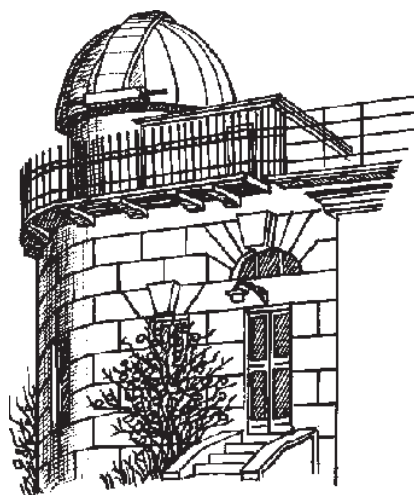


# **ODESSA ASTRONOMICAL PUBLICATIONS**

**Volume 29  
(2016)**



Astronomical Observatory  
of I. I. Mechnikov Odessa National University

# ODESSA ASTRONOMICAL PUBLICATIONS

Volume 29  
(2016)

*Editorial Board:*

S. M. Andrievsky – *Editor-in-Chief*  
V. V. Kovtyukh – *Executive Secretary*  
G. A. Garbuzov – *Associate Editor*

*Advisory Editors:*

I. L. Andronov, S. K. Aslanov, V. A. Avdyushev, A. V. Bagrov, A. A. Bazey, K. I. Churyumov,  
A. B. Fokin, V. G. Karetnikov, N. I. Koshkin, V. G. Lozitskiy, T. V. Mishenina, B. S. Novosyadlyj,  
V. E. Panchuk, Ya. V. Pavlenko, L. S. Pilyugin, V. Yu. Terebizh, V. V. Tsymbal, D. Turner,  
S. N. Udovichenko, O. M. Ulyanov, A. I. Zhuk

*Responsible for this Issue:* M. I. Ryabov, A. I. Zhuk

*Technical editing:* S. L. Strakhova

*Address:*

Astronomical Observatory, Odessa National University, E-mail: [astro@paco.odessa.ua](mailto:astro@paco.odessa.ua)  
T. G. Shevchenko Park, Odessa, 65014, UKRAINE <http://www.astro-observ.odessa.ua>  
Tel., Fax: + 38 048 722-84-42 <http://www.onu.edu.ua/en/science/>

*The electronic version of the journal is on the web page:* <http://www.onu.edu.ua/en/science/>

Одесские Астрономические Публикации  
Издается с 1946 года (издание возобновлено в 1993 г., №6)

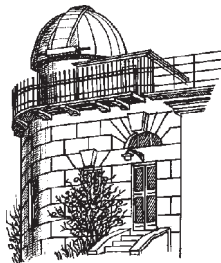
Свидетельство о государственной регистрации печатного средства массовой информации:  
серия КВ № 14722-3693Р от 30.10.2008 г.

Журнал включен в список ВАК Украины решением Президиума от 23.02.2011 №1-05/2.

Printed in UKRAINE  
ASTROPRINT PUBLISHING COMPANY

# ODESSA ASTRONOMICAL PUBLICATIONS

Volume 29  
(2016)



Odessa  
«AstroPrint»



## CONTENTS

**Cosmology, gravitation, astroparticle physics, high energy physics**

GRAVITY-ANTIGRAVITY INTERPLAY ON Mpc SCALE Chernin A.D. ....	6
PROBING AND IDENTIFYING NEW PHYSICS SCENARIOS AT INTERNATIONAL LINEAR COLLIDER Pankov A.A., Tsytrinov A.V. ....	9
HOT DENSE MAGNETIZED SPINOR MATTER IN PARTICLE AND ASTROPARTICLE PHYSICS: THE ROLE OF BOUNDARIES Sitenko Yu.A. ....	12
GRAVITY-DRIVEN ACCELERATION AND KINETIC INFLATION IN NONCOMMUTATIVE BRANS-DICKE SETTING Rasouli S.M.M., Paulo Vargas Moniz ....	19
TOWARD THE QUANTIZATION OF BLACK HOLES Gladush V.D. ....	25
QUASI-ANALYTICAL METHOD FOR IMAGES CONSTRUCTION FROM GRAVITATIONAL LENSES Kotvytskiy A.T., Bronza S.D. ....	28
X-RAY EMISSION AND ORIENTATION OF SELECTED PF GALAXY CLUSTERS Tugay A.V., Dylida S.S., Panko E.A. ....	34
NO THE HOLMBERG EFFECT FOR GALAXY PAIRS SELECTED FROM THE SDSS AT $Z \leq 0.06$ Dobrycheva D.V., Vavilova I.B. ....	37
THE SOLUTION OF THE COSMOLOGICAL CONSTANT PROBLEM AND THE FORMATION OF THE SPACE-TIME CONTINUUM Bukalov A.V. ....	42

**Astrophysics**

SOFT GAMMA REPEATERS AND ANOMALOUS X-RAY PULSARS BEYOND MAGNETARS Bisnovaty-Kogan G.S. ....	46
ISENTROPIC "SHOCK WAVES" IN NUMERICAL ASTROPHYSICS Moiseenko S.G., Bisnovaty-Kogan G.S. ....	54
UNIVERSALITY IN MAGNETOEMISSION OF COMPACT ASTROPHYSICAL OBJECTS Kondratyev V.N., Korovina Yu.V., Blanchard Ph. ....	58
NUCLEOSYNTHESIS AT MAGNETOROTATIONAL SUPERNOVA EXPLOSION AND GALACTIC CHEMICAL EVOLUTION Kondratyev V.N., Mishenina T.V. ....	60
THE CHEMICAL COMPOSITION OF THE ACTIVE STARS Glazunova L.V. ....	63
STRONTIUM ABUNDANCES IN COOL DWARF STARS OF GALACTIC THIN AND THICK DISKS Gorbaneva T.I., Mishenina T.V. ....	70
SEARCH FOR VARIABLE STARS AND THEIR STUDY Kokumbaeva R.I., Zakhzhay V.A., Khruslov A.V. ....	71
A TECHNIQUE FOR SIMULTANEOUS MEASUREMENT OF CIRCULAR AND LINEAR POLARIZATION WITH A SINGLE-CHANNEL POLARIMETER Kolesnikov S.V., Breus V.V., Kiselev N.N., Andronov I.L. ....	74
THE MEAN LIGHT CURVES OF THE MIRA-TYPE STARS IN THE H- AND K-BANDS Kudashkina L.S. ....	78
3D NUMERICAL HYDRODYNAMICAL SIMULATIONS OF A RADIATION-DRIVEN JET LAUNCH AND DISAPPEARING OVER LOW/HARD STATE Nazarenko V.V., Nazarenko S.V. ....	82
A SURVEY OF SEVERAL SPECTRAL LINES IN THE SPECTRA OF THE SUPERGIANT HD 14143 Maharramov Y.M. ....	87
THE CHANGING LOOK AGNS MONITORING PROJECT Oknyanskij V.L., Huseynov N.A., Lipunov V.M., Tatarnikov A.M., Shatsky N.I., Tsygankov S.S., Metlov V.G., Salmanov I.R., Gaskell C.M. ....	92
OPTICAL MONITORING OF NGC4151 DURING 110 YEARS Oknyanskij V.L., Metlova N.V., Huseynov N.A., Di-Fu Guo, Lyuty V.M. ....	95

PHOTOMETRIC OBSERVATIONS OF A NEW ECLIPSING BINARY NSVS 8213217 Udovichenko S.N. ....	98
EFFECTIVE TEMPERATURE AND RADIAL VELOCITY OF THE SMALL-AMPLITUDE CEPHEID POLARIS ( $\alpha$ UMi) IN 2015 Usenko I.A., Kovtyukh V.V., Miroshnichenko A.S., Danford S. ....	100
CHROMOSPHERIC ACTIVITY OF THE FLARE STAR YZ CMI IN QUIESCENCE ACCORDING TO THE FAST SPECTRAL MONITORING DATA Verlyuk I.A. ....	103
TWO-MATRIX PHOTOMETER CONTROL SYSTEM Zhantayev Zh.Sh., Kuratov K.S., Seytimbetov A.M., Mailybayev A.T., Alimgazinova N.Sh., Manapbayeva A.B., Kuratova A.K., Iztleuov N.T. ....	105
<b>Astroinformatics</b>	
ASTROINFORMATICS AS A NEW RESEARCH FIELD: UKRVO AND VIRGO RESOURCES Vavilova I.B. ....	109
THE INVESTIGATION OF THE FON3 CATALOGUE DATA USING WIELEN METHOD Akhmetov V.S. ....	116
BALDONE SCHMIDT (LATVIA) TELESCOPE ASTROPHOTOS ARCHIVE Eglite M., Eglitis I. ....	120
OBTAINING POSITIONS OF ASTEROIDS FROM DIGITIZED PROCESSING OF PHOTOGRAPHIC OBSERVATIONS IN BALDONE OBSERVATORY (CODE 069) Eglitis I., Eglite M., Shatokhina S.V., Andruk V.M. ....	123
UV-PHOTOMETRY WITH THE 1.2 M SCHMIDT TELESCOPE IN BALDONE Eglitis I., Eglite M., Pakuliak L.K., Andruk V.M. ....	126
STARS WITH HIGH PROPER MOTIONS IN THE MODERN CATALOGS OF THE CDS DATABASE Kryuchkovskiy V.F., Maigurova N.V. ....	129
FON: FROM START TO FINISH Pakuliak L.K., Andruk V.M., Golovnia V.V., Shatokhina S.V., Yizhakevych O.M., Ivanov G.A., Yatsenko A.I., Sergeeva T.P. ....	132
VIRTUAL OBSERVATORY AND COLITEC SOFTWARE: MODULES, FEATURES, METHODS Pohorelov A.V., Khlamov S.V., Savanevych V.E., Briukhovetskyi A.B., Vlasenko V.P. ....	136
ANALYSIS OF ASTEROID'S OBSERVATIONS IN OPEN PHOTOMETRIC DATABASES Pomazan A., Maigurova N. ....	141
UKRVO – FEATURES AND COMPARISON OF THE NEW CATALOGUE OF PHOTOGRAPHIC SURVEY OF THE NORTHERN SKY Protsyuk Yu., Relke E. ....	144
USING OF UKRVO DATA AND SOFTWARE FOR NEW REDUCTIONS OF PHOTOGRAPHIC OBSERVATIONS OF SELECTED MINOR PLANETS Protsyuk Yu., Maigurova N., Protsyuk S., Golovnia V. ....	147
SEARCH SMALL BODIES IMAGES IN COLLECTIONS DIGITIZED PHOTOGRAPHIC OBSERVATIONS OF PREVIOUS YEARS Shatokhina S., Kazantseva L., Kazantsev A., Andruk V., Golovnia V. ....	151
PHOTOGRAPHIC OBSERVATIONS OF MAJOR PLANETS AND THEIR MOONS DURING 1961-1990 AT THE MAO NAS OF UKRAINE Yizhakevych O.M., Andruk V.M., Pakuliak L.K. ....	155
THE EQUATORIAL COORDINATES AND B-MAGNITUDES OF THE STARS IN THE SOUTHERN HEMISPHERE ZONES BASED ON THE DIGITIZED ASTRONEGATIVES OF FON PROJECT AT THE ULUGH BEG ASTRONOMICAL INSTITUTE Yuldoshev Q.X., Muminov M.M., Ehgamberdiev Sh.A., Usmanov O.U., Relke H., Protsyuk Yu.I., Kovylianska O.E., Protsyuk S.V., Andruk V.N. ....	160
<b>Radioastronomy</b>	
THE PHYSICAL CONDITIONS OF THE CENTRAL PART OF ORION A HII REGION BY THE RADIO RECOMBINATION LINES AT 8 AND 13 MM Tsivilev A.P., Parfenov S.Yu., Krasnov V.V. ....	163
THE DAILY 110 MHZ RADIO WAVE SKY SURVEY: STATISTICAL ANALYSIS OF IMPULSE PHENOMENA FROM OBSERVATION IN 2012-2013 Samodurov V.A., Dumsky D.V., Isaev E.A., Rodin A.E., Kazancev A.N., Fedorova V.A., Belyatskij Yu.A. ...	167

ANGULAR STRUCTURE OF FRII RADIO SOURCES 3C169.1 AND 3C263 AT DECAMETER WAVELENGTHS Vashchishin R.V., Shepelev V.A., Lozinsky A.B., Lytvynenko O.A. ....	170
RELATIONS OF STRUCTURE COMPONENTS OF GIANT RADIO SOURCES Miroshnichenko A.P. ....	173
SPECIAL FIELDS OF THE GALAXY RADIO EMISSION Vasilenko N.M., Sidorchuk M.A. ....	177
PARAMETERS OF THE TRANSIENT SIGNALS DETECTED IN THE DECAMETER SURVEY OF THE NORTHERN SKY Kravtsov I.P., Zakharenko V.V., Vasylieva I.Y., Mykhailova S.S., Ulyanov O.M., Shevtsova A.I., Skoryk A.O. ....	179
CONNECTION BETWEEN THE SHOCK WAVE SPEED AND II TYPE RADIO BURSTS DRIFT VELOCITY Isaeva E.A., Kravetz R.O. ....	184
TOOLS AND METHODS OF LOW-FREQUENCY RADIO RECOMBINATION LINES INVESTIGATIONS Konovalenko A.A., Stepkin S.V., Mukha D.V., Vasilkovskiy E.V. ....	187
THE CURRENT STATE OF DATA TRANSMISSION CHANNELS FROM PUSHCHINO TO MOSCOW AND PERSPECTIVES Dumsky D.V., Isaev E.A., Samodurov V.A., Shatskaya M.V. ....	190
<b>Sun and Solar system</b>	
CYCLES AND ANTI-CYCLES OF SOLAR ACTIVITY Ryabov M.I. ....	192
THE DECADE-LONG INSTABILITIES IN EARTH'S ROTATION AS EVIDENCE OF LITHOSPHERIC DRIFT OVER THE ASTENOSPHERE Sidorenkov N.S. ....	196
«CHURYUMOV UNIFIED NETWORK»: NEW, IMPORTANT TASKS FOR ASTRONOMICAL OBSERVATORIES TO PROTECT SOCIETY IN THE ERA OF MODERN HYBRID WARS Churyumov K.I., Vidmachenko A.P., Steklov A.F., Dashkiev N.G., Romanyuk Ya.O., Stepakhno I.V. ....	200
INTERNATIONAL NETWORK OF PASSIVE CORRELATION RANGING FOR ORBIT DETERMINATION OF A GEOSTATIONARY SATELLITE Kaliuzhnyi M., Bushuev F., Shulga O., Sybiryakova Ye., Shakun L., Bezrukovs V., Moskalenko S., Kulishenko V., Malynovskiy Ye. ....	203
THE CHANGE INDICES OF SOLAR AND GEOMAGNETIC ACTIVITY AND THEIR INFLUENCE ON THE DINAMICS OF DRAG OF ARTIFICIAL SATELLITE Komendant V.H., Koshkin N.I., Ryabov M.I., Sukharev A.L. ....	207
PROBLEM OF MISTAKES IN DATABASES, PROCESSING AND INTERPRETATION OF OBSERVATIONS OF THE SUN. II. SOLAR FLARES Lozitska N.I. ....	211
MODERN CCD OBSERVATIONS OF SELECTED MINOR PLANETS FOR THE CONNECTION OF DYNAMIC AND KINEMATIC COORDINATE SYSTEMS Pomazan A., Maigurova N. ....	213
THE OBSERVATIONS OF ARTIFICIAL SATELLITES AND SPACE DEBRIS USING KT-50 TELESCOPE IN THE ODESSA UNIVERSITY Shakun L., Korobeynikova E., Koshkin N., Melikyants S., Strakhova S., Terpan S., Burlak N., Golubovskaya T., Dragomiretsky V., Ryabov A. ....	217
RESONANCES IN ASTEROID SYSTEMS Troianskyi V.V. ....	221
IS THERE 9-TH PLANET IN OUR SOLAR SYSTEM? Vidmachenko A.P. ....	224
SPECIFICATION OF LIMITS OF POSSIBLE EXISTENCE OF SATELLITES IN THE GRAVITATIONAL FIELD OF PLANETS Yasenev S.O., Radchenko K.O. ....	226
HIP 13962 – THE POSSIBLE FORMER MEMBER OF BINARY SYSTEM WITH SUPERNOVA Yushchenko V., Yushchenko A., Gopka V., Shavrina A., Kovtyukh V., Hong K.S., Mkrtychian D., A-Thano N. ....	229

## COSMOLOGY, GRAVITATION, ASTROPARTICLE PHYSICS, HIGH ENERGY PHYSICS

DOI: <http://dx.doi.org/10.18524/1810-4215.2016.29.84906>

# GRAVITY-ANTIGRAVITY INTERPLAY ON Mpc SCALE

A.D. Chernin

Sternberg Astronomical Institute, Moscow University,  
Universitetsky Pr. 13, Moscow, 119919, Russia, [chernin@sai.msu.ru](mailto:chernin@sai.msu.ru)

**ABSTRACT.** It is demonstrated that the major physical features of the local expansion flows of galaxies are due to antigravity domination in the dynamics of the systems.

**Keywords:** Cosmology: dark energy, local expansion flows.

### 1. Introduction

In 1998-99, the discovery of dark energy (Riess et al., 1998, Perlmutter et al. 1999) opened new wide perspectives in cosmology (see, for instance, Byrd et al. 2012, and references therein). With dark energy, a new "antigravity" force has entered the cosmic scene, and it has been soon realized that the gravity-antigravity interplay is the major dynamical factor that controls the global cosmological expansion at distances of 1 000 Mpc and more. The astronomical findings made near the cosmic horizon have provided us as well with new reliable grounds for better understanding of astronomical phenomena at relatively small, non-cosmological distances. In this way, it was found that the local expansion motions of galaxies at distances of the order of  $\sim 1$  Mpc are also ruled by gravity-antigravity interplay (Chernin 2001, 2008, 2013 and references therein). Local dynamical effects of dark energy are in the focus of our discussion here.

### 2. Local dark energy

Due to the cosmological discoveries (Riess et al., 1998, Perlmutter et al. 1999), we know now that dark matter and dark energy are the basic components of the present-day Universe. The fractions of dark energy and dark matter in the entire mass/energy balance of the observed Universe are about 70 and 26%, respectively. The usual (baryonic) matter constitutes about 4%. Dark matter and dark energy do not emit, absorb, or scatter light. They manifest themselves only by their gravity and antigravity, correspondingly. Antigravity was predicted theoretically by Einstein in 1917, when he introduced the cosmological constant  $\Lambda$  to the equations of General Relativity. This constant repre-

sents dark energy and antigravity produced by dark energy in physics and cosmology. In 1922-24, the possible existence of Einstein's antigravity was taken into account in Friedmann's cosmological model where  $\Lambda$  was treated as a theory empirical parameter which should be measured in astronomical observations.

The modern cosmological data show that antigravity is stronger than gravity in the observable Universe as a whole. Because of the antigravity domination the global expansion proceeds with acceleration: the relative velocities of receding galaxies increase with time. Antigravity dominates at present and during the last 7 Gyr of the cosmic evolution; in the unlimited future, antigravity domination will be even stronger than now.

Do dark energy and Einstein's antigravity exist not only at the global distances where it was initially discovered, but also at relatively small distances around the Milky Way Galaxy?

It comes from General Relativity that Einstein's antigravity is a universal (in the same sense as Newton's gravity) physical factor acting actually everywhere in space, on both global and local astronomical scales. The density of dark energy is the same everywhere in the Universe and it is given by Einstein's cosmological constant alone:  $\rho_\Lambda = \Lambda/(8\pi G)$ , where  $G$  is the Newtonian gravitational constant; the speed of light  $c = 1$  here; the dark energy density  $\rho_\Lambda$  is positive and its currently adopted value  $\rho_\Lambda \simeq 0.7 \times 10^{-29}$  g/cm<sup>3</sup>.

On these physical grounds and with the use of the recent most precise observational data on the local expansion flows and their environments (Karachentsev 2005, Karachentsev et al. 2003, 2006, 2007), we worked out a theory model which is a local counterpart of Friedmann's cosmological model. For our model, we adopt from General Relativity the macroscopic description (Gliner 1965) of dark energy as a vacuum-like continuous medium of perfectly uniform constant density with the equation of state

$$p_\Lambda = -\rho_\Lambda. \quad (1)$$

Here  $p_\Lambda$  is the dark energy pressure.

We take from General Relativity also an indication that the "effective gravitating density" is determined

by both density and pressure of the medium:

$$\rho_{eff} = \rho + 3p. \quad (2)$$

The effective density of dark energy,  $\rho_\Lambda + 3p_\Lambda = -2\rho_\Lambda < 0$ , is negative, and it is because of this sign minus that dark energy produces not attraction, but repulsion, or antigravity.

Finally, we borrow from General Relativity the Kottler exact solution for a spherically-symmetrical spacetime (known also as the Schwarzschild-de Sitter spacetime). The solution gives the metric outside a spherical matter mass  $M$  imbedded in the dark energy of the density  $\rho_\Lambda$ . We use the solution in the weak field approximation, when deviations from the Galilean metric are small; correspondingly, the velocities of the local motions are small compared to the speed of light and the spatial differences of the gravity-antigravity potential are small (in absolute value) compared to the speed of light squared. Then the Kottler solution is reduced to the Newtonian description in terms of the gravity-antigravity potential  $U$ :

$$Y^{1/2} \simeq 1 + U, \quad U(R) = -\frac{GM}{R} - \frac{4\pi G}{3}\rho_\Lambda R^2. \quad (3)$$

In this approximation, the force (per unit mass) comes from Eq.6:

$$F(R) = -\frac{dU}{dR} = -\frac{GM}{R^2} + \frac{8\pi G}{3}\rho_\Lambda R. \quad (4)$$

We see in the rhs here the sum of the Newtonian force of gravity produced by the mass  $M$  and Einstein's force of antigravity produced by dark energy (the forces are for unit mass, i.e. acceleration). It is also seen from Eq.4 that gravity dominates at small distances from the mass  $M$ , while antigravity is stronger than gravity at large distances. Gravity and antigravity balance at the distance

$$R = R_\Lambda = \left(\frac{M}{\frac{8\pi}{3}\rho_\Lambda}\right)^{1/3} \quad (5)$$

which is the radius of the "zero-gravity sphere" (Chernin 2001).

The zero-gravity radius  $R_\Lambda$  appears as the local spatial counterpart of the "zero-gravity moment" in the global expansion of the Universe which occurred about 7 Gyr ago.

### 3. Very Local Flow: a model

The nearest flow of galaxies is observed at the distances of 1-3 Mpc from the barycenter of the Local Group. This "Very Local Flow" (hereafter VLF) has been well studied in the recent observations (Karachentsev et al. 2003, 2006, 2007, and references therein). Basing on these data and the theory relations

of Sec. 2, we suggest a model of gravity-antigravity interplay which controls the dynamics of local flows of expansion (Chernin 2001, 2008, 2013). In application to the VLF, our model treats the Local Group as a spherical mass  $M = (3 \div 4) \times 10^{12} M_\odot$  with a radius  $\simeq 1$  Mpc. According to Eq.5, the zero-gravity radius of the group proves to be  $R_\Lambda = 1.1 - 1.3$  Mpc which is near its observed radial size. The model treats galaxies (dwarfs) of the expansion flow around the group as "light (test) particles" moving along radial trajectories in the force field produced by the matter mass  $M$  of the group and the dark energy uniform background in which both group and outflow are imbedded.

In the volume of the group,  $R < R_\Lambda$ , the gravity of the matter mass  $M$  is stronger than the antigravity produced by the dark energy background in the same volume. Because of this, the group is quasi-stationary and gravitationally bound. Outside the group, in the VLF area,  $R > R_\Lambda$ , the antigravity of dark energy dominates. Consequently, the VLF particles are unbound and moving with acceleration away from the group. The particle dynamics is ruled by the equation of motion which follows from Eq.4:

$$\ddot{R}(t) = -\frac{GM}{R^2} + \frac{8\pi G}{3}\rho_\Lambda R. \quad (6)$$

The sum in the rhs of Eq.10 is positive and growing with the distance at  $R > R_\Lambda$ , so that the acceleration of the particles is increasing with the distance.

The first integral of the equation of motion is the mechanical energy conservation law:

$$\frac{1}{2}\dot{R}^2 = \frac{GM}{R} + \frac{4\pi G}{3}\rho_\Lambda R^2 + E, \quad (7)$$

where  $\dot{R} = V$  is the particle radial velocity,  $E$  is a constant which is the total mechanical energy of the particle.

Eq.7 gives the radial phase trajectories of the accelerating flow in the velocity-distance space. As we may see, the model is completely compatible with the data by Karachentsev et al. (2006, 2006, 2007). It may also be seen from Eq.7 that the phase trajectories of the flow converge to the phase attractor of the system which is the straight line  $V = \dot{R} = H_\Lambda R$ . Here  $H_\Lambda = \left(\frac{8\pi}{3}G\rho_\Lambda\right)^{1/2}$  is the "asymptotic Hubble factor" which is a universal constant given by the dark energy density only:  $H_\Lambda = 61$  km/s/Mpc. The attractor indicates the evolutionary trend of the system: the flow gains its nearly linear kinematic structure with the growing distance.

Note that the asymptotic expansion rate  $H_\Lambda = \left(\frac{8\pi}{3}G\rho_\Lambda\right)^{1/2}$  is the same for both global cosmology and our local theory model.

Accelerating expansion flows of galaxies which are similar to the Very Local Flow are also found around several nearby groups and clusters of galaxies

(Karachentsev et al. 2007, Chernin 2013). Their spatial physical scales differ in an order of magnitude, from  $\sim 1$  to  $\sim 10$  Mpc. Nevertheless they all reveal the same nearly linear velocity-distance kinematic structure with time-rates about the Hubble's global factor. They constitute a new and rich class of extragalactic systems whose observational appearance, kinematic structure and evolution are completely due to the antigravity domination in their internal dynamics.

#### 4. Conclusion

The world of galaxies is a grandiose expansion flow studied first by Vesto Slipher, Ernst Öpik, George Lemaître and Edwin Hubble in 1910-20s. The most impressive discovery of that times is the linear velocity-distance relation,  $V = HR$ , known as Hubble's law of cosmic expansion, where  $V$  is the receding velocity of galaxies at the distance  $R$  and  $H$  is the "Hubble's factor" which is the expansion time-rate. Found at local distances of 1-30 Mpc, Hubble's law was widely interpreted as the major property of the whole Universe. Meanwhile cosmological implications based on Friedmann's uniform model are valid only for global distances of the order of 1 000 Mpc and larger where the spatial distribution of galaxies is statistically uniform. This important point was made by Sandage et al. (1972, 2006) and Zeldovich (1978, 1993) who seen Hubble's law at local distances "mysterious" and "surprising".

In this paper, the physics which is behind these systems is clarified. We show that the structure and evolution of the local flows are due to the gravity-antigravity interplay in their dynamics.

*Acknowledgements.* Fruitful discussions with G.S.Bisnovatyi-Kogan, N.V.Emelyanov and I.D.Karachentsev are highly appreciated.

#### References

- Byrd G.G., Chernin A.D., Teerikorpi P., Valtonen M.J.: 2012, *Paths to Dark Energy*. De Gruyter Pubs., Berlin/Boston.
- Chernin A.D.: 2001, *Physics-Uspekhi*, **44**, 1099.
- Chernin A.D.: 2008, *Physics-Uspekhi*, **51**, 253.
- Chernin A.D.: 2013, *Physics-Uspekhi*, **56**, 741.
- Gliner E.B.: 1965, *JETP*, **49**, 542.
- Karachentsev I.D.: 2005, *Astron. J.*, **129**, 178.
- Karachentsev I.D., Chernin A.D., Teerikorpi P.: 2003, *Astrophysics*, **46**, 491.
- Karachentsev I.D., Tully R.B., Dolphin A., et al.: 2007, *Astron. J.*, **133**, 504
- Karachentsev I.D., Dolphin A., Tully R.B., et al.: 2006, *Astron. J.*, **131**, 1361.
- Perlmutter S., Aldering G., Goldhaber G., et al.: 1999, *ApJ*, **517**, 565.
- Riess A.G., Filippenko A.V., Challis P., et al.: 1998, *AJ*, **116**, 1009.
- Sandage A., et al.: 1972, *Astrophys. J.*, **172**, 253.
- Sandage A. et al.: 2006, *Astrophys. J.*, bf 653, 843.
- Zeldovich Ya.B.: 1978, in "The Large Scale Structure of the Universe", eds. M. Longair and J. Einasto, *IAU*, p.409
- Zeldovich Ya.B.:1993, *Selected Works*, **vol.2**, *Particles, Nuclei, and the Universe*, Princeton Univ. Press, p. 123

DOI: <http://dx.doi.org/10.18524/1810-4215.2016.29.84931>

# PROBING AND IDENTIFYING NEW PHYSICS SCENARIOS AT INTERNATIONAL LINEAR COLLIDER

A.A. Pankov, A.V. Tsytrinov

Abdus Salam ICTP Affiliated Centre and Technical University of Gomel  
Gomel, 246746, Belarus, [pankov@ictp.it](mailto:pankov@ictp.it)

**ABSTRACT.** Many new physics scenarios are described by contact-like effective interactions that can manifest themselves in  $e^+e^-$  collisions through deviations of the observables from the Standard Model predictions. If such a deviation were observed, it would be important to identify the actual source among the possible non-standard interactions as many different new physics scenarios may lead to very similar experimental signatures. Here we study the possibility of uniquely identifying the indirect effects of  $s$ -channel sneutrino exchange with double polarization asymmetry, as predicted by supersymmetric theories with  $R$ -parity violation, against other new physics scenarios in process  $e^+e^- \rightarrow \mu^+\mu^-$  at the International Linear Collider.

**Keywords:** Elementary particles, Standard Model, physics beyond the Standard Model.

## 1. Introduction

Numerous new physics (NP) scenarios, candidates as solutions of Standard Model (SM) conceptual problems, are characterized by novel interactions mediated by exchanges of very heavy states with mass scales significantly greater than the electroweak scale. In many cases, theoretical considerations as well as current experimental constraints indicate that the new objects may be too heavy to be directly produced even at the highest energies of the CERN Large Hadron Collider (LHC) and at foreseen future colliders, such as the  $e^+e^-$  International Linear Collider (ILC). In this situation the new, non-standard, interactions would only be revealed by indirect, virtual, effects manifesting themselves as deviations from the predictions of the SM. In the case of indirect discovery the effects may be subtle since many different NP scenarios may lead to very similar experimental signatures and they may easily be confused in certain regions of the parameter space for each class of models.

There are many very different NP scenarios that predict new particle exchanges which can lead to contact interactions (CI) which may show up below direct production thresholds. These are compositeness (Eichten, 1983), a  $Z'$  boson from models with

an extended gauge sector, scalar or vector leptoquarks (Buchmuller, 1987),  $R$ -parity violating sneutrino ( $\tilde{\nu}$ ) exchange (Kalinowski, 1997), bi-lepton boson exchanges (Cuypers, 1998), anomalous gauge boson couplings (AGC) (Gounaris, 1997), virtual Kaluza-Klein (KK) graviton exchange in the context of gravity propagating in large extra dimensions, exchange of KK gauge boson towers or string excitations (Arkani-Hamed, 1998), *etc.* Of course, this list is not exhaustive, because other kinds of contact interactions may be at play.

If  $R$ -parity is violated it is possible that the exchange of sparticles can contribute significantly to SM processes and may even produce peaks or bumps in cross sections if they are kinematically accessible. Below threshold, these new spin-0 exchanges may make their manifestation known via indirect effects on observables (cross sections and asymmetries). Here we will address the question of whether the effects of the exchange of scalar (spin-0) sparticles can be differentiated at the ILC with a center of mass energy  $\sqrt{s} = 0.5 - 1$  TeV and time-integrated luminosity of  $\mathcal{L}_{\text{int}} = 0.5 - 1$  ab $^{-1}$  in process

$$e^+ + e^- \rightarrow \mu^+ + \mu^- \quad (\tau^- + \tau^+), \quad (1)$$

from those associated with the wide class of other contact interactions mentioned above. For details of the analysis and extended references, see (Tsytrinov, 2012; Moortgat-Pick, 2013).

## 2. Observables and NP parametrization in $\mu^+\mu^-$ production

For a sneutrino in an  $R$ -parity-violating theory, we take the basic couplings to leptons and quarks to be given by

$$\lambda_{ijk} L_i L_j \bar{E}_k + \lambda'_{ijk} L_i Q_j \bar{D}_k. \quad (2)$$

Here,  $L$  ( $Q$ ) are the left-handed lepton (quark) doublet superfields, and  $\bar{E}$  ( $\bar{D}$ ) are the corresponding left-handed singlet fields. If just the  $R$ -parity violating  $\lambda L L \bar{E}$  terms of the superpotential are present it is clear that observables associated with leptonic process (1) will be affected by the exchange of  $\tilde{\nu}$ 's in the  $t$ - or  $s$ -channels. For instance, in the case only one nonzero

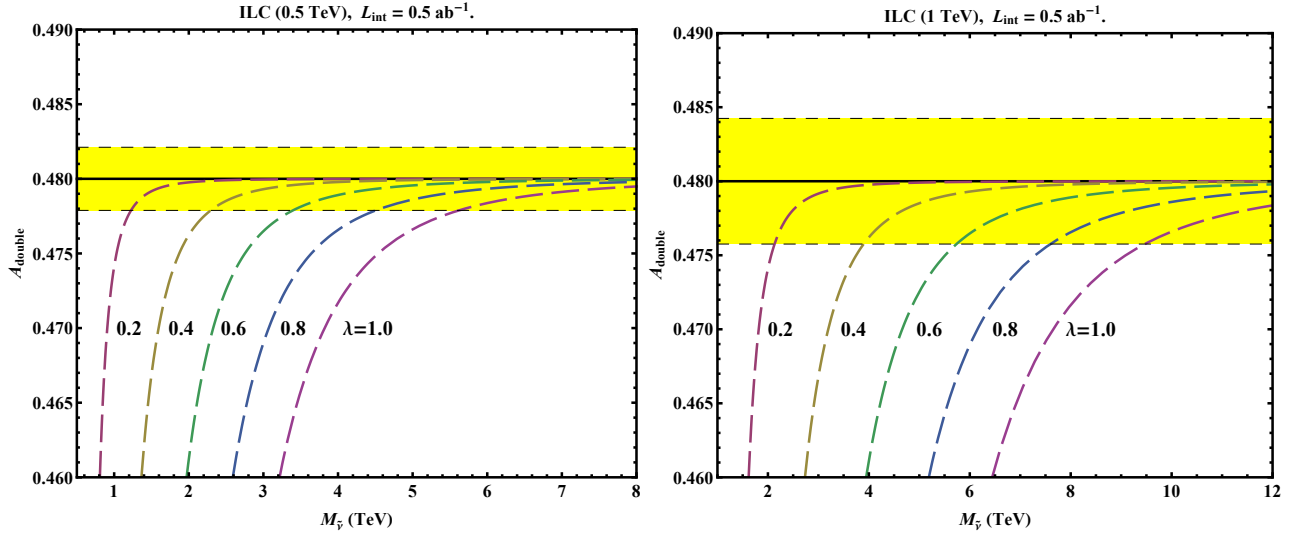


Figure 1:  $A_{\text{double}}^{\tilde{\nu}}$  asymmetry as a function of sneutrino mass  $M_{\tilde{\nu}}$  for different choices of  $\lambda$  (dashed lines) at the ILC with  $\sqrt{s} = 0.5$  TeV (left) and  $\sqrt{s} = 1.0$  TeV (right),  $\mathcal{L}_{\text{int}} = 0.5 \text{ ab}^{-1}$ . The horizontal solid line corresponds to  $A_{\text{double}}^{\text{SM}} = A_{\text{double}}^{\text{CI}} = 0.48$ . The expected SM uncertainty shown as yellow bands.

Yukawa coupling is present,  $\tilde{\nu}$ 's may contribute to, e.g.  $e^+e^- \rightarrow \mu^+\mu^-$  via  $t$ -channel exchange. In particular, if  $\lambda_{121}$ ,  $\lambda_{122}$ ,  $\lambda_{132}$ , or  $\lambda_{231}$  are nonzero, the  $\mu^+\mu^-$  pair production proceeds via additional  $t$ -channel sneutrino exchange mechanism. However, if only the product of Yukawa, e.g.  $\lambda_{131}\lambda_{232}$ , is nonzero the  $s$ -channel  $\tilde{\nu}_\tau$  exchange would contribute to the  $\mu^+\mu^-$  pair final state. Below we denote by  $\lambda$  the relevant Yukawa coupling from the superpotential (2) omitting the subscripts.

With  $P^-$  and  $P^+$  denoting the longitudinal polarizations of the electrons and positrons, respectively, and  $\theta$  the angle between the incoming electron and the outgoing muon in the c.m. frame, the differential cross section of process (1) in the presence of contact interactions can be expressed as ( $z \equiv \cos \theta$ ):

$$\frac{d\sigma^{\text{CI}}}{dz} = \frac{3}{8} [(1+z)^2 \sigma_+^{\text{CI}} + (1-z)^2 \sigma_-^{\text{CI}}]. \quad (3)$$

In terms of the helicity cross sections  $\sigma_{\alpha\beta}^{\text{CI}}$  (with  $\alpha, \beta = \text{L, R}$ ), directly related to the individual CI couplings  $\Delta_{\alpha\beta}$  (see Eq. (7)):

$$\begin{aligned} \sigma_+^{\text{CI}} &= \frac{1}{4} [(1-P^-)(1+P^+) \sigma_{\text{LL}}^{\text{CI}} + \\ &+ (1+P^-)(1-P^+) \sigma_{\text{RR}}^{\text{CI}}], \end{aligned} \quad (4)$$

$$\begin{aligned} \sigma_-^{\text{CI}} &= \frac{1}{4} [(1-P^-)(1+P^+) \sigma_{\text{LR}}^{\text{CI}} + \\ &+ (1+P^-)(1-P^+) \sigma_{\text{RL}}^{\text{CI}}], \end{aligned} \quad (5)$$

where the first (second) subscript refers to the chirality of the electron (muon) current. Moreover, in Eqs. (4) and (5):

$$\sigma_{\alpha\beta}^{\text{CI}} = \sigma_{\text{pt}} |\mathcal{M}_{\alpha\beta}^{\text{CI}}|^2, \quad (6)$$

where  $\sigma_{\text{pt}} \equiv \sigma(e^+e^- \rightarrow \gamma^* \rightarrow \mu^+\mu^-) = (4\pi\alpha_{\text{em}}^2)/(3s)$ . The helicity amplitudes  $\mathcal{M}_{\alpha\beta}^{\text{CI}}$  can be written as

$$\mathcal{M}_{\alpha\beta}^{\text{CI}} = \mathcal{M}_{\alpha\beta}^{\text{SM}} + \Delta_{\alpha\beta} = Q_e Q_\mu + g_\alpha^e g_\beta^\mu \chi_Z + \Delta_{\alpha\beta}, \quad (7)$$

where  $\chi_Z = s/(s - M_Z^2 + iM_Z\Gamma_Z)$  represents the  $Z$  propagator,  $g_L^l = (I_{3L}^l - Q_l s_W^2)/s_W c_W$  and  $g_R^l = -Q_l s_W^2/s_W c_W$  are the SM left- and right-handed lepton ( $l = e, \mu$ ) couplings of the  $Z$  with  $s_W^2 = 1 - c_W^2 \equiv \sin^2 \theta_W$  and  $Q_l$  the leptonic electric charge. The  $\Delta_{\alpha\beta}$  functions represent the contact interaction contributions coming from TeV-scale physics.

The structure of the differential cross section (3) is particularly interesting in that it is equally valid for a wide variety of NP models such as composite fermions, extra gauge boson  $Z'$ , AGC, TeV-scale extra dimensions and ADD model. Parametrization of the  $\Delta_{\alpha\beta}$  functions in different NP models ( $\alpha, \beta = \text{L, R}$ ) can be found in (Moortgat-Pick, 2013).

The doubly polarized total cross section can be obtained from Eq. (3) after integration over  $z$  within the interval  $-1 \leq z \leq 1$ . In the limit of  $s, t$  small compared to the CI mass scales, the result takes the form

$$\begin{aligned} \sigma^{\text{CI}} &= \sigma_+^{\text{CI}} + \sigma_-^{\text{CI}} = \\ &= \frac{1}{4} ((1-P^-)(1+P^+) (\sigma_{\text{LL}}^{\text{CI}} + \sigma_{\text{LR}}^{\text{CI}}) + \\ &+ (1+P^-)(1-P^+) (\sigma_{\text{RR}}^{\text{CI}} + \sigma_{\text{RL}}^{\text{CI}})). \end{aligned} \quad (8)$$

It is clear that the formula in the SM has the same form where one should replace the superscript CI  $\rightarrow$  SM in Eq. (8).

Since the  $\tilde{\nu}$  exchanged in the  $s$ -channel does not interfere with the  $s$ -channel SM  $\gamma$  and  $Z$  exchanges, the differential cross section with both electron and

positron beams polarized can be written as

$$\begin{aligned} \frac{d\sigma^{\tilde{\nu}}}{dz} &= \frac{3}{8} [(1+z)^2 \sigma_+^{\text{SM}} + (1-z)^2 \sigma_-^{\text{SM}} + \\ &+ 2 \frac{1+P^-P^+}{2} (\sigma_{\text{RL}}^{\tilde{\nu}} + \sigma_{\text{LR}}^{\tilde{\nu}})]. \end{aligned} \quad (9)$$

Here,  $\sigma_{\text{RL}}^{\tilde{\nu}} (= \sigma_{\text{LR}}^{\tilde{\nu}}) = \sigma_{\text{pt}} |\mathcal{M}_{\text{RL}}^{\tilde{\nu}}|^2$ ,  $\mathcal{M}_{\text{RL}}^{\tilde{\nu}} = \mathcal{M}_{\text{LR}}^{\tilde{\nu}} = \frac{1}{2} C_{\tilde{\nu}}^s \chi_{\tilde{\nu}}^s$ , and  $C_{\tilde{\nu}}^s$  and  $\chi_{\tilde{\nu}}^s$  denote the product of the  $R$ -parity violating couplings and the propagator of the exchanged sneutrino. For the  $s$ -channel  $\tilde{\nu}_\tau$  sneutrino exchange they read

$$C_{\tilde{\nu}}^s \chi_{\tilde{\nu}}^s = \frac{\lambda_{131} \lambda_{232}}{4\pi \alpha_{\text{em}}} \frac{s}{s - M_{\tilde{\nu}_\tau}^2 + i M_{\tilde{\nu}_\tau} \Gamma_{\tilde{\nu}_\tau}}. \quad (10)$$

Below we will use the abbreviation  $\lambda^2 = \lambda_{131} \lambda_{232}$ .

As seen from Eq. (9) the polarized differential cross section picks up a  $z$ -independent term in addition to the SM part. The corresponding total cross section can be written as

$$\begin{aligned} \sigma^{\tilde{\nu}} &= \frac{1}{4} (1 - P^-)(1 + P^+) (\sigma_{\text{LL}}^{\text{SM}} + \sigma_{\text{RR}}^{\text{SM}}) + \\ &+ \frac{1}{4} (1 + P^-)(1 - P^+) \times (\sigma_{\text{RR}}^{\text{SM}} + \sigma_{\text{LL}}^{\text{SM}}) + \\ &+ \frac{3}{2} \frac{1 + P^-P^+}{2} (\sigma_{\text{RL}}^{\tilde{\nu}} + \sigma_{\text{LR}}^{\tilde{\nu}}). \end{aligned} \quad (11)$$

It is possible to uniquely identify the effect of the  $s$  channel sneutrino exchange exploiting the double beam polarization asymmetry defined as (Osland, 2003)

$$A_{\text{double}} = \frac{(+, -) + (-, +) - (+, +) - (-, -)}{(+, -) + (-, +) + (+, +) + (-, -)}, \quad (12)$$

where  $(+, -) = \sigma(P_1, -P_2)$ , ..., and  $P_{1,2} = |P^{\cdot,+}|$ . From (8) and (12) one finds

$$A_{\text{double}}^{\text{SM}} = A_{\text{double}}^{\text{CI}} = P_1 P_2 = 0.48, \quad (13)$$

where the numerical value corresponds to electron and positron degrees of polarization:  $P_1 = 0.8$ ,  $P_2 = 0.6$ . This is because these contact interactions contribute to the same amplitudes as shown in (7). Eq. (13) demonstrates that  $A_{\text{double}}^{\text{SM}}$  and  $A_{\text{double}}^{\text{CI}}$  are indistinguishable for any values of the contact interaction parameters,  $\Delta_{\alpha\beta}$ , i.e.  $\Delta A_{\text{double}} = A_{\text{double}}^{\text{CI}} - A_{\text{double}}^{\text{SM}} = 0$ .

On the contrary, the  $\tilde{\nu}$  exchange in the  $s$ -channel will force this observable to a smaller value,  $\Delta A_{\text{double}} = A_{\text{double}}^{\tilde{\nu}} - A_{\text{double}}^{\text{SM}} \propto -P_1 P_2 |C_{\tilde{\nu}}^s \chi_{\tilde{\nu}}^s|^2 < 0$ . The value of  $A_{\text{double}}$  below  $P_1 P_2$  can provide a signature of scalar exchange in the  $s$ -channel. All those features in the  $A_{\text{double}}$  behavior are shown in Fig. 1.

In the numerical analysis, cross sections are evaluated including initial- and final-state radiation by means of the program ZFITTER, together with ZEFIT, with  $m_{\text{top}} = 175$  GeV and  $m_H = 125$  GeV.

As numerical inputs, we shall assume the identification efficiencies of  $\epsilon = 95\%$  for  $\mu^+ \mu^-$  final

states, integrated luminosity of  $\mathcal{L}_{\text{int}} = 0.5 \text{ ab}^{-1}$  with uncertainty  $\delta \mathcal{L}_{\text{int}} / \mathcal{L}_{\text{int}} = 0.5\%$ , and a fiducial experimental angular range  $|\cos \theta| \leq 0.99$ . Also, regarding electron and positron degrees of polarization, we shall consider the following values:  $P^- = \pm 0.8$ ;  $P^+ = \pm 0.6$ , with  $\delta P^- / P^- = \delta P^+ / P^+ = 0.5\%$ . Discovery and identification reaches on the sneutrino

Table 1: Discovery and identification reaches on sneutrino mass  $M_{\tilde{\nu}}$  (95% C.L.) in TeV as a function of  $\lambda$  for the process  $e^+ e^- \rightarrow \mu^+ \mu^-$  at the ILC.

$M_{\tilde{\nu}}$ (TeV)	$\lambda = 0.5$	$\lambda = 1.0$
Discovery (ILC 0.5 TeV)	3.0	5.9
ID (ILC 0.5 TeV)	2.4	4.7
Discovery (ILC 1 TeV)	5.1	10.0
ID (ILC 1 TeV)	4.1	8.0
Current limits	0.9	2.0

mass  $M_{\tilde{\nu}}$  (95% C.L.) listed in Table 1 are obtained from conventional  $\chi^2$  analysis. For comparison, current limits from low-energy data are also shown. From Table 1 one can see that identification of sneutrino exchange effects in the  $s$ -channel with  $A_{\text{double}}$  is feasible in the region of parameter and mass space far beyond the current limits.

### 3. Concluding remarks

In this note we have studied how uniquely identify the indirect (propagator) effects of spin-0 sneutrino predicted by supersymmetric theories with  $R$ -parity violation, against other new physics scenarios in high energy  $e^+ e^-$  annihilation into lepton-pairs at the ILC in process (1). To evaluate the identification reach on the sneutrino exchange signature, we develop a technique based on a double polarization asymmetry formed by polarizing both beams in the initial state, that is particularly suitable to directly test for such  $s$ -channel sneutrino exchange effects in the data analysis.

*Acknowledgements.* This research has been partially supported by the Abdus Salam ICTP (TRIL Programme), the Collaborative Research Center SFB676/1-2006 of the DFG at the Department of Physics of the University of Hamburg and the Belarusian Republican Foundation for Fundamental Research.

### References

- Arkani-Hamed N. et al.: 1998, *Phys. Lett. B*, **429**, 263.
- Buchmuller W.B. et al.: 1987, *Phys. Lett. B*, **191**, 442.
- Cuyper F. et al.: 1998, *Eur. Phys. J. C*, **2**, 503.
- Eichten E. et al.: 1983, *Phys. Rev. Lett.*, **50**, 811.
- Gounaris G.J. et al.: 1997, *Phys. Rev. D*, **56**, 3970.
- Kalinowski J. et al.: 1997, *Phys. Lett. B*, **406**, 314.
- Moortgat-Pick G. et al.: 2013, *Phys. Rev. D*, **87**, 095017.
- Osland P. et al.: 2003, *Phys. Rev. D*, **68**, 015007.
- Tsytrinov A.V. et al.: 2012, *Phys. Lett. B*, **718**, 94.

DOI: <http://dx.doi.org/10.18524/1810-4215.2016.29.84938>

# HOT DENSE MAGNETIZED SPINOR MATTER IN PARTICLE AND ASTROPARTICLE PHYSICS: THE ROLE OF BOUNDARIES

Yu.A. Sitenko

Bogolyubov Institute for Theoretical Physics, National Academy of Sciences of Ukraine,  
14-b Metrologichna Street, 03680 Kyiv, Ukraine

**ABSTRACT.** We study the influence of boundaries on chiral effects in hot dense relativistic spinor matter in a strong magnetic field which is orthogonal to the boundaries. The most general set of boundary conditions ensuring the confinement of matter within the boundaries is employed. We find that the chiral magnetic effect disappears, whereas the chiral separation effect stays on, becoming dependent on temperature and on a choice of boundary conditions. As temperature increases from zero to large values, a stepped-shape behaviour of the chiral separation effect as a function of chemical potential is changed to a smooth one. A choice of the boundary condition can facilitate either amplification or diminution of the chiral separation effect; in particular, the effect can persist even at zero chemical potential, if temperature is finite. This points at a significant role of boundaries for physical systems with hot dense magnetized spinor matter, i.e. compact astrophysical objects (neutron stars and magnetars), relativistic heavy-ion collisions, novel materials known as the Dirac and Weyl semimetals.

**Keywords:** hot dense matter, strong magnetic field, chiral effects.

## 1. Introduction

Properties of hot dense spinor matter in a strong magnetic field are intensively studied during the last decade. An interest to this subject is driven by diverse areas of contemporary physics, ranging from particle and astroparticle physics to cosmology and even condensed-matter physics. Relativistic heavy-ion collisions (Kharzeev D.E.: 2014), compact astrophysical objects (neutron stars and magnetars) (Ferrario L., Melatos A., and Zrake J.: 2015), the early universe (Tashiro H., Vachaspati T., and Vilenkin A.: 2012), novel materials known as the Dirac and Weyl semimetals (Vafeek O. and Vishwanath A.: 2014) are the main physical systems where such studies are relevant. In the case of temperature, chemical potential, and the inverse magnetic length exceeding considerably the mass of a relativistic quantized spinor matter field, it has

been shown in theory (Metlitski M.A. and Zhitnitsky A.R.: 2005; Fukushima K., Kharzeev D.E., and Warringa H.J.: 2008) that persistent and nondissipative currents emerge in thermal equilibrium, resulting in a variety of chiral effects in hot dense magnetized matter; see review in Miransky V.A. and Shovkovy I.A.: 2015, and references therein.

So far chiral effects were mostly considered in unbounded (infinite) matter, which may be relevant for cosmological applications, perhaps. For all other applications (to particle, astroparticle, and condensed matter physics), an account has to be taken of the finiteness of physical systems, and the role of boundaries in chiral effects in bounded matter has to be clearly exposed. The concept of quantized matter fields which are confined to bounded spatial regions is quite familiar in the context of condensed matter physics: collective excitations (e.g., spin waves and phonons) exist only inside material samples and do not spread outside. Nevertheless, a quest for boundary conditions ensuring the confinement of quantized matter was initiated in particle physics, in the context of a model description of hadrons as bags containing quarks (Bogolioubov P.N.: 1968; Chodos A., Jaffe R.L., Johnson K., Thorn C. B., and Weisskopf V.: 1974). Motivations for a concrete form of the boundary condition may differ in detail, but the key point is that the boundary condition has to forbid any flow of quark matter across the boundary, see Johnson K.: 1975. However, from this point of view, the bag boundary conditions proposed in Bogolioubov P.N.: 1968, and in Chodos A., Jaffe R.L., Johnson K., Thorn C. B., and Weisskopf V.: 1974 are not the most general ones. It has been rather recently realized that the most general boundary condition ensuring the confinement of relativistic quantized spinor matter within a simply connected boundary involves four arbitrary parameters (Akhmerov A.R. and Beenakker C.W.J.: 2008; Al-Hashimi M.H. and Wiese U.-J.: 2012), and the explicit form of such a condition has been given (Sitenko Yu.A.: 2015; Sitenko Yu.A. and Yushchenko S.A.: 2015; Sitenko Yu.A.: 2016a). To study an impact of the background magnetic field on confined matter, one has to choose the magnetic field configuration with respect to the boundary sur-

face. The primary interest is to understand the effect of a boundary which is transverse to the magnetic field strength lines. Then the simplest geometry is that of a slab in the uniform magnetic field directed perpendicular. It should be noted that such a geometry can be realized in condensed matter physics by putting slices of Dirac or Weyl semimetals in an external transverse magnetic field. Note also that the slab geometry is conventional in a setup for the Casimir effect (Casimir H.B.G.: 1948); see review in Bordag M., G. L. Klimchitskaya G. L., Mohideen U., and Mostepanenko V. M.: 2009.

As a first step toward the full theory of chiral effects in bounded matter, the chiral effects in dense magnetized ultrarelativistic spinor matter at zero temperature in a slab were considered in publication Gorbar E.V., Miransky V.A., Shovkovy I.A., and Sukhachov P.O.: 2015, with the use of the bag boundary condition of Bogolioubov P.N.: 1968. Our aim is to extend the consideration to the case of nonzero temperature and the most general boundary condition.

## 2. Thermal equilibrium for chiral spinor matter

We start with the operator of the second-quantized spinor field in a static background,

$$\hat{\Psi}(\mathbf{r}, t) = \sum_{E_\lambda > 0} e^{-iE_\lambda t} \langle \mathbf{r} | \lambda \rangle \hat{a}_\lambda + \sum_{E_\lambda < 0} e^{-iE_\lambda t} \langle \mathbf{r} | \lambda \rangle \hat{b}_\lambda^\dagger, \quad (1)$$

where  $\hat{a}_\lambda^\dagger$  and  $\hat{a}_\lambda$  ( $\hat{b}_\lambda^\dagger$  and  $\hat{b}_\lambda$ ) are the spinor particle (antiparticle) creation and destruction operators satisfying anticommutation relations,

$$\left[ \hat{a}_\lambda, \hat{a}_{\lambda'}^\dagger \right]_+ = \left[ \hat{b}_\lambda, \hat{b}_{\lambda'}^\dagger \right]_+ = \langle \lambda | \lambda' \rangle, \quad (2)$$

and  $\langle \mathbf{r} | \lambda \rangle$  is the solution to the stationary Dirac equation,

$$H \langle \mathbf{r} | \lambda \rangle = E_\lambda \langle \mathbf{r} | \lambda \rangle, \quad (3)$$

$H$  is the Dirac Hamiltonian,  $\lambda$  is the set of parameters (quantum numbers) specifying a one-particle state,  $E_\lambda$  is the energy of the state; wave functions  $\langle \mathbf{r} | \lambda \rangle$  satisfy the requirement of orthonormality

$$\int_{\Omega} d^3r \langle \lambda | \mathbf{r} \rangle \langle \mathbf{r} | \lambda' \rangle = \langle \lambda | \lambda' \rangle \quad (4)$$

and completeness

$$\sum \langle \mathbf{r} | \lambda \rangle \langle \lambda | \mathbf{r}' \rangle = I \delta(\mathbf{r} - \mathbf{r}'); \quad (5)$$

summation is over the whole set of states, and  $\Omega$  is the quantization volume.

Conventionally, the operators of dynamical variables (physical observables) in second-quantized theory are

defined as bilinears of the fermion field operator (1). One can define the fermion number operator,

$$\begin{aligned} \hat{N} &= \frac{1}{2} \int_{\Omega} d^3r (\hat{\Psi}^\dagger \hat{\Psi} - \hat{\Psi}^T \hat{\Psi}^{\dagger T}) \\ &= \sum \left[ \hat{a}_\lambda^\dagger \hat{a}_\lambda - \hat{b}_\lambda^\dagger \hat{b}_\lambda - \frac{1}{2} \text{sgn}(E_\lambda) \right], \end{aligned} \quad (6)$$

and the energy (temporal component of the energy-momentum vector) operator,

$$\begin{aligned} \hat{P}^0 &= \frac{1}{2} \int_{\Omega} d^3r (\hat{\Psi}^\dagger H \hat{\Psi} - \hat{\Psi}^T H^T \hat{\Psi}^{\dagger T}) \\ &= \sum |E_\lambda| \left( \hat{a}_\lambda^\dagger \hat{a}_\lambda + \hat{b}_\lambda^\dagger \hat{b}_\lambda - \frac{1}{2} \right), \end{aligned} \quad (7)$$

where superscript  $T$  denotes a transposition and  $\text{sgn}(u)$  is the sign function [ $\text{sgn}(\pm u) = \pm 1$  at  $u > 0$ ]. The average of operator  $\hat{U}$  over the grand canonical ensemble is defined as (see, e.g., Das A.: 1997)

$$\langle \hat{U} \rangle_{T, \mu} = \frac{\text{Sp} \hat{U} \exp \left[ -(\hat{P}^0 - \mu \hat{N})/T \right]}{\text{Sp} \exp \left[ -(\hat{P}^0 - \mu \hat{N})/T \right]}, \quad (8)$$

where equilibrium temperature  $T$  is defined in the units of the Boltzmann constant, chemical potential is denoted by  $\mu$ , and  $\text{Sp}$  denotes the trace or the sum over the expectation values in the Fock state basis created by operators in (2). Let us take operator  $\hat{U}$  in the form

$$\hat{U} = \frac{1}{2} \left( \hat{\Psi}^\dagger \Upsilon \hat{\Psi} - \hat{\Psi}^T \Upsilon^T \hat{\Psi}^{\dagger T} \right), \quad (9)$$

where  $\Upsilon$  is an element of the Dirac-Clifford algebra. The explicit form of  $\hat{U}$ ,  $\hat{P}^0$  and  $\hat{N}$  in terms of the creation and destruction operators is inserted in (9); then one obtains

$$\langle \hat{U} \rangle_{T, \mu} = -\frac{1}{2} \text{tr} \langle \mathbf{r} | \Upsilon \tanh[(H - \mu I)(2T)^{-1}] | \mathbf{r} \rangle, \quad (10)$$

where  $\text{tr}$  denotes the trace over spinor indices. We are considering the quantized charged spinor field in the background of a static uniform magnetic field with strength  $\mathbf{B} = \boldsymbol{\partial} \times \mathbf{A}$ , where  $\mathbf{A}$  is the vector potential of the magnetic field. Assuming that the magnetic field is strong (supercritical) and ultrarelativistic spinor matter is at high temperature and high density,

$$|eB| \gg m^2, \quad T \gg m, \quad |\mu| \gg m, \quad (11)$$

we shall neglect the mass of the spinor matter field, putting  $m = 0$  in the following. Thus the Dirac Hamiltonian takes form

$$H = -i\gamma^0 \boldsymbol{\gamma} \cdot (\boldsymbol{\partial} - ie\mathbf{A}), \quad (12)$$

where  $e$  is the charge of the matter field and natural units  $\hbar = c = 1$  are used. Owing to the presence of chiral symmetry,

$$[H, \gamma^5]_- = 0, \quad (13)$$

where  $\gamma^5 = -i\gamma^0\gamma^1\gamma^2\gamma^3$  ( $\gamma^0, \gamma^1, \gamma^2,$  and  $\gamma^3$  are the generating elements of the Dirac-Clifford algebra, and  $\gamma^5$  is defined according to Okun L.B.: 1982), one can introduce also the following average:

$$\langle \hat{U} \rangle_{T, \mu_5} = \frac{\text{Sp} \hat{U} \exp \left[ -(\hat{P}^0 - \mu_5 \hat{N}^5)/T \right]}{\text{Sp} \exp \left[ -(\hat{P}^0 - \mu_5 \hat{N}^5)/T \right]}, \quad (14)$$

where

$$\hat{N}^5 = \frac{1}{2} \int_{\Omega} d^3r (\hat{\Psi}^\dagger \gamma^5 \hat{\Psi} - \hat{\Psi}^T \gamma^{5T} \hat{\Psi}^\dagger) \quad (15)$$

is the axial charge and  $\mu_5$  is the chiral chemical potential. For operator  $\hat{U}$  in the form of (9), one obtains

$$\langle \hat{U} \rangle_{T, \mu_5} = -\frac{1}{2} \text{tr} \langle \mathbf{r} | \Upsilon \tanh[(H - \mu_5 \gamma^5)(2T)^{-1}] | \mathbf{r} \rangle, \quad (16)$$

Thus, there are two types of thermal averaging, when chiral symmetry is present. For instance, one can define the vector current density as either an average over the standard grand canonical ensemble,

$$\mathbf{J} = \langle \hat{U} \rangle_{T, \mu} \Big|_{\Upsilon = \gamma^0 \gamma}, \quad (17)$$

or an average over the grand canonical ensemble with the chiral chemical potential,

$$\mathbf{J} = \langle \hat{U} \rangle_{T, \mu_5} \Big|_{\Upsilon = \gamma^0 \gamma}. \quad (18)$$

As we shall see, there is no contradiction between these two different definitions of the same physical quantity, since at least one of them results in zero.

### 3. Chiral effects in the unbounded space

A solution to the Dirac equation in the background of a static uniform magnetic field is well described in the literature, see, e.g., Akhiezer A.I. and Berestetskij V.B.: 1965. The one-particle energy spectrum in the case of the massless spinor field is

$$E_{nk} = \pm \omega_{nk}, \quad \omega_{nk} = \sqrt{2n|eB| + k^2}, \\ -\infty < k < \infty, \quad n = 0, 1, 2, \dots, \quad (19)$$

$k$  is the value of the wave number vector along the magnetic field, and  $n$  numerates the Landau levels. A straightforward calculation of (18) with the use of the

explicit form of spinor wave functions of definite chiralities immediately yields

$$\mathbf{J} \equiv \langle \hat{U} \rangle_{T, \mu_5} \Big|_{\Upsilon = \gamma^0 \gamma} = -\frac{e\mathbf{B}}{2\pi^2} \mu_5, \quad (20)$$

whereas (17) turns out to be zero. Similarly, one can calculate the axial charge density,

$$J^{05} \equiv \langle \hat{U} \rangle_{T, \mu, \mu_5} \Big|_{\Upsilon = \gamma^5} = \frac{|eB|}{2\pi^2} \left\{ \mu_5 \right. \\ \left. + \sum_{n=1}^{\infty} \int_0^{\infty} dk \frac{\sinh[(\mu_5 + \mu)/T]}{\cosh[(\mu_5 + \mu)/T] + \cosh(\sqrt{2n|eB| + k^2}/T)} \right. \\ \left. + \sum_{n=1}^{\infty} \int_0^{\infty} dk \frac{\sinh[(\mu_5 - \mu)/T]}{\cosh[(\mu_5 - \mu)/T] + \cosh(\sqrt{2n|eB| + k^2}/T)} \right\}, \quad (21)$$

and the axial current density,

$$\mathbf{J}^5 \equiv \langle \hat{U} \rangle_{T, \mu} \Big|_{\Upsilon = \gamma^0 \gamma \gamma^5} = -\frac{e\mathbf{B}}{2\pi^2} \mu. \quad (22)$$

Note that  $\mathbf{J}$  (20) and  $\mathbf{J}^5$  (22) are known as the chiral magnetic (Fukushima K., Kharzeev D.E., and Warringa H.J.: 2008) and chiral separation (Metlitski M.A. and Zhitnitsky A.R.: 2005) effects, respectively. Only the lowest Landau level ( $n = 0$ ) contributes to (20) and (22), and both effects are of topological origin, being related to a quantum anomaly, see Alekseev A.Y., Cheianov V.V., and Frohlich J.: 1998; Giovannini M. and Shaposhnikov M.: 1998; Son D.T. and Zhitnitsky A.R.: 2004; Kharzeev D.E., McLerran L.D., and Warringa H.J.: 2008; Basar G. and Dunne G.V.: 2013. Defining the left and right current densities,

$$\mathbf{J}_L = \frac{1}{2} (\mathbf{J} + \mathbf{J}^5) \quad (23)$$

and

$$\mathbf{J}_R = \frac{1}{2} (\mathbf{J} - \mathbf{J}^5), \quad (24)$$

as well as the left and right chemical potentials,

$$\mu_L = \mu + \mu_5 \quad (25)$$

and

$$\mu_R = \mu - \mu_5, \quad (26)$$

one can rewrite (20) and (22) as

$$\mathbf{J}_L = -\frac{e\mathbf{B}}{4\pi^2} \mu_L \quad (27)$$

and

$$\mathbf{J}_R = \frac{e\mathbf{B}}{4\pi^2} \mu_R. \quad (28)$$

Actually, the chiral magnetic effect was first discovered in the form of (27) in Vilenkin A.: 1980 (with a missing extra factor of 1/2).

#### 4. Chiral effects in a slab

To study an influence of a background magnetic field on the properties of hot dense spinor matter, one has to account for the fact that the realistic physical systems are bounded. Our interest is in an effect of the static magnetic field with strength lines which are orthogonal to a boundary. Then, as was already noted, the simplest geometry of a material sample is that of a straight slab in the uniform magnetic field directed perpendicular. The one-particle energy spectrum in this case is [cf. (19)]

$$E_{nl} = \pm\omega_{nl}, \quad \omega_{nl} = \sqrt{2n|eB| + k_l^2}, \quad n = 0, 1, 2, \dots, \quad (29)$$

where the values of the wave number vector along the magnetic field,  $k_l$ , are to be determined by the boundary condition.

The most general boundary condition ensuring the confinement of relativistic spinor matter within a simply connected boundary is (see Sitenko Yu.A. and Yushchenko S.A.: 2015; Sitenko Yu.A.: 2016a)

$$\left\{ I - \gamma^0 \left[ e^{i\varphi\gamma^5} \cos \theta + (\gamma^1 \cos \varsigma + \gamma^2 \sin \varsigma) \sin \theta \right] e^{i\tilde{\varphi}\gamma^0(\boldsymbol{\gamma}\cdot\mathbf{n})} \right\} \times \chi(\mathbf{r}) \Big|_{\mathbf{r} \in \partial\Omega} = 0, \quad (30)$$

where  $\mathbf{n}$  is the unit normal to surface  $\partial\Omega$  bounding spatial region  $\Omega$  and  $\chi(\mathbf{r})$  is the confined spinor matter wave function,  $\mathbf{r} \in \Omega$ ; matrices  $\gamma^1$  and  $\gamma^2$  in (30) are chosen to obey condition

$$[\gamma^1, \boldsymbol{\gamma} \cdot \mathbf{n}]_+ = [\gamma^2, \boldsymbol{\gamma} \cdot \mathbf{n}]_+ = [\gamma^1, \gamma^2]_+ = 0, \quad (31)$$

and the boundary parameters in (30) are chosen to vary as

$$\begin{aligned} -\frac{\pi}{2} < \varphi \leq \frac{\pi}{2}, \quad -\frac{\pi}{2} \leq \tilde{\varphi} < \frac{\pi}{2}, \\ 0 \leq \theta < \pi, \quad 0 \leq \varsigma < 2\pi. \end{aligned} \quad (32)$$

The MIT bag boundary condition (Johnson K.: 1975),

$$(I + i\boldsymbol{\gamma} \cdot \mathbf{n})\chi(\mathbf{r}) \Big|_{\mathbf{r} \in \partial\Omega} = 0, \quad (33)$$

is obtained from (30) at  $\varphi = \theta = 0$ ,  $\tilde{\varphi} = -\pi/2$ .

The boundary parameters in (30) can be interpreted as the self-adjoint extension parameters. The self-adjointness of the one-particle energy (Dirac Hamiltonian in the case of relativistic spinor matter) operator in first-quantized theory is required by general principles of comprehensibility and mathematical consistency; see, e.g., Bonneau G., Faraut J., and Valent G.: 2001. To put it simply, a multiple action is well defined for a self-adjoint operator only, allowing for the

construction of functions of the operator, such as resolvent, evolution, heat kernel and zeta-function operators, with further implications upon second quantization.

In the case of a disconnected boundary consisting of two simply connected components,  $\partial\Omega = \partial\Omega^{(+)} \cup \partial\Omega^{(-)}$ , there are in general eight boundary parameters:  $\varphi_+$ ,  $\tilde{\varphi}_+$ ,  $\theta_+$ , and  $\varsigma_+$  corresponding to  $\partial\Omega^{(+)}$ ; and  $\varphi_-$ ,  $\tilde{\varphi}_-$ ,  $\theta_-$ , and  $\varsigma_-$  corresponding to  $\partial\Omega^{(-)}$ . If spatial region  $\Omega$  has the form of a slab bounded by parallel planes,  $\partial\Omega^{(+)}$  and  $\partial\Omega^{(-)}$ , separated by distance  $a$ , then the boundary condition takes form

$$(I - K^{(\pm)})\chi(\mathbf{r}) \Big|_{z=\pm a/2} = 0, \quad (34)$$

where

$$\begin{aligned} K^{(\pm)} = & \gamma^0 \left[ e^{i\varphi_{\pm}\gamma^5} \cos \theta_{\pm} \right. \\ & \left. + (\gamma^1 \cos \varsigma_{\pm} + \gamma^2 \sin \varsigma_{\pm}) \sin \theta_{\pm} \right] e^{\pm i\tilde{\varphi}_{\pm}\gamma^0\gamma^z}, \end{aligned} \quad (35)$$

coordinates  $\mathbf{r} = (x, y, z)$  are chosen in such a way that  $x$  and  $y$  are tangential to the boundary, while  $z$  is normal to it, and the position of  $\partial\Omega^{(\pm)}$  is identified with  $z = \pm a/2$ . The confinement of matter inside the slab means that the vector bilinear,  $\chi^\dagger(\mathbf{r})\gamma^0\gamma^z\chi(\mathbf{r})$ , vanishes at the slab boundaries,

$$\chi^\dagger(\mathbf{r})\gamma^0\gamma^z\chi(\mathbf{r}) \Big|_{z=\pm a/2} = 0, \quad (36)$$

and this is ensured by condition (34). As to the axial bilinear,  $\chi^\dagger(\mathbf{r})\gamma^0\gamma^z\gamma^5\chi(\mathbf{r})$ , it vanishes at the slab boundaries,

$$\chi^\dagger(\mathbf{r})\gamma^0\gamma^z\gamma^5\chi(\mathbf{r}) \Big|_{z=\pm a/2} = 0, \quad (37)$$

in the case of  $\theta_+ = \theta_- = \pi/2$  only, that is due to relation

$$[K^{(\pm)} \Big|_{\theta_{\pm}=\pi/2}, \gamma^5]_- = 0. \quad (38)$$

However, note that, as a massless spinor particle is reflected from an impenetrable boundary, its helicity is flipped. Since the chirality equals plus or minus the helicity, chiral symmetry has to be necessarily broken by the confining boundary condition. Thus the case of  $\theta_+ = \theta_- = \pi/2$  is not acceptable on the physical grounds. Moreover, there is a symmetry with respect to rotations around a normal to the slab, and the cases differing by values of  $\varsigma_+$  and  $\varsigma_-$  are physically indistinguishable, since they are related by such a rotation. The only way to avoid the unphysical degeneracy of boundary conditions with different values of  $\varsigma_+$  and  $\varsigma_-$  is to fix  $\theta_+ = \theta_- = 0$ . Then  $\chi^\dagger(\mathbf{r})\gamma^0\gamma^z\gamma^5\chi(\mathbf{r})$  is non-vanishing at the slab boundaries, and the boundary condition takes form

$$\left\{ I - \gamma^0 \exp \left[ i \left( \varphi_{\pm}\gamma^5 \pm \tilde{\varphi}_{\pm}\gamma^0\gamma^z \right) \right] \right\} \chi(\mathbf{r}) \Big|_{z=\pm a/2} = 0. \quad (39)$$

Condition (39) determines the spectrum of the wave number vector in the  $z$  direction,  $k_l$ . The requirement that this spectrum be real and unambiguous yields constraint (see Sitenko Yu.A. and Yushchenko S.A.: 2015; Sitenko Yu.A.: 2016a)

$$\varphi_+ = \varphi_- = \varphi, \quad \tilde{\varphi}_+ = \tilde{\varphi}_- = \tilde{\varphi}; \quad (40)$$

then the  $k_l$  spectrum is determined implicitly from relation

$$k_l \sin \tilde{\varphi} \cos(k_l a) + (E_{\dots l} \cos \tilde{\varphi} - m \cos \varphi) \sin(k_l a) = 0, \quad (41)$$

where  $m$  is the mass of the spinor matter field and  $E_{\dots l}$  is the energy of the one-particle state. In the case of the massless spinor matter field,  $m = 0$ , and the background uniform magnetic field perpendicular to the slab,  $\mathbf{B} = (0, 0, B)$ ,  $E_{\dots l}$  takes the form of  $E_{nl}$  (29), and relation (41) is reduced to

$$k_l \sin \tilde{\varphi} \cos(k_l a) + E_{nl} \cos \tilde{\varphi} \sin(k_l a) = 0, \quad (42)$$

depending on one parameter only, although the boundary condition depends on two parameters,

$$\{I - \gamma^0 \exp [i(\varphi \gamma^5 \pm \tilde{\varphi} \gamma^0 \gamma^z)]\} \chi(\mathbf{r})|_{z=\pm a/2} = 0. \quad (43)$$

Using the explicit form of standing waves with the  $k_l$  spectrum determined by (42), one can compute the averages of type (8). As to the averages of type (14), they cannot be defined, because the confining boundary condition necessarily breaks chiral symmetry: standing waves inside a slab are formed from counterpropagating waves of opposite chiralities. It is straightforward to check the validity of relations

$$\mathbf{J} = J^{05} = 0. \quad (44)$$

Similarly, the components of the axial current density, which are orthogonal to the direction of the magnetic field, vanish as well,

$$J^{x5} = J^{y5} = 0. \quad (45)$$

As to the component of the axial current density, which is along the magnetic field, only the lowest Landau level ( $n = 0$ ) contributes to it, and hence the  $z$  component of the axial current density is

$$J^{z5} = -\frac{eB}{2\pi a} \left[ \sum_{k_l^{(+)} > 0} f_+(k_l^{(+)}) - \sum_{k_l^{(-)} > 0} f_-(k_l^{(-)}) - \frac{1}{2} \sum_{k_l^{(+)} > 0} 1 + \frac{1}{2} \sum_{k_l^{(-)} > 0} 1 \right], \quad (46)$$

where

$$f_{\pm}(k) = \left[ e^{(k \mp \mu)/T} + 1 \right]^{-1}, \quad (47)$$

and the two last sums which are independent of temperature and chemical potential correspond to the contribution of the vacuum fluctuations. The calculation of the sums over  $l$  yields (see Sitenko Yu.A.: 2016b, 2016c)

$$J^{z5} = -\frac{eB}{2\pi a} \times \left\{ \operatorname{sgn}(\mu) F \left( |\mu|a + \operatorname{sgn}(\mu) [\tilde{\varphi} - \operatorname{sgn}(\tilde{\varphi})\pi/2]; Ta \right) - \frac{1}{\pi} [\tilde{\varphi} - \operatorname{sgn}(\tilde{\varphi})\pi/2] \right\}, \quad (48)$$

where

$$F(s; t) = \frac{s}{\pi} - \frac{1}{\pi} \int_0^\infty dv \frac{\sin(2s) \sinh(\pi/t)}{[\cos(2s) + \cosh(2v)][\cosh(\pi/t) + \cos(v/t)]} + \frac{\sinh \{[\arctan(\tans)]/t\}}{\cosh[\pi/(2t)] + \cosh \{[\arctan(\tans)]/t\}}. \quad (49)$$

In view of relation

$$\lim_{a \rightarrow \infty} \frac{1}{a} F(|\mu|a; Ta) = |\mu|/\pi, \quad (50)$$

the case of a magnetic field filling the whole (infinite) space (Metlitski M.A. and Zhitnitsky A.R.: 2005) is obtained from (48) as a limiting case [cf. (22)],

$$\lim_{a \rightarrow \infty} J^{z5} = -\frac{eB}{2\pi^2} \mu. \quad (51)$$

Unlike this unrealistic case, the realistic case of a magnetic field confined to a slab of finite width is temperature dependent, see (48) and (49). In particular, we get

$$\lim_{T \rightarrow 0} J^{z5} = -\frac{eB}{2\pi a} \times \left[ \operatorname{sgn}(\mu) \left[ \frac{|\mu|a + \operatorname{sgn}(\mu)\tilde{\varphi}}{\pi} + \Theta(-\mu\tilde{\varphi}) \right] - \frac{\tilde{\varphi}}{\pi} + \frac{1}{2} \operatorname{sgn}(\tilde{\varphi}) \right] \quad (52)$$

and

$$\lim_{T \rightarrow \infty} J^{z5} = -\frac{eB}{2\pi^2} \mu; \quad (53)$$

here  $\llbracket u \rrbracket$  denotes the integer part of quantity  $u$  (i.e. the integer which is less than or equal to  $u$ ), and  $\Theta(u) = \frac{1}{2}[1 + \operatorname{sgn}(u)]$  is the step function. As follows from (48), the boundary condition that is parametrized by  $\tilde{\varphi}$  can serve as a source which is additional to the spinor matter density: the contribution of the boundary to the axial current effectively enhances or diminishes the

contribution of the chemical potential. Because of the boundary condition, the chiral separation effect can be nonvanishing even at zero chemical potential,

$$J^{z5}|_{\mu=0} = -\frac{eB}{2\pi a} \left\{ F(\tilde{\varphi} - \text{sgn}(\tilde{\varphi})\pi/2; Ta) - \frac{1}{\pi} [\tilde{\varphi} - \text{sgn}(\tilde{\varphi})\pi/2] \right\}; \quad (54)$$

the latter vanishes in the limit of infinite temperature,

$$\lim_{T \rightarrow \infty} J^{z5}|_{\mu=0} = 0. \quad (55)$$

The trivial boundary condition,  $\tilde{\varphi} = -\pi/2$ , yields spectrum  $k_l = (l + \frac{1}{2})\frac{\pi}{a}$  ( $l = 0, 1, 2, \dots$ ), which is the same in the setups of both bag models (Bogolioubov P.N.: 1968) and (Chodos A., Jaffe R.L., Johnson K., Thorn C. B., and Weisskopf V.: 1974). The axial current density at zero temperature for this case was obtained in Gorbar E.V., Miransky V.A., Shovkovy I.A., and Sukhachov P.O.: 2015,

$$J^{z5}|_{T=0, \tilde{\varphi}=-\pi/2} = -\frac{eB}{2\pi a} \text{sgn}(\mu) \left[ \frac{|\mu|a}{\pi} + \frac{1}{2} \right]. \quad (56)$$

The "bosonic-type" spectrum,  $k_l = l\frac{\pi}{a}$  ( $l = 0, 1, 2, \dots$ ), is yielded by  $\tilde{\varphi} = 0$ , and, due to the contribution of the vacuum fluctuations, the axial current density is continuous at this point,

$$\lim_{\tilde{\varphi} \rightarrow 0_+} J^{z5} = \lim_{\tilde{\varphi} \rightarrow 0_-} J^{z5}. \quad (57)$$

## 5. Summary and discussion

We have considered the influence of boundaries on chiral effects in hot dense magnetized relativistic spinor matter. An issue of the confining boundary condition plays the key role in this study. In the absence of boundaries there exist the chiral magnetic effect which is exhibited by the nondissipative vector current along the magnetic field, see (20), and the chiral separation effect which is exhibited by the nondissipative axial current in the same direction, see (22); both currents are temperature independent. As boundaries are introduced and the matter volume is shrunk to a slab which is transverse to the magnetic field, the fate of these currents is different. The axial current stays on, becoming dependent on temperature and on a choice of boundary conditions, see (48) and (49); as temperature increases from zero to large values, a stepped-shape behaviour of the axial current density as a function of chemical potential is changed to a smooth one, see (52) and (53). The vector current, as well as the axial charge, is extinct, see (44), because of boundary condition (36). Thus, the chiral magnetic effect in a slab is eliminated by the confining boundary condition.

Magnetic fields of the order of the QCD energy scale squared can be produced in the quark-gluon plasma created in relativistic heavy-ion collisions (as a result of electric currents from the colliding charged ions); see Kharzeev D.E.: 2014. Magnetic fields up to  $10^{15}$  Gauss may exist in some compact stars (magnetars); see Glendenning N.K.: 2000; Turola R, Zane S., and Watts A.L.: 2015. Even stronger fields are generated in progenitor magnetars during the core collapse after the supernovae explosion (Ferrario L., Melatos A., and Zrake J.: 2015). It has been claimed that the chiral magnetic effect (20) plays a significant role in these processes; see Boyarsky A., Ruchayskiy O., and Shaposhnikov M.: 2012; Sigl G. and Leite N.: 2016. Another claim is that the chiral magnetic effect is responsible for a solution of the problem of large kicks of pulsars (Charbonneau J. and Zhitnitsky A.: 2010; Charbonneau J., Hoffman, and Heyl J.: 2010). The latter problem is that pulsars exhibit rapid proper motion with velocities ranging from 100 to 1600 km/s, and about 15% of pulsars has velocities above 1000 km/s (Arzoumanian Z., Chernoff D.F., and Cordes J.M.: 2002). Large velocities are unambiguously confirmed with the model independent measurement of pulsar B1505+55 moving at  $1083_{-90}^{+103}$  km/s (Chatterjee S., Vlemmings W.H.T., Brisken W.F., et al: 2005). Persistent topological current (20) has been proposed in the capacity of an engine which pushes a fast pulsar like a rocket (Charbonneau J. and Zhitnitsky A.: 2010).

However, if finiteness of a physical system in the direction of the magnetic field is taken into account, then the topological vector current, as well as the axial charge, disappears, that is due to the boundary condition confining spinor (electron, quark, or nucleon) matter inside the magnetar. This circumstance changes essentially the whole picture of the large kick mechanism. The only necessary ingredients are a strong magnetic field and the high density of the relativistic charged spinor matter in the core of a compact star (magnetar or protomagnetar). Such an environment develops axial currents with the specific temperature dependence which is almost stepped-shape in the case of degenerate matter ( $T \ll |\mu|$ ) and a somewhat smooth otherwise, see (48), (49), (52), and (53). The pertinent carriers of these currents are electrons in the case of the nuclear matter, or electrons and quarks in the case of the deconfined quark matter (in supposed quark stars). Since the currents are persistent, they are capable of delivering the asymmetry of neutrinos created by weak interaction from the interior to the surface without dissipation, thus producing a proper motion of the star as a whole. The details of the mechanism are yet to be elaborated.

*Acknowledgements.* I would like to thank the Organizers of the XVI Odessa Gamow International Conference-School "Astronomy and beyond: Astro-

physics, Cosmology, Cosmomicrophysics, Astroparticle Physics, Radioastronomy and Astrobiology” for kind hospitality during this interesting and inspiring meeting. The work was supported by the National Academy of Sciences of Ukraine (Project No.0112U000054) and by the ICTP – SEENET-MTP Grant PRJ-09 “Strings and Cosmology”.

## References

- Akhiezer A.I. and Berestetskij V.B.: 1965, *Quantum Electrodynamics* (Interscience, New York).
- Akhmerov A.R. and Beenakker C.W.J.: 2008, *Phys. Rev. B*, **77**, 085423.
- Alekseev A.Y., Cheianov V.V., and Frohlich J.: 1998, *Phys. Rev. Lett.*, **81**, 3503.
- Al-Hashimi M.H. and Wiese U.-J.: 2012, *Ann. Phys. (Amsterdam)*, **327**, 1.
- Arzoumanian Z., Chernoff D.F., and Cordes J.M.: 2002, *Astrophys. J.*, **568**, 289.
- Basar G. and Dunne G.V.: 2013, *Lect. Notes Phys.*, **871**, 261.
- Bogolioubov P.N.: 1968, *Ann. Inst. Henri Poincaré A* **8**, 163.
- Bonneau G., Faraut J., and Valent G.: 2001, *Amer. J. Phys.*, **69**, 322.
- Bordag M., G.L. Klimchitskaya G.L., Mohideen U., Mostepanenko V.M.: 2009, *Advances in the Casimir Effect* (Oxford University Press, Oxford).
- Boyarsky A., Ruchayskiy O., Shaposhnikov M.: 2012, *Phys. Rev. Lett.* **109**, 111602.
- Casimir H.B.G.: 1948, *Proc. Kon. Ned. Akad. Wetenschap B* **51**, 793.
- Charbonneau J., Hoffman, and Heyl J.: 2010, *Mon. Not. Roy. Astron. Soc.* **404**, L119.
- Charbonneau J. and Zhitnitsky A.: 2010, *J. Cosmol. Astropart. Phys.* 08 (2010) 010.
- Chatterjee S., Vlemmings W.H.T., Brisken W.F. et al: 2005, *Astrophys. J.* **630**, L61.
- Chodos A., Jaffe R.L., Johnson K., Thorn C.B., Weisskopf V.: 1974, *Phys. Rev. D* **9**, 3471.
- Das A.: 1997, *Finite Temperature Field Theory* (World Scientific, Singapore).
- Ferrario L., Melatos A., Zrake J.: 2015, *Space Sci. Rev.*, **191**, 77.
- Fukushima K., Kharzeev D.E., Warringa H.J.: 2008, *Phys. Rev. D*, **78**, 074033.
- Giovannini M. and Shaposhnikov M.: 1998, *Phys. Rev. D* **57**, 2186.
- Glendenning N.K.: 2000, *Compact Stars: Nuclear Physics, Particle Physics, and General Relativity* (Spriger, New York).
- Gorbar E.V., Miransky V.A., Shovkovy I.A., Sukhachov P.O.: 2015, *Phys. Rev. B* **92**, 245440.
- Johnson K.: 1975, *Acta Phys. Pol. B* **6**, 865.
- Kharzeev D.E.: 2014, *Prog. Part. Nucl. Phys.*, **75**, 133.
- Kharzeev D.E., McLerran L.D., Warringa H.J.: 2008, *Nucl. Phys. A*, **803**, 227.
- Metlitski M.A. and Zhitnitsky A.R.: 2005, *Phys. Rev. D*, **72**, 045011.
- Miransky V.A. and Shovkovy I.A.: 2015, *Phys. Rep.*, **576**, 1.
- Okun L.B.: 1982, *Leptons and Quarks* (Elsevier Science Publishers B.V., Amsterdam).
- Sigl G. and Leite N.: 2016, *J. Cosmol. Astropart. Phys.* 01 (2016) 025.
- Sitenko Yu.A.: 2015, *Phys. Rev. D* **91**, 085012.
- Sitenko Yu.A.: 2016a, *J. Phys. Conf. Ser.* **670**, 012048.
- Sitenko Yu.A.: 2016b, *Europhys. Lett.* **114**, 61001.
- Sitenko Yu.A.: 2016c, *Phys. Rev. D* **94**, 085014.
- Sitenko Yu.A. and Yushchenko S.A.: 2015, *Int. J. Mod. Phys. A* **30**, 1550184.
- Son D.T. and Zhitnitsky A.R.: 2004, *Phys. Rev. D* **70**, 074018.
- Tashiro H., Vachaspati T., and Vilenkin A.: 2012, *Phys. Rev. D* **86**, 105033.
- Turola R, Zane S., and Watts A.L.: 2015, *Rep. Prog. Phys.* **78**, 116901.
- Vafeek O. and Vishwanath A.: 2014, *Annu. Rev. Condens. Matter Phys.* **5**, 83.
- Vilenkin A.: 1980, *Phys. Rev. D* **22**, 3080.

DOI: <http://dx.doi.org/10.18524/1810-4215.2016.29.84956>

# GRAVITY-DRIVEN ACCELERATION AND KINETIC INFLATION IN NONCOMMUTATIVE BRANS-DICKE SETTING

S.M.M. Rasouli<sup>1,2,3</sup>, Paulo Vargas Moniz<sup>1,2</sup>

<sup>1</sup> Departamento de Física, Universidade da Beira Interior,  
Rua Marquês d'Avila e Bolama, 6200 Covilhã, Portugal,  
*mrasouli@ubi.pt, pmoniz@ubi.pt*

<sup>2</sup> Centro de Matemática e Aplicações (CMA - UBI), Universidade da Beira Interior,  
Rua Marquês d'Avila e Bolama, 6200 Covilhã, Portugal

<sup>3</sup> Physics Group, Qazvin Branch, Islamic Azad University, Qazvin, Iran

**ABSTRACT.** By assuming the spatially flat FLRW line-element and employing the Hamiltonian formalism, a noncommutative (NC) setting of the Brans-Dicke (BD) theory is introduced. We investigate gravity-driven acceleration and kinetic inflation in this NC BD cosmology. Despite to the commutative case, in which both the scale factor and BD scalar field are obtained in power-law forms (in terms of the cosmic time), in our herein NC model, we see that the power-law scalar factor is multiplied by a dynamical exponential warp factor. This warp factor depends on not only the noncommutative parameter but also the momentum conjugate associated to the BD scalar field. For very small values of this parameter, we obtain an appropriate inflationary solution, which can overcome problems within standard BD cosmology in a more efficient manner. Moreover, we see that a graceful exit from an early acceleration epoch towards a decelerating radiation epoch is provided. For late times, due to the presence of the NC parameter, we obtain a zero acceleration epoch, which can be interpreted as the coarse-grained explanation.

## 1. Introduction

In the BD setting employed in [1, 2], a variable BD coupling parameter rather than a constant one has been supposed. Then, without introducing any scalar potential or cosmological constant, an accelerated expanding universe, from the kinetic energy density of a dynamical Planck mass, has been obtained. In [2], it has been argued that, to meet sufficient inflation, the scale factor in the Einstein frame must accelerate. However, there is no source to get an accelerating scale factor in that frame. In other words, in the commutative case of the BD theory [3] (in the Jordan frame), even by assuming variable  $\omega$ , there is a fundamental problem with kinetic inflation: regardless of the form

of  $\omega(\phi)$ , all the D branch<sup>1</sup> solutions are encountered with the graceful exit problem [2].

In our herein NC BD setting<sup>2</sup>, which, regardless of varying  $\omega$ , can be considered as a generalized set up of [2], we will obtain an accelerating scale factor for the early Universe, without encountering the above-mentioned problems of [2]. Moreover, we will show that requirements of an inflationary epoch (specially, the nominal as well as sufficient conditions) are satisfied in a more convenient manner when the noncommutativity parameter is present.

In this paper, by assuming a spatially flat FLRW universe, a generalized BD theory, and introducing a particular NC Poisson bracket between the BD scalar field and the logarithm of scale factor, we review the solutions (associated to the NC equations of motion) and discuss the effects of noncommutativity.

## 2. Noncommutative Brans-Dicke Cosmological Setting

We start with the spatially flat FLRW metric as the background geometry, namely

$$ds^2 = -N^2(t)dt^2 + e^{2\alpha(t)}(dx^2 + dy^2 + dz^2), \quad (1)$$

where  $a(t) = e^{\alpha(t)}$  is the scale factor and  $N(t)$  is a lapse function.

To get a general set of the field equations, let us start with the Lagrangian associated to the (generalized<sup>3</sup>) BD theory in the Jordan frame as

$$\mathcal{L}[g, \phi] = \sqrt{-g} \left[ \phi R - \frac{\omega(\phi)}{\phi} g^{\mu\nu} \nabla_\mu \phi \nabla_\nu \phi - V(\phi) \right] \quad (2)$$

<sup>1</sup>We will introduce the D and X branches later.

<sup>2</sup>Most of the discussions of this work has been reported in our previous paper [4].

<sup>3</sup>It has been recently shown [5, 6] that, instead of adding a scalar potential to BD action, such a scalar potential can be induced from the geometry of an extra dimension.

$$+ \sqrt{-g}\mathcal{L}_{\text{matt}},$$

where  $\mathcal{L}_{\text{matt}} = 16\pi\rho(\alpha)$  is the Lagrangian density of ordinary matter ( $\rho$  is the energy density), which does not explicitly depend on the BD scalar field  $\phi$ . The BD parameter  $\omega(\phi)$  is a function of the BD scalar field and varies with the space-time point;  $V(\phi)$  is the scalar potential, the greek indices run from zero to 3 and  $R$  is the Ricci scalar associated to the metric  $g_{\mu\nu}$ , whose determinant is denoted by  $g$ . Therefore, the Hamiltonian of the model is given by

$$\mathcal{H} = -\frac{Ne^{-3\alpha}}{2\chi\phi} \left[ \frac{\omega(\phi)}{6} P_\alpha^2 - \phi^2 P_\phi^2 + \phi P_\alpha P_\phi \right] \quad (3)$$

$$+ Ne^{3\alpha} (V - 16\pi\rho),$$

where  $\chi \equiv 2\omega + 3$ , and  $P_\alpha, P_\phi$  are the conjugate momenta associated to  $\alpha$  and  $\phi$ , respectively. In this work, we work with the comoving gauge, namely, we set  $N = 1$ . Instead of the commutative phase space where the Poisson algebra is given by  $\{\alpha, \phi\} = 0$ ,  $\{P_\alpha, P_\phi\} = 0$ ,  $\{\alpha, P_\alpha\} = 1$  and  $\{\phi, P_\phi\} = 1$ , to investigate the effects of a classical evolution of the noncommutativity on the cosmological equations of motion, we presume the following Poisson commutation relations between the variables as  $\{\alpha, \phi\} = \theta$ ,  $\{P_\alpha, P_\phi\} = 0$ ,  $\{\alpha, P_\alpha\} = 1$  and  $\{\phi, P_\phi\} = 1$  where the NC parameter  $\theta$  is taken as a constant. Employing these noncommutation relations and the Hamiltonian (3) leads us to deformed equations of motion as

$$\dot{\alpha} = -\frac{e^{-3\alpha}}{2\chi\phi} \left[ \frac{\omega(\phi)}{3} P_\alpha + \phi P_\phi \right]$$

$$- \frac{\theta e^{-3\alpha}}{2\chi\phi} \left[ \frac{1}{6} \frac{d\omega(\phi)}{d\phi} P_\alpha^2 - 2\phi P_\phi^2 + P_\alpha P_\phi \right]$$

$$+ \frac{\theta e^{3\alpha}}{\phi} \left[ V(\phi) + \phi \frac{dV(\phi)}{d\phi} - 16\pi\rho \right], \quad (4)$$

$$\dot{P}_\alpha = e^{3\alpha} \left[ -6V(\phi) + 16\pi \left( 6\rho + \frac{d\rho}{d\alpha} \right) \right], \quad (5)$$

$$\dot{\phi} = -\frac{e^{-3\alpha}}{2\chi} (P_\alpha - 2\phi P_\phi)$$

$$- \theta e^{3\alpha} \left[ 6V(\phi) - 16\pi \left( 6\rho + \frac{d\rho}{d\alpha} \right) \right]. \quad (6)$$

$$\dot{P}_\phi = \frac{e^{-3\alpha}}{2\chi\phi} \left[ (P_\alpha - 2\phi P_\phi) P_\phi + \frac{1}{6} P_\alpha^2 \frac{d\omega(\phi)}{d\phi} \right]$$

$$- \frac{e^{3\alpha}}{\phi} \left[ V(\phi) + \phi \frac{dV(\phi)}{d\phi} - 16\pi\rho \right], \quad (7)$$

where a dot denotes the differentiation with respect to the cosmic time and we have assumed  $\phi = \phi(t)$ . We should note that the equations of motion associated to the momenta  $P_\alpha$  and  $P_\phi$ , under the proposed NC deformation, are the same as ones in the commutative case and, obviously, in the limit  $\theta \rightarrow 0$ , Eqs. (4) and (6) are reduced to the corresponding standard commutative equations.

In what follows, we investigate the cosmological implications of this NC BD setting for a very simple case in which the BD parameter is a constant and the scalar potential and the ordinary matter are absent.

### 3. Gravity-Driven acceleration for cosmological models in the noncommutative BD Setting

As mentioned, we would like to assume a very simple case in which we set  $\omega(\phi) = \omega = \text{constant}$ ,  $\rho = 0$  and  $V(\phi) = 0$ . Therefore, from (5), we get  $\dot{P}_\alpha = 0$ , which gives a constant of motion. Thus, we get  $P_\alpha = c_1$ ; also, Eqs. (4) and (7) give  $P_\phi = c_2^\pm \phi^{-1}$  where  $c_1$  and  $c_2^\pm \neq 0$  are the integration constants. These constants are not independent; by substituting them into the Hamiltonian constraint, we obtain  $c_1^\pm = (3|c_2|/\omega) [-\text{sgn}(c_2) \pm \xi]$  where  $\xi \equiv \sqrt{\chi/3}$ ,  $\omega \neq 0$  and  $\text{sgn}(x) = x/|x|$  is the signum function. Thus, from (6),  $\dot{\phi}$  can be given by

$$\dot{\phi} = -\frac{f^\pm}{\xi\alpha^3} \quad \text{where} \quad f^\pm \equiv \frac{|c_2|}{2\omega} [-\text{sgn}(c_2)\xi \pm 1]. \quad (8)$$

By employing the obtained expressions associated to the momenta and the integration constants, from Eqs. (4) and (6) we obtain

$$H = h^\pm \left( \frac{\dot{\phi}}{\phi} \right) \quad \text{where} \quad h^\pm \equiv g^\pm + \frac{c_2\theta}{\phi}, \quad (9)$$

where  $H = \dot{a}/a$  is the Hubble constant and  $g^\pm \equiv -\frac{1}{2} [1 \pm \text{sgn}(c_2)\xi]$ . We should note that the above equations corresponding with each sign of<sup>4</sup>  $c_2$  yield two branches for the Hubble parameter. If we assume an attractive gravity [7], i.e.,  $\phi > 0$ , the values of  $\dot{\phi}$  as well as  $h$  corresponding to each branch<sup>5</sup> must be specified to get an expansion or contraction universes. For instance, in a special case, by setting  $c_2 > 0$  and  $\theta = 0$ , we obtain  $H = -\frac{\dot{\phi}}{2\phi} (1 \pm \xi)$ . In this case, for  $\xi < 1$ ,  $H > 0$  only when  $\dot{\phi} < 0$ , and  $H < 0$  only when  $\dot{\phi} > 0$  (for both of the branches). While, for  $\xi > 1$ , to have a positive Hubble expansion we must choose the upper sign for  $\dot{\phi} < 0$  and the lower sign for  $\dot{\phi} > 0$ .

Now, let us investigate a general case. We get the acceleration of the scale factor as  $\frac{\ddot{a}}{a} = -\frac{1}{6\phi} [\rho^{(\phi)} + 3p^{(\phi)}] = -\left(\frac{\dot{\phi}}{\phi}\right)^2 \left( 2h^2 + h + \frac{c_2\theta}{\phi} \right)$ , where

<sup>4</sup>For simplicity of expressing the quantities, we will sometimes drop the index  $\pm$ .

<sup>5</sup>Following [8, 1, 2], we will call the branches as follows. As in the Einstein frame, one of the branches always yields an expanding universe, while the other gives a contracting universe. Therefore, the solutions correspond to the former, and the latter are called the X branch and D branch, respectively. In our herein model, when  $c_2 > 0$ , X branch and D branch solutions correspond to the upper sign and lower sign solutions, respectively. When  $c_2 < 0$ , we note the transformations derived after Eq. (16).

the energy density and pressure associated to the BD scalar field are given by [6]

$$\rho^{(\phi)} \equiv -T_0^{0(\phi)} = 3h^2 \left( \frac{\dot{\phi}^2}{\phi} \right), \quad (10)$$

$$p^{(\phi)} \equiv T_i^i(\phi) = \left( 3h^2 + 2h + \frac{2c_2\theta}{\phi} \right) \left( \frac{\dot{\phi}^2}{\phi} \right), \quad (11)$$

where  $i = 1, 2, 3$  (with no sum) and we have employed relations (8) and (9). Therefore, in order to get an accelerating universe, the following constraint must be satisfied

$$2h^2 + h + \frac{c_2\theta}{\phi} < 0. \quad (12)$$

As  $\rho^{(\phi)} > 0$ , relation (11) and constraint (12) dictate that the pressure must take negative values.

From (9), we get a relation between the scale factor and the BD scalar field as

$$a(t) = a_i [\phi(t)]^g e^{-c_2\theta\phi^{-1}}, \quad (13)$$

where  $a_i = e^{\alpha_i}$  is an integration constant, which corresponds to  $\alpha$  in a specific time. Eq. (13) indicates that the NC parameter appears in the power of an exponential warp factor. We can easily show that this time-dependent warp factor appears in the differential equation associated to  $\phi$  [see Eq. (14)] and makes it a very complicated differential equation, such that we have to solve it numerically instead. Employing Eqs. (13) and (8), we get a differential equation for the BD scalar field as

$$\dot{\phi}\phi^{3g} e^{-3c_2\theta\phi^{-1}} = -\frac{f}{a_i^3\xi}, \quad (14)$$

where, according to (8),  $f$  depends on  $c_2$  and  $\omega$ .

In the commutative case, dependent on the value of  $\omega$ , we obtain two different types of solutions: (i) when  $g = -1/3$  (or  $\omega = -4/3$ ), which corresponds to both the lower sign (when  $c_2 > 0$ ) and the upper sign (when  $c_2 < 0$ ), the solutions correspond to the de Sitter-like space as  $a(t) = a_i\phi_i^{-\frac{1}{3}}e^{mt}$  and  $\phi(t) = \phi_i e^{-3mt}$ , where  $\phi_i$  is an integration constant, and  $m \equiv \frac{-|c_2|}{8a_i^3}[-\text{sgn}(c_2) \pm 3]$ , ii) for  $\omega \neq -4/3$ , we obtain the generalized version of the well-known O'Hanlon-Tupper solution [9, 7] as  $a(t) = \tilde{a}_i(t - t_{\text{ini}})^{r_{\pm}}$  and  $\phi(t) = \phi_i(t - t_{\text{ini}})^{s_{\pm}}$  with

$$\tilde{\phi}_i = \left\{ \frac{|c_2|}{2a_i^3\omega} \left[ \text{sgn}(c_2) \mp \frac{(\omega + 1)}{\xi} \right] \right\}^{s_{\pm}},$$

$$\tilde{a}_i = a_i\tilde{\phi}_i^g = a_i \left\{ \frac{|c_2|}{2a_i^3\omega} \left[ \text{sgn}(c_2) \mp \frac{(\omega + 1)}{\xi} \right] \right\}^{r_{\pm}},$$

where  $t_{\text{ini}}$  is an integration constant and the exponents  $r_{\pm}$  and  $s_{\pm}$  are given by

$$r_{\pm} = \frac{1}{3\omega + 4} [\omega + 1 \pm \text{sgn}(c_2)\xi], \quad (15)$$

$$s_{\pm} = \frac{1 \mp 3\text{sgn}(c_2)\xi}{3\omega + 4}.$$

Here, we should explain the role of the parameters present in the model. For a particular case where  $c_2 > 0$  (or  $c_2 < 0$ ), we get the solutions corresponding to  $(r_+, s_+)$  and  $(r_-, s_-)$  known as the fast and slow solutions, respectively [7].

By assuming  $\omega \neq -4/3$  and redefining  $\Phi \equiv -\ln(G\phi)$  (where  $G$  is the gravitational constant), it has been shown [10] that there are duality transformations as

$$\alpha \rightarrow \left( \frac{3\omega + 2}{3\omega + 4} \right) \alpha - 2 \left( \frac{\omega + 1}{3\omega + 4} \right) \Phi, \quad (16)$$

$$\Phi \rightarrow - \left( \frac{6}{3\omega + 4} \right) \alpha - \left( \frac{3\omega + 2}{3\omega + 4} \right) \Phi,$$

under which the slow and fast solutions are interchanged [11], namely,  $(r_{\pm}, s_{\pm}) \longleftrightarrow (r_{\mp}, s_{\mp})$ . However, in our model for  $\theta = 0$  herein, from (15), without considering the duality transformations (16), we can see that the sign of the integration constant  $c_2$  is responsible for the mentioned role, interchanging the lower-upper solutions. More precisely, under interchanging  $c_2 > 0 \leftrightarrow c_2 < 0$ , the parameters  $c_1$ ,  $g$ , and  $f$  transform as  $(c_1^{\pm}, f^{\pm}, g^{\pm}) \longleftrightarrow (-c_1^{\mp}, -f^{\mp}, g^{\mp})$ , and, consequently, we get  $(r_{\pm}, s_{\pm}) \longleftrightarrow (r_{\mp}, s_{\mp})$ . Also for the general NC case, as seen from (9), the general duality transformations, not only depend on the  $f$ ,  $g$ , and the integration constants  $c_1$  and  $c_2$  but also may depend on the noncommutativity parameter.

In our model, due to presence of the three parameters  $c_2$ ,  $\omega$  and  $\theta$ , we can obtain a good variety of solutions for X and D branches, for more detail, see [4]. Here, we are only interested in summarizing some of the results of Case Ia, namely, the lower sign with  $c_2 > 0$ ,  $-3/2 < \omega < -4/3$  and  $\theta < 0$ : (i) For very small negative values for the noncommutative parameter, we have shown that the scale factor starts from a singular point at  $t = 0$  and increases for both of the commutative and NC cases. However, it always does not have the same behavior for these cases. For the commutative case, we always get  $\ddot{a} > 0$ , while for the noncommutative case, for the very early times, we have  $\ddot{a} > 0$ , but at the special point, it turns to be negative; namely, after a very small time, the phase changes and we obtain a decelerating universe. (ii) The scalar field always drops for both of the commutative and NC cases. (iii) The larger the integration constant  $c_2$ , the shorter the time of the accelerating phase. (iv) The smaller the  $|\theta|$ , the larger the slope of  $a(t)$ , namely  $\dot{a}$ . (v) In the late times, by assuming the same initial values for the parameters (except  $\theta$ ),  $\phi(t)$  tends to zero for both the commutative and NC cases. However, for the large values of the cosmic time, in the commutative case,  $\ddot{a}$  never takes a constant value. While, in the NC case, we get a zero acceleration epoch.

## 5. Kinetic inflation

In the previous section, by proposing a NC setting for the BD theory, we have mentioned that how we can overcome the graceful exit problem. However, these features alone do not guarantee a scenario for the resolution of the problems with the standard cosmology.

In this section, we first investigate the nominal condition [1] for the acceleration associated to the inflation, namely,

$$d^{\text{Hor}} > H^{-1}, \quad \text{where} \quad d^{\text{Hor}}(t) = a(t) \int_{t_i}^t dt'/a'. \quad (17)$$

Then, in the rest of this section, we will study the condition for sufficient inflation.

Employing Eqs. (8), (9), and after some manipulations, we obtain

$$\frac{d \ln(a^2 \phi)}{dt} = \pm(2h + 1) \left( \frac{\dot{\phi}}{\phi} \right). \quad (18)$$

Using (8) and integrating over  $dt$ , we get

$$d^{\text{Hor}} = \frac{a^3 \phi}{|f|} - \frac{2c_2}{2g + 1} d^{\text{NC}} \quad (19)$$

up to a constant of integration. In Eq. (19), we introduced a NC contribution of distance,  $d^{\text{NC}}$ , as  $d^{\text{NC}} \equiv \frac{\theta a}{c_2} \int P'_\phi dt'/a'$ . We expect that  $d^{\text{NC}}$  can add a positive value to the  $d^{\text{Hor}}$  to properly assist in satisfying the requirement associated to the horizon problem. In order to compare, by the aid of (8), we rewrite Eq. (9) as  $H = |f|h/(\xi a^3 \phi)$ . Employing this result and (19) in the nominal condition (17) yields

$$D^{\text{NC}} \equiv d^{\text{Hor}} - H^{-1} = \frac{\phi a^3}{|f|} \left( 1 + \frac{\xi}{h} \right) - \frac{2d^{\text{NC}}}{2g + 1} > 0. \quad (20)$$

Obviously, when  $\theta$  goes to zero then  $d^{\text{NC}}$  vanishes, and, thus, the relation associated to the horizon distance of the commutative case is recovered. Therefore, the resulted relation is the same as corresponding one in Ref. [1] provided that the BD coupling parameter takes constant values within. Consequently, when  $\theta = 0$  the only acceptable result is  $0 < \xi < 1$  ( $-3/2 < \omega < 0$ ), which is obtained by choosing either the upper sign for  $c_2 > 0$  or the lower sign for  $c_2 < 0$ .

For our herein NC case, it is important to emphasize that the NC parameter plays a significant role in determining whether the constraint (20) is satisfied or not. As an example, for both the commutative and the NC (case Ia) cases, in Fig. 1, we have plotted  $D^{\text{NC}}$  versus cosmic time. This figure shows that the constraint (20), at all times, for the NC case can be easier satisfied than its corresponding commutative case.

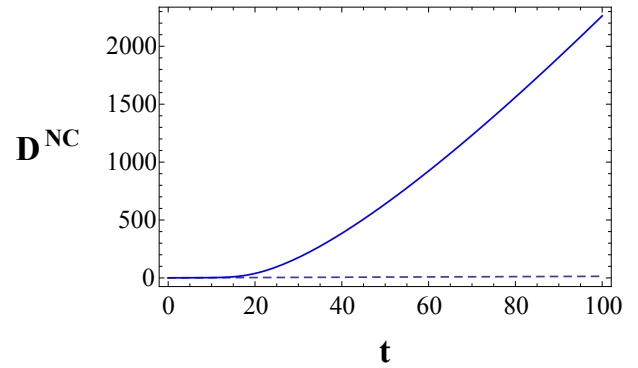


Figure 1: The behavior of the  $D^{\text{NC}}$ , the quantity which defined as in (20), versus cosmic time. The dashed and solid curves are associated to the commutative and NC cases, respectively. This figure is plotted (as an example) to show that the nominal condition (17) for the NC solutions (particularly for the case Ia) can be easily satisfied. The initial values are  $\omega = -1.4$ ,  $a_0 = 1 = c_2$ ,  $\theta = 0$  (dashed curve) and  $\theta = -0.000001$  (solid curve) [4].

In what follows, we investigate the condition for sufficient inflation, which is constrained as [2]

$$\frac{d_*^{\text{Hor}}}{a_*} > \frac{1}{H_0 a_0}. \quad (21)$$

The quantity appeared in lhs of the above inequality is comoving size of a causally connected region at a specific earlier time  $t_*$ . From relation (18), for the specific time  $t_*$ , we obtain

$$d_*^{\text{Hor}} = \left. \frac{a^3 \phi (1 - \delta)}{f \text{sgn}(c_2)} - \frac{2}{2g + 1} d^{\text{NC}} \right|_*. \quad (22)$$

We should note that the integration constant, which was removed in relation (19), has now been included in  $\delta \equiv \frac{a_*^2 \phi_i}{a^2 \phi}$  where the subscript  $i$  stands for initial values. By assuming that  $\phi > 0$ , we always have  $\delta \geq 0$ . In order to construct the inequality (21) in our herein NC model, which can be appropriately compared with the corresponding commutative one, we have employed a few assumptions and a lot of manipulations. Let us here just express the final result [4]:

$$\frac{a_*^2 \phi_*}{a_{\text{end}}^2 \phi_{\text{end}}} \gtrsim \left( \frac{M_0}{\sqrt{\bar{\alpha}_0 T_0}} \right) (1 - \delta_*)^{-1} \xi^2 \quad (23)$$

$$\times \frac{1}{4\pi \epsilon |f| (g + \frac{c_2 \theta}{\phi})^2 \left[ 1 - \frac{2d_*^{\text{NC}}}{(2g+1)|f|(1-\delta_*)a_*^3 \phi_*} \right]},$$

where the time  $t_{\text{end}}$  is devoted to the end of inflation in which the entropy is produced. The subscript 0 stand for the present epoch,  $M_0$  is the value of the Planck mass today and  $\bar{\alpha}_0 = \gamma(t_0)\eta_0 = (8\pi/3)(\pi^2/30)\bar{g}(t_0)\eta_0$ ,

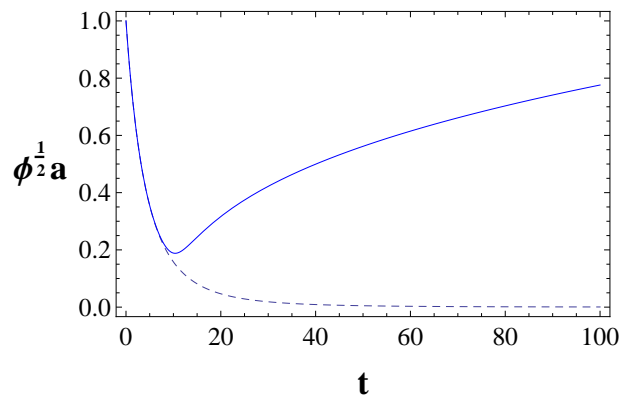


Figure 2: The time behavior of  $a\phi^{1/2}$  for the commutative case (dashed curve) and NC case (solid curve). The initial conditions are  $c_2 = 1 = a_0$ ,  $\omega = -1.36$  and  $\theta = -0.000001$  for the NC case [4].

in which  $\eta_0$  is for the ratio today of the energy density in matter to that in radiation. The constraint (23) is the generalized (noncommutative) version of the one resulted in [2] provided the BD coupling is taken as a constant therein.

We should note that, in the commutative case, the constraint (21), even with assuming a favorite set of initial conditions, implies that the quantity  $a^2\phi$  decreases with the cosmic time, which also indicates that the Planck mass must decrease during inflation. Consequently, to get an admissible result, a branch change must be induced [2].

In the NC case, considering the lower sign with  $c_2 > 0$  (D branch) and employing (18), (9) and the expression for  $g^\pm$ , we obtain  $d\ln(a\phi^{1/2})/dt = -|f|/(2\xi a^3\phi) \left[ \text{sgn}(c_2)\xi + \frac{2c_2\theta}{\phi} \right]$ , which, for the commutative case, is reduced to  $d\ln(a\phi^{1/2})/dt = -|f|/(2a^3\phi)$ . It is easy to show that that, for the commutative case, the quantity  $a\phi^{1/2}$  always decreases with the cosmic time, see Fig. 2. We should emphasize that such a result is not in agreement with the observational data [4].

For a general NC case, fortunately, for  $c_2 > 0$ ,  $\theta < 0$ , and lower case, i.e., the D branch, we have shown numerically that at the early times,  $a\phi^{1/2}$  behaves similar to its corresponding in the commutative case. However, after reaching a nonzero minimum, it starts to increase, see Fig. 2.

## 6. Conclusions

In this paper, we have introduced a NC BD setting. Such a scenario bears much resemblance to the settings assumed in NC quantum cosmology or a few classical noncommutative gravitational/cosmological investigations in theories alternative to general relativity [15, 13, 12, 14].

We have constructed a NC generalized BD setting to include key ideas of duality and branch changing as well as gravity-driven acceleration and kinetic inflation. Then, we have assumed that  $N = 1$  and there is neither a scalar potential nor a cosmological constant. Moreover, we have assumed that the Lagrangian density of the ordinary matter is absent.

In this scenario, we have found that the power-law scale factor of the Universe is not similar to the commutative case, but instead it is generalized to be multiplied with a time-dependent exponential warp factor. Moreover, we have seen that the BD scalar field is not in the form of a simple power function of time (similar to its corresponding commutative case), but instead, it can be obtained from a more complicated differential equation.

For  $\theta = 0$ , we have shown that our herein model yields an extended model of the de Sitter-like space and O'Hanlon-Tupper solutions. In the latter, the integration constants play the role of the duality transformations introduced in the context of the BD theory [11].

For case Ia, we have shown that the scale factor always accelerates in the commutative case, while, for the NC case, it accelerates only for very early times, and after a very short time, it turns to give a decelerated universe. Consequently, our model can be an appropriate inflationary model, in which we can overcome the graceful exit problem. Moreover, contrary to the commutative model in which the scale factor always accelerates in late times, we get a zero acceleration epoch for the Universe in the NC case. It has believed that this result can be interpreted as coarse-grained explanation of the quantum gravity footprint.

We have shown that both the nominal and sufficient requirements associated to the inflation can be fully satisfied in our NC model.

In the BD theory with a variable  $\omega$  [2], for a kinetic inflation model, all the accelerations in the D branch suffer from the graceful exit problem. However, for our NC model, we have shown that this problem is appropriately solved due to the presence of the NC parameter: at the very early times, although, the same as the commutative case,  $a\phi^{1/2}$  decreases with the cosmic time, while after a very short time, it starts to increase with time, which is in agreement with observations.

*Acknowledgements.* S. M. M. Rasouli is grateful for the support of Grant No. SFRH/BPD/82479/2011 from the Portuguese Agency Fundação para a Ciência e Tecnologia. He is also extremely grateful to the organizers of the 16-th Gamow International Conference/Summer School, specially, prof. Alexander Zhuk, for their warm hospitality during his attendance at the conference as well as his visiting time. This research work was supported by Grants No. CERN/FP/123618/2011 and No. PEst-OE/MAT/UI0212/2014.

### References

- [1] J. J. Levin, *Phys. Rev. D* **51**, 462 (1995).
- [2] J. J. Levin, *Phys. Rev. D* **51**, 1536 (1995).
- [3] C. Brans and R.H. Dicke, *Phys. Rev.* **124**, 925 (1961).
- [4] S.M.M. Rasouli and P.V. Moniz, *Phys. Rev. D* **90**, 083533 (2014).
- [5] S.M. M. Rasouli, M. Farhoudi and H. R. Sepangi, *Classical Quantum Gravity* **28**, 155004 (2011); S. M. M. Rasouli, *Prog. Math. Rel., Gravit. Cosmol.* **60**, 371 (2014).
- [6] S.M. M. Rasouli, M. Farhoudi and P. V. Moniz, *Classical Quantum Gravity* **31**, 115002 (2014).
- [7] V. Faraoni, *Cosmology in Scalar Tensor Gravity* (Kluwer Academic, Dordrecht, 2004).
- [8] R. Brustein and G. Veneziano, *Phys. Lett. B* **329**, 429 (1994).
- [9] J. O'Hanlon and B.O.J. Tupper, *Nuovo Cimento Soc. Ital. Fis.* **7B**, 305 (1972);
- [10] G. Veneziano, *Phys. Lett. B* **265**, 287 (1991).
- [11] J. E. Lidsey, *Phys. Rev. D* **52**, R5407 (1995); *Classical Quantum Gravity* **13**, 2449 (1996).
- [12] S. M. M. Rasouli, M. Farhoudi and N. Khosravi, *Gen. Rel. Grav.* **43**, 2895 (2011).
- [13] S. M. M. Rasouli, A. H. Ziaie, J. Marto, and P. V. Moniz, *Phys. Rev. D* **89** 044028 (2014).
- [14] S. M. M. Rasouli, A. H. Ziaie, S. Jalalzadeh and P. V. Moniz, *Annals of Phys.* **375** 154 (2016).
- [15] W. Guzmán, M. Sabido and J. Socorro, *Phys. Lett. B* **697**, 271 (2011).

DOI: <http://dx.doi.org/10.18524/1810-4215.2016.29.84957>

## TOWARD THE QUANTIZATION OF BLACK HOLES

V.D. Gladush

Dnepropetrovsk National University, Gagarin Ave, 725014, Ukraine,  
*vgladush@gmail.com*

**ABSTRACT.** In order to construct a quantum model of black hole (BH), we introduce a modified description of classical space-time BH (the Schwarzschild solution). We develop the Lagrangian formalism of the vacuum gravitational field in spherically symmetric space-time, divided on the two regions: R- and T-regions. Initial metrics in their regions are taken in the scale-invariant form and depend on a timelike coordinate in T-region and space-like coordinate in R-region. We introduce the Hamiltonian and mass function, which corresponding evolutional coordinate ( $t$  or  $r$ ) in each of regions. Their Poisson brackets are proportional Hamiltonian constraint. Further we construct the quantum operators of Hamilton and masse. Their commutator are proportional to the Hamilton operator. System of Wheeler-De Witt equation and equation on the own values of mass operator, together with the compatibility condition, allow to find wave functions in every region. These wave functions form the common wave function of BH with the continuous masse spectrum.

**Keywords:** Black hole, mass function, Hamiltonian constraint, quantum, mass operator, compatibility condition.

## 1. Introduction

Beginning with article Bekenstein (1974) it is considered that BH has a discrete mass spectrum. This connect with the idea of quantizing the horizon area of BH. The last was based on the fact that the horizon area of a nonextremal BH behaves in a sense as an adiabatic invariant (Christodoulou, 1970,1971). In what follows, these ideas developed in numerous works (See e.g., Mukhanov, 1986; Bekenstein et al, 1995; Barvinsky et al, 1996, 2001; Hod, 1998; Khriplovich 1998, 2002, 2004, 2008, etc). On the other hand, the known approaches (Thiemann at all, 1993, Kastrup at all, 1994, Kuchař, 1994) to the canonical quantization of the spherically-symmetric gravitational field give the continuous mass spectrum. Formal canonical approach (Cavaglia et al, 1995,1996) gives an analogical result. These approaches can be related by postulating periodic boundary conditions in

time for the plane waves and by identifying the period  $\Delta$  in real time with the period  $\Delta_H = 8\pi G M/c^3$  in Euclidean time (Kastrup, 1996). This yields the mass spectrum  $M_n = (1/2)m_P\sqrt{n}$ ,  $n = 1, 2, \dots$ . In the work Jalalzadeh et al (2011) by using the modification of gauge multiplier and with the application of Wheeler-DeWitt approach the discrete mass spectrum of BH was also got. In this work we, on the basis of simple geometrodynamical approach with the use of DeWitt equation and quantum mass operator, we construct quantum model of BH with the continuous mass spectrum.

## 2. Classic space-time description

## 2.1. Actions, Lagrangians and supermetrics in the R- and T-regions

Spherically-symmetric space-time (ST) with the metric

$$ds^2 = h(r, t) (dx^0)^2 - g(r, t) dr^2 - R^2(r, t) d\sigma^2, \quad (1)$$

where  $d\sigma^2 = d\theta^2 + \sin^2\theta d\alpha^2$ , has the scalar curvature

$$\begin{aligned} {}^{(4)}R &= 2 \left\{ -1 - \frac{R}{g} R_{,0} (\ln(hR))_{,0} + \right. \\ &\quad \left. + \frac{R}{h} R_{,1} (\ln(gR))_{,1} \right\} \sin\theta + (\operatorname{div}\vec{V}) \sin\theta. \end{aligned} \quad (2)$$

Here  $R_{,0} = \partial R/\partial x^0$ ,  $R_{,1} = \partial R/\partial r$ ,  $\operatorname{div}\vec{V}$  is divergence some vector  $\vec{V}$ . Action for a free gravitational field

$$S = -\frac{c^3}{16\pi\kappa} \int_{V^4} \sqrt{-g} {}^{(4)}R d^4x, \quad (3)$$

after reduction and rejection of the surface term, can be written as

$$S = \int_{V^2} \tilde{L} dx^0 dr, \quad (4)$$

where  $\tilde{L}$  – effective Lagrangian

$$\tilde{L} = \frac{c^3 R}{2\kappa} \left\{ \sqrt{\frac{h}{g}} R_{,r} (\ln(hR))_{,r} - \sqrt{\frac{g}{h}} R_{,0} (\ln(gR))_{,0} + 1 \right\}. \quad (5)$$

Information about the ST structure is contained in the term  $(\nabla R)^2 = \gamma^{ab} R_{,a} R_{,b}$ . The surface  $R(r, x^0) = R_g = \text{const}$ , for which the equality  $(\nabla R)^2 = 0$  holds, divides ST on two parts: T- and R-regions. Besides, in T:  $(\nabla R)^2 > 0$ , and in R:  $(\nabla R)^2 < 0$ . Taking into account the Birkhoff theorem, in the R- or T-region can be chosen such coordinate systems in which metrical coefficients depend only on space-like  $r$  or timelike  $x^0$  coordinate, so that:

$$ds_+^2 = h_+(r) (dx^0)^2 - g_+(r) dr^2 - R_+^2(r) d\sigma^2, \quad (6)$$

$$ds_-^2 = h_-(x^0) (dx^0)^2 - g_-(x^0) dr^2 - R_-^2(x^0) d\sigma^2. \quad (7)$$

We will define the dimensionless variables  $\zeta_{\pm}$ ,  $\tau_{\pm}$ :

$$r = \frac{R_g}{2} \zeta_{\pm}, \quad x^0 = \frac{R_g}{2} \tau_{\pm}, \quad r_g = \frac{R_g}{2} \zeta_g, \quad x_g^0 = \frac{R_g}{2} \tau_g, \quad (8)$$

where  $\{\zeta_-, \tau_-\} \in T$ ,  $\{\zeta_+, \tau_+\} \in R$ . Then

$$ds_+^2 = h_+(\zeta_+) (d\tau_-)^2 - g_+(\zeta_+) (d\zeta_+)^2 - R_+^2(\zeta_+) d\sigma^2,$$

$$ds_-^2 = h_-(\tau_-) (d\tau_-)^2 - g_-(\tau_-) (d\zeta_-)^2 - R_-^2(\tau_-) d\sigma^2.$$

By virtue of additivity, the action can be rewritten as follows

$$S = S_- + S_+ = \int_0^{x_g} L_- d\tau_- + \int_{x_g}^{\infty} L_+ d\zeta_+, \quad (9)$$

$$L_- = \frac{s_0}{2} \sqrt{h_- g_-} \left\{ -\frac{R_-}{h_-} R_{-,0} (\ln(g_- R_-))_{,0} + 1 \right\}, \quad (10)$$

$$L_+ = \frac{s_0}{2} \sqrt{h_+ g_+} \left\{ \frac{R_+}{g_+} R_{+,1} (\ln(h_+ R_+))_{,1} + 1 \right\}, \quad (11)$$

where  $s_0 = R_g^2 c^3 / 4\kappa$ . In (9) integration on  $\zeta_-$  and  $\tau_+$  is executed in the interval  $l = \zeta_{-2} - \zeta_{-1} = \tau_{+2} - \tau_{+1} = 1$ . We will enter the new field variables:

$$h_- = \frac{n_- + u_-}{n_- - u_-} N_-^2, \quad g_- = \frac{n_- - u_-}{n_- + u_-}, \quad R_- = \frac{R_g}{2} (n_- + u_-), \quad (12)$$

$$h_+ = \frac{u_+ - n_+}{u_+ + n_+}, \quad g_+ = \frac{u_+ + n_+}{u_+ - n_+} N_+^2, \quad R_+ = \frac{R_g}{2} (u_+ + n_+). \quad (13)$$

Then metrics and Lagrangians take the form of

$$ds_-^2 = \frac{R_g^2}{4} \left\{ N_-^2 \frac{n_- + u_-}{n_- - u_-} d\tau_-^2 - \frac{n_- - u_-}{n_- + u_-} d\zeta_-^2 - (n_- + u_-)^2 d\sigma^2 \right\}, \quad |u_-| < n_-, \quad (14)$$

$$L_- = \frac{s_0}{2} \left\{ \frac{1}{N_-} (u_-^2 - n_-^2) + N_- \right\}, \quad (15)$$

$$ds_+^2 = \frac{R_g^2}{4} \left\{ \frac{u_+ - n_+}{u_+ + n_+} d\tau_+^2 - N_+^2 \frac{u_+ + n_+}{u_+ - n_+} d\zeta_+^2 - (u_+ + n_+)^2 d\sigma^2 \right\}, \quad 0 < n_+ < u_+ < \infty, \quad (16)$$

$$L_+ = \frac{s_0}{2} \left\{ \frac{1}{N_+} (u_+^2 - n_+^2) + N_+ \right\}, \quad (17)$$

where  $\tau_{\pm} = \partial/\partial\tau_{\pm}$ ,  $\zeta_{\pm} = \partial/\partial\zeta_{\pm}$ . The requirement  $\delta S = 0$  with respect variations  $\delta N$  leads to constrains

$$\frac{\partial L_-}{\partial N_-} = 0 \implies u_-^2 - n_-^2 = N_-^2, \quad (18)$$

$$\frac{\partial L_+}{\partial N_+} = 0 \implies u_+^2 - n_+^2 = N_+^2. \quad (19)$$

Except the Lagrange multipliers  $N$  from  $L$ , we get Lagrangians and actions of the system in both minisuperspaces:

$$L_- = s_0 \sqrt{u_-^2 - n_-^2}, \quad L_+ = s_0 \sqrt{u_+^2 - n_+^2}, \quad (20)$$

$$S_- = s_0 \int_0^{\zeta_g} \sqrt{u_-^2 - n_-^2} d\tau_- = s_0 \int_0^{\zeta_g} d\Omega_-, \quad (21)$$

$$S_+ = s_0 \int_{\zeta_g}^{\infty} \sqrt{u_+^2 - n_+^2} d\zeta_+ = s_0 \int_{\zeta_g}^{\infty} d\Omega_+. \quad (22)$$

Here  $d\Omega_{\pm}^2 = du_{\pm}^2 - dn_{\pm}^2 > 0$  are metrics on the minisuperspaces. Using the gauge condition  $N = 1$ , the constrains can be rewritten in the form

$$u_-^2 - n_-^2 = 1, \quad u_+^2 - n_+^2 = 1. \quad (23)$$

Therewith the initial actions (9) we reduced to the actions (21) and (22) for the geodesic equations in the minisuperspaces.

## 2.2. Hamiltonian and general solution of Einstein equations

From the Lagrangian (15) where  $N_- = 1$ , we obtain the momentums and in T-region

$$P_{u_-} = s_0 u_{-, \tau_-}, \quad P_{n_-} = -s_0 n_{-, \tau_-}, \quad (24)$$

$$H_-(q, q) = \frac{s_0}{2} (u_{-, \tau_-}^2 - n_{-, \tau_-}^2 - 1), \quad (25)$$

$$H_-(p, q) = \frac{1}{2s_0} (P_{u_-}^2 - P_{n_-}^2) - \frac{s_0}{2}. \quad (26)$$

In R-region, by analogy, from (17) we obtain

$$P_{u_+} = s_0 u_{+, \zeta_+}, \quad P_{n_+} = -s_0 n_{+, \zeta_+}, \quad (27)$$

$$H_+(q', q) = \frac{s_0}{2} (u_{+, \zeta_+}^2 - n_{+, \zeta_+}^2 - 1), \quad (28)$$

$$H_+(p, q) = \frac{1}{2s_0} (P_{u_+}^2 - P_{n_+}^2) - \frac{s_0}{2}, \quad (29)$$

where an evolutionary coordinate is the spacelike coordinate  $\zeta_+$ .

Easily to see that momentums  $P_{u_{\pm}}, P_{n_{\pm}}$  are saved, and Hamiltonians  $H_{\pm}$  are vanished by virtue of the constrains (23). Hence we obtain the general solutions of geodesic equations on the minisuperspaces in the R- and T-regions

$$u_- = \frac{1}{s_0} P_{u_-} \tau_- + C_{u_-}, \quad n_- = -\frac{1}{s_0} P_{n_-} \tau_- + C_{n_-}, \quad (30)$$

$$u_+ = \frac{1}{s_0} P_{u_+} \zeta_+ + C_{u_+}, \quad n_+ = -\frac{1}{s_0} P_{n_+} \zeta_+ + C_{n_+}, \quad (31)$$

$$R_+ = \frac{r}{s_0} (P_{u_+} - P_{n_+}) + \frac{1}{2} R_g (C_{u_+} + C_{n_+}), \quad (32)$$

where momentums obey the constrains

$$P_{u_-}^2 - P_{n_-}^2 = P_{u_+}^2 - P_{n_+}^2 = s_0^2. \quad (33)$$

If one substitutes these expression for  $u_{\pm}$  in metrics (14,16), and taking into account constrains (33), one gets the general solutions Einstein equations in the R- and T-regions for the calibrations  $N = 1$ .

### 2.3. Matching conditions

Since the surface  $R(r, x^0) = R_g$  divides ST on the T- and R-regions with the metrics (14) and (16), then there is a problem finding of the matching conditions. Foremost the first quadratic forms of the sections  $\tau = \zeta = const$  must be equal.

$$(ds_-^2)_{\tau=\zeta_g} = (ds_+^2)_{\zeta_+=\zeta_g} \quad \tau_- = \zeta_+ = \zeta_g, \quad (34)$$

From here, supposing  $\zeta_- = \tau_+$ , we obtain

$$u_- = u_+, \quad n_- = n_+ \text{ at } \tau_- = \zeta_+ = \zeta_g.$$

Now, we consider variations of the action  $S$  at  $N = 1$ :

$$\delta S = \delta S_- + \delta S_+ = \int_0^{\zeta_g} \delta L_- d\tau_- + \int_{\zeta_g}^{\infty} \delta L_+ d\zeta_+. \quad (35)$$

From here, at the fixed boundary conditions we obtain the motion equations in the T- and R-regions:

$$u_{-, \tau_- \tau_-} = 0, \quad n_{-, \tau_- \tau_-} = 0, \quad (36)$$

$$n_{+, \zeta_+ \zeta_+} = 0, \quad u_{+, \zeta_+ \zeta_+} = 0. \quad (37)$$

Let now the fields on the infinity and in the center are fixed, and on the boundary of the T- and R-regions they are free. Then using (35) we find

$$\delta S = s_0 [(u_{+, \zeta_+} - u_{-, \tau_-}) \delta u_- - \quad (38)$$

$$- (n_{-, \tau_-} - n_{+, \zeta_+}) \delta n_-]_{\tau=\zeta=\zeta_g}. \quad (39)$$

By virtue of the  $\delta S = 0$  and arbitrariness of value  $\{\delta u_-, \delta n_-\}$  from here follows the matching conditions of the derivatives. As a result, we obtain

$$u_- = u_+, \quad n_- = n_+, \quad (40)$$

$$u_{-, \tau_-} = u_{+, \zeta_+}, \quad n_{-, \tau_-} = n_{+, \zeta_+}. \quad (41)$$

### 2.4. Mass function in the R- and T-regions

From the definition of the mass function

$$M = \frac{c^2}{2\kappa} R (1 + \gamma^{ab} R_{,a} R_{,b}) \quad (42)$$

we obtain the mass functions in the T- and R-regions as the functions of the velocities and coordinates:

$$M_- = \frac{c^2 R_g}{4\kappa} (n_- + u_- + (n_- - u_-) (n_{-, \tau_-} + u_{-, \tau_-})^2), \quad (43)$$

$$M_+ = \frac{c^2 R_g}{4\kappa} (u_+ + n_+ - (u_+ - n_+) (u_{+, \zeta_+} + n_{+, \zeta_+})^2). \quad (44)$$

or, as the functions of the momentums and coordinates

$$M_- = \frac{c^2 R_g}{4\kappa} (n_- + u_- + \frac{1}{s_0^2} (n_- - u_-) (P_{u_-} - P_{n_-})^2), \quad (45)$$

$$M_+ = \frac{c^2 R_g}{4\kappa} (u_+ + n_+ - \frac{1}{s_0^2} (u_+ - n_+) (P_{u_+} - P_{n_+})^2), \quad (46)$$

Using the motion equations or constrains, it is easy to show that the derivatives of the mass functions with respect to evolutional coordinates  $\tau_-$ , or  $\zeta_+$  in the T- or R-fields, respectively, as well as Poisson brackets between Hamiltonians and mass functions, vanish

$$(M_{\pm})_{, \pm} = \{M_{\pm}, H_{\pm}\} = \frac{2R_g}{4\kappa s_0^2} (P_{u_{\pm}} - P_{n_{\pm}}) H_{\pm} = 0.$$

Here  $(M_-)_{, -} = \partial M_- / \partial \tau_-$  and  $(M_+)_{, +} = \partial M_+ / \partial \zeta_+$ . Thus, the dynamical quantities  $M_{\pm}(p, q)$  are the integrals of motion.

### 2.5. The construction of metrics with the help of constrains and mass functions

Let us assume that  $M(q, p) = m$ . This implies

$$u_{\pm} + n_{\pm} - \frac{1}{s_0^2} (u_{\pm} - n_{\pm}) (P_{u_{\pm}} - P_{n_{\pm}})^2 = \frac{4\kappa m}{c^2 R_g}.$$

Taking into account the constrains (33) from here we find

$$P_{u_{\pm}} = \pm \frac{s_0 (u_{\pm} - 2\kappa m / c^2 R_g)}{\sqrt{(u_{\pm} - 2\kappa m / c^2 R_g)^2 - (n_{\pm} - 2\kappa m / c^2 R_g)^2}}, \quad (47)$$

$$P_{n_{\pm}} = \mp \frac{s_0 (n_{\pm} - 2\kappa m / c^2 R_g)}{\sqrt{(u_{\pm} - 2\kappa m / c^2 R_g)^2 - (n_{\pm} - 2\kappa m / c^2 R_g)^2}}. \quad (48)$$

Further, from the general solutions (30) and (30), we obtain  $u(0) = C_u$ ,  $n(0) = C_n$ . Hence

$$P_{u_{\pm}} = \pm \epsilon_2 \frac{s_0 (C_{u_{\pm}} - 2\kappa m / c^2 R_g)}{\sqrt{(C_{u_{\pm}} - 2\kappa m / c^2 R_g)^2 - (C_{n_{\pm}} - 2\kappa m / c^2 R_g)^2}}, \quad (49)$$

$$P_{n_{\pm}} = -\epsilon_2 \frac{s_0 (C_{n_{\pm}} - 2\kappa m / c^2 R_g)}{\sqrt{(C_{u_{\pm}} - 2\kappa m / c^2 R_g)^2 - (C_{n_{\pm}} - 2\kappa m / c^2 R_g)^2}}. \quad (50)$$

From the last expression in the (13) it follows that  $u_+ = 2R_+/R_g - n_+$ . Then from the metric (16), using the (8) and (13), we find that  $g_{00} = 1 - n_+R_g/R_+$ . Owing to asymptotic condition  $g_{00} = 1 - R_g/R_+$  when  $R_+ \rightarrow \infty$ , where  $R_g = 2\kappa m/c^2$ , it follows from this  $n_+ \rightarrow 1$  and  $s_0 = \kappa m^2/c$ . Then from (31) we have  $P_{n_+} = 0$ ,  $C_{n_+} = 1$  and momentum constrain (33) gives  $P_{u_+} = s_0$ . Here we confined oneself to a positive value. As a result, the solution (31), takes the form  $u_+ = \zeta_+ + C_{u_+}$ ,  $n_+ = 1$ . Assumed that that  $C_{u_+} = 0$  and substituting the obtained solution in (16), where  $N_+ = 1$ , we obtain the Schwarzschild solution in a scale-invariant form

$$ds_+^2 = \frac{R_g^2}{4} \left\{ \frac{\zeta_+ - 1}{\zeta_+ + 1} d\tau_+^2 - \frac{\zeta_+ + 1}{\zeta_+ - 1} d\zeta_+^2 - (\zeta_+ + 1)^2 d\sigma^2 \right\}, \quad (51)$$

Finally, using (32), we find  $R = r + \kappa m/c^2$ . Taking into account the relations  $u_+ = \zeta_+$ ,  $n_+ = 1$ , (8) and (16) we come to the standard expression for the Schwarzschild metric.

In order to find the metric in the T-region we use the solution (30), the matching conditions (40), and the metric (14). As a result we obtain a trajectory of the system  $\{u_- = \tau, n_- = 1\}$  in the minisuperspace and the metric of ST in the scale-invariant form

$$ds_-^2 = \frac{R_g^2}{4} \left\{ \frac{1 + \tau_-}{1 - \tau_-} d\tau_-^2 - \frac{1 - \tau_-}{1 + \tau_-} d\zeta_-^2 - (1 + \tau_-)^2 d\sigma^2 \right\}. \quad (52)$$

### 3. Quantum description

#### 3.1. Quantization in the T-region

When choosing a method of quantization by the formula  $\hat{H} \sim \Delta + qR$  (choice of the order for operators) we can use the usual covariant quantization, assuming  $\hat{H} \sim \Delta$ , because minisuperspace is flat. With this in mind, we have transformed the classical action and the metric of minisuperspace to the maximum simple Lorentzian form. Here evolution variable is the dimensionless timelike coordinate  $\tau$ , the generalized coordinates and velocities are  $\{u_-, n_-\}$  and  $\{u_-, \tau_-, n_-, \tau_-\}$ , the momentums are  $\{P_{u_-}, P_{n_-}\}$ . We define the momentum operators by the standard formulae

$$\hat{P}_{n_-} = -i\hbar \frac{\partial}{\partial n_-}, \quad \hat{P}_{u_-} = -i\hbar \frac{\partial}{\partial u_-}. \quad (53)$$

Then the Hamiltonian has the form

$$\hat{H}_- = -\frac{\hbar^2 c}{2\kappa m^2} \left( \frac{\partial^2}{\partial u_-^2} - \frac{\partial^2}{\partial n_-^2} \right) - \frac{\kappa m^2}{2c}. \quad (54)$$

The Hamilton constrain leads to the DeWitt equation

$$\hat{H}_- \Psi_- = 0 \Rightarrow \left( \frac{\partial^2}{\partial u_-^2} - \frac{\partial^2}{\partial n_-^2} \right) \Psi_- + \mu^4 \Psi_- = 0, \quad (55)$$

where  $\mu = \sqrt{s_0/\hbar} = m/m_{pl}$ ,  $m_{pl} = \sqrt{c\hbar/\kappa}$ . The mass function in the T-region corresponds to the mass operator

$$\hat{M}_- = \frac{m}{2} \left( u_- + n_- + \frac{u_- - n_-}{\mu^4} \left( \frac{\partial}{\partial u_-} - \frac{\partial}{\partial n_-} \right)^2 \right). \quad (56)$$

Further, we introduce the light coordinates in the minisuperspace of the T-region

$$\xi_- = u_- - n_-, \quad \eta_- = u_- + n_-. \quad (57)$$

Then the Hamiltonian, DeWitt equation and mass operator take the forms

$$\hat{H}_- = -\frac{2c\hbar^2}{\kappa m^2} \frac{\partial^2}{\partial \xi_- \partial \eta_-} - \frac{\kappa m^2}{2c}, \quad (58)$$

$$\frac{\partial^2 \Psi_-}{\partial \xi_- \partial \eta_-} + \frac{\mu^4}{4} \Psi_- = 0, \quad (59)$$

$$\hat{M}_- = \frac{m}{2} \left( \eta_- + \frac{4}{\mu^4} \xi_- \frac{\partial^2}{\partial \xi_-^2} \right). \quad (60)$$

We consider the operator commutator

$$\left[ \hat{H}_-, \hat{M}_- \right] \Psi_- = \frac{4}{\mu^4} \hat{H}_- \frac{\partial \Psi_-}{\partial \xi_-} = \frac{4}{\mu^4} \frac{\partial}{\partial \xi_-} \left( \hat{H}_- \Psi_- \right), \quad (61)$$

We see that commutator vanishes on constrain  $\hat{H}_- \Psi_- = 0$ . Therefore, the eigenvalue problem of the mass operator:  $\hat{M}_- \Psi_- = m \Psi_-$  is necessary to solve together with the finding of the wave functions, satisfying DeWitt equation. Thus the need to solve together a system of equations

$$\frac{\partial^2 \Psi_-}{\partial \xi_- \partial \eta_-} = -\frac{\mu^4}{4} \Psi_-, \quad \mu^4 = \frac{m^4}{m_{pl}^4}, \quad (62)$$

$$\frac{\partial^2 \Psi_-}{\partial \xi_-^2} = -\frac{\mu^4}{4} \left( \frac{\eta_- - 2}{\xi_-} \right) \Psi_-. \quad (63)$$

The compatibility condition leads to the equation

$$\xi_- \frac{\partial \Psi_-}{\partial \xi_-} + (2 - \eta_-) \frac{\partial \Psi_-}{\partial \eta_-} = \Psi_-. \quad (64)$$

Hence we find the  $\Psi_- = \xi_- G(Z)$ , where  $G(Z)$  is the arbitrary function of argument  $Z = \xi_- (2 - \eta_-)$ . Substituting the  $\Psi_-$  into DeWitt equation (62), we get

$$Z \frac{d^2 G}{dZ^2} + 2 \frac{dG}{dZ} - \frac{\mu^4}{4} G = 0. \quad (65)$$

Its general solution

$$G = \frac{1}{\sqrt{Z}} \left\{ C_1 J_1 \left( \sqrt{-\mu^4 Z} \right) + C_2 Y_1 \left( \sqrt{-\mu^4 Z} \right) \right\}. \quad (66)$$

where  $J_1(x)$  and  $Y_1(x)$  are the Bessel functions of the first and second kind. Thus, the common wave function of the Hamiltonian and the mass operator takes the form

$$\Psi_- = \frac{\xi_-}{\sqrt{Z_-}} \left\{ C_1 J_1 \left( \mu^2 \sqrt{-Z_-} \right) + C_2 Y_1 \left( \mu^2 \sqrt{-Z_-} \right) \right\}. \quad (67)$$

Returning to the variables  $\{u_-, n_-\}$ , we find

$$\Psi_- = \frac{u_- - n_-}{\sqrt{(n_- - 1)^2 - (u_- - 1)^2}} \cdot \left\{ C_1 J_1 \left( \mu^2 \sqrt{(u_- - 1)^2 - (n_- - 1)^2} \right) + C_2 Y_1 \left( \mu^2 \sqrt{(u_- - 1)^2 - (n_- - 1)^2} \right) \right\}.$$

The minisuperspace metric  $d\Omega_-^2 = du_-^2 - dn_-^2 > 0$  in the T-region gives the physically admissible timelike directions  $(u_- - 1)^2 - (n_- - 1)^2 > 0$  of the vector  $\xi_-^a = u_- - 1, n_- - 1$ . For the regularity of the wave function, on the light-cone  $(u_- - 1)^2 - (n_- - 1)^2 = 0$  in the minisuperspace, we suppose that  $C_2 = 0$ . As a result, the wave function of the black hole with the mass  $m$  in T-region takes the form:

$$\Psi_- = \frac{C_-(u_- - n_-)J_1\left(\mu^2\sqrt{(u_- - 1)^2 - (n_- - 1)^2}\right)}{\sqrt{(n_- - 1)^2 - (u_- - 1)^2}}. \quad (68)$$

The found wave function depends on the square two-dimensional vector  $\xi_-^a = \{u_- - 1, n_- - 1\}$  with initial point  $\{1, 1\}$ . In the physical region the wave function oscillates and decreases. Outside the light cone, it decreases monotonically

### 3.2. Quantization in the R-region

Here the formal evolution variable is the dimensionless spacelike coordinate  $\zeta$ , the generalized coordinates and velocities are  $\{n_+, u_+\}$   $\{u_{+, \zeta_+}, n_{+, \zeta_+}\}$ , the momentums are  $\{P_{u_+}, P_{n_+}\}$ . We define formally momentum operators by the formulae

$$\hat{P}_{u_+} = -i\hbar\frac{\partial}{\partial u_+}, \quad \hat{P}_{n_+} = -i\hbar\frac{\partial}{\partial n_+}. \quad (69)$$

The Hamiltonian has the form

$$\hat{H}_+ = -\frac{c\hbar^2}{2\kappa m^2}\left(\frac{\partial^2}{\partial u_+^2} - \frac{\partial^2}{\partial n_+^2}\right) - \frac{\kappa m^2}{2c}, \quad (70)$$

The Hamilton constrain  $H_+ = 0$  leads to the DeWitt equation:

$$\hat{H}_+\Psi_+ = 0 \Rightarrow \left(\frac{\partial^2}{\partial u_+^2} - \frac{\partial^2}{\partial n_+^2}\right)\Psi_+ + \mu^4\Psi_+ = 0. \quad (71)$$

The mass function corresponds to the mass operator

$$\hat{M}_+ = \frac{m}{2}\left(u_+ + n_+ + \frac{u_+ - n_+}{\mu^4}\left(\frac{\partial}{\partial u_+} - \frac{\partial}{\partial n_+}\right)^2\right) \quad (72)$$

We introduce the light coordinates in the minisuperspace of the R-region

$$\xi_+ = n_+ - u_+, \quad \eta_+ = n_+ + u_+. \quad (73)$$

Then the Hamiltonian, DeWitt equation and mass operator take the forms

$$\hat{H}_+\Psi_+ = \frac{2c\hbar^2}{\kappa m^2}\frac{\partial^2\Psi_+}{\partial\eta_+\partial\xi_+} - \frac{\kappa m^2}{2c}\Psi_+, \quad (74)$$

$$\frac{\partial^2\Psi_+}{\partial\eta_+\partial\xi_+} - \frac{\mu^4}{4}\Psi_+ = 0. \quad (75)$$

$$\hat{M}_+ = \frac{m}{2}\left(\eta_+ - \frac{4}{\mu^4}\xi_+\frac{\partial^2}{\partial\xi_+^2}\right). \quad (76)$$

The commutator of the Hamilton and the mass operator

$$\left[\hat{H}_+, \hat{M}_+\right]\Psi_+ = \frac{4}{\mu^4}\hat{H}_+\frac{\partial\Psi_+}{\partial\xi_+} = \frac{4}{\mu^4}\frac{\partial}{\partial\xi_+}\left(\hat{H}_+\Psi_+\right). \quad (77)$$

vanishes on the constrain  $\hat{H}_+\Psi_+ = 0$ . Therefore, the eigenvalue problem of the mass operator:  $\hat{M}_+\Psi_+ = m\Psi_+$  should be solved together with the finding of the wave functions, satisfying DeWitt equation. So necessary to solve together a system of equations

$$\frac{\partial^2\Psi_+}{\partial\eta_+\partial\xi_+} = \frac{\mu^4}{4}\Psi_+, \quad (78)$$

$$\frac{\partial^2\Psi_+}{\partial\xi_+^2} = \frac{\mu^4}{4}\left(\frac{\eta_+ - 2}{\xi_+}\right)\Psi_+. \quad (79)$$

The compatibility condition leads to the equation

$$\xi_+\frac{\partial\Psi_+}{\partial\xi_+} + (2 - \eta_+)\frac{\partial\Psi_+}{\partial\eta_+} = \Psi_+, \quad (80)$$

From here we find that  $\Psi_+ = \xi_+G_+(\tilde{Z})$ , where  $\tilde{Z} = \xi_+(2 - \eta_+)$ . Substituting this relation into DeWitt equation we derive the equation for the function  $G_+(\tilde{Z})$ :

$$\tilde{Z}\frac{d^2G_+}{d\tilde{Z}^2} + 2\frac{dG_+}{d\tilde{Z}} + \frac{\mu^4}{4}G_+ = 0. \quad (81)$$

Its general solution taking into account the formula  $\Psi_+ = \xi_+G_+(\tilde{Z})$  leads to the wave function of the state with a certain mass

$$\Psi_+ = \frac{\xi_+}{\sqrt{\tilde{Z}}}\left\{C_1J_1\left(\mu^2\sqrt{\tilde{Z}}\right) + C_2Y_1\left(\mu^2\sqrt{\tilde{Z}}\right)\right\}. \quad (82)$$

Take into consideration that  $\tilde{Z} = (u_+ - 1)^2 - (n_+ - 1)^2$ , from the regularity condition of the wave function on the light cone, we get  $C_2 = 0$ . As a result, wave function of BH with the mass  $m$  in the R-region takes the form:

$$\Psi_+ = \frac{C_+(u_+ - n_+)J_1\left(\mu^2\sqrt{(u_+ - 1)^2 - (n_+ - 1)^2}\right)}{\sqrt{(u_+ - 1)^2 - (n_+ - 1)^2}}. \quad (83)$$

The found wave function describes the standing decreasing spherical wave in the minisuperspace of the R-region.

## 4. Conclusion

The resulting wave function (68), (83) satisfy the matching conditions (40). Furthermore in full minisuperspace R- and T- regions, we can enter the general

smooth coordinates by the formulae

$$\begin{aligned} u &= \begin{cases} u_- = \eta_-, & -1 < \eta_- < 1 \\ u_+ = \zeta_+, & 1 < \zeta_+ < \infty \end{cases}, \\ n &= \begin{cases} n_- = 1, & -1 < \eta_- < 1 \\ n_+ = 1, & 1 < \zeta_+ < \infty \end{cases} = 1. \end{aligned}$$

Herewith the common wave function of the BH for the whole space  $V^4 = T \cup R$  has the form

$$\Psi = \frac{A(u-n)}{\sqrt{(n-1)^2 - (u-1)^2}} J_1(\mu^2 \sqrt{(u-1)^2 - (n-1)^2}). \quad (84)$$

It corresponds to the state with a certain mass  $m = \mu m_{pl}$ . The mass spectrum obtained continuously. This is in agreement c other works (See e.g., Cavaglia' at all, 1995), where other methods are used. Interesting to note that formal quantization in R-region with spacelike evolution coordinate gives the same wave function that and in the T-region with the timelike evolution coordinate.

## References

- Bekenstein J.D.: 1974, Lett. Nuovo Cimento, **11**, 467.  
 Christodoulou D.: 1970, Phys. Rev. Lett, **25**, 1596.  
 Christodoulou D. at all.: 1971, Phys. Rev. **D4**, 3552.  
 Mukhanov V.F.: 1986, JETP Lett. **44**, 63.  
 Bekenstein J.D. at all.: 1995, gr-qc/9505012.  
 Barvinsky A. at all.: 1996, gr-qc/9607030.  
 Barvinsky A. at all.: 2001, Cl. Quant Grav, **18**, 4845.  
 Hod S.: 1998, Phys. Rev. Lett. **81**, 4293.  
 Khriplovich I.B.: 1998, Phys. Lett. **B431**, 19.  
 Khriplovich I.B.: 2004, ZhETF **126**, 527.  
 Khriplovich I.B.: 2008, Phys. Atom. Nucl. **71**, 671.  
 Thiemann T. at all.: 1993, Nucl. Phys. **B399**, 211.  
 Kastrup H.A. at all.: 1994, Nucl. Phys. **B425**, 665.  
 Kuchař K.: 1994, Phys. Rev. **D50**, 3961.  
 Kastrup H.A.: 1996, Phys. Lett. **B385**, 75.  
 Cavaglia' M. at all.: 1995, Int.J.Mod.Phys. **D4**, 661.  
 Cavaglia' M. at all.: 1996, Int.J.Mod.Phys. **D5** 227.  
 Jalalzadeh S. at all.: 2012, Int. J. Th. Ph. **51**, 263.



where the number of rows with coefficients  $a_i$  is equal to  $m = \deg g(x)$ , and the number of rows with equal coefficients  $b_j$  is equal to  $n = \deg f(x)$ .

The resultant and Sylvester matrix connects the following

**Theorem 1.** Let  $R(f, g)$  – the resultant of  $f$  and  $g$ , and  $S(f, g)$  – they Sylvester matrix, then:

$$R(f, g) = \det S(f, g) \quad (6)$$

The proof of Theorem 1, see. eg, (Lang 1965, Van Der Waerden 1971).

We have the following

**Theorem 2.** The polynomials  $f$  and  $g$  have a common root, if and only if,

$$R(f, g) = 0. \quad (7)$$

The modern proof of Theorem 2 sees. Eg., (Lang, 1965; Van Der Waerden, 1971).

From Theorem 2 follow

**Theorem 3.** Let  $A = A(x_1, x_2)$  and  $B = B(x_1, x_2)$  are polynomials of two variables  $x_1$  and  $x_2$ . System of equations

$$\begin{cases} A(x_1, x_2) = 0 \\ B(x_1, x_2) = 0 \end{cases}, \quad (8)$$

has a solution, if and only if, at least one of the results  $R_{x_1}(A, B)$ ,  $R_{x_2}(A, B)$  is zero.

The proof of Theorem 3, see. Eg (Walker, 1950; Van Der Waerden, 1971).

There is also

**Theorem 4.** The polynomials  $A = A(x_1, x_2)$  and  $B = B(x_1, x_2)$  have a common component, if and only if, at least one of the results,  $R_{x_1}(A, B)$ ,  $R_{x_2}(A, B)$  is identically equal to zero.

### 3. The algorithm for constructing images for $N$ -point lens

Theorems 1-3 we use the algorithm for solving the problem of calculating the coordinates of the image points. The right parts the equations of system (3), are rational functions of the variables  $x_1$  and  $x_2$ . We transform each equation of the system (3) in a polynomial equation, and we obtain a system of equations:

$$\begin{cases} F_1(x_1, x_2, y_1) = 0 \\ F_2(x_1, x_2, y_2) = 0 \end{cases}. \quad (9)$$

We apply to the system (9) Theorem 4. Let's see has the common component the equations of system. If there is a common component, we separate it. In this case, the system (9) is divided into several sub-systems with the equations without common components. If there is no common components, we are using theorem 3, and we are eliminate from system (9) of the variable  $x_1$ , and then the variable  $x_2$ . The two obtained

equations form a system

$$\begin{cases} R_1(x_2, y_1, y_2) = 0 \\ R_2(x_1, y_1, y_2) = 0 \end{cases}. \quad (10)$$

System (10) from the system (9), but in general it is not equivalent. The first equation of the system is a polynomial in the variable  $x_2$ . The second – a polynomial in the variable  $x_1$ . The variables  $y_1$  and  $y_2$  we believe parameters. We compute the set of roots of each of  $R_1$  and  $R_2$  polynomials and select them to a subset of real roots. Determine the direct multiplication of the sets of real roots of polynomials. We check each pair of direct multiplication so that it satisfies the system (9). This selection is completely defines the set of solutions of this system. Thus, in the first stage, a solution of (3) we are reduced to the computation of roots of polynomials in one variable. We achieve this by using analytical methods of classical algebraic geometry. In the second stage, we apply approximate methods of calculation. The problem is reduced to the computation of roots of polynomials in one variable over the field of complex numbers.

### 4. The binary lens

The binary lens (in the case of  $N = 2$ ) were studied in many works, see. Eg, (Schneider et al., 1999, Schneider et al., 1986, Asada 2002, Cassan 2008, Witt 1990). To demonstrate the method, we consider the two-point gravitational lens with equal masses  $m_1 = m_2 = 1/2$ . Point masses are on the  $x$  – axis at a distance  $a$  from the origin to (Figure 1).

$$\begin{cases} y_1 = x_1 - \frac{1}{2} \frac{x_1 - a}{(x_1 - a)^2 + x_2^2} - \frac{1}{2} \frac{x_1 + a}{(x_1 + a)^2 + x_2^2} \\ y_2 = x_2 - \frac{1}{2} \frac{x_2}{(x_1 - a)^2 + x_2^2} - \frac{1}{2} \frac{x_2}{(x_1 + a)^2 + x_2^2} \end{cases}. \quad (11)$$

In this case, the system (3) takes the form: We transform the system (11) to (9) and we represent the polynomials  $F_1$  and  $F_2$  in the lexicographical form in ascending powers of the variable  $x_1$ . We have:

$$\begin{cases} F_1 = -y_1(a^4 + 2a^2x_2^2 + x_2^4) + (a^2 - x_2^2 + (a^2 + x_2^2)^2)x_1 + 2y_1(a^2 - x_2^2)x_1^2 + (2x_2^2 - 1 - 2a^2)x_1^3 - y_1x_1^4 + x_1^5, \\ F_2 = (-a^2x_2 - x_2^3 + (a^2 + x_2^2)^2(x_2 - y_2)) - (x_2 + 2(a^2 - x_2^2)(x_2 - y_2))x_1^2 + (x_2 - y_2)x_1^4. \end{cases} \quad (12)$$

With the resultant  $R_1 = R(F_1, F_2)$  exclude from the system (12) variable  $x_1$ . Sylvester matrix  $S_1 = S(F_1, F_2)$  is of the order  $\deg F_1 + \deg F_2 = 9$ . Since

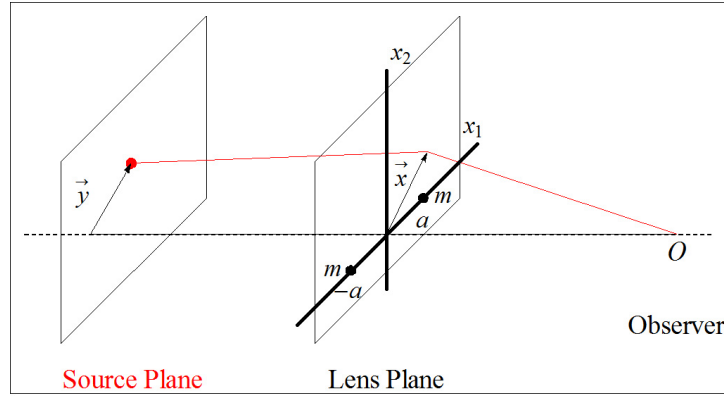


Figure 1: The binary gravitational lens.

$R_1 = \det S_1$ , we have:

$$\begin{aligned}
 R_1(x_2, y_1, y_2) = & 4a^4x_2^2(a^2 + x_2^2)(-a^2y_2^3 - \\
 & -y_2^2(1 - a^2 + 4a^4 + 4a^2y_1^2 + 4a^2y_2^2)x_2 - \\
 & -y_2(4a^2 - 4a^4 + 4a^6 + y_1^2 + 4a^2y_1^2 - \\
 & -8a^4y_1^2 + 4a^2y_1^4 + 5y_2^2 - 4a^2y_2^2 + \\
 & +8a^4y_2^2 + 8a^2y_1^2y_2^2 + 4a^2y_2^4)x_2^2 + \\
 & +(4a^6 - 4a^4 + y_1^2 + 4a^2y_1^2 - 8a^4y_1^2 + \\
 & +4a^2y_1^4 + y_2^2 - 12a^2y_2^2 + 8a^4y_2^2 - 8y_1^2y_2^2 + \\
 & +8a^2y_1^2y_2^2 - 8y_2^4 + 4a^2y_2^4)x_2^3 - \\
 & -4y_2(a^4 - a^2 - y_1^2 - 2a^2y_1^2 + y_1^4 - \\
 & -y_2^2 + 2a^2y_2^2 + 2y_1^2y_2^2 + y_2^4)x_2^4 + \\
 & +4(a^4 + 2a^2(y_2^2 - y_1^2) + (y_1^2 + y_2^2)^2)x_2^5).
 \end{aligned} \tag{13}$$

Similarly calculate the resultant  $R_2$ :

$$\begin{aligned}
 R_2(x_1, y_1, y_2) = & 4a^4x_1^2(a^2 - x_1^2)(-a^2y_1^3 + \\
 & +y_1^2(1 + a^2 + 4a^4 - 4a^2y_1^2 - 4a^2y_2^2)x_1 - \\
 & -y_1(4a^2 + 4a^4 + 4a^6 - 5y_1^2 - 4a^2y_1^2 - \\
 & -8a^4y_1^2 + 4a^2y_1^4 - y_2^2 + 4a^2y_2^2 + \\
 & +8a^4y_2^2 + 8a^2y_1^2y_2^2 + 4a^2y_2^4)x_1^2 + \\
 & +(4a^4 + 4a^6 - y_1^2 - 12a^2y_1^2 - 8a^4y_1^2 + \\
 & +8y_1^4 + 4a^2y_1^4 - y_2^2 + 4a^2y_2^2 + 8a^4y_2^2 + \\
 & +8y_1^2y_2^2 + 8a^2y_1^2y_2^2 + 4a^2y_2^4)x_1^3 + \\
 & +4y_1(a^2 + a^4 - y_1^2 - 2a^2y_1^2 + y_1^4 - \\
 & -y_2^2 + 2a^2y_2^2 + 2y_1^2y_2^2 + y_2^4)x_1^4 - \\
 & -4(a^4 - 2a^2y_1^2 + y_1^4 + 2a^2y_2^2 + 2y_1^2y_2^2 + y_2^4)x_1^5).
 \end{aligned} \tag{14}$$

If there are the coordinates  $y_1$  and  $y_2$  of source, coordinates of images  $x_1$  and  $x_2$  can be calculated in several ways.

The first method. Numerically solve the equations  $R_1(y_1, y_2, x_2) = 0$  and  $R_2(y_1, y_2, x_1) = 0$ . Determine the sets of their roots  $x_1^{(i)}\{x_1^{(1)}, x_1^{(2)} \dots x_1^{(p)}\}$  and  $x_2^{(j)}\{x_2^{(1)}, x_2^{(2)} \dots x_2^{(q)}\}$ , respectively. Select a subsets of real roots. Determine their direct multiplication of. Couples  $(x_1^{(i)}, x_2^{(j)})$  – elements of direct multiplication, substitute into the original system of equations (11). Choose solutions that satisfy the system. It uniquely identifies the set of solutions of the system (11).

The second method. Numerically solve one of the equations (14), such as the first. Calculate the set of its roots  $x_2^{(j)}\{x_2^{(1)}, x_2^{(2)} \dots x_2^{(q)}\}$ . Select a subset of real roots. Each of the real roots substitute into the equation of system (11). Find the solutions  $x_1^{(i)}\{x_1^{(1)}, x_1^{(2)} \dots x_1^{(p)}\}$  that correspond to each of the roots of  $x_2$ .

## 5. Conclusions

In this article we offer a quasi-analytic method of solution of the vector equation  $N$ -point gravitational lens. The method consists of two main stages. Analytical stage, in which we reduce the problem to the solution of systems of polynomial equations, which, in turn, reduce to the problem of finding the roots of polynomials in one variable. The numerical stage, in which we calculate the roots of polynomials in one variable. A complete solution we get when we separate real solutions and we tested them. Thus, our method is both more accurate and faster.

## References

- Blioch P.V., Minakov A.A.: 1989, *Gravitacionnyye linzy*, 240 p.
- Weinberg S.: 1972, *Gravitation and Cosmology*, 696.
- Landau L.D., Lifshitz E.M.: 1988, *The classical Theory of Fields*, **V.2**, 512 p.
- Zakharov A.F.: 1997, *Gravitacionnyye linzy i mikro-linzy*, 328 p.
- Schneider P., Ehlers J., Falco E.E.: 1999, *Gravitational lenses*, 560 p.
- Chwolson O.: 1924, *Astr. Nachrichten.*, **221**, 329.
- Einstein A.: 1936 *Science.*, **2188**, 506.
- Schneider P., Weiss A.: 1986, *Astr. Ap.*, **164**, 237.
- Asada H.: 2002, *Astron. Astrophys.*, **390**, L11.
- Cassan A.: 2008, *Astron. Astrophys.*, **491**, 587.
- Witt H.J.: 1990, *Astron. Astrophys.*, **236**, 311.
- Lang S.: 1965, *Algebra*, 564 p.
- Walker R.J.: 1950, *Algebraic curves*, 236 p.
- Van Der Waerden B.L.: 1971, *Algebra I, II*, 456 p.

DOI: <http://dx.doi.org/10.18524/1810-4215.2016.29.84961>

# X-RAY EMISSION AND ORIENTATION OF SELECTED PF GALAXY CLUSTERS

A.V. Tugay<sup>1</sup>, S.S. Dylida<sup>1</sup>, E.A. Panko<sup>2</sup>

<sup>1</sup> Astronomy and Space Physics Department, Faculty of Physics,  
Taras Shevchenko National University of Kyiv,  
Glushkova ave., 4, Kyiv, 03127, Ukraine, [tugay.anatoliy@gmail.com](mailto:tugay.anatoliy@gmail.com)

<sup>2</sup> Department of Theoretical Physics and Astronomy,  
I.I. Mechnikov Odessa National University,  
Shevchenko Park, Odessa, 65014, Ukraine, [panko.elena@gmail.com](mailto:panko.elena@gmail.com)

**ABSTRACT.** X-ray counterparts for 35 galaxy clusters contained in the PF catalogue of galaxy clusters and groups were found in XMM-Newton archive. 22 ones (all from ACO catalogue) have extended elliptic X-ray haloes appropriate for determination of orientation. Position angles and eccentricities were calculated and compared with cluster orientations optical band.

**Keywords:** Galaxies: clusters; X-rays: galaxies: clusters.

## 1. Introduction

The study of morphology of galaxy clusters is important for understanding the large scale structure of Universe. Orientation of galaxies and clusters may give information about clusterisation and cosmologic evolution. The best way to consider orientation of extragalactic objects is the usage of special large and uniform catalog of galaxy clusters. Clusters are also suitable for orientation analysis in X-ray band because they contain a haloes of hot intergalactic gas.

Since (Binggeli, 1984) orientation of galaxies in clusters was the subject of numerous studies. Orientations of galaxies in 247 rich Abell clusters were studied in detail in Godlowski et al. (2010) and Panko et al. (2013) with corresponding statistical analysis and simulations. Orientation of galaxies from compact sample can be numerically described by the distribution of anisotropy parameter. The parameter was calculated for edge-on galaxies in Parnovsky & Tugay (2007) and for nearby galaxy groups in Godlowski et al. (2012). Orientation of galaxies in nearby groups was studied by Pajowska et al. (2012) too.

## 2. Observational data

Our study in optic band based on PF catalogue of galaxy clusters and groups data. The catalogue contains 6188 structures of southern sky (Panko & Flin, 2006). Orientations and shapes of PF clusters were calculated taking into consideration galaxy 2D locations in the cluster field using the covariance ellipse method (Carter & Metcalfe, 1980; Biernacka et al., 2007). To select PF clusters counterparts in X-rays we used Xgal list of all X-ray extragalactic sources observed by XMM-Newton space observatory (Tugay, 2012). Xgal includes 5021 sources and approximately 30% of them are galaxy clusters. In the current study we found PF clusters counterparts in X-rays, calculated their orientations and eccentricities in X-ray band and compared obtained values with optical data, including the anisotropy signs in distribution of galaxies inside the clusters.

## 3. Method

Cross-correlation of PF and Xgal objects was performed on the base of condition of appearing Xgal source within PF cluster radius. We found 35 Xgal sources counterparts in PF catalogue. To estimate orientation of X-ray halo we selected at XMM images pixels with certain numbers of detected photons (two, three, four etc). Then we approximated each set of pixels with ellipse by the minimal square method and found positional angle  $PA$  and eccentricity  $e$ . We succeeded to find X-ray orientation for 28 Abell clusters (Abell, Corwin & Olowin, 1989) from PF catalog but 6 of them have no appropriate optical orientation. Common results are presented in Table 1. Table 2 shows PF clusters with X-ray sources that are inappropriate for orientation determination by any reason.

Table 1: Orientation and eccentricities of X-ray PF galaxy clusters.

PF	ACO	$PA$	$PA_X$	$e_{PF}$	$e_X$
0004-3606	2717	160	36±17	0.29	0.37±0.08
0009-3469	2721	93	12±6	0.23	0.67±0.02
0022-1954	13	102	57±3	0.13	0.64±0.04
0034-2570	22	174	105±7	0.13	0.58±0.17
0042-3308	S 41	163	118±1	0.14	0.60±0.01
0068-2875	2811	119	65±10	0.24	0.48±0.05
0082-2951	S 84	6	58±11	0.17	0.48±0.06
0104-2195	133	65	16±6	0.09	0.55±0.03
0115-4600	2877	179	41±29	0.17	0.29±0.09
0168-5458	2933	70	22±3	0.08	0.75±0.30
0229-4765	S 239	148	198±8	0.16	0.59±0.06
0329-4427	3112	17	12±1	0.14	0.63±0.02
0350-5258	3128	162	139±5	0.14	0.91±0.05
0370-5364	3158	56	11±6	0.11	0.50±0.05
0480-3720	514	61	35±1	0.20	0.67±0.01
0500-3868	3301	43	69±3	0.08	0.48±0.02
2020-5671	3667	39	31±5	0.13	0.74±0.06
2070-3523	3705	122	115±6	0.29	0.47±0.04
2149-5088	3771	0	148±58	0.13	0.62±0.19
2181-3068	3814	60	16±4	0.17	0.50±0.03
2187-1958	2384	167	104±5	0.29	0.81±0.05
2229-3570	3854	27	57±10	0.29	0.41±0.10

### 3. The general notes on selected clusters

Here are general notes on selected clusters.

A 2717, A 2877, A S 1111. These clusters look like spherical, but for first and second ones we determined  $PA$ .

A 13, A 2811, A O S 84, A S 239, A O 3158, A 3667, A 3771, A 3856. Orientation of cluster core differs from periphery. We didn't determine  $PA$  for A C 3856.

Double clusters: A 2933, A 3128, A 2384.

Faint clusters: A S 41, A 514, A 3301.

A 3705 - a pair of interacting clusters, but  $PA$  was found by X-ray image.

Clusters with undefined orientation or with large differences in optical and X-ray  $PA$  are presented in Table 3.

Except for 22 clusters with both optical and X-ray orientation there are 13 PF clusters with X-ray sources for which it is impossible to compare orientations.

4 point X-ray sources were found within PF clusters. No X-ray haloes of galaxy clusters were detected for these systems.

1. PF 0120-3828. BAX 017.9025-38.1867 cluster. X-ray source 2MASXJ00570192-3806028 galaxy (only 3 references in SIMBAD).

2. PF 0093-2244. MCXC J0056.9-2213 cluster. X-ray source RBS139 Seyfert 1 galaxy.

Table 2: PF clusters with X-ray sources not suitable for comparison of orientation.

PF	ACO	$PA$	$PA_X$	note
0093-2244	MCXC	131	-	point source
0120-3828	BAX	106	-	point source
0263-5237	3038	146	-	point source
0408-3720	new	180	-	point source
0451-6138	3266	106	-	interacting
0532-2498	Snow 20	24	-	point source
2230-3890	3856	-	50±4	diff. orient.
2256-3778	3888	-	166±6	
2277-5266	3911	-	50±4	
2323-4265	S 1101	-	147±1	
2331-4225	S 1111	-	-	spherical
2378-2816	4038	-	32±6	
2395-3453	4059	-	58±5	

3. PF 0263-5237. Abell 3038 cluster. X-ray source ESO 198-24 Seyfert 1 galaxy.

4. PF 0532-2498. Snow 20 cluster (T.Snow, 1970). X-ray source - IC 411 galaxy (9 references).

PF 0408-3720 cluster was unknown in previous works. In the region of this cluster we found ESO 359-19 Seyfert 1 galaxy.

A 3266 - complex system of interacting clusters inappropriate for orientation estimation in X-rays.

7 PF clusters (bottom of Table 2) have no anisotropy

Table 3: Notes on large differences in orientation. Most of such clusters has near-spherical X-ray halo. Optical orientation of last 5 clusters can not be determined because of their diffuse structure.

PF	ACO	$PA$	$PA_X$	$e_X$
0034-2570	22	174	$105\pm 7$	0.13
0042-3308	S 41	163	$118\pm 1$	0.14
0068-2875	2811	119	$65\pm 10$	0.24
0229-4765	S 239	148	$198\pm 8$	0.16
0350-5258	3128	162	$139\pm 5$	0.14
0500-3868	3301	43	$69\pm 3$	0.08
2070-3523	3705	122	$115\pm 6$	0.29
2149-5088	3771	0	$148\pm 58$	0.13
2187-1958	2384	167	$104\pm 5$	0.29
2230-3890	3856	-	$50\pm 4$	differs
2256-3778	3888	-	$166\pm 6$	
2277-5266	3911	-	$50\pm 4$	
2323-4265	S 1101	-	$147\pm 1$	
2395-3453	4059	-	$58\pm 5$	

signs in optical band, according to Panko (2013) criteria, so we excluded them from comparison with X-ray data. Specifically, A 3856 shows different orientation of the core and periphery of X-ray halo; A 1111 has spherical halo; other clusters include A 1101, A 3888, A 3911, A 4038 and A 4059.

#### 4. Results and conclusion

Analysis of Table 1 shows that  $PA$  tend to correlate. Eccentricity is larger in X-rays because visible hot gas halo lies close to the center of cluster in the region of larger potential. The correlation of orientation in two bands leads to issue that galaxies and gas halo in clusters are involved in significant gravitational interaction but the processes of cluster evolution continue in the current cosmological era.

*Acknowledgements.* This research has made use of NASA's Astrophysics Data System.

#### References

- Abell G.O., Corwin H.G., Olowin R.P.: 1989, *ApJS*, **70**, 1.
- Biernacka M., Flin P., Panko E., Juszczyk T.: 2007, *Odessa Astron. Publ.*, **20**, 26.
- Binggeli B.: 1984, *A&A*, **107**, 338.
- Carter D., Metcalf, N.: 1980, *MNRAS*, **191**, 325.
- Godlowski W., Piwowarska P., Panko E., Flin P.: 2010, *ApJ*, **723**, 985.
- Godlowski M., Panko E., Pajowska P., Flin P.: 2012, *JPhSt.*, **16**, 3901.
- Pajowska P., Godlowski M., Panko E., Flin P.: 2012, *JPhSt.*, **16**, 4901.
- Panko E.A.: 2013, *Odessa Astron. Publ.*, **26**, 90.
- Panko E., Flin P.: 2006, *JAD.*, **12**, 1.
- Panko E., Piwowarska P., Godlowska J., Godlowski W., Flin P.: 2013, *Ap.*, **56**, 322.
- Parnovsky S., Tugay A.: 2007, *JPhSt.*, **11**, 366.
- Tugay A.V.: 2012, *Odessa Astron. Publ.*, **25**, 142. <http://arxiv.org/abs/1311.4333>.

DOI: <http://dx.doi.org/10.18524/1810-4215.2016.29.85268>

# NO THE HOLMBERG EFFECT FOR GALAXY PAIRS SELECTED FROM THE SDSS DR9 AT $Z \leq 0.06$

D.V. Dobrycheva, I.B. Vavilova

Main Astronomical Observatory of the National Academy of Sciences of Ukraine  
*daria@mao.kiev.ua, irivav@mao.kiev.ua*

**ABSTRACT.** We studied the Holmberg effect in galaxy pairs selected from the SDSS DR9, where 60561 galaxies were limited by redshift  $0.02 < z < 0.06$  and absolute magnitude:  $M_r \leq -20.7^m$  for central galaxies (N=18578) and  $M_r > -21.5^m$  for neighbor galaxies (N=41983). We have made a morphological classification for each galaxy using both the visual inspection and machine learning methods. We considered four morphological types of galaxy pairs (E, early, and L, late, types) for testing the Holmberg effect: E-E, E-L, L-E, L-L (first companion of pairs is a central galaxy and second one is a faint satellite galaxy). We concluded about the absence of the Holmberg effect:  $R_{g-i} = 0.3$  for L-E pairs at  $0.04 < z \leq 0.06$  and  $R_{g-i} = 0.2$  for E-E and E-L pairs at  $0.02 \leq z \leq 0.04$ .

Summarizing, a correlation of color indices in pairs for the samples of galaxies composed with the half of large sky surveys likely SDSS was not confirmed or confirmed partially. The Holmberg effect is rather connected with morphological types of galaxies than with their color indices. Taking into account a scenario of the secular evolution, the presence of at least one elliptical galaxy in pair may be indicator of previous mergers in the earlier epoch. So, figuring manifestations of the Holmberg effect in its original interpretation no longer seems such urgent.

**Keywords:** galaxies: color indices.

## 1. Introduction

In 1958, Holmberg has found a color indices (B-V) dependence for 32 pairs of galaxies with a correlation coefficient of  $R = +0.80 \pm 0.6$  using the difference in the radial velocity of pair components  $\Delta V \leq 250$  km/s as a selection criteria (Holmberg, 1958). Later on such a correlation of color indices in the close paired galaxies was called the ‘‘Holmberg effect’’ and tested many times for different galaxy samples. The interest to this effect is caused that it may be explained as a tendency to have similar morphological types for galaxies, which are evolving together.

We note below several results obtained in 1980-2000

before the era of big data, which were in favor of this effect. Tomov (1979) has obtained (B-V) and (U-B) color indices for 105 pairs of galaxies from RC2 Catalog by de Vaucouleurs and confirmed the effect. Then, Demin et al. (1984) have continued work with this sample and found a ‘‘color indices - morphological types’’ relation for pairs with a different morphological types of galaxies (E - elliptical, S - spiral) with correlation coefficients  $R_{B-V(U-B)} \sim 0.7 - 0.8$  for E-E and S-S pairs,  $R_{B-V(U-B)} \sim 0.5 - 0.6$  for E-S pairs. Reshetnikov (1998) in his work with a sample of 24 interacting galaxies selected from the catalogs by Arp, by Vorontsov-Velyaminov, and by Karachentsev (issued in 1966, 1959, and 1972, respectively) obtained  $R_{B-V(U-B)} \sim 0.8 - 0.9$ . Hernandez-Toledo et al. (2001) for a sample of 45 S-S paired galaxies from the catalog by Karachentsev of 1972 year have resulted as  $R_{B-V} = 0.77$ .

One of the explanation of such a linear correlation for pairs with different morphological composition was that the evolution of galaxies in pairs is occurring in parallel under the influence of a common gravitational interaction and mutual gas dynamic processes over several billion years (Karachentsev, 1987) and can provide, for example, the periodic bursts in S-S pairs from starforming regions originating simultaneously in both components (Demin, 1984).

It is important to emphasize that in those years the data on the radial velocities were sparsed as well as only several dozens gravitationally connected galaxy pairs were known. The selection criteria were based on the two-dimensional projected sky separation and galaxy diameter. For example, when later on, Franco-Balderas et al. (2003, 2004) reexamined a morphological classification of galaxy pairs from the Karachentsev’s catalog and remeasured their photometric parameters, they obtained that the Holmberg effect is a very weak or entirely absent for these objects.

The era of big data and surveys likely SDSS allowed us to compile more wider samples of galaxies with a good quality photometric and spectroscopic properties. Looking ahead, we say that significant correlations of the color indices for galaxies in pairs were not found in studies of samples from the SDSS survey.

Table 1: Correlation coefficients, R, of color indices ( $M_g - M_i$ ) of galaxies in pairs from SDSS DR9 sample

Morph. type	Sub-sample	N pairs	R, SDSS pairs	R, random pairs
L-L	1	35	0.05	0.006
	2	87	0.17	0.00001
L-E	1	24	0.02	0.007
	2	62	0.3	0.003
E-E	1	174	0.2	0.0001
	2	289	0.05	0.001
E-L	1	106	0.2	0.001
	2	229	0.15	0.006

In this work we examine the presence of Holmberg effect both for a new sample of galaxy pairs selected from SDSS DR9 at  $z \leq 0.1$  by the three-dimensional Voronoi tessellation method (Dobrycheva, 2015) and for several aforementioned samples of galaxies, for which we updated their color indices by reducing to the SDSS colorimetry. These results are presented in Section 2 and 3, respectively. Their comparison with results obtained for others SDSS samples and concluding remarks are given in Section 4.

## 2. The Holmberg effect verification for the paired galaxies from SDSS DR9

### 2.1. The sample of galaxy pairs from SDSS DR9

The studied sample of paired galaxies selected from SDSS DR9 is described in our papers (Dobrycheva, 2013; Dobrycheva et al., 2015). It is consisted of  $N = 60561$  galaxies with redshifts  $0.02 \leq z \leq 0.06$  and absolute magnitudes  $-24^m \leq M_r \leq -19.4^m$ . We determined the absolute magnitudes as follows:

$$M_r = m_r - 5 * \lg(D_L) - 25 - ext_r - K(z)_r,$$

where  $m_r$  - visual magnitude in  $r$  band,  $D_L$  - distance luminosity,  $ext_r$  - the Galactic absorption in  $r$  band by Schlegel et al. (1998),  $K(z)_r$  - k-correction in  $r$  band according to Chilingarian et al. (2010, 2012). We determined the color indices using the following formulas:

$$M_g - M_i = (m_g - m_i) - (ext_g - ext_i) - (K(z)_g - K(z)_i),$$

where  $m_g$  and  $m_i$  - visual magnitude in  $g$  and  $i$  band;  $ext_g$  and  $ext_i$  - the Galactic absorption in  $g$  and  $i$  band;  $K(z)_g$  and  $K(z)_i$  - k-correction in  $g$  and  $i$  band, respectively.

We divided the studied sample into subsamples of the central galaxies ( $M_r \leq -20.7^m$ ,  $N=18578$ ) and their neighbors ( $-20.7^m < M_r \leq -19.4^m$ ,  $N=41983$ ) (see Figure 1). We applied the 3D Voronoi tessellation method (Elyiv et al., 2009)) to identify galaxy paired systems as “the central galaxy - the closest neigh-

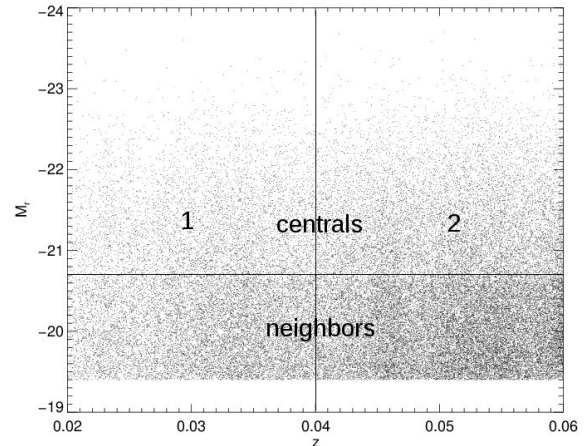


Figure 1: The absolute magnitude of galaxies as a function of redshift for central galaxies ( $N=18578$ ) and their neighbors ( $N=41983$ ) selected from SDSS DR9 at  $0.02 \leq z \leq 0.06$ .

bor” determining a distance between the components up to 100 kpc. Such approach allowed us to consider the central galaxies from the central sample as the cores of the Voronoi cell, whereas the neighbors as the galaxies, which hit in the field of the Voronoi cell, from the neighbors sample. To study the Holmberg effect we divided our sample into two subsamples by redshift:

- 1)  $0.02 \leq z < 0.04$ ,  $M_r \leq -20.7^m$ ;
- 2)  $0.04 < z \leq 0.06$ ,  $M_r \leq -20.7^m$  (Figure 1).

### 2.2. Verification of the Holmberg effect

We calculate the correlation coefficients, R, between color indices  $M_g - M_i$  for central galaxy and the nearest neighbor (up to 100 kpc between components) for the aforementioned galaxy sample. The relationships for pairs with different morphological composition are presented in Figure 3, 4, where the first symbol (E-E, E-L, S-S, S-L) indicates the type of central galaxy. We compared these results with those for pairs, where one galaxy was taken from a sample of central galaxies and other one was selected randomly from a sample of the nearest neighbors. Repeating this procedure 100 times for random choice of color indices ( $M_g - M_i$ ) of neighbor galaxy, we determined the average value. The obtained results are given in Table 1, where column 1 represents morphological types of galaxies in pair; column 2 - index number of subsamples (see Section 2.1 and Figure 1); N - number of pairs; R, SDSS pairs, and R, random pairs, are the correlation coefficients by Kolmogorov-Smirnov test for galaxy pairs from SDSS and random galaxy pairs,

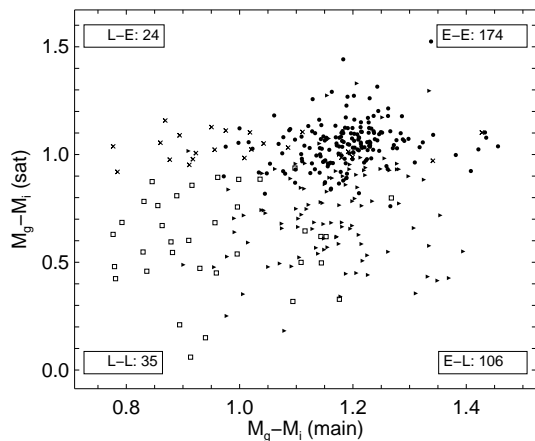


Figure 2: Relationships of color indices ( $M_g - M_i$ ) for the components of galaxy pairs from SDSS DR9 (sub-sample 1 from Figure 1). The abscissa corresponds to the component of a pair with bigger color indices.

respectively. One can see that there is no correlation between color indices in the studied galaxy pairs, for example, even the biggest values of coefficients are  $R_{g-i} = 0.3$  for L-E pairs at  $0.04 < z \leq 0.06$  and  $R_{g-i} = 0.2$  for E-E and E-L pairs at  $0.02 \leq z \leq 0.04$ .

### 3. The Holmberg effect verification for the paired galaxies from other samples

#### 3.1. The updated galaxy sample by Tomov, which is cross-matched with SDSS DR13

We inspected the sample of galaxy pairs by Tomov (1979) reducing their data to the SDSS DR13. First of all, we determined for 69 pairs of galaxies (after cross-matching) their morphological types visually by the SDSS Navigate tools using the simplest scheme into E (early) type, which includes E, S0, S0a types, and L (late), which includes types from Sa to Irr. We used NED (NASA/IPAC Extragalactic Database) for updating radial velocity for all galaxies. We remind that Demin (1981), when analyzing this sample, has proposed a criterion for physical pair based on the difference of the radial velocities of components: it does not exceed a value of  $V \leq 300$  km/s. Using this criterion we excluded 17 optical pairs of galaxies. The absolute magnitudes  $M_r$  and color indices  $M_g - M_i$  for the rest of 104 galaxies were redetermined according to the formulas described in Section 2.1. As a result, these pairs of galaxies have  $0.0009 < z < 0.04$ ; relationships of color indices ( $M_g - M_i$ ) for galaxies of L-L, L-E, E-E, E-L pairs are illustrated in Figure 4.

Finally, after taking into account the confidence

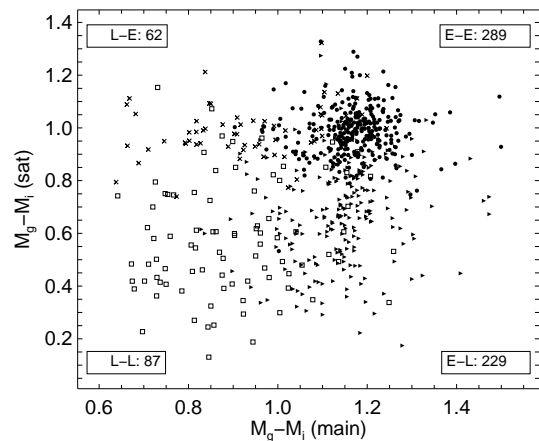


Figure 3: Relationships of color indices ( $M_g - M_i$ ) for the components of galaxy pairs from SDSS DR9 (sub-sample 2 from Figure 1). The abscissa corresponds to the component of a pair with bigger color indices.

Table 2: Correlation coefficients for color indices ( $M_g - M_i$ ) of 34 galaxy pairs from sample by Tomov (1979), which are reduced and cross-matched with SDSS DR13 data

Type of pairs	N pairs	R, Tomov's pairs	R, random pairs
L-L	16	0.30	0.02
L-E	0	0	0.01
E-E	15	0.48	0.07
E-L	3	0.52	0.01

interval and relationships of color indices ( $M_g - M_i$ ), the galaxy sample by Tomov, which is cross-matched with SDSS DR13, contained 34 pairs. We determined the correlation coefficients for color indices in the same way as for our sample of paired galaxies from SDSS DR9. One can see (Table 2) that its biggest value is  $R_{g-i} \sim 0.5$  for E-E and E-L pairs and this is not in favor of the presence of the Holmberg effect due to a weak statistics and significance level.

#### 3.2. The Catalog of galaxy pairs in the Local Supercluster, which is cross-matched with SDSS DR13

We have taken the Catalog of pairs of galaxies in the Local Supercluster (Karachentsev et al., 2008) to test the Holmberg effect. This catalog contains 509 pairs with line-of-sight velocities  $V_{LG} < 3500$  km/s. The component line-of-sight velocity differences and projected distances of the double systems have power-law distributions with the median values of 35 km/s and 123 kpc, respectively. We cross-matched

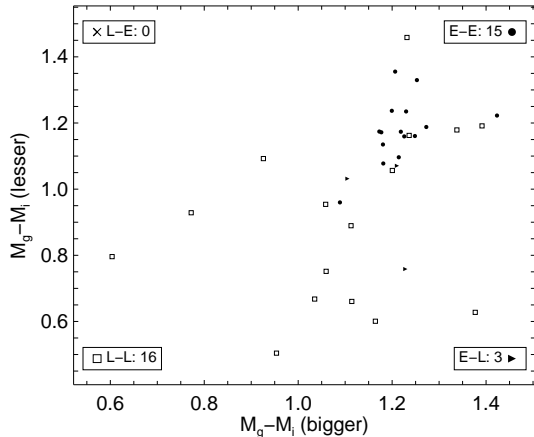


Figure 4: Relationships of color indices ( $M_g - M_i$ ) for the components of physical pairs of galaxies from Tomov's sample (1979) within confidence interval. The abscissa corresponds to the component of a pair with bigger absolute magnitude.

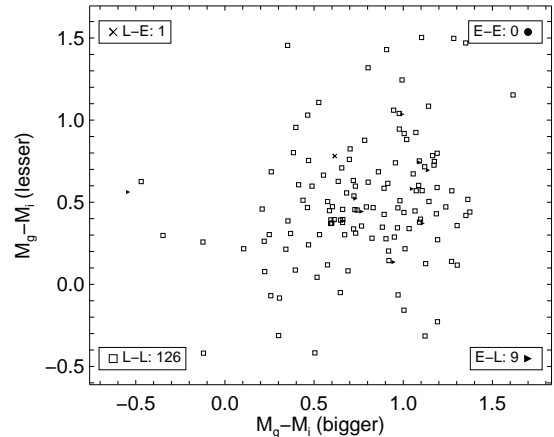


Figure 5: Relationships of color indices ( $M_g - M_i$ ) within confidence interval for the components of galaxy pairs in the Local Supercluster (Karachentsev et al., 2008), which are cross-matched with SDSS DR13. The abscissa corresponds to the component of a pair with bigger absolute magnitude.

Table 3: Correlation coefficients for color indices ( $M_g - M_i$ ) of 136 galaxy pairs in the local Supercluster, which are reduced and cross-matched with SDSS DR13 data

Type of pairs	N pairs	R, LS pairs	R, random pairs
L-L	126	0.26	0.002
L-E	1	-	0.005
E-E	0	-	-
E-L	9	0.07	0.04

this catalog with SDSS DR13 data and turned out that SDSS DR13 covers only 242 from 509 galaxy pairs. We used NED (NASA/IPAC Extragalactic Database) for updating radial velocity of galaxies. The morphological types for each galaxies were determined by the authors of this catalog, we grouped only them onto early (E) and late (L) types. The absolute magnitudes  $M_r$  and color indices  $M_g - M_i$  for 484 galaxies were calculated as it is described in Section 2.1. After determination of relationships of color indices ( $M_g - M_i$ ) between components of pairs and taking into account the confidence interval, we obtained 136 pairs (see Table 3 and Figure 5). One can see that there is no correlation of color indices, the biggest value of correlation coefficient is  $R_{g-i} \sim 0.26$  for L-L galaxy pairs.

#### 4. Discussion and concluding remarks

The SDSS has allowed to examine the Holmberg effect based on the high quality colorimetry.

Allam et al. (2004) using 1479 merging pairs from SDSS (Stoughton et al., 2002) found that the level of significance of the correlation apparently depends on the color indices: the highest ( $> 12\sigma$ ) for the  $g-r$  (closest SDSS analog to B-V) and the lowest ( $< 2\sigma$ ) for the  $i-z$  color indices. They obtained  $R_{g-r} = 0.38 \pm 0.03$  for galaxies in pairs and explained a weak correlation in terms of random star formation in merging systems. Deng et al. (2008) investigated the Holmberg effect for the Main galaxy pairs of the SDSS DR4 (Adelman-McCarthy et al., 2006) and found that except for  $i-z$  color the color indices between two components of the Main galaxy pairs have larger correlation coefficient. They have noticed weak tendencies indicating the Holmberg effect and absence of the significant dependences. But it is noteworthy that the Luminous Red Galaxy pair sample (Eisenstein et al., 2001) does not exhibit a statistically significant Holmberg effect.

Summarizing, we may note that for the samples of galaxies composed with the half of large sky surveys likely SDSS, this effect was not confirmed (Franco-Balderas et al., 2003; 2004; Allam et al., 2004; Melnyk et al., 2012; Dobrycheva et al., 2015) or confirmed partially/low significance level (Deng et al., 2008, 2010). In this work we verified the Holmberg effect with the sample of about 1000 paired galaxies selected from SDSS DR9 at  $z < 0.06$  and not found a correlation between their  $g-i$  color indices. This effect in the modern interpretation is rather connected with morphological types of galaxies than with their color indices.

In accordance with the hierarchical scenario of structure formation and the important role of small and

large interactions, the elliptical galaxies could be formed by the merger of late-type galaxies. The well-known relation “morphology-density” (Kauffmann et al., 2004; Tinker et al., 2013; Kovac et al., 2014; Wetzel, 2014), which manifests itself even on the scale of small groups (Karatsentsev, 1987; Melnyk et al., 2006; Vavilova et al., 2009; Melnyk et al., 2012; Dobrycheva et al., 2015) testifies to this. It is known also the observational asymmetry in distribution of the early-type galaxies from large to low redshifts (Baldry et al., 2014; Cucciati et al., 2006; Tal et al., 2014). In other words, the presence of at least one elliptical galaxy in the pair may be indicator of previous mergers in the earlier epoch. So, figuring manifestations of the Holmberg effect in its original interpretation no longer seems such urgent.

Following the link below you will get access to the studied sample of galaxies ( $0.02 < z < 0.04$ ) selected from the SDSS DR9 and described in Section 2.1 of this paper: [ftp.mao.kiev.ua/pub/astro/cats/galaxies/gal\\_sam\\_SDS\\_SDR9\\_z\\_from\\_0.02\\_to\\_0.06.csv](ftp.mao.kiev.ua/pub/astro/cats/galaxies/gal_sam_SDS_SDR9_z_from_0.02_to_0.06.csv).

Following the link below you will get access to the complete sample of galaxies at  $z < 0.1$  selected from the SDSS DR9 and described in papers by Dobrycheva (2013) and Dobrycheva et al. (2015): [ftp.mao.kiev.ua/pub/astro/cats/galaxies/gal\\_sam\\_SDS\\_SDR9\\_z\\_to\\_0.1.csv](ftp.mao.kiev.ua/pub/astro/cats/galaxies/gal_sam_SDS_SDR9_z_to_0.1.csv).

*Acknowledgments.* We thank the scientific group working on the Sloan Digital Sky Survey <http://www.sdss3.org>. Funding from SDSS-III has been provided by the Alfred P. Sloan Foundation and the U.S. Dept. of Energy Office of Science. This work was partially supported in frame of the Target Program of the Scientific Space Research of the NAS of Ukraine.

## References

- Adelman-McCarthy J.K., Agueros M.A., Allam S.S. et al.: 2006, *ApJ*, **162**, 38.
- Allam D. Tucker Smith et al.: 2004, *ApJ*, **127**, 1883.
- Baldry I.K., Glazebrook K., Brinkmann J. et al.: 2004, *ApJ*, **600**, 681.
- Chilingarian I., Melchior A.-L., Zolotukhin I.: 2010, *MNRAS*, **405**, 1409.
- Chilingarian I., Zolotukhin I.: 2012, *MNRAS*, **419**, 1727.
- Cucciati O., Iovino A., Marinoni C. et al.: 2006, *A&A*, **458**, 39.
- Demin V.V., Dibai E.A., Tomov A.N.: 1981, *AZh*, **582**, 925.
- Demin V.V., Zasov A.N., Dibai E.A. et al.: 1984, *AZh*, **61**, 625.
- Deng X.-F., He J.-Z., Jiang P. et al.: 2008, *ApJ*, **677**, 1040.
- Deng X.-F., Xin Y., Peng J., Wu P.: 2010, *Ap*, **53**, 342.
- Deng X.-F., He J.-Z., Wen X.-Q. et al.: 2008, *ChJPh*, **46**, 517.
- Dobrycheva D.: 2013, *Odessa Astron. Publ.*, **26/2**, 187.
- Dobrycheva D.V., Melnyk O.V., Vavilova I.B., Elyiv A.A.: 2015, *Ap*, **58**, 168.
- Eisenstein D.J., Annis J., Gunn J.E. et al.: 2001, *AJ*, **122**, 2267.
- Elyiv A., Melnyk O., Vavilova I.: 2009, *MNRAS*, **394**, 1409.
- Franco-Balderas A., Hernandez-Telode H.M., Dultzin-Hacyan D. et al.: 2003, *A&A*, **367**, 1029.
- Franco-Balderas A., Hernandez-Telode H.M., Dultzin-Hacyan D. et al.: 2004, *A&A*, **417**, 411.
- Hernandez-Toledo H.M., Puerari I.: 2001, *A&A*, **379**, 54.
- Holmberg E.: 1958, *Lund Medd. Astron. Obs. Ser. II*, **136**, 103.
- Karachentsev I.D., Makarov D.I.: 2008, *AstBu*, **63**, 299.
- Karachentsev I.D.: 1987, *Double galaxies, Moscow: Nauka*, 280.
- Kauffmann G., White S.D.M., Heckman T.M. et al.: 2004, *MNRAS*, **353**, 713.
- Kovac K., Lilly S.J., Knobel C. et al.: 2014, *MNRAS*, **438**, 717.
- Melnyk O.V., Elyiv A.A., Vavilova I.B.: 2006, *KFNT*, **22**, 283.
- Melnyk O.V., Dobrycheva D.V., Vavilovav I.B.: 2012, *Ap* **55**, 293.
- Reshetnikov V. P.: 1998, *AstL*, **24**, 153.
- Schlegel D.J., Funkbeiner D.P., Davis M.: 1998, *ApJ*, **500**, 525.
- Stoughton C., Lupton R.H., Bernardi M. et al.: 2002, *AJ*, **123**, 485.
- Tal T., Dekel A., Oesch P. et al.: 2014, *ApJ*, **789**, 164.
- Tinker J.L., Leauthaud A., Bundy K. et al.: 2013, *ApJ*, **778**, 93.
- Tomov A.N.: 1979, *Candidate's dissertation*.
- Vavilova I.B., Melnyk O.V., Elyiv A.A.: 2009, *Astron. Nachr.*, **330**, 1004.
- Wetzel A.R., Tinker J.L., Conroy C. et al.: 2014, *MNRAS*, **439**, 2687.

DOI: <http://dx.doi.org/10.18524/1810-4215.2016.29.84962>

# THE SOLUTION OF THE COSMOLOGICAL CONSTANT PROBLEM AND THE FORMATION OF THE SPACE-TIME CONTINUUM

Aleksandr V. Bukalov

The Centre for Physical and Space Research, International Institute of Socionics,  
Melnikova str., 12, Kyiv-050, 04050, Ukraine, [bukalov.physics@socionic.info](mailto:bukalov.physics@socionic.info)

**ABSTRACT.** The application of the microscopic theory of superconductivity to describe the early Universe makes it possible to solve the problem of dark energy. In the cosmological models with superconductivity (CMS) this problem is solved in a natural way: dark energy is the result of pairing of primary fermions with the Planck mass, and its calculated density is equal to  $6 \cdot 10^{-30} \text{ g/cm}^3$  and is in good agreement with data of PLANK collaboration. At the same time the birth of space-time domains can also be described in the proposed model. Characteristic parameters of interaction of primary fermions determine the changes of the scale and values of different, but conjugate with each other, phase transitions – for the dark energy, the observed evolving Universe and other component of the condensate of primary fermions.

**Keywords:** gravity, superfluid gas, fermions, evolution of the universe, dark energy, vacuum energy.

## 1. Introduction

It was provided a number of approaches for solve the problem of the cosmological constant and dark energy (Weinberg, 1989). Previously we described the process of formation of dark energy as a condensate of primary fermions, by analogy with the theory of superconductivity by Bardeen-Cooper-Schrieffer (BCS) (Bardeen, Cooper & Schrieffer, 1957). The vacuum was regarded as an analogue of a crystal at Planck distances (Fomin, 1990). However, we can consider the more general problem of the formation of Bose condensate from Fermi gas, which gives better understanding of the dark energy nature and a new approach to solving the problem of the cosmological constant and dark energy. At the present time the dark energy manifests itself as anti-gravity, not only on a cosmological scale, but on the scale of galaxy groups (Karachentsev et al., 2009; Bisnovatyi-Kogan & Chernin, 2012; Chernin et al., 2013; Eingorn & Zhuk, 2012; Brienkov, Eingorn & Zhuk, 2015; Bukalov, 2015).

## 2. The energy spectrum of the superfluid gas and density of dark energy

Let us consider the degenerate almost ideal Fermi gas with attraction between the particles, which are the primary fermions with a mass close to the Planck mass:  $M \approx M_p$ . It is well known, that even in the presence of an arbitrarily

weak attraction between the particles, the ground state of the system is unstable respect to the restructuring, changing whole system and lowering its energy (Bardeen, Cooper & Schrieffer, 1957; Pitaevskii & Lifshitz, 1980). This instability arises from the Cooper effect, i.e. aspiration to the formation of bound states of fermions pairs that are in the  $p$ -space near the Fermi surface and have momenta equal in direction and antiparallel spins. For consideration of this problem, following to (Pitaevskii & Lifshitz, 1980), we introduce the Bogolyubov transformation of the operators, which bring together the operators of the particles with opposite momenta and spins:

$$\hat{b}_{p^-} = u_p \hat{a}_{p^-} + v_p \hat{a}_{-p,+}^+, \quad \hat{b}_{p^+} = u_p \hat{a}_{p^+} - v_p \hat{a}_{-p,-}^+ \quad (1)$$

The indexes + and – refer to the two values of the spin projection. With gas isotropy the coefficients  $u_p$ ,  $v_p$  can depend only on the absolute value of the momentum  $p$ . The operators comply with the creation and annihilation of quasiparticles on condition:

$$\hat{b}_{p\alpha}^+ \hat{b}_{p\alpha}^+ + \hat{b}_{p\alpha}^+ \hat{b}_{p\alpha}^- = 1, \quad (2)$$

where the index  $\alpha$  numbers the two values of the spin projection. Other pairs of operators are anticommutative. Therefore, the transform coefficients are imposed a condition:

$$u_p^2 + v_p^2 = 1. \quad (3)$$

The transformation inverse to (1) takes the form

$$\hat{a}_{p^-} = u_p \hat{b}_{p^-} + v_p \hat{b}_{-p,-}^+, \quad \hat{a}_{p^+} = u_p \hat{b}_{p^+} - v_p \hat{b}_{-p,+}^+ \quad (4)$$

Due to the primary role of the interaction between pairs of particles with opposite momenta and spins we write only the Hamiltonian with the members, in which  $p_1 = -p_2 \equiv p$ ,  $p'_1 = -p'_2 \equiv p'$ . It is following:

$$\hat{H} = \sum_{p\alpha} \frac{p^2}{2m} \hat{a}_{p\alpha}^+ \hat{a}_{p\alpha} - \frac{g}{V} \sum_{pp'} \hat{a}_{p^+}^+ \hat{a}_{-p'}^+ \hat{a}_{-p,-}^- \hat{a}_{p^+}^-, \quad (5)$$

where  $g = 4\pi\hbar^2 |b|/m$  is a “coupling constant”,  $b < 0$  is the scattering length.

For the account of constancy of the number of particles in the system a new Hamiltonian is introduced as a difference  $\hat{H}' = \hat{H} - \mu \hat{N}$ , where  $\hat{N} = \sum_{p\alpha} \hat{a}_{p\alpha}^+ \hat{a}_{p\alpha}$  is a particle

number operator. In this case the chemical potential is determined by the condition that the average value  $\bar{N}$  is equal to a given number of particles in the system (Pitaevskii & Lifshitz, 1980).

Introducing  $\eta_p = p^2 / 2m - \mu$  and  $\mu \approx p_F^2 / 2m$ , we get near the Fermi surface  $\eta_p = v_F(p - p_F)$ , where  $v_F = p_F / m$ . Subtract  $\mu \hat{N}$  from the expression (5). Then

$$\hat{H}' = \sum_{p\alpha} \eta_p \hat{a}_{p\alpha}^+ \hat{a}_{p\alpha} - \frac{g}{V} \sum_{pp'} \hat{a}_{p'+}^+ \hat{a}_{-p'}^+ \hat{a}_{-p,-} \hat{a}_{p+}. \quad (6)$$

Making the transformation (4) with (2) and (3) and replacing  $p$  by  $-p$ , we get

$$\begin{aligned} \hat{H}' = & 2 \sum_p \eta_p v_p^2 + \sum_p \eta_p |u_p^2 - v_p^2| |\hat{b}_{p+}^+ \hat{b}_{p+} + \hat{b}_{p-}^+ \hat{b}_{p-}| + \\ & + 2 \sum_p \eta_p u_p v_p |\hat{b}_{p+}^+ \hat{b}_{-p,-}^+ + \hat{b}_{-p,+}^+ \hat{b}_{p+}| - \frac{g}{V} \sum_{pp'} \eta_p \hat{B}_p^+ \hat{B}_{p'}^+, \end{aligned} \quad (7)$$

$$\hat{B}_p = u_p^2 \hat{b}_{-p,-}^+ \hat{b}_{p+}^+ - v_p^2 \hat{b}_{p+}^+ \hat{b}_{-p,-}^+ + v_p u_p |\hat{b}_{-p,-}^+ \hat{b}_{-p,-}^+ - \hat{b}_{p+}^+ \hat{b}_{p+}^+|.$$

The choice of the coefficients  $u_p$ ,  $v_p$  can be carried out from the condition of minimum energy  $E$  of the system at a given entropy. The entropy is determined by the combinatorial expression (Pitaevskii & Lifshitz, 1980):

$$S = - \sum_{p\alpha} [n_{p\alpha} \ln n_{p\alpha} + (1 - n_{p\alpha}) \ln(1 - n_{p\alpha})].$$

In the Hamiltonian (7) diagonal matrix elements have only members, containing products  $\hat{b}_{p\alpha}^+ \hat{b}_{p\alpha} = n_{p\alpha}$ ,  $\hat{b}_{p\alpha}^+ \hat{b}_{p\alpha}^+ 1 - n_{p\alpha}$ . Therefore, we find

$$\begin{aligned} E = & 2 \sum_p \eta_p v_p^2 + \sum_p \eta_p |u_p^2 - v_p^2| |n_{p+} + n_{p-}| - \\ & - \frac{g}{V} \left[ \sum_p u_p v_p (1 - n_{p+} - n_{p-}) \right]^2. \end{aligned} \quad (8)$$

Varying this expression on the parameters  $u_p$  (taking into account the relation (3)), we obtain as the condition for the minimum

$$\begin{aligned} \frac{\delta E}{\delta u_p} = & - \frac{2}{v_p} (1 - n_{p+} - n_{p-}) \left[ 2 \eta_p u_p v_p - \right. \\ & \left. - \frac{g}{V} (u_p^2 - v_p^2) \sum_{p'} u_{p'} v_{p'} (1 - n_{p'+} - n_{p'-}) \right] = 0. \end{aligned}$$

Hence, we find the equation

$$2 \eta_p u_p v_p = \Delta (u_p^2 - v_p^2), \quad (9)$$

where  $\Delta$  is the sum of:

$$\Delta = \frac{g}{V} \sum_p u_p v_p (1 - n_{p+} - n_{p-}). \quad (10)$$

From (9) and (3) we express  $u_p$ ,  $v_p$  via  $\eta_p$  and  $\Delta$ :

$$\left. \begin{aligned} u_p^2 \\ v_p^2 \end{aligned} \right\} = \frac{1}{2} \left( 1 \pm \frac{\eta_p}{\sqrt{\Delta^2 + \eta_p^2}} \right). \quad (11)$$

Substituting these values in the (10), we obtain an equation that determines  $\Delta$ :

$$\frac{g}{2V} \sum_p \frac{1 - n_{p+} - n_{p-}}{\sqrt{\Delta^2 + \eta_p^2}} = 1.$$

In equilibrium, the occupation numbers of quasiparticles does not depend on the spin direction and are given by the Fermi distribution with zero chemical potential:

$n_{p+} = n_{p-} \equiv n_p = [e^{\varepsilon/T} + 1]^{-1}$ . Going also from summation to integration over  $p$ -space, we can write this equation in the form

$$\frac{g}{2} \int \frac{1 - 2n_p}{\sqrt{\Delta^2 + \eta_p^2}} \frac{d^3 p}{(2\pi\hbar)^3} = 1. \quad (12)$$

When  $T = 0$  quasiparticles are absent,  $\Delta = \Delta_0$ , so that  $n_p = 0$  and the equation (12) takes the form

$$\frac{g}{2(2\pi\hbar)^3} \int \frac{4\pi p^2 dp}{\sqrt{\Delta_0^2 + \eta_p^2}} = 1. \quad (13)$$

The main contribution to the integral in (13) comes from momentum range, in which  $\Delta_0 \ll v_F |p_F - p| \ll v_F p_F \sim \mu$  and the integral is logarithmic ( $\Delta_0$  is small in comparison with  $\mu$ , that confirmed by the result). After cutting the logarithmic integral for  $\eta = \tilde{\varepsilon} \sim \mu$  we obtain

$$\int \frac{p^2 dp}{[\Delta_0^2 + v_F^2 (p_F - p)^2]^{1/2}} \approx \frac{p_F^2}{v_F} \int \frac{d\eta}{(\Delta_0^2 + \eta^2)^{1/2}} \approx \frac{2p_F^2}{v_F} \ln \frac{\tilde{\varepsilon}}{\Delta_0}.$$

Here  $g m p_F \ln(\tilde{\varepsilon} / \Delta_0) / 2\pi^2 \hbar^3 = 1$ , and

$\Delta_0 = \tilde{\varepsilon} \exp[-2\pi^2 \hbar^3 / g m p_F] = \tilde{\varepsilon} \exp[-\pi \hbar / 2 p_F |b|]$  or  $\Delta_0 = \tilde{\varepsilon} \exp(-2 / g \chi_F)$ , where  $\chi_F = m p_F / \pi^2 \hbar^3$  is the energy density of the particle states on the Fermi surface ( $\chi d\varepsilon$  is the number of states in the interval  $d\varepsilon$ ).

Let us consider the shape of the energy spectrum of the system. The energy of the elementary excitations is  $\varepsilon_{p+} = \varepsilon_{p-} \equiv \varepsilon(p)$ . It is the change in energy of the entire system when changing the quasiparticle occupation numbers:  $\varepsilon = \delta E / \delta n_{p\alpha} |_{u_p v_p}$ . The calculating of  $\varepsilon(p)$  gives

(Pitaevskii & Lifshitz, 1980):  $\varepsilon(p) = \sqrt{\Delta^2 + \eta_p^2}$ . Thus, the energy of quasiparticles can not be less than  $\Delta$ . For  $p = p_F$   $\varepsilon(p) = \Delta$ . Therefore, the excited states of the system are separated from the main energy gap, as well as the quasi-particles must appear in pairs, it is possible to write down the value of this gap as  $2\Delta$ . From  $\varepsilon(p) \neq 0$  it follows that the Fermi gas has superfluidity. Thus from quasiparticles with energies  $\varepsilon(p)$  a gas appears, which moves translationally as a single unit relative to the fluid with velocity  $v$ . Such gas from quasiparticle corresponds to the normal component of the superfluid. The rest of the liquid will behave like a superfluid component. The density of such superfluid liquid is equal to the sum of the normal and superfluid components:  $\rho = \rho_n + \rho_s$ . An important property of superfluid motion is its potentiality:  $\text{rot } v_s = 0$ . The energy  $2\Delta$  is the energy of the Cooper pairs. It must be expended to break a pair. The value of the distance between the particles with correlated momenta, or the coherence length, is

$\xi_0 = \pi v_F / \Delta_0 = \hbar e^{2p_F |b|} / p_F$ .

From thermodynamics of superfluid Fermi gas it follows (Pitaevskii & Lifshitz, 1980) that  $\Delta = 0$ , when

$$T_c = \gamma \Delta_0 / \pi \approx 0.57 \Delta_0$$

$$\Delta = T_c \sqrt{\frac{8\pi^2}{7\zeta(3)} \left(1 - \frac{T}{T_c}\right)} = 3.063 T_c \sqrt{1 - \frac{T}{T_c}}. \quad (14)$$

We calculate the heat capacity of the gas. At low temperatures, we start from the formula

$$\delta E = \sum_p \varepsilon (\delta n_{p+} + \delta n_{p-}) = 2 \sum_p \varepsilon \delta n_p$$

to change the total energy by varying the quasiparticle occupation numbers. Divided into  $\delta T$  and go from summation to integration, we obtain the heat capacity:

$$C = V \frac{mp_F}{\pi^2 \hbar^3} \int_{-\infty}^{\infty} \varepsilon \frac{\partial n}{\partial T} d\eta, \text{ where } V \text{ is a volume.}$$

When  $T \ll \Delta$  quasi-particle distribution function is  $n \approx e^{-\varepsilon/T}$ , and their energy is  $\varepsilon \approx \Delta_0 + \eta^2 / 2\Delta_0$ . We integrate and get:

$$C = V \frac{\sqrt{2} mp_F \Delta_0^{5/2}}{\pi^{3/2} \hbar^3 T^{3/2}} e^{-\Delta_0/T}. \quad (15)$$

Thus, for  $T \rightarrow 0$  the heat capacity decreases exponentially. This is a direct consequence of the presence of the gap in the energy spectrum. The difference between the basic levels of the superfluid and normal systems is (Pitaevskii L.P., Lifshitz E.M., 1980):

$$E_s - E_n = -V \frac{mp_F}{4\pi^2 \hbar^3} \Delta_0^2. \quad (16)$$

The sign “-” in (16) is the instability of the “normal” ground state in the case of attraction between gas particles. On one particle it falls  $\sim \Delta^2 / \mu$ . We apply the theory outlined above to description the dark energy of the Universe and calculation of its density. We transform (16) into the expression for the density:

$$-\Delta \rho = \frac{E_s - E_n}{V} = -\frac{mp_F}{4\pi^2 \hbar^3} \Delta_0^2. \quad (17)$$

The observed density of dark energy can be regarded as the binding energy of the fermions. Therefore, considering it as the difference between the densities of the energies of the levels of the superfluid and normal systems, it is necessary to attribute this difference as negative, indicating instability of the normal ground state for an arbitrarily small attraction between fermions, according to (17).

With  $\Delta \rho = \rho_{DE} = \frac{1}{8\pi G_N} \Lambda = \frac{mp_F}{4\pi^2 \hbar^3} \Delta_0^2$  we choose, for example,  $v_F = \pi c / 8$ , in order to the fermion velocity on the Fermi surface was lower than the speed of light. Then

$$\Delta_0 = \tilde{\varepsilon} e^{-\frac{\pi \hbar}{2p_F |\lambda|}} = M_p e^{-\frac{\pi \hbar}{2p_F |\lambda|}} / 4\pi = M_p e^{-\frac{\pi \lambda_i}{2|\lambda|}} /$$

$$/4\pi = M_p e^{-\frac{1}{\lambda_i}} / 4\pi, \text{ where } M_p \text{ is the Planck mass.}$$

At  $\Lambda = \Delta_0^2 / 4 = \tilde{\varepsilon}^2 e^{-2\frac{\pi \hbar}{2p_F |\lambda|}} = \tilde{\varepsilon}^2 e^{-2/\lambda_i}$ , where  $\lambda_i$  is the constant of fermions interaction. We estimate the value of  $\lambda_i$ . Since  $\Lambda^{1/2} = \tilde{\varepsilon} / e^{1/\lambda_i} = M_p / e^{1/\lambda_i} C$ , then assuming a natural cutoff parameter of maximum energy equal to  $\tilde{\varepsilon} = M_p$ , when  $\lambda_i \cong \alpha_{em} = (137.0599)^{-1}$  and  $C = 8\pi$ , we obtain:

$$\rho_{DE} = \frac{1}{4\pi G_N} \frac{1}{8\pi t_p e^{1/\lambda_i}} = \frac{1}{256\pi^3 G_N^2} \frac{c^5}{\hbar e^{2\alpha_{em}^{-1}}}, \quad (18)$$

$\rho_{DE} = 6.09 \cdot 10^{-27} \text{ kg/m}^3$  in excellent agreement with the PLANK data (Planck Collaboration, 2013).

Thus, at the present time, at  $z = 0$ , the observed density of dark energy interaction parameter of primary fermions is very close to the electromagnetic fine structure constant  $\alpha_{em}$  or equal to it. There are two possibilities: either the interaction of fermions has electromagnetic nature, or the equality  $\lambda_i \cong \alpha_{em}^{-1}$  points to the existence of “shadow” or “mirror” long-range interactions, like the electromagnetic ones, for the charges of the shadow sector of matter, manifests itself as a primary condensate of fermions, or dark energy.

The density of the normal and superfluid systems of energy close to the Planck density, and dark energy is a small contribution to this density, making  $10^{-120} \rho_p$  at the present time, but in the grand unification epoch it was  $10^{-12} \rho_p$ . Therefore formally the quantum field theory correctly estimates the true vacuum energy density as the Planck density, but it is the density of the superfluid system, without making a direct contribution to the observed forms of energy, and therefore, into gravity. This contribution is made by only the energy of the system of fermions. If  $\lambda$  coincides with the  $\alpha_{em}$  or changed synchronously as a constant of shadow interaction, then it is possible to evaluate the dynamics of changes of  $\lambda = \alpha_{em}$  depending on the energy density in the early Universe. Let us consider the process of formation of modern values of dark energy in the hot early Universe. As we know from quantum electrodynamics, the value of the electromagnetic fine structure constant is a function of the four-momentum  $Q^2$ :

$$\alpha_i^{-1} = \alpha_{em} - \frac{\beta}{3\pi} \ln \left( \frac{Q}{2m_e} \right)^2, \quad (19)$$

where  $m_e$  is the electron mass,  $\alpha_{em} = e^2 / \hbar c$  is the fine structure constant. Then, the effective density of dark energy is:

$$\rho_{DE} = \frac{\Lambda}{8\pi G_N} = \frac{c^5}{256\pi^3 G_N^2 \hbar e^{2\left(\alpha_{em}^{-1} - \frac{\beta}{3\pi} \ln \left( \frac{Q}{2m_e} \right)^2\right)}} = \frac{c^5}{256\pi^3 G_N^2 \hbar e^{2\alpha_{em}^{-1}}} \left( \frac{Q}{2m_e} \right)^{\frac{4\beta}{3\pi}}, \quad (20)$$

where  $Q = kT / c$  is momentum of radiation quanta and matter in the early Universe:

Thus, the density of dark energy as the binding energy of fermions is controlled by the density of radiation energy and substance. At the same time  $\rho_{DE}$  reaches a minimum and becomes constant at  $Qc = 2m_e c^2 = 1.022 \text{ MeV}$ . For energy GUT  $\mu_{GUT} \approx 10^{15} \text{ eV}$  we have

$$\alpha^{-1}(\mu_{GUT}) = \alpha^{-1}(\mu_0) - \frac{\beta_i}{2\pi} \ln \left( \frac{\mu_{GUT}}{\mu_0} \right). \quad (21)$$

The law of variation of  $\lambda_i$  determines the dynamics of change in  $\Lambda$ . Before the start of transition to the superconducting state, with  $\lambda_i^{-1} \rightarrow 0$ ,  $\rho_s = 0$  and

$$\rho_n = \rho_p = \frac{1}{4\pi G_N (8\pi t_p)^2}. \quad (22)$$

In general  $\rho_s = \rho_p |1 - e^{-2\lambda_i^{-1}}|$ .

$$\rho_{DE} = \frac{|\hbar\omega_p|^4}{256\pi^3 e^{2\alpha^{-1}(\mu_0)}} \left( \frac{\mu_{GUT}}{\mu_0} \right)^{\frac{2\beta_i}{\pi}}. \quad (23)$$

To determine the law of variation of  $\alpha_i^{-1}$  we will look at some aspects of the Universe formation. If the Universe started from the Planck density  $\rho_p \sim M_p^4$ , then up to the moment of the phase transition it expanded in vacuum-like state. The scale factor  $a$  as the radius of the Universe at the moment of transition from the vacuum-like in a hot state was  $a = R_\Lambda = R_H T_{CMBR} / T_{GUT} = \Lambda_i^{-1/2} = 8\pi t_p e^{\alpha_i^{-1}}$ , where  $R_H = c/H$  is a modern value of the Hubble radius,  $T_{CMBR}$  is the CMB temperature. At the same time  $\tau_V$  is a parameter for the phase transition. At the moment of the phase transition we can estimate the radius of the Universe  $R_U$ , and accordingly the value  $\alpha_i^{-1}$  depending on the value of the energy gap  $\Delta_{DE}$ . For example, when  $\rho_{DE} = \langle \phi \rangle^4 = (246.3 \text{ GeV})^4$ ,  $\alpha_i^{-1} = 73.1$  and  $k_B T_{GUT} = 1.35 \cdot 10^{15} \text{ GeV}$ , then  $a = 2.292 \text{ sm}$ .

Because dark energy is the only one of the components of the observable Universe, but it is comparable to other, so it is rightful to consider the energy density of the entire observable Universe as evolving dynamically changing difference of density of normal and superfluid fermion systems, i.e. being in a state of a phase transition with changing energy density. Then the density  $\Delta\rho$  can be identified with the critical density of the Universe. When

$$\Delta\rho = \rho_c = \frac{3}{8\pi G_N} H_0^2 = \frac{mp_F}{4\pi^2 \hbar^3} \Delta_0^2 \quad \text{and} \quad m = M_p, \quad \text{choose}$$

$p_F = \pi M_p c / 4$ , in order to the fermion velocity on the Fermi surface will be lower than the speed of light. Then the square of the dynamically changing energy gap determines the Hubble radius:  $\Delta_0^2 = 6H_0^2$ . That means that the time parameter  $t_H$  is a function of the occurring phase transition of type II, corresponding to the Universe evolution and the variable  $\lambda_j$ :

$$\Delta_j = \frac{\tilde{\xi}}{e^{2p_i |b|}} = \frac{M_p}{4\pi e^{2p_i |b|}} = \frac{M_p}{4\pi e^{\frac{\pi\lambda_i}{2|b|}}} = \frac{M_p}{4\pi e^{\frac{1}{\lambda_j}}}. \quad (24)$$

From  $t_H = H_0^{-1} = 1.4 \cdot 10^{10} \text{ years}$ ,  $t_H = 8\pi t_p e^{\lambda_j^{-1}} = 8\pi t_p e^{\frac{\pi\lambda_i}{2|b|}}$ ,  $\lambda_j^{-1} = \pi\lambda_{F_j} / 2|b| \approx 137 \cong \alpha_{em}^{-1}$  at  $z = 0$ , where  $\alpha_{em}$  is the fine structure constant.

The critical density corresponds to the Hubble parameter with a value  $H_0 = 69.76 \text{ km/s/Mpc}$  is

$$\begin{aligned} \rho_c &= \frac{3}{8\pi G_N} H_0^2 = \frac{3}{8\pi G_N} \left( \frac{1}{8\pi t_p e^{\lambda_j^{-1}}} \right)^2 \\ &= \frac{3}{8\pi G_N} \left( \frac{1}{8\pi t_p} e^{\frac{\pi\lambda_i}{2|b|}} \right)^2 \approx 9.14 \cdot 10^{-30} \text{ g/sm}^3. \end{aligned} \quad (25)$$

This value  $\rho_c$  is in good agreement with the PLANK results (Planck Collaboration, 2013). It should be noted that the proximity of the dark energy density value of the critical density of matter and generally can be explained by the proximity or the equality of the interaction parameters at the present time. Such equality can be explained by the approximation of the various parameters  $\lambda_i$  to a single value, similar to the parameters behavior in the grand unification epoch:  $\lambda_i \cong \lambda_j \cong \lambda_z \cong \lambda_{em}$ . Thus, the observed dark energy and matter can be regarded as a set of quasi-particles with energy of communication of primary fermions. Therefore, the observed world can be seen as the difference between two energy levels of a fermion system, which density is close to the Planck density:  $\rho_n = \rho_p \approx 3M_p^4 / 8\pi$ ,  $\rho_s = \rho_n - \rho_c = 3(M_p^4 - M_p^2 \Delta_j^2) / 8\pi$

Thus, we can describe the observed critical density of the Universe as the difference between the densities of the superfluid and normal fermion systems, and this process is dynamic, providing the energy difference, which coincides with the energy of the observable Universe. Therefore, in the beginning we can start from the Planck density, when  $\rho_s = 0$ , to  $\rho_{p_n} - \rho_{s(t)} = \rho_{GUT}$  and then to

$\rho_s \rightarrow \rho_p |1 - e^{2/\lambda_j}|$ . Thus, the energy density of the superfluid fermion systems can be increased from zero to a density close to the Planck density.

## References

- Bardeen J., Cooper L., Schrieffer J.R.: 1957, *Phys. Rev.*, **108**, 1175–1204.
- Bisnovaty-Kogan G.S., Chernin A.D.: 2012, *Astrophys. Space Sci.*, **338**, 337.
- Brilenkov R., Eingorn M., Zhuk A.: 2015, arXiv: 1507.07234.
- Bukalov A.V.: 2015, *Odessa Astron. Publ.*, **28/2**, 114.
- Chernin A.D. et al.: 2013, *Astron. Astrophys.*, **553**, 101.
- Eingorn M., Zhuk A.: 2012, arXiv:1205.2384.
- Fomin P.I.: 1990, *Probl. phys. kinetics and physics of solid body*, 387–398.
- Karachentsev I.D. et al.: 2009, *MNRAS*, **393**, 1265.
- Planck Collaboration: arXiv:1303.5062 [astro-ph.CO].
- Pitaevskii L.P., Lifshitz E.M.: 1980, *Statistical Physics Part 2*.
- Weinberg S.: 1989, *Reviews of Modern Physics*, **61**, 1–23.

## ASTROPHYSICS

DOI: <http://dx.doi.org/10.18524/1810-4215.2016.29.84971>

## SOFT GAMMA REPEATERS AND ANOMALOUS X-RAY PULSARS BEYOND MAGNETARS

G.S.Bisnovaty-Kogan<sup>1,2</sup><sup>1</sup> Space Research Institute, Profsoyuznaya str. 84/32, Moscow 117997, Russia, [kgogan@iki.rssi.ru](mailto:kgogan@iki.rssi.ru)<sup>2</sup> National Research Nuclear University "MEPHI", Kashirskoye Shosse, 31, Moscow 115409, Russia

**ABSTRACT.** The observational properties of Soft Gamma Repeaters and Anomalous X-ray Pulsars (SGR/AXP) indicate to necessity of the energy source different from a rotational energy of a neutron star. The model, where the source of the energy is connected with a magnetic field dissipation in a highly magnetized neutron star (magnetar) is analyzed. Some observational inconsistencies are indicated for this interpretation. Slow rotating radiopulsars with very high magnetic fields were discovered, which don't show any features of SGR, there are SGR/AXP in which an upper limit of the dipole magnetic field strength corresponds to average magnetic field of radio pulsars. The energy source, connected with the nuclear energy of superheavy nuclei stored in the nonequilibrium layer of low mass neutron star is discussed. The losses of rotational energy, observed in SGR/AXP are connected with a magnetised stellar wind, induced by the bursting events near the neutron star surface.

**Keywords:** Stars: neutron - stars: magnetars - stars: activity

## 1. Introduction

Neutron stars (NS) are formed as a result of a collapse of the core of a massive star with a mass  $M > \sim 12M_{\odot}$ . Conservation of the magnetic flux gives an estimation of NS magnetic field as  $B_{ns} = B_s(R_s/R_{ns})^2$ ,  $B_s = 10 \div 100$  Gs, at  $R \sim (3 \div 10)R_{\odot}$ ,  $R_{ns} = 10$  km,  $B_{ns} = 4 \cdot 10^{11} \div 5 \cdot 10^{13}$  Gs (Ginzburg, 1964).

Estimation of the NS magnetic field is obtained in radio pulsars by measurements of their rotational period and its time derivative, in the model of a dipole radiation, or pulsar wind model (Pacini, 1967; Goldreich & Julian, 1969) Timing observations of single radiopulsars give the following estimation  $B_{ns} = 2 \cdot 10^{11} \div 5 \cdot 10^{13}$  Gs (Lorimer, 2005).

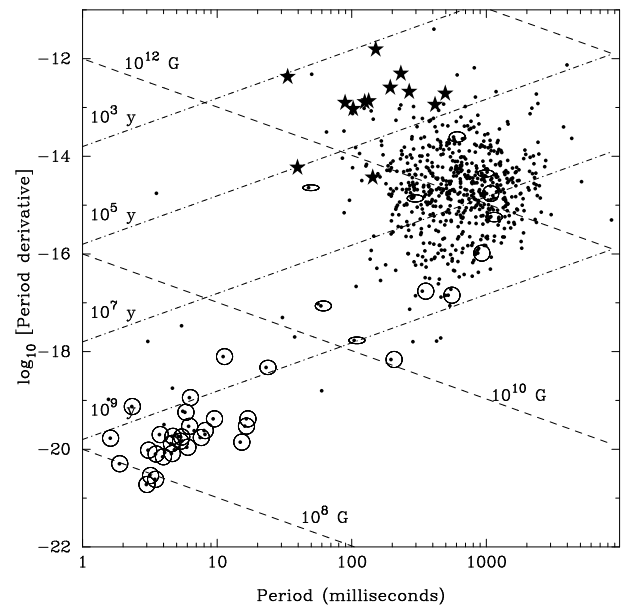


Figure 1:  $P - \dot{P}$  diagram for radiopulsars. Pulsars in binary systems with low-eccentricity orbits are encircled, and in high-eccentricity orbits are marked with ellipses. Stars show pulsars suspected to be connected with supernova remnants, from Lorimer (2005).

The pulsars with a small magnetic field in the left lower angle decrease their magnetic field during recycling by accretion in a close binary. see Bisnovaty-Kogan (2006).

SGR are single neutron stars with periods  $2 \div 8$  seconds They produce "giant bursts", when their luminosity  $L$  in the peak increase  $5 \div 6$  orders of magnitude. Having a slow rotation, and small rotational energy, their observed average luminosity exceeds rotational loss of energy more than 10 times, and orders of magnitude during the giant outbursts.

It was suggested by Duncan and Thompson (1995), that the source of energy is their huge magnetic field, 2 or 3 order of a magnitude larger, then the average field in radiopulsars. Such objects were called magnetars.

## 2. SGR, giant bursts, and short GRB

First two Soft Gamma Repeaters (SGR) had been discovered by KONUS group in 1979. The first one, FXP 0520 - 66, was discovered after the famous giant 5 March 1979 burst (Mazets et al., 1979b,c; Golenetskii et al., 1979), see also Mazets et al. (1982). In another source B1900+14 only small recurrent bursts had been observed (Mazets et al., 1979a). Now these sources are known under names SGR 0520 - 66 and SGR 1900+14 respectively. The third SGR 1806-20 was identified as a repetitive source by Laros et al. (1986a,b). The first detection of this source as GRB070179 was reported by Mazets et al. (1981), and it was indicated by Mazets et al. (1982), that this source, having an unusually soft spectrum, can belong to a separate class of repetitive GRB, similar to FXP0520 - 66 and B1900+14. This suggestion was completely confirmed. The fourth known SGR 1627-41, showing giant burst, was discovered in 1998 almost simultaneously by BATSE (Kouveliotou et al., 1998a), and BeppoSAX (Feroci et al., 1998). The giant bursts had been observed until now in 4 sources.

### 2.1. SGR0526-66

It was discovered due to a giant burst of 5 March 1979, projected to the edge of the SNR N49 in LMC, and described by (Mazets et al. 1979b,c; Golenetskii et al. 1979, Mazets et al. 1982). Accepting the distance 55 kpc to LMC, the peak luminosity in the region  $E_\gamma > 30$  keV was  $L_p \geq 3.6 \times 10^{45}$  ergs/s, the total energy release in the peak  $Q_p \geq 1.6 \times 10^{44}$  ergs, in the subsequent tail  $Q_t = 3.6 \times 10^{44}$  ergs. The short recurrent bursts have peak luminosities in this region  $L_p^{rec} = 3 \times 10^{41} - 3 \times 10^{42}$  ergs/s, and energy release  $Q_p^{rec} = 5 \times 10^{40} - 7 \times 10^{42}$  ergs. The tail was observed about 3 minutes and had regular pulsations with the period  $P \approx 8$  s. There was not a chance to measure  $\dot{P}$  in this object.

### 2.2. SGR1900+14

Recurrent bursts from this source had been first observed by Mazets et al. (1979a). Detailed observations of this source are described by Mazets et al. (1999b,c), Kouveliotou et al. (1999), Woods et al. (1999). The giant burst was observed 27 August, 1998. The source lies close to the less than  $10^4$  year old SNR G42.8+0.6, situated at distance  $\sim 10$  kpc. Pulsations had been observed in the giant burst, as well as in the X-ray emission observed in this source in quiescence by RXTE and ASCA.  $\dot{P}$  was measured, being strongly variable. Accepting the distance 10 kpc, this source had in the region  $E_\gamma > 15$

keV:  $L_p > 3.7 \times 10^{44}$  ergs/s,  $Q_p > 6.8 \times 10^{43}$  ergs,  $Q_t = 5.2 \times 10^{43}$  ergs,  $L_p^{rec} = 2 \times 10^{40} - 4 \times 10^{41}$  ergs/s,  $Q_p^{rec} = 2 \times 10^{39} - 6 \times 10^{41}$  ergs,  $P = 5.16$  s,  $\dot{P} = 5 \times 10^{-11} - 1.5 \times 10^{-10}$  s/s. The X-ray pulsar in the error box of this source was discovered by Hurley et al. (1999b). This source was discovered also in radio band, at frequency 111 MHz as a faint,  $L_r^{max} = 50$  mJy, radiopulsar (Shitov, 1999), with the same  $P$  and variable  $\dot{P}$ , good corresponding to X-ray and gamma-ray observations. The values of  $P$  and average  $\dot{P}$  correspond to the rate of a loss of rotational energy  $\dot{E}_{rot} = 3.5 \times 10^{34}$  ergs/s, and magnetic field  $B = 8 \times 10^{14}$  Gs. The age of the pulsar estimated as  $\tau_p = P/2\dot{P} = 700$  years is much less than the estimated age of the close nearby SNR. Note that the observed X-ray luminosity of this object  $L_x = 2 \times 10^{35} - 2 \times 10^{36}$  ergs/s is much higher, than rate of a loss of rotational energy, what means that rotation cannot be a source of energy in these objects. It was suggested that the main source of energy comes from a magnetic field annihilation, and such objects had been called as magnetars by Duncan and Thompson (1992).

### 2.3. SGR1806-20

The giant burst from this source was observed in December 27, 2004 (Palmer et al., 2005; Mazets et al., 2005; Frederiks et al., 2007a). Recurrent bursts had been studied by Kouveliotou et al. (1998b), Hurley et al. (1999a). Connection with the Galactic radio SNR G10.0-03 was found. The source has a small but significant displacement from that of the non-thermal core of this SNR. The distance to SNR is estimated as 14.5 kpc. The X-ray source observed by ASCA and RXTE in this object shows regular pulsations with a period  $P = 7.47$  s, and average  $\dot{P} = 8.3 \times 10^{-11}$  s/s. As in the previous case, it leads to the pulsar age  $\tau_p \sim 1500$  years, much smaller than the age of SNR, estimated by  $10^4$  years. These values of  $P$  and  $\dot{P}$  correspond to  $B = 8 \times 10^{14}$  Gs.  $\dot{P}$  is not constant, uniform set of observations by RXTE gave much smaller and less definite value  $\dot{P} = 2.8(1.4) \times 10^{-11}$  s/s, the value in brackets gives  $1\sigma$  error. The peak luminosity in the burst reaches  $L_p^{rec} \sim 10^{41}$  ergs/s in the region 25-60 keV, the X-ray luminosity in 2-10 keV band is  $L_x \approx 2 \times 10^{35}$  ergs/s is also much higher than the rate of the loss of rotational energy (for average  $\dot{P}$ )  $\dot{E}_{rot} \approx 10^{33}$  ergs/s. The burst of December 27, 2004 in SGR 1806-20 was the greatest flare,  $\sim 100$  times brighter than ever. It was detected by many satellites: Swift, RHESSI, Konus-Wind, Coronas-F, Integral, HEND et al.

Very strong luminosity of this outburst permitted to observe the signal, reflected from the moon by the HELICON instrument on the board of the satellite

Coronas-F, what permitted to reconstruct a full light curve of the outburst (Mazets et al., 2005; Frederiks et al., 2007a).

#### 2.4. SRG1627-41

Here the giant burst was observed 18 June 1998, in addition to numerous soft recurrent bursts. Its position coincides with the SNR G337.0-0.1, assuming 5.8 kpc distance. Some evidences was obtained for a possible periodicity of 6.7 s, but giant burst did not show any periodic signal (Mazets et al., 1999a), contrary to three other giant burst in SGR. The following characteristics had been observed with a time resolution 2 ms at photon energy  $E_\gamma > 15$  keV:  $L_p \sim 8 \times 10^{43}$  ergs/s,  $Q_p \sim 3 \times 10^{42}$  ergs, no tail of the giant burst had been observed.  $L_p^{rec} = 4 \times 10^{40} - 4 \times 10^{41}$  ergs/s,  $Q^{rec} = 10^{39} - 3 \times 10^{40}$  ergs. Periodicity in this source is not certain.

#### 2.5. SRG giant bursts in other galaxies

The similarity between giant bursts in SGR, and short GRB was noticed by Mazets et al. (1999c), Bisnovatyi-Kogan (1999). The experiment KONUS-WIND had observed two short GRB, interpreted as giant bursts of SGR. The first one, GRB070201, was observed in M31 (Andromeda), 1 February, 2007. The energy of the burst is equal to  $1 \cdot E^{45}$  erg, in consistence with giant bursts of other SGR Mazets et al. (2008). The second short burst, GRB051103, was observed in the galaxy M81, 3 November 2005. The energy of the burst is equal to  $7 \cdot E^{46}$  erg (Golenetskii et al., 2005; Frederiks et al., 2007).

### 3. Estimations of the magnetic fields in SGR/AXP

Despite the fact, that rotation energy losses are much smaller than the observed luminosity, for estimation of the magnetic field strength in these objects used the same procedure as in radio pulsars, based on measurements of  $P$  and  $\dot{P}$ . The first measurements have been done for SGR 1900 + 14, in different epochs by measurements of satellites RXTE and ASCA (Kouveliotou et al., 1999), presented in Figs.2-4.

The pulse shape is changing from one epoch to another, inducing errors in finding derivative of the period. The big jump in  $\dot{P}$ , visible in Fig 4 looks out surprising. for magnetic dipole losses, because it needs a considerable jump in the magnetic field strength, prohibited by self induction effects. Contrary, in the model of pulsar wind rotational energy losses it looks quite reasonable, that these losses strongly increase during the giant burst, when the  $\dot{P}$  jump was observed.

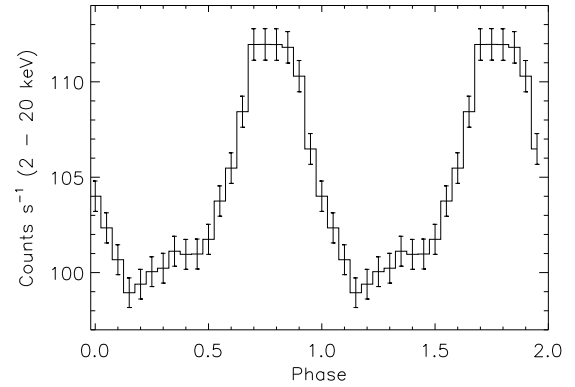


Figure 2: The epoch folded pulse profile of SGR 1900 + 14 (2-20 keV) for the May 1998 RXTE observations, from Kouveliotou et al. (1999).

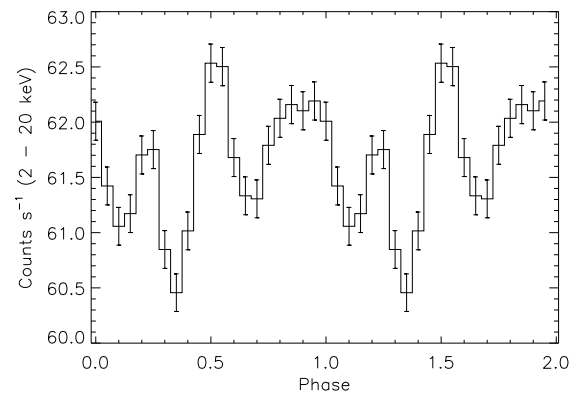


Figure 3: The epoch folded pulse profile of SGR 1900 + 14 (2-20 keV) for the August 28, 1998 RXTE observation. The plot is exhibiting two phase cycles, from Kouveliotou et al. (1999).

### 4. Radiopulsars with very high magnetic fields and slow rotation

Radio pulsars are rotating neutron stars that emit beams of radio waves from regions above their magnetic poles. Popular theories of the emission mechanism require continuous electron-positron pair production, with the potential responsible for accelerating the particles being inversely related to the spin period. Pair production will stop when the potential drops below a threshold, so the models predict that radio emission will cease when the period exceeds a value that depends on the magnetic field strength and configuration. It was shown by Young et al. (1999a,b) that the pulsar J2144-3933 has a period of 8.51s, which is by far the longest of any known radio pulsar. Moreover, under the usual model assumptions, based on the neutron-star

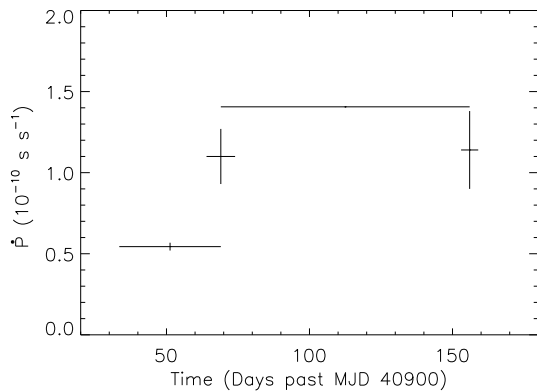


Figure 4: The evolution of Period derivative versus time since the first period measurement of SGR 1900+14 with ASCA by Hurley et al. (1999a). The time is given in Modified Julian Days (MJDs), from Kouveliotou et al. (1999)

equations of state, this slowly rotating pulsar should not be emitting a radio beam. Therefore either the model assumptions are wrong, or current theories of radio emission must be revised. The period 8.51 second is characteristic for SGR/AXP objects, but this pulsar does not show any violent behaviour, and behave like ordinary radio pulsar.

Soon after this discovery, several other radio pulsars were found, where also  $\dot{P}$ , and therefore magnetic field strength was measured (Manchester et al., 2001; Camilo et al., 2000; McLaughlin et al., 2003; 2004). These pulsars include:

1. PSR J1119 - 6127,  $P = 0.407$  s,  
 $\dot{P} = 4.0 \cdot 10^{-12}$  s/s,  $B = 4.1 \cdot 10^{13}$  G;
2. PSR J1814 - 1744,  $P = 3.975$  s,  
 $\dot{P} = 7.4 \cdot 10^{-13}$  s/s,  $B = 5.5 \cdot 10^{13}$  G;

It was noted by Camilo et al. (2000), that "Both PSR J1119 6127 and PSR J1814 1744 show apparently normal radio emission in a regime of magnetic field strength where some models predict that no emission should occur. Also, PSR J1814 1744 has spin parameters similar to the anomalous X-ray pulsar (AXP) IE 2259 + 586, but shows no discernible X-ray emission. If AXPs are isolated, high magnetic field neutron stars (magnetars), these results suggest that their unusual attributes are unlikely to be merely a consequence of their very high inferred magnetic fields."

3. PSR J1847 - 0130,  $P=6.7$  s,  $\dot{P} = 1.3 \cdot 10^{-12}$  s/s,  
 $B=9.4 \cdot 10^{13}$  G.

It was noted in the paper of McLaughlin et al. (2003), with the title "PSR J18470130: A RADIO PULSAR WITH MAGNETAR SPIN CHARACTERISTICS", that "The properties of this pulsar prove that inferred dipolar magnetic field strength and period cannot alone be responsible for the unusual high-energy properties

of the magnetars and create new challenges for understanding the possible relationship between these two manifestations of young neutron stars."

4. PSR J1718 - 37184,  $P= 3.4$  s,  $B = 7.4 \cdot 10^{13}$  G.

It was noted in the paper of McLaughlin et al. (2004), that "These fields are similar to those of the anomalous X-ray pulsars (AXPs), which growing evidence suggests are magnetars. The lack of AXP-like X-ray emission from these radio pulsars (and the non-detection of radio emission from the AXPs) creates new challenges for understanding pulsar emission physics and the relationship between these classes of apparently young neutron stars."

## 5. SGR/AXP with low magnetic fields and moderate rotation

SGR/AXP J1550-5418 (1E 1547.0-5408) was visible in radio band, showing pulsations with a period  $P = 2.069$  s (Camilo et al., 2007). The pulsations with the same period have been observed first only in the soft X ray band by XMM-Newton (Halpern et al., 2008). In the hard X ray region statistics of photons was not enough for detection of pulsations. In the strong outbursts in 2008 October and in 2009 January and March, observed by Fermi gamma-ray burst monitor, the period of 2.1s was clearly visible up to the energy  $\sim 110$  keV (Kaneko et al., 2010). The INTEGRAL detected pulsed soft gamma-rays from SGR/AXP 1E1547.0-5408 during its Jan-2009 outburst, in the energy band  $20 \div 150$  keV, showing a periodicity with  $P=2.1$ s (Kuiper et al., 2009). This object is the only SGR/AXP with a relatively low period, all previous has periods exceeding  $\sim 4$ s.

A low-magnetic-field SGR0418+5729 was detected by Fermi gamma-ray burst detector (Rea et al., 2010). This soft gamma repeater with low magnetic field SGR0418+5729 was recently detected after it emitted bursts similar to those of magnetars. It was noted by Rea et al. (2010) that "X-ray observations show that its dipolar magnetic field cannot be greater than  $7.5 \cdot 10^{12}$  Gauss, well in the range of ordinary radio pulsars, implying that a high surface dipolar magnetic field is not necessarily required for magnetar-like activity".

## 6. The Magnetar Model

In the paper of Duncan and Thompson (1992) was claimed, that dynamo mechanism in the new born rapidly rotating star may generate NS with a very strong magnetic field  $10^{14} \div 10^{15}$  G, called magnetars. These magnetars could be responsible for cosmological GRB, and may represent a plausible model for SGR. In the subsequent paper (Duncan & Thompson, 1995)

the connection between magnetars and SGR was developed in more details. The authors presented a model for SGRs, and the energetic 1979 March 5 burst, based on the existence of neutron stars with magnetic fields much stronger than those of ordinary pulsars.

Subsequent observations of  $P$  and  $\dot{P}$  in several SGR (McGill, 2014), seems to support this model. However, when the rotation energy losses are much less than observed X-ray luminosity,  $B$  estimations using  $\dot{P}$  are not justified, because magnetic stellar wind could be the main mechanism of angular momentum losses. The jump in  $\dot{P}$  observed in the giant burst of PSR1900+14 (Fig.4) is plausibly explained by a corresponding increase of the magnetic stellar wind power, while the jump in the dipole magnetic field strength is hardly possible. The jumps in  $\dot{P}$ , as well as in the pulse form (Figs.2,3) have not been seen in the radio pulsars. In the fall-back accretion model of SGR (Chatterjee et al., 2000; Alpar, 2001; Trümper et al., 2010; 2013) the estimations of the magnetic field using  $P$  and  $\dot{P}$  give the values characteristic for usual radiopulsars, when there is a presence of a large scale magnetic field in the fall back accretion disk (Bisnovatyi-Kogan & Ikhsanov, 2014).

When the energy density of the magnetic field is much larger than that of matter, as expected in the surface layers of the magnetar, the instability should be suppressed by magnetic forces. The observations of radio pulsars, showing no traces of bursts, with magnetar magnetic fields and slow rotation (Section ), detection of SGR with a small rotational period and low magnetic field, estimated from  $P$  and  $\dot{P}$  values similar to radio pulsars (Section ), gives a strong indication that inferred dipolar magnetic field strength and period cannot alone be responsible for the unusual high-energy properties of SGR/AXP. Therefore, another characteristic parameter should be responsible for a violent behaviour of SGR/AXP. The unusually low mass of the neutron star was suggested by Bisnovatyi-Kogan (2012), Bisnovatyi-Kogan and Ikhsanov (2014) as a parameter, distinguishing SGR/AXP neutron stars from the majority of neutron stars in radio pulsars and close X-ray binaries.

## 7. Angular momentum losses by a magnetized stellar wind

A magnetic stellar wind carries away the stellar angular momentum  $J$  as (Weber & Davis, 1967)

$$\dot{J}_{wind} = \frac{2}{3} \dot{M} \Omega r_A^2, \quad (1)$$

here  $r_A$  is Alfvén radius, where the energy density of the wind  $E_w$  is equal to the magnetic energy density  $E_B = B^2/(8\pi)$ . We consider the wind with a constant outflowing velocity  $w$ , which energy density is  $E_w =$

$0.5\rho w^2$ . In a stationary wind with a mass loss rate  $\dot{M}$  the density is equal to

$$\rho = \frac{\dot{M}}{4\pi w r_A^2}. \quad (2)$$

For the dipole stellar field we have  $B = \mu/r^3$ , where  $\mu = B_s r_*^3$  is the magnetic dipole moment of the star. At the Alfvén radius we have

$$\rho_A = \frac{\dot{M}}{4\pi w r_A^2}, \quad E_{wA} = \frac{\dot{M} w}{8\pi r_A^2}, \quad E_{BA} = \frac{\mu^2}{8\pi r_A^6}. \quad (3)$$

From the definition of the Alfvén radius  $r_A$  we obtain its value as

$$E_{wA} = E_{BA}, \quad r_A^4 = \frac{\mu^2}{\dot{M} w}. \quad (4)$$

The angular momentum of the star  $J = I\Omega$ , and when the wind losses (1) are the most important, we obtain the value of stellar magnetic field as

$$B_{wind}^2 = \frac{9}{4} \frac{I^2 \dot{\Omega}^2 w}{\Omega^2 \dot{M} r_*^6}. \quad (5)$$

The angular momentum and energy losses by the dipole radiation which are main losses in ordinary radiopulsars are written as (Pacini, 1967; Goldreich & Julian, 1969)

$$L = \frac{B_s^2 \Omega^4 r_*^6}{c^3}, \quad \dot{E} = I\Omega\dot{\Omega} = L, \quad \dot{J}_{PRS} = \frac{L}{\Omega}. \quad (6)$$

We obtain from (6) the magnetic field if the dipole radiation losses are the most important

$$B_{PSR}^2 = \frac{3Ic^3\dot{\Omega}}{2\Omega^3 r_*^6}. \quad (7)$$

The ratio of these two values is written as

$$\frac{B_{PSR}^2}{B_{wind}^2} = \frac{2c^3\dot{M}}{3I\Omega\dot{\Omega}w} = \frac{4}{3} \frac{\dot{M} w^2/2}{I\Omega\dot{\Omega}} \left(\frac{c}{w}\right)^3 = \frac{4}{3} \frac{F_{wind}}{\dot{E}_{rot}} \left(\frac{c}{w}\right)^3. \quad (8)$$

Here  $F_{wind}$  is the the energy flux carried away by the wind, and  $\dot{E}_{rot}$  is rate of the loss of rotational energy. For estimation of the energy flux carried away by the wind could be used the average X and  $\gamma$ -ray luminosity of SGR/AXP  $L_{x\gamma}$ , and the wind velocity is of the order of the free fall velocity of the neutron star. For low mass neutron star  $M \leq 0.8M_\odot$  we have  $v_{ff} = \sqrt{\frac{2GM}{r_*}} \approx (c/3)$  at  $M = 0.6M_\odot$ ,  $r_* = 15\text{km}$ , and

$$\frac{B_{PSR}^2}{B_{wind}^2} = 36 \frac{L_{x\gamma}}{\dot{E}_{rot}}. \quad (9)$$

Using data from McGill (2014) and (9) we obtain for the magnetic fields of SGR 0526-66, SGR 1806-20,

SGR 1900+14 the values  $10^{13}$ ,  $1.7 \cdot 10^{14}$ ,  $6 \cdot 10^{13}$  Gs respectively. While the mechanical loss of the energy could exceed  $L_{x\gamma}$ , these values of the magnetic field are suppose to be the upper limit if the magnetic field of these SGR, see Bisnovaty-Kogan (2017).

### 8. Model of nuclear explosion

It was shown by Bisnovaty-Kogan and Chechetkin (1974), that in the neutron star crust full thermodynamic equilibrium is not reached, and a non-equilibrium layer is formed there during a neutron star cooling, see also Bisnovaty-Kogan (2001).

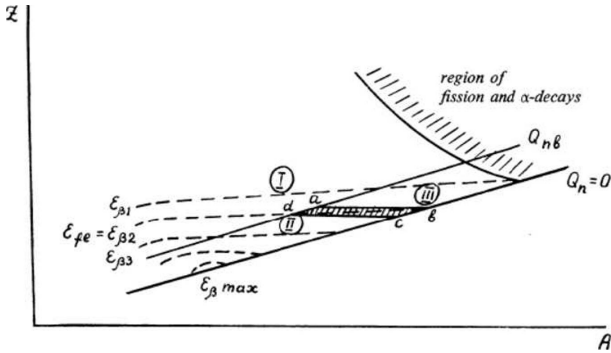


Figure 5: The formation of chemical composition at the stage of limiting equilibrium. The thick line  $Q_n = 0$  defines the boundary of the region of existence of nuclei, the line  $Q_{nb}$  separates region I, where photo-disintegration of neutrons is impossible from regions II and III. The dashed lines indicate a level of constant  $\varepsilon_\beta = Q_p - Q_n$ ;  $\varepsilon_{\beta 1} < \varepsilon_{\beta 2} < \dots < \varepsilon_{\beta max}$ . In region I we have  $Q_n > Q_{nb}$ ; in region II we have  $Q_n < Q_{nb}$ ,  $\varepsilon_{fe} < \varepsilon_\beta$ ; and in region III we have  $Q_n < Q_{nb}$ ,  $\varepsilon_{fe} > \varepsilon_\beta$ . The line with the attached shading indicates a region of fission and  $\alpha$ -decay. The shaded region  $abcd$  determines the boundaries for the values of  $(A, Z)$  with a limited equilibrium situation, at given values of  $Q_{nb}(T)$  and  $\varepsilon_{fe}(\rho)$ , from Bisnovaty-Kogan and Chechetkin (1974).

The non-equilibrium layer is formed in the region of densities and pressure  $\rho_2 < \rho < \rho_1$ ,  $P_1 < P < P_2$ , with

$$\begin{aligned} \rho_1 &\simeq \mu_e 10^6 \left( \frac{8}{0.511} \right)^3 \simeq 3.8 \cdot 10^9 \mu_e \text{ g/cm}^3 \\ &\simeq 1.5 \cdot 10^{10} \text{ g/cm}^3 \end{aligned}$$

$$\begin{aligned} \rho_2 &\simeq \mu_e 10^6 \left( \frac{33}{0.511} \right)^3 \simeq 2.7 \cdot 10^{11} \mu_e \text{ g/cm}^3 \\ &\simeq 10^{12} \text{ g/cm}^3 \end{aligned}$$

$P_1 = 7.1 \cdot 10^{27}$  in cgs units,  $P_2 = 2.1 \cdot 10^{30}$  in cgs units.

The mass of the non-equilibrium layer is defined as (Bisnovaty-Kogan & Chechetkin, 1974)

$$\begin{aligned} M_{nl} &= \frac{4\pi R^4}{GM} (P_2 - P_1) \simeq 0.1(P_2 - P_1) \simeq 2 \cdot 10^{29} \text{ g} \\ &\simeq 10^{-4} M_\odot, \end{aligned}$$

and the energy stored in this non-equilibrium layer is estimated as

$$E_{nl} \simeq 4 \cdot 10^{17} (P_2 - P_1) \approx 10^{48} \text{ erg}$$

Here a neutron star of a large ( $\sim 2 M_\odot$ ) was considered, where the nonequilibrium layer is relatively thin, and its mass, and the energy store are estimated in the approximation of a flat layer. The nuclei in the non-equilibrium layer are overabundant with neutrons, so the number of nucleons per one electron is taken as  $\mu_e \simeq 4$ , and the energy release in the nuclear reaction of fission is about  $5 \cdot 10^{-3} c^2$  erg/g. Soon after discovery of gamma ray bursts the model of nuclear explosion was suggested (Bisnovaty-Kogan et al., 1975), in which the non-equilibrium layer matter is brought to lower densities during a starquake. At the beginning GRB have been considered as objects inside the Galaxy, and the outburst was connected with period jumps in the neutron star rotation similar to those observed in the Crab nebula pulsar. It was suggested that: "Ejection of matter from the neutron stars may be related to the observed jumps of periods of pulsars. From the observed gain of kinetic energy of the filaments of the Crab Nebula ( $\sim 2 \cdot 10^{41}$  erg) the mass of the ejected material may be estimated as ( $\sim 10^{21}$  g). This leads to energies of the  $\gamma$ -ray bursts of the order of  $10^{38} - 10^{39}$  erg, which agrees fully with observations at the mean distance up to the sources 0.25 kpc". A more detailed model of the strong 5 March 1979 burst, now classified as SGR 0526-66 in LMC, was considered by Bisnovaty-Kogan and Chechetkin (1981). It was identified with an explosion on the NS inside the galactic disk, at a distance  $\sim 100$  ps. The schematic picture of the nuclear explosion of the matter from the non-equilibrium layer is presented in Fig.6.

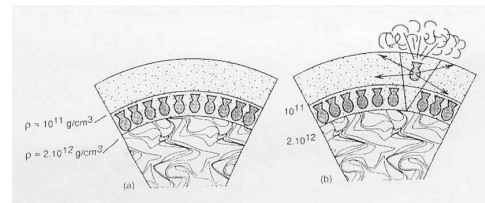


Figure 6: The schematic picture of non-equilibrium layer in the neutron star: a) in a quiescent stage; b) after starquake and nuclear explosion, from Bisnovaty-Kogan (1992).

Cosmological origin of GRB, and identification of a group of non-stationary sources inside Galaxy as SGR/AXP lead to considerable revision of the older model, presented by Bisnovaty-Kogan et al. (1975). It becomes clear that SGR represent a very rare and very special type of objects, which produce bursts much more powerful, than it was thought before from comparison with quakes in Crab nebula pulsar. Besides, the SGR are the only sources for which the nuclear explosions could be applied, because the energy release in the cosmological GRB highly exceed the energy store in the non-equilibrium layer.

It was suggested by Bisnovaty-Kogan (2012, 2015), Bisnovaty-Kogan and Ikhsanov (2014), that the property, making the SGR neutron star so different from much more numerous of them in radio pulsars, single and binary X ray sources, is connected with the value of their mass, but not the magnetic field strength, see Camilo (2000), McLaughlin (2003), and Section . Namely, it was suggested that the neutron stars in SRG/AXP have anomalously low mass,  $(0.4 \div 0.8)M_{\odot}$ , compared to the well measured masses in binary systems of two neutron stars, where neutron stars have masses  $\geq 1.23 M_{\odot}$  (Ferdman et al., 2014). The violent behaviour of the low-mass NS may be connected with much thicker and more massive non-equilibrium layer, and accretion from the fall-back highly magnetized accretion disk could trigger the instability, leading to outbursts explosions (Bisnovaty-Kogan & Ikhsanov, 2014). The NS radius is increasing with mass rather slowly, and in a flat approximation the mass of non-equilibrium layer is inversely proportional to the mass. In Sect. the calculated mass of the non-equilibrium layer  $M_{nl} \approx 10^{-4}M_{\odot}$  was belonged to the neutron star with the mass  $\sim 2 M_{\odot}$  (see Bethe & Johnson, 1975; Malone et al., 1975). It follows from calculations of neutron star models that for  $M_{ns} = 0.45 M_{\odot}$  the mass of the non-equilibrium layer is  $\sim 7$  times larger (Bisnovaty-Kogan & Ikhsanov, 2014). The energy store reaches  $\sim 10^{49}$  erg, what is enough for  $\sim 1000$  giant bursts.

The observational evidences for existence of neutron stars with masses, less than the Chandrasekhar white dwarf mass limit have been obtained by Janssen et al. (2008). Observations of the binary pulsar system J1518-4904 indicated the masses of the components to be  $m_p = 0.72(+0.51, -0.58)M_{\odot}$ ,  $m_e = 2.00(+0.58, -0.51)M_{\odot}$  with a 95.4% probability. It was suggested by Bisnovaty-Kogan and Ikhsanov (2014) that low mass neutron stars could be formed in the scenario of the off-center explosion (Branch & Nomoto, 1986), but more detailed numerical investigation is needed to prove it. X-ray radiation of SGR/AXP in quiescent states was explained as a fall back accretion from the disk with a large scale poloidal magnetic field, what could also be a trigger for development of instability, leading to

the mixing in the neutron star envelope, and nuclear explosion of the matter from the non-equilibrium layer.

## 9. Conclusions

1. SGR are highly active, slowly rotating neutron stars.
2. Nonequilibrium layer (NL) is formed in the neutron star crust, during NS cooling, or during accretion onto it. It may be important for NS cooling, glitches, and explosions connected with SGR.
3. The mass and the energy store in NL increase rapidly with decreasing of NS mass.
4. The properties of pulsar with high magnetic fields prove that inferred dipolar magnetic field strength and period cannot alone be responsible for the unusual high-energy properties of SGR/AXP. The NL in low mass NS may be responsible for bursts and explosions in them.
5. The upper boundary of the magnetic fields in 3 most famous SGR, measured by the average  $L_{x\gamma}$  luminosity is about one order of magnitude lower than the values obtained using the pulsar-like energy losses of the rotational energy of the neutron star.
6. Magnetar model of SGR, in which the energy of the observed bursts is provided by magnetic field annihilation, seems to be not relevant. Observations of quiet radiopulsars with a "magnetar" magnetic field, and of a low-field "magnetar", is the most important indication to that conclusion. A rapid growth of rotational periods, what is a favorite argument for a "magnetar" origin, is naturally explained by action of the magnetic stellar wind. Besides, the high pressure of the magnetic field suppresses convection, which is needed in all annihilation models.

*Acknowledgements.* This work was supported partially by RFBR grant 14-02-00728, President RF grant NSh-261.2014.2, and RAS presidium programm P-7b.

## References

- Alpar M.A.: 2001, *ApJ*, **554**, 1245.  
 Bethe H.A., Johnson M.B.: 1974, *Nuclear Physics*, **A230**, 1.  
 Bisnovaty-Kogan G.S.: 1992, *Proc. Conf. Taos (USA) "Gamma-ray bursts - Observations, analyses and theories"*, (A93-20206 06-90), p. 89.  
 Bisnovaty-Kogan G.S.: 1999, *Proc. Vulcano Workshop 1999, Memorie della Societa Astronomica Italiana*, 2002, **73**, 318.  
 Bisnovaty-Kogan G.S.: 2001, *Stellar Physics. Vol.1. Fundamental concepts and stellar equilibrium*, Springer.  
 Bisnovaty-Kogan G.S.: 2006, *Physics Uspekhi*, **49**, 53.

- Bisnovatyi-Kogan G.S.: 2012, *Proc. Workshop "Gamma-Ray Bursts: Probing the Science, Progenitors and their Environment"* Moscow, 13 - 15 June 2012, pp.1-4; <http://www.exul.ru/workshop2012/Proceedings2012.pdf>
- Bisnovatyi-Kogan G.S.: 2015, *Astron. Astrophys. Transactions*, **29**, 165.
- Bisnovatyi-Kogan G.S.: 2017, in *Handbook of Supernovae*, A.W. Alsabti, P. Murdin (Eds.) Springer International Publishing
- Bisnovatyi-Kogan G.S., Chechetkin V.M.: 1974, *Ap. Space Sci.*, **26**, 25.
- Bisnovatyi-Kogan G.S., Chechetkin V.M.: 1981, *Sov. Astron.*, **58**, 561.
- Bisnovatyi-Kogan G.S. et al.: 1975, *Ap. Space Sci.*, **35**, 23.
- Bisnovatyi-Kogan G.S., Ikhsanov N.R.: 2014, *Astronomy Reports*, **58**, 217.
- Branch D., Nomoto K.: 1986, *Astron. Astrophys.*, **164**, L13.
- Camilo F. et al.: 2000, *ApJ*, **541**, 367.
- Camilo F. et al.: 2007, *ApJ Lett.*, **666**, L93.
- Chatterjee P. et al.: 2000, *ApJ*, **534**, 373.
- Duncan R.C., Thompson C.: 1992, *ApJ Lett.*, **392**, L9.
- Duncan R.C., Thompson C.: 1995, *MNRAS*, **275**, 255.
- Ferdman R.D. et al.: 2014, *MNRAS*, **443**, 2183.
- Feroci M. et al.: 1998, *GCN*, No. 111.
- Frederiks D.D. et al.: 2007a, *Astron. Lett.*, **33**, 1.
- Frederiks D.D. et al.: 2007b, *Astron. Lett.*, **33**, 19.
- Ginzburg V.L.: 1964, *Soviet Physics Doklady*, **9**, 329.
- Goldreich P., Julian W.H.: 1969, *ApJ*, **157**, 869.
- Golenetskii S.V. et al.: 1979, *Sov. Astron. Letters*, **5**, 340.
- Golenetskii et al.: 2005, *GCN*, No. 4197.
- Halpern J.P. et al.: 2008, *ApJ*, **676**, 1178.
- Hurley K. et al.: 1999a, *ApJ*, **523**, L37.
- Hurley K. et al.: 1999b, *ApJ*, **510**, L111.
- Janssen G.H. et al.: 2008, *Astron. Astrophys.*, **490**, 753.
- Kaneko Y. et al.: 2010, *ApJ*, **710**, 1335.
- Kouveliotou C. et al.: 1998a, *The Astronomer's Telegram*, No. 29
- Kouveliotou C. et al.: 1998b, *Nature*, **393**, 235.
- Kouveliotou C. et al.: 1999, *ApJ Lett.*, **510**, L115.
- Kuiper L. et al.: 2009, *The Astronomer's Telegram*, No. 1921.
- Laros J.G. et al.: 1986a, *Bulletin of the AAS*, **18**, 928.
- Laros J.G. et al.: 1986b, *Nature*, **322**, 152.
- Lorimer D.R.: 2005, *Living Reviews in Relativity*, **8**, 7.
- Manchester R.N. et al.: 2001, *MNRAS*, bf 328, 17.
- Mazets E.P. et al.: 1979a, *Sov. Astron. Letters*, **5**, 343.
- Mazets E.P. et al.: 1979b, *Sov. Astron. Letters*, **5**, 163.
- Mazets E.P. et al.: 1979c, *Nature*, **282**, 587.
- Mazets E.P. et al.: 1981, *Ap. Space Sci.*, **80**, 3.
- Mazets E.P. et al.: 1982, *Ap. Space Sci.*, **84**, 173.
- Mazets E.P. et al.: 1999a, *ApJ Lett.*, **519**, L151.
- Mazets E.P. et al.: 1999b, *Astron. Letters*, **25**, 628.
- Mazets E.P. et al.: 1999c, *Astron. Letters*, **25**, 635.
- Mazets E.P. et al.: 2005, *astro-ph/0502541*.
- Mazets E.P. et al.: 2008, *ApJ*, **680**, 545.
- McGill Pulsar Group 2014, *McGill Online Magnetar Catalog*. <http://www.physics.mcgill.ca/pulsar/magnetar/main.html>.
- McLaughlin M.A. et al.: 2003, *ApJ Lett.*, **591**, L135.
- McLaughlin M.A. et al.: 2004, in *Young Neutron Stars and Their Environments IAU Symp. No. 218*. Eds. F. Camilo and B.M. Gaensler. (Astron. Soc. Pacific, San Francisco, 2004), p.255.
- Malone R.C. et al.: 1975, *ApJ*, **199**, 741.
- Pacini F. 1967, *Nature*, **216**, 567.
- Palmer D.M. et al.: 2005, *Nature*, **434**, 1107.
- Rea N. et al.: 2010, *Science*, **330**, 944.
- Shitov Yu.P.: 1999, *IAU Circ.*, No. 7110, Feb. 17.
- Trümper J.E. et al.: 2010, *Astron. Astrophys.*, **518**, A46.
- Trümper J.E. et al.: 2013, *ApJ*, **764**, 49.
- Weber E.J. and Davis L.J.: 1967, *ApJ*, **148**, 217.
- Woods P.M. et al.: 1999, *ApJ*, **524**, L55.
- Young M.D. et al.: 1999a, *Nature*, **400**, 848.
- Young M.D. et al.: 1999b, *ASP Conference Series*, **202**, 185.

DOI: <http://dx.doi.org/10.18524/1810-4215.2016.29.84972>

# ISENTROPIC "SHOCK WAVES" IN NUMERICAL ASTROPHYSICS

S.G. Moiseenko<sup>1</sup>, G.S. Bisnovaty-Kogan<sup>1,2</sup><sup>1</sup> Space Research Institute, Profsoyuznaya str. 84/32, Moscow, 117997 Russia,<sup>2</sup> National Research Nuclear University MEPhI, Kashirskoe sh. 31, Moscow, 115409 Russia  
*moiseenko@iki.rssi.ru, gkogan@iki.rssi.ru*

**ABSTRACT.** Numerical simulations of the cold supersonic flows in different astrophysical problems meets with the loss of precision difficulty. For to overcome the difficulty it was suggested earlier to use conservation entropy equation instead of energy conservation law. In the paper we analyse quantitatively the error what appears in the shocked flow when isentropic equations are used. The isentropic equations of gas dynamics can be used only when there are no shocks in the solution or when they are weak and do not significantly affect the flow. The results described here were represented as a talk at the 16-th Gamow Summer School: "Astronomy and beyond: Astrophysics, Cosmology, Cosmobiophysics, Astroparticle Physics, Radioastronomy and Astrobiology" 14-20 August, 2016, Odessa, Ukraine. The complete paper is published in Bisnovaty-Kogan & Moiseenko, 2016.

**Keywords:** Shock waves, Numerical hydrodynamics.

## 1. Introduction

In numerical simulations of astrophysical problems, instead of the energy equation, sometimes the equation for the density of entropy is used, which is assumed to be conserved throughout the flow, including at discontinuities in the form of shock waves. As a rule, this approach is used for modelling of cold supersonic gas flows. In these flows the internal energy density of the gas is considerably lower than the kinetic energy density. Large numerical errors can appear in temperature (pressure) calculations for flows of such kind. This approach is mostly used in astrophysics, where crude, approximate numerical results may be acceptable when there is large scatter in the observational data and in their interpretation. Qualitatively such numerical approach was probably discussed for the first time in the paper by Ryu et al. (1993). Although the use of such isentropic schemes has continued (see for

example B[2,3], the errors in the law of energy conservation due to the application of entropy conservation at strong discontinuities have not been analysed. Evidently, an isentropic jump requires removal of energy from the post-shock gas, since the entropy of the gas in a real jump (shock wave) increases, and heat extraction is needed to conserve it. If  $S_1$  and  $S_2$  are the entropies of the gas ahead of and after the jump, then  $S_2 = S_1$  for an isentropic shock and  $S_2 > S_1$  for a Hugoniot adiabat. According to the second law of thermodynamics, in order to reduce the entropy to  $S_1$  after the jump, it is necessary to lose an amount of heat (i.e., reduce the energy by  $\Delta Q = \bar{T} \cdot (S_2 - S_1)$ , where  $\bar{T}$  is the average temperature over the thickness of the shock.

In this paper we consider the conditions at an "isentropic" discontinuity for power law equations of state of the form  $P = K(S)\rho^\gamma$  and make a quantitative estimate of the numerical errors in the conservation of energy.

## 2. Conditions at discontinuities: the Hugoniot adiabat and an "isentropic" discontinuity

### 2.1. Hugoniot adiabat

The conditions at a plane discontinuity in the Hugoniot adiabat are reduced to the conservation of mass, momentum, and energy, which for a discontinuity reference frame have the form (Loytsansky, 1987):

$$\rho_1 v_1 = \rho_2 v_2, \quad (1)$$

$$P_1 + \rho_1 v_1^2 = P_2 + \rho_2 v_2^2, \quad (2)$$

$$E_1 + \frac{P_1}{\rho_1} + \frac{v_1^2}{2} = E_2 + \frac{P_2}{\rho_2} + \frac{v_2^2}{2}. \quad (3)$$

Equation of state:  $P = K(S)\rho^\gamma$ . Expression for the internal energy:

$$E = \frac{1}{\gamma - 1} \frac{P}{\rho} = \frac{K(S)}{\gamma - 1} \rho^{\gamma-1}. \quad (4)$$

Here  $v$  is the velocity,  $\rho$  is the density,  $P$  is the pressure,  $T$  is the temperature,  $\gamma$  is the adiabatic index,  $E$

is the internal energy, and  $S$  is the entropy. A subscript "1" indicates a quantity ahead of the front and "2" behind the front. Equations (1- 3) yield an equation for the Hugoniot adiabat (Loitsyanskii, 1987), which relates the density and pressure ahead of and after the jump:

$$\frac{P_2}{P_1} = \frac{(\gamma + 1)\rho_2 - (\gamma - 1)\rho_1}{(\gamma + 1)\rho_1 - (\gamma - 1)\rho_2}, \quad (5)$$

as well as the relationship of other parameters before and after the jump:

$$v_1 - v_2 = \frac{\sqrt{2}(P_2 - P_1)}{\sqrt{\rho}((\gamma - 1)P_1 + (\gamma + 1)P_2)^{1/2}} \quad (6)$$

Introducing the Mach number of the shock wave  $M_1 = \frac{v_1}{c_1}$  we obtain (Landay& Lifshitz, 1988 ):

$$\frac{\rho_2}{\rho_1} = \frac{v_1}{v_2} = \frac{(\gamma + 1)M_1^2}{(\gamma - 1)M_1^2 + 2}, \quad (7)$$

$$\frac{P_2}{P_1} = \frac{2\gamma}{\gamma - 1}M_1^2 - \frac{\gamma - 1}{\gamma + 1}, \quad (8)$$

$$\frac{T_2}{T_1} = 1 + \frac{2(\gamma - 1)}{(\gamma + 1)^2 M_1^2} (M_1^2 - 1)(1 + \gamma M_1^2), \quad (9)$$

$$M_2^2 = \frac{2 + (\gamma - 1)M_1^2}{2\gamma M_1^2 - (\gamma - 1)}. \quad (10)$$

### 2.1. "Isenropic" discontinuity

For an "isentropic" discontinuity, the energy equation (3) is replaced by an equation for the conservation of entropy, which for an ideal gas with the equation of state  $P = \rho \Re T$  and an adiabatic index  $\gamma$ , takes the form

$$S = \frac{\Re}{\gamma - 1} \ln \left( \frac{P}{\rho^\gamma} \right) + C_1. \quad (11)$$

Since the gas constant  $\Re$  and  $C_1$  are assumed to be the same before and after the discontinuity, the conservation of entropy can be written in the form

$$\frac{P_1}{\rho_1^\gamma} = \frac{P_2}{\rho_2^\gamma}. \quad (12)$$

From equations (1) and (2) excluding  $v_2$  we get

$$P_1 + \rho_1 v_1^2 = P_2 + \frac{\rho_1^2}{\rho_2} v_1^2. \quad (13)$$

Defining sound speed as  $c = \sqrt{\gamma \frac{P}{\rho}}$ , we get

$$\frac{1}{\gamma} c_1^2 + v_1^2 = \frac{P_2}{P_1} \frac{c_1^2}{\gamma} + \frac{\rho_1}{\rho_2} v_1^2. \quad (14)$$

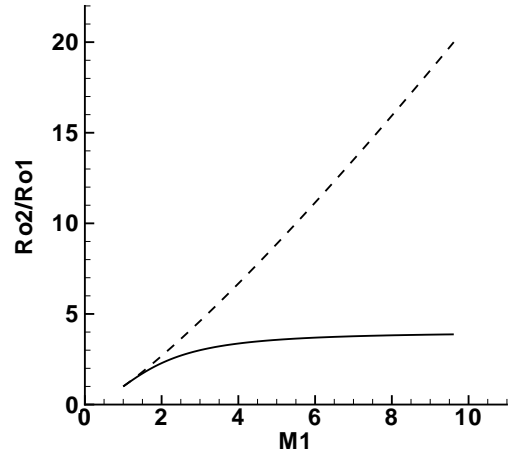


Figure 1: The ratio of the post- and pre-discontinuity densities  $\rho_2$  and  $\rho_1$  as a function of the Mach number  $M_1$  ahead of a discontinuity (the Mach number of the shock). The smooth curve is for an adiabatic shock wave and the dashed curve, for an "isentropic" discontinuity.

Using (12) and define the post-shock Mach number as  $M_2 = \frac{v_2}{c_2}$ , we obtain

$$\frac{1}{\gamma} c_1^2 + v_1^2 = \left( \frac{\rho_2}{\rho_1} \right)^\gamma \frac{c_1^2}{\gamma} + \frac{\rho_1}{\rho_2} v_1^2, \quad (15)$$

$$M_1^2 + \frac{1}{\gamma} = \left( \frac{\rho_2}{\rho_1} \right)^\gamma \frac{1}{\gamma} + \frac{\rho_1}{\rho_2} M_1^2. \quad (16)$$

Using the notation  $x = \frac{\rho_2}{\rho_1}$  we obtain

$$M_1^2 = \frac{x^\gamma - 1}{\gamma} \frac{x}{x - 1}; \quad (17)$$

$$\frac{P_2}{P_1} = x^\gamma; \quad \frac{T_2}{T_1} = x^{\gamma-1}; \quad \frac{v_2}{v_1} = \frac{1}{x}; \quad \frac{c_2}{c_1} = x^{\frac{\gamma-1}{2}}. \quad (18)$$

The post-shock Mach number can be written in the following form

$$M_2^2 = v_2^2 \frac{\rho_2}{\gamma P_2} = \frac{v_1^2}{\gamma x^2} \frac{x \rho_1}{P_1} \frac{P_1}{P_2} = \frac{v_1^2}{\gamma x} \frac{\rho_1}{P_1} \frac{1}{x^\gamma} = \frac{M_1^2}{x^{\gamma+1}} \quad (19)$$

The plots for the following values  $x = \frac{\rho_2}{\rho_1}(M_1)$ ,  $\frac{P_2}{P_1}(M_1)$ ,  $\frac{T_2}{T_1}(M_1)$ , and  $\frac{v_2}{v_1}(M_1)$  are at the Figures (1-4) for a Hugoniot adiabat and for an "isentropic" jump for the adiabatic index  $\gamma = 5/3$ .

The total energies before and after the jump, including the work of pressure forces, are given by

$$\varepsilon_1 = E_1 + \frac{P_1}{\rho_1} + \frac{v_1^2}{2} = \frac{\gamma}{\gamma - 1} \frac{P_1}{\rho_1} + \frac{v_1}{2} = \frac{c_1}{\gamma - 1} + \frac{v_1^2}{2} = c_1^2 \left( \frac{M_1^2}{2} + \frac{1}{\gamma - 1} \right), \quad (20)$$

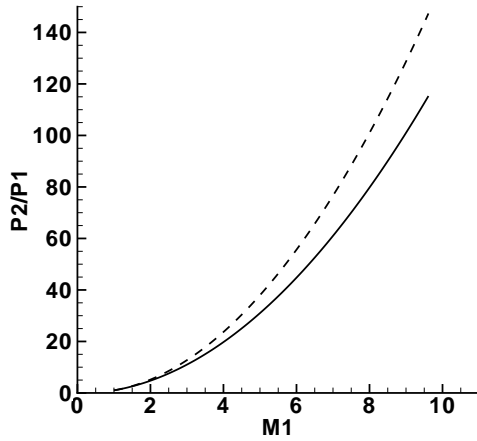


Figure 2: The ratio of the post- and pre-discontinuity pressures  $P_2$  and  $P_1$  as a function of the Mach number  $M_1$  ahead of a discontinuity (the Mach number of the shock). The smooth curve is for an adiabatic shock wave and the dashed curve, for an "isentropic" discontinuity.

$$\varepsilon_2 = E_2 + \frac{P_2}{\rho_2} + \frac{v_2^2}{2} = c_2^2 \left( \frac{M_2^2}{2} + \frac{1}{\gamma - 1} \right). \quad (21)$$

For  $M_1 \gg 1$  we have

$$M_1^2 = \frac{x^\gamma}{\gamma}, \quad M_2^2 = \frac{1}{\gamma x}. \quad (22)$$

The relative change in the total energy at an "isentropic" jump is

$$\frac{\varepsilon_2 - \varepsilon_1}{\varepsilon_1} = \frac{\frac{\gamma}{\gamma-1} \frac{P_2}{\rho_2} + \frac{v_2^2}{2}}{\frac{\gamma}{\gamma-1} \frac{P_1}{\rho_1} + \frac{v_1^2}{2}} - 1. \quad (23)$$

Taking into account (18) we obtain

$$\frac{\varepsilon_2 - \varepsilon_1}{\varepsilon_1} = \frac{\frac{1}{\gamma-1} (x^{\gamma-1} - 1) + \frac{M_1^2}{2} \left( \frac{1}{x^2} - 1 \right)}{\frac{1}{\gamma-1} + \frac{M_1}{2}}. \quad (24)$$

Here  $x$  is an implicit function of  $M_1$  determined by (17). Figure 5 is a plot of the relative change in the total energy for a gas passing through an "isentropic" jump as a function of the Mach number of the upstream flow. These plots show that as the amplitude of a strong discontinuity (jump) increases, the parameters behind it are significantly different for the adiabatic and "isentropic" cases. Thus, for an "isentropic" jump the density behind the jump can increase infinitely for  $M_1 \rightarrow \infty$ , while for an adiabatic shock the density behind it can increase only by a factor of  $\frac{\gamma+1}{\gamma-1}$ . The velocity of the gas passing through an "isentropic" jump tends to zero with increasing  $M_1$ , while in the adiabatic case it falls only by a factor of  $\frac{\gamma-1}{\gamma+1}$  for  $M_1 \rightarrow \infty$ .

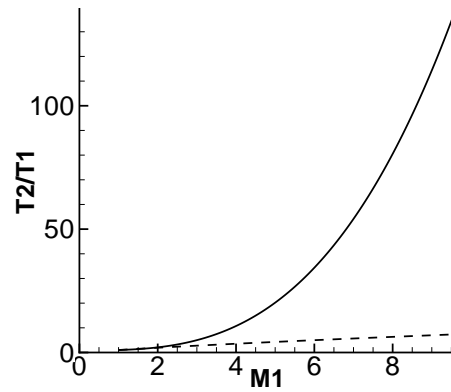


Figure 3: The ratio of the post- and pre-discontinuity temperatures  $T_2$  and  $T_1$  as a function of the Mach number  $M_1$  ahead of a discontinuity (the Mach number of the shock). The smooth curve is for an adiabatic shock wave and the dashed curve, for an "isentropic" discontinuity.

### 3. On the possibility of using the isentropic equations for numerical modelling

Using the "isentropic" equations for modelling gas flows can lead to substantial errors when shock waves are present. The size of the errors increases with increasing shock intensity.

In numerical simulations of supernova explosions (see e.g. Moiseenoo et al., 2015), the shock Mach number is  $\sim 30$ . With this shock amplitude, numerical modelling of a supernova with the isentropic equations would lead to errors of an order of magnitude in the post-shock parameters.

An isentropic system of gas dynamic equations has been used in a numerical simulation of the dynamics of supernova bubbles (Bychkov et al., 2006). The supernova shock wave, however, has a large amplitude (the Mach number of the shock wave from the supernova can reach tens) and substantially determines the structure of the flow after the shock front.

In the monograph by Bisikalo et al. (2013) devoted to the simulations of close binary systems authors note that gas flows appear for which the total energy density of the gas is mainly determined by the kinetic energy density. In this situation, when conservation of the total energy is used, large numerical errors may arise in calculating the temperature of the flow. The "isentropic" equations can be used for modelling this kind of flow if shock waves do not appear or have small amplitudes. The calculations show that shock waves do develop in simulations of close binary systems (i.e., a "hot line", "hot point"), where the Mach number of the upstream flow can be  $\geq 4$  and substantially determine the flow structure; using the "isentropic" equations may in-

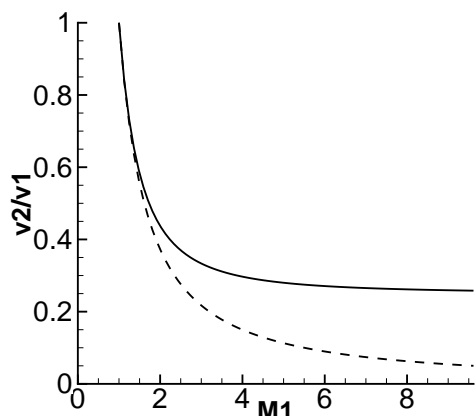


Figure 4: The ratio of the post- and pre-discontinuity velocities  $v_2$  and  $v_1$  as a function of the Mach number  $M_1$  ahead of a discontinuity (the Mach number of the shock). The smooth curve is for an adiabatic shock wave and the dashed curve, for an "isentropic" discontinuity.

produce substantial numerical errors in calculations of post-shock gas flow.

In order to overcome the difficulties in calculating cold supersonic flows, it was proposed by Ryu et al. (1993) that simultaneous calculations be done using the conservation equation for the total energy and the entropy equation. In the part of the flow where there were no shocks, the entropy equation was used. Where shock waves developed, the energy equation was used. A number of criteria were introduced for determining which of these equations should be used in solving the general system of gas dynamic equations. The introduction of a "double energy formalism" has been proposed (Bryan et al., 1995), where the entropy calculations include a calculation of the time variation in the internal energy as well as in the total energy. In the case of a highly supersonic flow, the pressure and temperature of the gas were calculated using the internal energy equation; otherwise, the equation for the total energy balance was used.

When irregular, moveable grids with a variable structure are used (Springel, 2010), models of cold and rapid flows using the total energy balance equation may lead to numerical errors in calculating the temperature, since even small errors in calculating the total energy (associated, for example, with the grid reconstruction and remapping of the parameters) can lead to substantial errors in calculating the internal energy. It was suggested in (Springel, 2010) that the amplitude of the developing shock waves be estimated. When the shock Mach number does not exceed  $\sim 1.1$ , it is suggested that the entropy balance equation be used. Another approach proposed in the same paper assumes

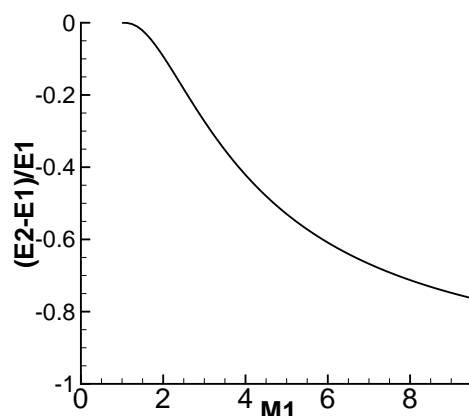


Figure 5: The relative change in the total energy for gas passing through an "isentropic" jump as a function of Mach number  $M_1$  of the incident flow (the Mach number of the shock wave).

a comparison of the internal energy of a cell with its kinetic energy at each step. In calculations of flows with gravitation, the criterion for choosing the energy or entropy equation might be to compare the force created by the gas flow with the acceleration of gravity. If the internal energy of the gas is low compared to the gravitational energy, then the entropy equation is used.

*Acknowledgements* This work was supported by a grant from the Russian Science Foundation (project No. 15-12-30016).

## References

- Bisikalo D.V., Zhilkin A.G., Boyarchuk A.A.: *Gas Dynamics of Close Binary Stars* [in Russian], Moscow: Fizmatlit, 2013, 632 pp.
- Bisnovatyi-Kogan G.S., Moiseenko S.G.: 2016, *Astrophys.*, **59**, 1.
- Bryan G.L., Norman M.L., Stone J.M., Cen R., Ostriker J.P.: 1995, *Comput. Phys. Commun.*, **89**, 149.
- Bychkov V., Popov M.V., Oparin A.M., Stenflo L., Chechetkin V. M.: 2006, *Astron. Zh.*, **83**, 337.
- Landau L.D., Lifshitz E.M.: *Hydrodynamics* [in Russian], Moscow: Nauka, 1988, 736 pp.
- Loitsyanskii L.G.: *Mechanics of Liquids and Gases* [in Russian], Moscow: Nauka, 1987, 840 pp.
- Moiseenko S.G., Bisnovatyi-Kogan G.S.: 2015, *Astron. Rep.*, **59**, 573.
- Spergel V.: 2010, *Month. Not. Roy. Astr. Soc.*, **401**, 791.
- Ryu D., Ostriker J.P., Kang H., Cen R.: 1993, *ApJ*, **414**, 1.
- Zhilkin A.G., Bisikalo D.V.: 2010, *Astron. Zh.*, **87**, 913.

DOI: <http://dx.doi.org/10.18524/1810-4215.2016.29.84976>

# UNIVERSALITY IN MAGNETOEMISSION OF COMPACT ASTROPHYSICAL OBJECTS

V. N. Kondratyev<sup>1,2</sup>, Yu. V. Korovina<sup>3</sup>, Ph. Blanchard<sup>2</sup><sup>1</sup> Physics Department, Taras Shevchenko National University of Kyiv, 03022-UA Kyiv, Ukraine, [vkondrat@univ.kiev.ua](mailto:vkondrat@univ.kiev.ua)<sup>2</sup> Faculty of Physics, Bielefeld University, D-33501 Bielefeld, Germany<sup>3</sup> Moscow Institute of Open Education, 125167-RU Moscow, Russia

**ABSTRACT.** Magnetodynamics of inhomogeneous crusty nuclear matter is considered accounting for quantum fluctuations and ferromagnetic coupling. We show that anomalies in nuclide magnetic moments give rise to erratic jumps in magnetotransport of neutron star crusts. Universal properties of such a noise are favorably compared with statistical and temporal features of Soft Gamma Repeating bursts.

**Keywords:** Soft gamma repeaters. – neutron stars: magnetic field.

## 1. Introduction

The pioneering evidence for ultramagnetized astrophysical objects (“magnetars”) is associated with the discovery Mazets et.al (1979) of March 5, 1979 event from SGR 0526-66. The magnetar concept (e.g., Kondratyev, 2002; Svinkin et al., 2015) and refs. therein) is strongly corroborated by further observations of soft gamma repeaters (SGRs) and anomalous X-ray pulsars (AXPs). The observed SGR properties indicate (Kondratyev, 2002; Svinkin et al., 2015) significant higher multipole magnetic fields being substantially larger than the corresponding dipole component  $B_{\text{dip}} \sim 10^{15}$  G. Assuming a noticeable contribution of magnetic pressure in a balance of crust forces in neutron star (NS) we write

$$dB_n^2/dR \sim 8\pi GM n(R)/R^2, \quad (1)$$

where the gravitational constant  $G$ , and the star mass  $M(R)$  within radius  $R$  is related to the matter density  $n(R)$  as  $4\pi R^2 n(R) = dM/dR$ . Substituting this relation into Eq. (1) and integrating over NS crust area, we obtain for the field strength  $B \sim 10^{1.5}$  TeraTesla ( $M/M_\odot$ )(10km/R)<sup>2</sup>, with the solar mass  $M_\odot$ . Thus field toroidal components can reach tens teratesla (TT) that is consistent with estimates (Kondratyev, 2014) based on the supernova explosion energy. Such fields (ie, in excess of 0.1 TT) can affect the structure and properties of atomic nuclei (see. (Kondratyev, 2002; 2014) and refs. therein), In this contribution the randomly jumping interacting moments (RJIM) model (Kondratyev, 2002) is further extended for an analysis of SGR burts.

## 2. Modeling NS Crust Magnetodynamics

The RJIM model for magnetodynamics simulations in NS crust has already been described in(Kondratyev 2002) and refs. therein. We briefly remind that in simulations of demagnetization dynamics we use a very general form for magnetic moments  $m$  of atomic nuclei  $m = \mu \sum_n v_n \theta(b - b_n) = Ig$  with the nucleon magneton  $\mu$ , spin  $I$  and nuclear g-factor  $g$ , as well as step function  $\theta(x)$  depending on a local magnetic field  $b$ . Atomic nuclei occupied a volume  $V_D$  contribute to the magnetization  $P = m/V_D$ . Taking  $g = 3$  for nuclear component of magnetic induction we get

$$P = 1.5 \text{ TG } In / (10^{13} \text{ g/cm}^3), \quad (2)$$

In a case of comparable sizes for nucleus and occupied volume  $V_D$  (i.e.,  $n \sim 10^{13.5} \text{ g/cm}^3$ ) internuclear interaction is ferromagnetic (Kondratyev&Lutz, 1999; Kondratyev, 2002). Taking for magnetic coupling strength between nearest-neighbor (nn) elements the value  $J$  total Hamiltonian  $H$  for atomic nuclei array in a field  $H$  can be expressed as follows:

$$H = -\sum_i m_i b_i \quad (3)$$

through an interaction of magnetic moment  $m_i$  with a local field  $b_i = H(t) + J \sum_{j \subset nn} P_j + h_i$ . Here the sum runs over  $nn$  elements and random fields  $h_i$  with Gaussian distribution with a width  $R$ , called the disorder (Kondratyev, 1994; 2002), which allow to take into account the inhomogeneity, disorder and fluctuations.

## 3. RJIM model Implications in SGR-Burst Activity

Let us consider adiabatically changing in time crust magnetic field  $H$ . When the local field value  $b_i$  of a certain NS crust domain becomes less than certain value  $b_i$  magnetization is changing stepwise. Due to the ferromagnetic interaction moment hopping may be triggered for the nearest neighbors, which in turn may cause some discontinuity point for their neighbors, and so forth, producing, thereby, avalanches. The linear speed  $c_m$  of the avalanche propagation is determined by the ratio of a lattice constant  $a \sim 20$  fm and the relaxation time  $t_N \sim 10^{220.5}$  s for nuclear

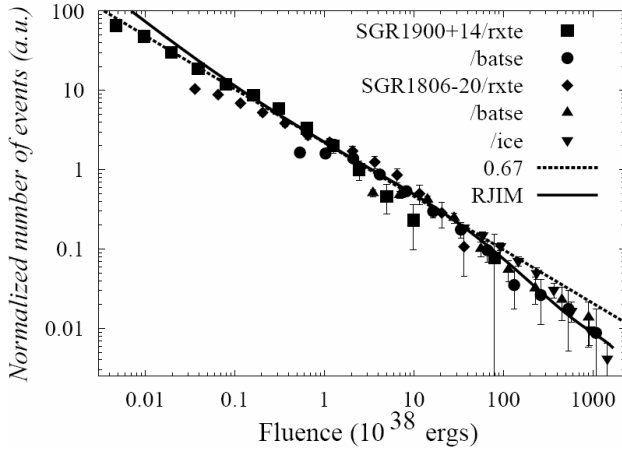


Figure 1: Normalized cumulative energy distributions of SGR-bursts are compared with the results of RJIM for the cubic lattice of a size  $(150)^3$  represented by the solid line. The data of the RXTE and BATSE observations for SGR 1900+14 from (Gogus et al., 1999) are shown by squares and circles, respectively. RXTE (diamonds), BATSE (up-triangles), and ICE (down-triangles) data for SGR 1806-20 are from (Gogus et al., 2000). The dashed line denotes the power law distribution.

re-configuration associated with magnetic response,  $c_m \sim a/t_N \sim 10^8$  cm/s (for more details see [3]). Then for outer crusts of a linear size,  $l_{\text{crust}} \sim 100$  m, an estimate of the avalanche spanning time,  $t_{\text{av}} \sim l_{\text{crust}}/c_m \sim 0.1$  ms, is consistent with the rising time for giant flares of SGR (Mazets et al 1979, Kondratyev 2002, Svinkin et al 2015). The field  $H(t)$  remains almost constant on the time scale  $t_{\text{av}}$ , while the magnetization reduces sharply on a value proportional to the avalanche size. The corresponding excess of magnetic energy is released in the magnetosphere and estimated as

$$E = H \Delta P V_a = 10^{41} \text{ Ergs} \quad (4)$$

$$(H/TT) (\Delta n / 10^{13} \text{ g/cm}^3) (V_a / 10^6 \text{ m}^3).$$

For a field strength  $H \sim 3TT$ , typical magnetar crust density  $n \sim 10^{13.5} \text{ g/cm}^3$ , and avalanche linear size of order of outer NS crust thickness, 100 m (i.e.,  $V_a$  about  $10^6 \text{ m}^3$ ) the amount of energy obtained from Eq. (3) is consistent with an energy of soft gamma-ray bursts.

Since the velocity of magnetoplasma waves (i.e., Alfvén waves) is close to the speed of light  $c$ , the linear size of the strongly excited magnetosphere region exceeds the value  $R_{\text{ex}} \sim l_{\text{crust}} c/c_m \sim 10$  km, comparable to NS radius. Subsequent development and cooling of photon-electron-positron plasma via gamma-ray emission from this region generates a short-duration ( $\sim 100$  ms) SGR-burst event with rising and decaying fronts of light curve  $\sim 10$  ms (Kondratyev 2002). Figure 1 represents the cumulative distributions of detected burst energy, i.e. the burst number with an energy exceeding certain value. We assume nearly isotropic emission accounting for a source remoteness. The RJIM results are in a good agreement with observations for 7 periods of energy. The obtained event number dependence is well fitted by the power law with an exponent 0.67, which corresponds to the value 1.67 for the differential distribution and provides a signal of self-organized criticality in the burst statistics.

For a constant change rate  $\dot{B}$  of the magnetic field the inter-avalanche field interval is proportional to the time interval (i.e. waiting time) between the induced bursts.

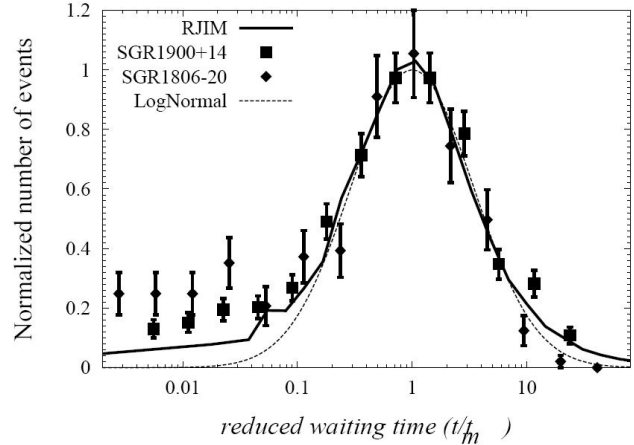


Figure 2: The reduced waiting time distribution between the successive RXTE/PCA bursts from SGR 1900+14 (squares) (Gogus et al., 1999) and SGR 1806-20 (diamonds) (Gogus et al., 2000) are compared with the waiting time distribution between avalanches (solid curve). The dashed line represents the fit to the lognormal distribution of the width 3.6.

Taking the respective normalized values, i.e. inter-burst time and inter-avalanche field, we compare the theoretical predictions with observations in Fig. 2. As seen in Fig. 2 for different SGRs the waiting time distributions as a function of the reduced time obey universal function. The data are well reproduced by simulations and fitted at a maximum by the lognormal function. Such a property points out the single time scale for SGR-burst triggering processes. Within RJIM model such a time-scale is determined by the ratio of the disorder parameter  $R$  and the field change rate  $\tau = R/\dot{B}$ . Therefore, the scaling with respective time leads to an universal function.

#### 4. Conclusion

We considered magnetodynamics of inhomogeneous nuclear matter relevant for neutron star crusts. Accounting for inter-nuclide magnetic coupling, we show that quantum fluctuations in nuclear magnetic reactivity give rise to erratic jumps in magnetotransport of neutron star crusts. The resulting sharp energy releases lead to gamma-ray bursts. The properties of such a noise are favorably compared with burst statistics of Soft Gamma Repeaters. As is shown the predicted by RJIM model scaling properties for, e.g., the burst intensity and waiting time distributions, are in a good agreement with SGR observations supporting thereby the credibility of RJIM model.

**Acknowledgements.** This work is supported in part by Integral scientific data center, the Swiss National Science Foundation (SCOPEs project No. IZ73Z0152485) and the Alexander von Humboldt Foundation.

#### References

- Gogus E. et al.: 1999, *Ap.J. Letters*, **526**, L93.
- Gogus E. et al.: 2000, *Ap.J. Letters*, **532**, L121.
- Kondratyev V.N.: 1994, *Phys. Lett.*, A **190**, 465.
- Kondratyev V.N., Lutz H.O.: 1999, *Eur. Phys. J. D* **9**, 483.
- Kondratyev V.N.: 2002, *Phys. Rev. Lett.*, **88**, 221101.
- Kondratyev V.N.: 2014, *EPJA.*, **50**, 7.
- Kondratyev V.N., Korovina Yu.V.: 2015, *JETP L*, **102**, 131.
- Mazets E.P. et al.: 1979, *Nature (London)*, **282**, 587.
- Svinkin D.S. et al.: 2015, *Mon. Not. R. Astron. Soc.*, **447**, 1028.

DOI: <http://dx.doi.org/10.18524/1810-4215.2016.29.84978>

# NUCLEOSYNTHESIS AT MAGNETOROTATIONAL SUPERNOVA EXPLOSION AND GALACTIC CHEMICAL EVOLUTION

V. N. Kondratyev<sup>1,2</sup>, T. V. Mishenina<sup>3</sup><sup>1</sup> Physics Department, Taras Shevchenko National University of Kyiv, 03022-UA Kyiv, Ukraine, [vkondrat@univ.kiev.ua](mailto:vkondrat@univ.kiev.ua)<sup>2</sup> Faculty of Physics, Bielefeld University, D-33501 Bielefeld, Germany<sup>3</sup> Astronomical Observatory, Odessa National University, 65014-UA Odessa, Ukraine, [tmishenina@ukr.net](mailto:tmishenina@ukr.net)

**ABSTRACT.** Synthesis of chemical elements is investigated at conditions of magnetorotational instabilities in astrophysical plasma at supernova explosion. Effects of ultra-strong nuclear magnetization are demonstrated to enhance the portion of titanium product. The relation to an excess of <sup>44</sup>Ti revealed from the Integral mission data and galactic chemical evolution is discussed.

**Keywords:** Stars: supernovae, magnetic field. – Nucleosynthesis: abundances, the Galaxy chemical evolution.

## 1. Introduction

Major nucleosynthetic contributions to nuclide enrichment during galactic chemical evolution, plausibly, come from synthesis of heavy atomic nuclei in Supernovae (SNe) (Woosley, Heger & Weaver, 2002). Magnetorotational instabilities (MRI) and/or dynamo action represent perhaps main respective explosion mechanism. Then for magnetic field geometry one gets, see Fig. 1. Maximum field intensity at distances smaller than a radius  $r_0$  from a center of the vortex dynamo process can be taken as a constant  $H_0$ . Strong magnetization of the MRI central region stabilizes magnetic fluxes  $\Phi_0$  also for field decaying components. Respectively, in conditions of a constant flux at radius  $r > r_0$  the dependence of strength  $H$  on distance  $r$  can be represented as  $H = \Phi_0 / \pi r^2$ . Comparable values for magnetic pressure gradients and gravitational force, i.e.,  $dH^2(r)/dr = 4H_0^2/b^2 r_a \sim 8\pi GM n(R)/R^2$ , determine the radius  $r_a$  relative to the MRI center corresponding to material irruption. Here the gravitational constant  $G$ , the star mass  $M$  inside the bifurcation radius  $R$  is related to the matter density  $n(R)$  as  $4\pi R^2 n(R) = -dM/dR$ . Additional constraints on MRI parameters are given by shock wave energy  $E_s$ , see (Kondratyev & Korovina, 2015),  $H_0^2 r_0^2 \sim 8 E_s / [L(2-b^{-1})]$ , where  $L$  is total length of MRI areas,  $b = (r_a/r_0)^2$ . For typical SN Type II values  $R \sim 30$  km,  $E_s \sim 10^{51.5}$  ergs at  $H_0 \sim 3$  TT one obtains  $r_0 \sim 10^{-0.5}$  km and  $b \sim 10$ . Nuclides produced at such fields (i.e., larger than 0.1 TT) contain an information on matter structure and explosion mechanisms (see Kondratyev et al., 2004; 2014; and refs. therein). In this contribution we analyze MRI effect in nuclide production and galactic chemical evolution.

## 2. MRI explosive nucleosynthesis

Abundances of iron group and nearby nuclides are described very successfully within nuclear statistical equilibrium (NSE) approach for over half a century (Woosley, Heger & Weaver, 2002). At such conditions nuclide abundance is determined mainly by the binding energy of corresponding atomic nuclei. The magnetic effects in the NSE were considered by Kondratyev (2014 and refs. therein). Recall that at temperatures ( $T \leq 10^{9.5}$  K) and field strengths ( $H \geq 0.1$  TT), the magnetic field dependence of relative output value  $y = Y(H)/Y(0)$  is determined by a change in the binding energy of nuclei in a field and can be written in the following form

$$y = \exp\{\Delta B / kT\}. \quad (1)$$

We consider examples of <sup>56</sup>Ni and <sup>44</sup>Ti. Such a choice of symmetric nuclei, double magic and anti-magic for vanishing magnetization, gives a clear picture of magnetic effects in the formation of chemical elements and fundamental conclusions about transmutation and synthesis of nuclei in ultramagnetized plasma.

The binding energy  $B$  can be written as  $B = B_{\text{LDM}} + C_n + C_p$ , where shell corrections  $C_i$  for protons and neutrons, and the component  $B_{\text{LDM}}$  is calculated in semiclassical liquid drop model and varies only slightly in the magnetic field, according to the Bohr-van Leuven theorem, see (Kondratyev, 2014).

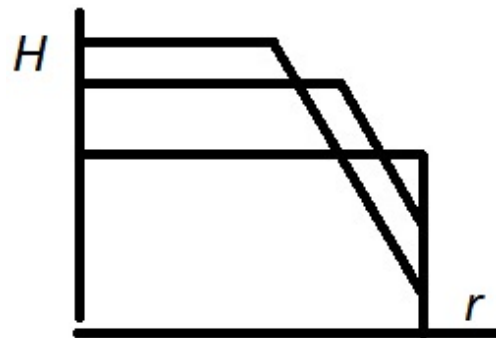


Figure 1: Schematic view of magnetic field geometry for MR grain in Supernova.

Spin magnetization of Pauli type dominates for the neutron magnetic reactivity. Interaction of a field and the spin-magnetic moment corresponding to a spin projection  $m_n$  on a field vector gives rise to a linear shift of energy levels  $\Delta = m_n g_n \omega_L$ , where  $\omega_L = \mu_N H$  with nucleon magneton  $\mu_N$ , and  $g_n$  – neutron  $g$ – factor. Accordingly, the shell energy in a field  $H$  is modified as follows

$$C_n(H) = C_n^+(E_F + \Delta) + C_n^-(E_F - \Delta), \quad (2)$$

where the indices + and – indicate a sign of the projection of spin magnetic moment on field direction. The proton magnetic response is represented by a superposition of the field interaction with spin and orbital magnetic moments and exceeds the neutron component for an open shell.

As is demonstrated by Kondratyev & Korovina (2015) at field strengths  $H < 10$  TT, the binding energy shows nearly linear  $H$  dependence for considered nuclei  $B = B_0 + \kappa_i H$  [MeV] with magnetic susceptibility parameters  $\kappa_i$  depending on a nucleus  $nucleus = {}^A_Z N$ . For  ${}^{44}\text{Ti}$  the value of this parameter is positive  $\kappa_{\text{Ti}} \sim 0.3$  MeV/TT, and in case of  ${}^{56}\text{Ni}$  it becomes negative  $\kappa_{\text{Ni}} \sim -0.3$  MeV/TT. Evidently, for anti-magic at zero field strength nuclei the shell energy always increases with field  $H$ , and for magic one – decreases, indicating positive and negative values of magnetic susceptibility  $\kappa_i$ , respectively. Then for an average relative yield over MRI region  $V$ , see sect. 1,  $\langle y \rangle = V^{-1} \int_V d^3 r y(H(\mathbf{r}))$  one gets

(Kondratyev & Korovina, 2015)

$$\begin{aligned} \langle y \rangle &= b^{-1} \left( \exp\{a\} + \int_1^b \exp\{a/x\} dx \right) \\ &= \left( \exp\{a/b\} + \frac{a}{b} [\text{Ei}(a) - \text{Ei}(a/b)] \right), \end{aligned} \quad (3)$$

where  $a = \kappa_i H_0 / kT$ ,  $b = (r_a/r_0)^2$ . The radius  $r_0$  relative to the MRI center corresponds to a maximum in field strength  $H_0$ , and radius  $r_a$  is determined from conditions of comparable values for magnetic pressure gradients and gravitational force at  $R$  corresponding to material irruption, i.e.,  $dH^2(r)/dr = 4H_0^2/b^2 r_a \sim 8\pi GM n(R)/R^2$ . Here the gravitational constant  $G$ , and the star mass  $M$  inside the bifurcation radius  $R$  is related to the matter density  $n(R)$  as  $4\pi R^2 n(R) = -dM/dR$ , and the integral exponential function  $\text{Ei}(x) = \int_{-\infty}^x \frac{\exp\{t\}}{t} dt$ .

In Fig. 2 one sees significant difference for magnetic field dependence of nuclide output, magic and anti-magic at vanishing field. For anti-magic nuclei and, therefore, increasing binding energy with increasing field strength or positive magnetic susceptibility relative volume of nucleosynthesis increases significantly with increasing  $a$ . At the same time, the relative production of magic nuclides, i.e., negative value  $a$ , is not substantially changed with increasing field. This behavior significantly differs from the case of a spatially uniform magnetization, see Fig. 2, which corresponds to the exponential dependence of  $\langle y \rangle$  or  $b = 1$  in Eq. (3). In this case the coefficients of suppression and

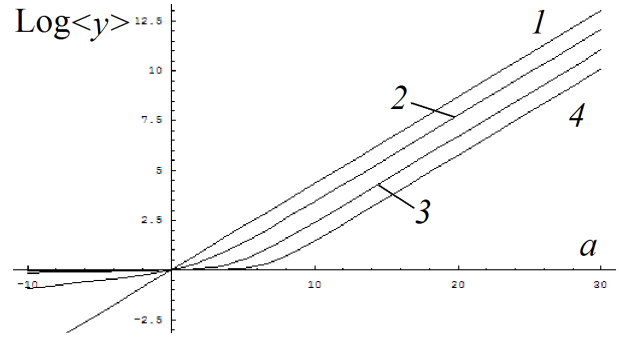


Figure 2: Relative yield of nucleosynthesis products depending on a parameter  $a$  at values  $b = 1, 9, 100, 900$  indicated by lines 1, 2, 3, 4, respectively.

enhancement are the same with the same absolute value of  $a$ . The presence of the diffusion layer, corresponding to a fade-out field strength with increasing  $r$  (or  $b > 1$ ) in a real MRI region leads to substantial differences of relevant factors. Significant increase in a synthesis of anti-magic nuclei is accompanied by a slight change in mass volume magic nuclides. Model predictions in the absence of magnetic effects, see. (Woosley, Heger & Weaver, 2002), give the mass of initially synthesized  ${}^{44}\text{Ti}$ ,  $M_{\text{Ti}} \sim 10^{-5} M_{\text{Sun}}$  (in solar masses  $M_{\text{Sun}}$ ). For realistic characteristics of Type II SN explosion (sect. 1) enhancement factor  $\langle y \rangle_{\text{Ti}} \sim 30 - 300$  corresponds to a mass  $M_{\text{Ti}} \sim 10^{-3.5} - 10^{-2.5} M_{\text{Sun}}$ . It is worthy to notice that not all the material ejected from the central part of a star is formed in MRI areas, see (Kondratyev, 2014). Such an enhancement of  ${}^{44}\text{Ti}$  is in an agreement with direct observations in young SN II remnants (Kondratyev & Korovina, 2015)  $M_{\text{Ti}} \sim 10^{-3.5} M_{\text{Sun}}$ . At the same time for SN I the  ${}^{44}\text{Ti}$  volume is significantly smaller (Kondratyev, Korovina & Mishenina, 2015). One might expect, therefore, noticeable correlations in enrichment of anti-magic nuclides with other metals, e.g.,  ${}^{56}\text{Fe}$ ,  ${}^{48}\text{Ti}$ ,  ${}^{26}\text{Al}$ .

### 3. Galactic chemical evolution: magic and anti-magic nuclides

An important application of the nucleosynthesis computations is represented by a description of the enrichment of our Galaxy and the Universe as a whole with various chemical elements. Despite considerable progress in the chemical evolution modeling, as well as in the nucleosynthesis computations, a number of issues remain unresolved. In this paper, we dwell on potential sources of calcium and titanium production.

For this purpose we use the abundances of these elements, which we had obtained earlier for the Galactic disc dwarfs (Mishenina et al., 2008), and compared them with the chemical evolution computations (Timmes, Woosley & Weaver, 1995) (Figs. 3, 4). In the study (Timmes, Woosley & Weaver 1995) the yields of isotopes  ${}^{48}\text{Ti}$  and  ${}^{44}\text{Ca}$ , produced by massive supernovae, from Woosley & Weaver (1995) were used to develop a Galactic chemical evolution model. As can be seen from Figs. 3 and 4, the employed data describe the trend of  $[\text{Ca}/\text{Fe}]$  vs.  $[\text{Fe}/\text{H}]$  quite well; however, the adopted yield of isotope  ${}^{48}\text{Ti}$  is insufficient to describe the behavior of  $[\text{Ti}/\text{Fe}]$  vs.  $[\text{Fe}/\text{H}]$ . A similar pattern for calcium and titanium is presented in

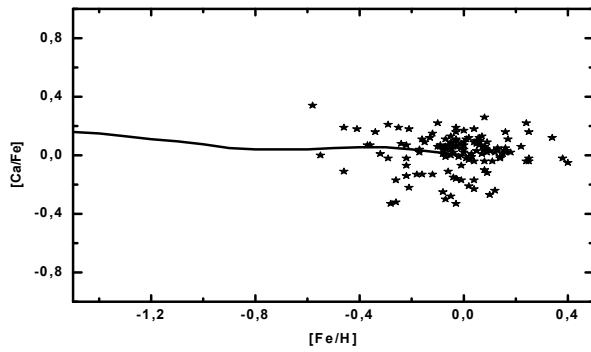


Figure 3: Comparison of observed abundance of Ca (Mishenina et al. 2008, marked as asterisks) with the trend of galactic chemical evolution (Timmes, Woosley & Weaver 1995, marked as solid line).

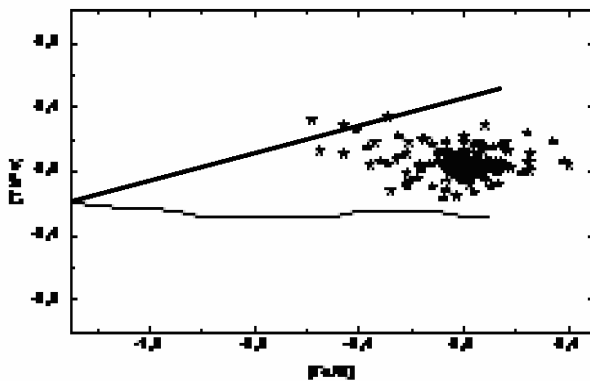


Figure 4: The same as Figure 3, but for Ti abundance. Thick solid line shows magnetic enhancement, see eq. (3) and discussion therein.

the study by Timmes, Woosley & Weaver (1995; see their Figs. 25 and 27). It proves that the investigated sources of calcium production, such as massive stars, are dominant suppliers of calcium in the interstellar medium while further improved computations for the titanium sources are required. In respect with titanium the authors point out that "both the  $^{48}\text{Ti}$  yield and the ration  $[\text{Ti}/\text{Fe}]$  are sensitive to the parameters of the explosion and the amount of material that falls back onto the neutron star". The nucleosynthesis computations (Woosley & Weaver, 1995) were carried out not accounting for the magnetic field.

We suggest another possible mechanism of additional titanium enrichment when taking into account the increased yield of anti-magic nuclides in ultramagnetized astrophysical plasma. As is seen on an example of the radioactive isotope  $^{44}\text{Ti}$  the direct observational data, see sect. 1, confirm such an enrichment which can be understood in terms of magnetic effects. The resulting enrichments of M44 isobars are collaborated with observational data (Kondratyev, 2014; Magkotsios, 2010). The proton magnetic reactivity dominates in a change of binding energy, see Eq. (2). Therefore, one can expect to meet a noticeable increase in production of other titanium isotopes, as well. At the same time a yield calcium isotopes can be

expected unchanged because of the proton shell closure, see Eq. (3).

#### 4. Conclusion

Nucleosynthesis at magnetorotational supernova explosion was considered by employing arguments of nuclear statistical equilibrium. Magic-antimagic switches in the nuclear shell structure in varying magnetic field lead to an increase of titanium binding energy and, consequently, to a noticeable increase of the portion of  $^{44}\text{Ti}$  in explosive nucleosynthesis products. Magnetic effects in nuclide creation are favorably compared to observational Integral data and galactic chemical composition.

*Acknowledgements.* This work is supported in part by Integral scientific data center and by the Swiss National Science Foundation (SCOPE project No.~IZ73Z0152485).

#### References

- Kondratyev V.N. et al.: 2004, *Proc. 54th Intern.Symp. on Nuclear Spectroscopy and Structure of Atomic Nuclei* (Belgorod, Russia), p. 83.  
 Kondratyev V.N.: 2014, *EPJ A*, **50**, 7.  
 Kondratyev V.N., Korovina Yu.V.: 2015, *JETP Letters* **102**, 131.  
 Kondratyev V.N., Korovina Yu.V., Mishenina T.V.: 2015, *Odessa Astron. Publ.*, **28**, 168.  
 Mishenina T.V., Soubiran C., Bienayme O. et al.: 2008, *Astron. Astrophys.*, **489**, 923.  
 Magkotsios G. et al.: 2010, *Astrophys. J. Suppl. Ser.*, **191**, 66.  
 Woosley S.E. & Weaver T.A.: 1995, *Astrophys. J. Suppl. Ser.*, **101**, 181.  
 Woosley S.E., Heger A., Weaver T.A.: 2002, *Rev. Mod. Phys.*, **74**, 1015.  
 Timmes F.X., Woosley S.E., Weaver T.A.: 1995, *Astrophys. J. Suppl. Ser.*, **98**, 617.

DOI: <http://dx.doi.org/10.18524/1810-4215.2016.29.84982>

## THE CHEMICAL COMPOSITION OF THE ACTIVE STARS

L. V. Glazunova<sup>1,2</sup><sup>1</sup> Department of Astronomy, Odessa National University  
T.G.Shevchenko Park, Odessa 65014 Ukraine, [astro@paco.odessa.ua](mailto:astro@paco.odessa.ua)<sup>2</sup> Odessa National Academy of Telecommunications,  
Kuznechnaya street 1, Odessa, 65029, Ukraine

**ABSTRACT.** The comparison of the results of the studies of the active stars' chemical composition obtained by different authors has been performed. It was concluded that the difference between the abundances of some elements in active and inactive stars becomes significant ( $> 3\sigma$ ) only for the active stars with high chromospheric activity ( $lgR'_{HK} > -4$ ). This is the case primarily for the light elements, namely Li, Na and Al, as well as heavy elements with  $Z > 30$ .

**Key words:** Stars: RS CVn end BY Dra binaries, abundances – stars: individual: LX Per, OU Gem, BY Dra.

## 1. Introduction

Stars with outer convective envelopes and luminosity classes V to III with the observed emission in the CaII *H&K* lines, the light curve peculiarities, as well as enhanced X-ray and microwave emission, are termed as active stars (Berdugina, 2005). One of the quantitative measures of chromospheric activity is the activity index  $lgR'_{HK} = lg(F_{HK}/\sigma T_{eff}^4)$ , which was first introduced by Noyes et al. (1984). This index describes the correlation between the emission flux in the CaII *H&K* lines and luminosity of a star. Several types of active stars of widely differing masses and in different evolutionary stages have been discovered to date; these are young T Tauri (T Tau) stars which have not yet reached the Main Sequence (MS); RS Canum Venaticorum (RS CVn) stars which represent evolved synchronized fast-rotating components of close binary systems; W Ursae Majoris (W UMa) stars; cool low-mass dwarf BY Draconis (BY Dra) stars; and single giants of the FK Comae (FK Com) type. Objects within such a range of evolutionary states have one common feature they all have outer convective envelopes and high rates of spin resulting in the magnetic field enhancement. The highest chromospheric activity is exhibited by the RS CVn binaries and the BY Dra type low-mass dwarfs (Strassmeier, 2005).

The RS CVn stars are close detached binary systems with the orbital periods from several days to several

tens of days; in these binaries, one component is usually a G-K subgiant, while another one is a low-mass main-sequence star. The chromospheric activity of the subgiant is deemed to be related with its rather rapid rotation as a close binary component. The activity of these stars was first detected from the sinusoidal variations in their light curve, which did not coincide with the binary orbital period. The associated brightness variations are considered to be related with the presence of dark spots on the subgiants surface; these are similar to sunspots, but are relatively larger (covering up to 20% of the disc area in some binary systems). The amplitude of the binary brightness variations related to these spots is from several hundredths to several tenths of a magnitude. The difference between the spot and disc temperatures can reach as high as 1500 K. The chromospheric activity index is higher than  $-4.0$  dex.

The BY Dra type stars are main-sequence dwarfs with spectral types G, K and M and masses  $0.08 \div 0.5M_{\odot}$ . High magnetic activity is exhibited as strong optical flares and periodical variations in the brightness of the out-of-eclipse portions of the light curve with amplitudes of up to  $0.1^m$ . This peculiarity is due to large spots on the stellar surface (covering up to 10% of the stellar surface).

Such high chromospheric activity on the stellar surface is likely to affect not only resonance, but also subordinate spectral lines, resulting in altered surface chemical composition. The investigated peculiarities of the chemical composition of active stars can be an additional indicator of physical processes on their surfaces.

## 2. The chemical composition of inactive stars with outer convective envelopes and luminosity classes V to III

Before proceeding to a discussion of the chemical composition of chromospherically active stars, the peculiarities and errors in determinations of the chemical composition of late-type inactive stars in our Galaxy should be considered. This can be done by exemplify-

ing the study of the chemical composition of the HR 1614 moving group dwarfs by De Silva et al. (2007), in which the abundances of 13 elements were determined from high-dispersion spectra of 14 cluster stars and four field stars. The reported mean standard deviation (deviation) of the derived iron abundances in the cluster stars was  $\sigma = \pm 0.033$  dex, while the intrinsic accuracy of the model atmospheric parameters was as follows:  $T_{eff} = \pm 50$  K,  $\lg g = \pm 0.1$ ,  $\xi = \pm 0.1$  km s<sup>-1</sup>. A noticeable difference (exceeding 3  $\sigma$ ) between the mean abundance estimates and the solar values was observed for the light elements, such as Na ( $-0.09 \pm 0.08$  dex) and Al ( $-0.13 \pm 0.06$  dex), and for heavier elements with  $Z > 39$ , namely Zr ( $-0.15 \pm 0.07$  dex) and Nd ( $-0.21 \pm 0.02$  dex); the overabundance of barium ( $+0.15 \pm 0.05$  dex) was also observed. The field stars exhibited the same tendency in the estimated elemental abundance dynamics as that observed in the cluster stars, with the only exception being a much narrower scatter of the elemental abundance determinations: Na ( $-0.18 \pm 0.04$  dex), Al ( $-0.2 \pm 0.05$  dex), Zr ( $-0.15 \pm 0.04$  dex) and Ba ( $+0.25 \pm 0.03$  dex). These four stars have almost equal gravitational acceleration; and it is this parameter which has the most direct effect on the level of errors in the determination of the atmospheric abundances of these elements.

The abundances of 23 elements in 276 dwarfs of the population of the thin and thick components of the Galactic disc were determined in the studies by Mishenina et al. (2004, 2008, 2013). The intrinsic accuracy in the determinations of the model atmospheric parameters were expected to be as follows:  $T_{eff} = \pm 100$  K;  $\lg g = \pm 0.2$ ;  $\xi = \pm 0.2$  km s<sup>-1</sup>. Standard deviation of the estimated abundances of the light elements ( $Z < 13$ ) was  $\sigma = \pm 0.15$  dex, which was twice as high as that for the iron-group elements ( $\sigma = \pm 0.08$  dex). The dispersion of the estimated abundances of the heavy elements ( $Z > 38$ ) was  $0.12 \div 0.14$  dex for cooler stars ( $T_{eff} = 5000$  K) and  $0.08 \div 0.10$  dex for hotter stars ( $T_{eff} = 6000$  K). The authors deduced the following conclusions:

- A decrease in the abundances of  $\alpha$ -elements, in particular for O, Mg, Si and Ti, was observed with increasing metallicity though the dispersion of the estimated Ca abundances was higher.
- High dispersion observed for Al is likely to be caused by the NLTE-effects, and it may be reduced when these effects are taken into account.
- High dispersion observed for Na remains at the same level even when the NLTE effects are factored in. This can be due to the fact that many sources contribute to the Na production, which results in its highly inhomogeneous distribution in the interstellar medium.
- High dispersion in the Ba and La abundance estimates is likely due to high uncertainties in the stellar age determinations, which resulted in the uncertain-

ties in the determined contributions of the slow  $s$ - and rapid  $r$ - neutron-capture processes, which are the main donors of these elements.

As can be seen, the dispersion of the estimated elemental abundances in the studies by Mishenina et al. are consistent with that reported by De Silva et al. (2007), given the error in the model parameter determinations in the latter study is half that in the former ones. For several elements the differences between the stellar abundance determinations and solar values are so small (within  $2\sigma$ ) that can not be reckoned as significant. However, we can unambiguously assert that the error in the determinations of the atmospheric abundances of certain chemical elements (such as Na, Al, Ba and possibly some others) in dwarfs is by a factor of two or even three greater than that for other elements.

The analysis of the chemical composition of cool giants in our Galaxy can be exemplified by the study of Reddy et al. (2012) concerned with the determination of mean abundances of 22 chemical elements in the giants belonging to clusters of different ages. The intrinsic accuracy in the determinations of the model atmospheric parameters were expected to be as follows:  $\delta T_{eff} = \pm 100$  K;  $\delta \lg g = \pm 0.25$ ;  $\delta \xi = \pm 0.2$  km s<sup>-1</sup>. The mean dispersion of the estimated abundances for all investigated elements was 0.03–0.05 dex. The distribution of elements by their atomic numbers is typical for giants as such: the excess in the abundance estimates when compared to the solar values, which was 0.1 dex for the light elements ( $\alpha$ -elements) and 0.2 dex for the heavy elements ( $s$ - and  $r$ -elements), is accounted for by the evolutionary change in the elemental abundances of the giant atmosphere.

### 3. The study of the chemical composition of active stars

A comparison between the elemental abundances in active (30) and inactive (101) dwarf stars was conducted in the study by Mishenina et al. (2008), and the following conclusions were inferred from the results obtained:

- both active and inactive dwarfs have shown almost the same correlations between the elemental abundances and metallicities;
- the lithium abundance determinations appeared not to be dependent on the stellar indices of chromospheric activity.

It is noteworthy that among the stars which had been assigned as active stars by various criteria, this study was focused on the stars with low chromospheric activity indices (lower than  $-4.32$  dex). The most comprehensive study of the chemical composition of active stars with high chromospheric activity indices was performed by Morel et al. (2006), who investigated the

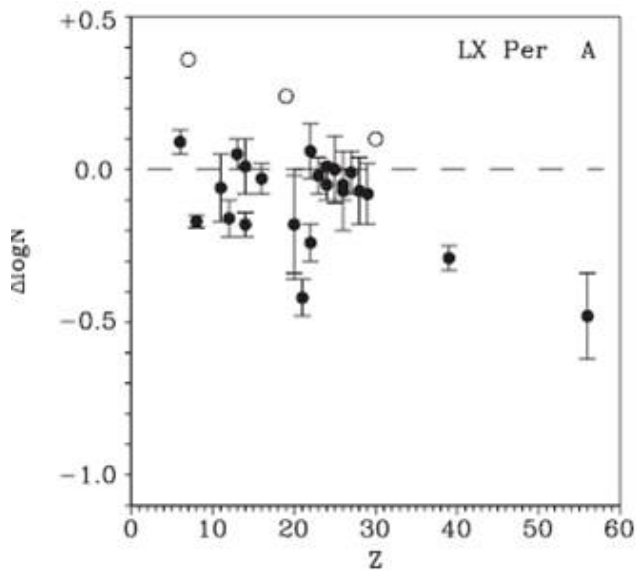


Figure 1: The distribution of the chemical elements in the atmospheres of the LX Per binary components (A component).

abundances of 10 elements with atomic numbers in the range 11 to 28, and 56 (Ba) in eight RS CVn stars with the index  $\lg R'_{HK}$  ranged from  $-3.83$  to  $-3.69$ . The largest difference between the abundance estimates and solar values was reported for Na ( $+0.4 \pm 0.1$  dex) and Al ( $+0.3 \pm 0.1$  dex); this difference was less significant for other  $\alpha$ -elements, while the scatter of barium abundances was rather wide ( $+0.2 \pm 0.2$  dex) in both active and inactive stars. These elements are noticeably sensitive to the NLTE-effects.

As shown by theoretical calculations performed in Lind et al. (2011), the error in the abundance determinations for these elements is expected to be not lower than  $0.1 \div 0.15$  dex, which is rather consistent with the dispersion of the abundance estimates for these elements in inactive late-type dwarfs. Hence, such a large difference between the abundances of certain elements and the solar values (especially for Na and Al) is due to their sensitivity to the NLTE-effects, which are considerably enhanced in active stars. The increased abundances of the elements sensitive to the NLTE effects in chromospherically active stars (with  $\lg R'_{HK} > -4$ ) are well illustrated in the study by Morel & Micela (2004) concerned with the investigation of the oxygen atmospheric abundances in active and inactive stars from the OI 6300 Å line, which is not sensitive to the NLTE-effects, and from the OI 7774 Å triplet, which is sensitive to the NLTE-effects. As reported in this study, the oxygen abundances derived from the OI 7774 Å triplet were on average  $1.0 \pm 0.2$  dex higher than those determined from the OI 6300 Å line.

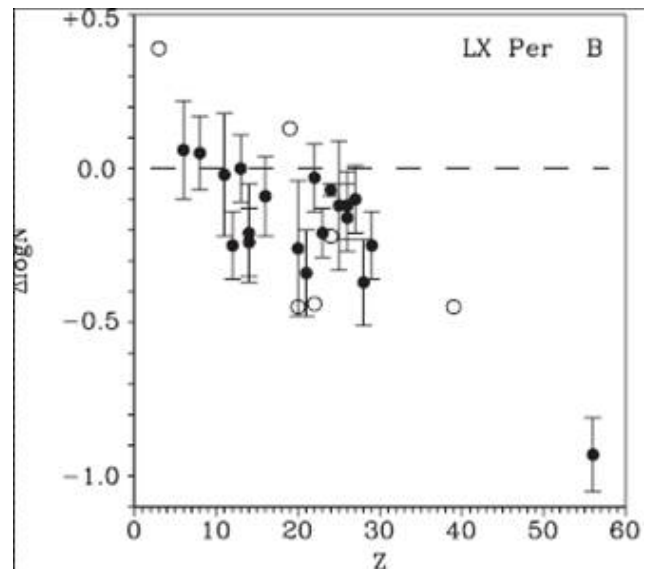


Figure 2: The distribution of the chemical elements in the atmospheres of the LX Per binary components (B component).

#### 4. The in-depth analysis of the chemical composition in the atmospheres of active stars by exemplifying certain binary systems

Let us consider in more detail the results and problems related to the abundance determinations in active stars exemplifying the most prominent representatives of the RS CVn stars, which have been the subject of numerous studies. There are very few investigations of the chemical composition of active stars in binaries with well-known parameters of the binary system and its components; and this can be an essential factor in drawing conclusions on the pattern of the abundance variations. Just several rather bright RS CVn and BY Dra stars have been thoroughly investigated to date.

Lambda Andromedae ( $\lambda$  And) is a RS CVn-type binary system (Tautvaisiene et al., 2010) with the rotation period of the active star subgiant  $P_{rot} = 54$  days and orbital period  $P_{orb} = 21$  days; the secondary component of the binary is a white dwarf. The effective temperature of the subgiant  $T_{eff} = 4830$  K; its projected rotational velocity  $v \sin i = 6.5$  km/s; its activity index  $\lg R'_{HK} = -3.68$ , and metallicity  $[Fe/H] = -0.53$  dex. As shown by the results of photometric observations (Frasca et al., 2008), in this binary system the spots on the subgiants surface cover up to 12% of the surface area while their temperature is 800 K lower than the photospheric one. The investigation of the atmospheric abundances of the  $\lambda$  And binary subgiant, which is a bright star, have been numerous reported. The scatter of the elemental abundances es-

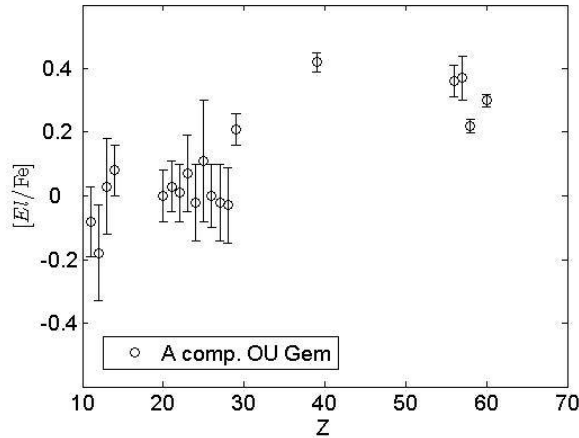


Figure 3: The distribution of the chemical elements in the atmospheres of the OU Gem binary components (A component).

timated in different studies of the subgiant is very wide ( $\pm 0.25$  dex on average), though the error in the abundance determinations averages to  $\pm 0.05$  dex. Such a wide scatter resulted from the employment of different model parameters of the subgiants atmosphere due to the spotted stellar surface associated with the mean effective temperature variations with the rotation phase, rather than from the errors in simulations. The mean abundance of the chemical elements generated in different nuclear processes is on average higher than the solar values; these differences amount to  $[\alpha/Fe] = 0.4$  dex,  $[s/Fe] = 0.2$  dex and  $[r/Fe] = 0.4$  dex. We suggest that such differences can be related to two processes:

- 1) the enrichment in the heavy elements resulted from the exchange of matter between a massive star (which is a white dwarf in this case) and less massive star (which is a subgiant in this case);

- 2) substantial NLTE-effects. A noticeable atmospheric lithium deficit in the active star ( $-0.5$  dex) should also be noted.

29 Dra is a RS CVn-type star (Barisevicius et al. 2010), its one component is a subgiant whose rotation period  $V_{rot} = 32$  days while the secondary component is a white dwarf. The effective temperature of the subgiant  $T_{eff} = 4720$  K; its projected rotational velocity  $v \sin i = 6.7$  km/s; the activity index  $\lg R'_{HK} = -4.65$ , and the atmospheric metallicity  $[Fe/H] = -0.20 \pm 0.05$  dex. This binary system has also been widely investigated. In contrast to the  $\lambda$  And binary system, whose chromospheric activity is higher, the scatter of the elemental abundances in 29 Dra is far narrower ( $< 0.1$  dex). This indicates that the model atmospheric parameters are less dependent on the rotation phase of the subgiant. The relative abundances of the iron-group elements, as well as  $s$ - and

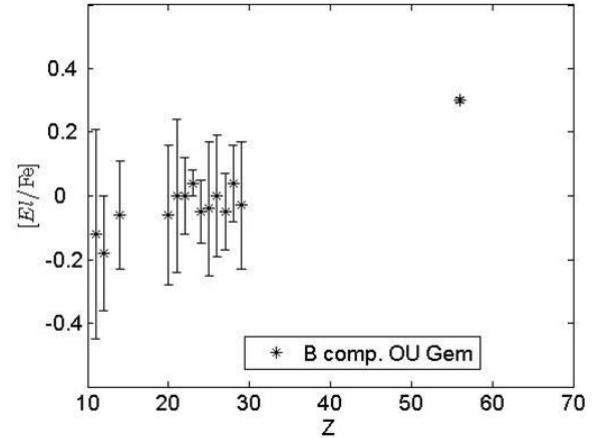


Figure 4: The distribution of the chemical elements in the atmospheres of the OU Gem binary components (B component).

$r$ -process elements, equal to solar ones. The abundance of  $\alpha$ -process elements is 0.1 dex higher than the solar value. Such a difference between the abundance estimates for  $\alpha$ -process elements and the solar values is likely to be mainly due to the exchange of matter in the binary with a more massive star evolving to become a white dwarf; and to a lesser extent, it may be accounted for by the NLTE-effects related to the chromospheric activity of the subgiant. A noticeable atmospheric lithium deficit in the active star ( $-0.45$  dex) should also be noted.

Thus, it was not a right selection of the two RS CVn-type binary systems, namely 29 Dra and  $\lambda$  And, as target ones to investigate the chemical composition of chromospherically active stars, because the elemental abundances in the primary components atmosphere may significantly vary at the stage of exchange of matter in the course of the binary evolution, though the contribution from the secondary component, which is a white dwarf, to the combined spectrum is near-zero in these binaries. The studies of the  $\lambda$  And binary system have also shown the dependence of the subgiants model atmospheric parameters on the phases of its rotation. Hence, the active stars in the 29 Dra and  $\lambda$  And binary systems cannot be used as target ones to study the impact of the chromospheric activity on the formation of the spectral lines.

The studies of another bright star of the RS CVn type, namely 33 Piscium (33 Psc) (Barisevicius et al., 2011), have been performed many times. This binary system contains a subgiant along with a late-type main-sequence star whose contribution to the combined spectrum of the binary is insignificant. The subgiant exhibits low chromospheric activity ( $\lg R'_{HK} < -4.7$ ). The orbital period of the binary

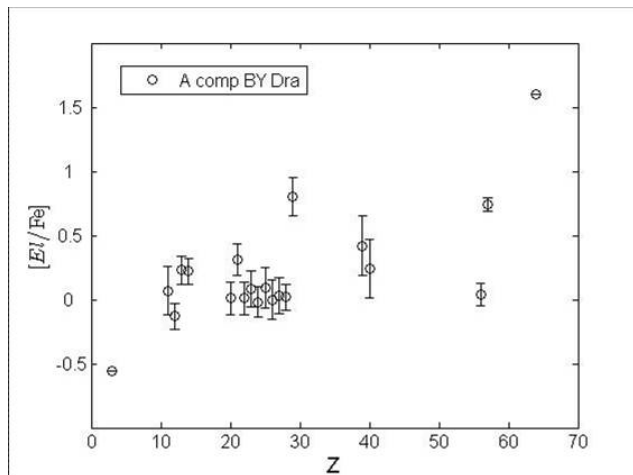


Figure 5: The distribution of the chemical elements in the atmospheres of the BY Dra binary components (A component).

system  $P_{orb} = 73$  days; the effective temperature of the subgiant  $T_{eff} = 4750$  K; its projected rotational velocity  $v \sin i = 2$  km/s and atmospheric metallicity  $[Fe/H] = -0.09 \pm 0.06$  dex. The scatter of the abundance estimates for different elements reported in different studies is within the error in the model determinations, except for certain lines. On average, the relative abundances of all elements are typical for the main-sequence stars and subgiants and almost equal to the solar ones.

##### 5. The investigation of the chemical composition of chromospherically active stars from the composite spectra of binary systems

The results of in-depth studies of a number of RS CVn and BY Dra binary systems with combined spectra, i.e. the spectra exhibiting the lines from both binary components, are also available at present. LX Persei (LX Per) is an eclipsing spectroscopic binary of the RS CVn type (Kang et al., 2013), which contains a main-sequence star and an active subgiant. The orbital period of the binary  $P_{orb} = 8$  days; the effective temperatures of the primary (A) and secondary (B) components are  $T_A = 6200$  K and  $T_B = 4790 \pm 230$  K, respectively; the ratio of the components luminosities  $L_A/L_B = 0.90$ ; the projected rotational velocities of the A and B components  $v \sin i_A = 9.1$  and  $v \sin i_B = 21$  km/s, respectively; the activity index of the subgiant  $\lg R'_{HK} = -4.55$ ; the metallicities of the A and B components  $[Fe/H]_A = -0.05 \pm 0.05$  dex and  $[Fe/H]_B = -0.12 \pm 0.11$  dex, respectively. The out-of-eclipse portion of the light curve shows peculiar variations with amplitudes ranging from 0.03 to 0.08<sup>m</sup>,

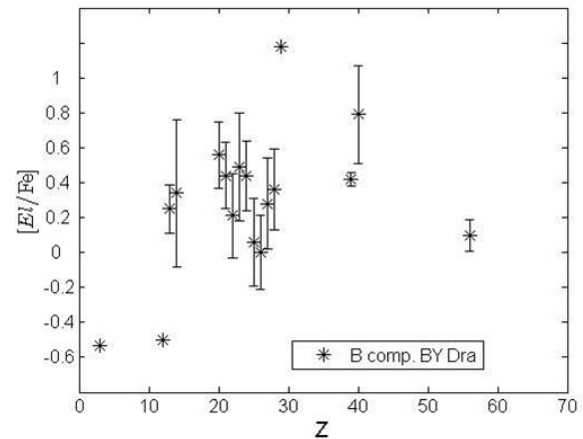


Figure 6: The distribution of the chemical elements in the atmospheres of the BY Dra binary components (B component).

though these variations showed no periodicity typical for the RS CVn stars. Fig. 1 presents the distribution of the chemical elements in both binary components (Kang et al. 2013). As is seen in Fig. 1,2 the elemental abundances in both components show significant peculiar variations, which exceed several-fold the error in the abundance determinations. Though there are not many lines of the heavy elements ( $Z > 40$ ), their abundance estimates show the most pronounced difference, such as a considerable deficit, when compared to the solar values; however, the barium lines can be reliably observed. Evolutionary changes in the abundances of the heavy elements imply their increase, rather than decrease; overlooking the NLTE-effects can also result in the increased.

Such a peculiar pattern of the distribution of the heavy elements has been obtained for the first time, and the authors suggested it can be due to the accretion of material from the gas-dust shell, in which the separation of the gas and dust components had occurred. This explanation cannot be deemed as credible, especially with regard to the stars with outer convective envelope. Accretion of material from the gas-dust shells is not a rare case in binary systems; however, such a peculiar pattern of the distribution of the chemical elements in the atmospheres of the binary components has not yet been observed. However, it must be admitted that there are just few studies of the atmospheric elemental abundances in the binary components, especially from the combined spectra, available as of today. The cause of such a pattern of the elemental distribution may be sought in the peculiarities of the binary system itself. The most pronounced feature of this binary is the rotational velocities of its components (9 and 21 km/sec), which are higher than those typical for

the stars with the outer convection envelopes, as well as a noticeable peculiar variations in the CaII H&K emission lines (from 3 to 10Å) while the  $H_\alpha$  emission remains practically unaltered (Wieler, 1978).

OU Geminorum (OU Gem) is a spectroscopic binary system consisting of two main-sequence BY Dra-type stars (Glazunova et al., 2014); its orbital period  $P_{orb} = 7$  days; the rotation period of the primary component (determined from the light curve plotted from photometric observations)  $P_{rot} = 7.4$  days; the effective temperatures of the primary (A) and secondary (B) components  $T_A = 5025$  K and  $T_B = 4500$  K, respectively; the ratio of the components luminosities  $L_A/L_B = 3.0$ ; the projected rotational velocities of the A and B components  $vsini_A = 6.0$  and  $vsini_B = 6.5$  km/sec, respectively; the activity indices of the A and B components  $\lg R'_{HKA} = -4.39$  and  $\lg R'_{HKB} = -4.5$ , respectively; the atmospheric metallicities of the A and B components  $[Fe/H]_A = -0.2 \pm 0.1$  dex and  $[Fe/H]_B = -0.15 \pm 0.19$  dex, respectively. Fig. 3,4 shows the distribution of the chemical elements in the atmospheres of the binary components adopted from the study Glazunova et al. (2014). As is seen in Fig. 3,4 the distribution of the light elements in the atmospheres of both binary components is typical for the main-sequence cool stars as described above. The heavy elements ( $Z > 40$ ) are noticeably overabundant in the atmospheres of both components. The lithium lines cannot be observed in the binary spectrum, which may be indicative of the low atmospheric abundance of this element in both components (less  $-0.5$  dex).

BY Draconis (By Dra) is a spectroscopic binary system consisting of two main-sequence stars which exhibit very high CaII H&K emission, i.e. both binary components are chromospherically active stars. Moreover, this binary system has a visual component, which is also a main-sequence star. The orbital period of the binary system  $P_{orb} = 6$  days; the rotation period of the primary component (determined from the light curve)  $P_{rot} = 3.8$  days; the effective temperatures of the primary (A) and secondary (B) components  $T_A = 4560 \pm 150$  K and  $T_B = 4430$  K, respectively; the ratio of the components luminosities  $L_A/L_B = 2.3$ ; the projected rotational velocities of the A and B components  $vsini_A = 8.0$  and  $vsini_B = 7.5$  km/sec, respectively; the activity index of the primary component  $\lg R'_{HK} = -3.45$ ; the atmospheric metallicities of the A and B components  $[Fe/H]_A = 0.04 \pm 0.15$  dex and  $[Fe/H]_B = -0.04 \pm 0.21$  dex, respectively. According to research, the spot on the primary components surface resulting in a photometric wave with an amplitude of 0.2 m covers up to 20% of its disc area; the spot temperature is 300 K lower than the photospheric one (Chugainov, 1976). Fig. 5,6 shows the distribution of the chemical elements in the atmospheres of both binary components according to the results of the examination of two spectra

performed by Glazunova & Kovtyukh (2014). As is seen from Fig. 3, with the 0.1 dex mean error in the determinations of the atmospheric abundances in the primary component, the abundance estimates of the elements with  $Z < 29$  are almost similar to the solar values, with the only exception being lithium, which is significantly underabundant in the atmospheres of both components. The scatter of the estimated abundances of the elements with  $Z > 29$  considerably exceeds the error in their determinations. However, the derived abundance of barium ( $Z = 56$ ) is practically similar to the solar value.

## 6. Conclusions and discussion

Based on the reported results of very few studies concerned with the investigation of the chemical composition of active stars and on our studies of two active binary systems of the BY Dra type, it is impossible to infer an unambiguous conclusion about the values and reasons for the variations in the atmospheric elemental abundances in active stars. We may only discuss the following tendencies in the elemental abundance dynamics in these stars:

- There is a noticeable increase in the abundances of the light elements ( $Z < 20$ ), which are sensitive to the NLTE-effects, in active stars with the chromospheric activity indices  $\lg R'_{HK} > -4.0$ ;
- An excess of the heavy elements ( $Z > 39$ ) has been observed in three active stars with rather high activity indices ( $> -4.5$ ), namely in the  $\lambda$  And, OU Gem and BY Dra binaries;
- The dispersion of the barium abundance estimates in different active binaries, as well as in inactive dwarfs, is rather wide ranging within  $0.15 \div 0.2$  dex;
- A significant underabundance of the heavy elements, including barium, may be observed in certain active binary systems (e.g. LX Per);
- Lithium is noticeably underabundant in active stars compared to inactive stars with the similar temperature range.

## References

- Barisevicius G., Tautvaisiene G., Berdyugina S., Chorniy Y., Ilyin I.: 2010, *Baltic Astr.*, **19**, 157.  
 Berdyugina S.V.: 2005, *Living Reviews in Solar Phys.*, **2**, 8.  
 Chugainov P.F.: 1976, *Izvestia Krymskoj Astrof. Obs.*, **55**, 94 (in Russian).  
 De Silva G.M., Freeman K.C., Bland-Hawthorn J., Asplund M., Bessell M.S.: 2007, *Astr. J.*, **133**, 694.  
 Frasca A., Biazzo K., Tas G., Evren S., Lanzafame A.S.: 2008, *Astr. & Astroph.*, **479**, 557.  
 Glazunova L.V., Mishenina T.V., Soubiran C., Kovtyukh V.V.: 2014, *Mon. Not. RAS*, **444**, 1901.

- Kang Y-W, Yushchenko A.V., Hong K., Guinan E.F., Gopka V.F.: 2013, *Astron. J.*, **145**,167.
- Lind K., Asplund M., Barklem P.S., Belyaev A.E.: 2013, *Astron. & Astroph.*, **528**, 9.
- Mishenina T.V., Pignatari M., Korotin S.A., Soubiran C., Charbonnel C., Thielemann F.-K., Gorbaneva T.I., Basak N.Yu.: 2013, *Astron. & Astroph.*, **489**, 12.
- Mishenina T.V., Soubiran C., Bienayme O., Korotin S.A., Belik S.I., Usenko I.A., Kovtyukh V.V.: 2008, *Astron. & Astroph.*, **489**, 923.
- Morel T., Micela G., Favata F.: 2006, *Astroph. & Space Sc.*, **304**, 185.
- Morel T., Micela G.: 2004, *Astron. & Astroph.*, **423**, 677.
- Noyes et al.: 1984, *Astroph. J.*, **279**, 763.
- Reddy A., Giridhar S., Lambert D.: 2012, *Mon. Not. RAS*, **419**, 1350.
- Strassmeier K.G.: 2005, *Astron. Nachr.*, **326**, 269.
- Tautvaisiene G., Barisevicius G., Berdyugina S., Chorniy Y., Ilyin I.: 2010, *Baltic Astr.*, **19**, 95.
- Weiler E.J.: 1978, *Mon. Not. RAS.*, **77**, 182.

DOI: <http://dx.doi.org/10.18524/1810-4215.2016.29.84992>

# STRONTIUM ABUNDANCES IN COOL DWARF STARS OF GALACTIC THIN AND THICK DISKS

T.I.Gorbaneva, T.V.Mishenina

Astronomical Observatory, Odessa National University

T.G.Shevchenko Park, Odessa 65014 Ukraine, [clumpstars@ukr.net](mailto:clumpstars@ukr.net), [tmishenina@ukr.net](mailto:tmishenina@ukr.net)

**ABSTRACT.** We revise the strontium abundances in FGK stars with metallicities ranging from  $-1.0 < [\text{Fe}/\text{H}] < +0.3$ . The observed stars belong to the substructures of the Galaxy thick and thin discs. The observations were conducted using the 1.93 m telescope at Observatoire de Haute-Provence (OHP, France) equipped with the echelle type spectrographs ELODIE and SOPHIE. The values of the Sr abundance were obtained using synthetic spectra using LTE model atmosphere. The comparison of our data with models of chemical evolution was made.

**Keywords:** stars: abundances

Strontium, as one of the abundant neutron-capture elements, has been extensively investigated in the past few decades. The data obtained will allow exploring ways of production and enrichment by strontium of the galactic substructures and the Galaxy generally.

The high-resolution echelle spectrographs SOPHIE ( $R = 75000$ ) and ELODIE ( $R = 42000$ ) on board 1.93m telescope of OHP (France) for the wavelengths range 4400–6800 Å were used. Spectral processing carried out by (Katz et al., 1998; Galazutdinov, 1992).

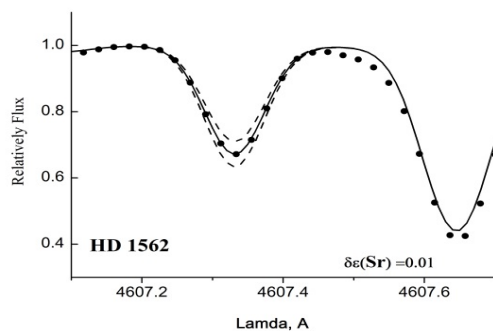


Figure 1: Spectrum synthesis fitting of observed profiles of SrI line 4607 Å

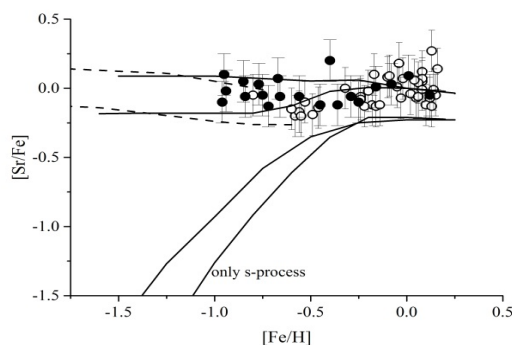


Figure 2: The run of  $[\text{Sr}/\text{Fe}]$  with  $[\text{Fe}/\text{H}]$ .

The effective temperatures  $T_{\text{eff}}$ , the surface gravities  $\log g$ , the microturbulent velocity  $V_t$ , and metallicities of the studied stars were estimated earlier in our paper (Mishenina et al., 2013; Kovtyukh et al., 2003).

Determination of the Sr abundance was made by STARSPT LTE spectral synthesis code (Tsymbal, 1996) from the Sr I line 4607 Å. The example of comparison of synthetic and observed spectra for Sr line is shown in Fig.1. The mean determination error is  $\pm 0.15$ . Departures from NLTE for 4607 Å: the correction is positive, from 0.1 to 0.2 dex (Bergemann et al., 2012). The dependence of the obtained LTE strontium abundance versus  $[\text{Fe}/\text{H}]$  is presented in Fig.2. The thin and thick disc stars are marked as open and black circles, correspondingly.

## Results & conclusions

To provide diagnostics of the types of n-capture processes forming Sr, we used the calculations of the Galactic enrichment by Travaglio et al. (2004) and Serminato et al. (2009). Both these models taken into account the contribution of s-process yields from asymptotic giant branch (AGB) stars and a primary (weak s-process component) and r-process production in the Galaxy from Type II supernovae stars (bottom line – Serminato et al. (2009), top – Travaglio et al. (2004) for thin disc and by dotted line for thick at Fig.2). The primary process (or LEPP) is also taken into account in model of Travaglio et al. (2004). Serminato et al. (2009) used first the r-process residual method ( $s = 1 - r$ ) and then the r – contribution from Type II Supernovae. Both models (Travaglio et al., 2004; Serminato et al., 2009) describe quite the behavior of a thin disc stars, albeit in some different ways. Note, the models which consider only the contribution in n-capture enrichment from s-process do not depict well the observation.

*Acknowledgments.* This work was supported by the Swiss National Science Foundation (SCOPES project No. IZ73Z0-52485).

## References

- Galazutdinov G.A.: 1992, *Preprint SAO RAS*, n92.
- Katz et al.: 1998, *Astron. Astrophys.*, **338**, 151.
- Kovtyukh et al.: 2003, *Astron. Astrophys.*, **411**, 559.
- Mishenina et al.: 2013, *Astron. Astrophys.*, **552**, 128.
- Bergemann et al.: 2012, *Astron. Astrophys.*, **546**, A90.
- Tsymbal V.V.: 1996, *ASP Conf. Ser.*, **108**, 198.
- Travaglio et al.: 2004, *Astrophys. J.*, **601**, 864.
- Serminato et al.: 2009, *Publ. Astron. Soc. of Aust.*, **26**, 153.

DOI: <http://dx.doi.org/10.18524/1810-4215.2016.29.84994>

## SEARCH FOR VARIABLE STARS AND THEIR STUDY

R.I.Kokumbaeva<sup>1</sup>, V.A.Zakhzhay<sup>2</sup>, A.V.Khruslov<sup>3,4</sup><sup>1</sup> Fesenkov Astrophysical Institute, Observatory str., 23, 050020, Almaty, Kazakhstan, [raushan.raushan@mail.ru](mailto:raushan.raushan@mail.ru)<sup>2</sup> V.N. Karazin Kharkiv National University, Svobody pl, 61077, Kharkiv, Ukraine, [zhvladimir@mail.ru](mailto:zhvladimir@mail.ru)<sup>3</sup> Sternberg Astronomical Institute, Moscow State University, Universitetsky pr., 13, 119992, Moscow, Russia, [khruslov@bk.ru](mailto:khruslov@bk.ru)<sup>4</sup> Institute of Astronomy, Russian Academy of Sciences, Pyatnitskaya str., 48, 119017, Moscow, Russia

**ABSTRACT.** We search for variable stars and study them using our CCD observations, observations available in the CSS, NSVS, ASAS-3 and Super-WASP online public archives.

Our CCD observations were performed using the Zeiss-1000 telescope of the V.G. Fesenkov Astrophysical Institute's Tien-Shan Astronomical Observatory. Earlier, as a result of our search using CCD images, we detected 27 new variable stars; using the NSVS and SuperWASP databases, we detected 12 new red semiregular and irregular variable stars.

In this paper, we present our study of seven known variables based on the ASAS-3 and SuperWASP databases. All these stars remained poorly studied, their light elements were unknown, variability types were considered preliminary only. We studied two eclipsing variables (FY And and V2250 Sgr) and five Mira-stars (BZ Sco, CZ Sco, FK Sco, V880 Sco and V1818 Sgr).

**Keywords:** stars: variables: eclipsing binary, Mira-stars – stars: individual: FY And, V2250 Sgr, BZ Sco, CZ Sco, FK Sco, V880 Sco, V1818 Sgr

## 1. Introduction

We search for variable stars and study them using our CCD observations, observations available in the Catalina Surveys (Drake et al. 2009), Northern Sky Variability Survey (NSVS, Woźniak et al. 2004), the All Sky Automated Survey (ASAS-3, Pojmanski 2002) and SuperWASP (Butters et al. 2010) online public archives.

Our CCD observations were performed using the Zeiss-1000 telescope of the V.G. Fesenkov Astrophysical Institute's Tien-Shan Astronomical Observatory (altitude 2759 meters above the sea level). The telescope has a 1000-mm mirror and the focal length of 6650 mm. The Apogee U9000 D9 CCD camera was used. The CCD observations were carried out in Johnson's *BVR* photometric system. We mainly observed moderate-density areas of the Milky Way. The images were subjected to photometric processing using MaxIm DL5 specialized software and to further interpretation of the data. The limiting magnitude of our search is about 20<sup>m</sup> *V*;

it is possible to separate star pairs with inter-component distances as small as 1–2 seconds of arc.

Using online archives, we not only search for new variables but also use them (especially the NSVS archive) to study known variable stars. The databases contain a large volume of information permitting to improve types of variable stars, their light elements, follow the behavior of variables during time intervals of long duration.

## 2. Search for new variables

As a result of our search using CCD images, we detected 27 new variable stars (Kusakin et al. 2013, Kusakin et al. 2014, Kusakin et al. 2015a, Kokumbaeva et al. 2016); among them there are 13 eclipsing variables (EW, EB types; classification according to the General Catalogue of Variable Stars, GCVS, Samus et al. 2007-2016), 5 red semiregular and irregular variables (M, SR, LB types), 5  $\delta$  Scuti variables, two RR Lyrae stars, 1 BY Draconis star and 1 ellipsoidal variable (ELL type). Some of them were earlier suspected from survey data. For several variables, the light elements were later improved (Khruslov & Kusakin 2014ab).

Using the NSVS and SuperWASP databases, we detected 12 new red semiregular and irregular variable stars (LB and SR types; Kusakin et al. 2015b).

## 3. Study of known variables

In this paper, we present our study of seven known variables based on the ASAS-3 and SuperWASP databases. All these stars remained poorly studied, their light elements were unknown, variability types were considered preliminary only. We studied two eclipsing variables and five Mira-stars.

### 3.1. FY And

The variability of FY And = S 10112 (RA = 23<sup>h</sup> 23<sup>m</sup> 28<sup>s</sup>.65; Dec = +50° 15' 57".9, J2000) was discovered by Hoffmeister (1967). The variable was classified as an Algol-type variable star without light elements, range 15<sup>m</sup> – 16<sup>m</sup>.5. The discoverer used 64 photographic plates to detect 2 times of minima and 1 small fading. Later, Busch

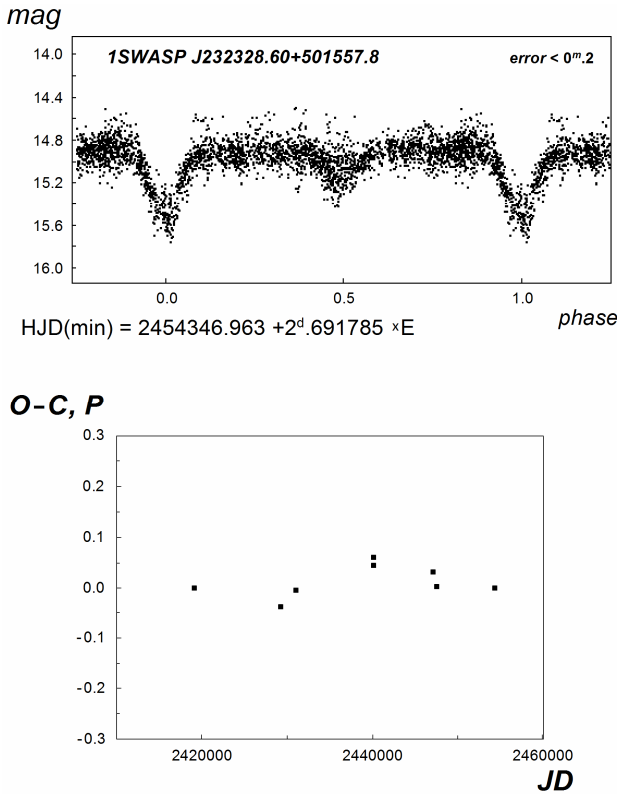


Figure 1: Light curve and O-C diagram for FY And.

& Häußler (1990) classified the variable as a possible eclipsing star, gave 5 moments of minima or fadings (the first of them coinciding with the latest by Hoffmeister) and a possible period  $P = 2.7$  days. The photographic magnitude range is  $15^m.55 - 16^m.40$ . In the GCVS (Samus et al. 2007-2016), the variable was classified as an Algol-type variable with the magnitude range  $15^m.6 - 16^m.4$ ; the variability period is not specified and the epoch of light minimum is given (the same as the latest one by Busch & Häußler).

We studied FY And using SuperWASP data and all times of minima. We confirm the eclipsing nature of this variable (EA type). The light elements are:

$$\text{HJD}(\text{minI}) = 2454346.963 + 2^d.691785 \times E.$$

From the 1SWASP data, the magnitude range is  $14^m.9 - 15^m.5$ ,  $\text{MinI} = 15^m.1$ ; the duration of the primary eclipse is  $D = 0.16$  P.

The SuperWASP observations, available as FITS tables, were converted into ASCII tables using the OMC2ASCII program as described by Sokolovsky (2007). From the SuperWASP data, we removed observations with errors exceeding  $0^m.20$ .

Additionally, we present the O-C diagram and the table of the all known eclipsing minima.

Table 1. Times of minima for FY And.

JD	O-C	Publication
241911.50	0.000	Hoffmeister (1967)
2429251.35	-0.038	Hoffmeister (1967)
2430998.410	-0.004	Hoffmeister (1967), Busch&Häußler (1990)
2440150.610	+0.045	Busch&Häußler (1990)
2440153.345	+0.061	Busch&Häußler (1990)
2447087.304	+0.032	Busch&Häußler (1990)
2447469.461	+0.003	Busch&Häußler (1990)
2454346.963	0.000	1SWASP data, this paper

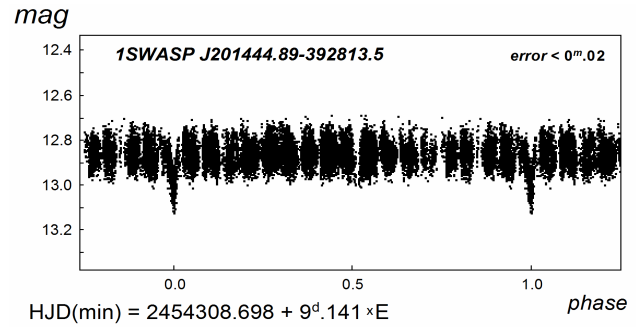


Figure 2: Light curve for V2250 Sgr.

### 3.2. V2250 Sgr

The variability of V2250 Sgr = S 7327 (RA =  $20^h 14^m 44^s.90$ ; Dec =  $-39^\circ 28' 13''.9$ , J2000) was discovered by Hoffmeister (1963). Following this publication, the variable was classified in the GCVS as an Algol-type variable star without light elements, magnitude range  $13^m.0 - 13^m.5$  (pg). We confirm the eclipsing nature of this variable according to data from SuperWASP. The light elements are:

$$\text{HJD}(\text{min}) = 2454308.698 + 9^d.141 \times E.$$

From the 1SWASP data, the magnitude range is  $12^m.85 - 13^m.05$ ; the duration of the eclipse is  $D = 0.025$  P. We removed observations with errors exceeding  $0^m.02$ .

### 3.3. Five southern Mira variables

We studied 5 red long-period variables, type M according to the GCVS, using ASAS-3 data. The results are presented in Table 2. In comments, we present the history of studies of these stars.

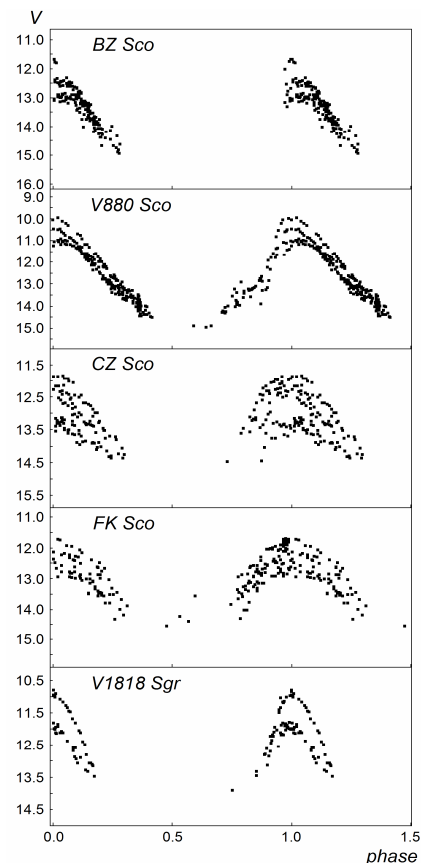


Figure 3: Light curves for five Mira stars.

Table 2. Light elements of the 5 southern Mira stars

No.	Variable	Coordinates (2000)	Type	V mag.	Period, days	Epoch, JD
1	BZ Sco	16 <sup>h</sup> 30 <sup>m</sup> 11 <sup>s</sup> .29 -36° 15' 06".7	M	11 <sup>m</sup> .7 – <15 <sup>m</sup> .0	369	2453769
2	V880 Sco	16 41 14.44 -34 07 32.8	M	10.0 – 15.0	389	2454528
3	CZ Sco	16 46 17.89 -31 02 06.8	M	11.9 – <14.4	216	2454615
4	FK Sco	17 01 54.07 -32 39 18.9	M	11.8 – <14.5	184	2453506
5	V1818 Sgr	18 06 57.91 -32 00 57.0	M	10.8 – <13.9	338	2454683

## Comments:

1. The variability of BZ Sco (HV 4023) was discovered by Luyten (1927). The variable was classified as a long-period variable star without light elements, magnitude range 15<sup>m</sup>.0 – <16<sup>m</sup>.0 (pg). The variable was classified in the GCVS as a possible Mira variable (M: type) without light elements. We confirm the Mira nature of this variable according to data from ASAS-3. The period is 369 days; a twice shorter period (184 days) is not excluded.

2. The variability of V880 Sco (AN 446.1935, HV 8933) was discovered by Luyten (1935); its magnitude range was 11<sup>m</sup>.0 – 15<sup>m</sup>.0 (pg). The variable was classified in the GCVS as a Mira variable (M type) without light elements. Sanduleak et al. (1995) give the spectral type M8e. We confirm the Mira nature of this variable according to data from ASAS-3.

3. The variability of CZ Sco (HV 4207) was discovered by Swope (1928). Following Swope (1928), the variable was not classified in the GCVS, with only the magnitude range (14<sup>m</sup>.8 – 16<sup>m</sup>.4 pg) given. Actually, it is a Mira variable star according to ASAS-3 data.

4. The variability of FK Sco (HV 4327) was discovered by Swope (1928). Following Swope (1928), the variable was not classified in the GCVS, with only the magnitude range given (14<sup>m</sup>.4 – < 16<sup>m</sup>.5 pg). Actually, it is a Mira variable star according to ASAS-3 data.

5. The variability of V1818 Sgr (AN 591.1933, HV 9242) was discovered by Luyten (1933), who gave the magnitude range 14<sup>m</sup>.8 – 16<sup>m</sup>.1 (pg). Plaut (1958) classified the variable as a possible Mira variable, with the time of maximum JD 2427860. It was not possible to derive the period. The magnitude in maximum is 13<sup>m</sup>.10, with the detected full amplitude > 1<sup>m</sup>.85 (pg). The variable was classified in the GCVS as a possible Mira variable (M: type); the period is not specified, and the magnitude range is presented as 13<sup>m</sup>.4 – 16<sup>m</sup>.1 (pg). We confirm the Mira nature of this variable according to data from ASAS-3.

*Acknowledgements.* The authors are grateful to Dr. V.P.Goranskij for providing light-curve analysis software. Thanks are due to Dr. N.N.Samus for helpful discussions. This study was supported by the Russian Foundation for Basic Research (grant 13-02-00664), the Basic Research Program P-7 of the Presidium of Russian Academy of Sciences, and also carried out in the framework of the project grant funding number 0075/GF4 Committee of Science, Ministry of Education and Science of the Republic of Kazakhstan «Studies of variable stars and metabolic processes with gas and dust disk».

## References

- Busch, H., Häußler, K.: 1990, *VSS*, **10**, 354.  
 Butters, O.W., West, R.G., Anderson, D.R., et al.: 2010, *Astron. Astrophys.*, **520**, L10.  
 Drake, A.J., Djorgovski, S.G., Mahabal, A., et al.: 2009, *ApJ*, **696**, 870.  
 Hoffmeister, C.: 1963, *VSS*, **6**, 1.  
 Hoffmeister C.: 1967, *AN*, **290**, 43.  
 Khruslov A.V., Kusakin A.V.: 2014a, *PZP*, **14**, 14.  
 Khruslov A.V., Kusakin A.V.: 2014b, *PZ*, **34**, 1.  
 Kokumbaeva R.I., Khruslov A.V., Kusakin A.V.: 2016, *NEWS of the National Academy of Sciences of the Republic of Kazakhstan*, Vol. 5 (No. 309), 35.  
 Kusakin A.V., Khruslov A.V., Kokumbaeva R.I.: 2013, *NEWS of the National Academy of Sciences of the Republic of Kazakhstan*, Vol. 5 (No. 291), 55.  
 Kusakin A.V., Khruslov A.V., Kokumbaeva R.I.: 2014, *NEWS of the National Academy of Sciences of the Republic of Kazakhstan*, Vol. 4 (No. 296), 51.  
 Kusakin A.V., Khruslov A.V., Kokumbaeva R.I., Reva I.V.: 2015a, *NEWS of the National Academy of Sciences of the Republic of Kazakhstan*, Vol. 5 (No. 303), 49.  
 Kusakin A.V., Khruslov A.V., Kokumbaeva R.I., Reva I.V.: 2015b, *NEWS of the National Academy of Sciences of the Republic of Kazakhstan*, Vol. 5 (No. 303), 55.  
 Luyten, W. J.: 1927, *Harvard College Observatory Bulletin*, **852**, 1.  
 Luyten, W. J.: 1933, *AN*, **250**, 259.  
 Luyten, W. J.: 1935, *AN*, **256**, 325.  
 Plaut, L.: 1958, *Annalen van de Sterrewachtte Leiden*, **21**, 217.  
 Pojmanski, G.: 2002, *Acta Astron.*, **52**, 397.  
 Sanduleak N., Stephenson C.B., and Bidelman W.P.: 1995, *IBVS*, **4230**, 1.  
 Samus N.N., Durlevich O.V., Goranskij V.P., Kazarovets E V., Kireeva N.N., Pastukhova E.N., Zharova A.V.: 2007-2016, *General Catalogue of Variable Stars*, Centre de Données Astronomiques de Strasbourg, B/gcvs.  
 Sokolovsky, K.V.: 2007, *PZP*, **7**, 30.  
 Swope, H. H.: 1928, *Harvard College Observatory Bulletin*, **857**, 1.  
 Woźniak, P.R., Vestrand, W.T., Akerlof, C.W., et al.: 2004, *AJ*, **127**, 2436.

DOI: <http://dx.doi.org/10.18524/1810-4215.2016.29.85015>

# A TECHNIQUE FOR SIMULTANEOUS MEASUREMENT OF CIRCULAR AND LINEAR POLARIZATION WITH A SINGLE-CHANNEL POLARIMETER

S.V. Kolesnikov<sup>1,2</sup>, V.V. Breus<sup>3</sup>, N.N. Kiselev<sup>1,4</sup>, I.L. Andronov<sup>3</sup><sup>1</sup> Crimean Astrophysical Observatory (CrAO), Krimea, Nauchny<sup>2</sup> Astronomical Observatory, I.I. Mechnikov Odessa National University (ONU) T.G.Shevchenko Park, Odessa 65014 Ukraine<sup>3</sup> Department of Mathematics, Physics and Astronomy, Odessa National Maritime University (ONMU), Mechnikova 34, Odessa 65029 Ukraine<sup>4</sup> Main Astronomical Observatory, National Academy of Sciences of Ukraine (MAO NASU), Zabolotnogo 27, Kyiv, Ukraine

**ABSTRACT.** We present a technique for simultaneous measurement of circular and linear polarization with the single-channel polarimeter, that is used in Crimean astrophysical observatory for many years. Methods and a computer program for data reduction is described. The algorithm is described, which have been used for photo-polarimetric monitoring of various astronomical objects cataclysmic variables, asteroids, comets.

**Key words:** Data reduction; Polarimetry; cataclysmic variable stars; asteroids; comets.

## 1. Introduction

The development of devices capable of measuring circular polarization of light became possible in the middle of the 20<sup>th</sup> century after the appearance of achromatic retarders. For us it became feasible in the middle of the 80's, following the development of multicomponent symmetric achromatic retarders by V.A. Kucherov (1986). Shakhovskoy N.M. et al. (2001) described a technique for circular polarization measuring using the CrAO 2.6-m Shajn mirror telescope (SMT) with a single-channel photopolarimeter, which uses the high-speed rotation of a quarter-wave retarder as a modulator. In that case the signal was integrated by four pulse counters over the time intervals corresponding to the 90 degree angles of the retarder rotation; at that, the angles of activity of the second pair of the pulse counters were shifted relative to those of the first pair by 45 degrees. In 2002, we modified the SMT polarimeter aiming to quasi-simultaneously measure all four Stokes parameters, namely I, Q, U and V. We still use a quarter-wave retarder as an analyser, which is continuously rotating at the rate of 33 rps, and a

Glan prism as a stationary polarizer. The switching unit of the polarimeter has been rearranged in such a way that the signal is integrated over the time intervals corresponding to the 22.5 degree angles of the retarder rotation, i.e. by eight pulse counters.

According to Serkowski (1974), the intensity of the light beam which has passed through such a device can be expressed by the following formula:

$$I'(\psi) = \frac{1}{2}(I + \frac{Q}{2}(1 + \cos 4\psi) + \frac{U}{2}\sin 4\psi - V\sin 2\psi) \quad (1)$$

where  $\psi$  is the angle of rotation of the retarder fast axis (hereinafter the major axis) relative to the analyser principal plane;  $I$  is the intensity of the incoming radiation;  $Q$  and  $U$  are the linear polarization parameters; and  $V$  is the circular polarization parameter. Having the dependencies (1) angularly integrated the equations for eight pulse counters ( $0^\circ - 22.5^\circ$ ,  $22.5^\circ - 45^\circ$ , ...,  $337.5^\circ - 360^\circ$ ) and taking into account repeating of counts in the range ( $180^\circ - 360^\circ$ ), the following expected values may be derived:

$$\begin{aligned} n_1 &= I_0 \cdot \frac{\pi}{8} + \frac{Q}{2} \cdot \frac{\pi}{8} + \frac{Q}{2} \cdot \frac{1}{4} + \frac{U}{2} \cdot \frac{1}{4} - V \cdot \left(\frac{1}{2} - \frac{\sqrt{2}}{4}\right) \\ n_2 &= I_0 \cdot \frac{\pi}{8} + \frac{Q}{2} \cdot \frac{\pi}{8} - \frac{Q}{2} \cdot \frac{1}{4} + \frac{U}{2} \cdot \frac{1}{4} - V \cdot \frac{\sqrt{2}}{4} \\ n_3 &= I_0 \cdot \frac{\pi}{8} + \frac{Q}{2} \cdot \frac{\pi}{8} - \frac{Q}{2} \cdot \frac{1}{4} - \frac{U}{2} \cdot \frac{1}{4} - V \cdot \frac{\sqrt{2}}{4} \\ n_4 &= I_0 \cdot \frac{\pi}{8} + \frac{Q}{2} \cdot \frac{\pi}{8} + \frac{Q}{2} \cdot \frac{1}{4} - \frac{U}{2} \cdot \frac{1}{4} - V \cdot \left(\frac{1}{2} - \frac{\sqrt{2}}{4}\right) \\ n_5 &= I_0 \cdot \frac{\pi}{8} + \frac{Q}{2} \cdot \frac{\pi}{8} + \frac{Q}{2} \cdot \frac{1}{4} + \frac{U}{2} \cdot \frac{1}{4} + V \cdot \left(\frac{1}{2} - \frac{\sqrt{2}}{4}\right) \\ n_6 &= I_0 \cdot \frac{\pi}{8} + \frac{Q}{2} \cdot \frac{\pi}{8} - \frac{Q}{2} \cdot \frac{1}{4} + \frac{U}{2} \cdot \frac{1}{4} + V \cdot \frac{\sqrt{2}}{4} \\ n_7 &= I_0 \cdot \frac{\pi}{8} + \frac{Q}{2} \cdot \frac{\pi}{8} - \frac{Q}{2} \cdot \frac{1}{4} - \frac{U}{2} \cdot \frac{1}{4} + V \cdot \frac{\sqrt{2}}{4} \end{aligned} \quad (2)$$

$$n_8 = I_0 \cdot \frac{\pi}{8} + \frac{Q}{2} \cdot \frac{\pi}{8} + \frac{Q}{2} \cdot \frac{1}{4} - \frac{U}{2} \cdot \frac{1}{4} + V \cdot \left(\frac{1}{2} - \frac{\sqrt{2}}{4}\right)$$

Note that the sky background effects should be eliminated from the values  $n_1, n_2, n_3, n_4, n_5, n_6, n_7$  and  $n_8$ . For this, the sky background should be measured prior and after the program object. The mean or interpolated sky background values at the instant of the object observation are subtracted from the observed values for the object for each of the eight channels.

The combination of the pulse counters readings enables to obtain the following dependencies for the Stokes parameters:

$$\begin{aligned} N &= n_1 + n_2 + n_3 + n_4 + n_5 + n_6 + n_7 + n_8 = \\ &= I_0 \cdot \frac{\pi}{2} \\ S_1 &= -n_1 + n_2 + n_3 + n_4 + n_5 - n_6 - n_7 - n_8 = \\ &= -V \cdot \sqrt{2} \\ S_2 &= -n_1 - n_2 - n_3 + n_4 + n_5 + n_6 + n_7 - n_8 = \quad (3) \\ &= V \cdot \sqrt{2} \\ S_3 &= n_1 + n_2 - n_3 - n_4 + n_5 + n_6 - n_7 - n_8 = U \\ S_4 &= n_1 - n_2 - n_3 + n_4 + n_5 - n_6 - n_7 + n_8 = Q \end{aligned}$$

As the parameter  $Q \leq 0.1$  for the majority of astronomical objects, when neglecting it, the first equation in the set (4) can be written down as  $I_0 = N/\pi$ . Hence, the standardized parameters  $u$  and  $q$  of the Stokes vector for the linear polarization expressed in per cent can be determined from the following formulae:

$$\begin{aligned} LP_1 &= 314.16 \cdot \frac{S_3}{N} = \frac{U}{I_0} = u \\ LP_2 &= 314.16 \cdot \frac{S_4}{N} = \frac{Q}{I_0} = q \end{aligned} \quad (4)$$

The Stokes parameters for the circular polarization are determined as follows:

$$\begin{aligned} CP_1 &= -S_1 \cdot \frac{157.08}{N} \\ CP_2 &= S_2 \cdot \frac{157.08}{N} \end{aligned} \quad (5)$$

According to the set of equations (4), the sum of pulses accumulated in all channels depends upon the parameter  $Q$ . Thus, in general, the second iteration is required to determine the final values of the polarization parameters, but it is only essential when the degree of linear polarization is above 10%.

The final equations for the degree  $p$  and the plane of linear polarization  $\theta$  are as follows:

$$\begin{aligned} p &= \frac{\sqrt{u^2 + q^2}}{I_0} \\ \theta &= \frac{1}{2} \arctan \frac{u}{q} \end{aligned} \quad (6)$$

The standard error of the circular and linear polarization can be determined from the following formulae:

$$\begin{aligned} \sigma_v &= 157.08 \frac{\sqrt{N + N_{bgr}}}{N} \\ \sigma_p &= 314.16 \frac{\sqrt{N + N_{bgr}}}{N} \end{aligned} \quad (7)$$

where  $N_{bgr}$  is the total number of the sky background pulses for eight pulse counters. According to [3], the error in the angle determination can be calculated by the following formula:  $\sigma_\theta = 28.65 \cdot \frac{\sigma_p}{p}$

## 2. Determination of the degree of circular polarization by the observed values $CP_1$ and $CP_2$

The parameters  $CP_1$  and  $CP_2$  are equivalent to the Stokes parameters for the linear polarization, namely  $q$  and  $u$ . Therefore,  $CP_1$  and  $CP_2$  are projections of the vector  $P_C$  on the  $O_X$  and  $O_Y$  axes under the statistical noise perturbations; hence, it is necessary to determine the degree of angle  $2\phi_0$ .

It can be done using the observations of a star with a wide range of circular polarization variation. To this end, at first, the correction for the zero point from the measured standards with zero polarization should be factored in, i.e. the instrumental polarization should be taken into account. And then, it is necessary to find such an angle of rotation of the coordinate system (i.e. rotation of the polarizer relative to the analyser) that one of the axes corresponds to the polarization while another one represents the noise.

Let us introduce a system of coordinates  $X$  and  $Y$  where the origin coincides with the mean values ( $< P_1 >$ ,  $< P_2 >$ ), and the  $O_X$  axis is tilted relative to  $P_1$  by an angle  $\phi$  (which equals to  $2\pi\phi_0$ ). Then,

$$\begin{aligned} P_1 &= \overline{P_1} + X \cos \phi - Y \sin \phi \\ P_2 &= \overline{P_2} + X \sin \phi + Y \cos \phi \\ X &= (P_1 - \overline{P_1}) \cos \phi + (P_2 - \overline{P_2}) \sin \phi \\ Y &= -(P_1 - \overline{P_1}) \sin \phi + (P_2 - \overline{P_2}) \cos \phi \end{aligned} \quad (8)$$

Let us calculate the second central moments for the variables  $P_1$  and  $P_2$ :

$$\begin{aligned} \mu_{ij} &= \langle (P_i - \overline{P_i})^2 (P_j - \overline{P_j})^2 \rangle \\ \langle X \rangle &= 0, \langle Y \rangle = 0, \\ \langle X^2 \rangle &= \mu_{11} \cos^2 \phi + 2\mu_{12} \cos \phi \sin \phi + \mu_{22} \sin^2 \phi = \\ &= \frac{1}{2}(\mu_{11} + \mu_{22}) + \frac{1}{2}(\mu_{11} - \mu_{22}) \cos 2\phi + \mu_{12} \sin 2\phi \\ \langle XY \rangle &= -(\mu_{11} - \mu_{22}) \cos \phi \sin \phi + \mu_{12}(\cos^2 \phi - \sin^2 \phi) = \\ &= -\frac{1}{2}(\mu_{11} - \mu_{22}) \sin 2\phi + \mu_{12} \cos 2\phi \quad (9) \\ \langle Y^2 \rangle &= \mu_{11} \sin^2 \phi + 2\mu_{12} \cos \phi \sin \phi + \mu_{22} \cos^2 \phi = \\ &= \frac{1}{2}(\mu_{11} + \mu_{22}) - \frac{1}{2}(\mu_{11} - \mu_{22}) \cos 2\phi - \mu_{12} \sin 2\phi \end{aligned}$$

These formulae are valid for any angle of rotation  $\phi$ , however, for the orthogonal regression, it is required to select such an angle that the joint moment. Thus,

$$\begin{aligned} \tan 2\phi &= \frac{2\mu_{12}}{\mu_{11} - \mu_{22}} \\ \sin 2\phi &= \frac{2\mu_{12}}{\sqrt{(\mu_{11} - \mu_{22})^2 + 4\mu_{12}^2}} \\ \cos 2\phi &= \frac{\mu_{11} - \mu_{22}}{\sqrt{(\mu_{11} - \mu_{22})^2 + 4\mu_{12}^2}} \end{aligned} \quad (10)$$

$$\begin{aligned} \langle X^2 \rangle &= \frac{1}{2}(\mu_{11} + \mu_{22}) + \frac{1}{2}\sqrt{(\mu_{11} - \mu_{22})^2 + 4\mu_{12}^2} \\ \langle XY \rangle &= 0 \\ \langle Y^2 \rangle &= \frac{1}{2}(\mu_{11} + \mu_{22}) - \frac{1}{2}\sqrt{(\mu_{11} - \mu_{22})^2 + 4\mu_{12}^2} \end{aligned}$$

In fact, there are four different roots  $\phi = \frac{1}{2} \arctan \lambda + \frac{k\pi}{2}$ ,  $k = 0, 1, 2, 3$  of the equation  $\tan 2\phi = \lambda$ .

Two of these four roots correspond to the direction of the major axis of the dispersion ellipse along the  $O_X$  axis while another two roots correspond to the direction along the  $O_Y$  axis. We select the main direction in the quadrant where the formulae for  $\sin 2\phi$  and  $\cos 2\phi$  are valid. Then, the variables  $X$  and  $Y$  have the highest and lowest dispersion, respectively, among all possible angles of rotation. It is rather common that the variable  $X$  is interpreted as a variable parameter with the observation noise while  $Y$  is interpreted as 'pure noise'.

The total Stokes parameters are calculated in the manner described. It follows from the above-presented formulae that using this technique the circular polarization parameters are determined more precisely than those for the linear polarization.

### 3. Computer program

To process the observation data obtained with the single-channel photopolarimeter, Breus (2007) has written the computer program "PolarObs", which carries out the techniques described above (see also Breus et al., 2007).

A data file is generated by the telescope observations; this file contains eight quasi-simultaneous measurements of the object's brightness for eight successive positions of the modulator and the instant of time at the end of a given observation. Information on the type of the object (such details as dark current, background, target star, reference star and standard), exposure time and number of observation in a series and spectral band-filter is also recorded in the data file by the polarimeter control program, written by a staff member of CrAO, D.N.Shakhovskoy.

The program automatically identifies the type of data sequence using keyword analysis, giving the user the option of accepting or changing the resulted type. Such a fashion allows of minimizing the amount of

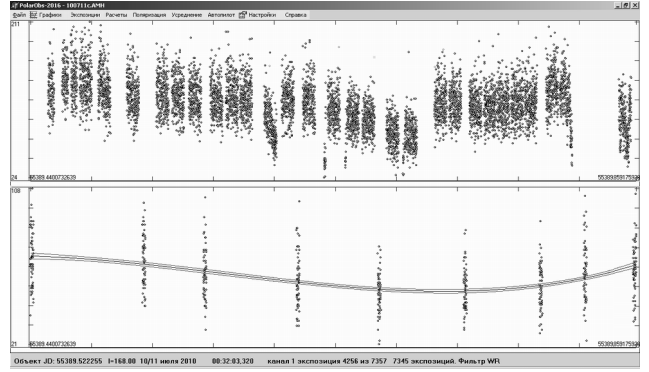


Figure 1: The main screen of PolarObs. Measurements of AM Her at the top and the background at the bottom.

clicking and key pressing which is more comfortable when processing a large set of data.

When the data set is open, the program exhibits two curves which represent the resulted measurements of the object's brightness (on the top of the screen) and sky background (on the bottom of the screen) for either of eight channels. Having the polynomial fitting of the background counts performed the obtained polynomial values are subtracted from the stars' counts for each channel individually. Subsequently, the user can compute the smoothing polynomial value for the reference star counts in order to determine the brightness of the target object. After that the program computes linear combinations (see 4) using fixed constants for each channel which results in the so-called 'vectors'  $S_1 - S_4$ . The first two vectors  $S_1$  and  $S_2$  are used later to compute the circular polarization parameters while another two vectors ( $S_3$  and  $S_4$ ) are used to obtain the linear polarization parameters. Having this step completed, it is possible to save the results obtained in a format of vectors of photometric observation, somehow similar to the Stokes parameters.

As the next step the user can analyse the diagram representing the correlation between  $S_2$  and  $S_1$  (for the circular polarization) and between  $S_4$  and  $S_3$  (for the linear polarization). In this view mode the calculated values of polarization, position angle and other data are shown under the diagram.

When processing the standards of zero or non-zero polarization, these data are considered to be and saved as the final results. When processing observations of a variable star or any other object it is necessary to account for the instrumental polarization. To this end, the coordinate system of the linear polarization diagram should be rotated by an angle determined from the standards of non-zero linear polarization.

To determine the circular polarization, it is necessary to rotate the coordinate system of the circular polarization diagram by a certain angle in such a way

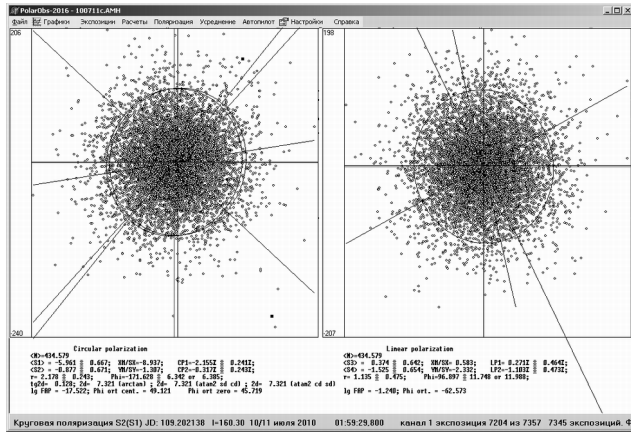


Figure 2: Diagram representing the correlation between  $S_2$  and  $S_1$  (left) and  $S_4$  and  $S_3$  (right)

that the line connecting the origin and the distribution centre coincides with the  $O_X$  axis.

The standardised values of the Stokes parameters can be the output to the files with extension \*.p on demand. These are delimited text files with spacebar and newline separated values which contain the following data:

- $JD$  is the Julian date;
- $F_t$  is the object brightness expressed as a ratio between the object counts and interpolated reference star count;
- $F_m$  is the object brightness expressed in magnitude units (related to the Pogson formula  $F_t$ );
- $CP_1^*, CP_2^*$  are the circular polarization values;
- $LP_1^*, LP_2^*$  are the linear polarization values;
- $\sigma_F, \sigma_{CP}, \sigma_{LP}$  are the errors in photometry, circular and linear polarization, respectively.

In the last step it is possible to perform either polynomial approximation or averaging of the standardised or not-standardised Stokes parameters. When averaging, the program gives an option to select statistically optimal number of points for averaging using three test-functions, such as the estimated error of a single measurement, average accuracy of the smoothed value and the signal-to-noise ratio.

The program was used to process the photopolarimetric observations of the stellar systems V405 Aur (Breus et al., 2013), BY Cam (Andronov et al., 2008), AM Her (Andronov et al., 2003) and QQ Vul (Andronov et al., 2010), as well as several comets (Kiselev et al., 2012; Rozenbush et al., 2007, 2009, 2014). Some results were reported in reviews on large scientific campaigns (Andronov et al., 2010; Vavilova et al., 2011, 2012).

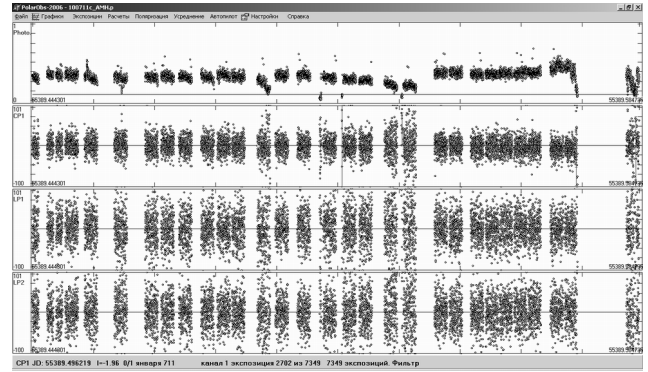


Figure 3: Viewing P-file - photometry (1), circular (2) and linear (3-4) polarization

### References

Andronov I.L. et al.: 2003, *Odessa Astron. Publ.*, **16**, 7.  
 Andronov I.L. et al.: 2008, *Central European Journal of Physics*, **6**(3), 385.  
 Andronov I.L. et al.: 2010, *Odessa Astron. Publ.*, **23**, 8.  
 Breus V.V. : 2007, *Odessa Astron. Publ.*, **20**, 32.  
 Breus V.V., Andronov I.L., Kolesnikov S.V., Shakhovskoy N.M.: 2007, *AATr*, **26**, 241.  
 Breus V. V. et al.: 2013, *JPhSt*, **17**, 3901.  
 Kiselev N.N. et al.: 2012, *LPI Contr.* **1667**, 6102.  
 Kucherov V.A.: 1986, *KPCB*, **2**, 59.  
 Rozenbush V.K. et al.: 2007, *The 10th Conference on Electromagnetic and Light Scattering, Bodrum, Turkey, Ed. by G.Videen et al.*  
 Rozenbush V.K. et al.: 2009, *Journal of Quantitative Spectroscopy and Radiative Transfer*, **110** (14), p. 1719.  
 Rozenbush V. et al.: 2014, *Asteroids, Comets, Meteors, Helsinki, Finland. Edited by K. Muinonen et al.*, p. 450.  
 Serkowski K.: 1974. *Planets, Stars and Nebulae, Studied with Photopolarimetry, ed. by Gehrels, Univ. of Arizona Press, Tucson*, p. 135.  
 Shakhovskoy N.M. et al.: 2001, *IzKry*, **97**, 91.  
 Vavilova I.B. et al.: 2011, *KosNT*, **17**, 74.  
 Vavilova I.B. et al.: 2012, *KPCB*, **28**, 85.

DOI: <http://dx.doi.org/10.18524/1810-4215.2016.29.85042>

# THE MEAN LIGHT CURVES OF THE MIRA-TYPE STARS IN THE H- AND K-BANDS

L. S. Kudashkina

Department “Mathematics, Physics and Astronomy”  
Odessa National Maritime University, Odessa, Ukraine, [kudals04@mail.ru](mailto:kudals04@mail.ru)

**ABSTRACT.** For nine Mira-type stars (o Cet, R Leo, S Car, U Her, X Oph, R Aql, RR Aql, S Ori, S Scl,) and one semi-regular star (L<sub>2</sub> Pup), the mean light curves have been obtained. The initial values of the brightness (observations) were fitted by a trigonometric polynomial of the statistically optimal order.

The Fourier coefficients and the additional parameters (degree of the trigonometric polynomial, amplitude of the brightness, the maximal slope of ascending and descending branch, semi-amplitudes and initial epochs for the brightness maximum (minimum magnitude) of each harmonic contribution, etc., were given in the tables reported earlier by Kudashkina (2016). In this study, we have received several interesting correlations between these parameters in the bands H and K. It was particularly noted the anomalous position on the figures of the star X Oph.

The mean light curves of the investigated stars are commonly symmetric in the near infrared region (H and K).

**Keywords:** Stars: Pulsating: Mira-type: SR

## 1. Introduction

This article is a continuation of the work on the Atlas of the mean light curves and catalogue of the characteristics of the long-period variable stars represented by Kudashkina (2003), Chinarova and Andronov (2000), Marsakova and Andronov (1998) and these works were done in a frame of activity of the “Ukrainian Virtual Observatory” (Vavilova et al., 2011, 2012) and “Inter-Longitude Astronomy” (Andronov et al., 2003). The “Stellar Bell” (pulsating stars) part of this campaign was reported by Andronov et al. (2014).

More details on observational bases, methods of processing of observations and methods of approximation of curves can be found in Andronov (2003) and Andronov and Marsakova (2006).

## 2. Data and analysis

For this investigation, the observational data of the near infrared bands (H and K) from the article «Infrared colours for Mira-like long-period variables found in the Hipparcos catalogue» by Whitelock et al. (2000) were used. 10 stars were processed: o Cet, R Leo, S Car, U Her, X Oph, R Aql, RR Aql, S Ori, S Scl, L<sub>2</sub> Pup (fig.1-2 and fig.5-6). As mentioned in the articles by Kudashkina (2015), Kudashkina and Andronov (1996), for the analysis we have used the program by Andronov (1994, 2003),

which allows the use of a trigonometric polynomial fit of the statistically optimal degree s:

$$m(t) = a_0 - \sum_{k=1}^s r_k \cos(2\pi k \cdot (t - T_{0k}) / P)$$

where  $r_k$  are semi-amplitudes and  $T_{0k}$  are initial epochs for the brightness maximum (minimum magnitude) of the wave with a period  $P=P/k$ .

The preliminary value of the period (from the General Catalogue of Variable Stars, (Samus et al. 2007-2015) was corrected using the method of differential corrections for each order  $s$  of the trigonometric polynomial (Andronov, 1994, 2003).

All computed parameters of light curves are subdivided into three groups: first, fundamental (period  $P$ , amplitude  $\Delta m = m_{\min} - m_{\max}$ , asymmetry  $f = \varphi_{\max} - \varphi_{\min}$ , degree of the trigonometric polynomial  $s$ ); second, parameters of the

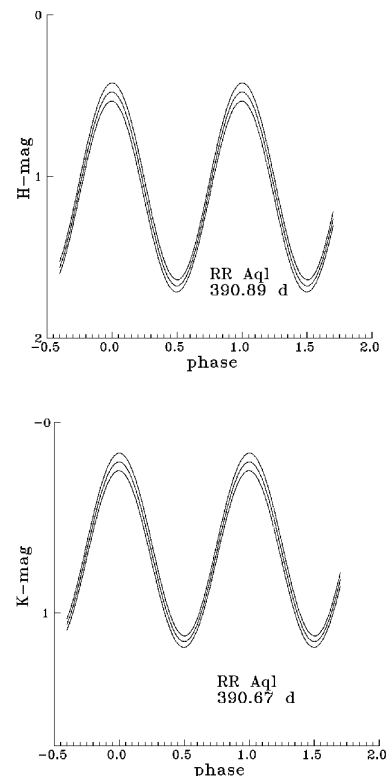


Figure 1: The mean light curves of the Mira-type stars in H and K bands. The best fit and the  $\pm 1\sigma$  error corridor are shown.

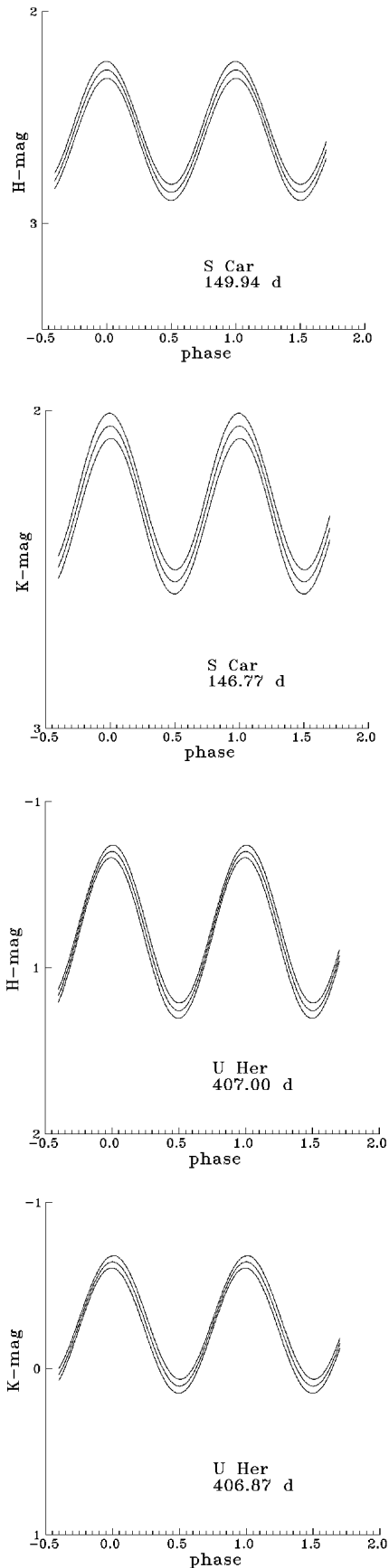


Figure 2: The mean light curves of the Mira-type stars in H and K bands. The best fit and the  $\pm 1\sigma$  error corridor are shown.

extremal slope of the light curve ( $m_i$  and  $m_d$  – the maximal slope of the incline for ascending and descending-branches;  $t_i$  and  $t_d$  – the characteristic time of the increase of brightness by  $1^m$  for ascending and descending branches); third, additional (parameters of harmonics).

The results were given in the tables reported earlier (Kudashkina, 2016). The main light curves are shown in Fig. 1, 2. The mean light curves for o Cet, R Aql and R Leo were given as well.

The regression lines and coefficient correlations were calculated for the next dependences:

- (1) period – amplitude “lgP –  $\Delta mag$  (H)”, “lgP –  $\Delta mag$  (K)”;
- (2) period – maximal slope of the incline for ascending and descending branches “lgP –  $m_i$  (H)”, “lgP –  $m_i$  (K)”, “lgP –  $m_d$  (H)”, “lgP –  $m_d$  (K)”;
- (3) period – characteristic time of the increase of brightness by 1m for ascending and descending branches “lgP –  $t_i$  (H)”, “lgP –  $t_i$  (K)”, “lgP –  $t_d$  (H)”, “lgP –  $t_d$  (K)”;
- (4) period – semiamplitude of the first harmonic “lgP –  $r_1$  (H)”, “lgP –  $r_1$  (K)”;
- (5) semiamplitude of the first harmonic – maximal slope of the incline for ascending and descending branches “ $r_1$  –  $m_i$  (H)”, “ $r_1$  –  $m_i$  (K)”, “ $r_1$  –  $m_d$  (H)”, “ $r_1$  –  $m_d$  (K)”;
- (6) semiamplitude of the first harmonic – characteristic time of the increase of brightness by  $1^m$  for ascending and descending branches “ $r_1$  –  $t_i$  (H)”, “ $r_1$  –  $t_i$  (K)”, “ $r_1$  –  $t_d$  (H)”, “ $r_1$  –  $t_d$  (K)”;
- (7) maximal slope of the incline for ascending branch – characteristic time of the increase of brightness by 1m for descending branch “ $m_i$  –  $t_d$  (H)”, “ $m_i$  –  $t_d$  (K)”;

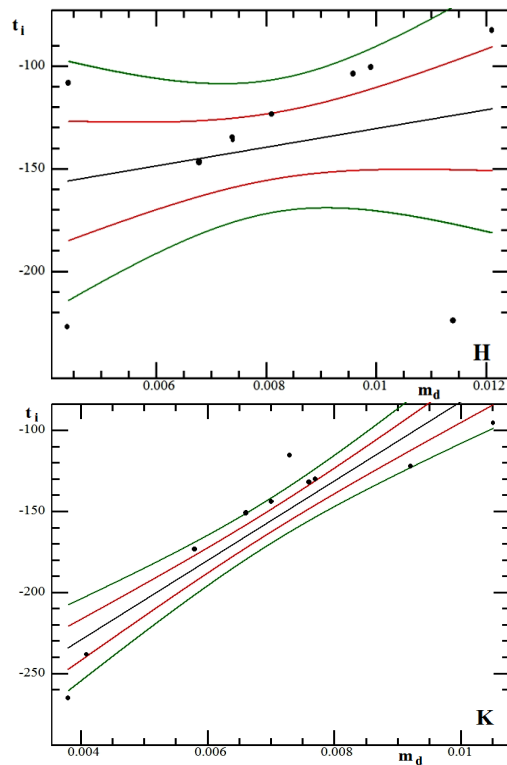


Figure 3: The dependencies between mutually inverse characteristics of the asymmetry of the branches. Index “i” corresponds to ascending branch, index “d” corresponds to the descending branch.

(8) maximal slope of the incline for descending branch – characteristic time of the increase of brightness by 1m for ascending branch “ $m_d - t_i$  (H)”, “ $m_d - t_i$  (K)”.

(9) difference of the amplitudes in the H – and K – band versus period  $\Delta m(H) - \Delta m(K) - \lg P$ .

### 3. Conclusions

For (8) the coefficient of the correlation for K – band  $\rho=0.92$  and  $\rho/\sigma_\rho=6.9$ . Meanwhile, the correlation coefficient for the H – band is only 0.24. Perhaps this is because the light curve in the K – band is more symmetrical than in the H – band.

For (1) the coefficients of the correlation are  $\rho=0.55$  and  $\rho/\sigma_\rho=1.9$  (H);  $\rho=0.54$  and  $\rho/\sigma_\rho=1.8$  (K).

For (4) the coefficients of the correlation are  $\rho=0.52$  and  $\rho/\sigma_\rho=1.7$  (H);  $\rho=0.52$  and  $\rho/\sigma_\rho=1.7$  (K).

For all other dependencies of the correlation coefficient less than 0.5 in absolute value and the ratio  $\rho/\sigma_\rho$  never exceeds 2.

Ratio (8) prompted the idea to test the dependence of the difference of the amplitudes of the rays H and K on the logarithm of the period (9).

For all ten stars of the dependence (9), the correlation coefficient is small enough ( $\rho=0.596$  and  $\rho/\sigma_\rho=1.8$ ). If we exclude two stars with highly asymmetric curves (S Ori and S Scl), the picture becomes different:  $\rho=0.70$  and  $\rho/\sigma_\rho=2.4$  (fig. 4). However, the star X Oph is also outstanding at the picture. This object is an anomalous

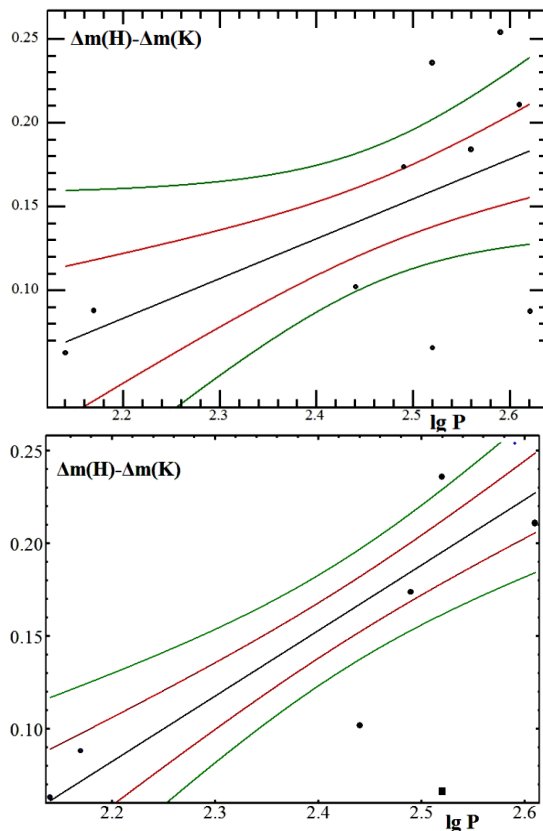


Figure 4: The dependence between  $\Delta m(H) - \Delta m(K)$  and  $\lg P$ . For the left dependence,  $\rho=0.596$  and  $\rho/\sigma_\rho=1.8$ . For the right dependence  $\rho=0.88$  and  $\rho/\sigma_\rho=4.2$ . At the bottom, the filled square shows the star X Oph, which was also excluded from the calculation.

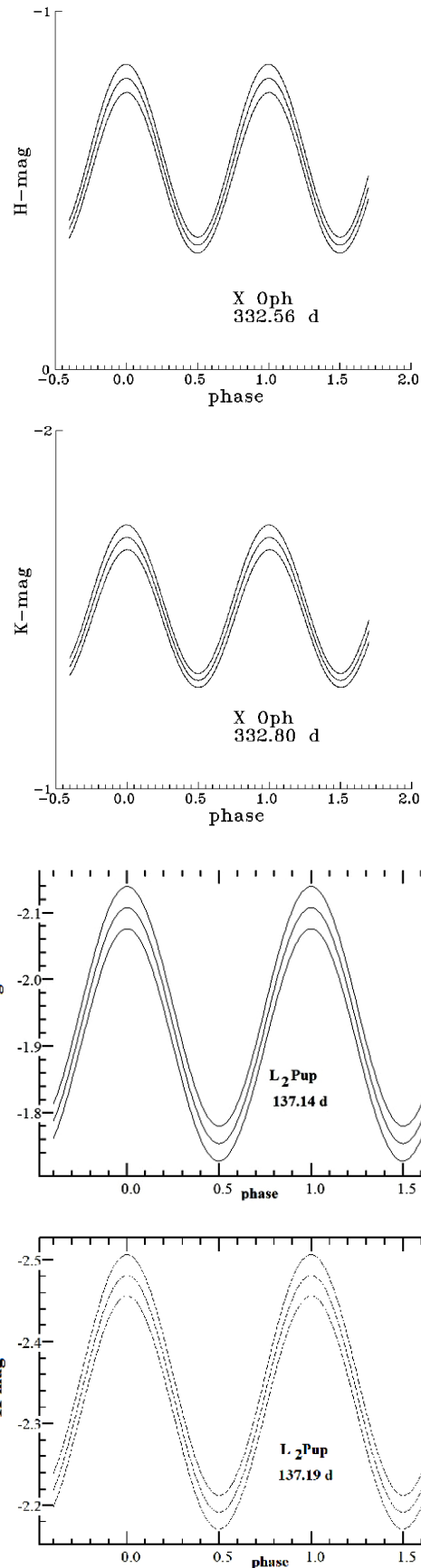


Figure 5: The mean light curves of the Mira-type stars in H and K bands. The best fit and the  $\pm 1\sigma$  error corridor are shown.

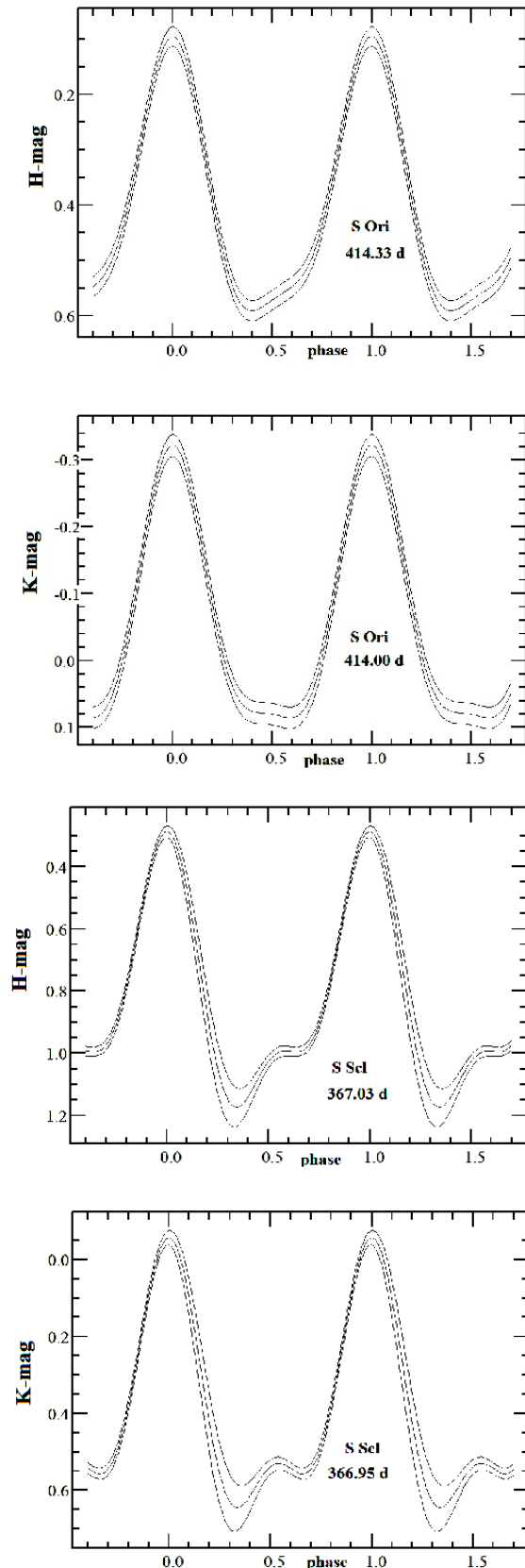


Figure 6: The mean light curves of the Mira-type stars in H and K bands. The best fit and the  $\pm 1\sigma$  error corridor are shown.

(small-amplitude) Mira-type star, which is also a spectral binary. Its features were discussed earlier (Andronov and Kudashkina, 2008). Also previously described features of the Mira-type stars R Aql, R Leo, U Her in the article Kudashkina and Rudnitskij (1988), in particular, we compared the behavior of the stars in the visual range and in the maser of the  $H_2O$  line.

All the figures were constructed with the program MCV (Andronov and Baklanov, 2004).

*Acknowledgements.* The authors are thankful to Prof. I.L. Andronov for useful discussions.

## References

- Andronov I.L.: 1994, *OAP*, **7**, 49. (1994OAP.....7...49A).
- Andronov I.L.: 2003, *ASPC* **292**, 391. (2003ASPC..292..391A).
- Andronov, I.L.; Antoniuk, K.A.; Augusto, P.; Baklanov, A.V.; Chinarova, L.L.; Chochol, D.; Efimov, Yu.S.; Gazeas, K.; Halevin, A.V.; Kim, Y.; Kolesnikov, S.V.; Kudashkina, L.S.; Marsakova, V.I.; Mason, P.A.; Niarchos, P.G.; Nogami, D.; Ostrova, N.I.; Patkos, L.; Pavlenko, E.P.; Shakhovskoy, N.M.; Tremko, J.; Yushchenko, A.V.; Zola, S.: 2003, *A&AT*, **22**, 4-5, 793. (2003A&AT...22..793A).
- Andronov I.L., Baklanov A.V.: 2004, *Astronomy School Reports*, **5**, 264. (2004AstSR...5..264A).
- Andronov I.L., Kudashkina L.S.: 2008, *OEJV*, **84**, 1. (2008OEJV...84....1A).
- Andronov I.L., Marsakova V.I.: 2006, *Astrophysics*, **49**, 506 (2006Ap.....49..506M).
- Andronov I.L., Marsakova V.I., Chinarova L.L.: 2014, *AASP*, **4**, 3. (2014AASP....4...3A).
- Chinarova L.L., Andronov I.L.: 2000, *OAP*, **13**, 116. (2000OAP....13..116C).
- Kudashkina L.S.: 2003, *KFNT*, **19**, 3, 193. (2003KFNT..19..193K).
- Kudashkina L.S.: 2016, <http://arxiv.org/abs/1607.03722>.
- Kudashkina L.S., Andronov I.L.: 1996, *OAP*, **9**, 108. (1996OAP.....9..108K).
- Kudashkina L.S., Rudnitskij G.M.: 1988, *Peremennye Zvezdy*, **22**, 925. (1988PZ.....22..925K)
- Marsakova V.I., Andronov I.L.: 1998, *OAP*, **11**, 79 (1998OAP....11...79M).
- Samus N.N., Durlevich O.V., Goranskij V.P., Kazarovets E. V., Kireeva N.N., Pastukhova E.N., Zharova A.V.: 2007-2015, *General Catalogue of Variable Stars*, VizieR On-line Data Catalog: B/gcvs (2009yCat....102025S)
- Vavilova I.B., Pakuliak L.K., Protsyuk Yu.I., Virun N.V., Kashuba S.G., Pikhun A.I., Andrievsky S.M., Mazhaev A.E., Kazantseva L.V., Shlyapnikov A.A., Shulga, A.V.; Zolotukhina A.V., Sergeeva T.P., Miroshnichenko A.P., Andronov I. L., Breus V.V., Virmina N.A.: 2011, *KosNT*, **17**, 4, 74. (2011KosNT..17d..74V).
- Vavilova I.B., Pakuliak L.K., Shlyapnikov A.A., Protsyuk Yu.I., Savanevich V.E., Andronov I.L., Andruk V.N., Kondrashova N.N., Baklanov A.V., Golovin, A.V., Fedorov P.N., Akhmetov V.S., Isak I.I., Mazhaev A.E., Golovnya V.V., Virun N.V., Zolotukhina A.V., Kazantseva L.V., Virmina N.A., Breus V.V., Kashuba S.G., Chinarova L.L., Kudashkina L.S., Epishev V.P.: 2012, *KPCB*, **28**, 2, 85. (2012KPCB...28..85V).
- Whitelock P.A., Marang F., Feast M.: 2000, *MNRAS*, **319**, 728. (2000MNRAS.319..728W).

DOI: <http://dx.doi.org/10.18524/1810-4215.2016.29.85048>

# 3D NUMERICAL HYDRODYNAMICAL SIMULATIONS OF A RADIATION-DRIVEN JET LAUNCH AND DISAPPEARING OVER LOW/HARD STATE

V.V. Nazarenko, S.V. Nazarenko

Astronomical Observatory, Odessa National University,  
Shevchenko Park, Odessa, 65014, Ukraine, [nazaret@te.net.ua](mailto:nazaret@te.net.ua)

**ABSTRACT.** In the present research we have calculated 3D numerical hydrodynamical simulations of a radiation-driven jet launch and disappearing over low/hard state. The calculations show that the jet launch occurs at the beginning of the low/hard state over 10-30 minutes of the orbital time. The jet disappearing occurs over the short time scale (of the order of 10-30 minutes of the orbital time) at the end of the low/hard state. The calculations also show that the temperature near the accretor is increased in 100-200 times over low/hard state relatively high/soft. The mass accretion rate in the disc is anti-correlated with the temperature near the accretor in our calculations.

**Keywords:** Stars: binaries - stars: jets - methods: numerical - hydrodynamics.

## 1. Introduction

The present research is concerned the 3D numerical hydrodynamical simulations of a radiation-driven jet launch and disappearing over low/hard states in microquasar on the base of Cyg X-1 binary parameters. The microquasars are that in semi-detached close binary systems in which the normal star (supergiant of O-B classes) overfill its Roche lobe and inflowing via  $L_1$ -stream in the compact objects (neutron star or black hole) Roche lobe in which accretion disc around the accretor is formed. Microquasar phenomenon is a launch and disappearing of relativistic jet along disc rotation axis in low/hard and high/soft states respectively. The observations show that jet velocities are about values: 0.25 and 0.98–0.99 of light speed. The observations also show that accretion disc luminosities in microquasars are about of 0.1–0.5 of critical luminosity (Fender et al., 1999; Fender, 2001; Mirabel, 2001; Fender, Gallo, Jonker, 2003; Fender, Belloni, Gallo, 2004; Gallo & Fender, 2005; Fender et al., 2006; Lachowicz et al., 2006; Gallo, 2007). The present work is the third one of own works which are devoted to 3D numerical hydrodynamical simulations of micro-

quasar phenomenon. We have simulated low/hard and high/soft states in accretion disc of microquasar Cyg X-1 taking into account the constant precession in the first work (Nazarenko V. & Nazarenko S., 2014) and undefined precession in the second one (Nazarenko V. & Nazarenko S., 2015). These results show the disc central part temperature is increased in 100–200 times over low/hard state relatively the central disc part temperature in high/soft state. The disc mass accretion rate is anti-correlated relatively the central disc part temperature time behaviour. The mass accretion rate is decreasing in 50–100 times over low/hard state relatively high/soft. The central disc part temperature is maximal at the beginning and at the end of the low/hard state. The transition between both states described above is order of 10–30 minutes of the orbital time. This time interval is very small value in respect to with the duration of both states described above since that of these states are about of half of the precession period (7–8 days in our calculations). In the first work (Nazarenko V. & Nazarenko S., 2014) the transitions between both states are regularly and happen every precession period. In the second work (Nazarenko V. & Nazarenko S., 2015) the transitions between both states are irregularly and are not every precession period. Such the numerical properties of the microquasar phenomenon calculated by us are close to the observational properties of classical microquasar Cyg X-1.

In the present work we complicate our simulations of microquasar phenomenon. For that we will calculate the radiation-driven jet formation along the disc rotation axis simultaneously with the simulation of low/hard and high/soft states in an accretion disc of classical microquasar Cyg X-1. Thus, our main task is to calculate the radiation-driven jet formation and its time behaviour over low/hard and high/soft states in classical microquasar Cyg X-1.

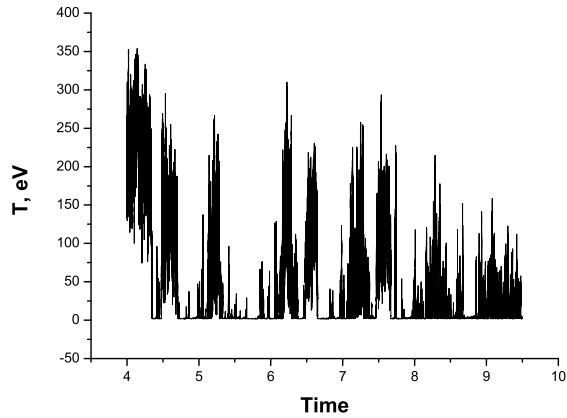


Figure 1: The time-dependences of the disc central part temperature.

## 2. Numerical algorithm

In the present research we use the numerical algorithm that is identical to our previous works. Shortly, the algorithm consists in the following. To calculate the accretion disc, we compute mass flow in the calculation area from initial to steady state. For that we use non-stationary hydrodynamical Euler equations which are resolved by astrophysical variant of the big particle code by Belotserkovskii & Davydov (1982). In the present research we use the radiation cooling model accordingly to Cox D.P. & Daltabuit E. (1971). To calculate mass flow in the calculation area we use rectangular coordinate system and numerical greed. The sell number in the numerical greed is  $110 \times 110 \times 148$ . To focus the jets along the disc rotation axes we will calculate the component of the radiation forces only. These radiation forces will be calculated by us in the approach of optically thin layers and in the approach of LTE and they may be written as follows:  $F_{rad} = \alpha * H/c$ , where  $\alpha$  is a coefficient of Thompsons scattering;  $H$  is radiation flux written as  $\sigma * T^4$ ;  $c$  is light speed. To simulate accretion disc precession we simulated slaved precession.

We use the following dimensionless units. The density is given in units of  $10^{11}$  particles per  $cm^3$ ; all the distances are given in units of the orbital separation; all temperatures are given in units of  $eV$ ; the velocities are given in  $km s^{-1}$ .

We cut the space around accretor with the radius of 0.05 to avoid the singularity in our calculations. We name this volume as Accretor-1 to distinguishit from real accretor.

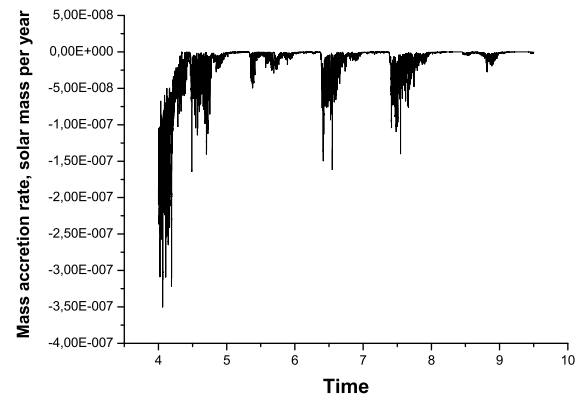


Figure 2: The time-dependences of the disc mass accretion rate.

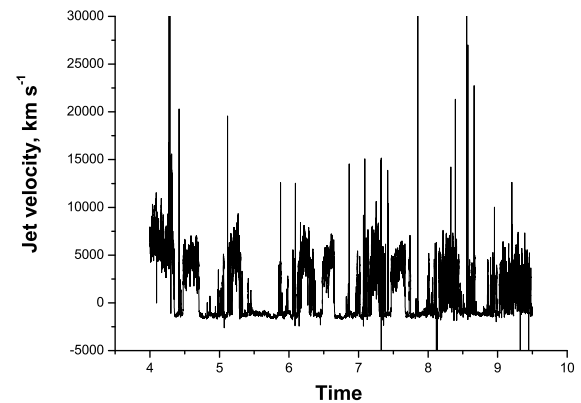


Figure 3: The time-dependences of the jet velocity.

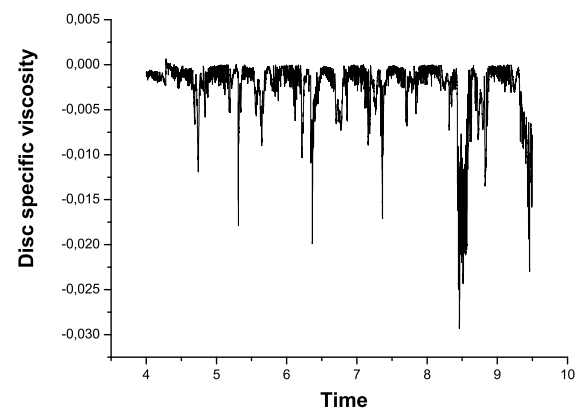


Figure 4: The time-dependences of the disc viscosity.

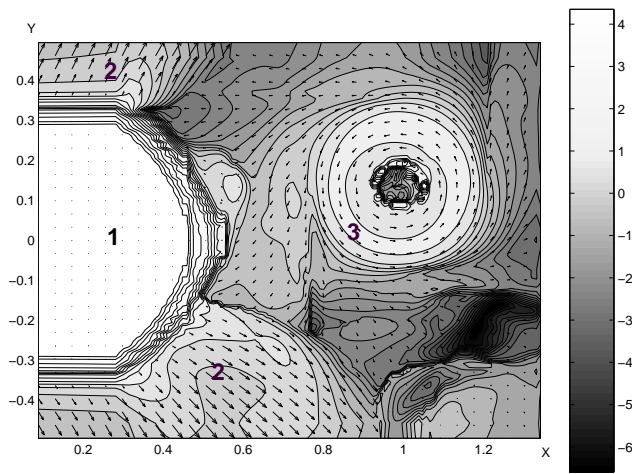


Figure 5: The cross-section of the calculation area by orbital plane and density contours on time 7.6 precession period.

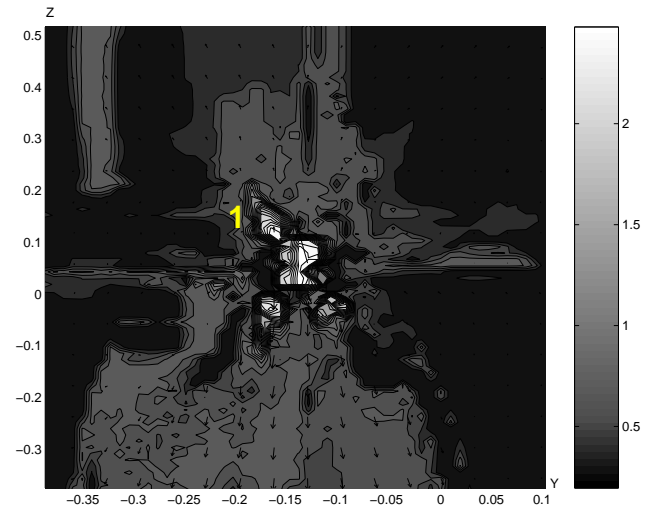


Figure 7: The cross-section of the calculation area by  $Z - Y$  plane laying on compact object centre on high resolution space scale and temperature contours on time 7.6 precession period.

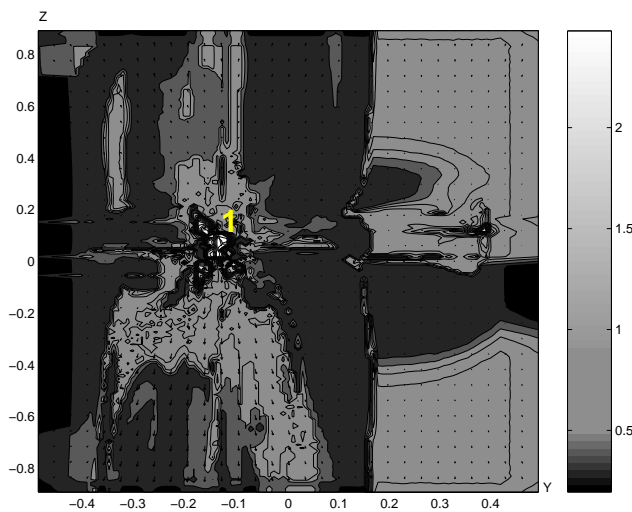


Figure 6: The cross-section of the calculation area by  $Z - Y$  plane laying on compact object centre on low resolution space scale and temperature contours on time 7.6 precession period.

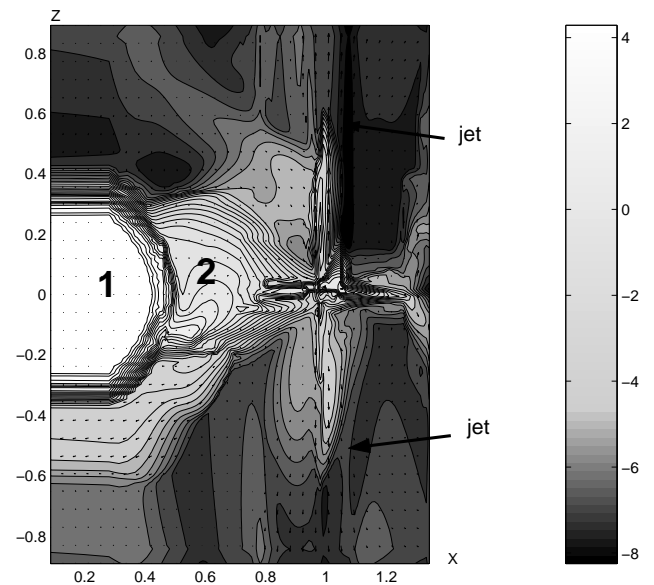


Figure 8: The cross-section of the calculation area by  $Z - X$  plane laying on line of centres and density contours on time 7.6 precession period.

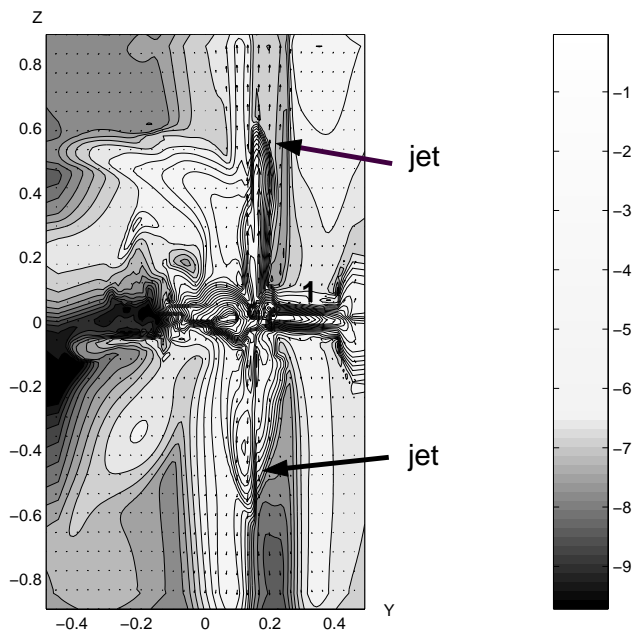


Figure 9: The cross-section of the calculation area by  $Z - Y$  plane laying on compact object centre and temperature contours on time 7.6 precession period.

### 3. Results

In our present simulations one-armed jets will be simulated in essential. By this reason we will show the jet parameters upper Acretor-1 only along the disk rotation axis at a height as high as 0.04.

The main results of the present research are plotted in Fig. 1-4. The time behaviour of the disc central part temperature is plotted in Fig. 1; the disc mass accretion rate is plotted in Fig. 2; jet velocity is plotted in Fig. 3; the accretion disc viscosity plotted in Fig. 4 is calculated as  $V_{rad} * r$ , where  $V_{rad}$  is radial velocity given in units of the orbital speed and  $r$  is the radial coordinate given in units of the orbital separation. The Fig. 1 shows that the temperatures in the disc central part are into two states: high and low. In the high state the temperatures are more high than the temperatures in the low states in 100-200 times approximately. The Fig. 2 shows that the mass accretion rate is anti-correlated with Fig. 1. When the temperature is high in Fig. 1, mass accretion rate is decreasing in 50-100 times. The key parameters in the present research are the jet velocities calculated along the disc rotation axis at a height as high as 0.04 (see Fig. 3). If jets are launching, the jet velocity is positive and on contrary when jets are disappearing, the jet velocity is negative (see Fig. 3) and an accretion process on compact object occurs. As Fig. 3 shows, the jet launch in the present research occurs suddenly, over 10-30 minutes of the orbital time, and its disap-

pearing is also occurring suddenly over the same time. Analysing the presenting Fig. 1-3 we may finally conclude that low/hard and high/soft states are simulated in our present research (Fender et al., 1999; Fender, 2001; Fender, Gallo, Jonker, 2003; Fender, Belloni, Gallo, 2004; Gallo & Fender, 2005; Fender et al., 2006). As Fig. 3 also shows, the jet velocities are maximal at the beginning and at the end of the low/hard state. This jet property may be explained very simply: the force accelerated jets is suddenly increased and is maximal at the beginning and the end of low/hard state but the jet mass is increased more gradually and is not maximal at the time pointed above. Such the circumstance finally results accordingly second Newtons law in the maximal jet velocity at the time stated above. The important parameter in the present research is an accretion disc specific viscosity. This parameter calculated in the present research (see Fig. 4) is maximal before a starting of jets. We may also mark that all the essential physical parameters of both states and jet production (see Fig. 1-4) are strong fluctuated over low/hard state in the present simulations.

The explanation of a mechanism of the jet production and low/hard and high/soft states generated in the present research is very simple: due to the precession of an accretion disc having being blowing by the donors wind in a disc in its central part to states are generated with high and low densities. When density is high in the disc centre and taking into account that optical thickness is less than 1 in this volume, the energy is very rapidly radiated due to radiation cooling and the temperature is very low in this state. On contrary, when the densities are low in the disc centre, the radiation cooling is not efficient in this volume and due to disc viscosity the kinetic energy of the disc rotation is instantaneously transformed into heat and the temperature is suddenly increased in this volume.

The cross-section of the calculation area by the disc plane (the density contours and velocity field; the precession phase is about of 5.75) is shown in Fig. 5 in which the donor (marked by number 1), donors wind (marked by number 2) and a disc (marked by number 3) are good seen. The cross-section of the calculation area by the  $Z - Y$  plane lying on the accretor (the temperature contours and velocity field; the precession phase is about of 7.6) is shown in Fig. 6 (the low resolution space scale) and Fig. 7 (the high resolution space scale). In this figure the high temperature region in the vicinity of the disc centre is very good seen (marked by number 1). This region has the strong warped form.

The cross-sections of the calculation area by  $Z - X$  plane on line of centres and the  $Z - Y$  plane line on compact object centre on time of jet launch of 7.6 precession period are shown in Fig. 8 and Fig. 9. In Fig. 8 the donor-star is marked by number 1 and the  $L_1$  stream is marked by number 2; in Fig. 9 the accretion disk is marked by number 1. As it is good

seen from Fig. 8-9 the two-armed jets are launching on the time of 7.6 precession period.

#### 4. Conclusions

To summarize the present simulations we may finally conclude that the essential numerical properties of both states, low/hard and high/soft, and jet production (the increasing of the disc central part temperature in low/hard state relatively high/soft; the decreasing of the disc mass accretion rate in low/hard state relatively high/soft; the transition between both states occurs at very short time scales it is the key property of the present simulations; the sudden jet production at the beginning of low/hard state; the maximal jet velocity occurs at the beginning and at the end of low/hard state) are close to the observed ones of classical microquasars.

#### References

- Belotserkovskii O.M., Davydov Yu.M.: 1982, *The large particles code in gas dynamics*, Moscow, Nauka, 391.
- Cox D. P., Daltabuit E.: 1971, *ApJ*, **167**, 113.
- Fender R. et al.: 1999, *ApJ*, **519**, 165.
- Fender R.: 2001, *MNRAS*, **322**, 31.
- Fender R.P., Gallo E., Jonker P.: 2003, *MNRAS*, **343**, 99.
- Fender R.P., Belloni T.M., Gallo E.: 2004, *MNRAS*, **355**, 1105.
- Fender R. et al.: 2006, *MNRAS*, **369**, 603.
- Gallo E., Fender R.P.: 2005, *MmSAI*, **76**, 600.
- Gallo E.: 2007, *Ap&SS*, **311**, 161.
- Lachowicz P. et al.: 2006, *MNRAS*, **368**, 1025.
- Mirabel I.F.: 2001, *ApSSS*, **276**, 319.
- Nazarenko V.V., Nazarenko S.V.: 2014, *Odessa Astron. Publ.*, **27**, 137.
- Nazarenko V.V., Nazarenko S.V.: 2015, *Odessa Astron. Publ.*, **28**, 171.

DOI: <http://dx.doi.org/10.18524/1810-4215.2016.29.85050>

# A SURVEY OF SEVERAL SPECTRAL LINES IN THE SPECTRA OF THE SUPERGIANT HD 14143

Y.M.Maharramov

Shamakhy Astrophysical Observatory, Azerbaijan National Academy of Sciences,  
Republic of Azerbaijan, [y\\_meherremov@rambler.ru](mailto:y_meherremov@rambler.ru)

**ABSTRACT.** Variations in the  $H_{\alpha}$ ,  $H_{\beta}$ , HeI, CII, SiIII, Al III, FeIII, NII, and OII lines in the spectrum of the star HD 14143 are investigated using observations carried out in 2013 with the 2-m telescope at the Shamakhy Astrophysical Observatory.

It has been revealed an anti-correlation between the variability of the radial velocity and spectral parameters of the absorption and emission components of the  $H_{\alpha}$  line in the spectrum of the star HD 14143. In addition, such anti-correlation has also been found out between the variability of the radial velocities of HeI and CII lines. At the same time the variabilities of the radial velocities of the absorption component of the  $H_{\alpha}$  and CII lines, as well as  $H_{\beta}$  and HeI lines correlate with each other.

**Key words:** Supergiant star, the profile of  $H_{\alpha}$  line, HD 14143

## 1. Introduction

The supergiant star HD14143 belongs to the stars with P Cyg profile of the  $H_{\alpha}$  line. According to (Barlow, 1977; Kraus et al., 2009; Vardya, 1984; Crowther et al., 2006), its spectral class is B2Ia, apparent magnitude is  $m_v = 6.66$  mag, mass is  $M/M_{\odot} = 28$ , radius is  $R/R_{\odot} = 52.9$ , luminosity is  $\log L/L_{\odot} = 5.42$ , effective temperature is  $T_{\text{eff}} = 18000$  K, mass-loss is  $\dot{M} = 1.05 \cdot 10^{-6} M_{\odot}/\text{year}$ , acceleration of gravity at the surface is  $\log g = 2.25$ , rotation speed is  $v \sin i = 76$  km/s, distance is  $D = 2.18$  kpc. It is believed that this star belongs to Per OB1 association (Lennon et al., 1993).

However, according to other authors (Lamers, 1981; Kudritzki et al., 1999; Tarafdar, 1988), the stellar parameters are somewhat different for HD14143 are:

$M_{\text{bol}} = -8.6$ ,  $T_{\text{eff}} = 17500$  K,  $T_{\text{eff}} = 20000$  K,  $R/R_{\odot} = 50.9$ ,  $R/R_{\odot} = 47.1$ ,  $R/R_{\odot} = 52$ ,  $M/M_{\odot} = 32$ ,  $\dot{M} = 0.30 \cdot 10^{-6} M_{\odot}/\text{year}$ ,  $\log g = 2.47$ ,  $\log g = 2.30$ ,  $\log L/L_{\odot} = 5.51$ ,  $\log L/L_{\odot} = 5.34$ ,  $B-V = 0.50$ ,  $E(B-V) = 0.65$

All earlier researchers of HD14143 performed only the determination of physical parameters of the supergiant star HD14143. Unfortunately, there are only little investigation concerning to the spectral and photometric observations of HD14143.

Note that due to the variable stellar wind and mass-loss rate, variations of the intensity, radial velocities, and P

Cygni profiles of lines of hydrogen, helium, and high-ionization ions are observed in the spectra of hot supergiants. From this point of view a study of the  $H_{\alpha}$  line is an especial interest. It is known that the  $H_{\alpha}$  line in the spectra of B supergiants has a clear P Cyg-type profile.

Generally, researchers noted that, the profile of  $H_{\alpha}$  line in the spectra of HD 14143 indicates variable structure, but the sequence of observations of all researchers was irregular and inadequate to trace in detail the changes in the spectra. Therefore they noted that more and systematic observations are needed to investigate this supergiant.

In the present paper, which is a sort of continuation of the above studies, we analyzed variations of the  $H_{\alpha}$  and  $H_{\beta}$  lines. In addition, we also investigated the variabilities of the HeI (5875.72, 5047.74, 5015.68, 4921.93 Å), CII (6578.05, 6582.88 Å), SiIII (5739.7 Å), Al III (5722.73, 5696.603 Å), Fe III (5193.91, 5156.11 Å), N II (5710.77, 5686.2, 5679.6, 5676.02, 5666.6, 5045.1, 5025.67, 5007.33, 5005.1, 5001.5, 4994.37, and 4987.38 Å) and OII (5160.02 Å) lines which formed deeper effective layers in the atmosphere of this star.

Our main aim is to study the observed peculiarities of these lines in the spectra. We believe our results will be of interest for further studies of this remarkable star.

## 2. Observation and processing

Spectral observations of the supergiant HD14143 in 2013 were carried out using a CCD detector in the echelle spectrometer mounted at the Cassegrain focus of the 2-m telescope of the Shamakhy Astrophysical Observatory (Mikhailov et al., 2005). The spectral resolution was  $R = 15000$  and the spectral range is  $\lambda\lambda 4700-6700\text{Å}$ . The Echelle spectra were processed with the standard technique using the DECH20 and DECH20t software (Galazutdinov, 1992).

Two spectra of the target star were obtained on each night. The signal-to-noise ratio was  $S/N = 150-200$ .

The average exposure was 1200-1500 s, depending on the weather conditions.

In addition to the observations of the target star, in order to check the stability of the instrument we also obtained numerous spectra of standard stars, the day and night background, and comparison spectra.

The measurement error for the equivalent widths ( $W$ ) does not exceed 5%, and error of the radial velocity ( $V_r$ ) is of the order of  $\pm 2$  km/s. Here ( $V_r$ ) are velocities of the

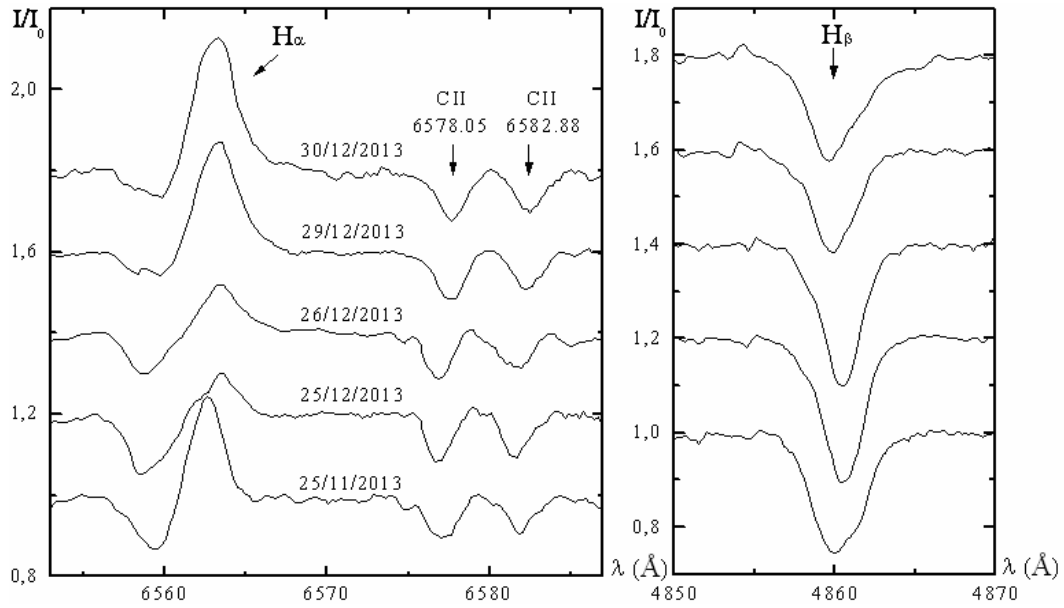


Figure 1: Profiles of the  $H_{\alpha}$ , CII and  $H_{\beta}$  lines in the spectra of HD 14143 observed in 2013.

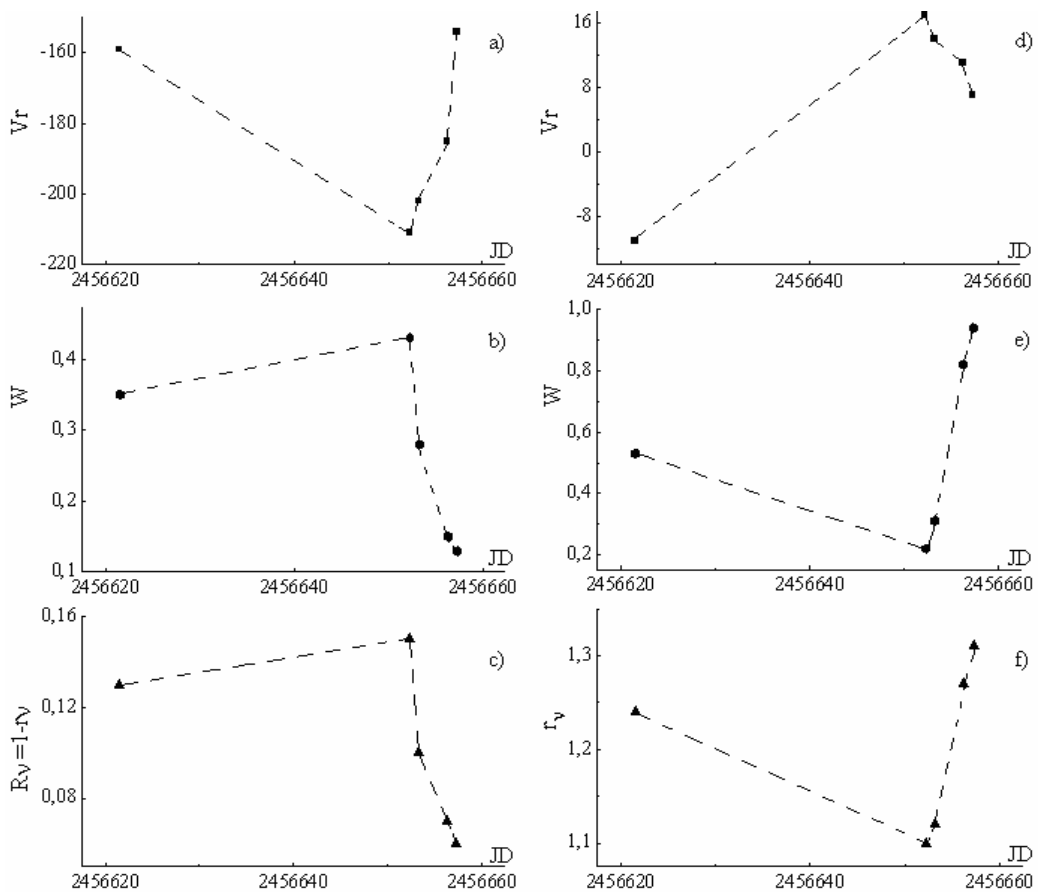


Figure 2: Variation with time of the radial velocities, equivalent widths, and depths (or residual intensities) in the  $H_{\alpha}$  line in the spectra of HD 14143. a), b), c) in the absorption; d), e), f) in the emission.

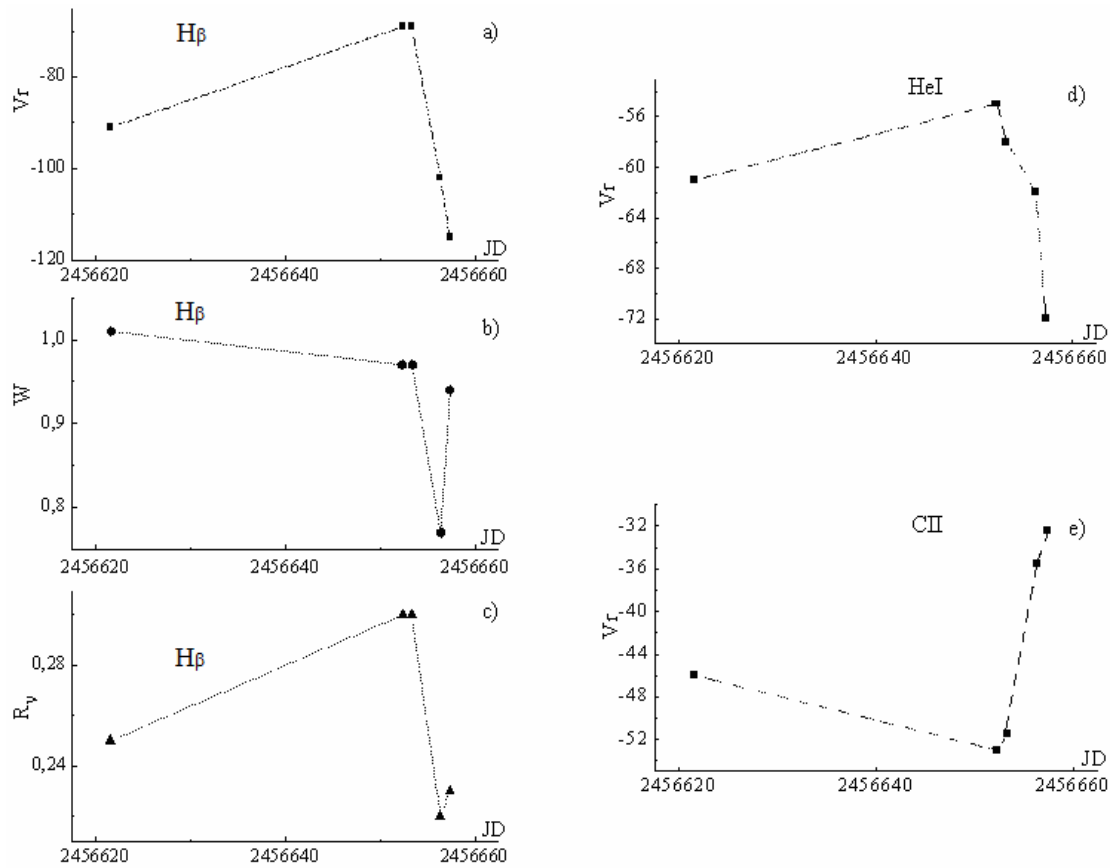


Figure 3: Variations of the radial velocities, and spectral parameters in the  $H\beta$ , HeI and CII lines.

absorption minima or emission maxima in the selected lines. Appropriate heliocentric corrections were included during data processing.

The profiles of the  $H\alpha$  line in the spectra of this star shows normal P Cyg profile in mainly. Our observations and measurements show that the most variability in the spectrum of HD14143 is displayed by the equivalent width, radial velocity and structures of the  $H\alpha$  line. Table 1 shows that the radial velocity and equivalent width of the absorption component of the  $H\alpha$  line varied between  $-227\div-159$  km/s and  $0.13\div0.43\text{\AA}$ , the emission component varied between  $-11\div+17$  km/s and  $0.22\div0.94\text{\AA}$ , and  $H\beta$  line varied between  $-115\div-69$  km/s and  $0.77\div1.01\text{\AA}$ , respectively. In addition, the depths of the absorption components of the  $H\alpha$  and  $H\beta$  lines varied between  $0.06\div0.15$  and  $0.22\div0.30$ , and the residual intensity of the emission component of the  $H\alpha$  line varied between  $1.10\div1.31$ , respectively.

As is shown from the measurements, in the radial velocity and spectral parameters of the  $H\alpha$  line, as well as the  $H\beta$  line significant changes happened, but the variability of the depth of the  $H\beta$  line is weaker.

In Table 1 the values of the radial velocity and spectral parameters of the  $H\alpha$  line and Figure 1 show that the intensity of emission component of the  $H\alpha$  line is stronger than the absorption one and both of the them changed substantially during observations.

We analyzed the spectra on December 29-30, 2013, and it is revealed that the second weaker components were observed in the violet side of the absorption component of  $H\alpha$  line. Table 1 shows that the depth and equivalent width of the absorption component of the  $H\alpha$  line are decreased and the residual intensity and equivalent width of the emission component of this line are increased substantially at that time.

Figure 1 and Table 1 also show that when the second weaker components were observed at the absorption component of  $H\alpha$  line, the  $H\beta$  line contours were shifted toward the violet, and its depth and equivalent width are relatively decreased.

At the same time the HeI line is displaced to the relatively violet side, but the CII lines shifted toward the red of the spectrum.

We also investigated the HeI, CII, Al III, FeIII, NII, NaID and OII lines in the spectra. We determined that the radial velocity of the CII lines vary between  $-54\div-31$  km/s. On the other hand, Figure 1 clearly shows that small components are observed and disappeared on the profiles of CII lines.

Unfortunately, the sequence of our observations was irregular, as well as because of a small number and due to low resolution we could not reveal in detail the structure of the  $H\alpha$  and CII profiles.

Table 1: Measurements of the parameters of the  $H_\alpha$  and  $H_\beta$  lines.

Date and JD	HD14143								
	$H_\alpha$ (abs)			$H_\alpha$ (em)			$H_\beta$		
	Vr (km/s)	W (Å)	$R_v$	Vr (km/s)	W (Å)	$r_v$	Vr (km/s)	W (Å)	$R_v$
25.11.2013 2456621,54	-159	0.35	0.13	-11	0.53	1.24	-91	1.01	0.25
25.12.2013 2456652,30	-211	0.43	0.15	17	0.22	1.10	-69	0,97	0.30
26.12.2013 2456653,28	-202	0.28	0.10	14	0.31	1.12	-69	0.97	0.30
29.12.2013 2456656,31	-210 -185	0.15	0.07	11	0.82	1.27	-102	0.77	0.22
30.12.2013 2456657,30	-227 -154	0.13	0.06	7	0.94	1.31	-115	0.94	0.23

Table 2: Measurements of parameters of the CII, HeI and NaI lines.

Date and JD	HD14143				
	Vr (km/s)				
	CII 6578.05Å	CII 6582.88Å	HeI 5875.72Å	NaI D1	NaI D2
25.11.2013 2456621,54	-46	-46	-61	-30	-25
25.12.2013 2456652,30	-52	-54	-55	-31	-27
26.12.2013 2456653,28	-51	-52	-58	-30	-27
29.12.2013 2456656,31	-33	-38	-62	-29	-28
30.12.2013 2456657,30	-31	-34	-72	-28	-25

Investigation of the HeI and NaID lines showed that the radial velocities of these lines vary between  $-72 \div -55$  km/s and  $-27.5 \pm 2.5$  km/s (Table 2), respectively, but profiles remain unchanged.

The averaged radial velocities of other ions are given in Table 3. Note that the considered spectra contain a lot of absorption lines formed in deeper layers of atmosphere. We measured the radial velocities of the selected absorption lines. As seen from the Table 3 averaged value of velocities of the selected absorption lines is  $-45.8$  km/s. This value is very close to the ( $V_{\text{sys}} = -47.0$ ) velocity of center of mass of the star HD14143 (*Simbad Astronomical Database*).

Table 3: Averaged radial velocities in the selected lines.

Elements	Vr, km/s Mean velocities
Si III	-45
Al III	-45
Fe III	-43
NII	-47
OII	-49

In addition, some results of the measurements in the spectra of HD14143 presented on a time scale in Figure 2 and 3. It has been revealed an anti-correlation between the radial velocity and spectral parameters of the absorption and emission components of the  $H_\alpha$  line, respectively (Fig.2). At the same time, such anti-correlation has been found out between the radial velocities of the HeI and CII lines (Fig.3d, e).

The variability of radial velocity, equivalent widths and depths of  $H_\beta$  line indicate repeating features too. But it shows that sometimes the variability of these quantities correlate with each other, but sometimes not (Fig. 3a, b, c).

Besides that, it has been revealed correlation between the variability of the radial velocities of the absorption component of the  $H_\alpha$  and CII lines, as well as between  $H_\beta$  and HeI lines.

### 3. Discussion

The  $H_\alpha$  line shows a P Cygni profile and is the only Balmer line showing emission in the spectrum. We have found out that all spectral parameters of the absorption and emission components of the  $H_\alpha$  observed in the atmosphere of the star HD14143 are significantly variable.

Table 1, 2 and Fig.1 show that on December 29-30, 2013, when the second weaker components were at the absorption component of the  $H_{\alpha}$  line the  $H_{\beta}$  and the HeI (5875.72 Å) lines shifted toward the violet, but the CII (6578.05, 6582.88 Å) lines shifted toward the red of the spectrum. This event can be explained by the complicated structure of the stellar wind.

On the other hand the formation small details in the profile of CII lines, as well as occasional shifts or disappearances of these components are interesting observational facts. As seen the deeper layers of the atmosphere of the star HD 14143 is an active variability. Detailed to investigate it is necessary to obtain many systematic observations with high resolution.

We noted above that there are correlations between the variabilities of the radial velocities and spectral parameters of the  $H_{\alpha}$ , CII,  $H_{\beta}$ , and HeI lines, respectively. Variabilities occur synchronously, or sometimes in an antiphase. We assume that these variabilities are caused by the pulsation or can be formed by the strong variable wind in the upper atmosphere of this star, i.e., in layers where the stellar wind is generated (Sobolev, 1947; Sobolev, 1985; De Jager, 1984; Cox, 1983). But a number of the observational materials is not enough, therefore it is not possible to reveal the quasiperiodicity of this variability.

In addition, Table 1 shows that when comparing with  $V_{\text{sys}}$ , on all dates  $H_{\alpha}$  and  $H_{\beta}$  absorption components are displaced to shorter wavelengths. But the averaged radial velocities of the all other selected absorption lines is very close to  $V_{\text{sys}}$ . We suppose it appears therefore that this star has an expanding outer envelope, whose density and velocity vary irregularly. The behavior of the inner atmosphere is peculiar, showing irregular changes in all line velocities. This star should be studied intensively for a full documentation of such changes.

#### 4. Conclusions

Sometimes the absorption component of  $H_{\alpha}$  line in the spectra of the star HD14143 is observed to be double. At that time the  $H_{\beta}$  and HeI (5875.72Å) lines shifted toward the violet, and the CII (6578.05, 6582.88Å) lines shifted toward the red of the spectrum. In addition, the small components are observed and disappeared on the profiles of CII lines. These events can be explained by the complicated structure of the stellar wind.

It has been revealed an anti-correlation between the variabilities of the radial velocity and spectral parameters of the absorption and emission components of  $H_{\alpha}$  line in the spectra of the star HD 14143. There is such anti-correlation between the variability of radial velocities of the HeI and CII lines. In addition, it has been revealed that the variabilities of the radial velocities of the absorption component of the  $H_{\alpha}$  and CII lines, as well as  $H_{\beta}$  and HeI lines correlate each other.

We assume that these variabilities are caused by the pulsation or can be formed by the strong variable wind in the upper atmosphere of this star, i.e., in layers where the stellar wind is generated

*Acknowledgements.* This work was supported by the scientific program for the priority fields of research of the National Academy of Sciences of Azerbaijan.

#### References

- Barlow M.J., Cohen M.: 1977, *Astrophys. J.*, **213**, 737.  
 Cox J.P.: 1983, *Theory of Stellar Pulsation*, Mir, Moscow (in Russian).  
 Crowther P.A., Lennon D.J., Walborn N.R.: 2006, *Astron. & Astrophys.*, **446**, 279.  
 De Jager C.: 1984, *The Brightest Stars*, Mir, Moscow (in Russian).  
 Galazutdinov G.A.: 1992, *Prepr. SAO RAS*, **92/2**.  
 Kraus M., Fernandes M.B., Kubat J.: 2009, *Astron. & Astrophys.*, **499**, 291.  
 Kudritzki R.P. et al.: 1999, *Astron. & Astrophys.*, **350**, 970.  
 Lamers H. J.G. L.M.: 1981, *Astrophys. J.*, **245**, 593.  
 Lennon D.J., Dufton P.L., Fitzsimmons A.: 1993, *Astron. & Astrophys., Suppl. Ser.*, **97**, 559.  
 Mikailov Kh.M., Khalilov V.M., Alekberov I.A.: 2005, *Tsirk. ShAO*, **109**, 21.  
 Tarafdar S.P.: 1988, *Astrophys. J.*, **331**, 932.  
 SIMBAD Astronomical Database (Strasbourg Astronomical Data Center), <http://simbad.u-strasbg.fr/Simbad/>.  
 Sobolev V.V.: 1947, *Moving Envelopes of Stars*, Leningrad, (in Russian).  
 Sobolev V. V.: 1985, *Course in Theoretical Astrophysics*, Nauka, Moscow (in Russian)  
 Tarafdar S.P.: 1988, *Astrophys. J.*, **331**, 932.  
 Vardya M.S.: 1984, *Astrophys. and Space Sci.*, **107**, 141.

DOI: <http://dx.doi.org/10.18524/1810-4215.2016.29.85054>

## THE CHANGING LOOK AGNS MONITORING PROJECT

V. L.Oknyanskij<sup>1</sup>, N.A.Huseynov<sup>2</sup>, V.M.Lipunov<sup>1</sup>, A.M.Tatarnikov<sup>1</sup>, N.I.Shatsky,  
S.S.Tsygankov<sup>3</sup>, V.G.Metlov<sup>1</sup>, I.R.Salmanov<sup>2</sup>, C.M.Gaskell<sup>4</sup>

<sup>1</sup> Sternberg Astronomical Institute, Moscow M.V. Lomonosov State University, Moscow, Russian Federation, [oknyan@mail.ru](mailto:oknyan@mail.ru)

<sup>2</sup> Shamakhy Astrophysical Observatory, National Academy of Sciences, Azerbaijan

<sup>3</sup> Tuorla Observatory, Department of Physics and Astronomy, University of Turku, Väisäläntie 20, FI-21500, Piikkiö, Finland

<sup>4</sup> Department of Astronomy and Astrophysics, University of California, Santa Cruz, USA

**ABSTRACT.** The Changing Look AGNs (CL AGNs) are objects which undergo dramatic variability of the emission line profiles and classification type of which can move from one spectral class to another within very short time interval (from days to years).

We start the project of spectral and photometric multiwavelength (from IR to X-ray) monitoring which include the selected set of AGNs also known as the CL AGNs.

We are going to use 2-m Zeiss telescope (ShAO) for optical spectral observations, 2.5-m telescope of SAI for IR *JHK* photometry and spectrophotometry, small telescopes Zeiss-600, AZT-5 for *BVRI* photometry.

We are also going to search for the new CL AGNs using the *MASTER* data. Furthermore, we can get historical light curves for the known and the new discovered objects using the *MASTER* opportunities.

We are planning to apply for X-ray and UV observations of some CL AGNs with the *SWIFT*.

We present some results of such monitoring of the transient object NGC2617.

The main goal of the project is to investigate the possibilities for the repeating cases of the strong changes of spectral type at the CL AGNs. Investigation of such type of objects can be very informative for understanding the nature of these fast variations as well as physics of the AGNs.

### 1. Introduction

The Changing Look AGNs (CL AGNs) are objects which undergo dramatic variability of the emission line profiles and classification type of which can move from one spectral class to another within very short time interval (from days to years). There are currently only some tens of cases of CL AGNs known. However, the small number of known CL AGNs is comparable to the number of AGNs which able to suspect, therefore, that perhaps every strongly variable AGN could be found to be a CL AGN if it is observed long enough. This assumption is supported by recent investigations (Runco et al., 2016)

which show that about 38% of 102 Seyferts changed type and about 3% of the objects demonstrate disappearance of  $H_{\beta}$  on time scale of 3-9 years. Also (MacLeod et al., 2016) estimate >15% for strongly variable luminous quasars have changing-look behavior on rest-frame timescales of 3000–4000 days. There different types of the CL cases:

1. Vanishing or strong decreasing of broad line components for some relatively short time from several months to several years (NGC 3616 (Andrillat, 1968), NGC 4151 (Lyutyj, Oknyanskij, Chuvaev 1984; Penston and Perez, 1984; Oknyansky, Lyuty and Chuvaev, 1991)), NGC7603, Mrk 372, 3C390.3, Mrk993, NGC7469 (Chuvaev, Lyutyi and Doroshenko, 1990), NGC6814 (Sekiguchi and Menzies, 1990), NGC5548 (Shapovalova et al., 2004)). It is known that type of change for 2 quasars SDSS J015957.64+003310.5 and the SDSS J101152.98+544206.4. (See more references at Shappee et al., 2014; Koay et al., 2016).

2. Appearing of broad line components in AGNs which are usually Sy2 for long time (Mrk 6, Mrk 1018, NGC 1097, NGC7582, Mrk 590, NGC 2617). In Some of these cases, there were registered returns to the usual low state with narrow type of lines after few years as it was in NGC7582 or after very long time as it happen for Mrk6 and Mrk590. For part of these objects changing look is connected with appearance of some blue shifted broad emission components (Mrk 6, 3C390.3).

3. More than 20 AGNs are changing look at X-ray spectral properties (see references at Richi et al., 2016). Some of these AGNs were also noted before as the changing look in optical spectral region (NGC4151 and Mrk 6).

4. Other CL AGNs which can not be from 1-3 type of cases. Those are objects with strong variation of continuum in hundreds of times without significant variations of lines. For example changing from QSO to BLac state ( QSO 1256+295 Wills et. al., 1983).

5. Tidal disruption of stars (TDE) observed in not AGN galaxies. These objects obtain AGN properties temporally.

Table 1: The CL AGNs selected for our project.

N	Galaxy	$\alpha$	$\delta$	V	Type	z
1	NGC 863	2 14 33	-00 45 58	13,80	Sa	0,0261
2	NGC 2617	8 35 38	-04 05 16	14,50	S0	0,0143
3	NGC 3227	0 23 30	+19 51 58	10,30	SBa	0,0039
4	NGC 3516	1 06 47	+72 34 09	11,30	SB0	0,0088
5	NGC 4151	2 10 32	+39 24 24	10,30	SBa	0,0033
6	NGC 4941	3 04 13	-05 33 05	11,20	SBa	0,0037
7	NGC 5548	4 17 59	+26 08 12	12,30	S0	0,017
8	NGC 6814	9 42 40	+10 19 28	11,30	SBb	0,0052
9	NGC 7469	3 03 15	+08 52 26	12,00	SBa	0,01639
10	3C 273	2 29 06	+02 03 08	12,90	QSO	0,158
11	3C 390.3	8 42 08	+79 46 17	15.38	S0	0,056

## 2. The list of selected objects

The main goal of the project is to investigate the possibilities for the repeating of cases of the strong changes of spectral type at the CL AGNs. Investigation of such type of objects can be very informative for understanding the nature of this fast variations as well as physics of the AGNs. So we were selecting the objects which have already known as CL cases in the past and are attractive for our observational opportunities (see Table 1).

## 3. Spectral and photometric multiwavelength monitoring

We are going to use 2-m Zeiss telescope (ShAO) for optical spectral observations, 2.5-m telescope of SAI for IR *JHK* photometry and spectrophotometry, small telescopes Zeiss-600, AZT-5 for *BVRI* photometry. We are also going to search for the new CL AGNs using the *MASTER* data (Lipunov et al. 2010). Moreover, we can get historical light curves for the known and the new discovered objects using the *MASTER* opportunities. We are planning to apply for X-ray and UV observations of some CL AGNs with the *SWIFT*. We have already got first results of such monitoring for the NGC 2617 during 2016.

## 4. NGC2617

Optical and near-infrared photometry, optical spectroscopy, and soft X-ray and UV monitoring of the changing look active galactic nucleus NGC 2617 show that it continues to have the appearance of a type 1 Seyfert

galaxy (Oknyansky et al., 2016a,b,c). An optical light curve for 2010–2016 indicates that the change of type probably occurred between October 2010 and February 2012 and was unconnected with the brightening in 2013. In 2016 NGC 2617 brightened again to the level of activity close to that of April 2013. We found variations in all passbands and in both the intensities and profiles of the broad Balmer lines. X-ray variations are well correlated with UV–optical variability and possibly lead by 1-3 days. The *K* band lags the *J* band by about  $22 \pm 2$  days but lags *H* by  $\sim 10$  days. *J* lags *B* by about 3 days. This could be because *J*-band variability arises from the outer edge of the accretion disc while *K*-band variability comes from thermal re-emission by dust. We found an increase in the *K*-band lag from 2013 to 2016 which could be due to dust sublimation. We propose that type changes are a result of increasing central luminosity causing sublimation of the innermost dust in the hollow bi-conical outflow.

## 5. Summary

We start the project of spectral and photometric multiwavelength (from IR to X-ray) monitoring which include the selected set of AGNs known already as the CL AGNs. We obtain first results for NGC2617.

The project is open for all interested in collaborations in these investigations.

*Acknowledgements.* We thank the SAI director, A.Cherepashchuk, and ShAO director, N.Jalilov, for granting us Director’s Discretionary Time for observations, and the staffs of the observatories. We also express our thanks to

N.Gehrels for approving the Swift ToO observation requests and the Swift ToO team for promptly scheduling and executing our observations. This work was supported in part by M.V.Lomonosov Moscow State University Program of Development, by the Russian Foundation for Basic Research through grant 14-02-01274 and by Russian Science Foundation through grant 16-12-00085.

### References

- Andrillat J.: 1968, *AJ*, **73**, 862.  
Chuvaev K.K., Lyutyi V.M., Doroshenko V.T.: 1990, *Soviet Astronomy Letters*, **16**, 372.  
MacLeod C.L. et al.: 2016, *MNRAS*, **457**, 389.  
Koay J.Y. et al.: 2016, **460**, 304.  
Lyutyj V.M., Oknyanskij V.L., Chuvaev K.K.: 1984, *Soviet Astronomy Letters*, **10**, 335.  
Lipunov V. et al.: 2010, *Adv. Astr.*, **2010**, 349171.  
Oknyanskii V.L., Lyutyi V.M., Chuvaev K.K.: 1991, *Soviet Astronomy Letters*, **17**, 100.  
Oknyansky V.L. et al.: 2016a, *ATel*, 9015.  
Oknyansky V.L. et al.: 2016b, *ATel*, 9030.  
Oknyansky V.L. et al.: 2016c, *ATel*, 9050.  
Penston M.V., Perez E.: 1984, *MNRAS*, **211**, 33P.  
Runco J.N. et al.: 2016, *ApJ*, **821**, 33.  
Richi C. et al.: 2016, *ApJ*, **820**, 5.  
Sekiguchi K., Menzies J.V.: 1990, *MNRAS*, **245**, 66.  
Shappee B.J. et al.: 2014, *ApJ*, **788**, 48.  
Shapovalova A.I. et al.: 2004, *A&A*, **422**, 925.  
Wills B.J. et al.: 1983, *ApJ*, **274**, 62.

DOI: <http://dx.doi.org/10.18524/1810-4215.2016.29.85058>

## OPTICAL MONITORING OF NGC4151 DURING 110 YEARS

V.L.Oknyanskij<sup>1</sup>, N.V.Metlova<sup>1</sup>, N.A.Huseynov<sup>2</sup>, Di-Fu Guo<sup>3</sup>, V.M.Lyuty<sup>1</sup>

<sup>1</sup> Sternberg Astronomical Institute, Moscow M.V.Lomonosov State University, Moscow, Russian Federation, [oknyan@mail.ru](mailto:oknyan@mail.ru)

<sup>2</sup> Shamakhy Astrophysical Observatory, National Academy of Sciences, Azerbaijan

<sup>3</sup> School of Space Science and Physics, Shandong University, Weihai, China

**ABSTRACT.** We present the historical light curve of NGC 4151 for 1906–2016. The light curve (Oknyanskij and Lyuty, 2007) is primarily based on our published photoelectric data (1968–2007, about 1040 nightly mean measurements (Oknyanskij and Lyuty, 2007)) and photographic estimates (mostly Odessa and Moscow plates taken in 1906 – 1982 (Oknyanskij, 1978, 1983), about 350 measurements). Additionally, we include all data obtained prior to 1968 (de Vaucouleurs and de Vaucouleurs, 1968; Barnes 1968; Sandage, 1967; Wisniewski and Kleinmann, 1968; Fitch et al., 1967) in total, 19 photoelectric observations from 1958–1967, were reduced by us to the same diaphragm aperture as that used in our measurements) as well as photographic data (Pacholczyk et al., 1983) (Harvard and Steward observatories' patrol plates taken in 1910–1968, about 210 measurements). The light curve includes our old and new photometrical data obtained during last years at SAI, ShAO and Weihai Observatory as well as other published data (Roberts and Rumstey, 2012; Schnülle et al., 2015). All these data were reduced to an uniform photometric system.

Applying Fourier (*CLEAN* algorithm) we have found periodic component ~16 years in the 110 years light curve. 40 years ago about the same "period" was firstly revealed from Odessa's photometrical data (Oknyanskij, 1977; 1978). This "period" seen in the light curve was then found independently in the spectral variability and interpreted as a case of the supermassive binary black hole (Bon et al., 2012). We interpret these circles as some accretion dynamic time.

**Keywords:** AGN, optical variability, historical light curves

### 1. Introduction

NGC4151 is one of the most popular and well studied AGNs, it is most bright and high variable object, which is very often used as an example object: typical Sy1, typical Sy1.5, typical object changing classification type between Sy1 and Sy1.9. Now about the same cases of changing spectral classification types were found for several tens of

AGNs. So it is more likely typical than untypical option for AGNs and it has to be explained in some unification model.

NGC 4151 – is one of the several Seyfert galaxies which were firstly discovered at 1967 as variable in optical region (Fitch et al., 1967). Shortly after that (at 1968) the photoelectric *UBV* monitoring of NGC 4151 object was started at Crimean Laboratory of Sternberg Astronomical Institute (Lyuty, 1977). Variability of the object before 1967 can be investigated only from the archive photographic observations and an insignificant number of isolated photoelectrical observations. First long term optical variability investigations using photographic archive data (Harvard plates taken in the years 1932–1952 and Steward plates taken in the years 1956–1968) were published (in graphic form only) by Pacholczyk (1971). Our long term photometry of NGC 4151 using Odessa plates (1952–1975) was published in table and graphic forms Oknyanskij (1978). Subsequently, Pacholczyk et al. (1983) published more complete photometrical data started from 1910 (in table form). Finally, variability of NGC 4151 during 1906–1911 years was investigated using old Moscow plates (Oknyanskij, 1983). The longest uniform series of photometric observations were obtained by one of us (Lyuty, 1977), and so all other observations, as far as possible, were reduced to the system of the series (see details at Lyuty and Oknyanskij, 1987). Long-term historical light curve, including photographic and photoelectric data, was published by Lyuty and Oknyanskij (1987), and then continued for the more than 100 years (Lyuty 2006; Oknyanskij and Lyuty, 2007; Oknyanskij et al. 2012; 2013). In Oknyanskij et al., (2014) we add to the light curve published data of Roberts and Rumstey (2012) reduced to our system. Our data were reproduced at historical light curves many times (for example by Czerny et al. (2003).

### 2. Historical light curve for 1906–2016

At the present work we continue the optical monitoring of NGC 4151. Our new data after 2010 (~200 nights) include the photoelectric *UBV* and CCD photometry with the same telescope 0.6-m and equipments at the Crimean Astronomical Station of the MSU (see details in Oknyanskij and Lyuty, 2007; Oknyanskij et al., 2013), CCD data, which

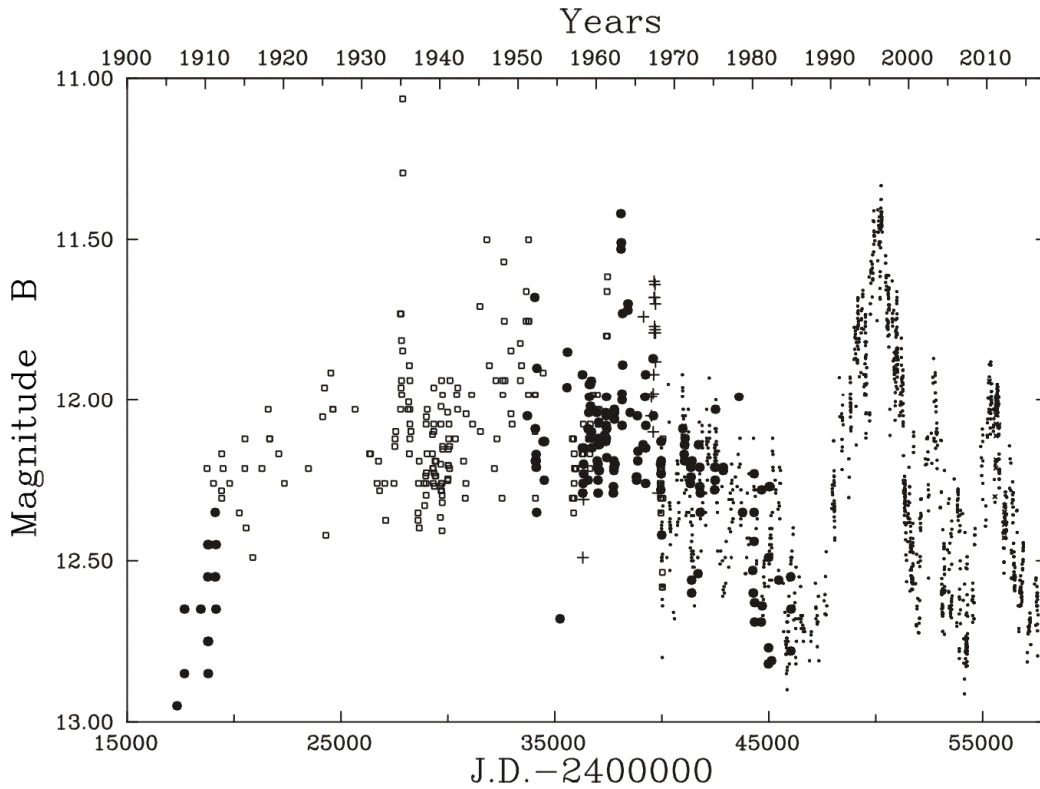


Figure 1: The historical light curve of NGC 4151. Filled circles – our photographic data, open circles – Pacholszyk et. al. (1983), pluses – photoelectric data obtained before 1968, dots – Crimean photoelectric monitoring, our new photoelectric and CCD data, other published CCD data transferred to our system (Roberts & Rumstay, 2012; Schnülle et al., 2015). The errors are of the order of 0.2 mag for Pachalcsyk’s data, 0.1 mag or better for our photographic points, and  $\sim 0.02$  mag or less for out photoelectric and CCD data.

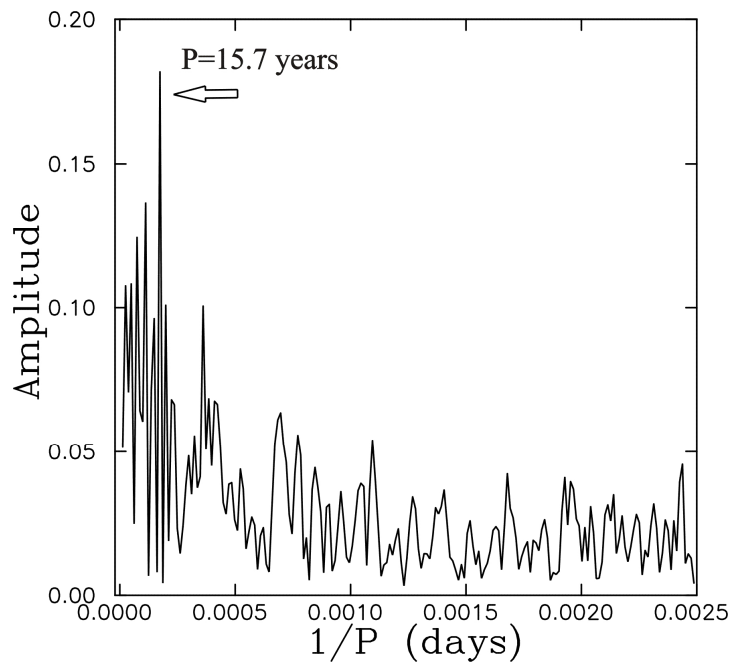


Figure 2: Relationship between the trial period  $P$  and its amplitude (in mag) obtained by the *CLEAN* method (Roberts et al., 1987). The regular component about 16 year which was firstly found 40 years ago (Oknyanskij, 1977) is most significant still in the variability during past 110 years.

were obtained with 0.6-m telescope at ShAO and the 1.0-m telescope at Weihai Observatory of Shandong University. We also added 29 points from Schnülle et al. (2015) reduced from  $z$  to our system in  $B$ .

The historical light curve for 1906–2016 years is presented at Fig. 1. At the light curve (Fig. 1) we can see different variable components: 1 – fast variations with time about tens of days, 2 – slow variations with time about several years, 3 – very slow component with time about tens of years. It is clearly seen that after minimuma at 1984 the type of variability is not the same as it was before: the amplitude of the fast variations become smaller compared to the slow ones. The most significant and long bright state during 1987–1997 happened just once during 110 years and can be connected with some unusual situation in the object, which increased the accretion rate very significantly.

## 2. Periodicity analysis

Applying Fourier (*CLEAN*) algorithm (Roberts et al., 1987) to the data from 1906 till 2016 (smoothed with steps of 100 days), we found out the periodical component  $P \sim 15.7$  years in 110 years light curve (see Fig. 2). Only on the base of the Odessa photometrical data (Oknyanskij 1977; 1978) nearly such period was revealed 40 years ago for the first time. Then presence of this periodic component was confirmed by us several times (Lyutyj and Oknyanskij, 1981; 1987; Oknyanskij and Lyuty 2007; Oknyanskij et al., 2007, 2013), and also, it was found independently from about the same data sets by Fun and Su (1999) and Guo et al. (2015). This “period” seen in the light curve was then found independently in the spectral variability and interpreted as a case of the supermassive binary black hole (Bon et al., 2012).

## 3. Summary

We present the historical light curve of NGC4151 for 1906–2016 which is longest known light curve among the variable Seyfert galaxies. The interval 1906–1966 is mostly presented by photographic estimates that were obtained using Moscow, Odessa, Harvard and Stewart old plates collections. All these data can be combined together and reduced to the same system as photoelectrical  $B$  observations just using magnitudes obtained with Odessa plates because these observations are overlap with photoelectric and other photographic data. The Pacholczyk (1983) magnitudes need some very big corrections in scale and zero point before plotting them together with other photometric data.

The historical light curve shows different components in variability. Very high and long active state during 1987–1998 was happened just once during 110 years. We again confirm the presence of the regular component about 16 years.

We interpret these circles as some typical accretion dynamic time for the object.

*Acknowledgements.* We are grateful to Dr. O.E. Mandel for assistance in photographic measurements. This work has been supported in part by the Russian Foundation for Basic Research through grant no. 14-02-01274.

## References

- Barnes T.G.: 1968, *Ap. Lett.*, **1**, 171.  
 Bon E. et al.: 2012., *ApJ*, **759**, 118.  
 Czerny B. et al.: 2003, *MNRAS*, **342**, 1222C.  
 de Vaucouleurs G., de Vaucouleurs A.G.: 1968, *Publications University of Texas, Series II*, **7**, 1.  
 Guo D.F. et al.: 2015, *RAA*, **14**, 923.  
 Fan J.H., Su C.Y.: 1999, *ChA&A*, **23**, 22.  
 Fitch W.S., Pacholczyk A.G., Weymann R.J.: 1967, *Astrophys. J.*, **150**, L67.  
 Lyutyi V.M., Oknyanskij V.L.: 1987, *Soviet Astronomy*, **31**, 245.  
 Lyuty V.M.: 2006, *ASP Conference Series*, **360**, 3.  
 Lyutyi V.M.: 1977, *Soviet. Astron.*, **21**, 655.  
 Lyutyj V.M., Oknyanskij V.L.: 1981, *Soviet Astron. Lett.*, **7**, 364.  
 Lyutyj V.M., Oknyanskij V.L.: 1987, *Soviet Astronomy*, **31**, 245.  
 Oknyanskij V.L.: 1977, *Astron. Tsirkulyar*, **944**, 2.  
 Oknyanskij V.L.: 1978, *Perem. Zvezdy Pr*, **21**, 71.  
 Oknyanskij V.L.: 1983, *Astron. Tsirkulyar*, **1300**, 1.  
 Oknyanskij V.L., Lyuty V.M.: 2007, *Peremen. Zvezdy Prilozhenie*, **7**, 28.  
 Oknyanskij V.L., Lyuty V.M.: 2007, *Odessa Astron. Publ.*, **20**, 160.  
 Oknyanskij et al.: 2012, *Odessa Astron. Publ.*, **25**, 179.  
 Oknyanskij et al.: 2013, *Odessa Astron. Publ.*, **26**, 212.  
 Oknyansky et al.: 2014, *Astron. Lett.*, **40**, 527.  
 Pacholczyk A.G.: 1971, *ApJ*, **163**, 149.  
 Pacholczyk A.G. et al.: 1983. *Ap. Let.*, **23**, 225.  
 Roberts D.H., Lehar J., Dreher J.W.: 1987, *AJ*, **93**, 968.  
 Roberts C.A., Rumstay K.R.: 2012, *JSARA*, **6**, 47.  
 Schnülle K. et al.: 2015, *A&A*, **578**, 57.  
 Sandage A.: 1967, *ApJ*, **150**, L177.  
 Wishnievski W.Z., Kleinmann D.E.: 1968, *ApJ*, **73**, 866.

DOI: <http://dx.doi.org/10.18524/1810-4215.2016.29.85060>

# PHOTOMETRIC OBSERVATIONS OF A NEW ECLIPSING BINARY NSVS 8213217

S.N. Udovichenko

Astronomical Observatory, Odessa National University  
Shevchenko Park, Odessa 65014, Ukraine, [udovich222@ukr.net](mailto:udovich222@ukr.net)

**ABSTRACT.** The photometric CCD observations for new suspected eclipsing binary NSVS 8213217 in Astronomical stations near Odessa (Ukraine) have been carried out. The light curves in V system were obtained and new adjusting period and light element was received. This star is identified as Algol-type eclipsing binary EA.

**Key words:** Stars: eclipsing binary variables: Algol-type - stars: individual: NSVS 8213217.

## 1. Introduction

NSVS 8213217 (UCAC4-574-077687, GSC 2126-2113), ( $\alpha_{J2000.0} = 19^h04^m43^s$ ;  $\delta_{J2000.0} = 24^\circ43'01''$ ) was suspected as possible eclipsing binary systems by Hoffman, Harrison, McNamara (2009) using automated variable star classification of Northern Sky Variability Survey. They determined the primary period as  $P=3^d.26268$ .

## 2. Observations

The photometric CCD observations in Astronomical stations near Odessa for this star were carried out together with others variable stars in Vulpecula constellation (in the field of Y Vul) during observational seasons 2011, 2012 and 2016 years. The 48 cm reflector AZT-3 with the f/4.5 Newtonian focus (F=2024 mm) equipped with CCD photometer UAI CCD (Sony ICX429ALL, 600x800 pixels) with V filter and Peltier cooler were used (Udovichenko, 2012). The exposure time for variable and comparison stars for the most part were chosen to except a saturation of frame and consist 90-120 sec. Two stars were chosen as comparison and check stars (comp=UCAC4-574-074580,  $m_V=12.93$ ; check=UCAC4-574-074571,  $m_V=14.15$ ). More then 2800 CCD frames with this star and comparison/check stars were gathered during 28 nights of observations. The reductions of the CCD frames were carried out using the CMUNIPACK (Motl) software. The standard procedure for the aperture photometry are composed of the dark-level and flat-field corrections

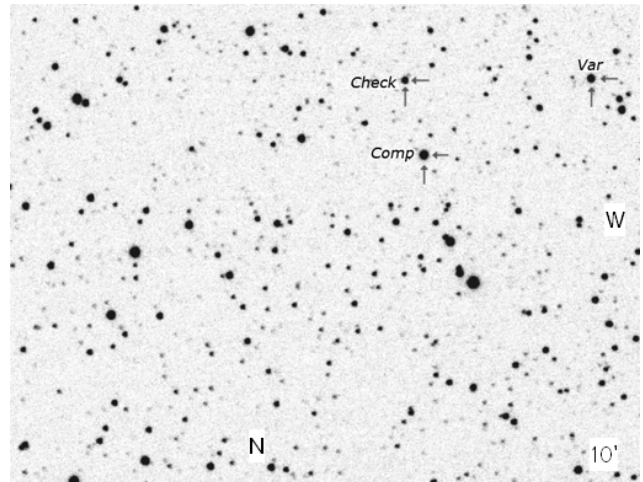


Figure 1: The finding chart NSVS 8213217 with the comparison and check stars marked.

and determination of the instrumental magnitude and precision. The all set of observations are shown in Table 1. The errors on individual data points vary between 0.005 mag to 0.015 mag.

At attempt to construct a phase curve it was found out, that the period  $P=3^d.26268$  offered by authors (Hoffman et al., 2009) is not absolutely exact. It was required to pick up new value of the period  $P=3^d.262215$  that individual light curves of primary eclipse, received throughout 6 years have coincided (Vstar software, Benn). The summary phase light curve NSVS 8213217 with new adjusted period are shown on Figure 2.

This curve was computed from elements:

$$\text{Min HJD} = 2455700.196 + 3.262215 \times E$$

and belonged to eclipsing binary variable EA. The initial epoch was measured from individual and summary curves of minima. The primary minimum is deep (about 0.7 mag), the secondary is not deep (about 0.1 mag) in V filter. There are 165 observations of NSVS 8213217 in Northern Sky Variability Survey (Woz-

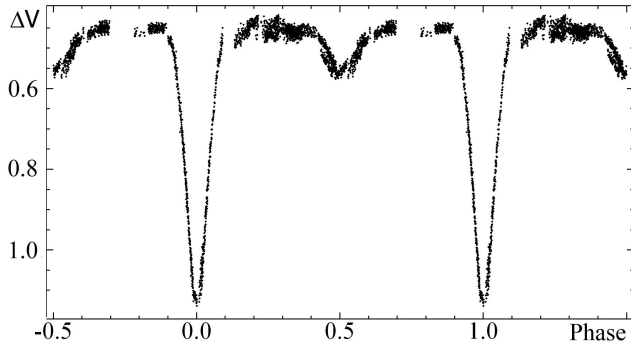


Figure 2: The phase light curve of NSVS 8213217.

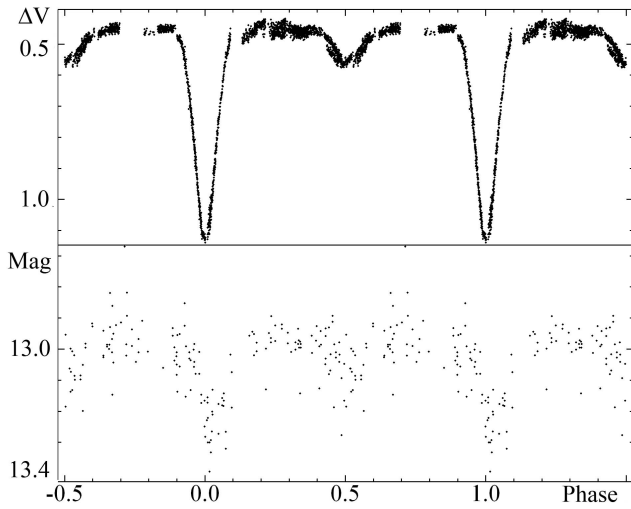


Figure 3: The phase light curve of NSVS 8213217 from this papers (top) and from NSVS data (bottom).

niak, 2004). The joint phase variation light curves from NSVS data of 1999-2000 years and our 2011-16 years, plotted with the same adjusted light elements are shown on Figure 3. This period has appeared available for all observations.

### 3. Conclusions

From photometric CCD observations it is found out:

1. The new suspected variable star NSVS 8213217 is Algol-type eclipsing binary EA.
2. New adjusting period and light element was received.
3. The period of light variation is stable during last 16 years.

Table 1: The times of observations NSVS 8213217

Time HJD	Number of frames
2455733.328 - 2455733.423	66
2455735.374 - 2455735.483	26
2455792.312 - 2455792.475	129
2455793.316 - 2455793.514	137
2455802.361 - 2455802.417	86
2455821.331 - 2455821.387	88
2455822.316 - 2456822.448	85
2455824.214 - 2455824.456	176
2455825.224 - 2455825.377	115
2456156.358 - 2456156.561	140
2456158.289 - 2456158.493	151
2456180.316 - 2456180.477	95
2456181.232 - 2456181.458	163
2457547.396 - 2457547.532	85
2457548.334 - 2457548.530	119
2457592.319 - 2457592.355	23
2457593.297 - 2457593.465	105
2457594.302 - 2457594.533	138
2457595.376 - 2457595.502	79
2457596.294 - 2457596.544	135
2457606.341 - 2457606.521	112
2457608.341 - 2457608.546	144
2457655.244 - 2457655.359	70
2457657.198 - 2457657.409	99
2457658.199 - 2457658.227	14
2457665.188 - 2457665.413	133
2457666.193 - 2457666.319	69
2457667.192 - 2457667.370	97

### References

Benn D.: [http://www.aavso.org/vstar/AAVSO\\_files](http://www.aavso.org/vstar/AAVSO_files).  
 Hoffman D.I., Harrison T.E., McNamara B.J.: 2009, *Astron. J.*, **138**, p.466-477.  
 Motl D.: <http://sourceforge.net/projects/c-munipack/files>  
 Udovichenko S.N.: 2012, *Odessa Astron. Publ.*, **25**, 32.  
 Wozniak P.R., Vestrand W.T., Akerlof C.W. et al.: 2004, *Astron. J.*, **127**, 2436.

DOI: <http://dx.doi.org/10.18524/1810-4215.2016.29.85061>

# EFFECTIVE TEMPERATURE AND RADIAL VELOCITY OF THE SMALL-AMPLITUDE CEPHEID POLARIS ( $\alpha$ UMi) IN 2015

I. A. Usenko<sup>1,2</sup>, V. V. Kovtyukh<sup>1</sup>, A. S. Miroschnichenko<sup>3</sup>, S. Danford<sup>3</sup>

<sup>1</sup> Astronomical Observatory, Odessa National University, Shevchenko Park, Odessa 65014, Ukraine, [igus99@ukr.net](mailto:igus99@ukr.net)

<sup>2</sup> Mykolaiv Astronomical Observatory, Mykolaiv 54030, Ukraine

<sup>3</sup> Dept. of Physics and Astronomy, University of North Carolina at Greensboro, Greensboro, NC, USA

**ABSTRACT.** We present the results of an analysis of 21 spectra of  $\alpha$  UMi (Polaris) obtained in September – December 2015. Frequency analysis shows an increase of the pulsation period up to 8.6 min in comparison to the 2007 observational set. The radial velocity amplitude comes to  $4.16 \text{ km s}^{-1}$ , and it approximately twice the one found in 2007. The average  $T_{\text{eff}} = 6017 \text{ K}$ , and it is close to the value determined for the 2001–2004 set. Therefore Polaris moves to the red edge of the Cepheid instability strip (CIS).

**Key words:** Stars: radial velocities; Cepheids: overtone pulsations; Cepheids: companions; Cepheids:  $\alpha$  UMi

## 1. Introduction

Polaris is the nearest Cepheid to us in the Galaxy. Being a small-amplitude pulsator (DCEPS) it has some specific features which testify about its peculiar character:

1. An abrupt decrease of the pulsation amplitude during forty years ( $5\text{--}6 \text{ km s}^{-1}$  before 1950 (Roemer, 1965) to  $0.05 \text{ km s}^{-1}$  in the 1980's (Ferne, Kamper & Seager, 1993)) and the beginning of its increase during the next 20 years (Dinshaw et al. 1987; Hatzes & Cochran 2000; Kamper 1996; Bruntt et al. 2008; Lee et al. 2008), – from  $1.5 \text{ km s}^{-1}$  in 1987 to  $2.4 \text{ km s}^{-1}$  in 2007.
2. According to Turner et al. (2005), both photometry and radial velocity data taken in 1896–2004 suggest an increase of the pulsation period by  $4.45 \pm 0.03 \text{ yr}^{-1}$  (from 3.966942 to 3.970691 days), except for a short-term slowdown of  $4.28 \pm 0.73 \text{ yr}^{-1}$  in 1963–1966. The period increase is an evidence of Polaris' redward crossing

of the Cepheid instability strip (hereafter CIS). According to Lee et al. (2008), the pulsation period increased up to 86 seconds in 2005–2007 (from 3.973000 to 3.97394 days), while the pulsation amplitude increased to  $2.2 \text{ km s}^{-1}$ .

3. Previous frequency analyses of the radial velocity data sets of 1987/88 (Dinshaw et al., 1989), 1992/93 (Hatzes & Cochran, 2000), Kamper (1996), Lee et al. (2008) revealed the presence of additional periods of 45.3, 40.2, 34, and 119 days, respectively, in addition to the main pulsation period of 3.97 days. These additional periods have been explained by the rotation of Polaris, existence of cool or macroturbulent velocity spots, or non-radial pulsations.

## 2. Observations and frequency analysis

Twenty one spectrum were taken in September–December 2015 with the 0.81 m telescope of the Three College Observatory (TCO), located in central North Carolina, USA. They were obtained with an échelle spectrograph manufactured by Shelyak Instruments<sup>1</sup> in a spectral range from 4250 to 7800 Å with a spectral resolving power of  $R \sim 10000$ . There are no gaps between the spectral orders. The data were reduced using the *échelle* package in IRAF.

The DECH30 package (Galazutdinov 2007) allows to measure the line depths and radial velocities using spectra in FITS format. Lines depths were used to determine the effective temperature (a method based on the spectroscopic criteria, Kovtyukh 2007). Derived values of the  $T_{\text{eff}}$  and radial velocity for each spectrum are given in Table 1.

In the next step we used the PERIOD04 program (Lenz & Breger, 2005) to calculate a Fourier power

<sup>1</sup><http://www.shelyak.com>

Table 1: Observational data of  $\alpha$  UMi

HJD 2450000+	$T_{\text{eff}}$ K	Phase	Metals	$RV$ ( $\text{km s}^{-1}$ )			
				NL	$H_{\alpha}$	$H_{\beta}$	$H_{\gamma}$
7283.656	6083±15	0.854	-17.57±1.48	149	-19.27	-17.18	-17.20
7284.715	6059±23	0.120	-19.10±1.63	139	-20.12	-17.79	-17.73
7311.627	6048±20	0.890	-11.93±1.38	104	-11.27	-10.04	-10.93
7312.630	6064±20	0.142	-18.73±1.71	114	-19.50	-17.67	-16.97
7313.632	6007±15	0.394	-15.00±1.59	129	-16.72	-15.51	-15.20
7314.583	5997±16	0.633	-15.83±1.19	119	-16.43	-14.96	-15.93
7316.650	6070±17	0.153	-18.19±1.72	121	-19.31	-17.13	-17.44
7317.625	5967±16	0.398	-15.52±1.56	91	-16.44	-14.48	-14.81
7318.599	6001±18	0.643	-14.93±1.29	118	-15.57	-14.18	-15.27
7319.535	6077±16	0.879	-17.36±1.36	118	-18.90	-16.85	-17.11
7337.676	5962±17	0.442	-16.08±1.08	132	-17.69	-15.21	-16.11
7338.548	6006±19	0.661	-15.35±1.67	125	-16.09	-14.61	-14.35
7339.657	6025±20	0.940	-18.54±1.45	141	-20.36	-17.74	-17.90
7340.667	6037±15	0.194	-17.65±1.35	134	-19.13	-16.87	-17.36
7343.559	6058±18	0.922	-18.55±3.36	139	-20.42	-18.33	-17.77
7349.546	5990±14	0.428	-15.15±1.37	138	-16.73	-14.34	-15.01
7350.581	6034±16	0.688	-14.43±1.62	123	-15.59	-15.06	-14.38
7365.541	6025±17	0.451	-15.14±1.47	147	-15.71	-14.34	-14.72
7366.563	5973±19	0.708	-15.20±1.52	121	-15.94	-14.26	-14.42
7372.638	5975±15	0.236	-17.76±1.48	154	-19.27	-17.18	-17.20
7376.586	6022±14	0.229	-16.60±1.34	161	-18.27	-15.92	-12.20

Phase is calculated using the ephemeris (1)

NL represents the number of metal lines whose radial velocities were measured

spectrum. It uses the Fourier and Fast Fourier Transform analysis with minimization of residuals of sinusoidal fits to the data.

The power spectrum was calculated over the frequency range  $0-1 \text{ d}^{-1}$  with a resolution of  $0.00002 \text{ d}^{-1}$ . The highest amplitude of  $1.70$  corresponds to a frequency of  $0.25126439 \text{ d}^{-1}$ , or  $3.97987156$  days, respectively. This period exceeds by  $8.5$  minutes the period of  $3.97394$  days determined from the 2007 observational set. The systemic velocity ( $\gamma$  - velocity) is equal to  $-16.70 \text{ km s}^{-1}$ .

The following ephemeris has been computed based on the radial velocity values:

$$RV_{\text{min}} = HJD\ 2457284.237 + 3.97987156 \times E \quad (1)$$

The radial velocity data for each spectrum folded with this period are given in Table 1.

The radial velocity and effective temperature of Polaris are shown in Figures 1 and 2 (data from the last three months of 2015).

The data were fitted with the sinusoidal curves. However, one value of  $-11.93 \pm 1.3 \text{ km s}^{-1}$  obtained on HJD 2457311.627 was excluded from the analysis. According to this approximation, the mean amplitude of the radial velocity curve is  $4.16 \text{ km s}^{-1}$ .

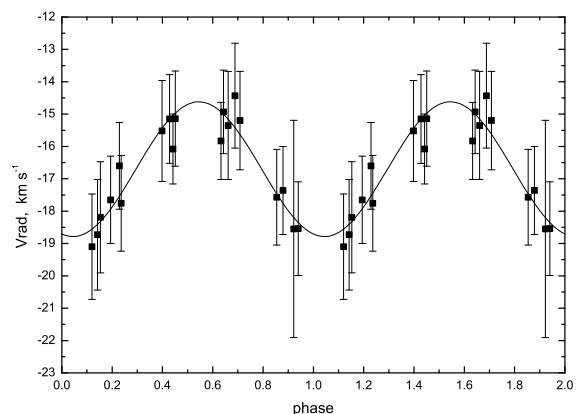


Figure 1: The radial velocity variations of Polaris during its pulsation period.

### 3. Summary

1. As seen from the results of our observations, the pulsation period of Polaris shows a considerable increase in comparison with estimates obtained in 2007 (Lee et al., 2008). This fact confirms the assumption that Polaris is moving to the red edge of the CIS;
2. The mean amplitude of the radial velocity nearly

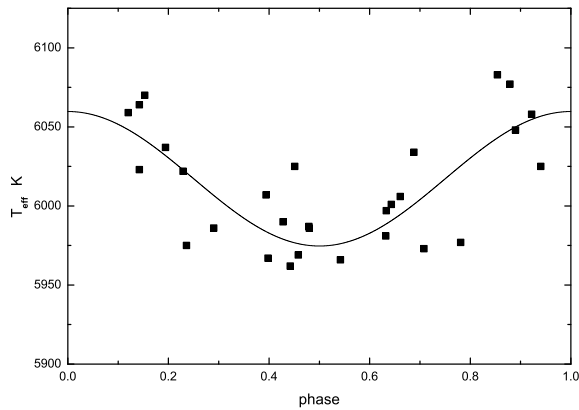


Figure 2:  $T_{\text{eff}}$  of Polaris during its pulsation period.

doubled during the last eight years in comparison to the 2007 observations by Lee et al. (2008).

3. The effective temperature of Polaris for this data set averages 6017 K. This value is close to 6015 K determined for the set of 2001–2004 data (Usenko et al., 2005).

## References

Bruntt H., Evans N.R., Stello D., Penny A.J., Eaton J.A., Buzasi D.L., Sasselov D.D., Preston H.L. & Miller-Ricci E.: 2008, *ApJ*, **683**, 433.

- Dinshaw N., Matthews J.M., Walker G.A.J., Hill G.M.: 1989, *AJ*, **98**, 2249.
- Evans N.R., Sasselov D.D. & Short C.I.: 2002, *ApJ*, **567**, 1121.
- Fernie J.D.: 1966, *AJ*, **71**, 731
- Fernie J.D., Kamper, K.W., & Seager, S.: 1993, *ApJ*, **416**, 820.
- Galazutdinov G.A.: 2007, <http://gazinur.com/DECH-software.html>
- Hatzes A.P., Cochrane W.D.: 2000, *AJ*, **120**, 979.
- Kamper K.W., Evans N.R. & Lyons R.W.: 1984, *JRASC*, **78**, 173.
- Kamper K.W.: 1996, *JRASC*, **90**, 140.
- Kamper K.W., Fernie J.D.: 1998, *AJ*, **116**, 936.
- Kovtuykh V.V.: 2007, *MNRAS*, **378**, 617.
- Lee B.-C., Mkrtichian D.E., Han I., Park M.-G. & Kim K.-M.: 2008, *AJ*, **135**, 2240.
- Lenz P., Breger M.: 2005, *Commun. Astroseismology*, **146**, 53.
- Roemer E.: 1965, *ApJ*, **141**, 1415.
- Turner D.G., Savoy J., Derrah J., Sabour M.A. & Berdnikov L.N.: 2005, *AJ*, **117**, 207.
- Usenko I.A., Miroshnichenko A.S., Klochkova V.G. & Yushkin M.V.: 2005, *MNRAS*, **362**, 1219.

DOI: <http://dx.doi.org/10.18524/1810-4215.2016.29.85064>

# CHROMOSPHERIC ACTIVITY OF THE FLARE STAR YZ CMi IN QUIESCENCE ACCORDING TO THE FAST SPECTRAL MONITORING DATA

Verlyuk I.A.

Main Astronomical Observatory of National Academy of Sciences of Ukraine,  
03680, Kiev, 27 Zabolotnoho St, Ukraine, [irina.verlyuk@gmail.com](mailto:irina.verlyuk@gmail.com)

**ABSTRACT.** Spectral monitoring of the flare star YZ CMi ( $U = 12.9$ ,  $B = 12.7$ ,  $V = 11.1$ ) was carried out on the Zeiss-600 telescope at the Peak Terskol Observatory. We used a low resolution grating spectrograph with spectral resolution of  $\sim 100 \text{ \AA}$  and time resolution from 2 to 30 s. The spectra of the star in the quiescent state show variability in the lines  $H_\beta$ ,  $H_\gamma$ , Mg b, possibly in  $\text{Ca II K} + H_\epsilon$ . Variations of the equivalent widths of the order of several percents were detected. The characteristic time of variations is about of a few minutes. The observed variations indicate the non-stationary activity of the flare star YZ CMi chromosphere in the quiescent state.

**Keywords:** Stars: variability – methods: statistical – stars: late-type

## 1. Introduction

Red dwarf star YZ CMi ( $dM 4.5e$ ,  $R = 0.36 R_{\text{sun}}$ ,  $M = 0.34 M_{\text{sun}}$ ,  $T = 2900 \text{ K}$ ) is one of the most bright and active flare star. According to the Crimean catalog of flare stars (Gershberg et al., 1999) optical photometry of flares contained in 164 articles, optical spectra of flares described in 55 papers. Studies of the star at quiescence state are practically absent.

In this paper, we show that the star YZ CMi demonstrates activity in the quiescent state. Activity appears in variations of chromospheric lines, in particular in lines of the triplet of magnesium Mg b ( $\lambda 5167$ ,  $\lambda 5173$ ,  $\lambda 5184 \text{ \AA}$ ) with amplitude of oscillation of about 2%. Fluctuations are quasi-periodic in character, in the period range from 40 to 70 seconds during the observation time of about 15 minutes.

## 2. Observations

An array of 500 spectra of YZ CMi and two comparison stars has been obtained with a low resolution grism spectrograph (Zhilyaev et al. 2012) mounted on the Zeiss 600 telescope, at the Peak Terskol Observatory, on November 6, 2009. A spectral resolution was about of 100 Angstroms and a time resolution of 2.78 seconds. Averaged spectra of YZ CMi at quiescence and two comparison stars are shown in Fig. 1.

## 3. Results

The Allan power spectra for YZ CMi (Fig. 2) demonstrates high-frequency activity in the lines of chromospheric hydrogen  $H_\beta$ ,  $H_\gamma$  and perhaps in  $H_\epsilon$  and  $\text{Ca II K}$  ( $3968 \text{ \AA}$ ), and in the triplet of magnesium Mg b ( $5168$ ,  $5173$ ,  $5184 \text{ \AA}$ ). The amplitude of the variations in the lines of Mg b, determined by Fourier power spectrum is about 2.2% (0.02 magnitudes).

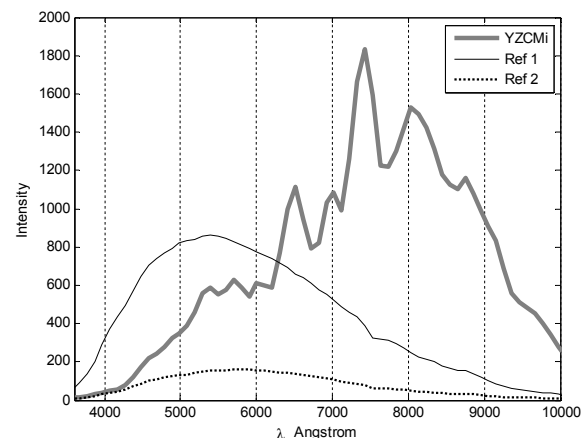


Figure 1: Averaged spectra of YZ CMi and two comparison stars.

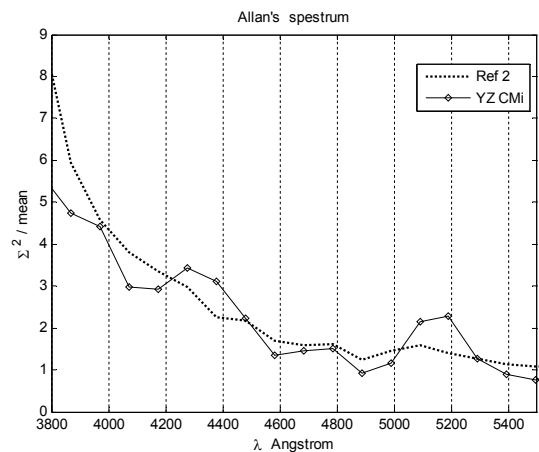


Figure 2: The Allan power spectra of YZ CMi and a reference star.

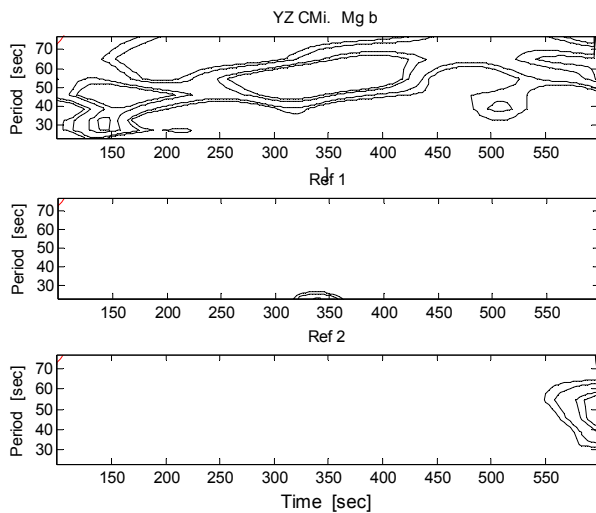


Figure 3: The wavelet power spectra of YZ CMi and comparison stars.

The Allan power spectrum is equal to power spectrum of variation (dispersion  $\Sigma^2$ ) relative to an average value of intensity. To calculate the spectrum the first differences of intensities in the spectra array are used (Zhang X. et al., 2008). For a Poisson random process, this ratio is equal to one. In the magnesium lines it is twice as large as can be seen in Fig. 2. The comparison star shows no variations in the power spectrum.

The wavelet power spectra of YZ CMi (Torrence et al., 1998, Fig. 3, top panel) and the comparison stars (middle and bottom panels) shows line intensity oscillations in chromospheric lines of triplet magnesium 5158Mg b (5168 - 5184 Å). YZ CMi for 15 minutes shows intensity oscillations with a period on average of about 50 seconds. Contours in the spectra correspond to significance levels of 90, 95, 99 % and more. The mentioned harmonic in the spectra of comparison stars are absent.

The time resolution in the wavelet power spectra is about of 100 seconds. Zug of oscillations of YZ CMi shows variations of oscillation period from 30 to 70 seconds. Thus, it is possible to estimate the average oscillation period of about 50 seconds. The relative amplitude of the oscillations is  $\Delta I / I = 2.2\%$ .

Fig. 4 demonstrates the global wavelet power spectrum of YZ CMi (Torrence et al., 1998), the Fourier power spectrum and the global wavelet power spectra of comparison stars. The power spectra of the comparison stars show the spectrum of the normal white noise, which has a chi-square distribution with two degree of freedom. The average value of the noise spectrum equals two. The value of the global wavelet power spectrum of YZ CMi at the maximum is equal to 5.65 and corresponds to the confidence level of 94%.

Thus, using the wavelet analysis we detected quasiperiodic pulsations of the chromospheric magnesium triplet lines with period of about 50 sec for a time of observation of 900 sec.

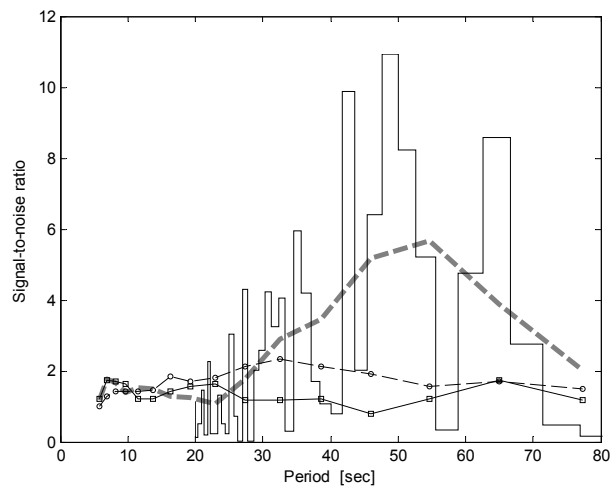


Figure 4: The global wavelet power spectrum of YZ CMi (thick line), the Fourier power spectrum (thin line) and the global wavelet power spectra of comparison stars (circles and squares).

#### 4. Diagnosis of oscillations

As part of the solar-stellar analogy, we can assume that the oscillations could be caused by the excitation of magnetohydrodynamic (MHD) oscillation of the flare loop (Stepanov et al., 2005). Plasma heating by MHD oscillations at the footing of the flare loop leads to the observed pulsations of YZ CMi in the optical range.

The diagnostic method of Stepanov et al. (2005) allows estimating the temperature, concentration of plasma and the intensity of the magnetic field of coronal loops from the observed characteristics of the light oscillations: the period, the modulation depth and decay time.

Clearly, there may be several coronal loops with different characteristics, which give rise to variations of the chromospheric lines of YZ CMi with different frequencies and decay time.

*Acknowledgements.* The author is thankful to M. Andreev for observations, to B. Zhilyaev for help with the calculations.

#### References

- Gershberg R.E. et al.: 1999, *A&ASS*, **139**, 555.  
 Zhilyaev B.E. et al.: 2012, in *Proc. of SPIE*, **8446**, 844681-1-10.  
 Zhang X. et al.: 2008, in *Proc. International Symposium on GPS/GNSS, Tokyo, Japan, 11-14 November 2008*, 127.  
 Torrence et al.: 1998, *Bull. Amer. Meteor. Soc.*, **79**, 61.  
 Stepanov A.V. et al.: 2005, *Astron. Letters*, **31**, 684.

DOI: <http://dx.doi.org/10.18524/1810-4215.2016.29.85068>

## TWO-MATRIX PHOTOMETER CONTROL SYSTEM

Zh.Sh. Zhantayev<sup>1</sup>, K.S. Kuratov<sup>1,2,3</sup>, A.M. Seytimbetov<sup>2</sup>, A.T. Mailybayev<sup>1,2</sup>,  
N.Sh. Alimgazina<sup>1,2</sup>, A.B. Manapbayeva<sup>2</sup>, A.K. Kuratova<sup>1,2</sup>, N.T. Iztleuov<sup>2</sup>

<sup>1</sup>National center of space researches and technologies, Almaty, Kazakhstan

<sup>2</sup>Al-Farabi Kazakh National University, Almaty, Kazakhstan

<sup>3</sup>Astrophysical institute named after V.G. Fesenkov, Almaty, Kazakhstan

*kenes\_kuratov@mail.ru, Nazgul.Alimgazina@kaznu.kz*

**ABSTRACT.** In this paper astronomical two-matrix photometer is described. It differs from common one CCD camera photometers by using the second CCD camera. It enables simultaneously to carry out the studied star and standard star light inputs measurements. The second camera application enables significantly to increase measurements accuracy and at least twice time decrease of one star observation. The significant increase of measurements accuracy is reached by carrying out simultaneous observations, and errors caused by the Earth atmosphere fluctuation are the same as for studied star so for standard star. Time decrease is reached by carrying out both stars simultaneous observations.

In the paper photometer's optical mechanics scheme is given. The motion mechanism of receiving and recording block with micrometer screw rotated by stepping motor is described. It is demonstrated that exact coordinates of matrix position attached to clutch on micrometer screw are shoot by absolute magnetic encoder.

The applied two-matrix photometer control system electronic equipment is described. The photometer operation control algorithm installed on Tien-Shan astronomical observatory 1-meter telescope is presented.

**Key words:** star, telescope, photometer, CCD-matrix, optical mechanics scheme, control system.

### 1. Introduction

In conducting astrophotometrical observations it's important to carry out measurements of the studied star and standard star simultaneously. But practically standard star is always located in some distance from the studied star so even in using CCD camera with maximum sizes (50x50 mm), it doesn't arrive at the emission receiver (matrix). All known photometers (for example, Liutyi et al. 2009) apply one matrix. Therefore observations are carried out separately (in order). Firstly, separate measurement worsens measurements accuracy due to different fluctuations over time in the Earth atmosphere, secondly, increases observational time on photometry of each studied object separately. This disadvantage can be eliminated only in simultaneous measurement of the studied star and standard star then atmosphere fluctuations effect will be the same on two stars.

Apart from in astrophysics there is a number of important tasks which can't be solved or difficult to solve

with existing photometers. For example, in astroseismic observations of faint objects, searching exoplanets and a number of other tasks where the studied star variations in brightness are small and fluctuations in the Earth atmosphere don't enable to conduct measurements or strongly distort them. In order to reveal such variations in light long-term observations applying complex mathematical analysis (e.g. Fourier analysis) are carried out. However, many such kind of tasks can't be solved by using one-matrix photometers and they aren't simply solved. In one-matrix photometers these variations in brightness "sink" in atmospheric fluctuations noises.

Thus, development of two-matrix photometer and putting it into the process of astronomical observations enable:

1. significantly to increase photometrical measurements accuracy due to conducting the studied star and standard star simultaneous observations;

2. to decrease twice the time of observations and, hence, more than twice improve observational time effectiveness on telescope;

3. to solve a number of tasks which are impossible to do with one-matrix photometer and extend the range of studied objects.

### 2. Equipment structure and algorithm of control

Development, manufacturing and adjustment of photometer optical-mechanical connection joint, electronic control schemes and software were required for creating astronomical two-matrix photometer.

Two one-meter telescopes of Tien-Shan astronomical observatories (TSAO) have Ritchey-Chrétien system which enables to create a big undistorted field in the telescope focus that gives additional advantages for two-matrix photometer operation.

One of CCD-matrix (main) is installed on telescope main optical axis from which the studied star measurements are carried out. The light flow from standard star with the help of diagonal mirror "placed out" onto photometer side surface with turn at 90° (degrees). Connection joint consisting of diagonal mirror, filters and CCD-matrixes is gathered into one optical block and has the possibility to move telescope focal plane on one of coordinates. Moving on the second coordinate is provided by photometer turn on telescope turning circle. This

responds to that standard stars can locate towards the studied star at different distances and in various positioned angles. Moving the second CCD-matrix in two directions, it's practically always possible to direct with coordinates onto standard star.

Optical scheme of photometer main channel (for the studied star observations) with Apogee U10 CCD-camera is presented in Fig. 1.

In the second channel simple matrix without cooling can be used. As standard star brightness is always higher so less sensitive CCD-receivers can be applied which have small sizes and weight. Small sizes and weight are essential, as optical block with matrix must move inside (relatively) photometer. The second channel mechanism of matrix moving operation principle is the following: with micro screw which has worm gear and is rotated with (SE) moves optical block with diagonal mirror, filters and CCD-matrix in one direction up to 14 cm with the possibility of crossing telescope main optical axis (MOA). In crossing telescope MOA there is appeared the possibility of both matrix testing and to determine instrumental recovery. Accurate coordinates of optical corrections block position is determined with absolute magnetic encoder which is hardly connected with micro screw (connected with micro screw from opposite side of SM).

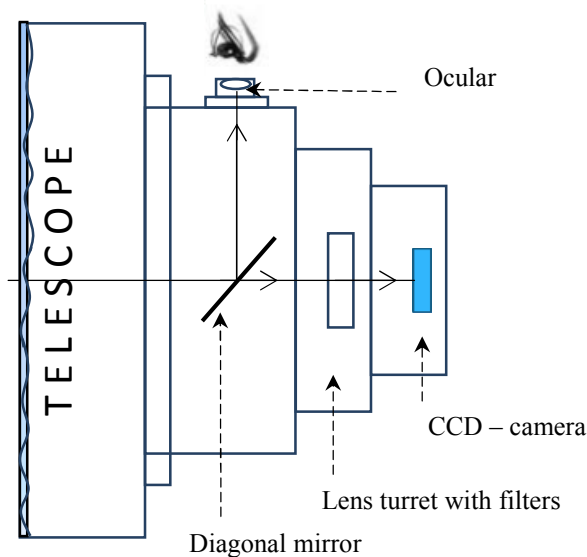


Figure 1: Optical scheme of photometer main channel

### 3. Electronic apparatus of two-matrix photometer control system (TMPCS)

In Fig. 3 TMPCS structural scheme is given.

Two-matrix photometer hardware structure includes the following components:

1. Micro controller platform of ARDUINO UNO (Petin 2015) type which is simply called microcontroller (MC) serves as the central control link. In fact, Arduino Uno model is the device on the basis of ATmega328 microcontroller. ATmega16U2 microcontroller provides the connection of receiver-transmitter with computer USB-port and in switching on to PC it enables Arduino to

be defined as virtual COM-port. 16U2 micro scheme weaving uses standard USB-COM driver therefore external drivers installation isn't required. At Windows platform only appropriate .inf-file is needed.

2. Electromechanical node (EMN) consists of 25 cm long micro screw which moves optical block consisting of diagonal mirror, turrets with filters and CCD-2 matrix. Moving is carried out with step engine (SE) which rotating micro screw moves optical block from the second matrix with installation accuracy up to 0.05  $\mu\text{m}$ . SE control (Kenio 1987) is carried out with A3967 EasyDriver V4.4. Driver control is carried out from Arduino controller with special programs.

3. As all telescope electronic nodes are connected with distributed net and are in significant distance then all nodes are connected with RS-485 [[www.radiomedtech.ucoz.ru//RS-485.pdf](http://www.radiomedtech.ucoz.ru//RS-485.pdf)] converters. RS-485 is chosen by us as it can lead up to 32 receivers with communication speed by specification up to 10 Mbd/sec at distance up to 1200 m.

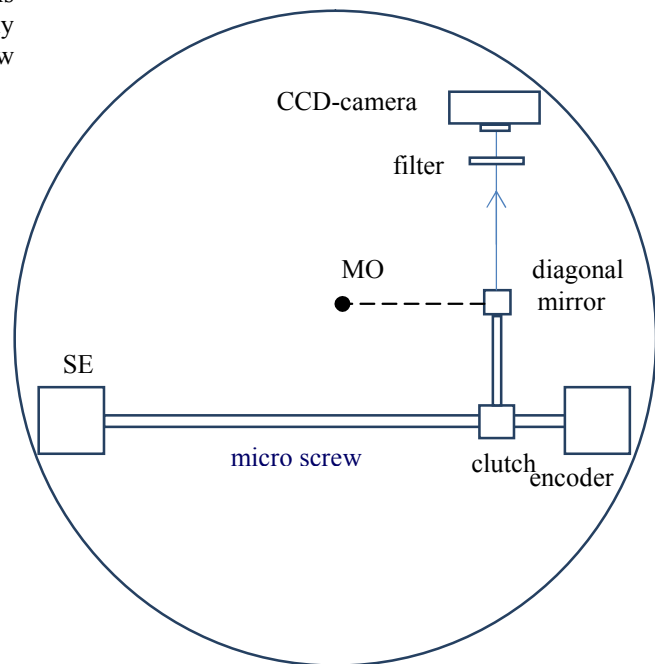


Figure 2: Optical-mechanical scheme of photometer second channel

4. Micro screw angle turn sensor (encoder) is used for carrying out the right system positioning and conducting the control at optical block moving from the second matrix in TMPCS. Baumer Electric CH-8501 absolute magnetic encoder which peculiarity is in saving angle turn data in voltage falling or disappearing, or in computer reboot is used as angle turn sensor. If in de-energized state the encoder shaft was turned onto definite angle or some number of turns so in voltage appearing encoder immediately gives shaft new actual angle position and factual number of turn. Thanks to this it isn't required after every switching on the system to produce moving of machine mechanical parts onto start-up position that is absolute encoders inarguable advantage.

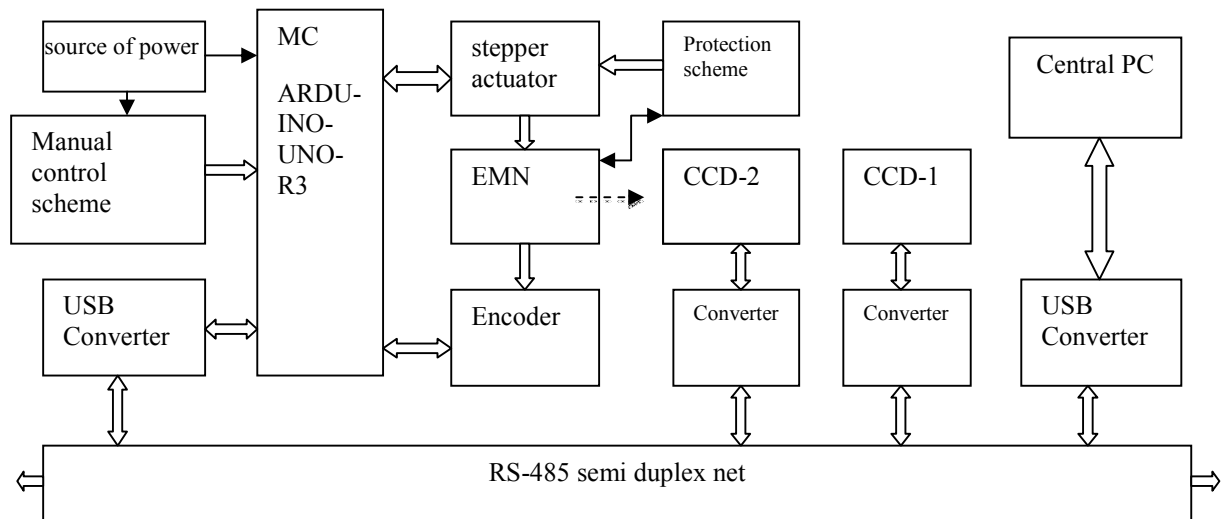


Figure 3: Structure of two-matrix photometer control system structure

5. Protection scheme includes mechanism of final switchers on both boundaries of optical block acceptable to move on micro screw which prevents mechanical breakdown and gives MC signal about reaching moving boundaries.

6. Manual control scheme enables to carry out button reset into initial position, gives commands on moving and movement direction option in testing mode.

#### 4. Algorithm of diagonal mirror moving control from MC

Software development is based on using Arduino (Sommer, 2015) development medium and contains the following main elements: text editor for writing a code, area for messages output, text console, toolbar with traditional buttons and main menu. This soft enables computer to interact with Arduino as for data transmission so for weaving the code into the controller.

In figure 4 algorithm flowchart of diagonal mirror moving control from MC is shown. In this algorithm of encoder code and final switcher values are used for reverse, the second matrix optical block moving is carried out with discrete steps which are alternated with periods of long home stations during which photometrical information about stellar objects picking up takes place. Movement control depends on triggers value “**Movement**” and “**Direction**” (moreover, MC definite output port bits are implied as these triggers), and discrete micro steps a number of which is given by programming subtracting counter and is defined by necessary moving accuracy.

#### 5. Conclusion

The developed two-matrix photometer is the astronomical measuring engine used in photometrical observations. Measuring engine distinctive feature lies in possibility to carry out simultaneous measurements of light flow from the studied star and standard star with increasing measurements accuracy and within less time.

Astronomy is the field of two-matrix photometer advantageous application: for researches of natural and artificial celestial objects.

#### References

- Liutyi V. M., Abdullaev B. I., Alekperov I. A., Giul'maliev N. I., Mikailov Kh. M., Rustamov B. N. : 2009, *Azerbaijani Astron. journal*, 2009. Vol. 3-4, p. 36 (in Russian).
- Petin V.A.: 2015 *Projects using Arduino controller*, S-Pb, BKhV-Peterburg, 464 pp. (in Russian).
- Kenio T. *Stepping motors and their microprocessor control systems*: 1987, Transl. English, M., Energoatomizdat, 200 pp. (in Russian).
- RS-485 interface: description, connection, [www.radiomedtech.ucoz.ru//RS-485.pdf](http://www.radiomedtech.ucoz.ru//RS-485.pdf) (in Russian)
- Sommer U. 2015: *Programming of Arduino/ Freeduino microcontroller boards*, S-Pb., BKhV-Peterburg, 256 pp. (in Russian).

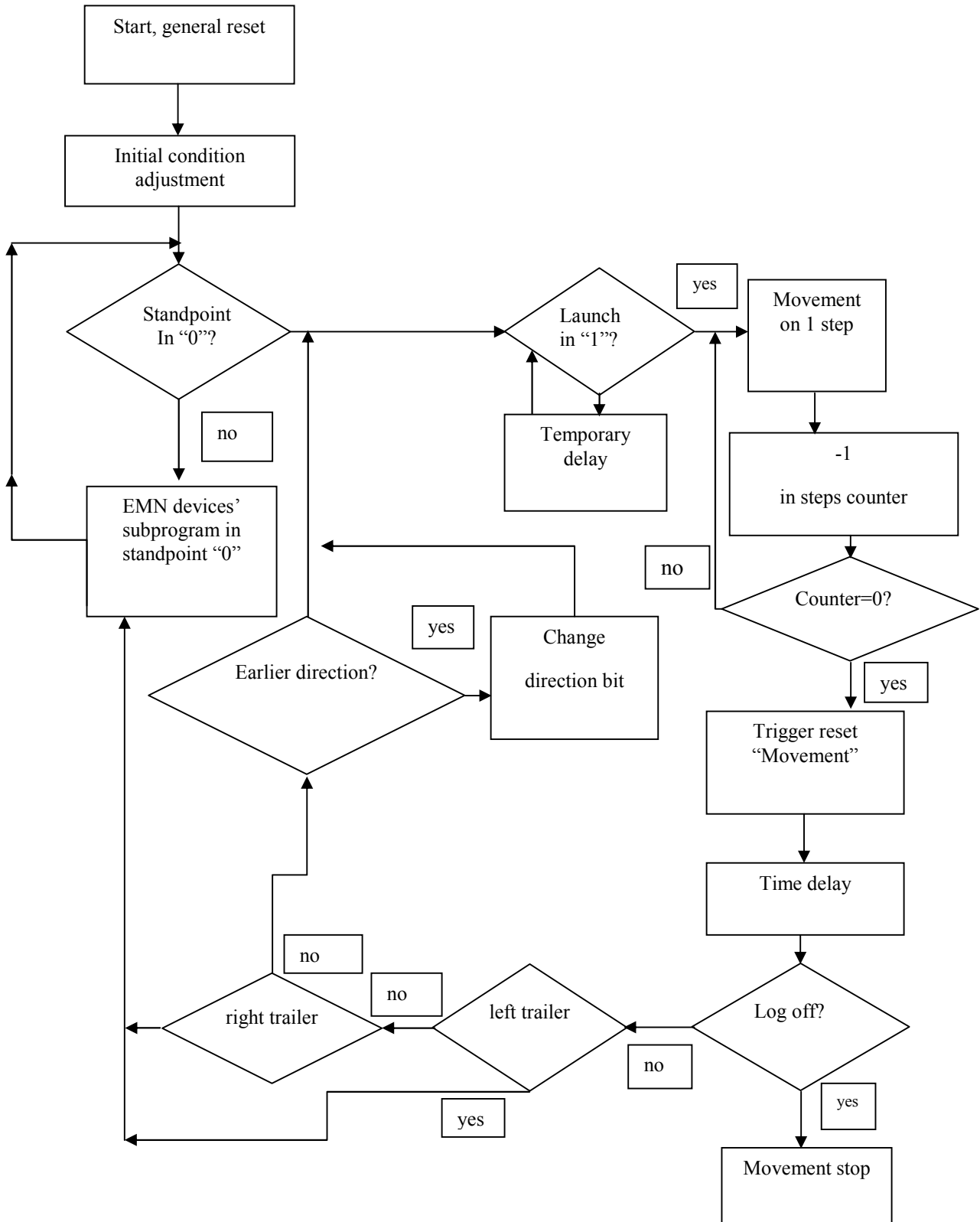


Figure 4: Algorithm of diagonal mirror moving control from MC

## ASTROINFORMATICS

DOI: <http://dx.doi.org/10.18524/1810-4215.2016.29.85269>ASTROINFORMATICS AS A NEW RESEARCH FIELD:  
UKRVO AND VIRGO RESOURCES

I.B. Vavilova

Main Astronomical Observatory, National Academy of Sciences of Ukraine,  
27 Akademika Zabolotnogo, Kyiv, 03143, Ukraine, [irivav@mao.kiev.ua](mailto:irivav@mao.kiev.ua)

**ABSTRACT.** The data-oriented astronomy has allowed classifying the *Astroinformatics* as a new academic research field, which covers various multi-disciplinary applications of the e-Astronomy. Among them are the data modeling, data mining, metadata standards development, data access, digital astronomical databases, image archives and visualization, machine learning, statistics and other computational methods and software for work with astronomical survey and catalogues with their tetra- to peta-scale astroinformation resource.

In this review we describe briefly the astroinformatics applications and software/services performed for different astronomical tasks in frame of the Virtual Roentgen and Gamma Observatory (VIRGO) and Ukrainian Virtual Observatory (UkrVO). Among them there are projects based on the archival space-born data of X-ray and gamma space observatories and on the Joint Digitized Archive (JDA) database of astroplate network collections. The UkrVO JDA DR1 deals with the star catalogues (FON, Polar zone, open clusters, GRB star fields) as well as the UkrVO JDA DR2 deals with the Solar System bodies (giant and small planets, satellites, astronomical heritage images).

**Keywords:** Astroinformatics: methods – Star catalogues – Galaxies – High-energy astrophysics

### 1. Introduction

Astroinformatics is introduced as the new data-oriented approach and advanced methodology for processing astronomical survey and catalogues with their tetra- to peta-scale astroinformation resource. Space observatories and ground-based telescopes provide a large volume of data over entire electromagnetic spectrum. Technical architecture (user layer, VO core layer, resource layer) for processing this resource was proposed by the IVOA Executive Committee. Such approach allows easy access to the metadata due to the interoperability between different astronomical archives and data centers.

“Many scientific disciplines are developing formal sub-disciplines that are information-rich and data-based, to such an extent that these are now stand-alone research and academic programs recognized on their own merits. In astronomy, peta-scale sky surveys will soon challenge our traditional research approaches and will radically transform how we train the next generation of astronomers, whose experiences with data are now increasingly more virtual (through

online databases) than physical (through trips to mountain-top observatories). We describe Astroinformatics as a rigorous approach to these challenges” (cited by “Astroinformatics: A 21st Century Approach to Astronomy”, Borne et al., 2009; see, also, Eastman et al., 2005; Gray et al., 2005; Butler, 2007; Cavuoti S., 2012; Vavilova et al., 2012a; Goodman et al., 2012; Borne, 2013; Brescia & Longo, 2013; Norris et al., 2013; Ruiz et al., 2014).

We note the WDC-Ukraine, which is a part of World Data Center System of the International Council of Science (ICSU). Among the basic tasks of WDC-Ukraine there is collection, handling and storage of science data and giving access to it for usage both in science research and study process. That include contemporary tutoring technologies and resources of e-libraries and archives; remote access to own information resources for the wide circle of scientists from the universities and science institutions of Ukraine. The resource of WDS-Ukraine is mainly used for geo-informatics, space weather, and astroinformatics projects.

The crucial role in promulgating new methods and services into the broader astronomy community belongs to the International Virtual Observatory Alliance (IVOA). At the beginning of the era of big data it initiated a creation of the national virtual observatories and development of the infrastructure of astronomical data center. Such centers give to users handy tools for data selection from large astronomical catalogues for a relatively small region of interest in the sky (see, for example, for GOODS: Giavalisco, 2004; for SDSS: D'Abrusco, 2007; “The National Virtual Observatory: Tools and Techniques for Astronomical Research, 2008), data standards and services for image processing (likely to Aladin) and manuals for processing the raw space-born data of various space missions (Chandra, XMM-Newton, Swift, NuStar, WISE, Kepler, GAIA, etc.). Besides the virtual observatories there are other sources for public outreach, for example, the well-known Astrostatistics and Astroinformatics Portal (ASAIP, <http://asaip.psu.edu>) (Feigelson, 2013; Feigelson, Hilbe (2014)); China Virtual Observatory Portal (Chen-zhou et al., 2012), Euro-VO (Buddelmeijer, 2013), Russia VO (Klipio et al., 2003); Data centers and systems as NED, HEASARC, SkyHound, NStED, SIMBAD, Planetary DS, and other (for a brief review on the multi-wave length surveys, see, Michaelian, 2016).

Ukraine Virtual Observatory (UkrVO) has been an IVOA member since 2011 (<http://ukr-vo.org/>). The cur-

rent UkrVO concept supports development of astro photo plate archives in the form of direct images of certain sky areas and celestial objects, as well as the spectra of celestial objects for multi-wave length studies of their properties (Vavilova et al., 2012b, 2014).

Virtual observatory VIRGO.UA for cosmology and high-energy astrophysics is a segment of VO “Infrastructure”, which deals with ensuring the provision of standards for Grid Services for virtual organizations (<http://virgoua.org/>).

In this review we describe briefly the astroinformatics applications and software/services performed for different astronomical tasks in frame of the Ukrainian virtual observatories – VIRGO and UkrVO.

## 2. Virtual Roentgen and Gamma Observatory (VIRGO) data center and services

Despite the overall success of the project VIRGO, number of Ukrainian astronomers who use the data of X-ray and gamma-ray observatories is still small. To overcome this problem, a web-based virtual observatory VIRGO (<http://skyview.virgoua.org>) as a “sky map” was developed (Figure 1). It allows visualizing the distribution parameter (intensity of signal, etc.) in space and the range energies setting by the user. From the analysis of such a large number of web interfaces it can be noted that the main progress in their development is associated with easier access to data and improve their visualization. Besides these two aspects, it was introduced a new approach to the quality of data provided by the user. In our opinion, one of the main reasons that an obstacle to the use of data in scientific studies, there is uncertainty value bias, which is usually not considered by the available standardized software. One of the examples of using these sky maps in 2–5 and 5–10 keV range with a public database of X-ray observations by XMM-Newton is a search of the dark matter decay line (Boyarsky et al., 2014; Savchenko, 2014; Yakubovsky et al., 2015).

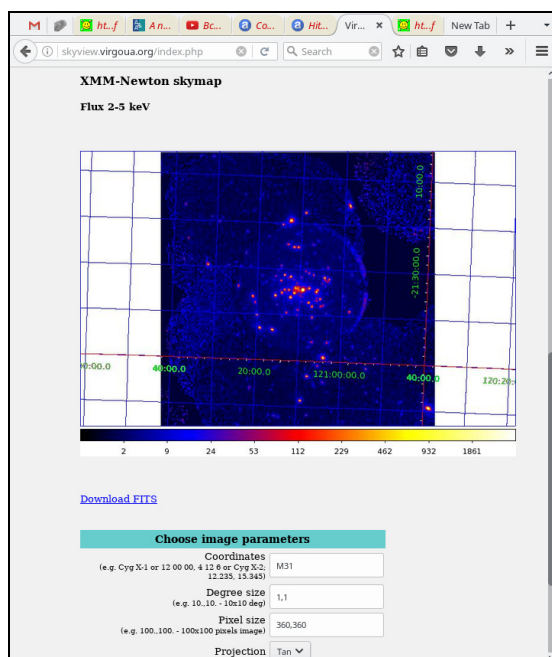


Figure 1: Screenshot of the interface “XMM-Newton sky map” (<http://skyview.virgoua.org>) from the VIRGO web-site.

The possibility of combining observational data obtained by ground-based telescopes and space observatories allows analyzing multi-wave physical properties of celestial bodies in more holistic measure. With this aim we prepared the new specially-oriented astro-space databases obtained with ground-based telescopes and space observatories. As a result, multi-wavelength spectral and physical properties of galaxies and galaxy clusters were analyzed in more details. These samples are as follows:

1) to study the spectral properties of quasars and the distribution of matter in intergalactic scales using Ly $\alpha$  forest (Ivashchenko et al., 2014; Torbaniuk O., :2015,:2016):

- sample of 3535 quasars from the SDSS DR7, redshift  $2.3 < z < 4.6$ ; spectrum of a good quality (high signal to noise ratio), available in the spectral view of the sky;
- sample of 33 quasars with  $z > 2$ , with high resolution spectra in publicly accessible ESO base;
- sample of 102643 quasars from the SDSS DR10 (including the sample “for composites” – 65976). Other objects: 11192 quasars with broad absorption lines (BAL); 6804 quasars with DLA- systems; 1248 quasars with absorption lines in Ly $\alpha$ ; 493 quasars in line with the absorption Ly $\beta$ ; 20 “normal” galaxies or galaxies with star-formation; 617 quasars with properly defined redshift; 1507 objects, whose spectra have low signal-to-noise (impossible to identification); 417 incomplete spectrum (for example, there is only part of the spectrum); 191 blazar’s candidate;

2) to study galaxies (including with active nuclei) in spite of their evolution and formation of large-scale structures in the Universe as well as the influence of the environment on the internal parameters of galaxies:

- sample of about 260,000 galaxies from SDSS DR9 up to  $z < 0.1$  to study their properties depending on environment, star-formation etc. (Dobrycheva, 2013; Dobrycheva et al., 2012, 2014, 2015);
- sample of 1429 active galactic nuclei (AGN) type I, 123 AGNs of type II, 10 BLRGs from SDSS DR7 with  $0.1 < z < 1.1$  in the field of view WiggleZ (Ivashchenko et al., 2015); and blazars (Vol’vach et al., 2011);
- sample of 95 AGNs selected from the 22-month Swift/BAT all-sky survey and spectra for these objects from XMM-Newton and INTEGRAL/IBIS in 0.5-250 keV (Vasylenko et al., 2015);
- sample of 62 2MIG isolated galaxies with active nuclei to  $z < 0.05$  (Chesnok et al., 2009; Chesnok, 2010; Pultova et al., 2015), which is considering as unique for recognizing their internal multiwavelength properties and physical parameters of accretion on the supermassive black holes outside of the environment.

3) to test cosmological parameters and the evolution of matter in a wide range of age of the Universe. The nature of dark components Universe – dark matter and dark energy – is one of the major challenges of modern cosmology. For this purpose, the key is the data on the CMB anisotropy obtained by WMAP and Planck, and data on the large-scale structure of the universe. Last baryon acoustic oscillations (BAO) include power spectra of galaxies, galaxy clusters, and Ly $\alpha$ -forest. However, information on the optimum cosmological model is important for data analysis of extragalactic observations.

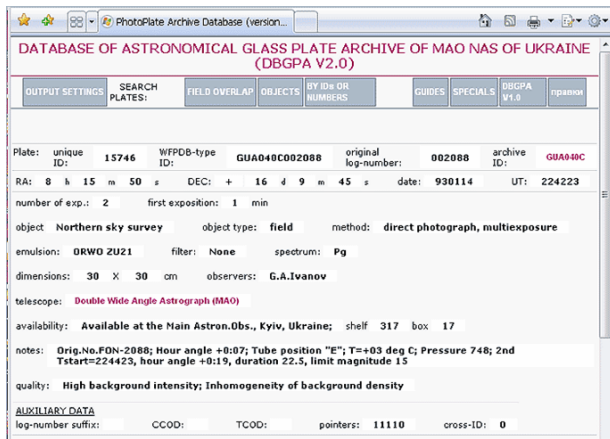


Figure 2: Screenshot of the interface of the UkrVO Joint Digitized Archive of astroplates, N=46 607 up to the current date (<http://gua.db.ukr-vo.org/archivespecial.php>; see, also, <http://www.skyarchive.org> for the wide-field astroplate database).

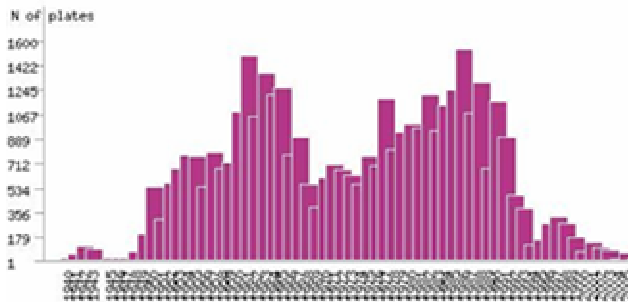


Figure 3: UkrVO Joint Digitized Archive of astroplates: distribution by years of observations.

- sample of about 130 galaxy clusters at  $z < 2$  observed by “Chandra” and other X-ray observatories (Babyk et al., 2014; Babyk, 2016) for determining a visible and dark matter content in galaxy clusters;
- sample of the power spectra of CMB temperature fluctuations obtained in space experiments WMAP (WMAP9) and Planck, supplemented by data on the CMB polarization; sample for measuring the Hubble constant with HST; sample for BAO from SDSS DR7, DR9 and 6dF [12]; the power spectra of galaxies from WiggleZ Dark Energy Survey; the distance to SN Ia from compilations of SNLS3 and Union2.1. It was obtained that a combination of data sets, which include BAO data, – Data Planck2013 +HST+BAO+SNLS3 – gives the most accurate determination of cosmological parameters from the narrowest confidence intervals (Novosyadlyj et al., 2014; Sergijenko et al., 2015).

### 3. UkrVO Joint Digitized Archive of Astroplates

The UkrVO’s development allows us 1) to save the unique astronomical observational heritage accumulated in observatories of Ukraine from the 1890-ies; 2) to open the wide on-line access to the joint database of digitized astronomic negatives and spectra for the national/foreign

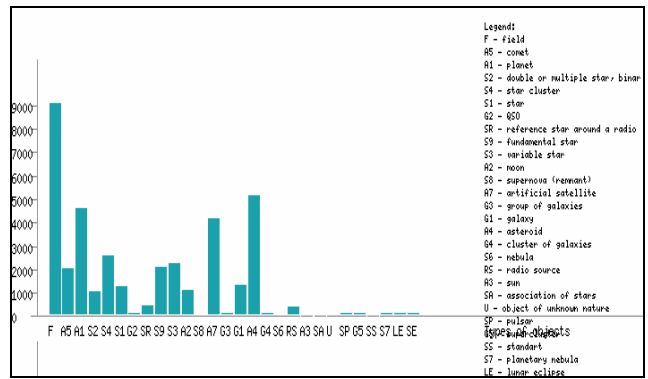


Figure 4: UkrVO Joint Digitized Archive of astroplates: distribution by research fields.

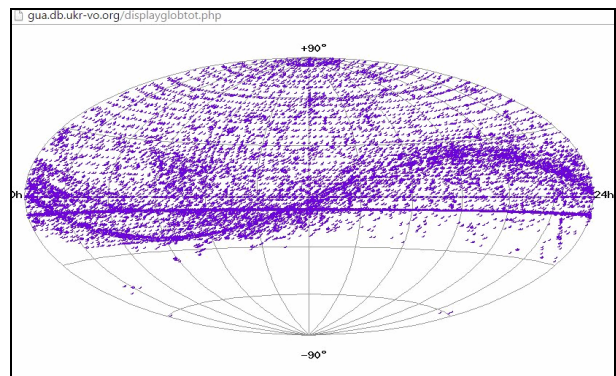


Figure 5: UkrVO Joint Digitized Archive of astroplates: distribution of astroplates over the sky (41,000 observations conducted with 32 telescopes of 20 to 412"/mm; exposure time is from 1 s to 1.5 h).

scientific community. The current state is available at the UkrVO web-site. At the initial stage, this task concluded in the creation and development of the Joint Digital Archive (JDA) of photographic observations. The total number of photographic plates in the UkrVO collection exceeds 300 thousands, including not only the positional but also the spectral and photometric observations. The current JDA version includes, at mainly, the positional observations of various celestial bodies. About 125,000 astroplates (Ukrainian Plate Archives) are included in the Wide-Field Plate Database by Tsvetkov M. (Kolev et al., 2012) (<http://www.wfpdb.org/catalogue.html>).

A preliminary processing of the digitized images of astroplates was done with a MIDAS/ ROMAFOT special software: registration of objects till  $16^m$ , determination of pixel coordinates and photometric values (Protsyuk et al., 2014a, 2016). The errors of Epson scanners arising during processing the astroplates were tested in works by Golovnya et al. (2010), Protsyuk et al. (2014b, 2014c). They are equal to  $\sigma_{x,y} = \pm 0.02-0.06$  px and  $\sigma_m = \pm 0.015-0.024$  mag for astrometry and photometry, respectively. Another software was developed for obtaining the equatorial coordinates and magnitudes of objects on the digitized astroplates (see, in detail, Andruk et al., 2015b).

Now the UkrVO JDA gives access to ~50,000 digitized astroplates of a good quality (its interface is illustrated in Figure 2). The UkrVO JDA Data releases, which were performed by scientists from Kyiv, Mykolaiv, Odesa,

L'viv and Crimea including those in a tight international cooperation, are in a final stage for issuing. UkrVO Data Release 1 deals with the star catalogues (FON, Polar zone, open clusters, GRB star fields). UkrVO Data Release 2 deals with the Solar System bodies (giant and small planets, astronomical heritage images). Source of these data: the digitized astroplates, which were organized as the UkrVO JDA database of astroplate network collections of different institutions as owners of these collections.

The histograms of a number of the digitized astroplates by years and by research fields, as well as distribution of objects over the sky are given in Figures 3-5, respectively.

### 3.1. UkrVO JDA Data Release 1: Star catalogues

Aforementioned software was tested many times and applied for creation of new catalogues and samples with different purposes (Andruk et al, 2015a, 2015b; Kazantseva et al, 2015; Muminov et al, 2016; Muminov et al, 2017; Protsyuk et al, 2014d; Yatsenko et al, 2011; Yizhakevych et al, 2014, 2015).

**Catalogue of the equatorial coordinates and the B-values of stars of a Kyiv part of the FON program.** This catalogue contains 19,568,347 stars and galaxies to  $B \leq 16.5^m$  for the 1988.1 epoch (Andruk et al., 2016a, 2016b; Pakuliak et al., 2016). Number of processed astroplates is 2260. Their digitization was carried out by Microtek Scan Maker 9800XL TMA and Epson Expression 10000XL, scanning mode – 1200 dpi, the size of most plates is 30x30 cm or 13000x13000 pixels. Coordinates of the stars and galaxies were obtained in the Tycho-2 catalogue system, B-magnitudes in photometric standards system (Andruk et al, 1995; Kornilov et al., 1991; Mermilliod, 1991; Relke et al., 2015). Intrinsic accuracy for all objects is  $\sigma_{\alpha\delta} = \pm 0.23''$  and  $\sigma_B = \pm 0.14^m$  (for stars in the range of  $B = 7^m - 14^m$ , errors are  $\sigma_{\alpha\delta} = \pm 0.10''$  and  $\sigma_B = \pm 0.07^m$ ) for the equatorial coordinates and B-magnitudes, respectively. Convergence between the determined and referenced positions is  $\sigma_{\alpha\delta} = \pm 0.06''$ , and the convergence with photoelectric star B-magnitudes is  $\sigma_B = \pm 0.15^m$ . Coordinate's errors related to the UCAC-4 are  $\sigma_{\alpha\delta} = \pm 0.30''$  (18,742,932 or 96.36% of objects were identified) (Zacharias et al., 2013).

**Catalogue of the equatorial coordinates and the B-magnitudes of the Kitab's part of the FON program.** Observations in frame of the FON program were conducted also at the Kitab Observatory (Academy of Sciences of Uzbekistan) from 1981 to 1996 with telescope DAZ telescope (F/D = 40/200). In 2015, about of 2600 astroplates were transported to the Institute of Astronomy in Tashkent (Uzbekistan), where their digitizing has started (Muminov et al., 2013). The digitized astroplates are being processed till now at this institute and also at the Walter Hohmann Observatory (Essen, Germany), Nikolaev Astronomical Observatory (Ukraine), and at the Main Astronomical Observatory NAS of Ukraine in Kyiv (1250 astronegatives up to current date). A preliminary estimation of intrinsic errors of this catalogue is based on the results of astronegatives for region  $\alpha$  [ $21^h, 3^h$ ],  $\delta$  [ $-2^\circ, -6^\circ$ ]: the averaged errors are  $\sigma_{\alpha\delta} = \pm 0.2''$  and  $\sigma_B = \pm 0.18^m$  (for stars with  $B < 14^m$  they are equal to  $0.1''$  and  $0.1^m$ ) for

the equatorial coordinates and B-magnitudes, respectively (Yuldoshev et al., 2016a, 2016b).

**U-magnitudes of stars and galaxies from the digitized astroplates of 1.2m Schmidt telescope in Baldone Observatory (Latvia).** Archives of the Schmidt telescope contains 734 astroplates in 253 regions of the sky captured in U-band close to the U-Johnson (Eglitis et al. 2016a, 2016b). At the moment, it is scanned about 300. The coordinates of stars and galaxies are obtained in Tycho-2 system, the U-values in the photoelectric standards.

Intrinsic accuracy for all objects is  $\sigma_{\alpha\delta} = \pm 0.28''$  and  $\sigma_B = \pm 0.20^m$  (for stars in the range of  $B = 8^m - 14^m$ , errors are  $\sigma_{\alpha\delta} = \pm 0.11''$  and  $\sigma_B = \pm 0.09^m$ ) for the equatorial coordinates and B-values, respectively. Systematic difference between common stars of this catalogue and Tycho-2 is  $\sigma_{\alpha\delta} = \pm 0.06''$  (for 5814 stars); for U-magnitudes  $\sigma_B = \pm 0.13^m$  (for 876 stars). These estimations have a preliminary character and based on the data of catalogue of positions and U-magnitudes for 68,784 stars and galaxies for 12 regions of the MEGA program (Andruk et al., 1995).

**Catalogues of position and proper motions of stars** (Protsyuk et al., 2014a, 2015a). In 2016, the catalogue of position and proper motions of stars in the areas around the Galactic open clusters was created by using photographic and CCD observations obtained with different telescopes in the 20-21 century.

Near 290 plates (20x20cm,  $5^\circ \times 5^\circ$ ), which have been obtained with the Zonal Astrograph of Nikolaev Astronomical Observatory (NAO) (D = 116 mm, F = 2040 mm, scale =  $101''/\text{mm}$ ) in 1962-1993, were scanned. In 2011-2015, more than 20,000 CCD frames were obtained with KT-50 telescope (D = 500 mm, F = 3000 mm,  $43' \times 38'$ , scale =  $0.8''/\text{pix}$ ) (Shulga et al., 2012). Totally more than 270 thousands FITS files from MAVO image archives with observational epoch from 1953 to 2010 were downloaded. All the data was processed and coordinates of all objects on the images were obtained.

Catalogue of position and proper motions of about 2.7 million stars ( $7-16^m$ ) in Tycho-2 system (NAO2015pm) was created. The accuracy of positions on both coordinates is ranged from  $0.02-0.04''$  for the stars of ( $7-12^m$ ) to  $0.08-0.11''$  for the stars of ( $14-16^m$ ). Intrinsic accuracy of proper motions is near  $0.04''/\text{year}$ . Systematic difference between common stars of NAO2015pm and XPM catalogues (Fedorov et al., 2009) is less than  $0.005''/\text{year}$  on both coordinates.

**Catalogues of stars in fields of Gamma-Ray Bursts.** GRBs are registered first by space observatories and transmit this information immediately for ground-based observatories, which, in own turn, may detect optical afterglow emitted during the next hours and days. Results on GRBs are published in the circulars GRB Coordinate Network (GCN Circulars). GRBs are occurring about once a day and have a uniform distribution on the celestial sphere.

Catalogues of stars in fields of GRBs allowed searching for optical counterparts of GRB in the past. With this aim we use astroplates from UkrVO JDA database (Sergeeva et al., 2004, Vavilova et al., 2012a,b, 2014a,b). The positional accuracy of selected objects is between  $\pm 0.3''$  and  $\pm 4.5''$  and the range of magnitudes is  $14^m - 19^m$ . GRBs and

all the objects are sought and identified on the digitized plates within the circle with a radius of dozens of arc minutes. The data on the equatorial coordinates and B-magnitudes of stars in GRB fields are obtained with LINUX/MIDAS/ROMA FOT software in Tycho-2 system (Andruk et al., 2010, 2016a; Yatsenko et al., 2011; Golovnya et al., 2010). They are as follows:  $\sigma_\alpha = \pm 0.17''$ ,  $\sigma_\delta = \pm 0.3''$  for coordinates and  $\sigma_m = \pm 0.3$  for B-magnitudes. Because of the expected optical image analogs of GRBs are very weak, we use only astroplates with exposure time more than 10 minutes (practically, they are all from the FON program collection). To clarify the parameters of stars and sizes of fields around GRBs, the maps of Digitized Sky Survey II (DSS2) and service Aladin v8.0 have being applied. The results of this work are published in GSN Circulars (see, for example, Golovnya, 2016). We note that the probability to find optical analogs of GRBs is small, especially when searching for them in the past.

3.2. UkrVO JDA Data Release 1: Software and web-services

The VizieR web service (Strasbourg, France) contains more than 15400 published astronomical catalogues. The **astronomical web-services (AWS)** of UkrVO (Mazhaev & Protsyuk, 2013) provide the automated search and selection of required data in accordance with the SCS standard for three catalogues compiled in Ukraine, namely, All-Sky Compiled Catalogue of 2.5 million stars (ASCC) by Kharchenko (2001), FONAC (Kislyuk and Yatsenko, 2005), XPM (Fedorov et al., 2009). The structure of AWS web address consists of path to script and search options after the question mark. The user can search in different areas of the sky and retrieve data from the astrometric catalogues. These AWS were inscribed into a register of the USA Virtual Astronomical Observatory (VAO). The register contains more than 17000 services.

“The high energy astrophysics science archive research center (HEASARC) validates each web service at least once per month. Using Data Discovery Tool (DDT) developed by the VAO, it is possible to retrieve data from all archives, which are inscribed in the VAO register. Illustration of the access with AWS by using Aladin GUI to XPM catalogue is given in Figure 6. It’s also possible with

this GUI to obtain access to two UkrVO JDA databases of observations conducted with astro photo plates and CCDs in the 20<sup>th</sup> and 21<sup>st</sup> centuries, respectively. Using the search results within metadata window of Aladin, one can download and visualize a preview image of a found photo plate” (cited by Mazhaev (2017)).

Special-oriented software has been developed for variable star research in the Odessa National Maritime University. We note MCV and VSCalc and describe ILA project.

The program **MCV ("Multi-Column View")** allows to make time series analysis of irregularly spaced data, particularly, having unique features: the approximation using combinations of algebraic and trigonometric polynomials simultaneously for up to 3 main periods (and harmonics); the periodogram analysis using the trigonometric polynomial of an user-defined degree superimposed on to an algebraic polynomial trend without a "pre-whitening"; the reduction of the CCD measurements using many stars in the field (the algorithm of the "artificial comparison star") and dozens of other features. At minimum, the program may be used for an automatic visualization of the (multi-) or one-column time series and preparation of graphs in the raster format. The description of the first version was published by Andronov and Baklanov (2004), but the program is regularly upgraded and new versions available at <http://soft.softodrom.ru/ap/Bred2i-p4726>.

Breus (2007a, b) proposed the **"Variable Stars Calculator" (VSCalc)** software, where 1) there is a possibility for reduction of visual observations and conversion of the photographic plate numbers in HJD (currently the database of the Odessa plate collection is available, but other files may be used as well); 2) the periodogram analysis may be carried out using the method by Lafler-Kinman-Kholopov; 3) the extrema may be determined using an algebraic polynomial of statistically optimal order.

Additional algorithms were realized in the programs **for vicinities of the extrema** by Andrych et al. (2015) and **for complete light curves** by Andronov et al. (2016). This method was improved for the multi-color observations by Andronov et al. (2015). The reduction of the photopolarimetric observations obtained at the 2.6m Shain telescope at the Crimean Astrophysical Observatory is carried out using the program "ZTSh-Server" (Breus et al., 2007b; Kolesnikov et al., 2016).

New programs are developed for automatic search for variable stars using measurements of all stars in the field and for the photometry of stars using overlapping images. The programs may be revised upon request.

Variability of stars was studied based on mathematical modeling of the observations from the following sources: own observations obtained in Poland, Slovakia (multi-color CCD photometry) and at the 2.6m Shain telescope of the Crimean Astrophysical observatory (photo-polarimetry); CCD observations within temporarily observational projects on the selected stars within an international project **"Inter-Longitude Astronomy" (ILA)** with participants from USA, Korea, Germany, Greece, Poland, Slovakia, Finland, Italy, Czechia, Hungary, France; observations with the ground-based CCD (Catalyna, ASAS, NSVS, WASP), visual (AAVSO, AFOEV, VSOLJ) and space (Hipparcos-Tycho, CHANDRA, UHURU, ROSAT) photometrical

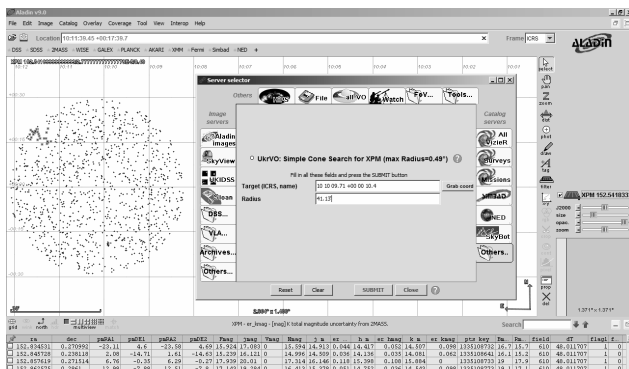


Figure 6: Screenshot of the GUI and search results for XPM catalogue (Fedorov et al., 2009) obtained with Aladin (AWS is developed by Mazhaev & Protsyuk, 2013).

surveys (see, a brief report, Andronov et al. (2010)). Highlights of the studies of the statistically optimal approximations of mean phase and individual light curves of pulsating and symbiotic variable stars were briefly reviewed by Andronov et al. (2014). Statistically optimal approximations of astronomical signals and their implications to classification and advanced study of eclipsing binaries were discussed by Andronov et al. (2016 b,c).

The main variable star research upon the "ILA" project is as follows (studies of selected objects, more than 1900):

- \* **"Polar"** ("Magnetic cataclysmic variables") – classical, eclipsing, asynchronous and intermediate polars, as well as the magnetic Dwarf Nova DO Dra; particularly, the spin evolution of white dwarfs in these objects; behavior in different luminosity states);

- \* **"Superhumper"** – "Non-magnetic cataclysmic variables" – superhumps, quasi-periodic and transient periodic oscillations in Nova-like stars and/or UGSU-type dwarf Novae;

- \* **"Eclipser"** – "Eclipsing Binary stars" – phenomenological modeling of the light curve using special patterns (shapes, profiles) of the phase-limited eclipses), determination of characteristics, studies of stability or variability of the period and shape of the light curve;

- \* **"Impactor"** – "Extreme direct impactors" – in interacting binary stars, a new subclass with a prototype star V361 Lyr;

- \* **"Symbiosis"** – "Symbiotic variable stars" – multi-component variability from minutes to decades;

- \* **"Stellar Bell"** – "Pulsating variable stars", currently of M, SR, RV, RR, DSct types;

- \* **"New Star"** – discovery, classification and determination of the phenomenological parameters of new variable stars.

The powerful **CoLiTec (Collection Light Technology)** software for the automated search for small celestial objects on a series of CCD frames has been developed within the UkrVO (<http://www.neoastrosoft.com/>). The core of this software is a new iteration method based on a sub-pixel Gaussian model of the discrete object image to estimate coordinates of celestial body. The method operates by continuous parameters (object's coordinates) in a discrete observational space (the set of pixel potentials) of the CCD frame. In this model, the kind of coordinate distribution of the photons hitting a pixel of the CCD frame is known a priori, while the associated parameters are determined from a real digital object image. The method is flexible in adapting to any form of object image, has high measurement accuracy along with a low calculating complexity (Savanevych et al., 2015a).

The comparative analysis of the processing of the same frames using CoLiTec and Astrometrica software says that in the case of low signal to noise ratios, the standard deviation of positional CCD measurements using the Astrometrica software is 30-50% greater than that of the CoLiTec software (Savanevych et al., 2015b). In 2014, the COLITEC software was recommended to all members of the *Gaia-FUN-SSO network* for analyzing observations as a tool to detect faint moving objects in frames.

The CoLiTex group developed also a new tool for the calibration of astronomical images – **FrameSmooth** – as a cross-platform module for brightness equalization of Co-

LiTec software. It allows processing images with any formats. Module is based on using the filter for brightness equalization, inverse median, and nonlinear high-frequency filters. It supports additional astronomical master-frames (Bias, Dark, DarkFlat and Flat) as well as OLDAS mode and feature for converting images in fits format were added (Dubovský et al., 2016). Figure 7 illustrates advantages of this method as comparing with traditional Muniwin method of calibration of the field of V1323 Her.

**Star catalogues, software and services of the Crimean Astronomical VO (CrAVO).** Information about archives of astronegatives obtained at the Crimean Astrophysical Observatory (CrAO) is located at the International Center in Sofia (<http://www.skyarchive.org/>); the data are available through a data base in the VizieR catalog VI/ 90 or with «CRI» key at: <http://draco.skyarchive.org/search/>. CrAVO data archives and catalogues are the part of the UkrVO astroinformatics resource (Shlyapnikov, 2007; Vavilova et al., 2012a).

The editable version of database consists of 39 catalogues prepared at the CrAO: some of them are digitized, 16 catalogues with the data on magnitudes and spectral classes of 34154 stars (**"Shajn Plan"**) are in processing (Gershberg et al., 2011; Fursiak, 2012; Shlyapnikov, 2013; Shlyapnikov et al., 2015).

Starting from 2013, a new database of spectral observations of celestial bodies has been forming (Gorbunov, Shlyapnikov, 2013; Pakuliak et al., 2014). They include spectroscopic observations conducted at the wide-angle astrographs with objective prism and reflectors ( $D = 1000, 1220$  and  $2600$  mm). The collection of spectroscopic



Figure 7: Field of variable star V1323 Her. From left to right: raw image, calibrated in usual way with the Muniwin, calibrated with FrameSmooth (see, in detail, presentation by Dubovský P.A., Savanevych V.E., Kudzej I. et al., [http://www.neoastrosoft.com/prague\\_2016\\_en/#more-3772](http://www.neoastrosoft.com/prague_2016_en/#more-3772) at the 48th Conference on variable stars research, Prague, 2016).

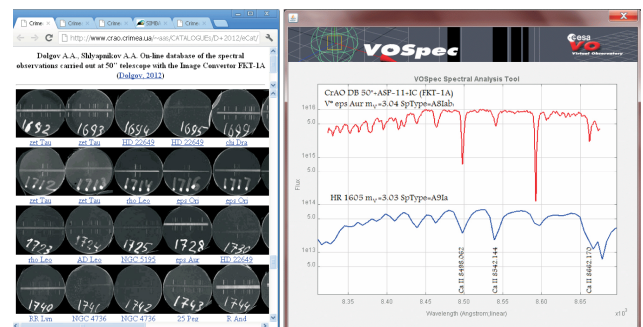


Figure 8: Example of the digitized spectrum with VOSpec from the database of spectral observations with 50-inch telescope at the CrAO.

observations with the objective prism consists of three parts in dependence on type of astrograph where this collection was obtained (Dolgov, Shlyapnikov, 2013). Parameters of astrographs (D/F in mm) and dispersion  $\sigma$  of digitized spectra in H $\gamma$  line ( $\text{\AA}/\text{pix}$ ) are as follows: Unar (D/F = 117/600,  $\sigma$  = 1.5), Dogmar (D/F = 167/750,  $\sigma$  = 1.4), 400-mm (D/F = 400/1600,  $\sigma$  = 1.5). Figure 8 gives an example of the digitized spectrum from the database of spectral observations with 50-inch telescope of the Crimean Astrophysical Observatory.

*Acknowledgements.* This work was partially supported in frame of the Target Complex Program of Scientific Space Research of the National Academy of Sciences of Ukraine (2012–2016).

## References

- Andronov I.L. et al.: 2010, *Odessa Astron. Publ.*, **23**, 8.  
 Andronov I. L. et al.: 2014, *AASP*, **4**, 3.  
 Andronov I. L. et al.: 2015, *JASS*, **32**, 127.  
 Andronov I.L. et al.: 2016a, *ASPC*, **505**, 101.  
 Andronov I. L. et al.: 2016b, *Phys J*, **2**, 140.  
 Andronov I. L. et al.: 2016c, *OEJV*, **176**, 35.  
 Andronov I. L., Baklanov A.V.: 2004, *AstSR*, **5**, 264.  
 Andrych K. D. et al.: 2015, *Odessa Astron. Publ.*, **28**, 158.  
 Andruk V. et al.: 1995, *Astron. Nachr.*, **316**, N4, 2.  
 Andruk V.M. et al.: 2015a, *Odessa Astron. Publ.*, **v.28/2**, 188.  
 Andruk V.M. et al.: 2015b, *Odessa Astron. Publ.*, **v.28/2**, 192.  
 Andruk V.M. et al.: 2016a, *Kinemat. Phys. Cel. Bodies*, **32**(1), 38.  
 Andruk V.M. et al.: 2016b, *Kinemat. Phys. Cel. Bodies*, **32**(5), 261.  
 Babyk I., Vavilova I.: 2014, *Astrophys. Space Sci.*, **349**, 1, 415.  
 Babyk Yu.V. et al.: 2014, *Astron. Reports*, **58**, 9, 587.  
 Babyk Yu. V.: 2016, *Astron. Reports*, **60**, 6, 542.  
 Boyarsky A. et al.: 2014, *Phys. Rev. Lett.*, **113**, 251301.  
 Breus V.V.: 2003, *Odessa Astron. Publ.*, **16**, 24.  
 Breus V.V.: 2007a, *Odessa Astron. Publ.*, **20**, 32.  
 Breus V.V. et al.: 2007b, *A&AT*, **26**, 241.  
 Borne K. et al.: 2009, *Astro2010: The Astronomy and Astrophysics Decadal Survey, Position Papers*, no. 6.  
 Borne K.: 2013, In: *Planets, Stars and Stellar Systems*, by Oswald T.D., Bond H.E., Springer, 2013, p. 403.  
 Brescia M., Longo G.: 2013, *Nuclear Instruments and Methods in Physics Research A*, **720**, 92.  
 Butler D.: 2007, *Nature*, **446**, 354.  
 Cavuoti S. et al.: 2012, *Proceedings of the SPIE*, 8451, article id. 845103, 13 pp.  
 Chenzhou C. et al.: 2012, *New Astronomy*, **17** (2), 167.  
 Chesnok N.G.: 2010, *Kosm. nauka tehnol.*, **16**(5), 77.  
 Chesnok N.G. et al.: 2009, *Kinemat. Phys. Cel. Bodies*, **25**(2), 107.  
 D'Abrusco R. et al.: 2007, *AphJ*, **663**(2), 752.  
 Dobrycheva D.V.: 2013, *Odessa Astron. Publ.*, **26**, 187.  
 Dobrycheva D. et al.: 2012, *Astrophysics*, **55**(3), 293.  
 Dobrycheva D. et al.: 2014, *Odessa Astron. Publ.*, **27**, 26.  
 Dobrycheva D.V et al.: 2015, *Astrophysics*, **58**(2), 168.  
 Dubrovsky P.A. et al.: 2016, in: *48th Conference on variable stars research*, Prague, 2016.  
 Dolgov A.A., Shlyapnikov A.: 2013, *Izv. KrAO*, **109**, 2, 165.  
 Eastman T. et al.: 2005, *Data Science Journal*, **4**, 67.  
 Eglitis I. et al.: 2016, *Odessa Astron. Publ.*, **29**, 126.  
 Feigelson E.D. et al.: 2013, ADASS XXII, *ASP Confer. Ser.*, **15**.  
 Feigelson E., Hilbe J. M.: 2014, *AAS Meeting #223*, id. 253.02.  
 Fedorov P. et al.: 2009, *MNRAS*, **393**, 133.  
 Fursiak Yu.A., Shlyapnikov A.A.: 2012, *AASP*, **2**(2), 197.  
 Gershberg, R. E. et al.: 2011, *Bull. CrAO*, **107**, 1, 11.  
 Giavalisco M. et al.: 2004, *AphJ*, **600**(2), L93.  
 Golovnya V.V.: 2016, *GCN Circulars*, No.19384, 1.  
 Golovnya V.V., Andruk V.M.: 2013, *Odessa Astron. Publ.*, **26/2**, 226.  
 Goodman A. et al.: 2012, ADASS XXI, *ASP Confer. Ser.*, **461**, 267.  
 Gorbunov M.A., Shlyapnikov A.A.: 2013, *Odessa Astron. Publ.*, **26/2**, 229.  
 Gray J. et al.: 2005, arxiv.org/abs/cs/0502008.  
 Ivashchenko G. et al.: 2014, *MNRAS*, **437**, 3343.  
 Ivashchenko G. et al.: 2015, *Kinemat. Phys. Cel. Bodies*, **31**(3), 1.  
 Kazantseva L. et al.: 2015, *Kinemat. Phys. Cel. Bodies*, **31**(1), 58.  
 Kislyuk V. S., Yatsenko A.I.: 2005, *Kinemat. Phys. Cel. Bodies Suppl.*, **5**, 33.  
 Kharchenko N.I.: 2001, *Kinemat. Phys. Cel. Bodies*, **17**(5), 409.  
 Klipio et al.: 2003, in ADASS XII, *ASP Confer. Se.*, **295**, 73.  
 Kolesnikov S.V. et al.: 2016, *Odessa Astron. Publ.*, **29**, 74.  
 Kolev A. et al.: 2012, *Publ. Astron. Soc. "Rudjer Boskovic"*, **11**, 219.  
 Kornilov V.G. et al.: 1991, *Trudy GAISH*, **63**, 1.  
 Malkov O. et al.: 2016, *Baltic Astronomy*, **25**(1), 107.  
 Mazhaev A., Protsyuk Y.: 2013, *Odessa Astron. Publ.*, **26/2**, 233.  
 Mazhaev A.: 2017, *Sci. innov.*, **13**(1).  
 Mermilliod J.C.: 1991, *Homogeneous means in UBVR system*.  
 Michaelian A.: 2016, *Baltic Astronomy*, **25**(1), 75.  
 Muminov M.M. et al.: 2013, *Izvestija GAO. Pulkovo*, **220**, 517.  
 Muminov M.M. et al.: 2016, *Izvestija GAO. Pulkovo*, **223**, 339.  
 Muminov M.M. et al.: 2017, *Bulgarian Astron. J.*, **26**, 1.  
 Norris R.P. et al.: 2013, *PASA*, **30**, 20.  
 Novosyadlyj B. et al.: 2014, *J. Cosmology and Astroparticle Phys.*, **5**, N 05, article id. 030.  
 Pakuliak L.K. et al.: 2012, *Proc. NAROO-GAIA*, 161.  
 Pakuliak L. et al.: 2014, *ASI Confer. Ser.*, **11**, 103.  
 Pakuliak L.K. et al.: 2016, *Odessa Astron. Publ.*, **29**, 132.  
 Protsyuk Yu.I. et al.: 2014a, *Odessa Astron. Publ.*, **27/1**, 59.  
 Protsyuk Yu.I. et al.: 2014b, *Odessa Astron. Publ.*, **27/1**, 61.  
 Protsyuk Yu.I. et al.: 2014b, *Odessa Astron. Publ.*, **27/1**, 63.  
 Protsyuk Yu.I. et al.: 2014d, *Kinemat. Phys. Cel. Bodies*, **30**(6), 296.  
 Protsyuk Yu. et al.: 2015a, *Odessa Astron. Publ.*, **28/2**, 202.  
 Protsyuk Yu.I. et al.: 2016, *Odessa Astron. Publ.*, **29**, 147.  
 Pulatova N.G. et al.: 2015, *MNRAS*, **447**(3), 2209.  
 Relke E. et al.: 2015, *Odessa Astron. Publ.*, **28/2**, 211.  
 Ruiz J.E. et al.: 2014, *Astronomy and Computing*, **7**, 3.  
 Savanevych V.E. et al.: 2015a, *MNRAS*, **451**, 3, 3287.  
 Savanevych V.E. et al.: 2015b, *Kinemat. Phys. Cel. Bodies*, **31**, 6, 302.  
 Savchenko D., Iakubovskiy D. : 2014, *AASP*, **4**, 51.  
 Sergeeva T.P. et al.: 2004, *Baltic Astron.*, **13**, 677.  
 Sergijenko O., Novosyadlyj B.: 2015, *Phys. Rev. D*, **91**, 083007.  
 Shlyapnikov A.: 2013, *Izvestiya KrAO*, **109**, 2, 169.  
 Shlyapnikov A. et al.: 2015, *Baltic Astron.*, **24**, 462.  
 Shulga A.V et al.: 2012, *Kosm. nauka tehnol.*, **18**(4), 52.  
 The National Virtual Observatory: Tools and Techniques for Astronomical Research: 2008, ASP, 382, [http://www.aspbks.org/a/volumes/table\\_of\\_contents/?book\\_id=420](http://www.aspbks.org/a/volumes/table_of_contents/?book_id=420)  
 Torbaniuk O.: 2015, *AASP*, **5**(2), 84.  
 Torbaniuk O.: 2016, *AASP*, **6**(2), 34.  
 Vasylenko A. et al.: 2015, *Aph.&Sp.Sci.*, **360**, id.37, 16p.  
 Vavilova I. et al.: 2012a, *Kinemat. Phys. Cel. Bodies*, **28**(2), 85.  
 Vavilova I.B. et al.: 2012b, *Baltic Astronomy*, **21**/3, 356.  
 Vavilova I.B. et al.: 2014, *Odessa Astron. Publ.*, **27/1**, 65.  
 Vavilova I. et al.: 2014, in: *Astroplate 2014*, Prague, Eds. Linda Mišková and Stanislav Vitek, 8.  
 Vavilova I. et al.: 2015, *Kosm. nauka tehnol.*, **21**(5), 94.  
 Vol'vach A.E. et al.: 2011, *Astron.Reports*, **55**(7), 608.  
 Yakubovskiy D.A. et al.: 2015, *Kosm. nauka tehnol.*, **21**(5), 90.  
 Yatsenko A.I. et al.: 2011, *Kinemat. Phys. Cel. Bodies*, **27**(5), 249.  
 Yizhakevych O. et al.: 2014, *Odessa Astron. Publ.*, **27/1**, 67.  
 Yizhakevych O. et al.: 2015, *Odessa Astron. Publ.*, **28/2**, 213.  
 Yuldoshev Q.X. et al.: 2016, *Odessa Astron. Publ.*, **29**, 160.  
 Zacharias N. et al.: 2013, *Astron. J.*, **145**, 44.

DOI: <http://dx.doi.org/10.18524/1810-4215.2016.29.85125>

## THE INVESTIGATION OF THE FON3 CATALOGUE DATA USING WIELEN METHOD

V.S.Akhmetov

Institute of Astronomy, V.N. Karazin Kharkiv National University,  
35 Sumska Str., 61022, Kharkiv, Ukraine, [akhmetovvs@gmail.com](mailto:akhmetovvs@gmail.com)

**ABSTRACT.** The method described by Wielen is very efficient provided the data under comparison are independent quantities. In this case, dispersion of position or magnitude differences is equal to the sum of their dispersions, because the index of correlation between the data is set zero. Using three or more independent catalogues, it is easy to estimate the external accuracy of each of them. For the cross-identification of objects, we have used the search window with a 0.5 arcsec radius. Final dispersions were calculated for every sub-range of magnitudes, for the stars with individual differences of position and magnitude exceeding three standard deviations being rejected. The following catalogues have been used for comparison with the FON3: XPM, PPMXL and UCAC4 in the Northern hemisphere. The dispersions of positions or magnitudes are calculated with the use of about 18 million common stars from these catalogues. The results presented in this work is consistent with analysis of the random errors of positions and magnitude that had been described by authors of FON3 catalog.

**Keywords:** Astrometry, astrometry-catalog, data analysis

### 1. Introduction

This paper presents some results of investigation of the FON3 catalogue of star positions and B-magnitudes in Northern Sky Survey (from  $-4^\circ$  to  $+90^\circ$ ). The FON3 catalog has been created under the motto of the rational use of resources accumulated in UkrVO JDA (Joint Digital Archive) in MAO NASU. The total amount of processed plates is 2260. Digitizing of astronegatives has been carried out with the help of Microtek ScanMaker 9800XL TMA and Epson Expression 10000XL scanners, with the scanning mode — 1200 dpi, the linear size of the plates — 30'30 cm or 13000'13000 pix. The catalog contains 19 451 751 stars and galaxies with B 16.5m for the epoch of 1988.1 (Andruk V.M. et al., 2010). The author of the FON3 catalog present internal accuracy for all objects is  $\sigma_{\alpha\delta} = 0.23''$  and  $\sigma_B = 0.14$  mag. For stars in the range of B =  $7^m$  -  $14^m$  errors are  $\sigma_{\alpha\delta} = 0.10''$  and  $\sigma_B = 0.07$ mag. Convergence between the calculated and reference positions is  $\sigma_{\alpha\delta} = 0.06''$ , and the convergence with photoelectric stellar B-magnitudes is  $\sigma_B = 0.15$ mag. (Andruk V. et al., 2016).

Using three or more independent catalogues, it is easy to estimate the external accuracy of each of them. For this purpose data from XPM, PPMXL and UCAC4 in the Northern hemisphere are used.

### 2. Estimation of external accuracy of the star positions and photometry by use of three independent data sets

The method used for estimation of external accuracy of the star positions was described by Wielen in 1995 (Wielen R. 1995). It is very robust under condition of the independence of the compared data. In such case the dispersion of the differences of positions or photometry is equal to the sum of their dispersions because their correlation coefficient is zero. With three or more independent catalogues it is easy to estimate the external accuracy of each of them:

$$\sigma_1 = \sqrt{\frac{D_{12} + D_{13} - D_{23}}{2}}$$

$$\sigma_2 = \sqrt{\frac{D_{12} + D_{23} - D_{13}}{2}}$$

$$\sigma_3 = \sqrt{\frac{D_{13} + D_{23} - D_{12}}{2}}$$

where  $D_{12}$ ,  $D_{13}$  and  $D_{23}$  are the dispersions of the differences of positions or magnitudes for three compared catalogues.

Before the calculation of the dispersions one should test that the correct values are obtained. The possible source of the incorrectness is the assumption that the means of the initial values are zero in the case when the catalogues with systematic errors have some non-zero means. If this non-zero mean is independent on magnitude or varies with it smoothly, then the dispersion of the differences of the positions or proper motions can be calculated. Otherwise, when the systematic differences change fast or disrupted the method does not work. Therefore it is important to determine the behavior of the systematic differences. Fortunately, in most cases the systematic differences of positions or photometry are some smooth functions of magnitude validating this method. Finally, in our case the dispersions are calculated for every small range of magnitude

with rejection of the stars with individual difference larger than 3 standard deviations.

The following catalogues have been used for the comparison with the FON3: UCAC4, PPMXL and XPM. It should be noted that the PPMXL and XPM proper motions were obtained with the use of the same schmidt plates. For the UCAC4 no schmidt plates were used. Consequently, the proper motions of the PPMXL and XPM are not independent. However the FON3-UCAC4-XPM and FON3-UCAC4-PPMXL datasets make the comparison possible.

### 3. Catalogs

Catalog UCAC4 is a compiled, all-sky star catalog covering mainly the 8 to 16 magnitude range in a single band-pass between V and R. Positional errors are about 15 to 20 mas for stars in the 10 to 14 mag range. Proper motions have been derived for most of the about 113 million stars utilizing about 140 other star catalogs with significant epoch difference to the UCAC CCD observations. All bright stars not observed with the astrograph have been added to UCAC4 from a set of Hipparcos and Tycho-2 stars. Thus UCAC4 should be complete from the brightest stars to about  $R=16$ , with the source of data indicated in flags. UCAC4 also provides a link to the original Hipparcos star number with additional data such as parallax found on a separate data file included in this release (Zacharias N. et al., 2013).

Catalog XPM is a combined data from the Two-Micron All Sky Survey (2MASS) and USNO-A2.0 catalogues in order to derive the absolute proper motions of about 300 million stars distributed all over the sky excluding a small region near the Galactic Centre, in the magnitude range  $12 < B < 19$  mag. The proper motions were derived from the 2MASS Point Sources and USNO-A2.0 catalogue positions with a mean epoch difference of about 45 years for the Northern hemisphere and about 17 years for the Southern one (Fedorov P. et al., 2009). The zero-point of the absolute proper motion frame (the 'absolute calibration') was specified with the use of about 1.45 million galaxies from 2MASS. Most of the systematic zonal errors inherent in the USNO-A2.0 catalogue were eliminated before the calculation of proper motions. The final version of the XPM catalogue contains about 314 million stellar positions and absolute proper motions. The mean formal error of absolute calibration is less than 1 mas/year (Fedorov P. et al., 2010).

PPMXL catalog contains about 900 million objects, some 410 million with 2MASS photometry, and is the largest collection of ICRS proper motions at present. The resulting typical individual mean errors of the proper motions range from 4 mas/year to more than 10 mas/year depending on observational history. The mean errors of positions at epoch 2000.0 are 80 to 120 mas, if 2MASS astrometry could be used, 150 to 300 mas else (Roesser S. et al., 2010).

### 4. Astronomical Database

To provide a quick and a simple access to modern astronomical catalogs that contain data of millions or billions celestial objects including stars, galaxies, quasars and others

the database has been developed. Modern astrometric catalogs obtained in last 20 years, are collected in this database using PostgreSQL server. The database contains about 30 catalogs with data more 1.5 Tb (Vavilova I.B. et al., 2012).

The main mission of creating the astronomical database is collect astronomical catalogs to provide a quick and a simple access to large dataset both for usual programs (TOPCAT, OriginLab, Microsoft Excel and others) and for a user's special programs.

To facilitate access to astronomical data from modern catalogs a web interface written in PHP programming language has been created. This web interface allows to select data containing in a small region of the celestial sphere <http://astrodata.univer.kharkov.ua/astrometry/db>.

The database allows the user to carry out data selection from the large astronomical catalogues by using: a network server, a internet browser, special scripts and programs. For cross-identification of objects and to calculate systematic errors and random accuracy of the star positions and photometry by use the database based on Wielen method the special program in C++ programming language has been developed.

### 5. Cross-identification of objects

In this paper star magnitudes of these catalogues are not used for cross-identification because of a significant difference in their band-pass and significant random and systematic errors of photometry. The cross-identification was carried out using only coordinates of objects. It should be noted that such cross-identification is usually named positional association and is not necessarily an exact identification.

To realize this method, the proper motions of catalog XPM has been used. In the first step a position of each objects in XPM catalog is calculated to epoch FON3 catalog by means of database.

The second step of cross-identification is a simple cross-match: each object of the catalog FON3 is compared with the object of the catalog XPM (on epoch FON3). If an angular distance is less than 0.5 arcsec it is common object. This procedure makes it possible to obtain lists of pairs of stars from both catalogs. The position difference between FON3 and XPM produced mainly only by the difference between random and systematic errors of both catalogues.

The corresponding procedure has been done for data UCAC4 and PPMXL catalogues. As result the FON3-UCAC4-XPM and FON3-UCAC4-PPMXL datasets about 18 million common stars have been obtained and then inserted to database for analysis.

### 6. The results of estimate the external accuracy and systematic errors data of catalogs

Below some results of investigations of the FON3, UCAC4, XPM and PPMXL catalogs are presented. For analysis of quality of the positions and photometry of the FON3 stars the different tests have been made.

Comparison of the FON3 data with UCAC4, XPM and PPMXL catalogs are shown in Figs 1 representing the systematic differences of positions in the sense FON3 minus catalogue, as well as their standard deviations as functions of stellar magnitude.

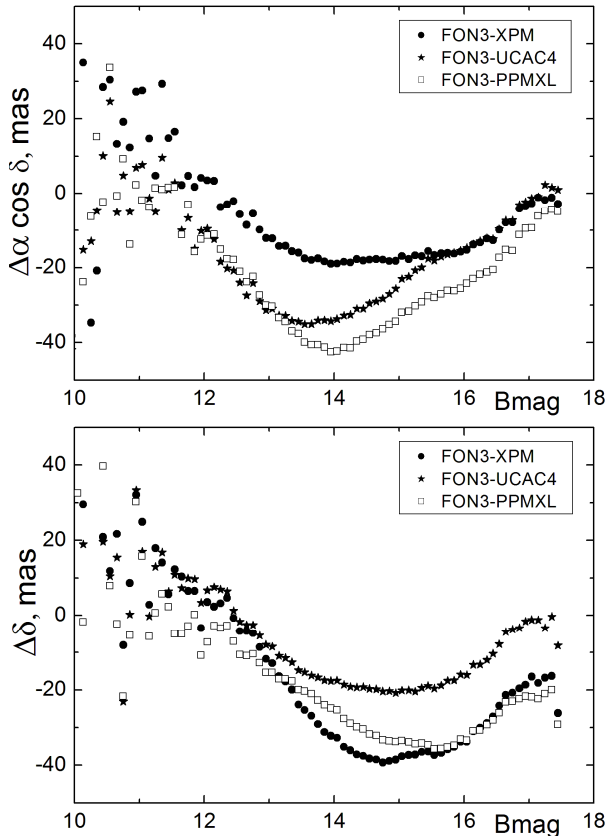


Figure 1: The systematic differences of the position FON3-XPM (black dots), FON3-UCAC4 (asterisks) and FON3-PPMXL (open rectangle) depending on the magnitude B of FON3.

The mean values of systematic differences of positions FON3-XPM, FON3-UCAC4, FON3-PPMXL are less than  $-40$  mas in the both coordinates. As showed in figure 1, the stars position of FON3 catalog are good agreement with XPM and UCAC4 in right ascension and declination correspondingly.

The external accuracy of stars position of FON3 catalogue are as functions of magnitude and equal 150 mas for brightest and up to 250 mas for faintest stars (Figure 2).

These external estimations of positional precision FON3 catalogue are in very good agreement with FON3 internal accuracy at the mean epoch observation.

The figure 3 is presented the systematic differences of star magnitudes in the sense FON3 minus catalogue, as well as their standard deviations as functions of stellar magnitude. The mean values of systematic differences of stellar magnitudes FON3-XPM, FON3-UCAC4, FON3-PPMXL are between  $-1$  up to  $2$  mag. As showed in figure 3, the stellar magnitudes of FON3 catalogue are good agreement with PPMXL catalogue data. The external accuracy of stellar magnitudes of FON3 catalogue are as functions of magnitude and equal 1 mag for brightest and  $0.3$  mag for faintest stars from  $13$  Bmag.

The noted facts should be taking into account in course that to creating catalog FON3 used data only plates of digitized astronegatives but do not used CCD observation.

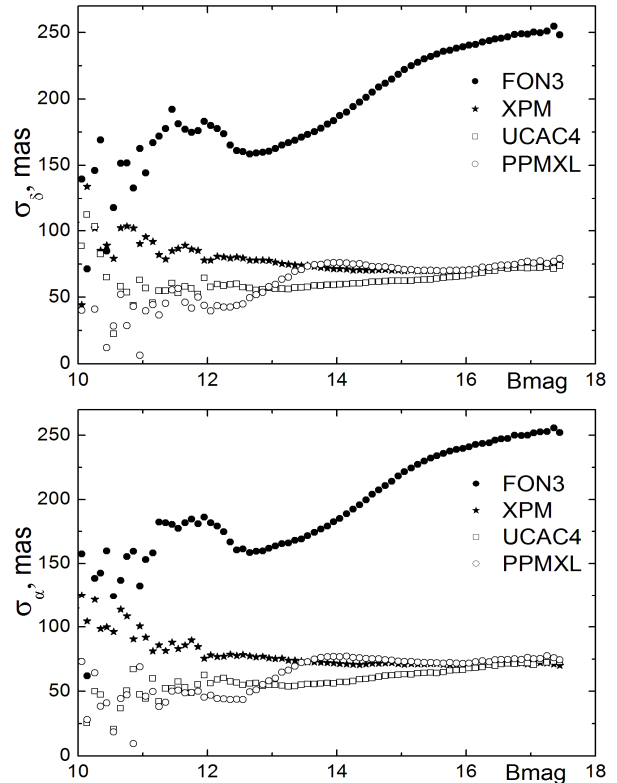


Figure 2: The standard deviations obtained by method Wielen of the position FON3 (black dots), XPM (asterisks), UCAC4 (open rectangle) and PPMXL (open circles) depending on the magnitude B of FON3.

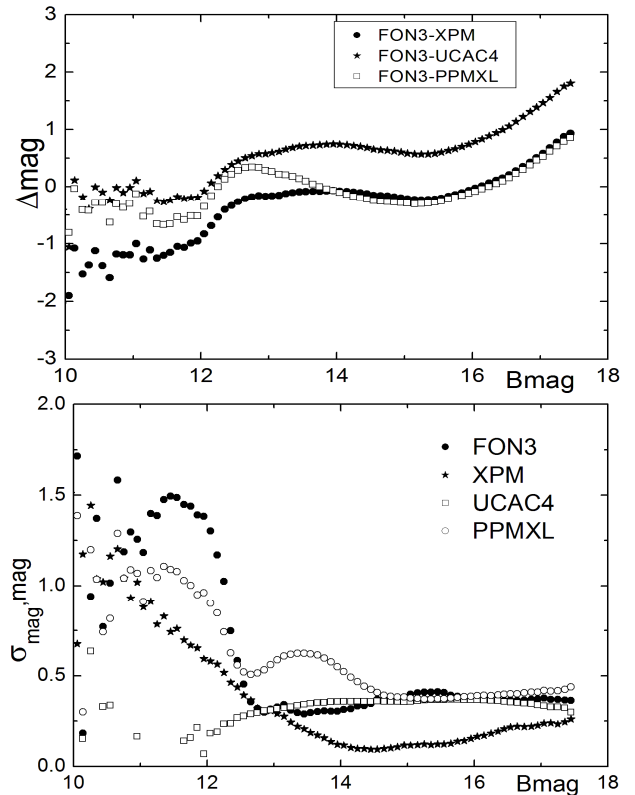


Figure 3: The systematic differences of the stellar magnitude FON3-XPM (black dots), FON3-UCAC4 (asterisks) and FON3-PPMXL (open rectangle) and their standard deviations obtained by method Wielen FON3 (black dots), XPM (asterisks), UCAC4 (open rectangle) and PPMXL (open circles) depending on the magnitude B of FON3 catalogue.

## 7. Conclusions

To summarize the work performed, we conclude the following.

The positions and photometry of FON3 stars were compared with same data of other modern astrometric catalogues.

The dispersion of positions and stellar magnitudes are calculated with the use of about 18 million common stars from FON3, XPM, UCAC4 and PPMXL catalogues.

The external accuracy of stars position of FON3 catalogue are good agreement with FON3 internal accuracy and equal 150 and 250 mas for brightest and faintest stars correspondingly.

The results that presented in this work are consistent with analysis of the random errors positions and stellar magnitudes that had been described by authors of FON3 catalog.

## References

- Andruk V. et al.: 2010, *Kinem. and Phys. of Cel. Bod.*, **26**, N3, 146.
- Andruk V. et al.: 2016, *Kinem. and Phys. of Cel. Bod.*, **32**, N5, 260.
- Fedorov P.N., Myznikov A.A., Akhmetov V.S.: 2009, *MNRAS*, **393**, 133.
- Fedorov P.N., Akhmetov V.S., Bobylev V.V., Gontcharov G.A.: 2011, *MNRAS*, **415**, 665.
- Vavilova I.B. et al.: 2012, *Kinem. and Phys. of Cel. Bod.*, **28**, N2, 85.
- Roeser S., Demleitner M., Schilbach E.: 2010, *AJ*, **139**, 2440.
- Wielen R., 1995, *A&A*, **302**, 613.
- Zacharias et al.: 2013, *AJ*, **145**, 44.

DOI: <http://dx.doi.org/10.18524/1810-4215.2016.29.85126>

## BALDONE SCHMIDT (LATVIA) TELESCOPE ASTROPHOTOS ARCHIVE

M. Eglite<sup>1</sup>, I. Eglitis<sup>2</sup>

<sup>1</sup>Institute of Astronomy, University of Latvia, 19 Raina blvd., Riga, LV-1586, Latvia,  
*eglitema@inbox.lv*

<sup>2</sup>Institute of Astronomy, University of Latvia, 19 Raina blvd., Riga, LV-1586, Latvia,  
*ilgmars@latnet.lv*

**ABSTRACT.** From 1967 to 2005, many astrophotos have been taken with the Baldone Schmidt telescope (80cmx120cmx240cm). These photos have being archived in the Institute of Astronomy of the University of Latvia (IAU code 069, longitude 24.4041 E, latitude 56.7734 N, altitude 103 m). There are over 22000 direct and 2300 spectral photos of different regions of the sky in this archive. There are also information on the photo materials type as well as the types of color filters used for photographing the sky fields and objects. The home page of the Institute of Astronomy's Baldone observatory ([www.baldoneobservatory.lu.lv](http://www.baldoneobservatory.lu.lv)) has the archive's description. Part of the description has also being published (Alksnis, et al., 1998).

**Keywords:** Schmidt telescope, wide field plate archive

### 1. Introduction

One of the main tasks of astronomers is to obtain observational data on various objects of the Universe and preserve these data for future use. The observational material subsequently forms the base for further studies and investigations. For over 100 years astronomers have gathered and stored photo collections on photographic glass and film photos. This has resulted to over 2 million wide field photos in Wide Field Imaging all over the world. From this quantity, more than 380000 of the wide field photos were taken with Schmidt telescopes (Tsvetkov et al., 1995). For more than 38 years, such an astronomical photo archive of photographic negatives, have been obtained with the Baldone Schmidt telescope. This is collected at the Astrophysical Observatory (IAU code 069) of the Institute of Astronomy, University of Latvia. The Baldone Schmidt telescope (80/120/240 cm) was first used in December 1996 on the hill Riekstkalns (longitude 24.4041 E, latitude 56.7734 N, altitude 103m) near Baldone city. The telescope ranges among the 12 biggest wide field Schmidt telescopes in the world (Table 1). By 2005, over 24300 photos have been taken with the Baldone Schmidt telescope.

### 2. Description of archive

The first astronomical photos were obtained in January 1967. The photos cover the field of 19 square degree, but the linear size of photoplates is 24x24 cm. Classically the scientific interests of the Latvian astronomers in the field of stellar astronomy were directed mainly to carbon stars. The implication was that most of the photos, both direct and spectral, obtained with the Baldone Schmidt telescope, covered the zone along the galactic equator, where the carbon stars are concentrated. The distribution of obtained direct and spectral photos, on the sky sphere, is presented in Figs. 1 and 2.

Table 1. The twelfth largest Schmidt-type telescopes in the world

Observatory	Aperture	From year	Country
Palomar	122	1947	U.S.A.
Bloemfontein	81	1950	South Africa
Hamburg-Calar Alto	80	1955	Germany-Spain
Tautenburg	134	1960	Germany
Byurakan	100	1961	Armenia
Kvistaberg	100	1964	Sweden
Baldone	80	1967	Latvia
La Silla	100	1969	ESO, Chile
Siding Spring	124	1973	Australia
Kiso	105	1974	Japan
Merida	100	1976	Venezuela
Calern	90	1976	France

Every photo taken with the Baldone Schmidt telescope has been taken in order to study a definite object and none stationary stars, especially carbon stars. Therefore, brightness and coordinates are only measured for these objects on the photos. On the average, about 95% to 99% of the information recorded on the photo remained unused. The glass and film photos are stored vertically in the rooms of the Schmidt telescope dome, which are no specially conditioned rooms, with temperature stabilization and less humidity. The photos are placed in original ORWO 24x24cm size plate standard packaging boxes.

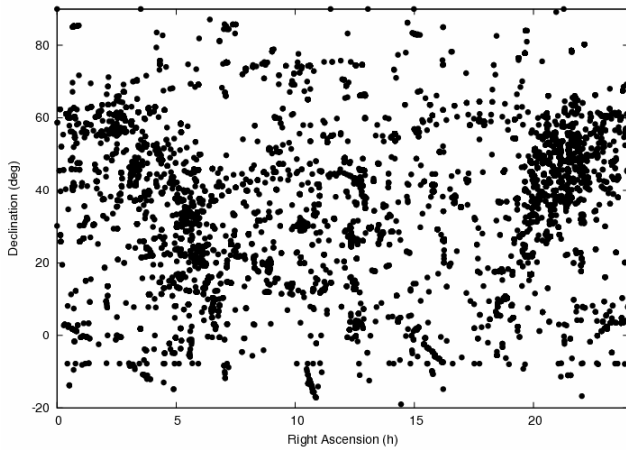


Figure 1: The distribution of the 22000 direct observations of the sky, made with the Baldone Schmidt telescope, in equatorial coordinates.

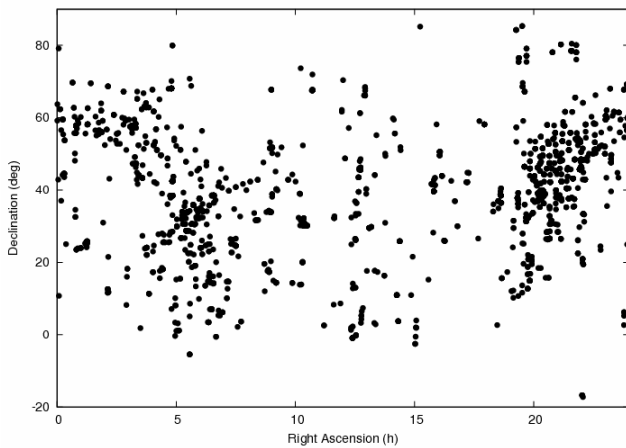


Figure 2: The distribution of the 2300 spectral observations of the sky, made with the Baldone Schmidt telescope, in equatorial coordinates.

The astroplates of the Baldone Schmidt telescope archive have been obtained mainly on the ORWO (East Germany) astronomical plates (Astro Platten ZU1, ZU2, ZU21, ZP1, ZP3). The plates have a size of 24x24cm. On the films (different versions of A500, A600, A700) of the Photographic Research Institute KAZNIIFOTOPROJEKT (Russia), most of the plates also have a size of 24x24 cm, while 1% have a size 13x18cm size. A small quantity is obtained on the Eastman Kodak mostly using IN plates in the USA.

For the stellar photometry the plates and light filters, were used. This provided a spectral sensitivity, close to the standard U, B, V system or the Becker's R- and Kron's I-magnitudes. In Table 2, the number (n) of direct photos taken with the emulsion type and filter combinations that is used most of the time, are listed.

The spectral photos have been obtained using 2 degree and 4 degree 80cm diameter objective prisms, which provide the resolution of about 200 and 450 at the hydrogen line H alpha respectively. For the searching of carbon stars, mostly the orthochromatic Kazan A600 astro films and the Kodak IN, infrared plates were used as detailed in Table 3.

Table 2. The combinations of the photo emulsions and filters used for the direct photos

Emulsion	Filter	n	Emulsion	Filter	n
	-			U	
ZU21	-	262	ZU21	UG1	337
ZU1	-	119	ZU2	UG1	229
ZP3	-	21	ZU21	UFS3	86
A500N	-	20	ZU1	UG1	62
	B			V	
ZU21	GG13	2783	A600N	ZS17	2102
ZU2	GG13	1692	A600	ZS17	1797
NT-1AS	GG13	337	A600U	ZS17	409
A500N	GG13	206	A600rP	ZS17	235
	R			I	
ZP1	RG1	7075	IN	KS19	877
ZP1	KS13	1692	IN	RG1+BG3	441
ZP3	RG1	764	I840	RG1	26
A700N	KS13	241	IVN	KS19	10

Table 3. The combinations of the photo emulsions and filters used for spectral photos

Emulsion	Filter	n	Emulsion	Filter	n
Blue spectrum			Yellow spectrum		
A600	GG13	98	A600	-	402
ZU2	-	68	A600N	GG5	167
ZU21	-	33	A600N	-	139
A600N	GG13	31	A600	GG5	134
Red spectrum			Near infrared spectrum		
103aF	-	123	IN	RG1	185
103aF	RG1	45	IVN	-	43
A700F	RG1	41	IN	-	37
A700N	-	37	I840	-	32

Many of the sky regions have been photographed tens and hundreds of times, in order to investigate variability of stars. The mostly photographed objects or regions are listed in Tables 4 for direct photos as well as the total number of photos (n) of the object obtained in 1967-2005.

Presently, the observational data and treated results are obtained in computer readable form, mainly online and stored in databases on the server of the Institute of Mathematics and Computer Science in University of Latvia ftp.e-spiets.lv. Nevertheless, the value of astronomical photo archives does not decrease. They contain information of the former changes in the optical range of cosmic objects at long time range. This information is very useful in current investigations and are therefore very relevant. This is more so, as the astronomers are gaining information in the whole range of the electromagnetic spectrum from gamma rays to radio waves.

### 3. Digitizing of archive

In the last 20 years, digitalization of astronomical information is taking place at a fast pace. From 2013, the regular digitization and processing of photographic astroplates started in Baldone observatory. The photos were digitized using Epson Expression 10000XL and 11000XL commercial scanners. The scanners had a resolution of 1200 dpi (or 2400 dpi). For processing, all images were transformed from TIFF format to the FITS format. This is achieved with an original program created at the Institute of Astronomy. Till this moment, more than 7000 photos

are digitized. Previously scans were tested, and the optimum mode of scanning was found (Protsyuk et al., 2014). Images were processed using advanced complex LINUX / MIDAS / ROMAPHOT programs (Andruk et al., 2015).

Scans are displayed on the server (ftp.e-spiets.lv) of the Institute of Mathematics and Computer Science in University of Latvia.

The digitizing of the UV-part of Baldone collection has started in June 2016 with two EPSON EXPRESSION 10000XL and three 11000XL flatbed scanners. Its photometric and astrometric characteristics were previously

The software was developed and implemented in Main Astronomical Observatory of the National Academy Science of Ukraine. The software is used to process the digitized astronomic photos as well as to obtain astrometric coordinates and photometric magnitudes of stars and compact galaxies.

Without these main tasks, the digitized photos of star fields allow to carry out a massive search for images of small bodies in the solar system. Furthermore, it allows for the determination of their coordinates. From the observations of earlier epoch, it is possible to extract information about the locations of these bodies (Eglitis et al., 2016).

Table 4. List of more observed objects in Baldone observatory from 1966 to 2005.

Object	n	Object	n	Object	n
CIT6	3164	IRC+20370	173	NGC 1817	91
Tr 2	831	Com.Halley	171	174,-3.5	91
M31	767	NGC 7419	169	CIT5	90
DY Per	440	V CrB	165	94,-10.5	89
BC 56	344	T Dra	144	NGC 2251	88
NGC 1245	300	IC 5146	142	CIT5+1245	87
90,-3.5	292	174,+7	139	NP Her	84
NGC 1664	287	94,+3.5	135	T Cnc+X Cnc	84
IRC+10216	262	94,0	134	Nova Cyg	79
NGC 7063	261	94,+7	131	Gal. II	77
86,+7	259	90,+3.5	129	NGC 7031	74
AFGL 2881	256	NGC 7092	125	U Cyg	74
Stock 4	254	NGC 1893	124	U Lyr	72
NGC 6871	243	CT Lac	124	NGC 659	72
94,-3.5	240	90,0	124	OW Aql	71
86,-7	234	94,+10.5	122	82,+7	69
NGC 7128	231	90,-7	122	82,+0	69
86,0	222	92,+6.5	121	RU Vir	68
86,-3.5	217	86,+10.5	120	CRL 3116	68
178,-7	210	94,-7	114	82,+3.5	66
86,+3.5	205	90,+1.3	114	Dol 2	64
178,+3.5	204	MQ Cyg	110	IC 1848	62
178,0	203	174,-7	107	Pluto	62
CIT6+SA54	199	174,0	107	82,-3.5	58
178,-3.5	183	174,+3.5	106	NML Tau	56
KL Cyg	180	NGC 457	103	82,-7	56
90,+7	180	SS Vir	98	NGC 7654	55
178,+7	175	BM Gem	96	V Cyg	55
NGC 7789	174	NGC 1528	94	EU And	54

#### 4. The electronic format of the plate archive

In Table 5, the description of the electronic format of the computer-readable catalogue at the link [www.baldoneobservatory.lu.lv](http://www.baldoneobservatory.lu.lv) is given. For more information on the Baldone Schmidt telescope plate archive contact e-mail: [astra@latnet.lv](mailto:astra@latnet.lv) or [ilgmars@latnet.lv](mailto:ilgmars@latnet.lv).

Table 5. The format of the plate archive.

Column heading	Bytes	Format	Units	Explanations
Plate No.	1-6	A6	---	Plate No.
Date	7-8	I2	y	Year
	9-10	I2	m	Month
	11-13	I2,1X	d	Day
	14-24	A11	---	Object
Object R.A.	25-27	I2,1X	h	Hours RA
	28-30	I2,1X	min	Minutes RA
	31-33	I2,1X	sec	Seconds RA
Object Dec.	34-37	I3,1X	o	Degrees Dec
	38-42	F4.1,1X	'	Minutes Dec
T exp. begin.	43-44	I2	h	Hours
	45-46	I2	min	Minutes
	47-49	I2,1X	sec	Seconds
T(exp)	50-53	I3,1X	min	Duration exp
Emulsion	54-60	A6	---	Emulsion type
Filter	61-67	A6,1X	---	Filter
System	68-69	A1,1X	---	System (Sp.Region)
Notes	70-71	A1,1X	---	Exposure
Notes	72-77	A6	---	Notes
Marker	78	A1	----	End of row

This investigation is supported by FP7 project „Nocturnal atmosphere”.

*Acknowledgements.* The Baldone Schmidt telescope photo archive could not be made without efforts of numerous staff members of the Baldone Astrophysical observatory. For the past 38 years or thereabout, the astronomers-observers, carried out observation of sky fields and other objects with the Schmidt telescope. The astronomers include A.Alksnis, I.Daube, L.Duncāns, I.Jurģitis, I.Platais, I.Pundure, A.Rudzinskis, P.Šimanskis, J.-I.Straume amongst others. Other staff members include laboratory assistants (I.Jurģitis, A.Birzvalks), who processed the exposed plates, assistants (Z.Jumiķe, M.Eglīte, V.Ozoliņa, D.Žaime), who copied the record book and made description on photos, and the technical staff (A.Avotiņš, J.Brenķis, V.Jumiķis, J.Kižla, G.Spulģis), who provided for the functioning of the telescope, assistants (V.Eglite, J.Kanopka) for major investment in digitizing astrophotos and researcher (V.Laposhka), who prepare programs for creating a virtual observatory needs.

#### References

- Alksnis A. et al.: 1998, *Baltic Astronomy*, **7**, 653.  
 Andruk V.M. et al.: 2015, [arxiv.org/abs/1512.05535](http://arxiv.org/abs/1512.05535).  
 Eglitis I. et al.: 2016, *Astroplate-2016, Prague*, In press.  
 Protsyuk Yu.I. et al.: 2014, *Odessa Astron. Publ.*, **27**, N1, 61.  
 Tsvetkov M. et al.: 1995, *PASP Conference Series*, **84**, 148.

DOI: <http://dx.doi.org/10.18524/1810-4215.2016.29.85128>

## OBTAINING POSITIONS OF ASTEROIDS FROM DIGITIZED PROCESSING OF PHOTOGRAPHIC OBSERVATIONS IN BALDONE OBSERVATORY (CODE 069)

I. Eglitis<sup>1</sup>, M. Eglite<sup>1</sup>, S.V. Shatokhina<sup>2</sup>, V.M. Andruk<sup>2</sup>

<sup>1</sup>Baldone Observatory, Institute of Astronomy, University of Latvia,  
Raina blvd. 19, Riga, LV 1586, Latvia, [ilgnars@latnet.lv](mailto:ilgnars@latnet.lv), [eglitema@inbox.lv](mailto:eglitema@inbox.lv)

<sup>2</sup>Main Astronomical Observatory of National Academy of Sciences,  
27 Akad. Zabolotnogo St., 03680, Kyiv, Ukraine, [svetash@mao.kiev.ua](mailto:svetash@mao.kiev.ua),  
[andruk@mao.kiev.ua](mailto:andruk@mao.kiev.ua)

**ABSTRACT.** Digital processing of photographic plates of star fields allows to determine with high accuracy the coordinates and stellar magnitudes for all registered objects on these plates. The processing results can be used for a broad search for images of small bodies of the Solar system and determination of their coordinates. From the observations of earlier epoch, we can extract information about the locations of these bodies well before discovering them. Modern approach to processing early photographic observations with new technologies can be an effective instrument for rediscovery of asteroids and correction their orbits. We analyzed the results of digital processing of observations of clusters in UBVR bands which were made on the 1.2-m Schmidt telescope of the Observatory of Institute of Astronomy of University of Latvia in Baldone (code 069). As a result 87 images of minor planets from 9.8 to 17.1 stellar magnitude and 2 images of comets were identified on 152 plates for 1967-1996. The catalogue of positions and stellar magnitudes of the searching asteroids was compiled. Among them 12 observations of asteroids are the earliest of the world's known observations of these asteroids. All positions of asteroids were compared with the ephemeris JPL DE431. Analysis was carried out.

**Keywords:** photographic archive – asteroids – catalogs – astrometric positions

### 1. Introduction

Baldone Observatory of Institute of Astronomy of Latvian University has the photographic collection more than 22000 plates obtained using 1.2 m Schmidt telescope (Eglitis et al., 2016d). The observational period started in 1966 and lasted for 39 years. The area of the sky, covered by a single plate is approximately 19 square degree and contains from 10 000 to 50 000 images of different celestial objects. The plate scale is of 72 "/mm. The observations were carried out with various filters and emulsions of astroplates. Combining emulsion ORWO ZU1 (ZU2 or ZU21 or Kodak 103aO or IIaO) with UG1 filter realizes U photometric band. Combining emulsion ORWO ZU2 (ZU21) with GG13 filter realizes B photometric band. Combining emulsion A600 with ZS17 filter or emulsion ORWO ZP1 with filter RG1 realizes V or R photometric band respec-

tively. As a result, photographic observational archive of Baldone observatory has about 700 U-plates, 5000 B-plates, 4500 V-plates and more than 10000 R-plates.

### 2. Results

From 2013 year the regular digitization and processing of photographic astroplates started in Baldone observatory. The plates were digitized using Epson Expression 10000XL and 11000XL commercial scanners with the resolution 1200 dpi (or 2400 dpi). For processing all images were transformed to the FITS format through GIMP ([www.gimp.org](http://www.gimp.org)) software packages and ImageMagic ([www.imagemagick.org](http://www.imagemagick.org)). Standard images were processed using advanced complex LINUX / MIDAS / ROMAPHOT programs. The software was developed and implemented in MAO NASU to process the digitized astronomic negative plates as well as to obtain the final product in the form of a catalogue of positions and stellar magnitudes for all registered objects on the plate. In detail, the process of digitization of images and their further processing and determination of coordinates and magnitudes are described in the series of publications (Andruk et al., 2005; 2007; 2010; 2014; 2015; 2016; Protsyuk et al., 2014a; 2014b). The results of the software testing are described in (Kazantseva et al., 2015; Yizhakevych et al., 2014; 2015; Protsyuk et al., 2014; Andruk et al., 2013).

Approbations of this software are the catalogs of stars coordinates and U-magnitudes and Pluto's positions received from observations in Baldone (Eglitis et al., 2016a; 2016c). The equatorial coordinates  $\alpha$ ,  $\delta$  and stellar magnitudes of all objects on the plates were obtained in the reference system of Tycho-2 at the epoch of exposition of each plate. Photographic  $U_{ph}$ -magnitudes of objects were calibrated with photoelectric  $U_{pe}$ -magnitudes.

The processing results of 152 observations of clusters and Pluto in UBVR bands in 1967-1996 were used for broad search for images of small bodies of the Solar system. As a result, 57 asteroids and 2 comets (31P/Schwassmann-Wachmann 2, C/1969 T1 (Tago-Sato-Kosaka)) were identified on these plates. From them 87 positions of asteroids and 2 positions of comets were received. These objects cover magnitude range from 9.8 to 17.1. All of them have orbit types: Main Belts, Hungarias and Mars-crosser.

Table 1 shows the number of asteroid's positions on all used plates with U, B, V, R filters. Figure 1 shows the distribution of all searching asteroids for all used plates and U-, B-, V-, R- plate's individual contribution in searching. More faint asteroids were identified only on astroplates with V, R filters.

For 33 U-plates the rms-error of coordinates of reduction to reference system is 0.10 arcsec for both coordinates. The rms-error of U-magnitude of calibration with photoelectric  $U_{pe}$ -magnitudes is 0.19. For single B, V, R-plates the accuracy values are presented in (Eglitis et al., 2016b). For several astroplates the digitizing six times in a row and further processing were performed to determine the accuracy of measurements of coordinates and magnitudes. According data analysis, the rms-error of measurements of coordinates increases to 0.25 arcsec with increasing asteroid's magnitude from 13 to 16 (Eglitis et al., 2016b).

Table 1. Astroplates used from Baldone astroplate archive.

Number of plates	Filter	Period of observations	Total number of positions of asteroids identified on plates	Number of positions of asteroids identified before discovering dates
143	U	1967-1987	45	9
7	B	1969-1996	16	2
1	V	1973	10	7
1	R	1973	16	12
$\Sigma=152$			87	30

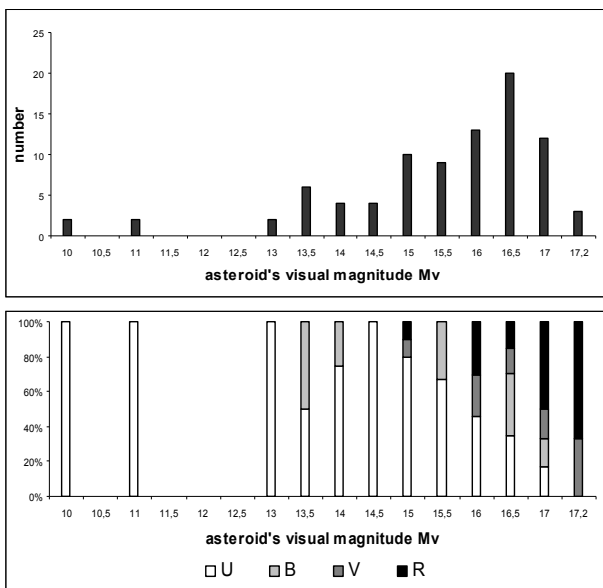


Figure 1: Distribution of all searching asteroids (top figure) and individual contribution U, B, V, R -plates (lower figure)

Full catalog of coordinates  $\alpha$ ,  $\delta$  and magnitudes of 87 positions of asteroids is given at <http://baldonesobservatorija.lv>. The comparison with the JPL DE431 ephemeris (<http://ssd.jpl.nasa.gov/horizons>) is given. 30 positions of asteroids from total searching quantity were observed many years before their discovering dates. Equatorial coordinates  $\alpha$ ,  $\delta$  and stellar magnitudes U (or B, or V, or R) and O-C differences in both coordinates, and U-Mv (B-Mv, V-Mv, Mv-R), where U – ultraviolet, B – blue, V – visual, R – red observed magnitudes, Mv -approximate visual asteroid's magnitude calculated by ephemeris JPL, presented in the Table 2. But 12 positions of asteroids in this table have the earliest chronologically observations among all known in the world. With bold font pointed these observations in this table. For several asteroids (31527, 2356, 2078) the distributions of all known observations in the world are presented on figures 2a,b,c. Observational data took from Minor Planet Center ([http://www.minorplanetcenter.net/db\\_search](http://www.minorplanetcenter.net/db_search)). With bold black color pointed observation in Baldone.

### 3. Conclusion

On photographic plates of Baldone Observatory can be detected asteroids with high accuracy up to 16-17 magnitude. Among those may be objects which discovered much later than observed. The presence of the archive of all observations in time scale 1966-2002 will give possibilities to select and process the interesting asteroids, including the bright Kuiper Belt objects. Cooperation with Ukrainian Virtual Observatory gives the opportunity to expand this work, involving numerous additional files of observations and, ultimately, to increase the number of new original positions. From this view Baldone observatory could compete with modern observations. A necessary condition for obtaining high-precision series of observations of asteroids is the presence of a confident moment of observations.

This investigation is supported by FP7 project „Nocturnal atmosphere”.

### References

Andruk V.M. et al.: 2005, *Kinematics and Physics of Celestial Bodies*, **21**, N5, 396.  
 Andruk V.M. et al.: 2007, *Journal of Physical Studies*, **11**, N3, 329.  
 Andruk V.M. et al.: 2010, *Kinematics and Physics of Celestial Bodies*, **26**, N3, 75.  
 Andruk V.M. et al.: 2013, *Odessa Astron. Publ.*, **26**, N2, 226-228.  
 Andruk V.M. et al.: 2014, *Odessa Astron. Publ.*, **27**, N1, 53.  
 Andruk V.M. et al.: 2015, 2015arXiv, In press.  
 Andruk V.M. et al.: 2016, *Kinematics and Physics of Celestial Bodies*, **32**, N1, 56.  
 Eglitis I. et al.: 2016a, Astrometry and photometry of Pluto from digitized photographic observations during 1961 to 1996, <http://www.astroplate.cz/abstracts>  
 Eglitis I. et al.: 2016b, Asteroids from digitized processing of photographic observations in Baldone, <http://www.astroplate.cz/abstracts>  
 Eglitis I. et al.: 2016c, U-magnitudes of stars and galaxies from the digitized astronegatives of Baldone Schmidt telescope, <http://www.astroplate.cz/abstracts>

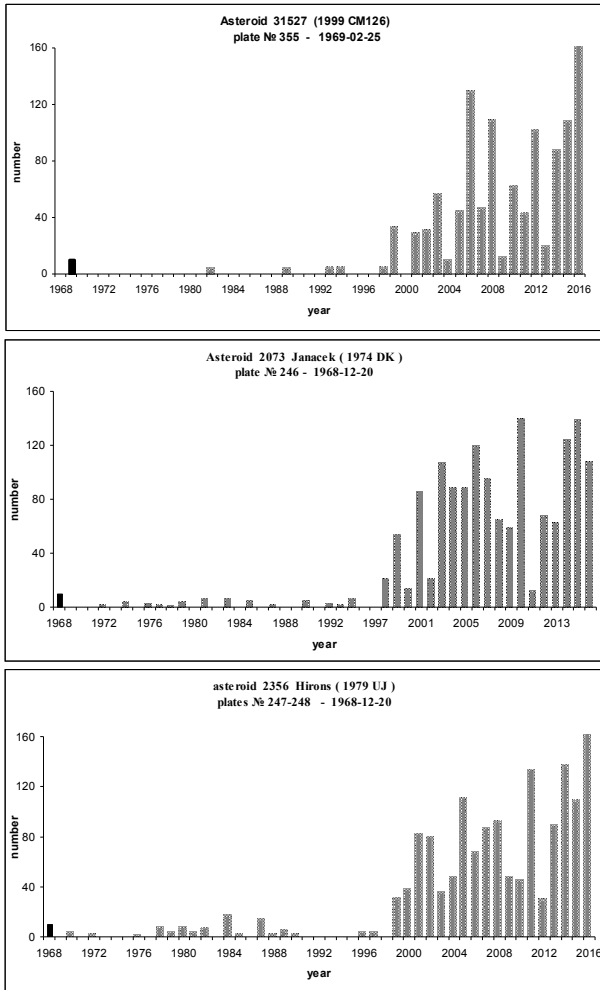


Figure 2a,b,c: Distributions on time scale of all known observations in the world for 31527, 2078, 2356 asteroids. With bold black color pointed observation in Baldone.

Table 2. Asteroids observed in Baldone before their discovering dates.

Object number name	RA, J2000.0 h m s	Dec, J2000.0 deg ' "	Magnitude	(O-C) <sub>RA</sub> arcsec	(O-C) <sub>Dec</sub> arcsec	U-Mv or B-Mv or Mv-R
Plate 26 (UT=1967-04-28.880787)						
2048 Dwornik (1973 QA)	121557.635	+265627.19	16.66 U	-.85	.03	.37
Plate 38 (UT=1967-05-12.878773)						
2048 Dwornik (1973 QA)	121521.343	+270852.92	-	-.55	-.89	-
Plate 246 (UT=1968-12-20.939583)						
2073 Janacek (1974 DK)	055815.208	+234757.40	16.04 U	-.96	.62	.59
2521 Heidi (1979 DK)	061008.994	+254139.11	16.22 U	.53	.13	.97
Plate 247 (UT=1968-12-20.961805)						
2356 Hiron (1979 UJ)	064122.935	+010604.39	16.75 U	.16	-.19	.95
Plate 355 (UT=1969-02-25.103587)						
31527 (1999 CM126)	123431.805	+264334.75	16.16 B	.03	-.58	-.29

Plate 2492 (UT=1973-01-01.869005)						
1964 Luyten (2007 P-L)	060210.229	+205211.52	16.94 V	-.57	-.23	1.13
2222 Lermontov (1977 ST1)	055721.505	+232045.48	14.22 V	-.51	-.67	-.59
4095 Ishizuchisan (1987 SG)	060542.953	+215512.14	15.87 V	-.75	.15	-.64
5588 Jennabelle (1990 SW3)	061027.128	+234945.76	16.50 V	.04	-2.00	.03
8260 (1984 SH)	060916.957	+215506.72	18.25 V	-.33	.60	1.27
14221 (1999 WL)	055455.643	+223031.62	16.36 V	.22	.09	-.11
26629 Zahller (2000 GZ132)	055505.199	+225921.89	16.88 V	.96	-.86	-.23
Plate 2496 (UT=1973-01-01.883241)						
1964 Luyten (2007 P-L)	060209.360	+205211.31	14.68 R	-.64	.17	1.13
2222 Lermontov (1977 ST1)	055720.803	+232046.92	13.56 R	.17	-.17	1.25
4095 Ishizuchisan (1987 SG)	060541.979	+215511.04	14.80 R	.04	-.15	1.71
5588 Jennabelle (1990 SW3)	061026.231	+234951.53	14.98 R	-.44	.23	1.50
5877 Toshimaihara (1990 FP)	055150.141	+232721.98	15.25 R	1.03	-.36	1.38
7346 Boulanger (1993 DQ2)	055557.298	+211840.79	15.40 R	.45	.10	1.38
8260 (1984 SH)	060915.903	+215507.20	16.67 R	-.70	-.18	.31
11974 Yasuhidefujita (1994 YF)	060111.237	+214944.57	15.63 R	.32	-.16	1.43
14221 (1999 WL)	055454.716	+223035.14	15.62 R	.56	-.06	.85
16506 (1990 UH1)	060319.833	+245725.71	14.57 R	.54	-.27	1.35
22282 (1985 RA)	061122.090	+233152.17	15.33 R	-.42	.17	1.21
26629 Zahller (2000 GZ132)	055504.277	+225918.46	16.12 R	.37	.23	.99
Plate 3511 (UT=1974-03-12.886782)						
2659 Millis (1981 JX)	060658.341	+222218.86	16.59 B	.38	1.06	-.18
Plate 4318 (UT=1975-05-08.893865)						
6785 (1990 VA7)	102220.190	+311948.67	16.52 U	-1.07	.16	.08
Plate 5912 (UT=1976-12-24.155115)						
3024 Hainan (1981 UW9)	102328.384	+285515.06	17.36 U	.37	.44	.67
Plate 15652 (UT=1987-03-24.954630)						
5914 Kathywhaler (1990 WK)	122048.075	+122110.13	17.13 U	.52	-.41	.70
Plate 15661 (UT=1987-03-25.929259)						
7472 Kumakiri (1992 CU)	123316.961	+131747.44	16.16 U	.35	.09	.28

Eglitis I. et al.: 2016d, *Odessa Astron. Publ.*, **29**, In press.  
 Kazantseva L.V. et al.: 2015, *Kinematics and Physics of Celestial Bodies*, **31**, **N1**, 37-54.  
 Protsyuk Yu.I. et al.: 2014, *Odessa Astron. Publ.*, **27**, **N1**, 61.  
 Protsyuk Yu.I. et al.: 2014, *Odessa Astron. Publ.*, **27**, **N1**, 59.  
 Yizhakevych O. et al.: 2014, *Odessa Astron. Publ.*, **27**, **N1**, 67.  
 Yizhakevych O. et al.: 2015, *Odessa Astron. Publ.*, **28**, **N2**, 213.

DOI: <http://dx.doi.org/10.18524/1810-4215.2016.29.85131>

## UV-PHOTOMETRY WITH THE 1.2 M SCHMIDT TELESCOPE IN BALDONE

I.Eglitis<sup>1</sup>, M.Eglite<sup>1</sup>, L.K.Pakuliak<sup>2</sup>, V.M.Andruk<sup>2</sup>

<sup>1</sup>Institute of Astronomy, University of Latvia, 19 Raina blvd., Riga, LV-1586, Latvia, [ilgmars@latnet.lv](mailto:ilgmars@latnet.lv)

<sup>2</sup>Main Astronomical Observatory of the National Academy of Sciences of Ukraine  
27 Akademika Zabolotnoho St., 03680 Kyiv, Ukraine, [andruk1058@ukr.net](mailto:andruk1058@ukr.net)

**ABSTRACT.** The University of Latvia's Institute of astronomy possesses a collection of 22 thousand photographic plates taken by the 1.2 m Schmidt telescope located at the Baldone observatory. Among others, there are 767 astro-negatives in this collection obtained in 314 sky areas using the Johnson U-filter. The field of view of each negative covers 19 square degrees. The plate scale is 72"/mm. The digitizing of the UV-collection has started in June 2016 with EPSON EXPRESSION 10000XL flatbed scanner. The general aim of the digitizing is to obtain UV-magnitudes and positions of all objects registered on the plates. Up to date near a half of the UV-collection is digitized. 24 digitized MEGA program plates of the collection were used for the preliminary investigation of the quality of photographic material and scanner systematic behavior. The catalog of positions and UV-magnitudes of 68.784 stars and galaxies for 12 regions allows evaluating the expected accuracy of the whole observed material. The estimated accuracy for all objects is  $\sigma_{\alpha\delta} = \pm 0.28''$  and  $\sigma_U = \pm 0.20^m$  for positions and brightness respectively. For the stars with  $U = 8^m - 14^m$  these errors are  $\sigma_{\alpha\delta} = \pm 0.11''$  and  $\sigma_U = \pm 0.09^m$ . The convergence of coordinates with respect to the coordinates of the reference system Tycho2 is  $\sigma_{\alpha\delta} = \pm 0.06''$ . The conformity with photoelectric Upe-magnitudes is  $\pm 0.13^m$ .

**Keywords:** digital image processing, ultraviolet, star catalogues

### 1. Introduction

The fields of interest of wide band UV-photometry used to be the vicinity of flare stars (or the supernova), the fields of active galaxy nuclei, the star formation regions, the fields of clusters, the dwarf nova, quasars and black holes (Wils, 2010; Krawchuk, 2013). However, UV photometric observational data are considerably less than those derived in the blue, visible and infrared spectral ranges as it is clear from the VisieR database collection of catalogs and publications.

Baldone Observatory of Institute of Astronomy, Latvian University possesses the photographic collection of 22 000 astroplates obtained using 1.2 m Schmidt telescope (Eglitis, 2016). The observational period started in 1966 and lasted for 39 years. The area of the sky, covered by a single plate is approximately 19 square degrees and contains from 10 000 to 50 000 images of different celestial objects. The

image scale is of 72 "/mm. Plates were obtained with two exposures of different duration with the shift of the telescope between them along both coordinates.

The digitizing of the UV-collection has started in June 2016 with EPSON EXPRESSION 10000XL flatbed scanner. Its photometric and astrometric characteristics were previously tested, and the optimum mode of scanning was found. Results of testing are given in (Protsyuk, 2014a; 2014b). Note, that random positional and photometric errors of the scanner for 1.2 m Schmidt telescope are 0.04" and 0.015<sup>m</sup> correspondingly.

### 2. Sequence of plate image processing

Next processes of digitized negatives' processing are tested in the series of works and were realized in catalogs of celestial objects (Protsyuk, 2014c, Kazantseva, 2015, Yizhakevych, 2015, Andruk, 2016a, Andruk, 2016b):

1. Preliminary image processing in MIDAS/ROMAFOT software to obtain pixel coordinates X, Y and instrumental estimations of magnitudes of fixed objects.
2. Separation of objects into sets of two expositions for each plate.
3. Selection of Tycho-2 reference stars' set into reference file for each plate.
4. The preliminary solution of equations for rectangular and equatorial coordinates of the set of reference stars.
5. Correction of the rectangular coordinates of objects for the scanner systematic errors.
6. The reduction of rectangular coordinates X, Y of all fixed objects into the Tycho-2 reference system.
7. The reduction of instrumental photometric estimations to the Johnson photoelectric  $U_{pe}$  magnitudes.

The detailed description of the above said procedures is given in (Andruk, 2015).

### 3. Astrometric reduction into Tycho2 reference system

For all plates the reduction model was represented in the form of complete polynomials of the 6-th degree, supplemented by the members of the equation accounting the effects of coma, distortion, and magnitude equation (Andruk, 2016a; Eglitis, 2016a). The results of the astro-

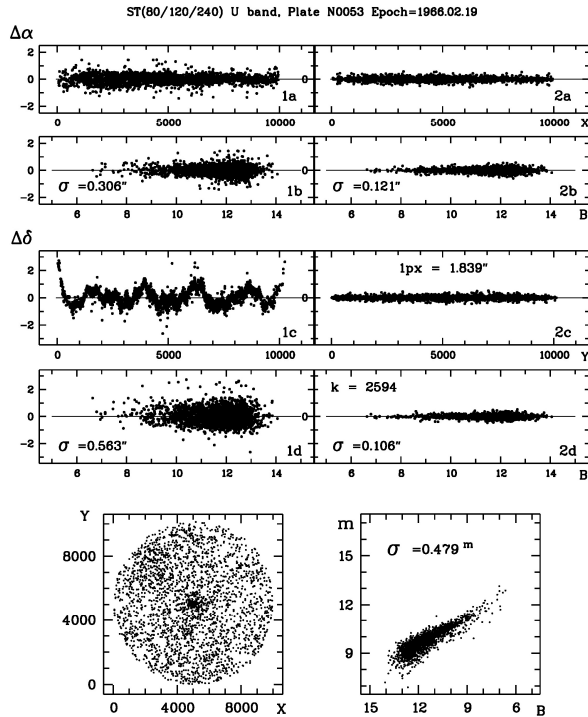


Figure 1: The results of the astrometric reduction into Tycho-2 system.

metric reduction are shown in Fig.1. The epoch of the plate is 1966.02.12. Left and right panels show the differences of equatorial coordinates  $\Delta\alpha$ ,  $\Delta\delta$  before and after the corrections for the systematic errors of the scanner. The differences of coordinates are represented in relation to pixel coordinates X,Y, and B-magnitudes from Tycho2. The lower panel depicts the distribution of Tycho2 stars over the field of the plate (on the left) and the connection of instrumental photometric m-values and B-magnitudes of Tycho2 (on the right).

#### 4. Photometric reduction into the photoelectric U-magnitudes

The data from (Andruk, 1995; 1996a; 1996b; 1996c; Relke, 2015) catalogs were used for the calibration of characteristic curves, accounting for the photometric error across the field of view and the reduction of instrumental photometric values into Johnson photoelectric  $U_{pe}$  magnitudes. Characteristic curves were restored using photometric data of both exposures. The approximation of characteristic curves and derivation of photographic magnitudes  $U_{ph}$  ( $U = U_{ph}$ ) for 24 plates were made by rms solution of the system of equations in the form of polynomials of the 5<sup>th</sup> degree. These equations describe the functional view of a characteristic curve with the members of equations accounting photometric error across the field of view (Andruk, 2016a; Eglitis, 2016a). The results of the photometric reduction for astronegatives with two exposures are represented in Fig. 2.

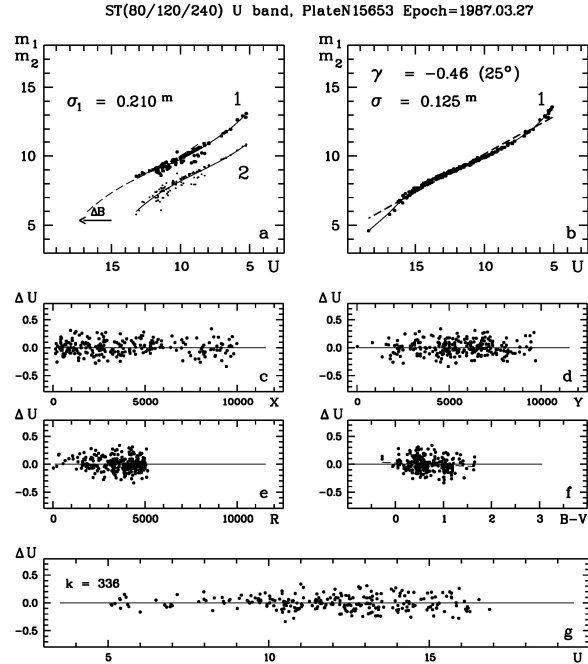


Figure 2: The results of the photometric solution for plates with two expositions.

Here, the steps of the characteristic curve restoration are depicted (a,b). Panels c-g show the differences  $\Delta U$  between U-magnitudes of stars calculated by characteristic curve and their photoelectric values.  $\Delta U$  are given in relation to coordinates X and Y, distances from the center of the plate R, color index B-V and photoelectric U-magnitudes.

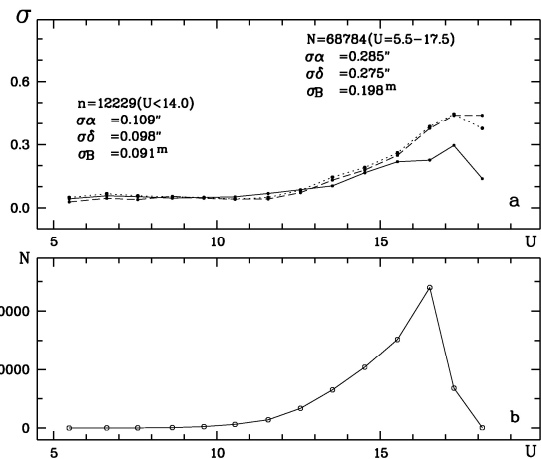


Figure 3: The trend of the internal errors for positions  $\sigma\alpha$ ,  $\sigma\delta$  and magnitudes  $\sigma U$  with U-magnitude (panel a) and the histogram of the distribution of the number of objects with U-magnitudes.

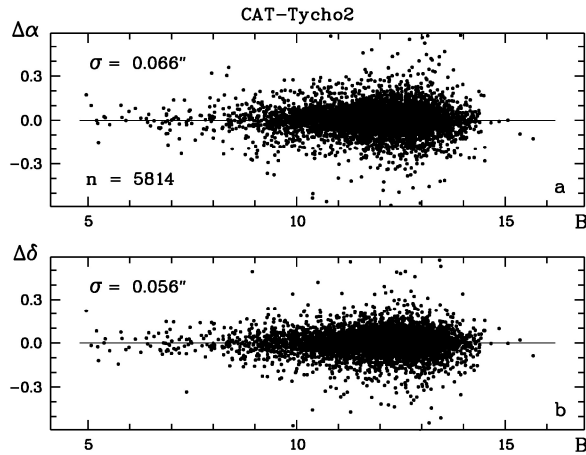


Figure 4: Positional errors for Tycho-2 stars in relation to B magnitudes from Tycho-2.

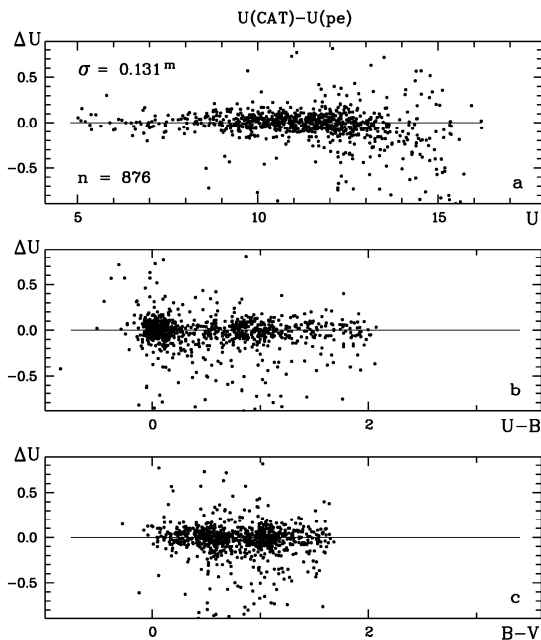


Figure 5: The comparison of derived U-magnitudes with photoelectric ones.

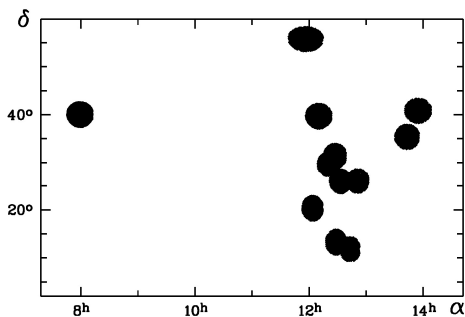


Figure 6: The distribution of 12 areas of MEGA program on the sky.

## 5. Catalog of U-magnitudes of MEGA program

After the treatment of 24 plates of MEGA program exposed in Baldone by 1.2 Schmidt telescope in U band, the catalog of positions and U-magnitudes for 68 784 stars and galaxies in 12 sky areas was made. Positions of objects are obtained in the system of Tycho-2, U-magnitudes are represented in the system of photoelectric standards. The internal accuracy for all objects is  $\sigma_{\alpha\delta} = \pm 0.28''$  and  $\sigma_U = \pm 0.20^m$ . For stars in the range of magnitudes  $U = 8^m - 14^m$  the correspondent errors are  $\sigma_{\alpha\delta} = \pm 0.11''$  and  $\sigma_U = \pm 0.09^m$  (Fig.3). The convergence of coordinates with the Tycho-2 reference system shown in Fig.4 is  $\sigma_{\alpha\delta} = \pm 0.06''$  (for 5 814 stars). The convergence with photoelectric  $U_{pe}$  magnitudes is  $\sigma_B = \pm 0.13^m$  (for 876 stars). The results of the comparison are given in Fig.5. The distribution of areas on the celestial sphere is represented in Fig.6.

## 6. Conclusion

For astronegatives with 2 exposures, the programing technique of characteristic curve restoration is developed and implemented for the creation of the catalog of positions and UV magnitudes of stars and galaxies. As a part of the UV collection is obtained with 1 exposure, it is necessary to find an empirical or analytical relation between measured and reference values of magnitudes in the case of absence of photoelectric standards in the section of extremely faint stars.

This investigation is supported by FP7 project „Nocturnal atmosphere”.

## References

- Andruk V. et al.: 1995, *Astron. Nachr.*, **316**, N4, 225.
- Andruk V.M. et al.: 1996a, *Astron. Nachr.*, **317**, N2, 49.
- Andruk V.M. et al.: 1996b, *Astron. Nachr.*, **317**, N2, 127.
- Andruk V.N.: 1996c, *Kinematic and Physics of Celestial Bodies*, **12**, N4, 60.
- Andruk V.M. et. al.: 2005, *Kinem. i Fizika Nebesn. Tel. Supl.* **N5**, 544 (in Ukraine).
- Andruk V.M. et al.: 2015, [arxiv.org/abs/1512.05535](https://arxiv.org/abs/1512.05535).
- Andruk V.M. et al.: 2016a, *Kinem. Phys. Cel. Bodies*, **32**, N1, 38.
- Andruk V.M. et al.: 2016b, *Kinem. Phys. Cel. Bodies*, **32**, N5, 261.
- Eglitis I. et al.: 2016a, *Astroplate-2016, Prague*, In press.
- Eglitis I. et al.: 2016b, *Odessa Astron. Publ.*, **29**, In press.
- Kazantseva L.V. et al.: 2015, *Kinem. Phys. Cel. Bodies*, **31**, N1, 58.
- Krawczyk C. et al.: 2013, *ApJ Suppl*, **206**, 1, 19.
- Protsyuk Yu.I. et al.: 2014a, *Odessa Astron. Publ.*, **27**, N1, 61.
- Protsyuk Yu.I. et al.: 2014b, *Odessa Astron. Publ.*, **27**, N1, 63.
- Protsyuk Yu.I. et al.: 2014, *Kinem. Phys. Cel. Bodies*, **30**, N6, 54.
- Relke E. et al.: 2015, *Odessa Astron. Publ.*, **28**, N2, 211.
- Yizhakevych O. et al.: 2015, *Odessa Astron. Publ.*, **28**, N2, 213.
- Wils P. et al.: 2010, *MNRAS*, **402**, 1, 436.

DOI: <http://dx.doi.org/10.18524/1810-4215.2016.29.85136>

## STARS WITH HIGH PROPER MOTIONS IN THE MODERN CATALOGS OF THE CDS DATABASE

V. F. Kryuchkovskiy, N. V. Maigurova

Research Institute "Mykolaiv Astronomical Observatory" (RI MAO)  
54030, Nikolaev, st. Observatornaya 1, selenion@yandex.ua

**ABSTRACT.** Stars with high proper motions, for the most part, are objects located in the solar neighborhood within 100 parsecs. These stars are important targets for a wide range of astrophysical problems, but the accuracy of the results depends on the completeness of the star samples. The uniform distribution over the celestial sphere is also important for kinematic studies. There are two catalogs of the fast stars in northern hemisphere, while only scattered lists of such stars are available for southern hemisphere. This paper presents the results of analysis of samples of stars with proper motions exceeding 150 mas/year from the modern catalogs of astronomical database CDS (PPMXL, SPM4, UCAC4, XPM, APOP, LSPM, Tycho2, URAT1 and WISE). Results of pairwise mutual cross-identification of the samples have shown that modern astrometric catalogs contain a significant number of false identifications of stars with large proper motions, and the total number of common stars in the resulting samples is extremely small and is not more than 20% on average.

**Keywords:** astronomical database, astronomical catalogs, stars: high proper motions stars

### 1. Introduction

Currently there are only a few ad hoc catalogs with the high proper motions (HPM) submitted in Strasburg database.

The most complete catalogs of stars with proper motions are the LSPM catalog based on the results of DSS scans from Palomar Sky Surveys (POSSI and POSSII) (Lepine et al., 2005) and compiled catalog **HPM-v2** maintained by the Main Astronomical Observatory of the National Academy of Sciences of Ukraine (Ivanov, 2008).

Both catalogs contain only stars in the Northern Hemisphere. The LSPM catalog contains 61 977 stars up to 21<sup>m</sup> with proper motions of more than 150 mas/yr. The catalog is 98% full for the stars up to 19<sup>m</sup>. The **HPM-v2 catalog** is created on the **FONAK 1.0** (Kislyuk et al., 1999) proper motions and 770 other available astronomical catalogs and sources. The catalog contains information about 618 238 stars with proper motions more than 40 mas/yr up to 16<sup>m</sup>. The limiting magnitude up to 17<sup>m</sup> for stars belong to double or multiple system.

The **NLTT Catalogue** (Luyten, 1980) and **Revised NLTT Catalog** (Salim, 2003) are catalogs that cover whole celestial sphere. **NLTT Catalogue** contains 58 845 stars with proper motions more than 200 mas/yr. **Revised NLTT Catalog** include 36 085 stars over whole sky, but

these catalogs are not complete and their stars are unevenly distributed over the sky (see Figure 1).

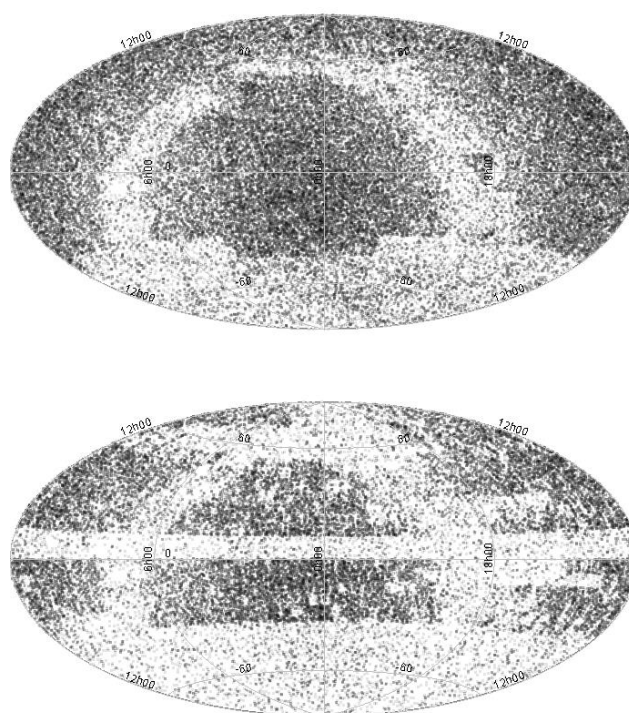


Figure 1: Distribution stars of the **NLTT** (up) и **Revised NLTT** (down) over celestial (Aitoff projection, equatorial coordinate system)

Over the last twenty years some large catalogs with stars proper motions become available for studies. Table 1 is given the catalog list that can be used for search and selection data with high proper motions stars. The list of catalogs in table 1 includes also catalog ALLWISE (Cutri et al., 2013). In this catalog, there are no proper motions. We used “d2M” field (distance separating the positions of the WISE source and associated 2MASS PSC (Cutri et al., 2003) source) for selection HPM stars. Since the mean observational epoch of WISE survey is 2010.55, only stars in range from 1.5” to 3.0” were chosen. The value 3.0 is declared as a maximal value which is used for cross-identification between 2MASS and ALLWISE data.

Table 1. Input catalogs.

Catalog, year	Limit Mag	Number of stars	Declination
LSPM, 2005	V 19.0	61 977	+0° — +90°
HPM-v2, 2008	V 16	618 238	-2.5° — +90°
APOP, 2015	R 20.8	100 774 150	-90° — +90°*
Tycho2, 2000	V 11.5	2 539 913	-90° — +90°
PPMXL, 2010	V 20	910 469 430	-90° — +90°
SPM4, 2011	V 17.5	103 319 647	-90° — -20°
UCAC4, 2012	R 16	113 780 093	-90° — +90°
URAT1, 2015	R 18.5	228 276 482	-24.8° — +90°
XPM, 2011	B 19	313 610 083	-90° — +90°
ALLWISE, 2013	W 17.1	747 634 026	-90° — +90°

\* - Except for  $\pm 20^\circ$  from Galactic Equator

## 2. Processing and Results

At the first stage samples of stars with proper motions more 150 mas/yr were selected from HPM-v2 catalog. Then cross-identification between HPM-v2 and LSPM catalogs in common declination zone were made. The size of search window was 1". The number of common stars was only 17 435. The distribution of HPM stars from **HPM-v2** (41 550 stars), **LSPM** (61 515 stars) and their common stars over celestial sphere are given in Figure 2. As can you see, if the initial samples have demonstrated conspicuous concentration of stars in the plane of the galactic equator then the distribution of the common stars is rather uniformly. Possible reasons for this fact are the difficulties in cross-identifying of the fields with high density of stars and large errors of the star proper motions in this region.

Table 2. Number of high proper motion stars.

Catalog	Number of stars with $PM \geq 150 \text{ мсд/год}$		
	All	$0 \leq \delta \leq 90$	$-90 \leq \delta < 0$
LSPM	61 977	61 977	0
Hpm-v2	41 550*	40 034	1 516
APOP	21 499	5 894	15 605
Tycho2	16 673	8 202	8 471
PPMXL	75 628 403	24 416 790	51 211 613
PPMXL*	5 679 268	1 869 585	3 809 683
SPM4	212 685	—	212 685
UCAC4	968 245	59 319	908 926
URAT1	690 982	547 135	143 847
WISE	11 902 471	4 263 856	7 638 615
XPM	4 272 089	144	4 271 945

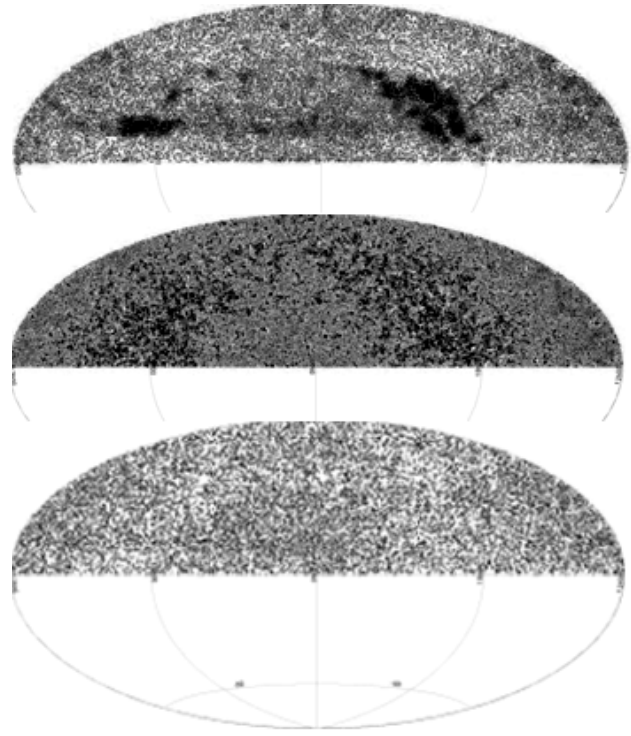


Figure 2: The distribution of HPM stars from **HPM-v2** (1), **LSPM** (2) and their common stars over celestial sphere (Aitoff projection, equatorial coordinate system).

At the next stage the samples with HPM stars were selected from the modern astrometric catalogs listed in the table 1. The table 2 contains the results of this selection separately for Northern and Southern hemisphere. As can be seen, the number of Southern HPM stars is several times higher than the number of Northern HPM stars in PPMXL (Roser, 2010), UCAC4 (Zacharias et al., 2012), URAT1 (Zacharias et al., 2015) catalogs.

For ALLWISE data the number of entries with “d2M” more 1.5” amounted to almost 12 million, and the number of HPM stars for Southern hemisphere here is also twice more than Northern one.

The HPM stars in XPM catalog (Fedorov et al., 2011) are almost lacking in the Northern hemisphere. Catalog XPM also contains incredibly large number of stars with high proper motions in Southern hemisphere.

The total number of HPM PPMXL stars exceeds 75 million. Roser et al. pointed to vast majority of PPMXL stars with high proper motion must be fakes. There are two lines corresponded PPMXL data in table 2. The second line (PPMXL\*) gives the number of HPM stars with 2MASS flag identification. The obtained number of the Southern HPM stars is comparable with value obtained for XPM catalog for this region. The possible explanation of this fact could be the same underlying surveys, but the distribution of HPM stars from PPMXL catalog (see figure 3) have shown the plate structure unlike a similar distribution for XPM catalog.

Probably, the most part of the Southern UCAC4 HPM stars are also fakes.

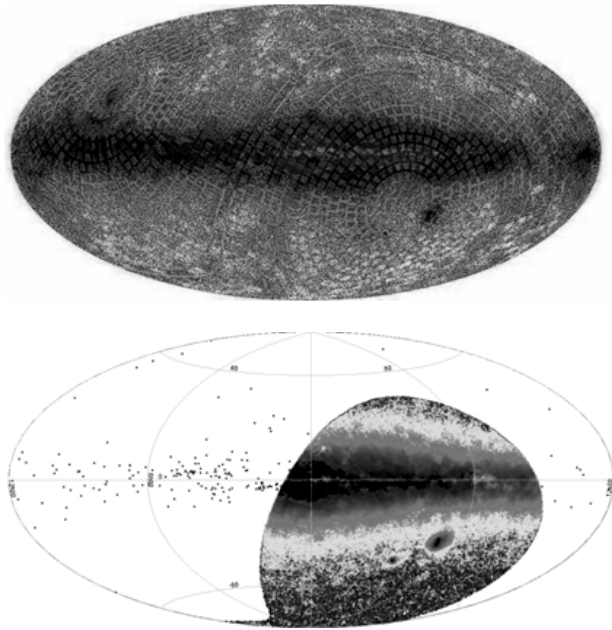


Figure 3: The distribution of HPM stars from **PPMXL** (up) and **XPM** (down) over celestial sphere (Aitoff projection, galactic coordinate system).

The pairwise mutual cross-identification of the selected HPM samples were performed. The results of search common HPM stars between different catalogs are given in table 3. The cross-identification was made with search radius of 1". The obtained number of common stars for all pairs is very small and not exceeds 5% of the total volume of compared samples.

Table 3. The results of the pairwise mutual cross-identifications between different catalogs.

Cross-matched Catalogs	Common stars		
	All	North	South
PPMXL-WISE	99 440	45 705	53 735
SPM4-WISE	13 539	-	13 539
UCAC4-WISE	44 585	24 968	19 617
URAT1-WISE	72 081	61 422	10 659
XPM-WISE	27 701	-	27 701
PPMXL-XPM	238 691	115	238 576
XPM-UCAC4	10 573	7	10 566
SPM4-UCAC4	17 910	-	17 910
URAT1-UCAC4	24 106	21 493	2 613

The cross-identification between **LSPM** catalog and some catalogs from table 1 was performed for samples of Northern declination zone. These results are given in table 4.

Taking into account the limiting magnitudes of the given catalogs, should be assumed that the URAT1 catalog is not complete with respect to the HPM stars in the Northern hemisphere.

Table 4. The cross-matching results with LSPM catalog.

Catalog	All	Common with LSPM
UCAC4	59 319	32 990
URAT1	547 135	36 777
HPM-v2	41 550	17 461
PPMXL*	1 869 585	51 054

### 3. Conclusions

The samples of stars with proper motions more 150 mas/year were chosen from some modern catalogs CDS database. The number of common HPM stars obtained from results of mutual pairwise cross-identifications between different catalogs is not more than 5 % of total volume of compared samples.

There are three main reasons complicated the studies of high proper motion stars:

- 1) actual proper motions accuracy in Galactic plane is much worse than declared accuracy of individual catalogs;
- 2) there are no whole celestial sphere catalogs with high accuracy astrometric positions for stars fainter than 16-17<sup>mag</sup>;
- 3) the different limiting magnitudes and photometric bands create certain complexities by doing catalogs cross-matching.

*Acknowledgements.* This research has made use of the **SIMBAD** database, operated at **CDS**, Strasbourg, France and **TOPCAT** software, data products from the **Wide-field Infrared Survey Explorer**, which is a joint project of the University of California, Los Angeles, and the Jet Propulsion Laboratory/California Institute of Technology, funded by the National Aeronautics and Space Administration.

### References

Lepine S. et al.: 2005, *AJ*, **129**, 1483.  
 Ivanov G.: 2008, *KFNT*, **24**, 480.  
 Kislyuk V.S. et al.: 1999, <http://cdsarc.u-strasbg.fr/viz-bin/Cat?I/261>.  
 Luyten W.J.: 1980, print University of Minnesota, Minneapolis, MN (USA), 16 p.  
 Salim S. et al.: 2003, *AphJ*, **582**, 1011.  
 Cutri R.M. et al.:2006, *AJ*, **131**, 1163.  
 Cutri R.M. et al.: 2013, *VizieR On-line Data Catalog: II/328*.  
 Roser S. et al.:2010, *AJ*, **139**, 2440.  
 Zacharias N. et al.:2013, *AJ*, **145**, 44.  
 Zacharias N. et al.:2015, *AJ*, **150**, 101.  
 Fedorov P.N. et al.:2011, *MNRAS*, **416**, 403.

DOI: <http://dx.doi.org/10.18524/1810-4215.2016.29.85140>

## FON: FROM START TO FINISH

L.K.Pakuliak, V.M.Andruk, V.V.Golovnia, S.V.Shatokhina, O.M.Yizhakevych,  
G.A.Ivanov, A.I.Yatsenko, T.P.Sergeeva

Main Astronomical Observatory of National Academy of Sciences,  
27 Akad. Zabolotnogo St., 03680, Kyiv, Ukraine, [andruk@mao.kiev.ua](mailto:andruk@mao.kiev.ua)

**ABSTRACT.** Almost 40-year history of FON project ended with the creation of the whole northern sky catalog of objects down to  $B \leq 16.5^m$ . The idea of 4-fold overlapping of the northern sky with 6 wide-field astrographs has not been realized in full. For historical reasons it has been transformed into the 2-fold overlapping observational program of MAO NAS of Ukraine, resulted in three versions of the multimillion catalog of positions, proper motions, and B-magnitudes of stars. The first version of 1.2 million stars had been finished before the 2000s and is based on the AC object list. The measurements of plates were made by automatic measuring complex PARSEC, specially developed for massive photographic reviews. As the input list was limited by AC objects, the most part of stars on the FON plates remained unmeasured. Principles of workflow organization of such works formed the basis for the further development of the project using the latest IT-technologies. For the creation of the second and the third versions of the catalog, the list of objects was obtained as a result of total digitizing of plates and their image processing. The final third version contains 19.5 million stars and galaxies with the maximum possible for the photographic astrometry accuracy. The collection of plates, obtained in other observatories – participants of the project, are partially safe and can be used for the same astrometric tasks.

**Keywords:** virtual observatory tools – astrometry – techniques: photometric – methods: data analysis – catalogs

### 1. Introduction

The plan of the photographic review of the northern sky (FON) was proposed in 1976 at MAO NAS of Ukraine by astronomers I.G.Kolchinsky and A.B.Onegina [Kolchinsky, 1977]. The idea arose after the acquisition of similar wide-angle astrographs of Carl Zeiss company with focal length 2 or 3 meters and aperture 40 cm in several observatories of the former USSR. For that moment, the Carte du Ciel project (CdC) was entirely completed. That project launched as far back as the end of XIX century and resulted in the compiled catalog of precise positions of stars down to  $11^m$  and the photographic atlas of stars down to  $14^m$  made by photographic plates of zone astrographs. The digitizing of CdC plates, made at Sternberg astronomical institute in Moscow in 80-s of the last century, ended with the creation on their basis the

Astrographic Catalogue (AC), containing 4 million stars at the epoch of observations and equinox B 1950.0. It was in the air, the idea of repetition of that project using modern instruments. The epoch difference for over 70 years provided the proper motions of a vast amount of stars with the best accuracy for that moment. It was possible on condition that the observational program, plate measurements and their treatment would be completed quickly.

The first condition was provided by similar instruments able to obtain the necessary photographic material during several years. After the thorough testing of instruments, the optimal overlapping scheme was proposed, and the common technique of observations was agreed [Kislyuk, 2000]. The optimal working field was accepted to be  $4^0 \times 4^0$  for all astrographs. In order to account the magnitude equation, the observations were carried out with two exposures of different duration with the shift of the tube between them along both coordinates. The short expositions are 18-22 seconds long, and the long one is 16-24 minutes.

The second condition of a successful project should be to develop and devise the automatic facilities for measurements of plates. A.V.Sergeev and O.E.Shornikov, engineers (for that moment) of Kazan Engelhardt observatory created the programming automatic measuring complex PARSEC designed for massive star measurements [Sergeev, 1991]. Five PARSEC complexes were installed in Nikolayev, Kiev, St.Petersburg (Pulkovo), Moscow (Zvenigorod), Kazan. Two of them (Kiev and Nikolayev) were involved into FON project.

PARSEC was able to measure the rectangular coordinates of star images with a repeatability  $\pm 0.6 - 2 \mu m$  in dependence on the quality of images and stellar magnitudes with an accuracy  $\pm 0.01 - 0.02^m$ . It had two modes of operation. The first one is the automatic scanning of all objects presented in the given area. The second mode was semi-automatic scanning the sample of objects with precalculated coordinates. This mode was used for the measurement procedure in FON project as the task was to obtain proper motions of stars. The number of objects measured per hour was 400 to 900 in dependence on precalculated coordinates' accuracy.

For the implementation of the third condition the starting point was the method of the processing the pool of the overlapped plates as the whole, using variables describing the common plate parameters together with individual ones. The method was mathematically developed and proved by H.Eichhorn [Eichhorn, 1963]. The solution of

the system of equations with tens of thousands of variables, as it was shown by H.Eichhorn, supposed to be the best way to account the instrumental aberrations and provide the homogeneous accuracy of the resulted catalog, obtained on the basis of the pool of overlapping plates. The main problem of the method was that the computing facilities, available at the time, were not able to execute that task entirely for such a system of equations. Therefore, in FON project the Eichhorn method was decided to apply partially, using the benefits of the overlapping without solving the joint bulky and often ill-conditioned systems of equations.

The FON project was supposed to provide the four-fold overlapping of the northern sky by several similar telescopes. Each observatory participating in the project had to carry out the one-fold covering of its part of the northern hemisphere with the shift of plate centers by  $2^\circ$  relative to other observatories in order to eventually obtain the four-fold overlapping. After the collapse of the USSR, the coordination of work was broken and some observatories could not complete their observations. On the same reason, the measurements of plates could not be conducted in most observatories. Therefore, the decision was made to enhance the MAO NASU observational program to the whole northern hemisphere including the most southern Kitab zone.

The regular observations started in 1982. During 15 years of observations (1980-1995) in MAO NASU, it was obtained near 2400 plates covering the sky from  $+2^\circ$  to  $+90^\circ$  on declination. Another 90 plates in  $-2^\circ$  to  $+2^\circ$  declination zone were received from Kitab observatory.

## 2. FONAC V1.0

The first version of the catalog was built on the basis of 1700 plates of best quality selected for measurements on MAO NASU PARSEC complex. Some of the plates were repeatedly measured in Nikolayev observatory to evaluate the accuracy of measurements. The input catalog for the measurements was AC. To ensure the stability of metrological characteristics of the measuring complex during the measurements the algorithms and programs for control and diagnostic of PARSEC equipment were devised and implemented. They provided the continuous monitoring of repeatability of measurements, the current analysis and registration of non-standard situations that arose in measuring process and during the preparation of input files for their further treatment. The time of measuring of one plate with the mean rate of 600 objects per hour varied from 1 and a half to 20 hours relatively to the number of stars fixed on the plate. All the measurements were carried out during 1991-1998.

For the optimization of the measurements and systematization of the accumulated data, the database with the control software was developed and implemented. The user interface allowed to create, replenish and correct the database of measured plates, to make a schedule of the measurements, to obtain the reference data about measured plates, to control the measurement process, to compose reports on measured declination zones, to prepare input files, to make the technical monitoring of measurement process and so on. The input files for measurements include lists of previously calculated rectangular

coordinates of objects, corrected for the distortion and coma effects. Lists were divided into blocks of 400 objects. Four control stars were measured at the start and the end of each block for the accounting of the instrument parameters' variations. Both expositions were measured for bright stars. For stars fainter than  $10.5^m$  only long exposition was taken into account. The software package includes Assembler, FORTRAN, and Pascal modules.

The initial reduction of measured coordinates was made with PPM star catalog as a reference. The reduction models were used in the form of incomplete cubic polynomials for each coordinate separately. Plate parameters were derived from the combined solution of connection equations for both exposures. To evaluate the number of significant members in the reduction model, the solution of conditional equations was made by Gram-Schmidt orthogonalization method. The errors of measurements, depending on brightness and a star position on a plate were accounted by constructing the aberration masks using data of GSC1.0. After the completion of HIPPARCOS mission catalogs and their derivative ones the re-reduction of measurements became possible. As a result, it ultimately gave the improvement of the accuracy of positions and proper motions of one and a half times. [Yatsenko, 2000]. The photometric reduction into B system was made using Tycho and USNO A2.0 catalogs. B-V color indices were obtained from Tycho and GSC 1.1 data.

The final reduction of measured coordinates was made with ACT catalog as a reference. ACT is based on data of AC2000, which is AC in the HIPPARCOS system, and Tycho. The result of final reduction was FONAC, the catalog of positions and proper motions based on the data of FON project and Astrographic Catalog [Kislyuk, 2000]. The first version of FONAC contains positions, proper motions and photometric data in  $B$ ,  $B - V$ ,  $B - R$  bands for 2 004 701 stars from AC list in the declination zone from  $-2^\circ$  to  $+90^\circ$ . The mean epoch of positions is 1988.19. For the determination of proper motions, AC2000 data was used as the first epoch. Photometric values of stars were derived from data of ACT, GSC 1.1, USNO A2.0. The accuracy of FONAC in dependence on object brightness is evaluated as  $\pm 0.18-0.25''$  for positions,  $\pm 3-5 \text{ mas/yr}$  for proper motions and  $\pm 0.18-0.25^m$  for brightness. As a rule, errors increase for stars brighter than  $7.5^m$  and fainter than  $11.5^m$ .

The main shortcoming of the first FONAC version was that it is created on the basis of the one-fold covering of the sky instead of the four-fold overlapping. In addition, the abilities of PARSEC measuring complex were limited by an AC input catalog data list. Limited magnitudes in it are  $\pm 13-13.5^m$  in B band. Therefore, after the completion of the first version, the most part of stars on the FON plates remained unmeasured ( $\sim 13.5-16.5^m$ ).

## 3. Ukrainian Virtual Observatory and new prospects of FON

In the 1990s, when the world has begun implementation of the ideas of digital astronomy, the IVOA (International Virtual Observatory Alliance) working group and IAU initiated the compilation of the catalogue of archives of astronegatives (Catalogue of Wide-

Field Plate Archives, <http://www.skyarchive.org/catalogue.html>, WFPDB – the archive of wide-angle photographic glass libraries) on data of ~200 astronomical institutions of the world. Those data had to be prepared in accordance with formats of data presentation devised by this group with the aim of their digitizing. The established database, obtained during the FON project workflow, became the basis for MAO WFPDB-archive creation and its inclusion into the global database of observations being a part of UkrVO Joint Digital Archive [Vavilova, 2012a, Vavilova, 2012b]. The development of information technologies and the upgrade of computer facilities make possible the complete digitizing of FON plates, their processing and data mining of all objects fixed on them.

In the early 2000s, it has started the mass digitization of negatives using flatbed scanners equipped with transparency module for digitizing of transparent media. The preceding thorough investigations of scanner digitizing capabilities, have shown that in the case of proper methods of scanning [Andruk, 2012, Protsyuk, 2014a, Protsyuk, 2014b] and development of the appropriate software [Andruk, 2014, Andruk, 2015a, Andruk, 2015b, Protsyuk, 2014a, Protsyuk, 2014b, Protsyuk, 2015, Kazantseva, 2015, Muminov, 2016, Vavilova, 2014, Yizhakevych, 2014, Yizhakevych, 2015, Yizhakevych, 2016, Yizhakevych, 2017] the feasibility exists to obtain coordinates and brightness of objects with the best accuracy possible for the photographic material. Two models of scanners were selected for FON plates digitizing, namely Microtek ScanMaker 9800XL TMA and Epson Expression 10000XL [Andruk, 2005a, Andruk, 2007, Andruk, 2010, Golovnya, 2010, Yatsenko, 2011]. The initial variant of plate image processing supposed to use two frames of each plate turned one to another by 90° with the aim of excluding the scanner errors along the axis of the matrix movement direction. That variant significantly increased the time consuming and the volumes of data storage. The preliminary version of FON comprehensive catalog included 15 million objects, was made using that method [Yatsenko, 2016].

#### 4. The final version of FONAC

When processing digital images the improved algorithms of primary treatment and the reduction were developed. They allowed to reject the technique of two frames and to eliminate the errors of scanning completely in the processing of one direct scan without prejudice to the final accuracy. Moreover, these algorithms made it possible to use the total field of the plate, that provides at least a 2-fold overlapping for 90% of objects and to exclude the images of the short exposure from the final processing. The software for plate image processing and the reduction of the measured coordinates and stellar magnitudes [Andruk, 2005, Andruk, 2015, ] has been developed on the basis of the standard MIDAS/ROMAFOT modules for the CCD images and supplemented with the special modules. The last ones implemented the algorithms of the treatment of broad star fields, the correction of scanner errors and the image geometry influence on a position of an object using the reference catalog data by successive approximation (3-4 steps). The application of the above said algorithms for the correction of primary data reduced

the reduction errors more than two times compared to non-corrected values and gave an average of 20% better the final accuracy in comparison with the two frames technology.

The final version of FONAC is based on the digital images of 2260 plates of Kiev and Kitab declination zones on which 153 million objects of various nature were registered. The catalog includes 19 568 347 stars and galaxies down to  $B \leq 16.5^m$  at the epoch 1988.1 [Andruk, 2016a, Andruk 2016b]. Each object was in an average obtained on 4 plates. 1,8 million entries in the catalog have only one image. Plate images were obtained in grey 16-bit color range with the resolution 1200 dpi. The astrometric reduction was made in the reference system of Tycho-2 at the epoch of plate expositions. The photometric reduction was carried out into the B – band of the system of photoelectric standards [Andruk, 1995, Andruk, 1996, Mermilliod, 1991, Kornilov, 1991, Relke, 2015]. In the overlapping areas positions and stellar magnitudes were obtained as a weighted average based on the weights derived for each object from the reduction of the individual plates. The convergence between obtained coordinates of objects and Tycho-2 values is  $\sigma_{\alpha\delta} = \pm 0.06''$ , the convergence with photoelectric B-values is  $\sigma_B = \pm 0.15^m$ . The comparison of the catalog with UCAC-4 shows the rms differences  $\sigma_{\alpha\delta} = \pm 0.30''$ . The final version of the catalog is supplemented by proper motions and stellar magnitudes  $f, B, V, r, i$  from UCAC-4 [Zacharias, 2013].

#### 5. Conclusion

Almost 40-year history of FON project ended with the creation of the whole northern sky catalog of objects down to  $B \leq 16.5^m$ . In the astrometry of the former USSR FON has become the only project of massive star catalogs from observations to catalog compilation and, from the very start to the finish made of the same team of participants. Unfortunately, the realities of life have not allowed implementing in full-scale the idea of I.Kolchinsky and A.Onegina of 4-fold sky overlapping by instruments of 6 observatories. In the final stage of the project, we used the plates of two observatories: Kiev and partially Kitab as well as several plates of Zelenchuk collection. The destiny of Abastumani and Zelechuk collections is unknown. The collection of Zvenigorod in its time was measured using the Moscow PARSEC complex and resulted in FOKAT stellar catalog. Now it is included in the database of Zvenigorod WFPDB-archive and is used for the solution of various special tasks where the time series of observations are required. The Dushanbe collection is safe and can be used for astrometric tasks. The Kitab collection is now being actively digitized and also used for the solution of various astrometric research tasks [Muminov, 2013, Muminov, 2014, Muminov, 2016a]. The FON project is unique with different standpoints, including the organization of mass measurements of astronomical photographic material containing millions of objects. The creation of automatic measuring complex required enormous technical and programming preparatory work starting from the selection of available stellar catalogs and assessment of their applicability to serve as input list of objects to the development of the hardware and software for general control of the process. Henceforward, the elaborated and practically tested principles of the massive meas-

urements organization became the cornerstone of the UKrVO archive databases and the system of their administration [Pakuliak, 2012], which, in turn, made it possible to return and raise the FON project at the state-of-the-art level.

*Acknowledgements.* The work was partially supported by Ukrainian Astronomical Association.

### References

- Andruk V. et al.: 1995, *Astron. Nachr.*, **316**, **N4**, 225.  
 Andruk V.N. 1996, *Kinem. i Fizika Nebesn. Tel.* **12**, **N4**, 60 (in Ukraine).  
 Andruk V.N. et al.: 2005, *Kinem. i Fizika Nebesn. Tel.* **21**, **N5**, 396 (in Ukraine).  
 Andruk V.M. et. al.: 2005, *Kinem. i Fizika Nebesn. Tel. Supl.* **N5**, 544 (in Ukraine).  
 Andruk V.M. et al.: 2010, *Kinem. Phys. Cel. Bodies*, **26**, **N3**, 75.  
 Andruk V., Pakuliak L.: 2007, *J. of Phys. Studies*. **11**, **N3**, 329 (in Ukraine)  
 Andruk V.M. et.al.: 2012, *Visnyk KNUA*, **49**, 11. (in Ukraine)  
 Andruk V.M. et al.: 2014, *Odessa Astron. Publ.*, **27**, **N1**, 53.  
 Andruk V.M. et al.: 2015, *Odessa Astron. Publ.*, **28**, **N2**, 192.  
 Andruk V.M. et al.: 2015, *Odessa Astron. Publ.*, **28**, **N2**, 188.  
 Andruk V.M. et al.: 2015, 2015, [arxiv.org/abs/1512.05535](https://arxiv.org/abs/1512.05535).  
 Andruk V.M. et al.: 2016, *Kinem. Phys. Cel. Bodies*, **32**, **N1**, 38.  
 Andruk V.M. et al.: 2016, *Kinem. Phys. Cel. Bodies*, **32**, **N5**, 261.  
 Golovnya V. Et al.: 2010, *J. of Phys. Studies*. **14**, **N2**, 2902 (in Ukraine)  
 Eichhorn H., Williams C. A.: 1963, *Astron. J.*, 68, N4, 221.  
 Kazantseva L.V. et al.: 2015, *Kinem. Phys. Cel. Bodies*, **31**, **N1**, 58.  
 Kislyuk V.S. et al.: 2000, *Kinem. Phys. Cel. Bodies*, **16**, **N6**, 483.  
 Kolchinsky I.G., Onegina A.B.: 1977, *Astrometriya i Astrofizika*, **N33**, 11.  
 Kornilov V.G. et al.: 1991, *Trudy GAIS*, **63**, 1.  
 Mermilliod J.C.: 1991, *Homogeneous means in the UBVR system*.  
 Muminov M.M. et al.: 2013, *Izvestija GAO. Pulkovo.*, **220**, 517.  
 Muminov M.M. et al.: 2014, *Odessa Astron. Publ.*, **27**, **N1**, 57.  
 Muminov M.M. et al.: 2016, *Izvestija GAO. Pulkovo.*, **223**, 339.  
 Muminov M.M. et al.: 2016, *Bulgarian Astron. J.*, **26**, 1.  
 Pakuliak L.K. et al.: 2012, *IAU Symp. No.285 Proc.*, 389.  
 Protsyuk Yu.I. et al.: 2014, *Odessa Astron. Publ.*, **27**, **N1**, 59.  
 Protsyuk Yu.I. et al.: 2014, *Odessa Astron. Publ.*, **27**, **N1**, 61.  
 Protsyuk Yu.I. et al.: 2014, *Odessa Astron. Publ.*, **27**, **N1**, 63.  
 Protsyuk Yu.I. et al.: 2014, *Kinem. Phys. Cel. Bodies*, **30**, **N6**, 54.  
 Protsyuk Yu.I. et al.: 2015, *Odessa Astron. Publ.*, **28**, **N2**, 202.  
 Relke E. et al.: 2015, *Odessa Astron. Publ.*, **28**, **N2**, 211.  
 Sergeev A. V. et.al.: 1991, *Astrophys. and Space Sci.*, 177, 329.  
 Vavilova I.B. et al.: 2012, *Kinem. Phys. Cel. Bodies*, **28**, **N2**, 85.  
 Vavilova I.B. et al.: 2012, *Baltic Ast.*, **21**, **N3**, 356.  
 Vavilova I.B. et al.: 2014, *Odessa Astron. Publ.*, **27**, **N1**, 65.  
 Yatsenko A.I. : 2000, *Kinem. Phys. Cel. Bodies*, **16**, **N1**, 67.  
 Yatsenko A.I. et al.: 2011, *Kinem. Phys. Cel. Bodies*, **27**, **N5**, 249.  
 Yatsenko A.I. et al.: 2016, *Kinem. Phys. Cel. Bodies*, **32**, **N3**, 75.  
 Yizhakevych O. et al.: 2014, *Odessa Astron. Publ.*, **27**, **N1**, 67.  
 Yizhakevych O. et al.: 2015, *Odessa Astron. Publ.*, **28**, **N2**, 213.  
 Yizhakevych O. et al.: 2016, *Odessa Astron. Publ.*, **29**, **N2**, In press.  
 Yizhakevych O. et al.: 2017, *Kinem. Phys. Cel. Bodies*, **33**, In press.  
 Zacharias N. et al.: 2013, *Astron. J.*, **145**, 44.

DOI: <http://dx.doi.org/10.18524/1810-4215.2016.29.85152>

## VIRTUAL OBSERVATORY AND COLITEC SOFTWARE: MODULES, FEATURES, METHODS

A.V.Pohorelov<sup>1</sup>, S.V.Khlamov<sup>1</sup>, V.E.Savanevych<sup>2</sup>, A.B.Briukhovetskyi<sup>2</sup>, V.P.Vlasenko<sup>2</sup>

<sup>1</sup> Kharkiv National University of Radio Electronics,  
14 Nauki Ave, Kharkiv UA-61166, Ukraine, [sergii.khlamov@gmail.com](mailto:sergii.khlamov@gmail.com)

<sup>2</sup> Western Radio Technical Surveillance Center, National Space Agency of Ukraine,  
Kosmonavtiv St, Mukachevo UA-89600, Ukraine, [vadym@savanevych.com](mailto:vadym@savanevych.com)

**ABSTRACT.** In this article we described complex processing system created by the CoLiTec project. This system includes features, user-friendly tools for processing control, results reviewing, integration with online catalogs and a lot of different computational modules that are based on the developed methods. Some of them are described in the article.

The main directions of the CoLiTec software development are the Virtual Observatory, software for automated asteroids and comets detection and software for brightness equalization.

The CoLiTec software is widely used in a number of observatories in the CIS. It has been used in about 700 000 observations, during which 1560 asteroids, including 5 NEO, 21 Trojan asteroids of Jupiter, 1 Centaur and four comets were discovered.

**Keywords:** Techniques: image processing, photometric – Astrometry – Methods: analytical, data analysis, numerical, statistical – Minor planets, asteroids – Comets: general – Stars: variables: other

### 1. Introduction

International efforts for collecting of the astronomical data sources led to creation of international alliance of national observatories (IVOA). It coordinates activities of standardization description, search, access and data publishing.

Alliance includes all virtual observatory projects, each of which solves its own scientific and technological problem. The main purpose of this organization became bringing together astronomical observation results of ground and space instruments, providing astronomers with powerful and easy-to-use instruments for accessing collected data.

The IVOA main purpose is to union national observatories in the international virtual observatory; to develop sets of standards and technologies; to combine archives of ground and space instruments that will provide researches a comfortable way to access them, as well as providing astronomers with powerful mechanisms for investigation of observational data.

Currently, there are twenty national and international projects of the Virtual Observatory (VO) in the world. Each of them share experience with another projects and

develop common standards for working with astronomical data. For example, US VO is focused on providing new research opportunities in astronomy to the community. As part of the community Spanish VO is focused on NEO detection. The main scientific area of Australian VO is creation of a theoretical astrophysical observatory for the galaxies simulation.

The International Virtual Observatory integrates enormous amount of data that contain various spectral ranges carrying unique information about celestial objects, which gives possibilities of their use in specific scientific applications, such as CoLiTec software (Savanevych et al., 2012).

The general tools for accessing information in IVOA are applications and services such as Astrogrid, Aladin, Topcat, SkyView. These tools allow users to work with surveys, catalogs and archives. Access to them is provided according to IVOA standards.

### 2. Virtual observatory

CoLiTec project develops the Virtual Observatory taking a part in the international astronomer community (Vavilova et al., 2012).

The first step was creating software for storing and publication of CCD-frames. It allows user to archive and search frames by specified parameters and may be accessed via Aladin.

The next step was creation of automatic frames loader in collaboration with Vihorlatsky observatory.

Frames uploaded through the web-interface are moderated and then processed with the On-Line Data Analysis System (OLDAS), as a part of the CoLiTec software. Processed frames are stored in the database from which they are published through SIAP protocol.

Processing sequence of Virtual Observatory server contains full stack of processing operations, that provided by the CoLiTec software (Savanevych et al., 2012).

At the first time CoLiTec project presented the national project of Ukrainian Virtual Observatory (UrkVO) as a part of the international astronomer community (Vavilova et al., 2012).

CoLiTec project created the software for storing and publication of CCD-frames that allows to archive and search frames by specified parameters (coordinates). Ex-

ternal access to the storage is provided of its own web-interface and can be accessed through Aladin. Software was implemented with using of VO technologies, including SIAP access protocol. It allows receiving the additional frames from external resources such as the SDSS and 2MASS.

Also CoLiTec project created the universal system for storing light curves of variable stars, together with a series of frames on which they were received - Vihorlatsky Virtual Observatory (ViVO). The system has the frames life-cycle which consists of the following steps:

- Collection step, that includes taking image of the sky area and its transformation to the fit format;
- Analyzing step contains moderation and preprocessing;
- Accumulation step allows to store collected data;
- Publication step provides access to already stored data.

At data collection step astronomer with a telescope and specified software takes images of the interesting sky areas and transform it to fit format.

Then user loads raw frames to the server via the web-interface. These raw frames will be moderated before its processing. At this stage faulty and unsupported frames are rejected. OLDAS system processes frames as soon as they successfully uploaded on the server. This technique allows to greatly speed up processing and provides user immediate notification of emerging issues. Processed data will be stored in the database and publishing via SIAP protocol.

The web-interface is the primary tool for frames uploading and management. It allows user to determine frames affiliation to the series and telescopes. Also you can view and edit the already uploaded series. Frames processing management allows user to select processing type (asteroids detection, frames background alignment, publishing). You can also start and stop processing, enable or disable notifications messaging.

The frame storage consists of two parts:

1. The first part is storage of fits metadata. It is the information obtained from fit header and it also includes fit path in file system.

Currently fits metadata keeps next information from fit header, such as right ascension, declination of the image center, exposure time, telescope parameters, with which the frame was received (latude, longitude, aperture), information about observer. Storage of fits metadata is implemented using PostgreSQL database.

2. The second part is storage of fits files that are stored as separate files in specified order. This avoids overhead connected with deployment and supporting of specialized storage facilities, such as file databases.

Data search inside the fit files is not expected, therefore selected storage method allows the conveniently control data placement on a different media with data compression.

Fits coverage from the storage can be represented on a celestial sphere, which is covered with a grid divided by segments. Also it contains main points of the poles, equator, current axis of rotation. Each point corresponds to one or more frames in this part of the sky.

According to IVOA recommendations for photometric data storing the software for frames storing extends with light curves and cross-references. This one allows receiv-

ing all relevant information such as required frames, light curves or photometric measurements (brightness).

ViVO provides flexibility and ability to convert values from IVOA existing formats of photometric data representing. This solution is based on the subject mediator that solves all IVOA requirements.

The subject mediator consists of the following elements: initial data format that will be converted (data from the storage); a set of conversion rules (for example, right ascension conversion from degrees to angular seconds); target formats with already specified structure, for example VSX, Vizier.

The developed system involves the ability to automatically publish loaded light curves in the catalogs of variable stars. In the absence of technical capability to send information to the directory (for example, publication to the magazine), the system will prepare the most complete data for publishing that will reduce time costs for user.

Publishing of results is performed in several formats:

- IVOA SOAP standard for photometric data;
- Vizier catalog, that provides access to data from Aladin software;
- The most widely known catalogs of variable stars such as IBVS, JAAVS, VSX.

ViVO web-interface represents light curves as a graph of brightness measurements variation. It is plotted by measurements from storage, data from different catalogs and telescopes. Detailed information about the appropriate magnitude and dimension of this frame is displayed after clicking on a point of the graph that represents the specific measurement.

### 3. CoLiTec software

Software for automated frames processing of asteroid surveys given as series of frames is necessary for the most effective astronomical observations.

This possibility is provided by the CoLiTec software allows not only to detect asteroids, but also to perform astrometric and photometric measurements in real time with the visual confirmation of processing results, <http://www.neoastrosoft.com> (Savanevych et al., 2012).

Full reliability of the detection of moving objects is retained up to the lower limit of SNR equal to 3 units in case of a minimum series consisting of four frames, with no stars covering of asteroid (Savanevych et al., 2015).

Detection of moving objects on the series of CCD-frames is performed in two stages.

Intraframe processing is designed to estimate the objects position at fixed times. Also cosmetic processing, frame alignment and brightness equalization are performed in this stage.

Interframe processing is used to detect and estimate objects trajectories. The core of CoLiTec software consists of preliminary objects detection based on accumulation of statistics that proportional to the signals energy along possible object motion paths. Such accumulation is performed by multivalued transformation of the objects coordinates that equivalent to the Hough space-time transformation (Savanevych et al., 2012) (see Figure 1).

CoLiTec software has the following features:

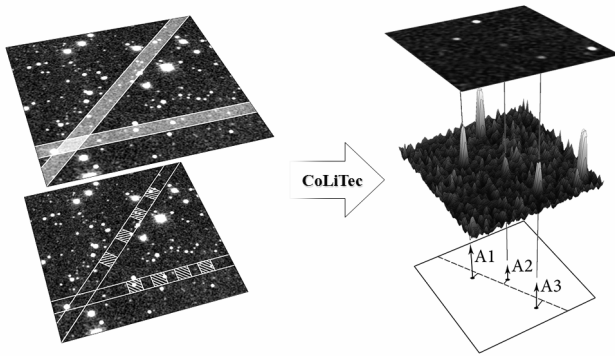


Figure 1: Algorithm for moving object detection

- Automatic detection of faint moving objects (SNR>2.5);
- Working with very wide field of view (up to 10 degrees<sup>2</sup>);
- FrameSmooth software for brightness equalization;
- Auto calibration and cosmetic correction;
- Fully automatic robust algorithm of astrometric reduction;
- Automatic rejection of the worst observations;
- Detection of very slow and very fast objects (from 0.7 to 40.0 pix./frame);
- LookSky – processing results viewer with user-friendly GUI;
- Multi-threaded support for multi-cores systems and local network;
- Processing pipeline managed by OLDAS (On-line Data Analysis System);
- CoLiTec Control Center (3C) with processing monitoring and logging.

These features allow effective using of CoLiTec software at the different observatories in the world.

The OLDAS mode is especially significant. It allows for near real-time data processing and assigns confirmation of the most interesting objects at the night of their preliminary discovery.

CoLiTec software equipped with the modern viewer of obtained results with a user-friendly GUI. LookSky runs independently of the main program and it can be used for independent review of CoLiTec processing results while the main program is processing data (see Figure 2).

Complex frame reduction was added in the last version of LookSky. This complex processing includes the following features:

- Frame processing by filter, background equalization;
- Coordinates reduction;
- Track and Stack;
- Search of objects by queries to the world Databases, such as Minor Planet Center, Variable Star Index, HyperLeda;
- Hand measuring.

A mobile version of the viewer is available. CoLiTec processing results can be monitored from anywhere in the world. It only requires any modern smartphones, a tablet or laptops running on any OS platform. After connection to our web-interface, you can perform different operations, for example, send a report to Minor Planet Center (MPC), including quick report to NEOCP.

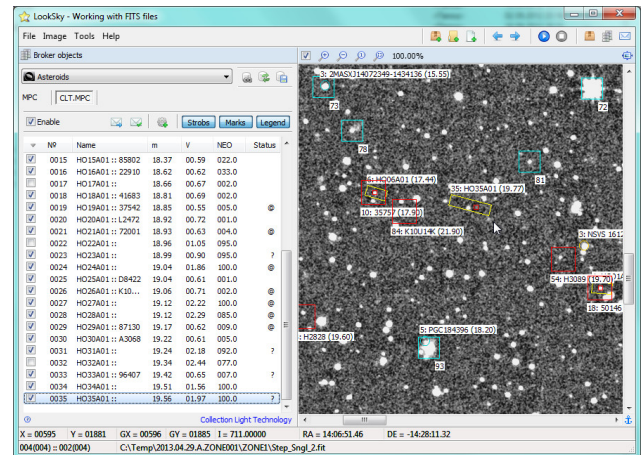


Figure 2: LookSky – processing results viewer with user-friendly GUI

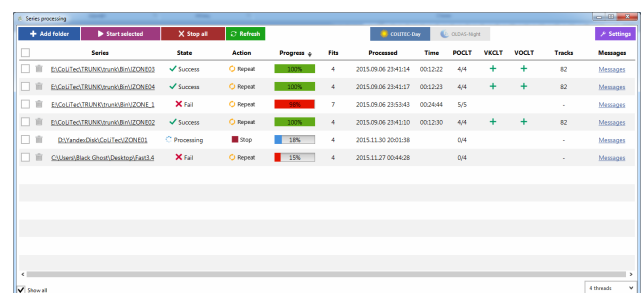


Figure 3: CoLiTec Control Center (3C) – system for managing the processing pipeline with user-friendly GUI

New principles and cross-platform technologies were applied to CoLiTec software. Some approaches for the quality control of performed process were refactored.

Java FX as cross-platform technology was used in GUI creation of basic modules. These modules are CoLiTec Control Center (see Figure 3), configuration editor ThresHolds and processing pipeline.

Some of the approaches for the quality control of performed process:

- Ordered storage of all required processing parameters allows extracting all necessary parameters for each module. Currently XML technology is used. These approaches are not only used in the configuration editor, but also at the each processing stage, as internal verification of the main processing bus.

- Multithreading, the ability to manage individual treatment processes. Tracking system of all running modules during processing was implemented. This system allows correct tracking, managing and terminating processes at any stage without data loss.

- System for deciding of the processing results allows to adapt the user settings and inform user about correct results at the each stage of processing.

Enhanced control of input and output data is held at the each stage of processing. It allows to detect damaged data from the existed one. The following sequence of the operations is performed for all modules at the each processing step.

CoLiTec software contains the system for monitoring processing messages with a detailed logging of handling process (see Figure 4). This approach is realized by change

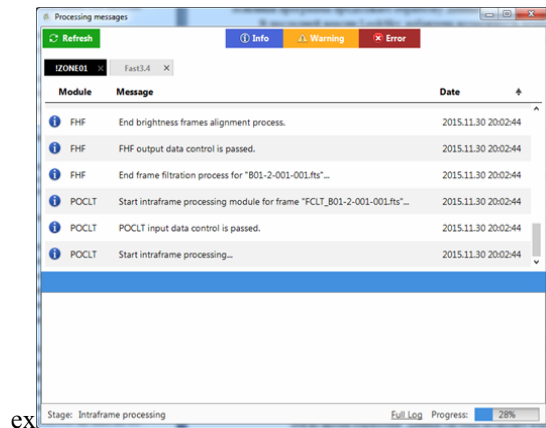


Figure 4: System for monitoring the processing messages with user-friendly GUI

data with a relational database. PostgreSQL was selected for such uses, because it may be applied on any operation systems.

CoLiTec software also includes the pipeline for digital video processing. It is presented as a flexible platform for receiving and processing video in any resolution, as well as easy integration of different modules required to improve image quality, delineation and recognition of moving objects in the video series.

CoLiTec software has abilities for detecting very slow and very fast objects. Range of visible velocities of detected asteroids is from 0.7 to 40.0 pixels per frame. For example, the faster NEO is K12C29D asteroid (40.0 pix./frame) (see Figure 5) or the slowest object is ISON C/2012 S1 comet 0.8 pix./frame).

These possibilities are provided by the different computational methods that developed by authors and implemented in the CoLiTec software.

One of them is a new iteration method for accurate estimation of asteroid coordinates, which is based on the subpixel Gaussian model of a discrete object image (Savanevych et al., 2015). This model of the object image takes into account a prior form of the object image and consequently it is adapted more easily to any forms of real image. The method operates by continuous parameters (asteroid coordinates) in a discrete observational space (the set of pixels potentials) of the CCD-frame.

In this model, a real coordinate distribution of photons hitting the pixels in the CCD-frame is not known and the form of this distribution is known a priori. It allows to determine associated parameters from a real digital object image. The advantages of subpixel Gaussian model become more obvious for the fainter celestial objects. This method has a high measurement accuracy along with a low calculating complexity due to a maximum likelihood procedure, which is implemented to obtain the best fit instead of a least-squares method and Levenberg-Marquardt algorithm for the minimization of the quadratic form (Savanevych et al., 2015).

The another method, which implemented in CoLiTec software, is the method for determining equatorial coordinates of celestial objects based on an assessment of their position in the digital frame (Pohorelov et al., 2016).

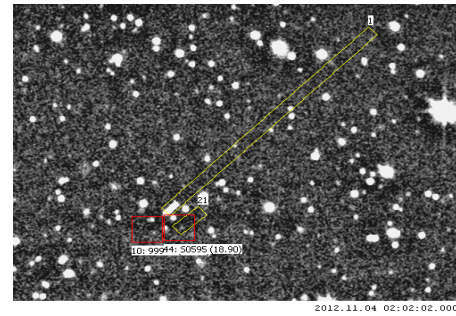


Figure 5: K12C29D asteroid – NEO (40.0 pix./frame)

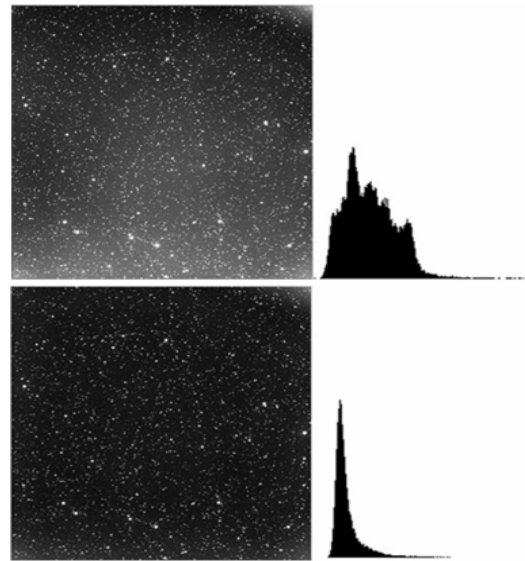


Figure 6: Frame filtration

Different reduction polynomial models (cubic and fifth-power) were implemented in this method. Also it allows to assess the significance of the reduction model coefficients and determine the influence of the polynomial model power on the accuracy of object's position assessment. The reduction models were built using the selected set of reference stars (for example, from UCAC4 catalog) (Zacharias et al., 2013). This method also takes into account the peculiarities of astronomical reduction in long-focus and short-focus optical systems.

CoLiTec software contains the module for brightness equalization of astronomical images. It based on the alignment of the interference substrate on the large CCD-frames without using of service (Master) frames (dark current frames – dark, noise reading frames – bias, «flat field» frames – flat).

Some cases when it is impossible to get Master-frames or calibration of received image don't lead to the desired result, for example, in the presence of ambient light. The images of celestial objects (stars and asteroids) in a separate frame are point, and with the atmosphere turbulence, can be presented as «blurred points», that produced slowly varying brightness changes (see Figure 6).

The method allows processing frames in the different frequency range. The stars and asteroids are formed by high-frequency spectral components of the image. However,

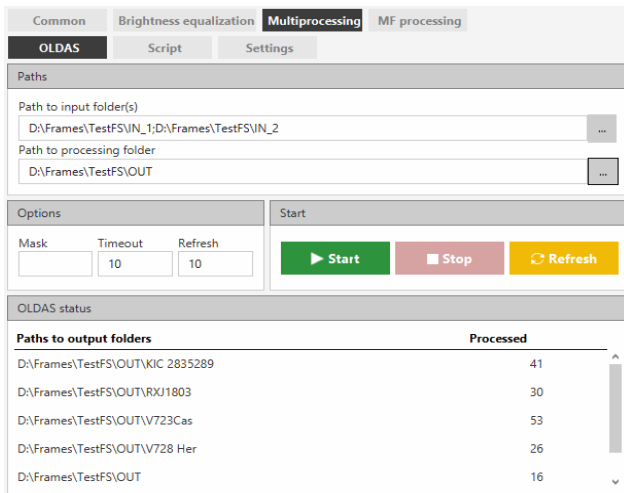


Figure 7: FrameSmooth – software for brightness equalization of astronomical frames with user-friendly GUI

the frame background is the low-frequency component. The subtraction of the low-frequency background variations allows leaving the unchanged high-frequency components of the image.

If the pulsed noise is the limited set of peak values against of zeros it is consider to use median filtering as a method for nonlinear image processing. The median filter is implemented as a local processing procedure by sliding window with specified sizes that includes an odd number of image counts. These filters increase twice signal and noise ratio (SNR) of objects images, including dim.

The range of mean values of background pixels brightness was reduced in two times by the 5% level of the maximum histogram value. This decrease is greater the larger the size of the window is being used.

These methods lead to increasing of astrometry accuracy indicators and stars photometry quality as well as the quality indicators of asteroids and comets detection.

They are implemented and successfully used as part of CoLiTec software of automated asteroids and comets discoveries on the series of CCD-frames and the FrameSmooth free software (see Figure 7).

The CoLiTec software is widely used in a number of observatories in the CIS. For the first time in the CIS, asteroids and comets were discovered in the automated mode using this software. It has been used in about 700 000 observations, during which four comets C/2011 X1 (Elenin), P/2011 NO1 (Elenin), C/2012 S1 (ISON) and P/2013 V3 (Nevski) out of seven discovered in the CIS and the Baltic States over the past 20 years were identified using CoLiTec. Thus, the comet C/2010 X1 (Elenin) was discovered on December 10, 2010, using the CoLiTec software. It was the first comet discovered by a CIS astronomer. In total, the CoLiTec software was used for discovery more than 1560 asteroids, including 5 NEO, 21 Trojan asteroids of Jupiter and 1 Centaur. Discovered asteroids include four of 16 asteroids detected during the whole history of astronomy of the Soviet Union, CIS, and Baltic states, approaching the Earth; and one of the two centaurs discovered in the CIS and Baltic states. Individual MPC electronic circulars were devoted to three asteroids (2011 HY52, 2011 QD23, 2011 RC17).

Approximately 80(86)% of positional CCD-measurements and 74(75)% of discoveries of asteroids were made using the CoLiTec software in 2012 (2011).

Considerable achievements of the CoLiTec software are associated with the detection of objects with near-zero apparent motion. For example, at the time of discovery, the image size of the comet C 2012 S1(ISON) was 5 pixels, and it shifted by 3 pixels for 4 frames (Khlamov et al., 2016). The Centaur 2013 UL10 was shifted by 10 pixels with the image size of 4-5 pixels at the time of discovery.

The CoLiTec project has been supported for several years by such organizations as ISON (Elenin et al., 2013), MAO NASU and RI NASU. In 2014, the CoLiTec software was recommended to all members of the Gaia-FUNSSO network (<https://gaiafunso.imcce.fr>) for analyzing observations as a tool for detecting faint moving objects on CCD-frames.

## References

- Savanevych V. E. et al.: 2012. CoLiTec software for automated detection of faint celestial bodies. *Space Science and Technology*, **18**, 39-46.
- Vavilova I. B. et al.: 2012. Astroinformation resource of the Ukrainian virtual observatory: Joint observational data archive, scientific tasks, and software. *Kinematics and Physics of Celestial Bodies*, **28**, 85-102.
- Vavilova I. B. et al.: 2012. UkrVO Joint Digitized Archive and Scientific Prospects. *Baltic Astronomy*, **21**, 356-365.
- Savanevych V. E. et al.: 2015. A new method based on the subpixel Gaussian model for accurate estimation of asteroid coordinates. *MNRAS*, **451**, 3287-3298.
- Savanevych V. E. et al.: 2015. Comparative analysis of the positional accuracy of CCD measurements of small bodies in the solar system software CoLiTec and Astrometrica. *Kinematics and Physics of Celestial Bodies*, **31**, 302-313.
- Pohorelov A. V. et al.: 2016. Investigation of the reduction model power influence on the accuracy of the object's position assessment using relative method. *Eastern-European Journal of Enterprise Technologies*, **82**, 42-49.
- Zacharias N. et al.: 2013. The fourth US naval observatory CCD astrograph catalog (UCAC4). *The Astronomical Journal*, **145**, 2.
- Khlamov S. V. et al.: 2016. Development of computational method for detection of the object's near-zero apparent motion on the series of CCD-frames. *Eastern-European Journal of Enterprise Technologies*, **80**, 41 - 48.
- Elenin L. et al.: 2013. Minor Planet Observations [H15 ISON-NM Observatory, Mayhill]. *Minor Planet Circulars*, **82692**, 1.
- Minor Planet Center, COMET C/2011 X1 (ELENIN):  
<http://www.minorplanetcenter.org/mpec/K10/K10XA1.html>
- Minor Planet Center, COMET P/2011 NO1 (ELENIN):  
<http://www.minorplanetcenter.org/mpec/K11/K11O10.html>
- Minor Planet Center, COMET C/2012 S1 (ISON):  
<http://www.minorplanetcenter.org/mpec/K12/K12S63.html>
- Minor Planet Center, COMET P/2013 V3 (NEVSKI):  
<http://www.minorplanetcenter.org/mpec/K13/K13V45.html>
- Minor Planet Center, 2011 HY52.:  
<http://www.minorplanetcenter.org/mpec/K11/K11J02.html>
- Minor Planet Center, 2011 QD23.:  
<http://www.minorplanetcenter.org/mpec/K11/K11Q39.html>
- Minor Planet Center, 2011 RC17.:  
<http://www.minorplanetcenter.org/mpec/K11/K11W34.html>

DOI: <http://dx.doi.org/10.18524/1810-4215.2016.29.85171>

## ANALYSIS OF ASTEROID'S OBSERVATIONS IN OPEN PHOTOMETRIC DATABASES

A. Pomazan, N. Maigurova

Research Institute "Nikolaev Astronomical Observatory",  
Observatorna 1, 54030, Mykolaiv, Ukraine, [antpomaz@gmail.com](mailto:antpomaz@gmail.com)

**ABSTRACT.** Today there are several open photometric databases containing important information for the study of the physical properties of asteroids. These databases are based on the results of various measurements of the different sets of objects. The study of statistical correlations between the various databases could significantly expand the list of asteroids with known physical parameters. We present the results of the comparative analysis of the determination of the albedo, diameters and absolute magnitudes of asteroids of five open sources (AKARI, IRAS, NEOWISE, HORIZONS and Pan-STARRS1). The infrared survey WISE (relatively to asteroids is NEOWISE project) and photometric survey Pan-STARRS1 are the widest databases of the absolute magnitudes and the albedo of asteroids providing information about 139356 and 248457 objects respectively. These surveys contain 73301 common asteroids. The obtained statistical relationships between the databases based on a common set of asteroids are presented.

**Keywords:** photometry observations, astronomical database, catalogs, asteroids

### 1. Introduction

Photometry is one of the main methods for studies of asteroids. Due to intensive photometric observations of asteroids in the last decades, huge information about the absolute magnitudes, periods of rotation around principle axis, sizes, shapes, colors and other characteristics of large number of asteroids was received.

According MPC database, the number of currently known asteroids with well-defined orbits is more than 720 thousands. Many ground-based (Pan-STARRS, SDSS MOC and etc.) and space (IRAS, AKARI, NEOWISE and etc.) surveys offer as well precisely determined orbital elements as a data of the photometric properties of asteroids. However, since each of the projects aimed to achieving specific goals they could provide a different set of photometric data. Analysis of the available data is a first step for further research of selected class of objects.

### 2. Brief overview of investigated photometric databases

5 surveys provided the photometric data were chosen for further investigation: IRAS, AKARI, NEOWISE, Pan-STARRS and SDSS MOC-3.

**IRAS** – Infrared Astronomical Satellite (Neugebauer et al., 1984), launched in 1983. The asteroid catalog was provided by Tedesco et al. (2002) as the supplemental IRAS minor planet survey (SIMPS). The SIMPS includes information for 2,470 asteroids.

**AKARI** – Japanese infrared satellite (Murakami et al., 2007), launched in 2006. The Asteroid catalog using AKARI (AcuA) (Usui et al., 2011) provides information for 5120 asteroids.

**NEOWISE** – is asteroid-hunting project of the Wide-field Infrared Survey Explorer (WISE) (Mainzer et al., 2011) mission. NEOWISE identified over 157,000 asteroids. 139356 asteroids were chosen from open databases for this research.

**Pan-STARRS** – the Panoramic Survey Telescope & Rapid Response System started operations in 2010 (Kaiser et al., 2010). The available data for 248457 asteroids (Veres et al., 2015) were used.

**SDSS MOC** – The Sloan Digital Sky Survey Moving Object Catalog provides information for all moving objects identified in the SDSS images. This data set contains Sloan Digital Sky Survey (SDSS) asteroid photometric observations classified according to the SDSS-based Asteroid Taxonomy (Carvano et al., 2010). This actual data set is the result of the taxonomic classification of third version of the SDSS MOC and contains 63468 asteroids. The SDSS MOC-4 is now available but not considered here.

Table 1 presents the availability of selected parameters in investigated surveys: the asteroid absolute magnitude (H), slope parameter (G), geometric visible albedo (pV), diameter (D), spectral type and the total number of asteroids.

Table 1. The availability of selected parameters in investigated surveys.

	H	G	pV	D	Spectral type	Data volume
IRAS	X		X	X		2470
AKARI	X	X	X	X		5199
NEOWISE	X	X	X	X		139356
Pan-STARRS	X	X			X	248457
SDSS MOC-3	X				X	63468

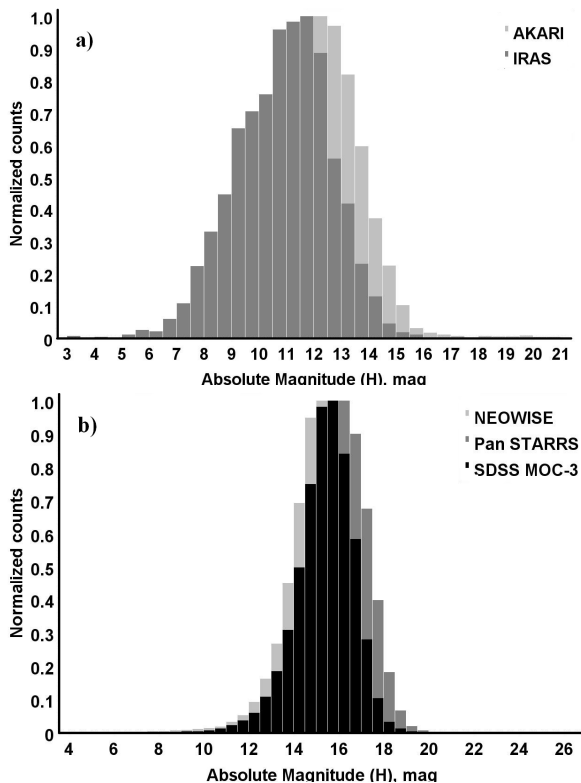


Figure 1: The distributions of absolute magnitude (H) values: a) – AKARI and IRAS surveys, b) – NEOWISE, Pan-STARRS and SDSS MOC-3

As can be seen, only the values of the absolute magnitude are available in each of the surveys. This is due to that the absolute magnitude is the main photometric parameters and available almost in all databases of asteroid observations (including MPC). Other parameters are partially overlapped because each of surveys was conducted for specific aims.

There are 328524 unique asteroids in foregoing surveys due to overlapping lists of objects. The cross-identification between infrared surveys (IRAS, AKARI, NEOWISE) shows 1993 common asteroids (Usui et al., 2014). The number of common asteroids between widest surveys (Pan-STARRS, NEOWISE, SDSS MOC-3) is 17888, the number of common asteroids for all 5 investigated surveys is only 362.

### 3. Analysis of absolute magnitude H

**AKARI:** The absolute magnitude (H) and slope parameter G were taken from the Asteroid Orbital Elements Database (Bowell et al. 1994) of Lowell Observatory at the epoch of 2010.

**IRAS:** The H- and G-values were mostly received from the MPC in 2001, where they were determined from ground-based observations in visible wavelengths.

**NEOWISE:** The absolute magnitudes H were taken from the Light Curve Database (Warner et al., 2009) when available otherwise, the values were taken from the MPC's orbital element file.

**SDSS MOC-3:** The H values were computed from observations.

**Pan-STARRS:** The H values were computed using both the Muinonen et al. (2010) and Bowell et al. (1989) phase functions (hereafter M10 and B89 respectively) from their own observations.

In Table 2 presents differences in H values between all 5 surveys.

The histograms of distributions of the absolute magnitude in investigated surveys are presented in Figure 1.

The peaks of distributions of absolute magnitude are 10.97 for IRAS, 12.08 for AKARI, 15.2 for NEOWISE, 16.12 for Pan-STARRS B89, 16.18 for Pan-STARRS M10 and 15.4 for SDSS MOC3.

Table 2. The residuals of values of the absolute magnitude between 5 processed surveys.

Residuals	AKARI	IRAS	NEOWISE	Pan-STARRS Bowell'89	Pan-STARRS Muinonen'10
IRAS	0.00±0.11 count 2104				
NEOWISE	0.00±0.22 count 4798	-0.01±0.23 count 2305			
Pan-STARRS Bowell'89	-0.24±0.38 count 3881	-0.20±0.37 count 1797	-0.33±0.29 count 73412		
Pan-STARRS Muinonen'10	-0.30±0.38 count 3881	-0.25±0.36 count 1797	-0.38±0.29 count 73412	-0.05±0.03 count 247458	
SDSS MOC-3	0.01±0.08 count 1367	0.00±0.04 count 601	-0.07±0.24 count 25877	0.22±0.34 count 40689	0.28±0.34 count 40689

#### 4. The slope parameter G

The parameter G is a one of parameters in phase function of brightness of asteroids. The slope parameter G determines how strongly the apparent brightness of an asteroid depends on the phase angle and accounts for the properties of scattered light on the asteroid's surfaces.

The vast majority of asteroids have no measured slope parameter so the average values of  $G=0.15$  are used for all asteroids that do not have a reported appropriate value.

**AKARI:** The survey has 105 asteroids that have value of slope parameter G different from 0.15.

**NEOWISE:** The survey has 96 such asteroids.

**Pan-STARRS:** As described in Veres et al. (2015), a Monte Carlo technique was used to calculate the slope parameters  $G_{B89}$  and  $G_{M10}$  with initial estimates based on measurements by Pravec et al. (2012) and Oszkiewicz et al. (2012) respectively.

The dense area near  $G_{B89}=0.2$  on Figure 2a and  $G_{M10}=0.5$  on Figure 2b could be explained by initial values for the Monte Carlo simulations of  $G=0.15$  for Bowell et al. (1989) phase function and  $G=0.53$  for Muinonen et al. (2010) phase function.

The dense area in the Figure 2b with mean value near  $G_{M10} = 0.2$  is due to a discontinuity in the two-parameter H,  $G_{12}$  phase function (Muinonen et al., 2010). This is caused by the Monte Carlo simulations performed by Veres et al. (2015), which have a propensity to drive the fitted  $G_{M10}$  value to 0.2 when the number of data points is small. This area contains about 30% of all  $G_{M10}$  values.

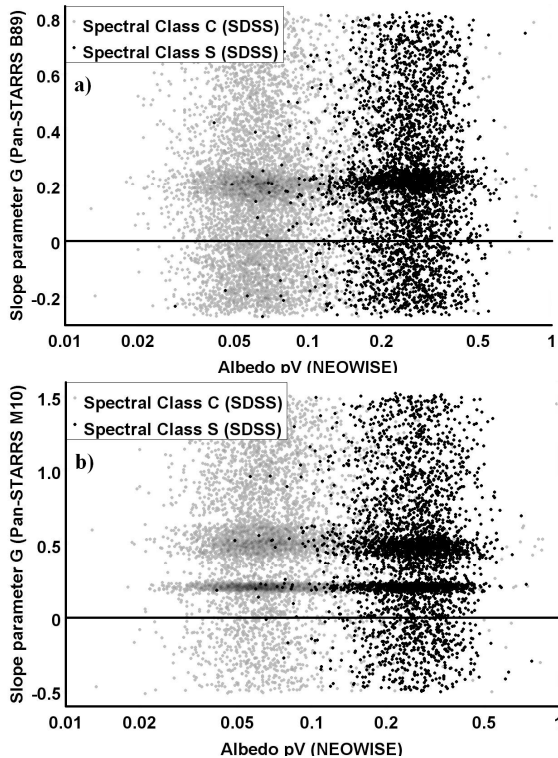


Figure 2: The slope parameter (Pan-STARRS) as function of albedo (NEOWISE) a) for phase function model of Bowell'89 and b) for Muinonen'10 for spectral class C (grey) and S (black).

#### 5. Conclusions

Five photometric surveys (IRAS, AKARI, NEOWISE, Pan-STARRS and SDSS MOC-3) were analyzed and 328524 unique asteroids were identified. 17888 common asteroids were detected between widest surveys (Pan-STARRS, NEOWISE, SDSS MOC-3) and only 362 one are common for all five investigated surveys.

Each of these surveys contains different photometric parameters and only values of absolute magnitude (H) are available for all of them. The distribution of H is shifted toward to fainter object for newer surveys (SDSS MOC-3, 2004; NEOWISE, 2010, Pan-STARRS, 2012). The peaks of the distributions are in range from 10.97 for IRAS to 16.18 for Pan-STARRS M10.

*Acknowledgements.* This research has made use of the VizieR catalogue access tool, CDS, Strasbourg, France; Tool for Operations on Catalogues And Tables (TOPCAT).

#### References

- Neugebauer G. et al.: 1984, *ApJ*, **278**, L1.  
 Tedesco E. F. et al.: 2002, *AJ*, **123**, 1056.  
 Murakami H. et al.: 2007, *PASJ*, **59**, S369.  
 Usui F., et al.: 2011, *PASJ*, **63**, 1117.  
 Mainzer A., et al.: 2011, *ApJ*, **731**, 53.  
 Kaiser N. et al.: 2010, *GAT III, SPIE Proc.*, **7733**.  
 Vereš P. et al.: 2015, *Icarus*, **261**, 34.  
 Carvano J. M. et al.: 2010, *A&A*, **510**, A43.  
 Usui F., et al.: 2014, *PASJ*, **66**, 56U.  
 Bowell E. et al.: 1994, *ACM*, 477.  
 Warner B. et al.: 2009, *Icarus*, **202**, 134.  
 Muinonen K. et al.: 2010, *Icarus*, **209**, 542.  
 Bowell E. et al.: 1989, *Asteroids II Proc.*, 524.  
 Pravec P. et al.: 2012, *Icarus*, **221**, 365.  
 Oszkiewicz D. et al.: 2012, *Icarus*, **219**, 283.

DOI: <http://dx.doi.org/10.18524/1810-4215.2016.29.85172>

## UKRVO – FEATURES AND COMPARISON OF THE NEW CATALOGUE OF PHOTOGRAPHIC SURVEY OF THE NORTHERN SKY

Protsyuk Yu.<sup>1</sup>, Relke E.<sup>2</sup>

<sup>1</sup> Research Institute: Nikolaev Astronomical Observatory, Ukraine, [yuri@nao.nikolaev.ua](mailto:yuri@nao.nikolaev.ua)

<sup>2</sup> Walter-Hohmann-Observatory, Germany, [helena\\_relke@yahoo.com](mailto:helena_relke@yahoo.com)

**ABSTRACT.** UkrVO plate archives contain information obtained at different observatories for a long time. With using data of photographic survey of the northern sky (FON project, from  $-4^\circ$  to  $90^\circ$ ) in Main Astronomical Observatory of National Academy of Science (MAO) new catalogue of positions and magnitudes was obtained. The catalogue contains coordinates and magnitudes of more than 19 million stars and galaxies from  $3^m$  to  $17.5^m$  for the mean epoch of 1988.3. Comparison with the catalogues UCAC4, PPMX, XPM was carried out. The differences of common stars positions between catalogues are from  $0.05''$ - $0.06''$  for the  $9$ - $11^m$  stars to  $0.30''$ - $0.40''$  for the  $5$ - $7^m$  and  $15$ - $16^m$  stars. The differences of common stars B-magnitudes between catalogues are from  $0.05^m$ - $0.10^m$  for the  $10$ - $11^m$  stars to  $0.4^m$ - $0.5^m$  for the  $6$ - $7^m$  and  $15$ - $16^m$  stars. The obtained results suggest the advisability of using the new catalogue for improving proper motions of stars within the range of  $8^m$ - $14^m$  magnitudes.

**Keywords:** Astrometry – catalogues – methods: data analysis

### 1. Introduction

UkrVO plate archives contain information obtained at different observatories for a long time (Vavilova et al., 2010, 2011, 2012a, 2012b, 2014). New catalogue FONAC3 obtained from the Photographic Survey of the Northern Sky (observation 1980-1995 from  $-4^\circ$  to  $90^\circ$ ) in Main Astronomical Observatory of National Academy of Science (MAO NASU) in 2016 (Andruk et al., 2015, 2016a, 2016b). For our extended comparison of the FONAC3 catalogue we used the UCAC4 (Zacharias et al., 2013), PPMX (Roeser et al., 2008) and XPM (Fedorov et al., 2009) catalogues and own special software (Protsyuk et al., 2014, 2015a, 2015b).

### 2. FONAC3 catalogue parameters

The catalogue contains coordinates and magnitudes of more than 19.5 million stars and galaxies from  $3^m$  to  $17.5^m$  for the mean epoch of 1988.3 (Figure 1). Mean errors of catalogue are 214 mas in right ascension and 197 mas in declination (Figure 2). The mean number of observations for most objects of the catalogue is 4 (Figure 3). The catalogue also includes near 1.9 million stars with one observation, 5.6 million with two observations and  $\sim 1.2$  million stars identified with the stars of the Tycho-2 catalogue.

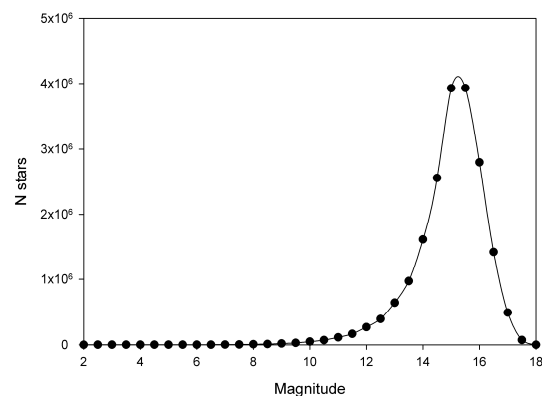


Figure 1: Distribution of stars of FONAC3 catalogue vs magnitude.

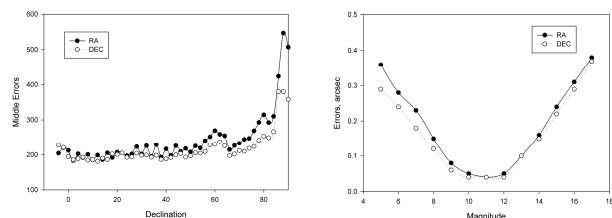


Figure 2: Standard deviations (SD) of catalogue positions vs declination (left) and vs magnitude (right).

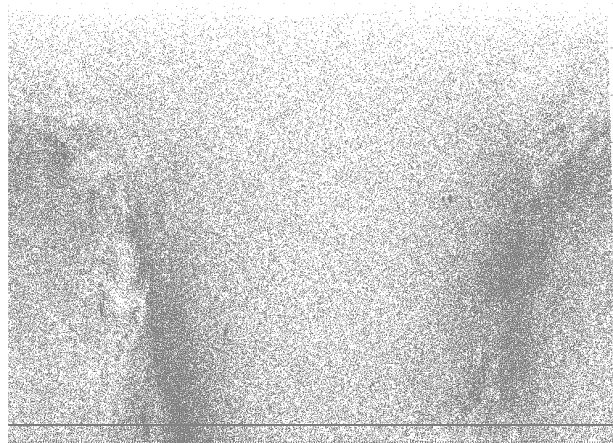


Figure 3. Distribution of density of FON catalogue in right ascension and declination.

### 3. Comparison with PPMX catalogue

PPMX catalogue contains more than 18 million stars up to 15.2 magnitude. In declination zone from -4 to 90 number of stars is near 9.5 million. We made cross-identification of FONAC3 and PPMX catalogues with the search window 1.5" and found near 7.67 million common stars. This amount is about 39% of the FONAC3 catalogue. Also, we identified 1.37 million common stars having B-magnitudes and used them for analysis of the FONAC3 catalogue magnitudes. Mean systematic differences between catalogues are  $63 \pm 218$  mas in right ascension,  $39 \pm 228$  mas in declination and  $0.04 \pm 0.19^m$  in B-magnitude. Distribution of RMS of differences between catalogues in coordinates and magnitudes are shown in Figures 4,5.

### 4. Comparison with XPM catalogue

The XPM catalogue contains of about 314 million stars in the magnitude range  $10^m < V < 20^m$ . We made cross-identification of FONAC3 and XPM catalogues with the search window 2.2" and found near 18.48 million common stars. This amount is about 94.4% of FONAC3 catalogue. From this set we used 16.64 million stars with two and more observations. Mean systematic differences between catalogues are 33 mas in right ascension, 52 mas in declination and  $0.06^m$  in B-magnitude. Mean (O-C) differences between

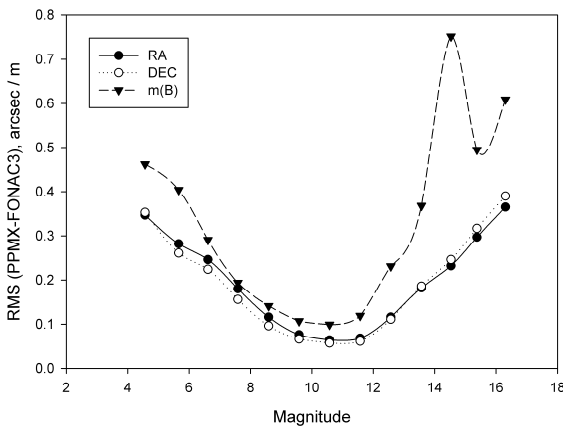


Figure 4: Distribution of RMS of differences PPMX-FONAC3 in coordinates and magnitudes vs magnitude

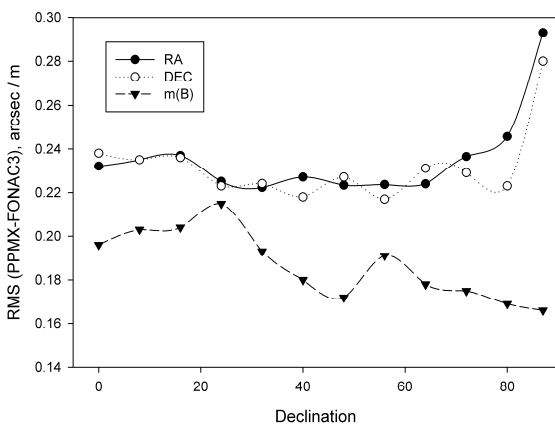


Figure 5: Distribution of RMS of differences PPMX-FONAC3 in coordinates and magnitudes vs declination.

XPM and FONAC3 catalogues are 305 mas in right ascension, 312 mas in declination and  $0.36^m$  in B-magnitude. Linear correlation of B-magnitude between catalogues is near 0.89. Distribution of mean (O-C) differences between catalogues in coordinates are shown in Figures 6,7.

### 5. Comparison with UCAC4 catalogue

The UCAC4 catalogue contains of about 113 million stars in the magnitude range  $8^m < V < 16^m$ . We carried out cross-identification of FONAC3 and UCAC4 catalogues with the search window 2.2" and found near 19.09 million common stars. This amount is about 97.6% of FONAC3 catalogue. From this set we used 17.2 million stars with two and more observations. Mean systematic differences between catalogues are 28 mas in right ascension, 38 mas in declination and  $-0.64^m$  in B-magnitude. Mean (O-C) differences between UCAC4 and FONAC3 catalogues are 302 mas in right ascension, 308 mas in declination and  $0.41^m$  in B-magnitude. Linear correlation of B-magnitudes between catalogues is near 0.87. Distribution of mean (O-C) differences between catalogues in coordinates are shown in Figures 8,9.

### 6. Conclusion

The study of the new catalogue FONAC3, including more than 19.5 million stars from  $3^m$  to  $17.5^m$  for the mean epoch 1988.3, and its comparison with catalogs UCAC4, PPMX and XPM was done (Figure 10-12).

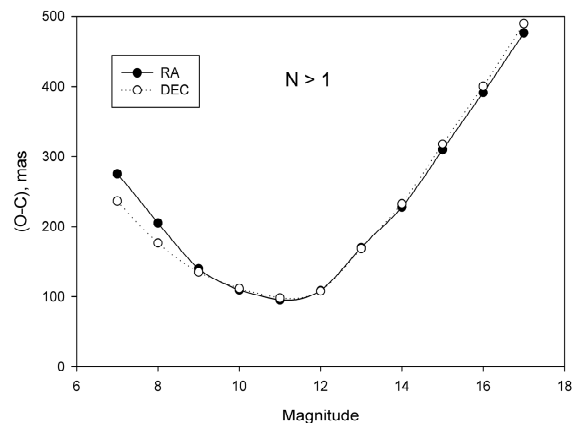


Figure 6: Distribution of mean (O-C) differences XPM-FONAC3 in coordinates vs magnitude.

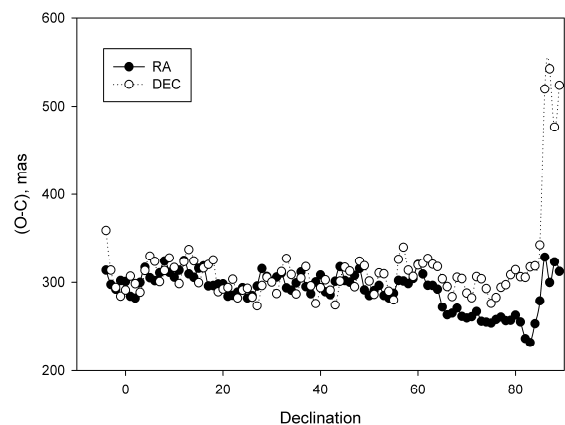


Figure 7: Distribution of mean (O-C) differences XPM-FONAC3 in coordinates vs declination.

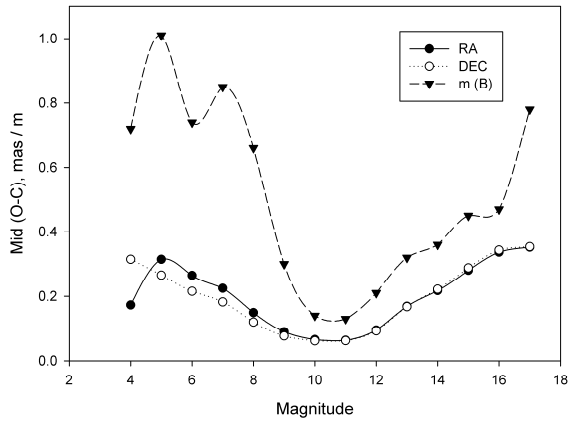


Figure 8: Distribution of mean (O-C) differences UCAC4-FONAC3 in coordinates and magnitudes vs magnitude.

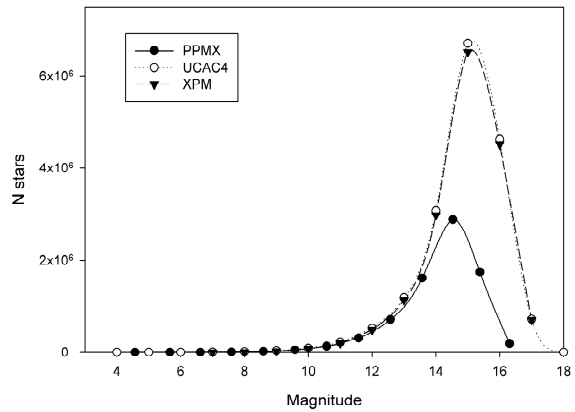


Figure 10: Distribution of common stars of FONAC3 catalogue with other catalogues vs magnitude.

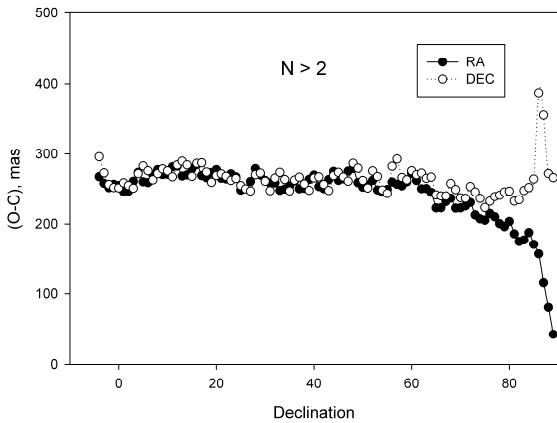


Figure 9: Distribution of mean (O-C) differences UCAC4-FONAC3 in coordinates vs declination for stars with more than two observations.

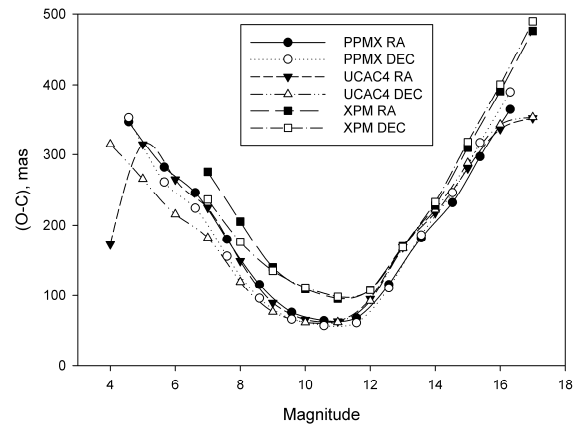


Figure 11: Distribution of mean (O-C) differences between FONAC3 and other catalogues in RA and DEC.

The most accurate part of the new catalogue includes about 5 million stars from  $8^m$  to  $14.5^m$  (Figure 11).

The convergence of the coordinates was better in comparison with UCAC4 and PPMX catalogues (Figure 11), the convergence of magnitudes was better for PPMX (Figure 12).

The XPM catalogue showed the worst convergence with FONAC3 in coordinates and in magnitudes (Figure 11-12).

In comparison with all catalogues the FONAC3 indicated low accuracy in the pole region.

These results suggest the feasibility of using this new catalogue to improve proper motions of stars in the range of  $8^m - 14^m$  and from  $-4^\circ$  to  $80^\circ$ .

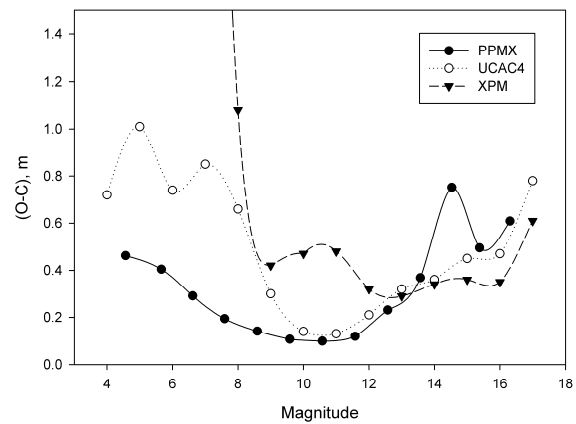


Figure 12: Distribution of mean (O-C) differences between FONAC3 and other catalogues in magnitude.

## References

- Andruk V. et al.: 2015, *arxiv.org/abs/1512.05535*  
 Andruk V. et al.: 2016, *Kinem. Phys. Cel. Bodies*, **32**, **N1**, 56.  
 Andruk V. et al.: 2016, *Kinem. Phys. Cel. Bodies*, **32**, **N5**, 1.  
 Fedorov P. et al.: 2009, *MNRAS*, **393**, 133.  
 Protsyuk Yu. et al.: 2014, *OAP*, **v.27/1**, 59.  
 Protsyuk Yu. et al.: 2015, *OAP*, **v.28/2**, 202.  
 Protsyuk Yu. et al.: 2015, *OAP*, **v.28/2**, 207.

- Roeser S. et al.: 2008, *A&A*, **488**, 401.  
 Vavilova I.B. et al.: 2010, *KosNT.*, **16**, **N5**, 62.  
 Vavilova I.B. et al.: 2011, *KosNT.*, **17**, **N4**, 74.  
 Vavilova I.B. et al.: 2012, *Kinem. Phys. Cel. Bodies*, **28**, **N2**, 85.  
 Vavilova I.B. et al.: 2012, *Baltic Ast.*, **21**, **N3**, 356.  
 Vavilova I.B. et al.: 2014, *OAP*, **v.27/1**, 65.  
 Zacharias N. et al.: 2013, *Astron. J.*, **145**, 44.

DOI: <http://dx.doi.org/10.18524/1810-4215.2016.29.85176>

## USING OF UKRVO DATA AND SOFTWARE FOR NEW REDUCTIONS OF PHOTOGRAPHIC OBSERVATIONS OF SELECTED MINOR PLANETS

Protsyuk Yu.<sup>1</sup>, Maigurova N.<sup>1</sup>, Protsyuk S.<sup>1</sup>, Golovnia V.<sup>2</sup>

<sup>1</sup> Research Institute: Nikolaev Astronomical Observatory, Ukraine, [yuri@nao.nikolaev.ua](mailto:yuri@nao.nikolaev.ua)

<sup>2</sup> Main Astronomical Observatory, National Academy of Sciences, Ukraine, [golov@mao.kiev.ua](mailto:golov@mao.kiev.ua)

**ABSTRACT.** The new reductions of available photographic plates of UkrVO digital archive containing images of selected minor planets were conducted. Data processing of these plates were carried out to check the possibility of obtaining the new positions with high accuracy in the system of Tycho2/UCAC4 reference catalogues. Archives of the Research Institute “Nikolaev Astronomical Observatory” (NAO) and Main Astronomical Observatory of National Academy of Science (MAO) were used. We have chosen near 60 plates from these archives. Observational epochs of the plates were in the range from 1974 to 1991. Usually, there were 3 exposures in each plate and each plate was scanned 6 times with 1600 dpi resolution. The full identification was conducted and coordinates of all objects were obtained with usage of different options of astrometric reductions. The inner accuracy of obtained positions is within of 0.03"-0.40". The comparison of the new topocentric positions of minor planets with Horizons ephemeris was made for calculation (O – C) residuals and their RMS. The matching with MPC data is present.

**Keywords:** Astrometry – methods: data analysis – virtual observatory tools – minor planets: general

### 1. Introduction

The photographic plates of UkrVO digital archive to check the possibility of obtaining the new positions of selected minor planets (MP) with high accuracy in the system of Tycho2 (Hog et al., 2000) and UCAC4 (Zacharias et al., 2013) reference catalogues were processed. The UkrVO digital archive contains image of plates from different Ukrainian telescopes (Vavilova et al, 2010, 2011, 2012a, 2012b, 2014a). The first investigation of minor planets with flatbed scanners in Ukraine started in 2013 (Golovnya et al., 2013). Then, we have studied dwarf and big planets (Kazantseva et al., 2015, Protsyuk et al., 2015e) and our methodics was significantly improved. The minor planets investigation is continued in this work.

In our new investigation we used plates only from two telescopes: the Zonal Astrograph of NAO (ZA, D/F = 12/204, 101 "/mm, FoV 5° x 5°, exposure 5-6 minutes) and the Double Wide-angle Astrograph (DWA, D/F = 40/200, 103 "/mm, FoV 8° x 8°, exposure 3-15 minutes)

of MAO (Protsyuk et al., 2014a, Vavilova et al, 2014b). Usually, there were 3 exposures in each plate and each plate was scanned 6 times with 1600 dpi resolution with same methodics (Protsyuk et al., 2014b, 2014c). In NAO we used Epson Perfection V750 Pro scanner and in MAO – Epson Expression 10000XL scanner.

### 2. Input data set

We have chosen asteroid (704) Interamnia (1910 KU, 1952 MW, H = 5.94 mag) as main object for our research. This planet was observed by both telescopes at about the same time. The apparent magnitude of the asteroids was near 11.0-11.5. The data reduction results of the measurement of these plates, made with "Ascorecord" measure machine in 20 century, were submitted in Minor Planet Center (MPC). We have also chosen (389) Industria (ZA, NAO) with magnitude near 12.0 and (1064) Aethusa (DWA, MAO) with magnitude near 13.5 as faint objects (Table 1).

Table 1. Selected minor planets

MP	N plates	Observatory	Epoch of observation	Mean Mag
704	29	NAO	1974.5-1985.8	11.1
704	20	MAO	1977.2-1982.2	11.5
389	4	NAO	1991.1-1991.3	12.0
1064	8	MAO	1979.6-1979.8	13.6

### 3. Data reduction

Detailed description of all steps of processing of digitized image of astro negatives, which containing preliminary filtering, choosing star shape objects and made reduction to the equatorial coordinates and magnitudes of a reference catalogues, are given in Protsyuk et al. (2014c, 2014d) and Andruk et al. (2014, 2015).

For choosing program for reduction we compare results from Kamasutra (00plate) and Plate Graf (plate\_gr) program (Protsyuk et al., 2014d) with same parameters (4 iteration with Tycho2 reference stars up to 12.5<sup>m</sup>, excluding the option of spectral class). Inner accuracy for 29 plates of NAO (MPC number 089) with Interamnia, received by two programs, are shown on Figure 1 and for 20

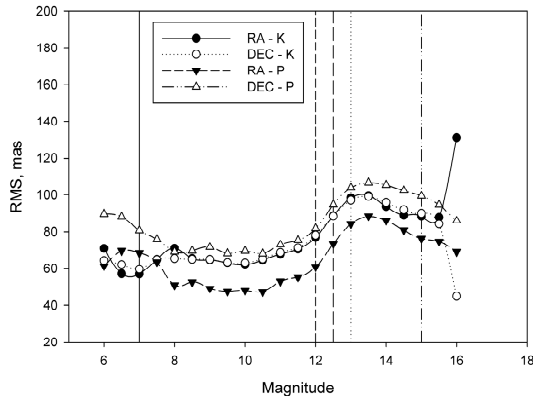


Figure 1: Inner accuracy for 29 plates of NAO received by Kamasutra (K) and Plate Graf (P)

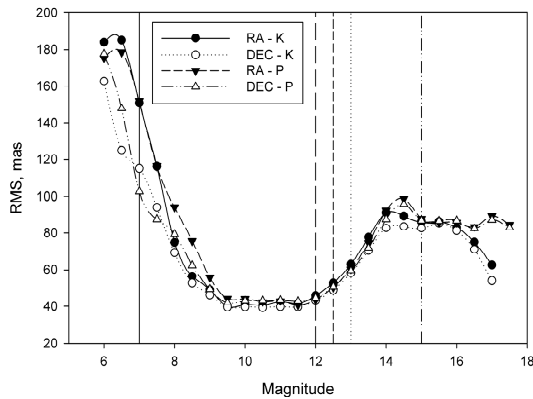


Figure 2: Inner accuracy for 20 plates of MAO received by program Kamasutra (K) and Plate Graf (P)

plates of MAO (MPC number 083) with one are shown on Figure 2.

For further research we chosen Plate Graf program due to the best accuracy results and speed of reduction. For example: time of reduction with one parameter set for 60 input data files of MAO's 4 plates with (389) Industria with usage Kamasutra was 7.5 hours and with usage Plate Graf – only 8 minutes.

In this study we are planning to find the best settings for Plate Graf program, which made all stars identification and astrometric reduction, and to compare obtained results with old one. Main of settings are: changing magnitude limit of reference stars from 12 to 15 with step  $0.5^m$ , choosing reference stars with different options of spectra, using 4 or 5 iteration and receiving mean coordinates from all 6 scans or best 5 scans.

For all plates we obtained totally 384 images in 1600 dpi resolution with several exposures and received 1130 input data files for all exposures. Next, we made near 50 thousands reduction of this 1130 input data files with different settings of Plate Graf program and received near 5 TB data for analysis. This data include, among others, position and instrumental magnitude for chosen asteroids and reference stars.

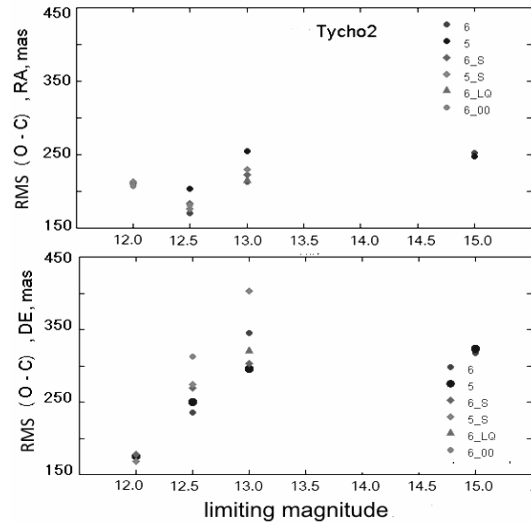


Figure 3: RMS of (O-C) of Interamnia, observed in NAO, for different settings of Plate Graf with Tycho2 reference catalogue

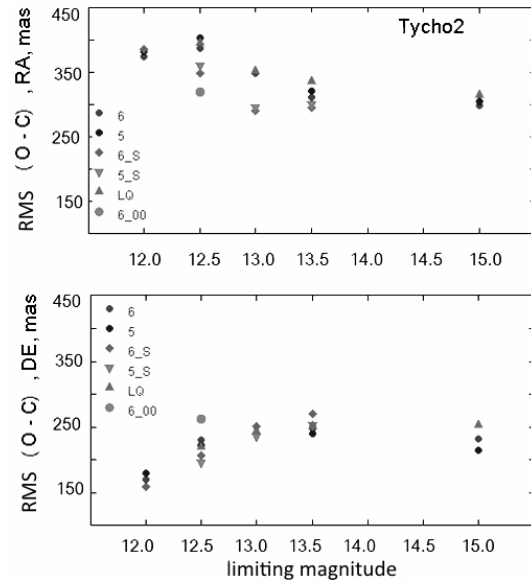


Figure 4: RMS of (O-C) of Interamnia, observed in MAO, for different settings of Plate Graf with Tycho2 reference catalogue

#### 4. Data analysis with different reduction settings

We compare our observed (O) position with calculated JPL ephemeris (C) from on-line service HORIZONS (HORIZONS, 2016). Figure 3,4 shown the RMS of (O-C) for different sets of limiting magnitudes, numbers of iteration and scans quality during processing data in Plate Graf with Tycho2 reference catalogue (RC T2). Figure 5,6 shown results of research for UCAC4 (RC U4) reference catalogue.

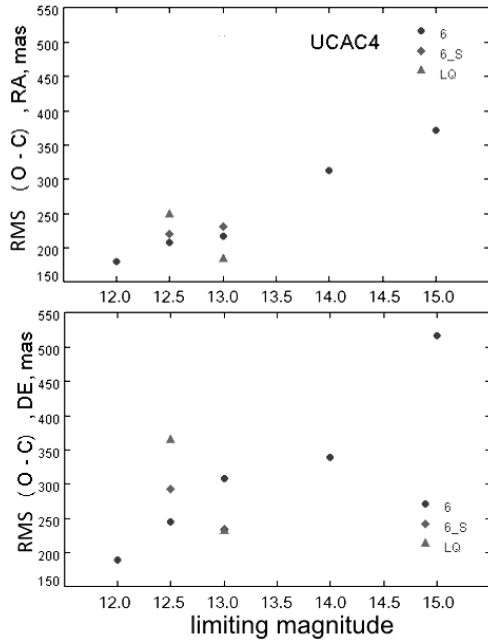


Figure 5: RMS of (O-C) of Interamnia (704), observed in NAO, for different settings of Plate Graf with UCAC4 reference catalogue

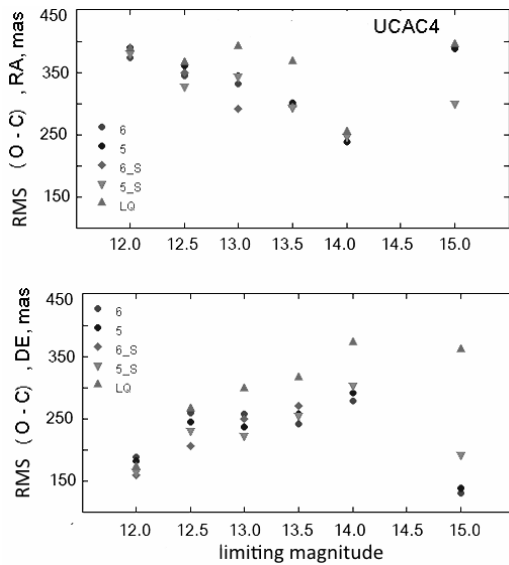


Figure 6: RMS of (O-C) of Interamnia (704), observed in MAO, for different settings of Plate Graf with UCAC4 reference catalogue

As can be seen, that the parameter "limiting magnitude of the reference catalogue" for NAO's observation provide the best results with 12 magnitude and for MAO's – gives the best results in the region of 13<sup>m</sup>-14<sup>m</sup>. This is due to the fact that the exposure time of the NAO's observation has been smaller on average and diameter of the ZA telescope is less than DWA more than 3 times. Results for most optimal settings are given in Table 2 and in Figure 7.

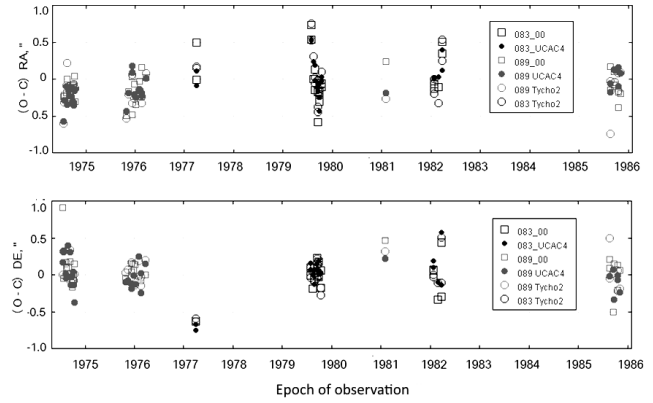


Figure 7: Reduction of Interamnia (704) observations for the selected option with different reference catalogues

Table 2. (O-C) for Interamnia obtained with optimal settings

Observatory	RC	m	(O-C) <sub>RA</sub> , mas	(O-C) <sub>DEC</sub> , mas
NAO	T2	12.0	-186 ± 207	45 ± 168
NAO	U4	12.0	-149 ± 178	-17 ± 188
MAO	T2	13.5	31 ± 311	-49 ± 247
MAO	U4	14.0	40 ± 237	-7 ± 278

### 5. Final analysis

For final analysis to compare our new results with old one we have used AstDyS-2 service (AstDyS-2, 2016). In this service we have chosen data from 083 Goloseevo, 084 Pulkovo and 089 Nikolaev observations (Figure 8, 9). Average (O-C) differences for all plates in our investigation and data from AstDyS-2 service are shown in Table 3.

As can be seen, that the new (O-C) differences obtained with ephemeris Horizons (JPL) and with previous "Ascrecord" measurements from AstDyS-2 database coincide within the limits set error. There were no significant accuracy improvement for NAO plates due to high precisions observations and performed reductions to HCRF/ACT reference system. We have obtained a significant improvement of random and systematic errors for MAO plates.

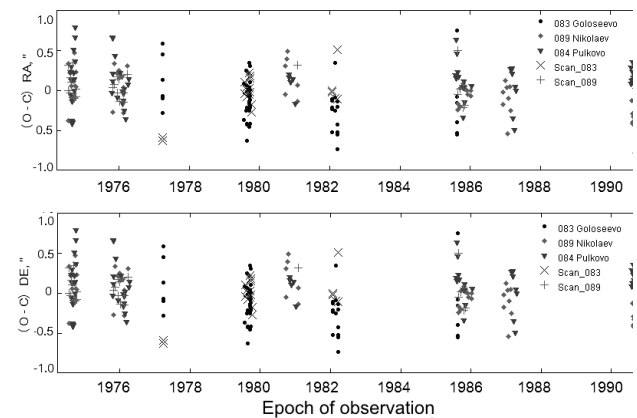


Figure 8: Comparing of new results (prefix scan\_) with old one

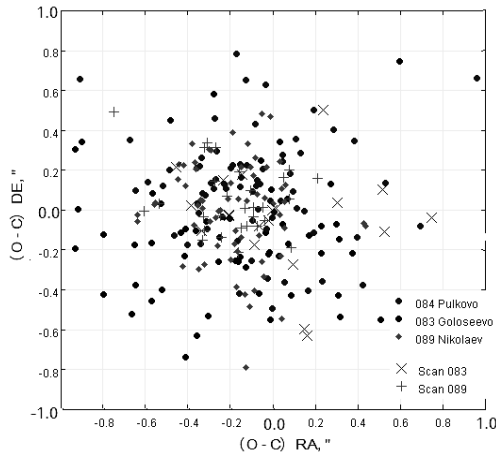


Figure 9: Compare of new results (prefix Scan) with old one

Table 3. Average (O-C) for old and new measurement

Observ. / MP	NAO (704)	MAO (704)	NAO (389)	MAO (1064)
N plates	65	55	4	-
Catalogue	ACT GSC	PPM	ACT GSC	-
<b>AstDyS</b> RA,mas	-185 ±206	-220 ±402	-218 ±332	-
<b>AstDyS</b> DEC,mas	-92 ±248	-157 ±296	-140 ±116	-
N plates	29	20	4	11
Catalogue	Tycho2	Tycho2	Tycho2	Tycho2
<b>New scan</b> RA, mas	-186 ±207	40 ±237	60 ±220	-455 ±514
<b>New scan</b> DEC, mas	45 ±168	7 ±278	158 ±227	-143 ±316
N plates	29	20	4	11
Catalogue	UCAC4	UCAC4	UCAC4	UCAC4
<b>New scan</b> RA, mas	-149 ±178	31 ±311	225 ±310	-460 ±368
<b>New scan</b> UCAC4 DEC, mas	-17 ±188	-49 ±247	113 ±243	-139 ±266

## 6. Conclusion

We chose 64 plates with 180 exposures of 3 minor planets observed in 1970-1990 from the archives of UkrVO.

Obtained 384 plates images with a resolution of 1600 dpi and processed in MIDAS environment to obtain X, Y, h / 2, I. Made identifying for 1130 processed data files.

More than 50 thousand reductions of data with different parameters were performed at total. The volume of reductions data is of about 5 TB.

We obtain the coordinates of minor planets for all variants of reductions.

A comparison of new (O-C) differences obtained with ephemeris Horizons (JPL) and with previous "Ascorecord" measurements from AstDyS-2 database was done.

New results for observations Interamnia in the NAO were shown a repetition of (O-C) system with improving accuracy. For MAO's observations improvement in the (O-C) system and noticeable improvement of accuracy were received.

These results are shown that reprocessing of old photographic plates with asteroid image, even on flatbed scanners, could give good results to reduce systematic errors in the positions of asteroids, associated with the use of old catalogues like PPM, SAO etc. Due to the high labor intensity, of course, this process should be selective. And plates for reprocessing should be chosen considering the quality and availability of plates, last history of the asteroid observations and precision of performed of old astrometric reductions.

## References

- AstDyS-2: 2016, <http://hamilton.dm.unipi.it/astdys/>  
 Andruk V. et al.: 2014, *Odessa Astron. Publ.*, **27/1**, 53.  
 Andruk V. et al.: 2015, *Odessa Astron. Publ.*, **28/2**, 192.  
 Hog E. et al.: 2000, *A&A*, **355**, L27.  
 HORIZONS: 2016, <http://ssd.jpl.nasa.gov/?horizons>.  
 Golovnya V. et al.: 2013, *Odessa Astron. Publ.*, **26/2**, 226.  
 Kazantseva L.V. et al.: 2015, *Kinem. Phys. Cel. Bodies*, **31**, **N1**, 37.  
 Protsyuk Yu. et al.: 2014, *ISBN: 978-80-7080-918-1*, 131.  
 Protsyuk Yu. et al.: 2014, *Kinem. Phys. Cel. Bodies*, **30**, **N6**, 296.  
 Protsyuk Yu. et al.: 2014, *Odessa Astron. Publ.*, **27/1**, 63.  
 Protsyuk Yu. et al.: 2014, *Odessa Astron. Publ.*, **27/1**, 59.  
 Protsyuk Yu.I. et al.: 2015, *Odessa Astron. Publ.*, **28**, **N2**, 204.  
 Vavilova I.B. et al.: 2010, *KosNT.*, **16**, **N5**, 62.  
 Vavilova I.B. et al.: 2011, *KosNT.*, **17**, **N4**, 74.  
 Vavilova I.B. et al.: 2012, *Kinem. Phys. Cel. Bodies*, **28**, **N2**, 85.  
 Vavilova I.B. et al.: 2012, *Baltic Ast.*, **21**, **N3**, 356.  
 Vavilova I.B. et al.: 2014, *Odessa Astron. Publ.*, **27/1**, 65.  
 Vavilova I. et al.: 2014, *ISBN: 978-80-7080-918-1*, 8.  
 Zacharias N. et al.: 2013, *Astron. J.*, **145**, 44

DOI: <http://dx.doi.org/10.18524/1810-4215.2016.29.85177>

## SEARCH SMALL BODIES IMAGES IN COLLECTIONS DIGITIZED PHOTOGRAPHIC OBSERVATIONS OF PREVIOUS YEARS

S. Shatokhina<sup>1</sup>, L. Kazantseva<sup>2</sup>, A. Kazantsev<sup>2</sup>, V. Andruk<sup>1</sup>, V. Golovnia<sup>1</sup>

<sup>1</sup> Main Astronomical Observatory of National Academy of Sciences, 27 Akad. Zabolotnogo St., 03680, Kyiv, Ukraine, [svetash@mao.kiev.ua](mailto:svetash@mao.kiev.ua), [andruk@mao.kiev.ua](mailto:andruk@mao.kiev.ua)

<sup>2</sup> Astronomical Observatory of Kiev National Taras Shevchenko University

3 Observatorna St., 04053, Kyiv, Ukraine, [KazL@ukr.net](mailto:KazL@ukr.net), [ankaz@observ.univ.kiev.ua](mailto:ankaz@observ.univ.kiev.ua)

**ABSTRACT.** Photographic observations of XX century is an important source of information on small bodies of the Solar system. The observations of chronologically earlier oppositions, photometric evaluation of brightness for long periods of time allow refining the orbits of asteroids and identifying various non-stationaries. Unfortunately international databases were contained a very little observable data for accurate estimates of geometric and kinematic parameters of asteroids.

We analyzed the results of digital processing of 338 photographic plates of Northern Sky Survey (FON) project. Modern approach to processing early observations using new digital technologies provides a sufficiently high accuracy of coordinates and magnitudes for all objects on astroplates. As a result 570 images of asteroids and 4 images of comets from 8-16 magnitudes were detected on these plates. Equatorial coordinates and stellar magnitudes of them were composed to catalog of asteroids. All positions were compared with ephemeris. Analysis of ephemeris calculations with known today about the several hundred small planets with observation data showed some interesting results.

**Keywords:** photographic archive – asteroids – catalogs – astrometric positions

### 1. Introduction

A broad searching of small bodies on photographic observations of previous years we planned to carry out on plates from Northern Sky Survey (FON) project. As the first result we used 338 photographic plates of FON project obtained with DWA (Double Wide-angle Astrograph, D/F=40/200, 103"/mm, h=186m) at the Main astronomical observatory in 1982-1994. These plates cover the area on celestial sphere from 0 to 24 hours in right ascension and from  $-4^\circ$  to  $+16^\circ$  in declination. The digitizing of astroplates has been performed using Microtek ScanMaker 9800XL TMA and Epson Expression 10000XL commercial scanners, with the resolution 1200 dpi. All scans of plates accumulated in Joint Digital Archive of Ukrainian virtual observatory. Standard images were processed using advanced complex LINUX / MIDAS / ROMAPHOT programs. The software was developed and implemented in MAO NASU to process the digitized astronomic negative plates as well as to obtain the final product in the form of a catalogue of positions and stellar magnitudes for all regis-

tered objects on the plate. In detail, the process of digitization of images and their further processing and determination of coordinates and magnitudes are described in the series of publications (Andruk et al., 2005; 2007; 2010; 2014; 2015; 2016; Protsyuk et al., 2014a; 2014b). The results of the software testing are described in (Kazantseva et al., 2015; Yizhakevych et al., 2014; 2015; Protsyuk et al., 2014; Andruk et al., 2013; Eglitis et al., 2016b; 2016c).

Digital processing of photographic plates of star fields allows to determine with high accuracy the coordinates and stellar magnitudes for all registered objects on these plates, such as stars, galaxies, small bodies, artificial satellites and artefacts.

At the first, the processing results of photographic plates of Northern Sky Survey project were used for composing of the catalog of star positions and B-magnitudes for 19451751 stars and galaxies with  $B < 16.$ <sup>m</sup> 5 (Andruk et al., 2016b).

Secondly, the processing results of these photographic plates had been used for a broad search for images of small bodies of the Solar system and determination of their coordinates. First test results of searching of Solar system bodies using plate archive of photographic observations were obtained earlier and described in (Shatokhina et al., 2005).

### 2. Results

376 asteroids from Main Belt and 2 comets (65P/Gunn [1982], 4P/Faye [1991]) were identified on plates. From them 570 positions of asteroids and 4 positions of comets were received and composed in total catalog. These objects cover magnitude range from 7.8 to 16.1. The equatorial coordinates  $\alpha$ ,  $\delta$  and stellar B-magnitudes of all small bodies on the plates were obtained in the reference system of Tycho-2 at the epoch of exposition of each plate. Photographic B-magnitudes of objects were calibrated with photoelectric standards.

Figure 1 shows the distribution of all searching asteroids for all used plates. More faint asteroids with 15-16 magnitude were identified on the astronegatives with high atmospheric transparency and good observing conditions only.

Almost every astronegative has images from 1 to 10 different asteroids. For example, Figure 2 shows mutual locations of 9 different asteroids from 10.<sup>m</sup>7 to 15.<sup>m</sup>0 magnitudes on the scan of plate GUA040C000887B.

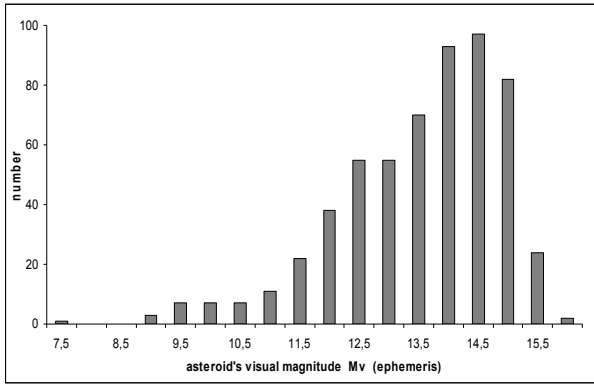


Figure 1: Distribution on magnitudes for 574 searching asteroids

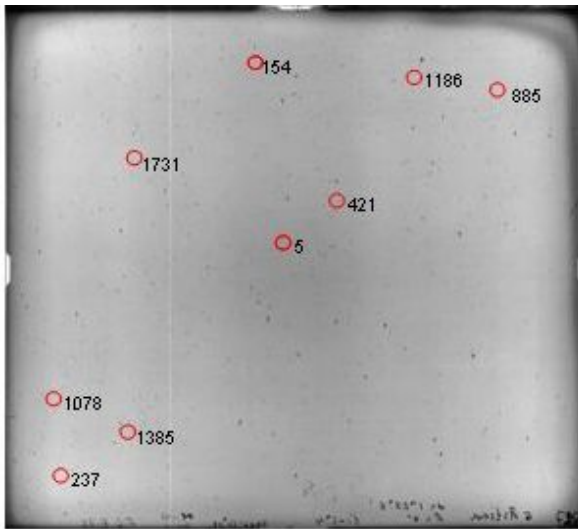


Figure 2: Images of 9 asteroids on scan of the plate GUA040C000887B.

From digital processing of photographic plates of FON project were obtained the mean internal errors equal 0.233 arcsec in both equatorial coordinates and 0.<sup>m</sup>14 in B magnitudes for all objects (Andruk et al., 2016b).

The comparison with the JPL DE431 ephemeris (<http://ssd.jpl.nasa.gov/horizons>) is given. The differences O-C on both coordinates and difference B-Mv (Mv – approximate visual magnitude calculated by ephemeris JPL) are received for all positions of asteroids and comets.

The most of searching asteroids have a single position in composed catalog. But 138 asteroids have a several positions from 2 to 5 during one opposition of asteroid. A range of changes in the differences O-C is 1 arcsec for such asteroids. We analyzed O-C of asteroids on different distances from center of plates. We analyzed O-C of asteroids on different values of asteroid's speed projection too. The significant dependencies O-C were not detected in analysis of these results.

Figure 3 shows changes of observed B magnitudes for 574 searching asteroids and comets. The small trend of B magnitudes observed for faint asteroids with 14-16 magnitudes in comparison with visual magnitudes calculated JPL. As a result, a lower value of color index observed for them. At the same time, the spread of values of B magnitude for faint asteroids increases.

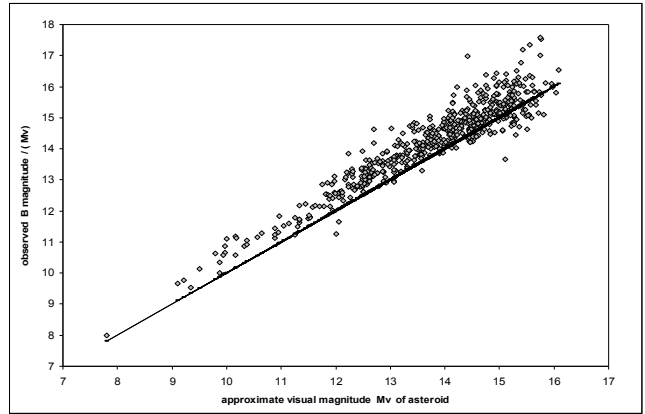


Figure 3: Changes of observed B magnitudes for 574 searching asteroids and comets along Mv asteroid's magnitude axis. (B magnitudes pointed gray color. Mv visual magnitudes pointed black color).

Eight asteroids of the total number in catalog were observed many years before dates of their discovery. For them equatorial coordinates  $\alpha$ ,  $\delta$  and stellar magnitudes B and O-C differences in both coordinates, and B-Mv, where B – blue observed magnitudes, Mv -approximate visual asteroid's magnitude calculated by ephemeris JPL, presented in the Table 1. Only 1 position of asteroid (20730) Jorgecarvano in this table have the earliest chronologically observations among all known in the world.

For asteroids (4816) Connelly and (20730) Jorgecarvano the distributions of all known observations in the world are presented on figure 4. Observational data took from Minor Planet Center ([http://www.minorplanetcenter.net/db\\_search](http://www.minorplanetcenter.net/db_search)). With bold black color pointed our observations

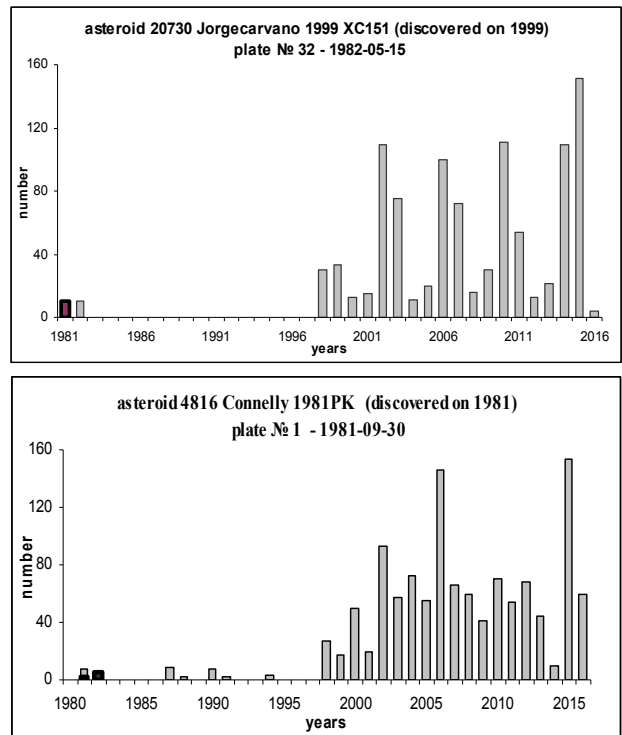


Figure 4: Distributions on time scale of all known observations in the world for 4816, 20730 asteroids.

Table 1 Asteroids observed before their discovering dates.

Object name	RA, J2000.0 h m s	Dec, J2000.0 deg ' "	Magnitu de	(O-C) <sub>RA</sub> arcsec	(O-C) <sub>Dec</sub> arcsec	B-Mv
Plate 1 UT=1981-09-30.762512						
(4816) Connolly 1981 PK	205232.895	+013454.26	16.31U	.57	-.74	.70
Plate 83 UT=1982-05-15.958641						
(7262) Sofue 1995 BX1	164301.910	-023619.46	15.14	-.59	-1.76	.16
Plate 82 UT=1982-05-15.958641						
(20730) Jorgecarvano 1999 XC151	161716.268	-023720.98	16.99U	.87	.56	1.25
Plate 274 UT=1982-07-14.702812						
(5001) EMP 1987 SB1	165147.325	-010355.78	15.99U	-1.15	-1.46	.02
Plate 1484 UT=1989-07-06.955139						
(13977) Frisch 1992 HJ7	195521.821	+085000.65	15.76B	-.24	.48	.78
Plate 1500 UT=1989-09-20.831430						
(14691) 2000 AK119	213153.404	+051221.23	15.77V	.11	-.80	.11
Plate 1513 UT=1989-10-19.872058						
(4290) Heisei 1989 UK3	005758.001	+154944.45	15.42R	-.60	.50	-.14
Plate 1618 UT=1990-03-01.044557						
(6518) Vernon 1990 FR	134123.217	+150003.62	16.36B	-.13	.77	.81

Similar (parallel) work was presented in Baldone observatory (Eglitis et al., 2016a). The faint asteroids up to 17 magnitudes were identified on the plate in Baldone observatory. Among them are much more interesting asteroids which discovered much later than observed.

Calculations evolution of asteroids with orbits MPC catalog from 2005 to 2016 were made earlier (Kazantsev et al., 2008). Differences semi-major axis of the orbits of asteroids between the catalog value in 2016 and calculated received.

The size and distribution of these values for albedo asteroids indicate the existence in the solar system is some non-gravitational effect. This effect is overwhelming growth of semi-major axis of the orbits of asteroids with small albedo.

Additional confirmation aforementioned effect, in principle, can be measured by the regulations asteroid on the plates of a few decades ago. More important differences in semi-major axis must meet greater values O-C.

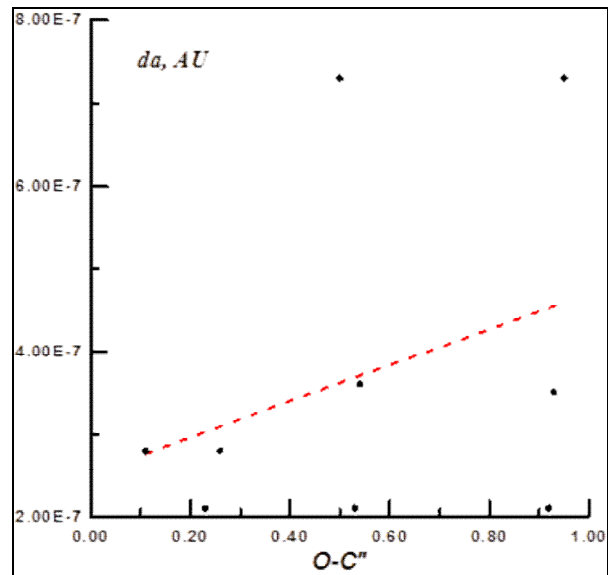


Figure 5: Distribution of values da (O-C) for O-C < 1'' and da > 2•10-7 a.o.

### 3. Conclusion

On photographic plates of Northern Sky Survey project can be detected asteroids with high accuracy up to 16-16.1 magnitude. Among those may be objects which discovered much later than observed. The presence of the archive of all observations at previous years will give possibilities to select and process the interesting asteroids. A necessary condition for obtaining high-precision series of observations of asteroids is the presence of a confident moment of time of observations.

### References

- Andruk V.M. et al.: 2005, *Kinem. and Phys. of Cel. Bodies*, **21**, **N5**, 396.
- Andruk V.M. et al.: 2007, *Journal of Physical Studies*, **11**, **N3**, 329.
- Andruk V.M. et al.: 2010, *Kinem. and Phys. of Cel. Bodies*, **26**, **N3**, 75.
- Andruk V.M. et al.: 2013, *Odessa Astron. Publ.*, **26**, **N2**, 226-228.
- Andruk V.M. et al.: 2014, *Odessa Astron. Publ.*, **27**, **N1**, 53.
- Andruk V.M. et al.: 2015, 2015arXiv, In press.
- Andruk V.M. et al.: 2016, *Kinem. and Phys. of Cel. Bodies*, **32**, **N1**, 56.
- Andruk V.M. et al.: 2016, *Kinem. Phys. Cel. Bodies*, **32**, **N5**, 261.
- Eglitis I. et al.: 2016, Asteroids from digitized processing of photographic observations in Baldone, <http://www.astroplate.cz/abstracts>.
- Eglitis I. et al.: 2016, Astrometry and photometry of Pluto from digitized photographic observations during 1961 to 1996, <http://www.astroplate.cz/abstracts>.
- Eglitis I. et al.: 2016, U-magnitudes of stars and galaxies from the digitized astronegatives of Baldone Schmidt telescope, <http://www.astroplate.cz/abstracts>.
- Kazantsev A.M. et al.: 2008, *Kinem. and Phys. of Cel. Bodies*, **24**, **N5**, 248-252.
- Kazantseva L.V. et al.: 2015, *Kinem. and Phys. of Cel. Bodies*, **31**, **N1**, 37-54.
- Protsyuk Yu.I. et al.: 2014, *Odessa Astron. Publ.*, **27**, **N1**, 61-62.
- Protsyuk Yu.I. et al.: 2014, *Odessa Astron. Publ.*, **27**, **N1**, 59-60.
- Yizhakevych O. et al.: 2014, *Odessa Astron. Publ.*, **27**, **N1**, 67.
- Yizhakevych O. et al.: 2015, *Odessa Astron. Publ.*, **28**, **N2**, 213.
- Shatokhina S. et al.: *Kinem. and Phys. of Cel. Bodies, Supp.* **N 5**, 2005, P.570-572.

DOI: <http://dx.doi.org/10.18524/1810-4215.2016.29.85181>

# PHOTOGRAPHIC OBSERVATIONS OF MAJOR PLANETS AND THEIR MOONS DURING 1961-1990 AT THE MAO NAS OF UKRAINE

O.M.Yizhakevych, V.M.Andruk, L.K.Pakuliak

Main Astronomical Observatory of National Academy of Sciences,  
27 Akad. Zabolotnogo St., 03680, Kyiv, Ukraine, izhak@mao.kiev.ua

**ABSTRACT.** We present the results of photographic observations' processing of Saturn's moons, Uranus, Neptune and their moons on the basis of MAO NAS of Ukraine photographic observational archive. The analysis of the results is given. Observations were obtained using 4 telescopes: Double Long-Focus Astrograph (DLFA, D/F = 400/5500), Zeiss Double Astrograph (DAZ, D/F= 400/3000), Reflector Zeiss-600 (D/F= 600/7500), Wide-angle Astrograph, (DWA, D/F= 400/2000). Observations were carried out during 1961 – 1990 (<http://gua.db.ukr-vo.org>). Digitizing of plates has been done by EPSON EXPRESSION 10000XL (EE) flatbed scanner in 16-bit gray color range with resolution 1200dpi. (Andruk et al.: 2005, 2012; Golovnja et al.: 2010; Protsyuk et al. 2014a, 2014b). The reduction of plates was made using the software developed in MAO NASU in the enhanced LINUX-MIDAS software kit. (Andruk V. et al.: 2016a, 2016b). Tycho2 was used as a reference system. The internal accuracy of the reduction for the first three instruments is  $\pm 0.08 - \pm 0.13$  arcsec for both coordinates. For the wide angle astrograph DWA, RMS errors appeared 2 – 2.5 times higher. The total amount of processed plates with images of Saturn's moons is **209 (511 frames)**, **33** plates contain the images of Uranus and U1,U2,U3,U4 moons, **29** plates have images of Neptune and N1 moon (Yizhakevych et al., 2015, 2016, 2017; Protsyuk et al., 2015). The online comparison of calculated positions of objects with IMCCE ephemeris data was made (<http://lnfm1.sai.msu.ru/neb/nss/nssephmf.htm>).

**Keywords:** Catalogs, Solar System Bodies, Saturn, Uranus, Neptune.

## 1. Introduction

The current work is the continuation of the preceding publications (Ivanov et al., 2013; Izhakevich et al., 1991; Kaltygina et al., 1992; Kulyk et al., 2012; Pakuliak et al., 1997a, 1997b, 2012; Shatokhina et al., 2005; Yizhakevych et al., 2014, Yizhakevich et al., (<http://gua.db.ukrvo.org/starcatalogs.php?whc=sat90>) and comprises the discussion of major planets' photographic observations' processing results. Using the observed data we obtained **1385** astrometric positions and magnitudes of 8 Saturn's moons S2, S3, S4, S5, S6, S7, S8, S9, **58** positions of Uranus, **66** positions of U1, U2, U3, U4 satellites of Uranus, **51** positions of Neptune, **9** positions of N1 moon of Neptune. All of them are obtained in the Tycho-2

reference frame. The analysis and the accuracy assessment of the obtained catalogs are considered.

## 2. Saturn's moons

From the total amount of photographic observations of Saturn, collected in MAO NASU ([DATABASE of JOINT PLATE ARCHIVE \(DBGPA V2.0\)](#)), we selected about 250 plates with the best quality of images. Taking into account, that each plate contains several exposures of different duration (from some seconds to some minutes), the total volume of processed material consists of **511 digital images**. The division of digital plate image into exposure frames and their further processing were done using the special software package (Andruk et al., 2014; 2015; Kazantseva et al., 2015).

Table 1 gives the data of the internal accuracy of the reduction of Saturn's moons' observations for each of 4 telescopes. Columns contain the telescope scale ("/pix), the mean number of Tycho-2 reference stars, unit weight RMS errors of magnitudes and positions, and a number of positions N by each telescope.

Table 1. The internal accuracy of the reduction of Saturn's moons' observations.

Telesc.	Scale "/pix	Ref. stars	rms <sub>mg</sub>	rms <sub><math>\alpha</math></sub>	rms <sub><math>\delta</math></sub>	N posit.
DLFA	0.79	75	0.27	0.09	0.09	1017
DWA	<b>2.17</b>	<b>610</b>	<b>0.27</b>	<b>0.23</b>	<b>0.22</b>	<b>101</b>
DAZ	1.45	142	0.34	0.09	0.10	95
Z600	0.59	16	0.37	0.09	0.11	172

From the Table 1, it is obvious that DWA observations (field  $8^{\circ} \times 8^{\circ}$ , scale 103"/mm) are the least suitable for such determinations because of internal errors which are more than twice higher than the other telescope ones. DWA observations (1978 – 1986, **13** nights) were not effective enough. Plates available for the processing are the ones containing mostly images of S5, S6, S8 moons. The possible reasons of the bad accuracy may be the poor resolution of images because of insufficient shift of telescope between the exposures and the telescope scale.

DLFA Saturn's moons observations occurred the most productive (1961- 1984, **57** nights) and durable. During the period, images of 7 main Saturn's moons S2-S8 were obtained.

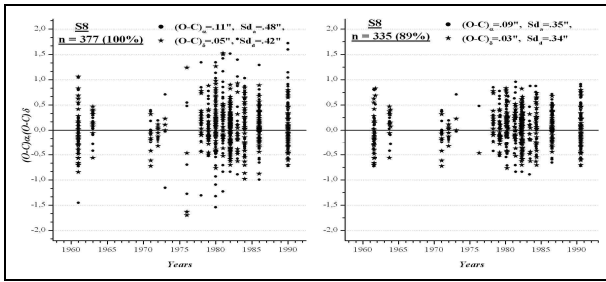


Figure 1: The distribution of S8 observations with dates and the dispersion of  $(O-C)_i$  in respect to their mean values.

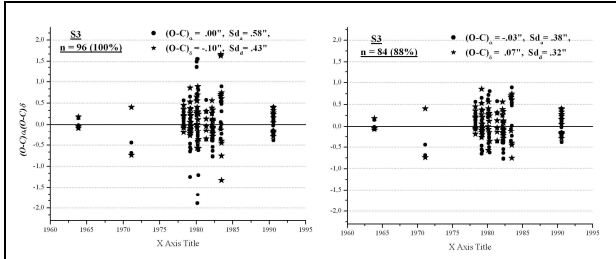


Figure 2: The distribution of S3 observations with dates and the dispersion of  $(O-C)_i$  relatively to their mean values.

The brief series of observations were obtained in Uzbekistan in the field conditions with the two other telescopes: **DAZ** in 1986 (7 nights) and **Z600** in 1990 (9 nights). The astrometric observations with Z600 reflector are among the first on using the reflector for the purposes of positional astrometry (Kaltygina et al., 1992).

The dispersion of values of random  $(O-C)_i$ , the mean values of  $(O-C)$  and standard deviations  $Sd$  were derived using the IMCCE ephemeris data (<http://lnfm1.sai.msu.ru/neb/nss/nssephmf.htm>) separately for each set of satellite positions. For S4, S5, S6, S8 with the wide sample of observations the standard deviations  $Sd$  became in the limits 0.41" to 0.48". For the other satellites with the small set of observations, these values are significantly larger. Table 2 and 2a show the statistical data of reduction for each moon separately. Here,  $N$  is the number of obtained positions, **Bph** is a photographic stellar magnitude with the standard deviation  $Sd_B$ ,  $(O-C)$  is mean values of residual deviation and  $Sd$  is a standard deviation for  $\alpha$  and  $\delta$  coordinates. The last column contains the following notations for telescopes: 1 corresponds to DLFA, 2 – DWA, 3 – DAZ, 4 – Z600.

Fig. 1 and Fig. 2 show the dispersion of values of random  $(O-C)_i$  in respect to their arithmetical mean value for two moons **S3** and **S8** on various volumes of samples: the left side shows the full sample, the right side – results after the elimination of observations with  $(O-C)_i$  exceeding or equal to  $2\sigma$ ". Dates of observations are given along the X-axis that helps to assess the intensity of observations during the 30 year period.

2.1. Application of  $2\sigma$ " criterion to all series of observations leads to the reduction of the sample volume by more than 10%-15% and to the mean decrease of the standard deviation  $Sd$  by 0.15". At the same time, the arithmetic mean values  $(O-C)$  for each satellite are reduced within the error of the mean, and the vast majority of  $(O-C)$  is

clustered around their arithmetic mean of  $\pm 1$ ". Table 2a shows the differences of statistical characteristics when applying the  $2\sigma$ " criterion to the samples with significantly different volumes for **S3** and **S8** satellites.

Table 2. The results of the reduction of Saturn's moons' photographic observations.

Obj.	N	$(O-C)_\alpha$	$Sd_\alpha$	$(O-C)_\delta$	$Sd_\delta$	Teles.
<b>S2</b>	<b>12</b>	0.48	<b>.68</b>	0.16	.48	1
<b>S3</b>	<b>96</b>	0.00	<b>.58</b>	0.10	.43	1,4
S4	183	0.07	.44	0.07	.42	1-4
S5	269	0.15	.47	0.07	.42	1-4
S6	435	0.09	.47	-0.03	.43	1-4
<b>S7</b>	<b>12</b>	-0.04	.47	0.10	<b>.63</b>	1,4
<b>S8</b>	<b>377</b>	0.11	.48	0.04	.41	1-4
S9	1	0.44		-0.27		4

Table 2a. The comparison of the results of the S3 and S8 reduction before and after the application of  $2\sigma$ " criterion.

N,	%	$(O-C)_\alpha$ "	$Sd_\alpha$ "	$(O-C)_\delta$ "	$Sd_\delta$ "
<b>S3, Bph=10.6 ± 0.08</b>					
96,	100	+0.00 ± 0.06	.58	+0.10 ± 0.04	.43
84,	88	-0.03 ± 0.04	.38	+0.07 ± 0.04	.32
<b>S8, Bph=11.9 ± 0.04</b>					
377,	100	+0.11 ± 0.02	.48	+0.04 ± 0.02	.41
335,	89	+0.09 ± 0.02	.35	+0.03 ± 0.02	.34

2. 2. The next step in the evaluation of the satellite reduction quality was made by determining the differential coordinates in the sense of "satellite minus satellite " and their comparison with theoretical data.

Table 3. The statistical characteristics of differential coordinates of Saturn's satellites by DLFA observations.

Si-Sj	N	$(O-C)_\alpha$	$Sd_\alpha$	$(O-C)_\delta$	$Sd_\delta$
S8-S2	6	-.05±.21	.52	.03±.08	.21
S6-S2	6	-.51±.18	.46	-.25±.13	.33
S5-S2	10	-.46±.25	.80	-.08±.09	.33
S4-S2	8	-.06±.29	.83	-.14±.10	.28
S3-S2	7	-.12±.20	.53	-.03±.08	.21
S8-S6	193	.01±.02	.28	.04±.02	.32
S5-S6	187	.02±.02	.24	-.06±.02	.25
S8-S3	43	.11±.05	.31	.02±.03	.22
S6-S3	68	.13±.04	.31	-.06±.03	.25
S5-S3	61	.10±.04	.29	.01±.03	.22
S8-S4	119	.00±.03	.31	.01±.03	.30
S6-S4	139	-.02±.02	.28	.00±.07	.17
S5-S4	125	.02±.02	.27	-.02±.02	.27
S3-S4	38	-.06±.04	.24	.11±.04	.25

Table 3 selectively for some pairs of satellites presents statistical characteristics of differential coordinates from observations at the **DLFA** telescope. First of all, these are the pairs formed by the combination of the **S2** satellite with other four ones. Positions of S2 (Enceladus) form the short-term observational series (n=12), obtained in 1979–1981 at DLFA. Here, the statistical data for other pairs of moons with the essentially larger number of observations

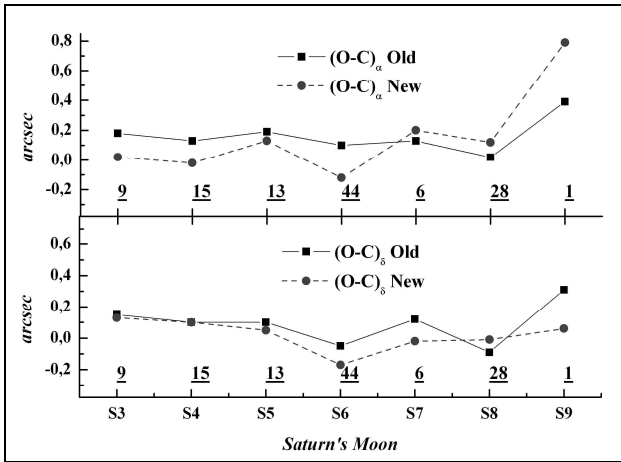


Figure 3: Matching of the mean values (O-C) obtained in the processing of Saturn’s moons’ observations using two techniques.

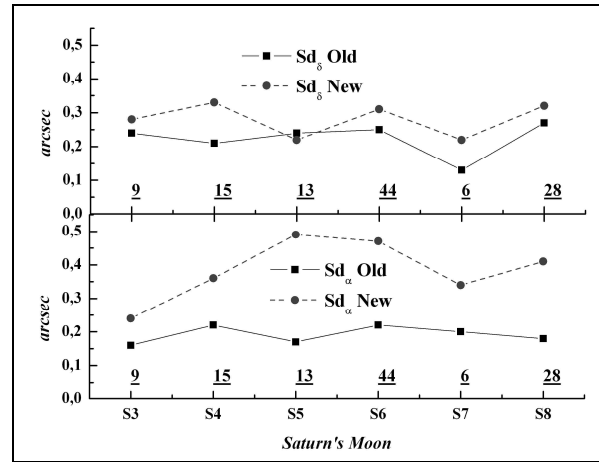


Figure 4: Matching of standard deviations Sdα and Sdδ obtained in the processing of Saturn’s moons’ observations using two techniques.

are given. For these pairs, values of Sd occurred two times lower than for pairs with S2. It may be due to small volumes of samples or the inaccuracy of S2 theoretical data. For the short-term observations and samples of small volumes, such type of analysis is not always unambiguous.

2. 3. One more step in the evaluation of the observation reduction quality was made by comparison of two techniques of processing the same series of photographic observations. We used the observations obtained by Z600 reflector in 1990. Both types of reduction are made in the same reference system of Tycho-2. In the first case we used the "classic" method of the reduction and in the last one the method of the reduction of digital plate images was applied.

It occurs that the number of positions of the same objects calculated with using two methods differs. The classic method gives 231 positions of 7 Saturn’s satellites. The modern technique gives only 172 positions. But, only in 119 cases, a match is found on objects and their moments of observations.

Fig. 3 and 4 show the differences in statistical characteristics for two different techniques of plate processing. The discrepancies of mean values of (O-C)α and (O-C)δ (Fig.3) on each satellite are small within the error of the mean. As for the differences in standard deviations Sd (Fig.4) on α coordinate, they are more significant while Sdδ doesn’t show any differences. The number of satellite positions is shown along X-axis.

The quantitative and qualitative difference in the results of reduction by using two techniques exists for other telescopes too. For example, earlier we had obtained 5 positions of S1 satellite close to Saturn (1980, DLFA). But processing of the digital image does not provide them. For S2 satellite 42 positions were previously determined from the observations obtained by tree telescopes DLFA, DWA, Z600 (1978-1990).

The digital image processing procedure has fixed only 12 positions of S2 obtained by DLFA (1979-1981). The cause of this disagreement may lay in the imperfection of the algorithm which evaluates the center and the quality of the satellite image and eliminates “trash” images. It requires the further study and improvement.

### 3. Uranus, Neptune and their moons

We have completed the processing of photographic observations of Uranus, Neptune and their moons obtained with three telescopes: DLFA, DWA, Z600 during 1963-1990 (Protsyuk et al., 2015; Yizhakevych, 2017a in press). The observational technique, as well as reduction one, were the same as for Saturn’s moons. We used 33 plates (or 20 observational nights) with Uranus images and 29 plates with Neptune (16 nights). Besides the images of major planets, we succeeded to identify and process 4 moons of Uranus, U1, U2, U3, U4 and one moon of the Neptune –N1. Finally, we obtained catalogs of astrometric positions of Uranus (n=61), its 4 satellites (n=56), Neptune (n=51) and its satellite N1 (n=9).

Table 4 contains the assessment of the internal accuracy of the reduction for Uranus and Neptune observations – RMS errors for both coordinates α, δ, and photographic stellar magnitude Bph. Here, as the volume of treated observations significantly yields the Saturn’s one, so the statistical parameters are determined less certain.

Table 4. The internal accuracy of the reduction of photographic plates with Uranus and Neptune images.

Tel..	Scale "/px	Ref. stars	Rms Bph	Rms α	Rms δ	N posit.
						Uran./Nept.
DLFA	0.79	97	.29	.06	.08	9 / 3
DWA	2.17	800	.32	.16	.20	29 / 33
Z600	0.59	16	.36	.09	.10	23 / 15
<b>Σ =</b>						<b>61 / 51</b>

Tables 5 and 6 comprise differences (O-C)<sub>i</sub> between observed and theoretical positions (DE405) of planets and their moons, mean values of (O-C) and standard deviations Sd on both coordinates. All the estimations are obtained online using IMCCE data.

Table 5. The results of the reduction of photographic observations of Neptune and its satellite N1.

Object	N	(O-C) <sub>α</sub>	Sd <sub>α</sub>	(O-C) <sub>δ</sub>	Sd <sub>δ</sub>	Tel.
N1	8	0.14	.41	0.25	.49	4
N1	1	0.95	-	-0.01	-	1
<b>Σ = 9</b>		0.23	.46	0.23	.46	
Neptune.	3	0.23	.46	0.07	1	1
Neptune	33	0.20	.68	-0.32	.98	2
Neptune	15	-0.06	.38	0.00	.44	4
<b>Σ = 51</b>		0.12	.60	-0.20	.83	

Table 6. The results of the reduction of photographic observations of Uranus and its satellites U1-U4.

Obj.	N	(O-C) <sub>α</sub>	Sd <sub>α</sub>	(O-C) <sub>δ</sub>	Sd <sub>δ</sub>	Tel.
U1	3	-0.30	1.18	0.78	.73	4
U2	8	-0.16	0.86	0.31	.39	4
U3	22	0.04	0.52	0.12	.31	4
U4	22	-0.09	0.56	0.10	.49	4
U4	1	0.00	-	-0.61	-	2
<b>Σ = 56</b>						
Uranus	9	0.86	0.61	-0.23	.61	1
Uranus	29	0.13	0.80	-0.22	.75	2
Uranus	23	0.15	0.66	0.06	.69	4
<b>Σ = 61</b>		0.24	0.76	-0.12	.74	

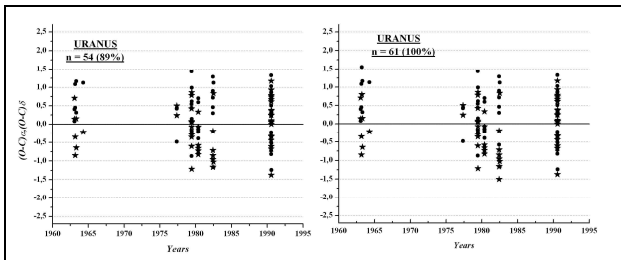


Figure 5: The distribution of Uranus observations with years and the dispersion of (O-C)<sub>i</sub> deviations

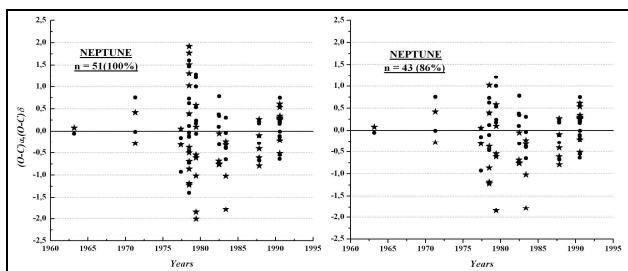


Figure 6: The distribution of Neptune observations with years and the dispersion of (O-C)<sub>i</sub> deviations

3.1. Fig. 5 and 6 demonstrate the distribution of observations of Uranus and Neptune during a 30-year observational period and the scatter of (O-C)<sub>i</sub> values relative to their arithmetic mean.

The (O-C)<sub>i</sub> scatter range is rather wide and is within ±2.0". After the elimination of positions with (O-C)<sub>i</sub> ≥ 2σ", the total amount of Uranus and Neptune positions decrease by 10-16%, and the range of (O-C)<sub>i</sub> scatter around the mean value narrowed to ± 1.5". Taking into account the paucity of samples (for Uranus number of

positions n is 61, for Neptune n=51), such narrowing has a significant effect on statistical parameters of a reduction, mainly on the standard deviations. It also casts doubt on the reliability of the evaluation of the material.

3.2. As in the case of Saturn, we have made the comparison of two techniques of processing procedure for U1, U2, U3, U4, N1 satellites (Z600, 1990). Fig. 7 demonstrates the differences between the standard deviations Sd<sub>α</sub> and Sd<sub>δ</sub> obtained using different techniques of reduction.

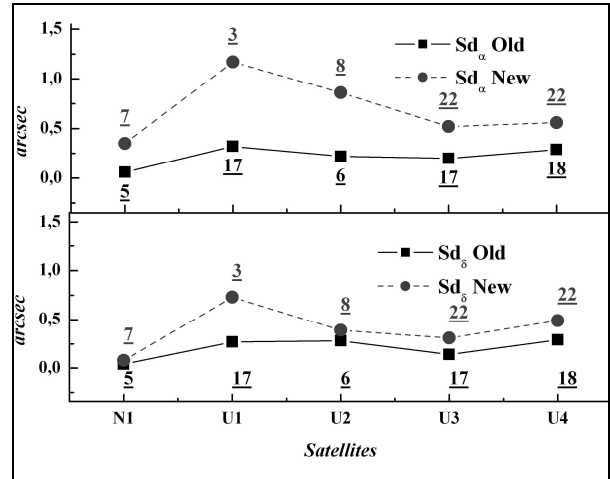


Figure 7: The comparison of reduction results made using two different processing procedures by comparison of standard deviations Sd<sub>α</sub> and Sd<sub>δ</sub>

Solid lines in Fig.7 represent the classic technique of the reduction, and the dashed ones describe the digital technique. Digits under the signs mark the number of positions. The remarkable divergence between two techniques on α coordinate may be the consequence of small volumes of samples.

#### 4. Conclusions

1. Processing of photographic observations of major planets and their moons was performed in the framework of UkrVO project (Vavilova et al., 2012a; 2012b; 2014a; 2014b).

2. We obtained astrometric catalogs of Saturn's satellites (n=1385 positions), Uranus (n=61), Neptune (n=51), Uranus's satellites U1 (n=3), U2 (n=8), U3 (n=22), U4 (n=22), Neptune's moon N1 (n=9) in Tycho-2 reference system. The internal accuracy of reduction in both coordinates is in the range 0.06"-0.11". For DWA telescope this accuracy is more than twice worse and is 0.16"- 0.23". The accuracy of photographic magnitudes varies from 0.27 mg to 0.37mg for all 4 telescopes.

3. The comparison of calculated positions with theory DE405 shows that the scatter of (O-C)<sub>i</sub> values is ± 2". Elimination of positions with (O-C)<sub>i</sub> ≥ 2σ" leads to the decrease of the sample volume by 10%-15% and to the reduction of standard deviation Sd approximately by 0.15". For narrow samples, the application of the (O-C)<sub>i</sub> ≥ 2σ" criterion can produce the erroneous conclusions.

4. The comparison of results obtained by the two techniques, classic and digital, shows the difference in the number of calculated positions for all objects. The reasons for these discrepancies are studied.

*Acknowledgments.* The authors are grateful Astro Spact Data Processing Center of MAO NASU for technical support

## References

- Andruk V. et al.: 2005, *Kinem.Phys. Sel. Bodies*, **21**, **N5**, 396.  
 Andruk V. et al.: 2012, *Visn. Kyiv Nat. Univ., Astronomia*, **48**, 35.  
 Andruk V. et al.: 2014, *Odessa Astron. Publ.*, **27/1**, 53.  
 Andruk V. et al.: 2015, [arxiv.org/abs/1512.05535](https://arxiv.org/abs/1512.05535).  
 Andruk V. et al.: 2016a, *Kinem.Phys.Sel. Bodies*, **32**, **N1**, 56.  
 Andruk V. et al.: 2016b, *Kinem.Phys.Sel. Bodies*, **32**, **N5**, 1.  
 Golovnja V. et al.: 2010, *Jurn. Phis. Studies*, **14**, **N2**.  
 Ivanov G. et al.: 2013, *Izvest. GAO in Pulkovo*, **220**, 501.  
 Izhakevich E. et al.: 1991, *Sient. Paper deposit.*, [1991PDRII4553 I](#).  
 Kaltygina S. et al., 1992, *Sient. Paper deposit.*, **N1044-Uk92**.  
 Kazantseva L. et al.: 2015, *Kinem. Phys. Sel. Bodies*, **28**, **N2**, 59.  
 Kulyk I. et al.: 2012, *IMCCE. Intern. Work. NAROO-GAIA, Paris Observatory*, 153, <hal-00758312>.  
 Pakuliak L.K. et al.: 1997a, *Newsletter IAU WG*, **9**, 13.  
 Pakuliak L. et al.: 1997b, *Baltic Astron.Vilnius*, **6**, **N2**, 251.  
 Pakuliak L. et al.: 2012, *IMCCE. Intern.l Workshop NAROO-GAIA, Paris Observatory*, 161, <hal-00821005>.  
 Protsyuk Yu.I. et al.: 2014a, *Odessa Astron. Publ.*, **27/1**, 61.  
 Protsyuk Yu.I. et al.: 2014b, *Odessa Astron. Publ.*, **27/1**, 63.  
 Protsyuk Yu.I. et al.: 2015, *Odessa Astron. Publ.*, **28/2**, 204.  
 Shatokhina S. et al.: 2005, *Kinem. Phys. Sel. Bodies Suppl.*, **N5**, 570.  
 Vavilova I. et al.: 2012a, *Baltic Astronomy*, **21**, **N3**, 356.  
 Vavilova I. et al.: 2012b, *Kinem. Phys. Sel. Bodies*, **28**, **N2**, 59.  
 Vavilova I. et al.: 2014a, *Proc. of the Workshop "ASTROPLATE", Prague*, 2014, 8.  
 Vavilova I. et al.: 2014b, *Odessa Astron. Publ.*, **27/1**, 65.  
 Yizhakevych O. et al.: 2014, *Odessa Astron. Publ.*, **27/1**, 67.  
 Yizhakevych E. et al.: 2015, *Odessa Astron. Publ.*, **28/2**, 213.  
 Yizhakevych O. et al.: 2016, *Visnyk Kyiv National Univ., Astronomia*, in press.  
 Yizhakevych O. et al.: 2017, *Kinem.Phys. Sel. Bodies*, **33**, in press.  
 Yizhakevich O. et al.: <http://gua.db.ukrvo.org/starcatalogs.php?whc=sat90>

DOI: <http://dx.doi.org/10.18524/1810-4215.2016.29.85182>

## THE EQUATORIAL COORDINATES AND B-MAGNITUDES OF THE STARS IN THE SOUTHERN HEMISPHERE ZONES BASED ON THE DIGITIZED ASTRONEGATIVES OF FON PROJECT AT THE ULUGH BEG ASTRONOMICAL INSTITUTE

Q.X. Yuldoshev<sup>1</sup>, M.M. Muminov<sup>2</sup>, Sh.A. Ehgamberdiev<sup>1</sup>, O.U. Usmanov<sup>1</sup>, H. Relke<sup>3</sup>, Yu.I. Protsyuk<sup>4</sup>, O.E. Kovylianska<sup>4</sup>, S.V. Protsyuk<sup>4</sup>, V.N. Andruk<sup>5</sup>

<sup>1</sup> Ulugh Beg Astronomical Institute of the Uzbek Academy of Sciences, 33 Astronomicheskaya St., 100052 Tashkent, Uzbekistan, [qudratillo@astrin.uz](mailto:qudratillo@astrin.uz)

<sup>2</sup> Andijan State University, 129 University Str., 170100 Andijan, Uzbekistan, [muminov\\_mm@mail.ru](mailto:muminov_mm@mail.ru)

<sup>3</sup> Walter Hohmann Observatory, Wallneyer St.159, 45133 Essen, Germany, [helena\\_relke@yahoo.com](mailto:helena_relke@yahoo.com)

<sup>4</sup> Research Institute "Nikolaev Astronomical Observatory", 1 Observatornaya St., 54030, Mykolaiv, Ukraine, [yuri@nao.nikolaev.ua](mailto:yuri@nao.nikolaev.ua)

<sup>5</sup> Main Astronomical Observatory of National Academy of Sciences, 27 Akad. Zabolotnogo St., 03680, Kyiv, Ukraine, [andruk@mao.kiev.ua](mailto:andruk@mao.kiev.ua)

**ABSTRACT.** FON (Russian abbreviation of the Photographic Sky Survey) were carried out at 6 observatories. The Kitab Observatory (KO) of Ulugh Beg Astronomical Institute (UBAI) of the Uzbek Academy of Sciences (UzAS) was involved in this project from 1981 to 1996. For the observations the Double Astrograph of Zeiss (DAZ, D/F = 40/300, 69"/mm) was used. On the FON project about 2600 photographic plates were exposed. In October, 2015 digitization of these astroplates were started using EPSON Expression 10000XL flatbed scanner with the spatial resolution of 1200 dpi and completed in June, 2016. The first stage of the work is the processing of the 2000 photographic plates in zones of the southern hemisphere with the declination between 0 and -20 degrees. The 1704 plates have already been processed. The equatorial coordinates  $\alpha$ ,  $\delta$  of stars and galaxies were determined in the system of the Tycho2 catalogue and the B-magnitudes in the system of the photoelectric standards. UBAI UzAS, Tashkent (Uzbekistan), ASU, Andijan (Uzbekistan), WHO, Essen (Germany), RI NAO, Nikolaev (Ukraine), MAO NASU, Kyiv (Ukraine) have taken part in the processing of the digitized images. For the data reduction the MIDAS package and software, developed in the MAO NASU were used. Based on the results of the processing of the astronegatives in the sectors of right ascension from 0 hours to 24 hours and declination from -20° to 0° the internal errors of the catalogue were estimated. The errors calculated for all stars are 0.17" and 0.18<sup>m</sup> respectively. For the stars brighter than 14 magnitude the errors are 0.08" and 0.07<sup>m</sup> for the equatorial coordinates and B-magnitudes respectively.

**Keywords:** photometric – methods: data analysis – catalogs, virtual observatory tools – astrometry – techniques

### 1. Introduction

The idea of the project "A photographic survey of the northern sky" (FON) was initiated by the main Astronomical Observatory of National Academy of Sciences of Ukraine (MAO NASU, Ukraine) [Kolchinsky, 1977]. The observatories of the former Soviet Union, such as Goloseevo, Zvenigorod, Dushanbe, Abastumani, Zelenchuk and Kitab realized this project using identical astrographs (with a diameter of 400 mm lens and a focal length of 2000 mm or 3000 mm) produced by the company Carl Zeiss Jena (GDR). On the Kitab observatory was installed a double Zeiss astrograph (F = 3000 mm, field of view 5.5° x 5.5° and scale 69"/mm). The photographing of the sky (from -20° to +30°) was done with a shift of the centers of photographic fields in 2 degrees on the declination, and with a difference of distances in 4 degrees on the right ascension between the centers of adjacent fields. The observation schema is represented in the Figure 1. Each field was photographed with two exposures (the long one: from 40 to 60 minutes and the short one: from 40 to 60 seconds) on the same photographic plate with the shift on both coordinates. The duration of the long exposure was selected in such a way to obtain images of stars down to 16-17 magnitude. On the Kitab observatory the photographic observations for the FON project were carried out from 1981 to 1996. More than 2600 photographic plates were received. In the observations were involved E. Rakhmatov, X. Rakhmatov, E. Mirmahmudov, L. Bash-tova, J. Ivanov and others. In October, 2015 all astronegatives were brought from Kitab observatory to Tashkent and systematized as an archive of the glass library of the AI UzAS. Since November 2015 have been scanned more than 2000 astronegatives in the areas from -18° to 0° using

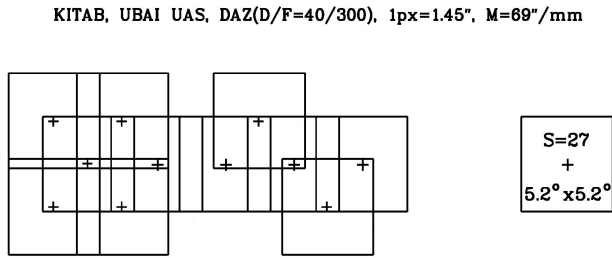


Figure 1: The scheme of the overlapping fields of the astronegatives for the Kitab's part of the FON project.

the Epson Expression 10000XL flatbed scanner and its base software product designed for the scanning with a spatial resolution of 1200 dpi and the size of fields up to 13000 x 13000 pixels (one pixel is equal 1.45"). By this time, for the Kyiv's part of the FON project in MAO NASU was developed a special software in LINUX/MIDAS/ROMAFOT environment, which has already been tested in various works (Andruk, 2005a; Andruk, 2005b; Andruk, 2007; Andruk, 2010; Eglitis, 2016a; Eglitis, 2016b; Kazantseva, 2015; Protsyuk, 2014a; Protsyuk, 2014d; Protsyuk, 2015; Vavilova 2012a; Vavilova, 2012b; Vavilova, 2014; Yatsenko, 2011; Yizhakevych, 2014; Yizhakevych, 2015; Yizhakevych, 2016). For all scans of the Kitab's part of the FON project were already received rectangular coordinates and instrumental stellar magnitudes of all registered objects and compiled preliminary catalogues of stars for all zones. The final result – the common catalogue will be obtained from the processing of single scans without rotating of the plates by 90°, which allows to save resources for storing and processing information twice without the compromising the accuracy of the results. The principles and steps of the processing of digitized photographic plates, which were briefly summarized in Andruk, 2015c, are already successfully applied for the processing of all scanned images of the Kitab's part of the FON project.

**2. The progress in the realisation of the Kitab's part of the FON project**

The common approach to the study of accuracy characteristics of scanners was implemented in the works (Golovnya, 2010; Protsyuk, 2014b; Protsyuk, 2014c). In this work for the digitization of the astronegatives was used the Epson Expression 10000XL scanner. The investigations of its astrometric and photometric characteristics were described in the works (Muminov, 2013; Muminov, 2014, Muminov, 2016). To obtain a star catalogue of equatorial coordinates and B-magnitudes were used the methods and programs for the processing of scans and the creating of catalogues presented in the works (Andruk, 2014; Andruk, 2015b; Andruk, 2016a; Andruk, 2016b; Pakuliak, 2016). The equatorial coordinates of stars and galaxies were obtained in the system of Tycho2 catalogue and the photographic B-magnitudes in the system of photoelectric standards (Andruk, 1995; Kornilov, 1991; Mermilliod, 1991; Relke, 2015). So far (September 2016) were processed N=1704 plates in ten areas, on which after mutual identifications for overlapping areas of the plates were found more than K=11.6 millions stars and galaxies from more than L=116

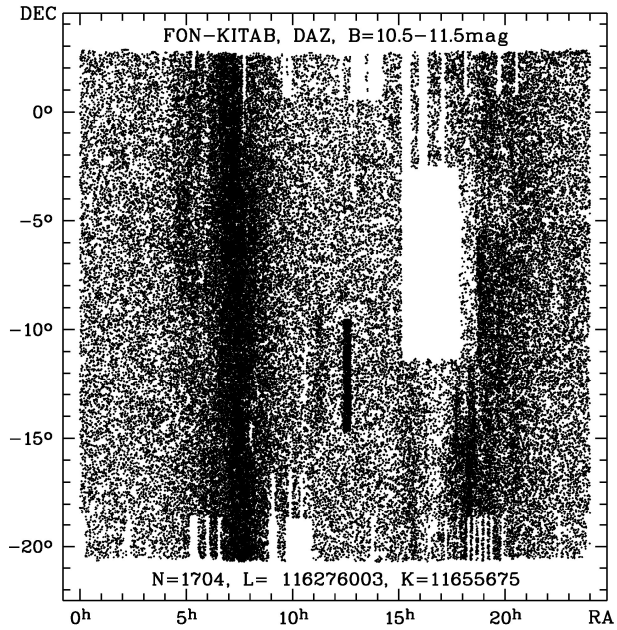


Figure 2: The progress in the processing of plates of the Kitab's part of the FON project.

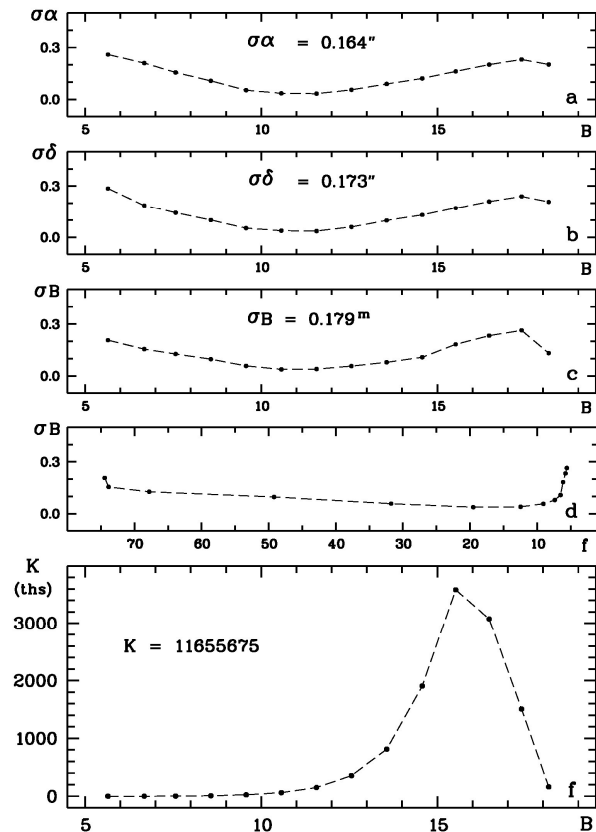


Figure 3: The errors of the determining of the equatorial coordinates and B magnitudes.

millions registered objects. These data for all zones are presented in the Figure 2. In the Figure 3 are given values of errors of the determined equatorial coordinates (a, b) and errors of the B-magnitudes (c, d) as well as the histogram of the distribution of stars and galaxies by magnitudes (f). Based on the results of the processing of these astronegatives were estimated internal catalogue errors. The mean

errors for all stars are 0.17" and 0.18<sup>m</sup> (for stars brighter than 14 magnitude -0.08" and 0.07<sup>m</sup>) in equatorial coordinates and magnitudes respectively.

## 6. Conclusion

The scanning, processing and creation of star catalogue in areas from -20 to 0 degrees of the Kitab's part of the FON project are planned to be finished by the end of 2016. The coordinates of stars and galaxies will be received in the system of Tycho-2 catalogue (mean epoch, 1984.9), B-magnitudes in the system of photoelectric standards. As photometric standards for the building of the characteristic curves of individual astronegatives were used photoelectric B-magnitude of stars from special catalogues. The convergence between the calculated and referenced positions is  $\sigma_{\alpha\delta} = \pm 0.056''$  and the convergence with photoelectric stellar B-magnitudes is equal  $\sigma_B = \pm 0.19^m$ . Differences relative to the UCAC4 catalogue are equal  $\sigma_{\alpha\delta} = \pm 0.29''$ .

The star catalogue of positions and B magnitudes of the Kitab's part of the FON project will be posted on the web-page of MAO NASU and website of UkrVO. The catalogue of stars and galaxies down to  $B \leq 17.5^m$  includes equatorial coordinates  $\alpha$ ,  $\delta$  on the individual epoch of the observations and on the Equinox 2000, stellar magnitudes in the B system, as well as the errors of the determinations of these values, the number of definitions and information in the form of average values for the diameter of star images ( $f$ ) and intensity values in the center of the object images ( $I_c$ ). Also in the catalogue will be included an additional information from the UCAC4 catalogue: the proper motions and stellar magnitudes in F, B, V, R, I bands (Zacharias, 2013).

Interim results on the progress and outcome of the creating a FON-Kitab catalogue (as well as works that were performed using FON software packages) were reported on the conferences Pulkovo-2013, Pulkovo-2015 (Russia, St.-Petersburg), Gamov-2016 (Odessa, Ukraine), Astroplate-2016 (Prague, Czech Republic) and others (Andruk, 2015a; Muminov, 2016).

*Acknowledgements.* The authors are thankful to anybody who has read this contribution to the end.

## References

- Andruk V. et al.: 1995, *Astron. Nachr.*, **316**, **N4**, 225.  
 Andruk V.N. et al.: 2005, *Kinem. i Fizika Nebesn. Tel.* **21**, **N5**, 396 (in Ukraine).  
 Andruk V.M. et. al.: 2005, *Kinem. i Fizika Nebesn. Tel. Supl.* **N5**, 544 (in Ukraine).  
 Andruk V., Pakuliak L.: 2007, *J. of Phys. Studies.* **11**, **N3**, 329 (in Ukraine)  
 Andruk V.M. et al.: 2010, *Kinem. Phys. Cel. Bodies*, **26**, **N3**, 75.  
 Andruk V.M. et al.: 2014, *Odessa Astron. Publ.*, **27**, **N1**, 53.  
 Andruk V.M. et al.: 2015, *Odessa Astron. Publ.*, **28**, **N2**, 188.  
 Andruk V.M. et al.: 2015, *Odessa Astron. Publ.*, **28**, **N2**, 192.  
 Andruk V.M. et al.: 2015, *arxiv.org/abs/1512.05535*.  
 Andruk V.M. et al.: 2016, *Kinem. Phys. Cel. Bodies*, **32**, **N1**, 38.  
 Andruk V.M. et al.: 2016, *Kinem. Phys. Cel. Bodies*, **32**, **N5**, 261.  
 Golovnya V. Et al.: 2010, *J. of Phys. Studies.* **14**, **N2**, 2902 (in Ukraine)  
 Eglitis I. et al.: 2016, *Odessa Astron. Publ.*, **29**, **N2**, In press.  
 Eglitis I. et al.: 2016, *Odessa Astron. Publ.*, **29**, **N2**, In press.  
 Kazantseva L.V. et al.: 2015, *Kinem. Phys. Cel. Bodies*, **31**, **N1**, 58.  
 Kolchinsky I.G., Onegina A.B.: 1977, *Astrometry and Astrophysics*, **N33**, 11.  
 Kornilov V.G. et al.: 1991, *Trudy GAIS*, **63**, 1.  
 Mermilliod J.C.: 1991, *Homogeneous means in the UBVR system*.  
 Muminov M.M. et al.: 2013, *Izvestija GAO. Pulkovo.*, **220**, 517.  
 Muminov M.M. et al.: 2014, *Odessa Astron. Publ.*, **27**, **N1**, 57.  
 Muminov M.M. et al.: 2016, *Izvestija GAO. Pulkovo.*, **223**, 339.  
 Muminov M.M. et al.: 2016, *Bulgarian Astron. J.*, **26**, 1. In press.  
 Pakuliak L.K. et al.: 2016, *Odessa Astron. Publ.*, **29**, **N2**, In press.  
 Protsyuk Yu.I. et al.: 2014, *Odessa Astron. Publ.*, **27**, **N1**, 59.  
 Protsyuk Yu.I. et al.: 2014, *Odessa Astron. Publ.*, **27**, **N1**, 61.  
 Protsyuk Yu.I. et al.: 2014, *Odessa Astron. Publ.*, **27**, **N1**, 63.  
 Protsyuk Yu.I. et al.: 2014, *Kinem. Phys. Cel. Bodies*, **30**, **N6**, 54.  
 Protsyuk Yu.I. et al.: 2015, *Odessa Astron. Publ.*, **28**, **N2**, 202.  
 Relke E. et al.: 2015, *Odessa Astron. Publ.*, **28**, **N2**, 211.  
 Vavilova I.B. et al.: 2012, *Kinem. Phys. Cel. Bodies*, **28**, **N2**, 85.  
 Vavilova I.B. et al.: 2012, *Baltic Ast.*, **21**, **N3**, 356.  
 Vavilova I.B. et al.: 2014, *Odessa Astron. Publ.*, **27**, **N1**, 65.  
 Yatsenko A.I. et al.: 2011, *Kinem. Phys. Cel. Bodies*, **27**, **N5**, 249.  
 Yizhakevych O. et al.: 2014, *Odessa Astron. Publ.*, **27**, **N1**, 67.  
 Yizhakevych O. et al.: 2015, *Odessa Astron. Publ.*, **28**, **N2**, 213.  
 Yizhakevych O. et al.: 2016, *Odessa Astron. Publ.*, **29**, **N2**, In press.  
 Yizhakevych O. et al.: 2017, *Kinem. Phys. Cel. Bodies*, **33**, In press.  
 Zacharias N. et al.: 2013, *Astron. J.*, **145**, 44.

## RADIOASTRONOMY

DOI: <http://dx.doi.org/10.18524/1810-4215.2016.29.85201>

## THE PHYSICAL CONDITIONS OF THE CENTRAL PART OF ORION A HII REGION BY THE RADIO RECOMBINATION LINES AT 8 AND 13 MM

Tsivilev A. P.<sup>1</sup>, Parfenov S. Yu.<sup>2</sup>, Krasnov V. V.<sup>1</sup><sup>1</sup>Pushchino Radio Astronomy Observatory (PRAO), Lebedev Physical Institute, Russia  
[tsivilev@prao.ru](mailto:tsivilev@prao.ru); [vvkras@sci.lebedev.ru](mailto:vvkras@sci.lebedev.ru)<sup>2</sup>Ural Federal University, Yekaterinburg, Russia

**ABSTRACT.** Observations of recombination radio lines (RRL) of hydrogen, helium (H, He) and carbon (C) were carried out in several positions of the HII region Orion A with RT22 radio telescope (Pushchino, Russia) at the wavelengths of 8 and 13 mm. The information about the ionization structure of the HII region was received. It is obtained that the measured helium abundance increases in the directions to "North" and "West" with a maximum at angular distances of 100-150" after which it declines. The maximum measured relative helium abundance,  $y^+ = n(\text{He}^+)/n(\text{H}^+)$ , is in the range of 9.4 – 11.0 %, therefore the actual He abundance  $n(\text{He})/n(\text{H})$  is  $\geq 9.4(\pm 0.5)$  %. With these estimates, the lower limit of the primordial helium abundance  $Y_p \geq 25.19(\pm 1.15)$  % should be expected. This limit is still not strong enough to assert the excess over  $Y_p$  predicted by the standard cosmological model ( $\approx 24.8\%$ ), but it admits the existence of unknown light particles. The  $y^+$  behavior and model calculations indicate that  $T_{\text{eff}}$  (effective temperature) of  $\theta^1$  Ori C star is 35000 – 37500 K, corresponding to the star spectral type of  $\approx$  O6.5 V, which is important for the calibration of hot OB-stars. Measured electron temperatures ( $T_e$ ) of the HII region, taking into account the deviations from the LTE, are in the range of 6600 – 8400 K and are strictly decreasing in direction to the "East". Alas information on the turbulent velocities of the ionized gas and its electron density was obtained.

**Keywords:** ISM: abundances – HII regions – Radio Lines: Orion Nebula

### 1. Introduction

Recombination radio lines (RRL), being one of the powerful tools for interstellar medium studies (Sorochenko & Gordon, 2003), *also allow* to check the standard cosmological model (SCM), in parts of primordial nucleosynthesis in the Universe that has taken place the first 2–3 minutes after the Bing Bang. Due to the Universe's expansion, only several light elements were produced during primordial nucleosynthesis which are helium-4 (hereafter, He), deuterium, helium-3, tritium and lithium. While almost all these elements are indicators of baryonic density of the Universe, the primordial helium-4 abundance also can be an indicator of the presence or absence of unknown light particles (Tsivilev et al., 2004,

2013; Tsivilev, 2009). The presence of unknown light particles may imply deviations from the SCM.

One of the most reliable methods of measurements of primordial helium abundance,  $Y_p = (\text{He}/\text{H})$ , is based on the optical and radio observations of H (hydrogen) and He (helium) recombination lines from HII regions. Optical observations can cover large number of sources including extragalactic ones. Comparing with optical observations, RRL observations are significantly less affected by systematic effects because, in radio range, helium can be treated as a hydrogen-like system with high accuracy meaning that coefficients of populations of identical hydrogen and helium levels are equal and canceled out in the  $(\text{He}/\text{H})$  ratio, thus, allowing to directly estimate the  $n(\text{He}^+)/n(\text{H}^+)$  value (see, e.g., Tsivilev, 2009; Tsivilev et al., 2013).

Our experience shows that moreover it is desirable to study the HII regions, especially their ionization structure, when estimating the He abundance in these HII regions. One of such HII regions is Orion A nebulae. We have been investigating this region for a long time (Tsivilev et al., 1986; Poppi et al., 2007; Tsivilev et al., 2014; Tsivilev, 2014) by observations of RRL which are mainly at the wavelengths of 8 and 13 mm. As a result of these investigations, we constructed the model of the HII region and obtained that the distribution of measured  $y^+ = n(\text{He}^+)/n(\text{H}^+)$  values has a maximum of  $y^+ = 10.0(\pm 0.8)$  %, that probably is close to the actual abundance of helium ( $n(\text{He})/n(\text{H})$ ) in this region (Poppi et al., 2007). In present study, we decided to repeat RRL observations in Orion A with RT22 radio telescope (Pushchino) at the 8 mm wavelength using an upgraded hardware in order to improve estimates of the position and value of the maximum of  $n(\text{He}^+)/n(\text{H}^+)$  distribution as well as to obtain physical parameters of the HII region and to obtain the new estimate of  $Y_p$ .

The positions in Orion A at which the new observations of H, He and C RRLs at 8 and 13 mm were carried out are shown in Figure 1. Part of the observations at 8 mm was published (Tsivilev, 2014), these positions are marked in Figure 1 as large circles with a size equal to the RT22 beam size at 8 mm.

### 2. Ionization Structure and Helium Abundance

In HII regions, the measured ( $y^+ = n(\text{He}^+)/n(\text{H}^+)$ ) and actual helium abundance ( $y = n(\text{He})/n(\text{H})$ ) are related through the structure factor R:

$$y^+ = R * y,$$

where  $R$  is determined by the ionization structure, i.e. by the ratio of sizes and emission measures of  $\text{He}^+$  и  $\text{H}^+$  zones (see, e.g., Tsvilev et al., 2013).

In our previous works (Tsvilev et al., 1986; Poppi et al., 2007), it was shown that the Orion A HII region has a “blister-type” structure with the core–halo density distribution. The current study, as well as previous ones, shows that ionized helium zone is smaller than ionized hydrogen zone, i.e. the factor  $R$  is lower than 1 and *has a different value in the core and halo*. The factor  $R$  is lower for the core (where we see the HII region is ionization bounded only) than for the halo, where we see the HII region is partly ionization bounded and partly density bounded, and the contribution of these parts into the observed emission varies with a position. In the positions, where the peak values of  $y^+$  are observed, the factor  $R$  probably is close to 1 (see Figure 9 in Poppi et al., 2007), i.e. one can directly measure the actual helium abundance in these positions.

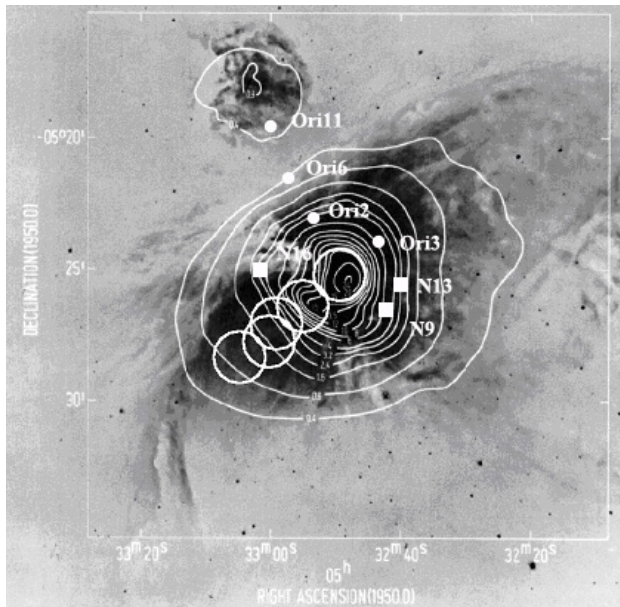


Figure 1: Optical image of Ori A region in  $\text{H}\alpha$  and  $\text{NII}$  lines from Hua & Louise (1982). Contours (faint white lines) designate 23 GHz continuum (Wilson & Pauls, 1984). Circles (large and small) and squares show positions at which our observations, respectively at 8 mm and 13 mm, were carried out.

Figure 2 shows the obtained distribution of  $n(\text{He}^+)/n(\text{H}^+)$  towards different directions in Orion A. In the previous study (Poppi et al., 2007), we found that the  $y^+$  maximum is located in positions Ori2 and Ori3 (see Figure 1). In this study, we obtained that the  $y^+$  maximum is located close to the position marked as N13 (see Figure 1) where measured  $y^+$  values are in the range of 9.4 – 11.0 %. For the established ionization structure, this means that the actual helium abundance in Orion A,  $n(\text{He})/n(\text{H})$ , should not be lower than 9.4( $\pm 0.5$ ) %. Further, in this position, we also can estimate the lower limit of primordial helium abundance ( $Y_p$ ). The helium abundance measured in the interstellar medium consists of  $\sim 90$  %, the one produced during the era of primordial nucleosynthesis in the Universe, and of  $\sim 10$  % one produced by

stars during their evolution (Hoyle & Teyler, 1964). To account the contribution of stars one can use the dependence of the helium abundance ( $Y$ , on a mass) on the abundance of heavy elements ( $Z$ ) (Tsvilev, 2009). Taking the slope of this dependence,  $dY/dZ = 1.62 (\pm 0.29)$ , from the literature (Izotov & Thuan, 2010) and the abundance of heavy elements in Orion A,  $Z = 0.0112 (\pm 0.0022)$  (Baldwin et al., 1991), we obtain:

$$Y_p \geq 25.19 (\pm 1.15) \%$$

This limit is still not strong enough to claim the overabundance comparing with  $Y_p$  predicted by the SCM ( $\approx 24.8\%$ ), however this limit admits the existence of unknown light particles in agreement with previous works (Tsvilev et al., 2004; 2013; Tsvilev, 2009).

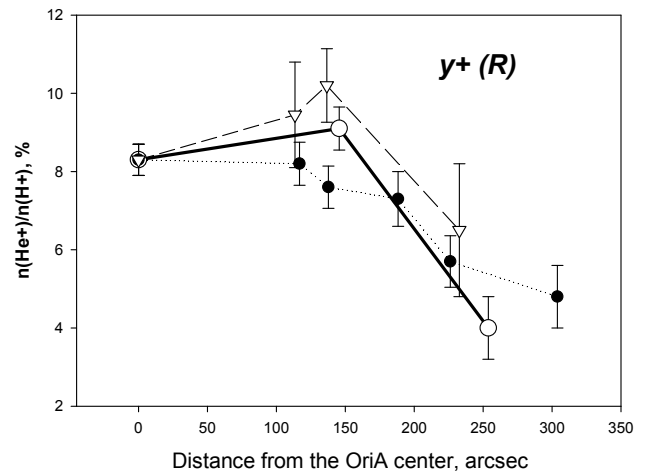


Figure 2: The distribution of measured  $y^+ = n(\text{He}^+)/n(\text{H}^+)$  values with the distance from the OriA center ( $\theta^1$  Ori C star). Black circles – in direction to the “East”: OriA – OriBar (large circles in Figure 1); white circles – in direction to the “North”: OriA – Ori6; open triangles – in direction to the “West”: OriA – Ori3 and N13.

### 3. Effective Temperature of $\theta^1$ Ori C Star

In figure 2, it is seen that, in directions to the “North” and “West”, the measured helium abundance increases with increasing distance from the OriA center ( $r$ ) and has a maximum at angular distances of 100–150” after which it goes down. In direction to the “East”, the measured  $y^+(r)$  always decreases with increasing  $r$  which means that along this direction the HII region is bounded by ionization only. This fact can be used to estimate the ionizing source (star or group of stars) of the HII region (Polyakov & Tsvilev, 2007). In the case of an ionization bounded HII region, the factor  $R$  will strongly depend on stellar properties, mainly on stellar effective temperature  $T_{\text{eff}}$  (Tsvilev et al., 2013). In Orion A, this star is  $\theta^1$  Ori C.

Our model calculations of  $y^+(r)$  behavior on the “East” direction show that  $T_{\text{eff}}$  of the ionizing source is in the range of 35000 – 36500 K. If one take into account that the HII region is ionized by not a single star but by a group of stars (Copetti & Bica, 1983) then the actual  $T_{\text{eff}}$  of  $\theta^1$  Ori C star should be higher (by  $\sim 1000$  K) and will be in the range of 36000 – 37500 K. This is in good agreement with our earlier estimates (Polyakov & Tsvilev, 2007).

Optical studies of Stahl et al. (2008) shown that the  $\theta^1$  Ori C spectral type is  $\sim O7 V$ . However, on our opinion, their data indicate that more likely the spectral type was  $\sim O6.5 V$  (see Figure 6 from Stahl et al., (2008)). It is known that one of the problems is a calibration of OB-stars, i.e. the correspondence of a given spectral type to  $T_{\text{eff}}$ . For example, for a star of O6.0 V spectral class Vacca et al. (1996) assign  $T_{\text{eff}} \approx 43\,600$  while Pottasch et al. (1979) assign much smaller value  $T_{\text{eff}} \approx 36\,500$  K.

Our data (see Figure 3) indicate in a favor of Pottasch et al. (1979) and Massey et al. (2005) calibrations, which is an important result.

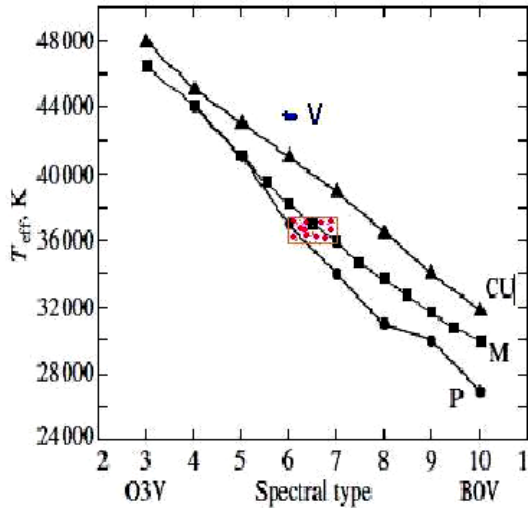


Figure 3: Spectral type- $T_{\text{eff}}$  calibration for OB-stars from P – Pottasch et al. (1979), M – Massey et al. (2005), CU – Conti & Underhill (1988), V – Vacca et al. (1996). Our estimates for  $\theta^1$  Ori C star are shown as a rectangle in the figure center.

#### 4. Electron Temperature of the Ionized Gas

The RRLs, using the line/continuum contrast, allow estimate electron temperature ( $T_e$ ) of the ionized gas (Sorochenko & Gordon, 2003). We made such estimates assuming LTE (local thermodynamic equilibrium) as well as non-LTE using tabulated departure coefficients from LTE of Salem & Brocklehurst (1979) and electron density values estimated by Mesa-Delgado et al. (2008) from optical observations. The results are shown in Figure 4 where it is clearly seen that, towards the “East” direction,  $T_e$  strictly decreases as the distance from the OriA center increases. The  $T_e$  decrease in direction to the “North” is doubtful. Optical data also show that  $T_e$  decreases with distance from the center (Mesa-Delgado et al., 2008). Such a decrease towards the region periphery can be related to either decreasing density (Wilson & Jaeger, 1987) or to an increase towards the region periphery of the abundance of heavy elements, especially oxygen and sulfur, which are cooling agents (Spitzer, 1981).

#### 5. Turbulent velocities of the Ionized Gas

According to RRL theory, line profile at the considered wavelengths has a Gaussian shape with the width that is a

convolution of thermal and turbulent broadening (Sorochenko & Gordon, 2003). As we have measured  $T_e$ , we can calculate thermal broadening and then extract turbulent one from the observed RRL width. In this way, we obtain turbulent velocities of the ionized gas ( $V_t$ ). Figure 5 shows the  $V_t$  distribution obtained using hydrogen as well as helium lines. It is seen that there is no clear dependence of  $V_t$  on the distance, however there is a weakly apparent peak at distances of 100-150" from the OriA center. This peak can represent the presence of boundary of the core of the HII region at these distances. The  $V_t$  values obtained are in good agreement with the previous measurements of, for example, Sorochenko & Berulis (1969).

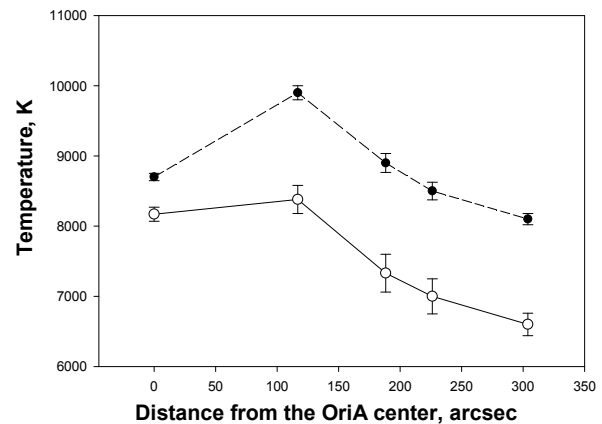
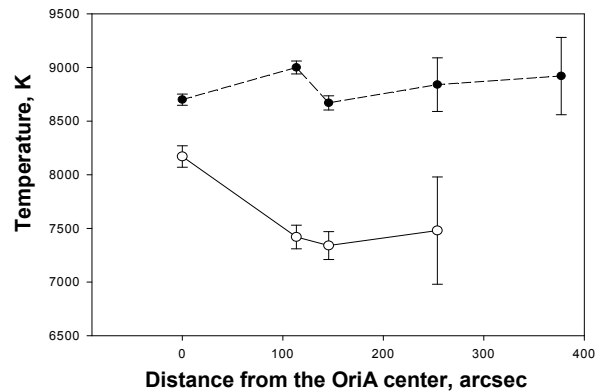


Figure 4: The dependence of electron temperature on the distance from the OriA center. Top panel shows the results obtained in direction to the “North”; bottom panel shows the results obtained in direction to the “East”. Open circles show the results obtained taking into account non-LTE effects; filled circles show the results obtained assuming LTE

#### 6. Electron density of the Ionized Gas

RRL theory (Sorochenko & Gordon, 2003) also predicts that for the quantum levels of atoms excited to principal quantum numbers of 100 and higher, Stark broadening due to collisions with electrons becomes apparent. Stark broadening is characterized by a Lorentz profile and an observed RRL has a Voigt profile. In the same spectrum at 13 mm (i.e. with the same frequency setup and angular

resolution), we see simultaneously H65 $\alpha$  and H93 $\gamma$  RRLs (see Figure 6). The observed line width of H93 $\gamma$  is higher than the one of H65 $\alpha$  in all observed positions. We suggested that H65 $\alpha$  is broadened only thermally while H93 $\gamma$  line is additionally broadened by Stark effect.

We have fitted H93 $\gamma$  RRL profile with Voigt function (Smirnov & Tsvilev, 1982) fixing Doppler width which was determined using H65 $\alpha$  RRL. In this way, we estimate Lorentz broadening that is proportional to electron density ( $N_e$ ) of the ionized gas and proportional to the principal quantum number of excited hydrogen level in the power of  $\approx 4.5$  (Sorochenko & Gordon, 2003).

As a result, we obtain  $N_e = (1.2 \pm 0.2) 10^5 \text{ cm}^{-3}$  for positions N9-N13 and  $N_e = (1.4 \pm 0.4) 10^5 \text{ cm}^{-3}$  for the nebulae center. This is higher by the order of magnitude than the value estimated by Smirnov et al. (1984) with RRL and the maximum value  $N_e \sim 2.5 \cdot 10^4 \text{ cm}^{-3}$  obtained by Mesa-Delgado et al. (2008) using optical observations. Further analysis is required to find out reasons for this inconsistency.

To save a space we do not present a table with estimated RRL parameters however we are ready to send this table on an e-mail on a request. To see shapes of the 8 mm spectra it is possible in Tsvilev (2014) paper.

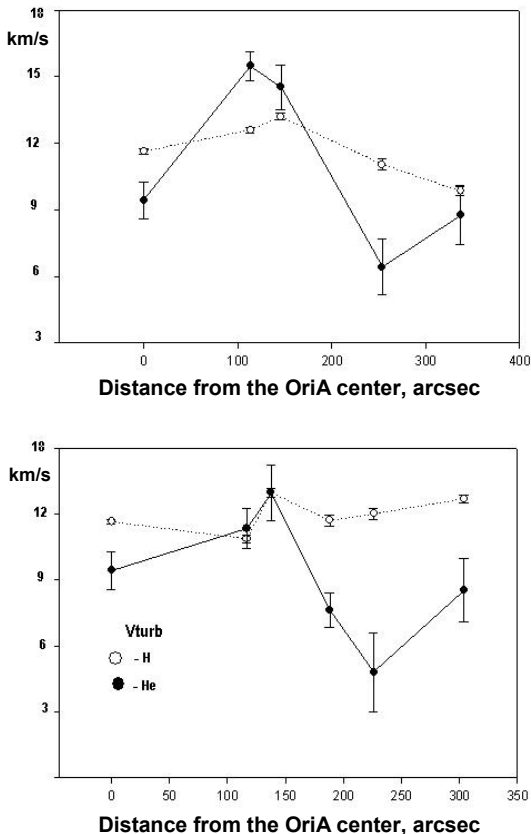


Figure 5: The dependence of turbulent velocities on the distance from the OriA center obtained using H (grey lines) and He (black line) RRLs. Top panel shows the results obtained in direction to the “North”; bottom panel shows the results obtained in direction to the “East”

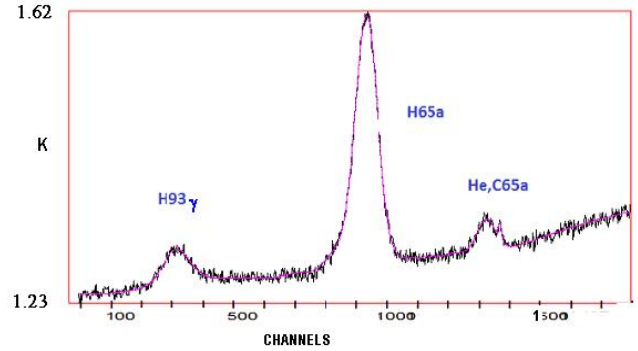


Figure 6: The spectrum at 13 mm averaged between positions N13 and N9. Ordinate is antenna temperature; abscissa is a spectral channel number, the frequency increases with increasing channel number. The smooth curve is the fitted spectrum.

*Acknowledgements.* The study was partially supported by the program of Presidium of RAS "The transient and explosive processes in astrophysics".

## References

- Sorochenko R.L., Gordon M.A.: 2003, *Radio Recombination Lines. Physics and Astronomy* (Fizmatlit, Moscow, 2003) [in Russian].
- Tsvilev A.P. et al.: 2004, *Odessa Astron. Publ.*, **17**, 103.
- Tsvilev A.P. et al.: 2013, *Astron. Lett.*, **39**, 737.
- Tsvilev A.P.: 2009, *Astron. Lett.*, **35**, 670.
- Tsvilev A.P. et al.: 1986, *Sov. Astron. Lett.*, **12**, 355.
- Poppi S. et al.: 2000, *A&A*, **464**, 995.
- Tsvilev A.P. et al.: 2014, *Odessa Astron. Publ.*, **27/2**, 80.
- Tsvilev A.P.: 2014, *Astron. Lett.*, **40**, 615.
- Hua C.T., Louise R.: 1982, *A&A SS*, **88**, 477.
- Wilson T.L., Pauls T.: 1984, *A&A*, **138**, 225.
- Hoyle F.R.S., Teyler R.J.: 1964, *Nature*, **203**, 1108.
- Izotov Y.I., Thuan T.X.: 2010, *ApJ*, **710**, L67.
- Baldwin J.A. et al.: 1991, *ApJ*, **374**, 580.
- Polyakov A.M., Tsvilev A.P.: 2007, *Astron. Lett.*, **33**, 34.
- Copetti M.V.F., Bica E.I.D.: 1983, *ApSS*, **91**, 381.
- Stahl O. et al.: 2008, arXiv:0805.0701v2.
- Vacca W.D. et al.: 1996, *ApJ*, **460**, 914.
- Pottasch S.R. et al.: 1979, *A&A*, **77**, 189.
- Massey P. et al.: 2005, *ApJ*, **627**, 477.
- Salem M., Brocklehurst M.: 1979, *ApJSS*, **39**, 633.
- Mesa-Delgado A. et al.: 2008, *ApJ*, **675**, 389.
- Wilson T.L., Jaeger B.: 1987, *A&A*, **184**, 291.
- Spitzer Jr.L.: 1981, *Physical Processes in the Interstellar Medium (MIR, Moscow, 1981)* [in Russian].
- Sorochenko R.L., Berulis I.I.: 1969, *Astroph. Lett.*, **4**, 173.
- Smirnov G.T., Tsvilev A.P.: 1982, *Sov. Astron.*, **26**, 616.
- Smirnov G.T. et al.: 1984, *A&A*, **135**, 116.
- Conti P.S., Underhill A.B.: 1988, *CNRS, (NASA, Washington, 1988)*, SP-497.

DOI: <http://dx.doi.org/10.18524/1810-4215.2016.29.85206>

## THE DAILY 110 MHz RADIO WAVE SKY SURVEY: STATISTICAL ANALYSIS OF IMPULSE PHENOMENA FROM OBSERVATION IN 2012-2013

V.A.Samodurov<sup>1,2</sup>, D.V.Dumsky<sup>1,2</sup>, E.A.Isaev<sup>1,2</sup>, A.E.Rodin<sup>1</sup>, A.N.Kazancev<sup>1</sup>,  
V.A.Fedorova<sup>1</sup>, Yu.A.Belyatskij<sup>1</sup>

<sup>1</sup> Pushchino Radio Astronomy Observatory ASC LPI, Pushchino, Russia, [sam@prao.ru](mailto:sam@prao.ru)

<sup>2</sup> National research university Higher school of economics, Moscow, Russia

**ABSTRACT.** On the Pushchino Radio Astronomy Observatory of Lebedev Physical Institute by radio telescope BSA (Big Scanning Antenna) in 2012 started daily multi-beam observations at the frequency range 109–112 MHz. The number of frequency bands range from 6 to 32, while the time constants range from 0.1 to 0.0125 sec. This data is an enormous opportunity for both short and long-term monitoring of various classes of radio sources (including radio transients), the Earth's ionosphere, interplanetary and interstellar plasma monitoring, search and monitoring for different classes of radio sources, etc. A specialized database was constructed to facilitate the large amount of observational data ([http://astro.prao.ru/cgi/out\\_img.cgi](http://astro.prao.ru/cgi/out_img.cgi)). We discuss in this paper method of allocation from the database for impulse data of various types. By using the database allocated 83096 individual impulses in declination from +3 to +42 degrees for July 2012 – October 2013 from pulsars, scintillation sources and so one. In result we constructed homogeneous sample suitable for statistical analyzes.

**Keywords:** radio survey, radio transients, monitoring, database

### 1. Observations

In 2012 the multi-beam feed array has become operational on the BSA FIAN radio telescope (Oreshko et al., 2012). As of July 2015 it is capable of 24-hour observation using 96 beams in declination of -8 to +42 degrees in the 109–111.5 MHz frequency band.

Radio Observatory of Lebedev Physical Institute in Pushchino has one of the most sensitive radio telescope at 110 MHz BSA (Big Scanning Antenna). Radio telescope originally worked in a range of 101–104 MHz, but in 1996 was rebuilt to a range of 109–112 MHz. In this range BSA telescope is the most sensitive in the world (and one of the most sensitive in the world in the meter wavelength range as a whole). Systemic equivalent flux density (SEFD) radio telescope is 34 Jy (Oreshko V.V. et al., 2012) at the zenith at a minimum temperature of the background, while a radio telescope LOFAR SEFD at a frequency of 120 MHz is about 2000 Jy (Van Haarlem et al., 2013). We need note that now the long-wave radio astronomy (in the range of 10 to 300 MHz) is experiencing a new wave of interest. There

is a wide class of scientific problems for this range (see., eg, Konovalenko et al., 2016). Existing radio telescopes (the most famous of them UTR-2 – Braude et al., 1978) are experiencing a rebirth, as the construction of new radio telescopes – except LOFAR (Van Haarlem M. P. et al., 2013) should be called GURT (Konovalenko et al., 2016) and LWA (Taylor et al., 2012).

Since 2012 BSA started multi-beams observations using 96 beams in declination from -8 up to +42 degrees in 6 and 32 frequency bands at 109–112 MHz and time sampling 0.1 s and 0.0125 s. The data stream in 32 bands and time sampling of 0.0125 s is producing 87.5 gigabytes per day. It was accumulated more than 70 TB (i.e. 3.5 TB with 100 ms time resolution from 2012 and 67 TB with 12.5 ms resolution from 2014).

The main technical parameters of the radio telescope BSA are:

- operating frequency band 109 – 112 MHz;
- the effective area of the antenna (maximum) – 47 000 square meters;
- the system noise temperature (minimum) – 560 K;
- antenna polarization – linear (horizontal, along the east-west direction);
- the number of beams today in registration – 96;
- the width of beam diagrams in the E-plane – 54 arcmin;
- the width of beam diagrams in the H-plane – 24 arcmin (zenith).

The sensitivity of the survey is 0.07 Jy at 100 ms time resolution and 0.2 Jy at 12.5 ms resolution.

Since July 2012 it was observed daily about 2 steradians, and starting April 2013 it is monitoring about 5 steradians for 50 degrees in declination. This is unique survey of North Hemisphere. Based on accumulated data and newly recording data we suggest to monitor and to search different types of astronomical phenomena. There are two main classes of the phenomenon which can be investigated using BSA data: long term monitoring (from daily up to yearly variations) and short transient detection (from ms to seconds). In this work we are testing short transient phenomena.

### 2. The selection methodic of pulse signals from data

We may found that for the case of source entering into the area of the main lobe of a ray diagram for example with  $S/N \geq 10$  detection criterion for sporadic (transient)

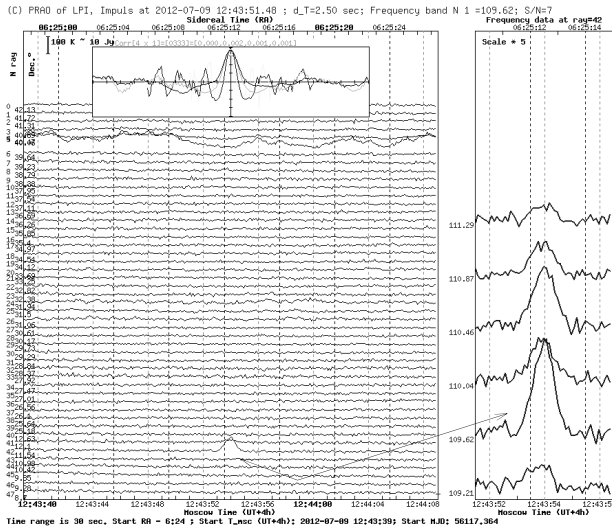


Figure 1: An example of one of the found pulse events: response from the passage of a satellite of the Earth (the International Space Station, showing the reflection area of about  $400 \text{ m}^2$ ) through the beam glissade aircraft radio beacon from one of the near airports. These beacons operate at frequencies around 110 MHz (BSA frequency range). The arrows indicate the selected pulse (width of about 1.5 sec): on the left, mainly boxing picture – temporary scan by BSA beams, in the right box – scan over 6 frequencies. The upper figure shows the result of boxing Pearson correlation results for the 3th time scales: they have the correlation is maximum at zero time scale for data from different observation frequency. At the top of the figure, on the 6th beam from above – an example of the scintillation point radio source. Such strong (single) order of magnitude as the scintillation of a second is usually also allocated as independent impulse events.

signal it have the following estimates. The unit reliably detectable pulse emission data on a band 415 kHz ( $\Delta t = 100 \text{ ms}$ ) will  $\geq 1,6 \text{ Jy}$ , for the band 78 kHz ( $\Delta t = 12,5 \text{ ms}$  that very goog for FRB searching work) –  $\geq 10,6 \text{ Jy}$ .

Note that for a recent LOFAR pulsar pilot survey (Coeenen, 2014), the authors have made a similar estimate with the same criterion of  $S/N = 10$  to find fast radio bursts (FRB – see Lorimer et al, 2007), and it was  $\geq 107 \text{ Jy}$  for  $\Delta t = 0,66 \text{ ms}$  (for our time scale  $\Delta t = 12,5 \text{ ms}$  it will move to  $\geq 25 \text{ Jy}$ ). So in result 32-frequency data from BSA with  $\Delta t = 12,5 \text{ ms}$  have good potential even in comparison with LOFAR, but in addition such survey we producing daily.

In this paper we worked until with 6-frequency data ( $\Delta t = 100 \text{ ms}$ ). We we chose also more soft detection criterions:  $S/N \geq 5$  for at least three of the six frequency bands. In our case signal  $S = S_{\max} - S_{\text{median}}$  for any 5 second data segment and  $N$  is dispersion of  $S$  on this data segment at some frequency band. In result we found usually all events on time scale from 0.1 to nearly 1 seconds. After we allow only events that found not more than in 1-3 ray. So interference signal eliminated that reflected usually on tens rays. We are deleted also region  $\delta \leq +3.5^\circ$  so as we have big interference unclear nature.

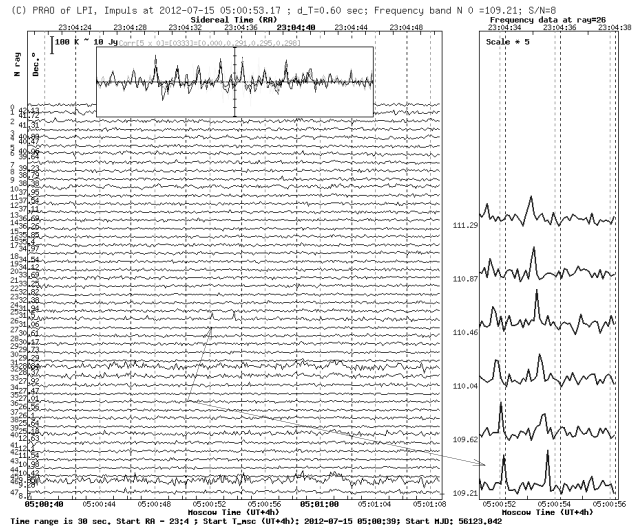


Figure 2: An example of one of the found pulse events: a response from one of the pulses (in the center of the figure) of the pulsar PSR2305+3000. The arrows indicate the selected impulse: to the left, mainly boxing picture – temporary scan beams on BSA, in the right box – scan a beam with impulse over 6 frequencies. In the right box clearly visible time drift along the frequency (here  $DM = 49,6 \text{ pc/cm}^3$ ). The upper figure shows the correlation boxing search result Pearson for the 3th time scales: they all showed a clear shift of the lower frequency data about the high-frequency band. This pulsar is bright enough ( $\sim 5 \text{ Jy}$ ) and noticeable series of pulses following each other with a period of  $P = 1,58 \text{ sec}$ . In total for PSR2305 + 3000 on the time interval 6.07.2012 – 10.20.2013 years allocated 334 pulse events.

### 3. The results of searching and sorting

In this work we discuss first results for short transient found from our database (Samodurov et al., 2015) in July 2012 – October 2013. We found 83096 events in diapason  $+3.5^\circ \leq \delta \leq +42.5^\circ$  which could be associated with pulsars, scintillation sources and fast radio transients. These found events are a homogenous sample suitable for statistical analysis. We found such classes of transient sources:

A) False signal so as interference, apparatuses and like unrealistic phenomena – 21962 events from 83096 or 26,43 %. They are:

- the impulses generated by far lobe diagram response on flush/deviation in strong radio sources (usually Sun): 5,87 % ;
- the impulses generated by apparatuses: 13,28 % ;
- the impulses generated by interference (man-made, thunderstorms): 3,94 % ;
- the impulses generated by different man-made reasons (for example overflights) and other: 3,34 % ;

B) Scintillation single signal produced by interstellar medium or ionosphere – 29283 events from 83096 or 35,23 %. They are:

- the scintillations with  $\Delta t \leq 1$  second (in base generated by interstellar medium): 27,38 % ;
  - the scintillations with  $1 \leq \Delta t \leq 5$  second: 6,78 % ;
  - the scintillations with  $\Delta t \geq 5$  second (in base generated by ionosphere): 0,60 % ;
  - other (satellites – fig. 1 and not clear reason): 0,40 %
- C) The single impulses with some dispersion time delay along frequencies bands, that are generated by pulsar (fig. 2) – 31851 events from 83096 or 38,33 %.

The most interesting results of the selection pulse last type. About 340 pulsars from ATNF pulsar catalog (Hobbs et al) falling within a declination band  $+3.5^\circ \leq \delta \leq +42.5^\circ$  and have periods of more than 0.3 seconds. We found in our sample pulses for 41 of them (even 2 pulsar found of having period 0.2-0.3 seconds). Pulse events number that found for these pulsars ranges from 1 (one) to thousands for the above observation time (an average of about one year).

The account of pulsars (for found sample from ATNF catalogue) with the different dispersion delay is varied:

- $DM < 16 \text{ pc/cm}^3$  : 9 units from 20;
- $DM < 50 \text{ pc/cm}^3$  : 37 units from 112;
- $50 \text{ pc/cm}^3 < DM < 100 \text{ pc/cm}^3$  : 4 units from 91;
- $DM > 100 \text{ pc/cm}^3$  : 0 units from 187.

This variation is clear so as good corresponding with distance to pulsars and its resulting brightness.

In end to end we found also of some pulses from candidates in new pulsars. We hope that after adding checking and analysis any from them really are unknown before pulsars.

#### 4. The future plans of data processing

Noticeably influence scattering pulsar pulse broadening on the effectiveness of the pulse discharge from the database. So ways of improving the search technique of pulse phenomena is now nearly clear: increase in analysis time (to appear from 5 sec to 15 sec) and the transition to data with  $\Delta t = 12.5$  ms and 32 frequency bands.

The database will updated by data for 2013-2016 for the subsequent stages of the work on the allocation of pulse phenomena. The database also will be expanded to the "fast" data (32 bands with a sampling time of 12.5 ms), which will dramatically expand the class to solve scientific problems: to investigate the fine structure of the giant pulses of pulsars, fine temporal structure of solar flares, to organize search FRB.

Indeed, the search for the FRB we need:

- Millisecond scale recording observations. The sampling of 12.5 ms at a frequency of 110 MHz for the BSA telescope essentially meets the necessary criteria;

– Large search area and the long-term observations. Some years continuous observations of the 40% sky now provide good base for statistics, and the accumulation of observations is continuing;

– The total bandwidth is 2.5 MHz, the difference between adjacent bandwidth of 78 KHz, while passing through the diagram BSA for about 5 minutes. These characteristics correspond to the available catch even short bursts of very high dispersion delays. Thus, it is easy to find that  $DM = 1000$  time delay in the region of 110 MHz with a difference frequency of 2 MHz is about 12 seconds, and for  $DM = 10,000$  – about 120 seconds, which is also less than the width of beam of BSA telescope. Thus, the BSA is suitable telescope for observation and search for FRB.

*Acknowledgements.* This work is supported by RFBR grant 14-07-00870a.

#### References

- Braude et al.: 1978, *Antenna*, **26**, 3–14.  
 Coenen, Thijs et al.: 2014, *A&A*, **570**, id.A60, 16.  
 Hobbs G., Manchester R. N. and Toomey L.: ATNF Pulsar Catalogue v1.54, [www.atnf.csiro.au/people/pulsar/psrcat/](http://www.atnf.csiro.au/people/pulsar/psrcat/).  
 Konovalenko A.A. et al: 2016, *Radiophysics and radioastronomy*, **21**, Issue 2, 83–131.  
 Lorimer D.R. et al.: 2007, *Science*, **318**, Is. 5851, 777–780.  
 Oreshko V.V. et al.: 2012, *Transactions of the Institute of Applied Astronomy (Russia)*, **24**, 80.  
 Samodurov V.A. et al.: 2015, *Transactions of conf. "Data Analytics and Management in Data Intensive Domains"* (DAMDID), 127–128.  
 Taylor G.B. et al.: 2012, *J. Astron. Instrum.*, **1**, 1–56.  
 Van Haarlem M.P. et al.: 2013, *Astron. Astrophys.*, **556**, id. A2.

DOI: <http://dx.doi.org/10.18524/1810-4215.2016.29.85207>

## ANGULAR STRUCTURE OF FR II RADIO SOURCES 3C169.1 AND 3C263 AT DECAMETER WAVELENGTHS

Vashchishin R.V.<sup>1</sup>, Shepelev V.A.<sup>2</sup>, Lozinsky A.B.<sup>3</sup>, Lytvynenko O.A.<sup>4</sup>

<sup>1</sup> Gravimetric Observatory of IGP NASU, Poltava,

<sup>2</sup> Institute of Radio Astronomy, National Academy of Sciences of Ukraine, Kharkiv,

<sup>3</sup> Physico-Mechanical Institute, National Academy of Sciences of Ukraine, Lviv,

<sup>4</sup> URAN-4 Laboratory of RI NASU, Odessa

**ABSTRACT.** The radio galaxy 3C169.1 and the quasar 3C263, located at nearly the same distance with red shift  $z > 0.6$ , have similar morphological and spectral characteristics. The maps of the sources obtained at decimeter and centimeter wavelengths have shown they are FR II radio sources with steep spectra and approximately equal angular sizes. The very first investigation of the sources structure at decimeter wavelengths is presented in the report. Observations were made using a network of the URAN decimeter interferometers with baselines 42 to 950 km and with maximum angular resolution of arcsec order of magnitude. The models of the image of these sources based on visibility functions measured have been obtained at frequencies of 20 and 25 MHz. They were composed of elliptical components with Gaussian brightness distribution. To facilitate the comparison of these low-frequency models with high-frequency radio images, the latter were converted to the similar models by fitting the Gaussian components to lobes and hot spots selected at the maps. Comparison of the models revealed changes in a structure of the sources caused by the frequency decrease.

**Keywords:** interferometer, brightness distribution, decimeter waves, radio galaxy, quasar.

### 1. Introduction

Observation of extragalactic radio sources at decimeter wavelengths with the URAN interferometers has revealed that their angular structure at low frequencies differs considerably from high-frequency images of the sources. The most obvious reason is a difference in spectra of source components which leads to essential changes of a ratio of their fluxes and results in modification of the source brightness distribution at low frequencies. The most prominent spectral phenomenon is synchrotron self-absorption of radio emission which is observed in the most compact details of the sources such as a core or hot spots. It often leads to disappearance of these compact

details in the decimeter range. An increase of an angular size of source lobes is other feature of brightness distribution observed at low frequencies. It is related to synchrotron losses in the most aged areas close to the core of the source. The losses make these areas less prominent at higher frequencies but keep them bright enough at lower ones. Such phenomenon has been revealed in radio galaxies studied with the URAN (Megn et al., 1999, Megn et al., 2003). Furthermore, an extended structure has been found out in some quasars at decimeters that significantly exceed the source dimensions measured at decimeter wavelengths (Megn et al., 1996, Megn et al., 2006). These components have large spectral indexes and low surface brightness that complicates their detection at higher frequencies. But at the same time they provide considerable part of the total source flux at the decimeter wavelengths.

It is generally accepted that radio galaxies and radio loud quasars have common physical nature and differences in their optical/UV properties is a result of orientation of a source axis relative to the line of sight. General radio properties of large-scale structure of radio galaxies and quasars have to be similar. Individual features of the source radio structure can be connected with age and power of the sources, their environment and a redshift.

The radio galaxy 3C169.1 and the quasar 3C263 are convenient pair of the sources to study of common properties and distinctions of the large-scale structure of extragalactic radio sources. These sources have approximately equal flux densities and angular dimensions; they are located practically at the same redshift of  $z \approx 0.6$  hence possess similar physical conditions in them. The radio sources have a similar spatial structure of FR II type according to their high-frequency maps. The goal of this study was to obtain the angular brightness distributions of these objects at decimeter wavelengths, to find a difference from their high frequency images, and also to compare the low frequency radio structures of the quasar and the radio galaxy.

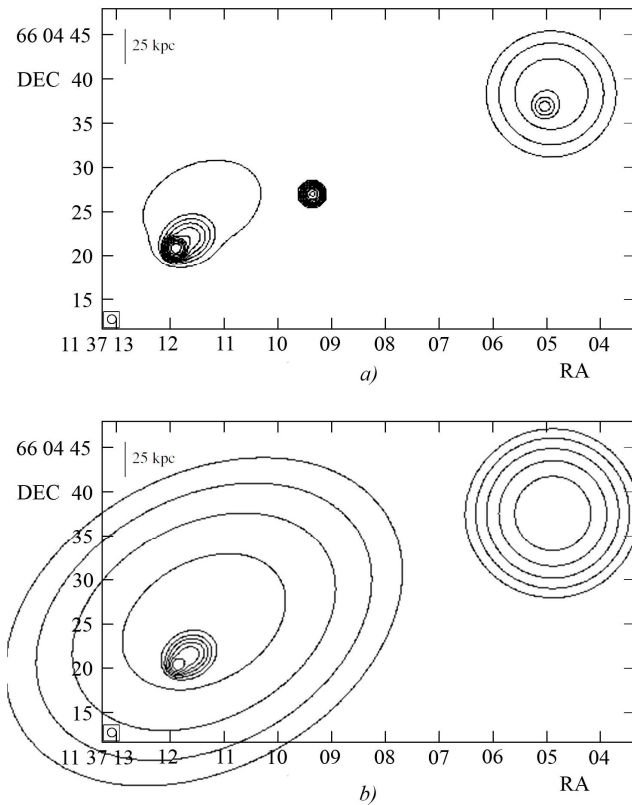


Figure 1: Models of brightness distribution of the quasar 3C263 at decimeter (a) and decameter (b) wavelengths

## 2. Observations and reduction

Radio galaxy 3C169.1 and quasar 3C263 were observed at frequencies of 20 and 25 MHz with the URAN radio interferometers (Megn et al., 1997, Megn et al., 1998) during 2011-2013. The observations were carried out in the range of  $\pm 2$  hours from the source culmination by seven minutes scans.

The arrays of radio telescopes URAN1-URAN4 have a possibility to receive the signals of two orthogonal linear polarizations to take into account Faraday rotation induced by Earth's ionosphere. Visibility functions were calculated using a software correlator by multiplication of signals recorded at each of the URAN radio telescopes with signal received by the North-South array of UTR-2.

Well-known technique of image reconstruction based on two-dimensional Fourier transform of complex visibilities cannot be used in observations at decameter wavelengths due to lack of a phase information. The method of model fitting using modulus of visibility functions was used instead to obtain brightness distribution of the radio sources.

The models were composed from elliptic components with Gaussian brightness distribution. Parameters of the models were fitted to obtain a good agreement of their spectrum of space frequencies with experimental hour angle dependences of the visibility amplitude (Megn et al., 2001).

At the first stage we used the maps of these objects obtained at higher frequencies to determine a quantity, dimension, form and relative position of the source components. For this purpose we calculate response of the

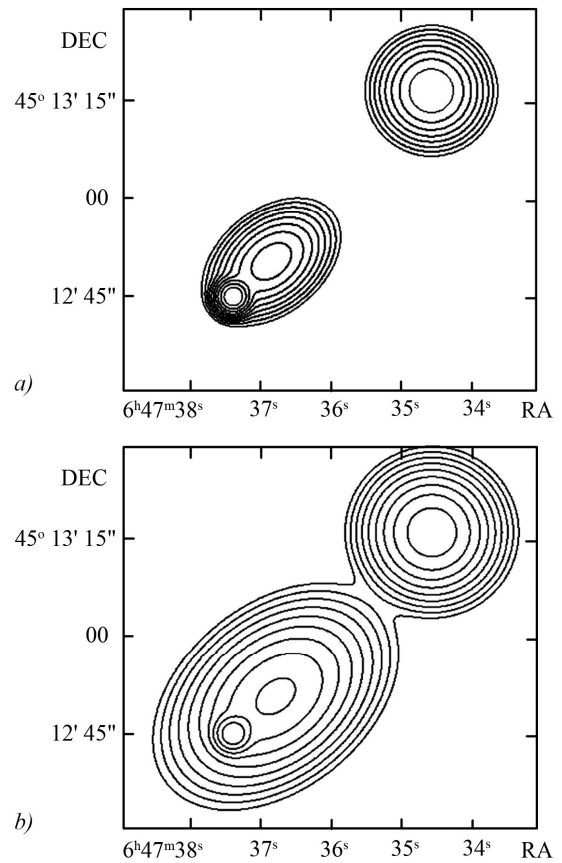


Figure 2: Models of brightness distribution of the radio galaxy 3C169.1 at decimeter (a) and decameter (b) wavelengths

map at space frequencies used in our observations with URAN and then fit simplest models to these calculated visibilities. The fitted model demonstrates how the source looks like from the "URAN's point of view" at high frequencies or at decameter wavelengths if its structure would not change with the frequency. Such models of brightness distribution are shown in the fig. 1a for the quasar 3C263 and fig. 2a for the radio galaxy 3C169.1.

The experimental visibility functions obtained in observations with the URAN interferometers differ significantly from the calculated map responses hence the angular structure of both sources was changed at decameter wavelengths.

At the second stage we fit a low frequency model to experimental data using models calculated above as an initial approximation to restrict the range of desired solutions and to eliminate ambiguities induced by a lack of the phase information. The models of the brightness distribution of the sources at frequency of 25 MHz obtained in this procedure are shown in the fig. 1b and fig. 2b for 3C263 and 3C169.1, respectively.

## 3. Discussion

To specify features of the source brightness distribution in the decameter range it is more convenient to compare the low frequency model with high frequency one rather than with the map. It allows determining the changes in flux density and dimensions of the source components

quantitatively. At high frequencies the main part of the flux of both sources is provided by the hot spots and the cores. At decameter wavelengths the cores radio emission is negligible and not detected with the URAN. The low frequency flux of the hot spots in both sources is much lower than emanation of the lobes that provide the main part of the sources emission at these wavelengths. The angular size of the lobes is enlarged significantly with frequency decrease, especially for south-east lobes, that are located closer to the observer in both radio sources. The farther lobes are increased modestly and hot spots in them, quite observable at the higher frequency, are not detected at the lower one.

Centers of the brightness distribution of the extended components in both objects are shifted to the core of the source. It can be explained by influence of synchrotron losses in the oldest parts of the lobes. These parts were formed at earlier stage of source expansion and they are located closer to the core. The synchrotron losses have reduced energy of this most aged population of relativistic electrons hence their radiation at higher frequencies is weakened comparatively to the lower frequencies. This effect leads to the shift of the brightness centers of the lobes in the core direction at lower frequencies. Position of the hot spots at the decameter wavelengths practically coincides with their coordinates in the decimeter range.

#### 4. Summary

The quasar 3C263 and the radio galaxy 3C169.1 were observed at the decameter wavelengths with the URAN interferometers. The models of the brightness distribution of the sources have been determined at low frequencies. It was found that at higher frequencies these objects have very similar properties. The radio sources have approximately equal angular sizes, flux densities, and ages and they are located at close redshifts. In the decameter range these quasar and radio galaxy also have similar angular structure but it differs significantly from their high frequency images. The compact details associated with the active cores of the sources are not detected. The lobes are enlarged noticeably and their relative brightness is increased compared to the hot spots. The extended structures whose size exceeds significantly source dimensions measured at high frequencies are not detected in both objects.

#### References

- Megn A.V. et al.: 1999, *ARep*, **43**, 428.
- Megn A.V. et al.: 2003, *ARep*, **47**, 1038.
- Megn A.V. et al.: 1996, *AstL*, **22**, 385.
- Megn A.V. et al.: 2006, *ARep*, **50**, 692.
- Megn A.V. et al.: 1997, *R&R*, **2**, 385.
- Megn A.V. et al.: 1998, *R&R*, **3**, 284.
- Megn A.V. et al.: 2001, *R&R*, **6**, 9.

DOI: <http://dx.doi.org/10.18524/1810-4215.2016.29.85208>

## RELATIONS OF STRUCTURE COMPONENTS OF GIANT RADIO SOURCES

A.P. Miroshnichenko

Institute of Radio Astronomy, NAS of Ukraine

4, Mystetstv Str., 61002, Kharkiv, Ukraine, [mir@rian.kharkov.ua](mailto:mir@rian.kharkov.ua)

**ABSTRACT.** Our previous estimates of physical parameters of galaxies and quasars with steep radio spectrum have showed their great radio luminosity and giant radio structure. Examination of the relations of corresponding monochromatic luminosities at different bands (from decametre to X-ray) allows estimate the comparative contribution of emission of structure components of sources. Using the sample of galaxies and quasars with steep radio spectrum from the UTR-2 catalogue we determine the contribution of emission of extensive radio lobes relatively central region, also relatively accretion disk, gas-dust torus, crown of accretion disk of given source. The particular interest has the relation of monochromatic luminosities of objects at near-infrared and X-ray bands, which corresponds to contribution of emission of gas-dust torus relatively emission of crown of accretion disk. The derived estimates of contribution of emission of components of giant sources reveal evolution effects at relations on redshift, linear size, age of examined sources.

**Keywords:** Galaxies – Quasars – Radio sources: giants

### 1. Introduction

Before (Miroshnichenko, 2012a, 2012b, 2013, 2014, 2015, 2016) we received estimates of the main physical parameters of quasars and galaxies with steep radio spectrum over the sample of sources from the UTR-2 catalogue at the decameter band. Note, that galaxies and quasars with steep low-frequency spectra have the great luminosity (by order of  $10^{28}$  W/Hz·ster at the frequency 25 MHz) and very extended radio structure with linear size by order of 1 Mpc, and characteristic age by order of 100 million years. So, steep-spectrum radio sources are peculiar objects with giant radio structure. It is important to study relations of emission of their different structure components.

### 2. Examination of emission relations of structure components

It is known from the observation data, the emission of separate components of the structure of extragalactic sources, mainly, corresponds to certain frequency bands. For instance, the emission of source at low frequencies, in particular, at decametre band, characterizes the extended component of structure, radio lobes. At the same time, the emission of central part of object displays more brightly at the high radio frequencies. The emission of accretion disk of source's active nucleus is presented, mainly at the optical

band. At that the X-ray emission of source is connected with crown of accretion disk. The emission of gas-dust torus surrounding accretion disk is observed at the infrared band, especially, at its near zone (near-IR). Examination of the relations of corresponding monochromatic luminosities of sources at different bands (from decametre to X-ray) allows estimate the comparative contribution of emission for structure components of sources. Note, that relation of flux densities of emission at different frequencies is identical to relation of corresponding monochromatic luminosities of a source. Also, it is important that relations of monochromatic luminosities are independent from the Universe model. Hence, these parameters allow study objectively the evolution effects for considered sources.

We consider that ratio of luminosities at 25 MHz and 5000 MHz,  $lg(S_{25}/S_{5000})$ , corresponds to contribution of emission of radio lobes relatively emission of the central region of source. Further, we suppose that contribution of emission of radio lobes: i) relatively of accretion disk emission – is ratio of luminosities at decameter and optical bands,  $lg(S_{25}/S_{opt})$ ; ii) relatively of torus emission of source – is ratio of luminosities at decametre and infrared bands,  $lg(S_{25}/S_{IR})$ ; iii) relatively of emission of accretion disk crown – is ratio of luminosities at decametre and X-ray bands,  $lg(S_{25}/S_X)$ . The pointed ratios are obtained for the sample of steep-spectrum sources to reveal evolution features of giant radio structures.

Earlier, we have compiled the sample of steep-spectrum sources at two fields of UTR-2 catalogue of extragalactic sources with given selection criteria (the value of spectral index at decametre band is greater than 1, the flux density of emission at frequency 25 MHz is  $S_{25} > 10$  Jy (Miroshnichenko, 2012a, 2012b, 2013). Our sample contains 130 galaxies and 91 quasars, including 78 galaxies and 55 quasars with linear steep spectra (spectral type S), and 52 galaxies and 36 quasars with steepness of their low-frequency spectra after a break (spectral type C+). We consider ratios of luminosities  $lg(S_{25}/S_{5000})$ ,  $lg(S_{25}/S_{opt})$ ,  $lg(S_{25}/S_{IR})$ ,  $lg(S_{25}/S_X)$ ,  $lg(S_{IR}/S_X)$ , determine relationship of these parameters on redshift  $z$ , linear size  $R$ , characteristic age  $t$ . These relationships are examined in each sub-sample of galaxies and quasars with steep radio spectrum:  $G_S$  (galaxies with linear steep spectrum S),  $G_C^+$  (galaxies with break steep spectrum C+),  $Q_S$  (quasars with S spectrum),  $Q_C^+$  (quasars with C+ spectrum).

As it means from derived mean values of luminosity ratios for extended radio lobes, these parameters are dependent from the spectral type of sources (see Table 1).

Table 1. Mean value of luminosity ratios of different structure components of galaxies and quasars with steep radio spectra S and C<sup>+</sup>.

		G <sub>S</sub>	Q <sub>S</sub>	G <sub>C<sup>+</sup></sub>	Q <sub>C<sup>+</sup></sub>
Ratio of emission of radio lobes and central region of source	$\langle \lg(S_{25}/S_{5000}) \rangle$	2.19 (+0.05)	2.08 (+0.08)	1.74 (+0.05)	1.69 (+0.08)
Ratio of emission of radio lobes and accretion disk of source	$\langle \lg(S_{25}/S_{opt}) \rangle$	5.64 (+0.12)	5.33 (+0.06)	5.15 (+0.12)	5.00 (+0.10)
Ratio of emission of radio lobes and torus of source	$\langle \lg(S_{25}/S_{IR}) \rangle$	4.58 (+0.17)	4.71 (+0.14)	3.67 (+0.19)	4.30 (+0.11)
Ratio of emission of radio lobes and accretion disk crown of source	$\langle \lg(S_{25}/S_X) \rangle$	9.03 (+0.23)	8.45 (+0.14)	7.89 (+0.33)	7.78 (+0.17)
Ratio of emission of torus and accretion disk crown of source	$\langle \lg(S_{IR}/S_X) \rangle$	4.53 (+0.36)	3.73 (+0.18)	4.68 (+0.47)	3.54 (+0.20)

For example, values of ratios  $\langle \lg(S_{25}/S_{5000}) \rangle$ ,  $\langle \lg(S_{25}/S_{opt}) \rangle$ ,  $\langle \lg(S_{25}/S_{IR}) \rangle$ ,  $\langle \lg(S_{25}/S_X) \rangle$  are greater for objects G<sub>S</sub> and Q<sub>C</sub>, then corresponding values for objects G<sub>C<sup>+</sup></sub> and Q<sub>C<sup>+</sup></sub>. At ones we can conclude on greater contribution of emission of radio lobes in galaxies and quasars with linear type of steep radio spectrum. At the same time as, galaxies and quasars with steep spectrum C<sup>+</sup> may possess more essential torus emission and accretion disk emission. Also, one can see from the Table 1, the mean value of ratio of torus emission and accretion disk emission for galaxies of both spectral type (S and C<sup>+</sup>) exceeds analogous value for quasars of both spectral types. This may indicate on more scaling, intensive tori in steep-spectrum galaxies in comparison with steep-spectrum quasars.

To study evolution of emission of structure components of sources with steep spectra S and C<sup>+</sup>, it is important to examine corresponding relationships on redshift, linear size, characteristic age of sources. Emission of radio lobes relatively emission of central region of objects ( $\lg(S_{25}/S_{5000})$ ) has very weak positive trend in relationship on redshift and linear size in all four subsamples (G<sub>S</sub>, G<sub>C<sup>+</sup></sub>, Q<sub>S</sub>, Q<sub>C<sup>+</sup></sub>). Meanwhile, the trend of decrease of value  $\lg(S_{25}/S_{5000})$  is observed in relationship on characteristic age. The relationship of emission ratio of radio lobes and accretion disk of sources ( $\lg(S_{25}/S_{opt})$ ) on redshift  $z$  is fitted by second power polynome for subsamples G<sub>S</sub> (with maximum at  $\lg(1+z) = 0,43$ , that is, at  $z = 1,69$ ) and G<sub>C<sup>+</sup></sub> (with maximum at  $\lg(1+z) = 0,28$ , that is, at  $z = 0,91$ ) (see Figure 1, Figure 2). Maximum of these relationships may evidence on the activity recurrence of giant sources. Linear trend of increase of  $\lg(S_{25}/S_{opt})$  at increase of  $\lg(1+z)$  is observed for subsamples of quasars Q<sub>S</sub> and Q<sub>C<sup>+</sup></sub> (Figure 1, Figure 2). At that, the positive trend in relationship  $\lg(S_{25}/S_{opt})$  on source linear size  $R$  is revealed for all types of objects in our sample (see, for example, Figure 3). Thus, the contribution of emission of radio lobes increases

at increase of linear size of steep-spectrum source. At that time, the examined sources display negative trend in relationship  $\lg(S_{25}/S_{opt})$  on characteristic age, that testifies on more intensive gas-dust torus in more old giant sources. This conclusion is confirmed by smaller mean value  $\langle \lg(S_{25}/S_{IR}) \rangle$  for G<sub>C<sup>+</sup></sub> and Q<sub>C<sup>+</sup></sub> in comparison with analogous values for G<sub>S</sub> and Q<sub>S</sub> (see Table 1).

Examination of mutual relationship for ratios of emission of two structure components of sample sources – contribution of emission of radio lobes relatively accretion disk emission and contribution of emission of radio lobes relatively torus emission – displays positive correlation of these parameters as well as evolution sequence of giant radio sources with steep spectrum. As one can see from Figure 4, galaxies and quasars with linear steep spectrum (S) cover region of more essential contribution of emission of radio lobes. On the other side, galaxies and quasars with steep spectrum C<sup>+</sup> correspond to region of smaller parameters of given structure components (see Figure 4). This peculiarity may be due to more intensive radiation of tori and accretion disks in objects with steep spectrum C<sup>+</sup>.

It is important to consider emission of spatially close structure components in source–torus emission relatively emission of accretion disk crown ( $\lg(S_{IR}/S_X)$ ). Decrease of value  $\lg(S_{IR}/S_X)$  at increase  $z$  for sample sources is found in relationship of this parameter on redshift  $z$ . Probably, the X-ray emission of accretion disk crown is more intensive for early cosmological epochs.

It is interesting, that relationship  $\lg(S_{IR}/S_X)$  on linear size of source  $R$  has the form of two branches (see Figure 5). Also, relationship  $\lg(S_{IR}/S_X)$  on  $R$  for G<sub>C<sup>+</sup></sub> and Q<sub>C<sup>+</sup></sub> has the form of two branches, but more spread (Figure 6). Such evolution form of  $\lg(S_{IR}/S_X)$  relatively linear size may indicate on activity recurrence of objects with giant radio structure.

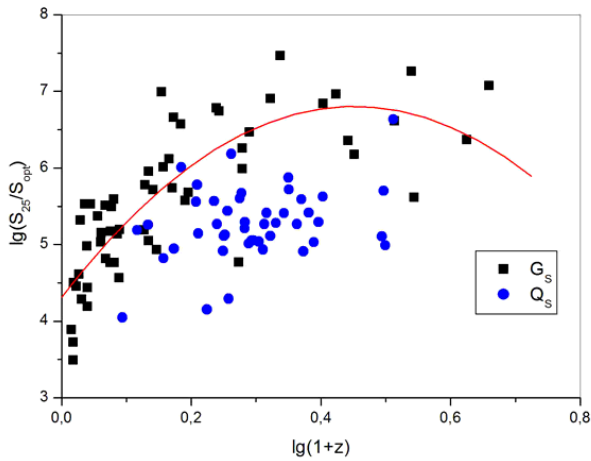


Figure 1: Ratio of emission of radio lobes and accretion disk versus redshift for galaxies and quasars with linear steep spectrum (fitting by second power polynome for  $G_S$  is marked by line)

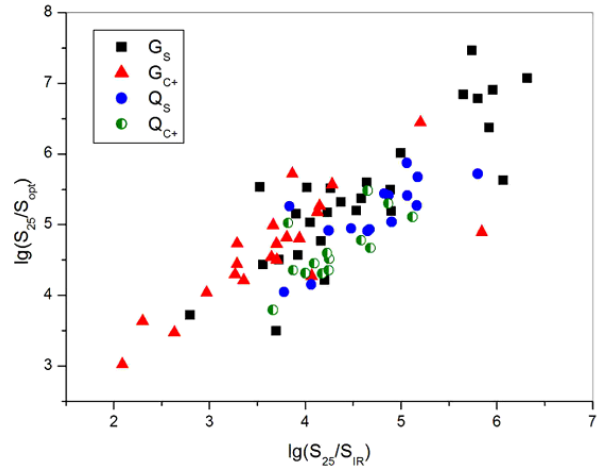


Figure 4: Ratio of emission of radio lobes and accretion disk versus ratio of emission of radio lobes and torus for galaxies and quasars with steep spectra S and C+ (evolution sequence)

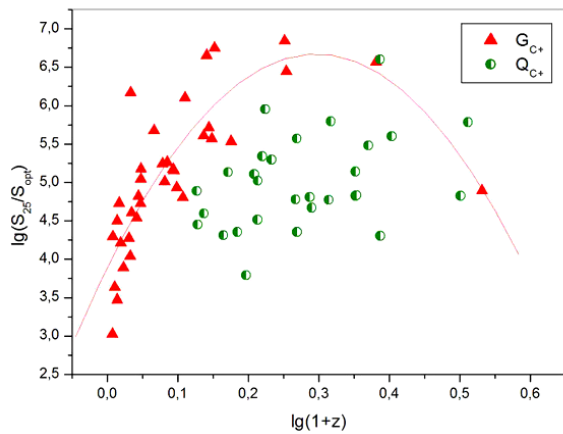


Figure 2: Ratio of emission of radio lobes and accretion disk versus redshift for galaxies and quasars with break steep spectrum (fitting by second power polynome for  $G_{C+}$  is marked by line)

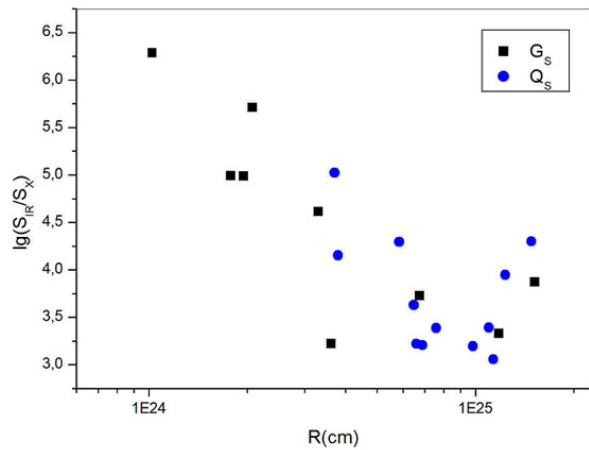


Figure 5: Ratio of emission of torus and accretion disk crown versus linear size for galaxies and quasars with linear steep spectrum

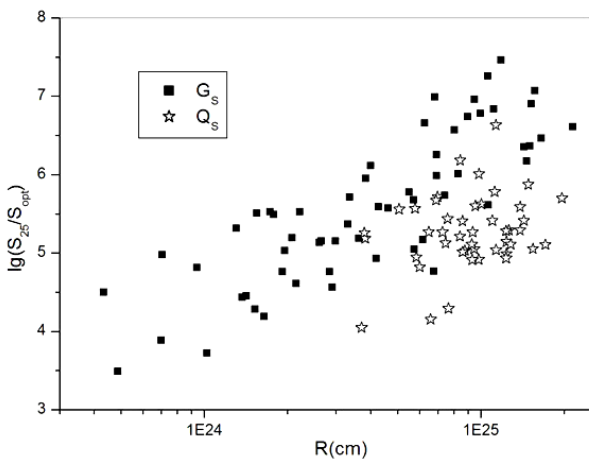


Figure 3: Ratio of emission of radio lobes and accretion disk versus linear size for galaxies and quasars with linear steep spectrum

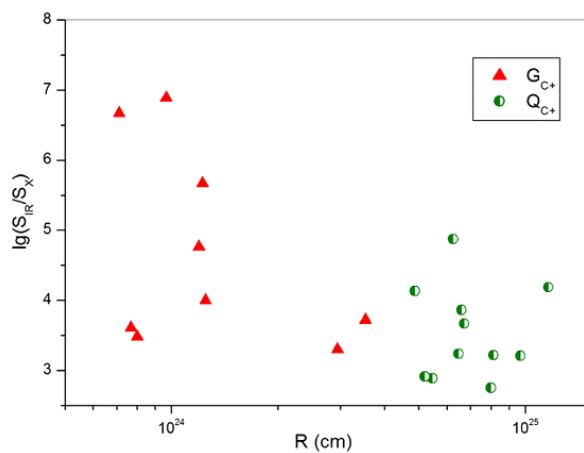


Figure 6: Ratio of emission of torus and accretion disk crown versus linear size for galaxies and quasars with break steep spectrum

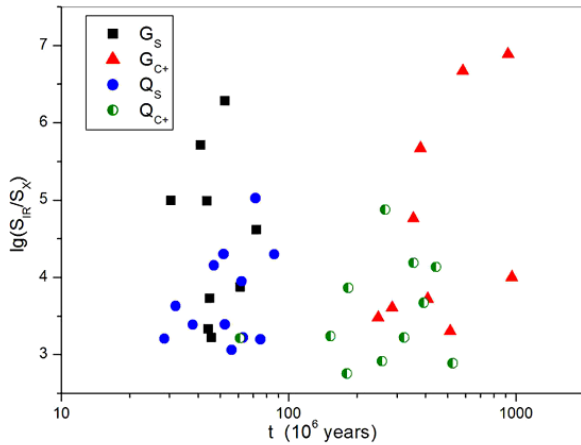


Figure 7: Ratio of emission of torus and accretion disk crown versus characteristic age for galaxies and quasars with steep spectra S and C+

The relationship of value  $lg(S_{IR}/S_X)$  on characteristic age of sources  $t$  is notable (Figure 7). Sample objects of spectral type C<sup>+</sup> ( $G_{C^+}$  and  $Q_{C^+}$ ) cover region of greater ages in comparison with objects of spectral type S ( $G_S$  and  $Q_S$ ) (see Figure 7). Radio sources with spectral type C<sup>+</sup> have, in average, characteristics age greater near one order, than analogous value for sources with linear steep spectrum S in our sample (Miroshnichenko, 2013). So, giant sources with steep spectrum C<sup>+</sup> may show more significant evolution effects in their structure components.

### 3. Conclusions

The comparative contribution of emission of structure components of sources is estimated for steep-spectrum galaxies and quasars from UTR-2 catalogue. This allows us to study the evolution effects of giant steep-spectrum radio sources. Main results of this study are next:

- Contribution of extended component (radio lobes) increases at the increasing of linear sizes of sources.
- Ratio of torus emission and disk crown of sources reveals two branches of evolution versus linear size and age of objects, indicating on the activity recurrence of nuclei of giant steep-spectrum sources.
- Galaxies and quasars with steep radio spectrum C<sup>+</sup>, having great characteristic age, display greater contribution of torus emission than objects with spectrum S.
- The evolution sequence is obtained for galaxies and quasars with steep radio spectra S and C<sup>+</sup>.

### References

- Miroshnichenko A.: 2012a, *Radio Physics and Radio Astronomy*, **3**, 215.  
 Miroshnichenko A.: 2012b, *Odessa Astron. Publ.*, **25**, 197.  
 Miroshnichenko A.: 2013, *Odessa Astron. Publ.*, **26/2**, 248.  
 Miroshnichenko A.: 2014, in: *Multiwavelength AGN Surveys and Studies*, Cambridge, 96.  
 Miroshnichenko A.: 2015, *Odessa Astron. Publ.*, **28/2**, 238.  
 Miroshnichenko A.: 2016, in: *Genesis and Growth of the Cosmic Web*, Cambridge, 631.

DOI: <http://dx.doi.org/10.18524/1810-4215.2016.29.85209>

## SPECIAL FIELDS OF THE GALAXY RADIO EMISSION

N.M.Vasilenko, M.A.Sidorchuk

Institute of Radio Astronomy, National Academy of Sciences of Ukraine  
Iskustv 4, 63014, Kharkov, Ukraine, [natamish@ukr.net](mailto:natamish@ukr.net), [sidor@rian.kharkov.ua](mailto:sidor@rian.kharkov.ua)

**ABSTRACT.** The brightness temperatures of radio emission were measured with the UTR-2 low-frequency radio telescope at frequencies 12.6, 14.7, 16.7, 20 and 25 MHz for the following Galaxy regions: the North Pole, the area of minimum radio brightness and the anticenter region. The brightness temperature spectrums of the galactic background radiation were constructed for the selected areas using the data at other different wavelengths. The brightness temperature spectral indices were determined for these areas at wavelengths ranging from meter to decameter.

**Keywords:** Galaxy: structure – radio continuum – spectral index: ISM – radiation mechanisms: non-thermal

## 1. Introduction

Large amount of sky surveys in a wide radio frequency range (see for example, Haslam et al., 1981; Roger et al., 1999; Wielebinski, 2004) showed that the radio emission is concentrated in the galactic plane with a maximum near the Galactic center and is extended up to high galactic latitudes, where demonstrates a sufficiently high intensity, especially at low frequencies. If not taking into account the ‘spurs’ and loops, the radio emission of the Galaxy can be divided into two components - the disk and the halo ones, symmetric with respect to the galactic plane. One can distinguish several specific areas of the galactic radio emission: the anticenter region, which characterizes the radiation of the Galaxy disk component, the areas of the minimum radiation and the Galactic poles, where the radio emission is mainly due to the Galaxy spherical halo. The knowledge of the radio emission spectral characteristics in these areas is extremely important for understanding the distribution and propagation of relativistic electrons and magnetic fields in the Galaxy.

As known, the brightness temperature ( $T$ ) frequency ( $\nu$ ) dependency is  $T(\nu) \sim \nu^{-\beta}$ : where  $\beta$  is the spectral index. The spectra were constructed by Bridle (1967), Cane (1979), Guzman et al. (2011) in these areas at different frequencies bands. Bridle (1967) has obtained the total background radiation spectral index  $\beta = 2.55 \pm 0.04$  between 13.15 and 404 MHz for the Galaxy North Pole. The same value of the total background average

spectral index ( $\beta = 2.55 \pm 0.03$ ) was obtained by Cane (1979) for the Galaxy poles at frequency range from 6 to 100 MHz. Based on these results Cane (1979) has constructed the radio sky model consisting only of two components, one of which is the disc of the uniform emission and absorption and another is the extragalactic background. Guzmán et al. (2011) determined the following spectral indices of the galactic radio emission brightness temperature: in the anticenter region  $\beta \approx 2.48$  between 10 and 1420 MHz; in the Northern sky minimum radio emission region  $\beta \approx 2.41$  at the same frequencies and for the Galaxy North Pole  $\beta \approx 2.53$  for frequencies between 2.3 and 1420 MHz. Guzmán et al. (2011) then used these results to evaluate and correct zero level offsets of the 408 MHz Haslam et al. (1981) and their all-sky 45 MHz surveys.

Here we present the constructed brightness temperature spectrum of the galactic radio emission at frequencies below 408MHz in the highlighted Galaxy regions, namely the anticenter region, the North Pole, and the Northern sky minimum radio brightness area. We used our Northern sky observational results at frequencies 12.6, 14.7, 16.7, 20 and 25 MHz (Vasilenko et al., 2006) and from the literature for the spectral studies.

## 2. The background spectrum of the Galaxy specific fields.

The brightness temperature of the sky in studied areas was obtained at decameter wavelengths using the UTR-2 radio telescope (Vasilenko et al., 2006). The angular resolution at frequencies 12.6, 14.7, 16.7, 20, and 25 MHz in the zenith direction is near 65' to 28' respectively. Also we used the brightness temperatures of these regions at frequencies below 408 MHz from the Guzmán's list (2011). We added to analysis the brightness temperatures from Haslam et al. (1981), Roger et al. (1999), Guzmán et al. (2011). The Metagalaxy brightness temperature  $T_M(\nu)$  was excluded from the sky total temperature using the expression (see Guzmán et al. (2011), Appendix A):

$$\log T_M(\nu) = 7.66 - 2.79 \log\left(\frac{\nu}{\text{MHz}}\right).$$

To study the spectral properties of the nonthermal radio emission at low frequencies we have limited to the

frequency range from 9 to 408 MHz. At frequencies below 9 MHz the observations were made with very low resolution and there is more pronounced absorption effect. We have analyzed the spectra at the following frequency bands: 9÷408 MHz, 9÷100 MHz and 9÷45 MHz to search for changes in the spectral index with a decreasing frequency. Brightness temperature spectra for each selected field were constructed at the above frequency bands at two stages: a) first, excluding brightness temperatures at decameter waves, which were defined by us and b) then with these brightness temperatures taken into account. The spectra were fitted with the least squares method. Figures 1a), b), c) show the spectrum in the log-log scale and fitted line for the three selected Galaxy regions in the frequency range 9÷100 MHz. As can be seen in this figures the brightness temperatures obtained by us and Roger, R. S. et al.(1999) are somewhat lower than the observed at similar frequencies, we assume that this is due to the telescopes low-resolution on which observations are made. The spectral indices of the galactic radio emission in the 9÷408 MHz range are greater than in the 9÷100 MHz range for all selected regions. The spectral indices taking into account our data, are less than without them in all these areas. The difference between spectral indices is greater for high-latitude regions - the North Pole and the minimum radiation area. The changes in the spectral index with a decreasing frequency may be due to changes of the spectrum of the extragalactic background with frequency. We show a significantly different Metagalaxy radiation spectrum with  $\beta_M \approx 2.41$  (Vasilenko et al., 2015) compared with  $\beta_M \approx 2.79$  Guzmán et al. (2011). The spectral indexes at frequencies between 9 and 45 have large errors than in other ranges. Spectral indices are shown in Table 1.

Table 1. The spectral indexes of the galactic brightness temperature.

Frequency band (MHz)	9÷408	9÷100	9÷45
Anticenter	2,48±0,04	2,44±0,03	2,35±0,14
North Pole	2,56±0,03	2,45±0,06	2,68±0,10
Min. North	2,51±0,09	2,37±0,09	2,4±0,15

### 3. Conclusions

Our spectral studies allow us to speak about existence of significant tendencies of change of the galactic radio emission spectral index with decreasing frequency. We assume that this may be due to changes in the spectrum of the extragalactic background. This work reveals the lack of ground-based high-resolution observations at low frequencies which does not allow identifying a possible break in the spectrum of the radio emission of the Galaxy in this frequency range.

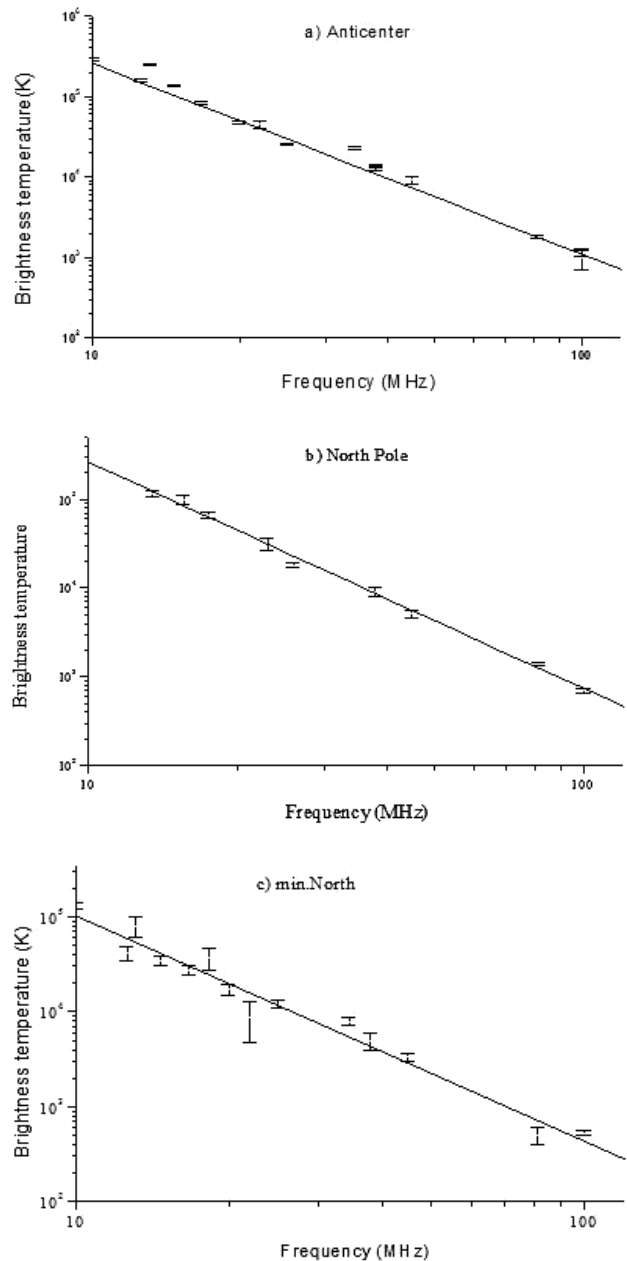


Figure 1: Brightness temperature spectra of the galactic radio emission and fitting of the line for three selected fields at frequency range 9÷100 MHz.

### References

- Bridle A.H.: 1967, *MNRAS*, **136**, 219.  
 Cane H.V.: 1979, *MNRAS*, **89**, 465.  
 Guzmán A.E. et al.: 2011, *A&A*, **525**, A138.  
 Haslam C.G.T. et al.: 1981, *A&A*, **100**, 209.  
 Roger R. S. et al.: 1999, *A&AS*.  
 Vasilenko N.M. et al.: 2006, *XXVth Gen.Ass.*, **JD12-45**, 370.  
 Vasilenko N.M. et al.: 2015, *RP&RA*, **20**, 205.  
 Wielebinski R.: 2004, *MIM Proc.*, 241.

DOI: <http://dx.doi.org/10.18524/1810-4215.2016.29.85210>

## PARAMETERS OF THE TRANSIENT SIGNALS DETECTED IN THE DECAMETER SURVEY OF THE NORTHERN SKY

I.P.Kravtsov<sup>1</sup>, V.V.Zakharenko<sup>1</sup>, I.Y.Vasylieva<sup>1</sup>, S.S.Mykhailova<sup>2</sup>,  
O.M.Ulyanov<sup>1</sup>, A.I.Shevtsova<sup>1</sup>, A.O.Skoryk<sup>1</sup>

<sup>1</sup> Institute of Radio Astronomy on National Academy of Sciences of Ukraine,  
Mystetstv str., 4, 61002, Kharkiv, Ukraine, *i.p.kravtsov@gmail.com*

<sup>2</sup> Department of Astronomy and Space Informatics, Physics School, Karazin Kharkiv National  
University, Svobody sq., 4, 61022, Kharkiv, Ukraine, *seychells\_sun@mail.ru*

**ABSTRACT.** Decameter all-sky Survey has been running at UTR-2 radio telescope over the past few years, about 70% of observational data are processed. The Survey is aimed at searching for pulsars and transient sources. Present work shows results of processing aforementioned part of data in order to find transient sources. The processing allowed detecting more than 500 signals. Distributions of the signals' parameters (dispersion measures, galactic latitudes, "signal-to-noise-ratios" etc.) are obtained, which give reason to consider the vast majority of these pulses the signals from cosmic sources.

**Keywords:** astronomical data bases: surveys – Galaxy: solar neighborhood – methods: data analysis

### 1. Introduction

Decameter survey of the Northern sky aimed at searching for pulsars and sources of transient radio emission (Vasylieva, 2014), which is held at the world's largest UTR-2 radio telescope, is the first survey of its kind in such a low-frequency range. The main risk of the automatic search (Vasylieva, 2013) for individual pulses (transient events) and their identification (determining the dispersion measure (DM), signal arrival directions, etc.) is a high probability of incorrect classification of the signals by their nature: signals from cosmic radio sources or interference of terrestrial origin.

That's why the routine for analysis and visualization of all data processing steps was developed at the next stage of "candidates" data processing and analysis (Zakharenko, 2015). Also, the possibility of Radio Frequency Interference (RFI) mitigation parameters tuning, filtering of low- and high-frequency interference, changing DM with a 0.002 pc/cc (parsec per cubic centimeter) step and some other are added to this routine. Despite the fact that each individual pulse cannot be unambiguously classified as interference or, vice versa, space radiation source, a large number of them allows to build a distribution on different parameters, such as DM, galactic latitude etc. Latter can be compared to the same characteristics of nearby pulsars, rotating radio transients (RRATs) or other types of neu-

tron stars, which can indirectly indicate that "candidates" belong either to cosmic radio sources or interference of terrestrial origin.

In order to estimate the possibility of detecting a significant number of pulsed sources of radio emission, the decameter census of known pulsars was held (Zakharenko, 2013). A very important result of this study was the confirmation of pulsar's pulse broadening towards lower frequencies. Earlier (due to the small number of detected pulsars) this phenomenon was not well substantiated in the decameter range. Figure 1 (bottom panel) shows the pulsar pulses broadening when the central frequency of observations changes from 100 MHz to 25 MHz. The amount of the broadening (top panel of the figure shows the extension of the radiation cone of pulsars for decameter waves compared to the meter ones) is 3.5 times at its maximum, and 1.6-1.8 times on average. This implies that we can expect detection of normal, giant or an anomalously intense pulses of pulsars (Ulyanov, 2006; Ulyanov, 2007), pulses of RRATs and other neutron stars which are oriented such that they cannot be detected at higher frequencies.

That is, considering the fact that neutron stars generate pulsed and transient radio emission, the number of transient signals can be much higher than that at high frequencies, even at 100 MHz (LOFAR).

The results of processing of approximately 70% of the Survey data and verification of nearly 1,000 "candidates" – individual pulses with the DMs which differ from the DMs of pulsars detected at the first stage – are presented in the present work. Thanks to the refining the dispersion measure, "signal-to-noise-ratio" (SNR) and pulse durations were refined. Section 2 describes the routine for processing the "candidates" data and the typical results of its work. Section 3 shows the distributions of various parameters of the "candidates". The final section provides the discussion of the results obtained after processing about 70% of the Survey data and suggests the direction of improving the processing routines and the further stages of data analysis.

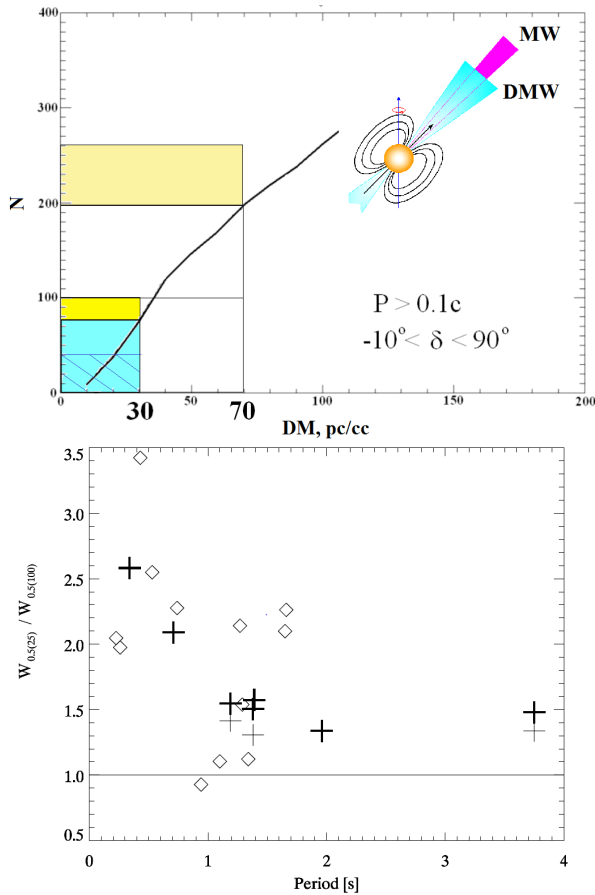


Figure 1: Top panel shows the extension of radiation cone at decameter waves compared to meter waves. The thick curve shows the number of known pulsars in the range of dispersion measures with 10 pc/cc step (Manchester, 2005). We consider that the extension will provide an opportunity to detect the pulsars, which aren't visible at higher frequencies (yellow rectangles). Bottom panel shows increasing of the «beaming fraction» (fraction of the period occupied by pulse or "opening" of the radiation cone) by 1.5-3 times (Relative expansion of the FWHM profile between frequencies 25 and 100 MHz as a function of period (Zakharenko, 2013, Fig. 11)).

## 2. Data Processing

The developed routine for transient signals analysis (Zakharenko, 2015) allowed to carry out the processing of each "candidate" out of about 1000. During the verification, the part of observational data which contains the supposed event is reprocessed by varying parameters of RFI mitigation, DM values etc. in order to obtain the maximum SNR of the transient signal. All these steps are visualized (displayed as a 2-dimensional spectrogram or integrated versus frequency and time). In addition the signal should satisfy the following criteria:

- to have a wide band (a few MHz);
- to be sufficiently homogeneous (without explicit narrowband or short spikes);
- to be present mostly in RFI-free frequency channels (in case of a significant number of polluted areas on the spectrogram, usually in a frequency range below 24 MHz).

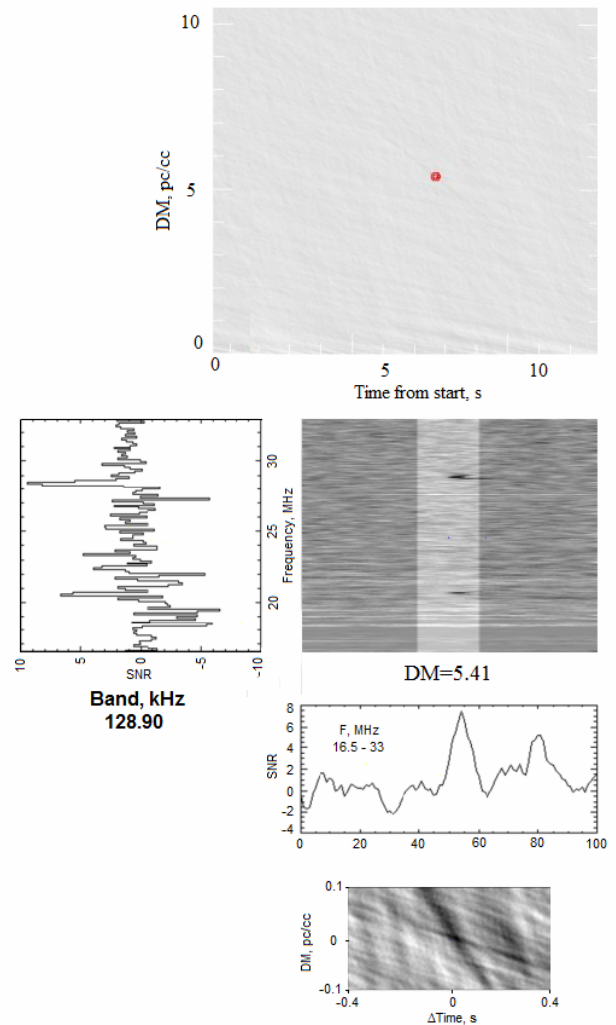


Figure 2: RFI which is identified by means of our developed verification routine and using the criteria set (see text).

Moreover, some RFI are repetitive. Individual pulses may appear relatively broadband. Such RFI must be analyzed using a toolkit for periodic signal analysis that is a part of the "candidates" analysis routine. If a sequence of pulses is found, usually the pulsar pulses can be distinguished from repetitive interference exactly by the broad band of their emission.

Such criteria cannot be programmed for automatic processing; therefore visual inspection with checking all the re-processing stages is used for "candidates" selection.

Examples of the obvious interference signals have been shown in earlier works (Vasylieva, 2014; Zakharenko, 2015).

Example of RFI which has been identified using the above-mentioned criteria are presented in Fig. 2.

## 3. Results

Currently, almost all observation sessions of the Survey have been carried out (Fig. 3). Fig. 4 shows the current status of the data processing (detected and verified signals are mapped there).

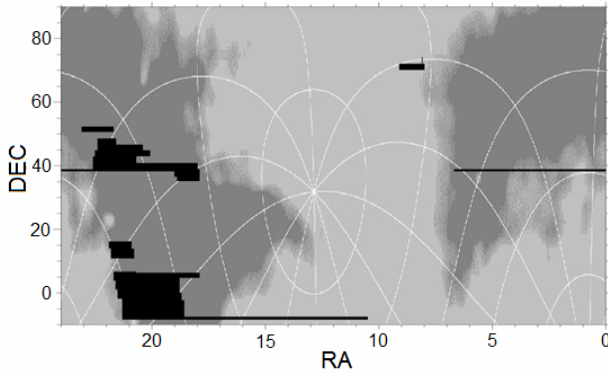


Figure 3: Current status of observations.

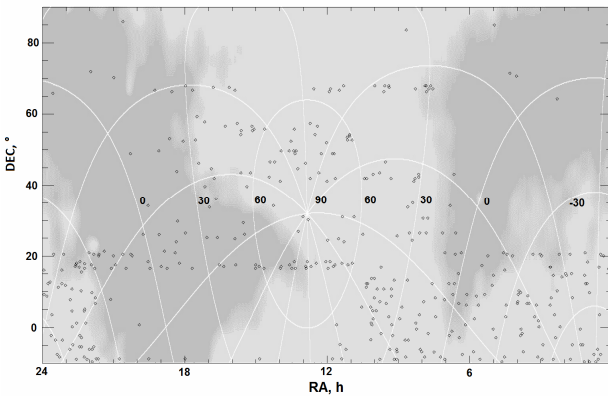


Figure 4: Transient signals at the sky map (about 70% of data are processed), verified by the developed routine.

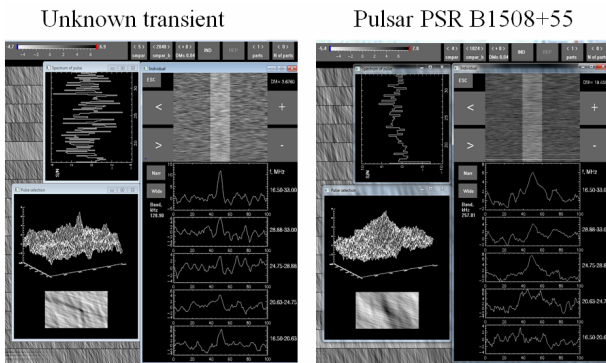


Figure 5: Presumably transient signal with  $DM = 3.676$  pc/cc (left panel) and individual pulse of PSR B1508+55 (right panel) with  $DM = 19.6$  pc/cc.

An example of "candidate" which with high probability is a pulse from the source of cosmic transient radio emission is shown in Fig. 5 in comparison with a pulse of a powerful well-known pulsar B1508+55. More broadband peaks (left panel, "highlighted" part of the spectrogram) are typical of the signals with a lower DM (Ulyanov, 2006).

Although it is impossible to claim doubtless classification of "candidates" (RFI / cosmic signal), we, nevertheless, can analyze distributions of certain properties of the detected signals. In the paper (Zakharenko, 2015) we presented distributions of DMs and galactic latitudes ( $b$ ) of some number of processed "candidates". Now, having more candidates, we can add distributions of other properties.

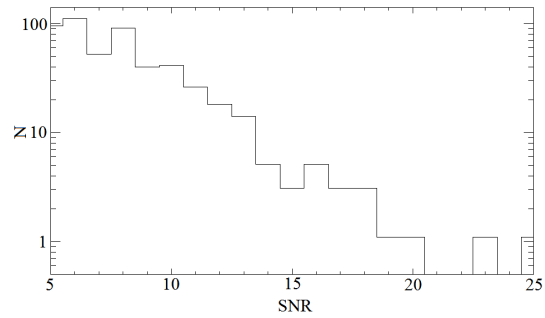
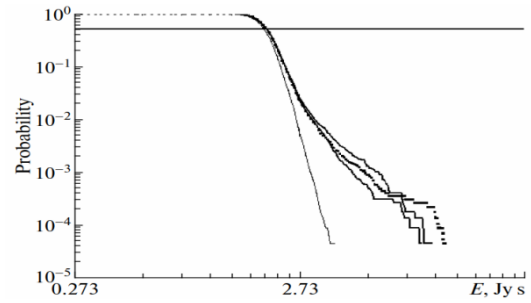


Figure 6: Distribution of detected pulses by SNR (bottom panel) and the distribution law of anomalously intense pulses of PSR B0809+74 by the energy (top panel, thin line – at the longitude of pulsar’s average profile, where the radiation is absent, the other (bold) curves – at different longitudes around the maximum of the average profile).

*The distribution of "signal-to-noise" ratio (SNR).* We obtain this parameter after tuning (by means of the aforementioned analysis routine), mainly of the DM parameter with a 0.002 pc/cc step for each of the detected events. This is necessary, because the step 0.01 pc/cc (which is used during the primary pipeline processing) is quite rough. Fig. 6 (bottom panel) shows the distribution of pulses by the SNR parameter. The top panel of the figure shows the integral distribution law of energies of anomalously intense pulses of the pulsar B0809+74 (Ulyanov, 2012) at different longitudes of average pulse profile. The similarity of the most intense ejections (bold curves) on the top panel and distributions of SNRs of the detected transients, which both obey the power law, is obvious.

*The distribution of the frequency of transient occurrence by the local time (LT).* The observations of the survey are carried out mostly from 18:00 LT to 6:00 LT with a half-hour additional overlap. Fig. 7 shows the distribution of the number of detected "candidates" depending on the local time (bottom panel). To observe one full sky "strip" in right ascension (24 hours), two observation sessions of the same declination are required, with a six months shift. The maximum similarity in terms of the RFI environment is thus for observations carried out near the days of spring and autumn equinoxes. In the ideal case of no RFI influence on the number of detected signals, it would be natural to assume the equiprobable appearance of transients independently of the observation time. But by analyzing (Fig. 7, top panel) the start and finish time of the corresponding observation "strips", it proves that coincidentally the beginning and the end of most strips of

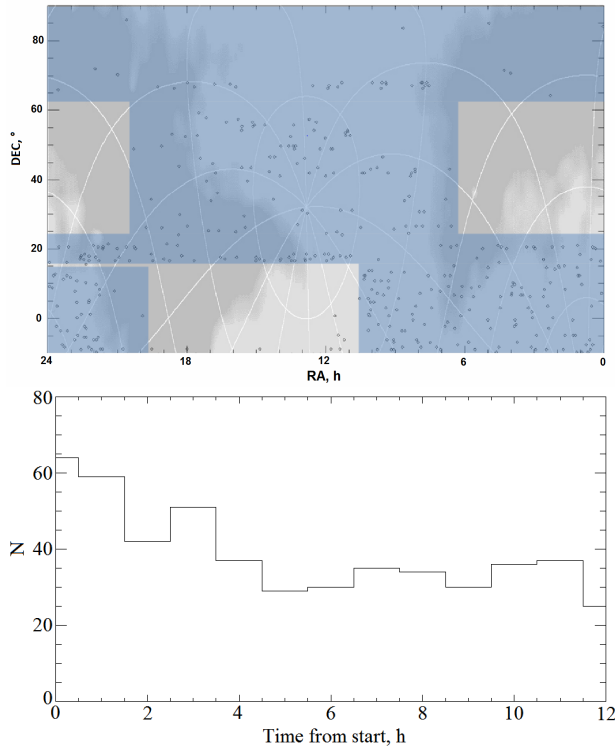


Figure 7: Bottom panel: the number of detected individual pulses depending on the observation time. Observation sessions began at 18:00 LT. Some sessions started in the range from 15:00 to 21:00 LT.

Top panel: current status of data processing, blue regions of the map indicate processed parts of the sky recordings.

fully or partly processed data (blue part) correspond to low galactic latitudes, where a maximum number of neutrons stars should be observed. So the maximum for the first two hours of observation and a slight increase of the number of "candidates" to the end of the 12-hour sessions can be caused both by the effect of unidentified RFI (which is more numerous in the daytime than at night), and the real distribution of cosmic sources of transient radio emission.

Two other distributions (of candidates' dispersion measures and galactic latitudes) have already been given based on a more limited dataset (about 30% of the Survey) in the paper (Zakharenko, 2015). In this paper we cleaned the set of "candidates" used previously from a few obvious interference and added the next part of the processed data (for now it is about 70% of the Survey).

*Distribution of candidates' DMs is presented in the bottom panel of Fig. 8.* The top panel shows the simulated distribution of pulsars by DM that can be discovered using the radio telescope under construction – SKA (Keane, 2015) based on the population synthesis and characteristic parameters of known pulsars (clear bars: strip 350-14000 MHz, gray ones: 50-350 MHz). At low DMs, the distance from the observer, the corresponding space volume, and the number of sources in it increase. Then due to scattering and weakening of the signal from more distant sources, the number of detectable sources starts to decrease. The same is true for our Survey (bottom panel of Fig. 8).

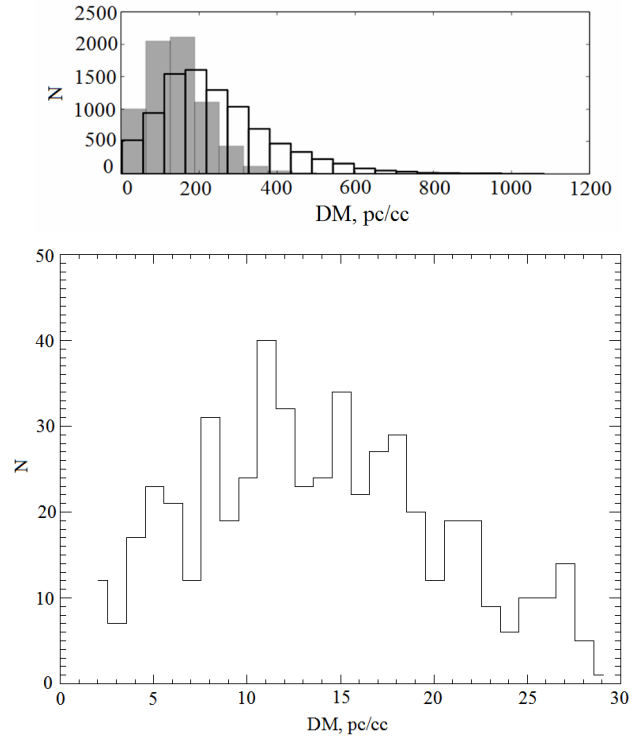


Figure 8: Simulated histograms of DM of pulsars, expected to be observed with SKA Phase 1, for SKA1-LOW (gray bars) and SKA1-MID (clear bars) (top panel) and DM distribution of the detected transients (bottom panel).

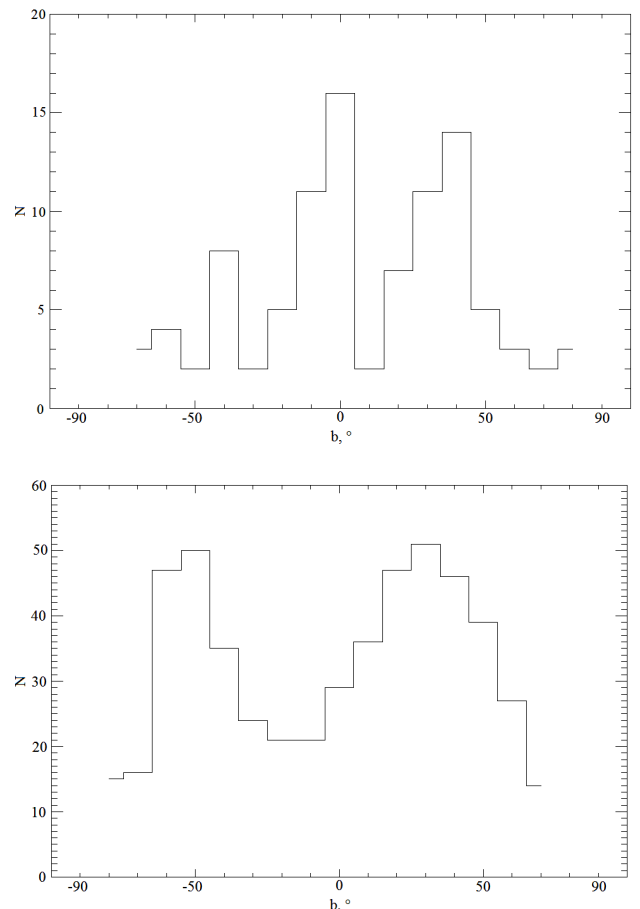


Figure 9: Galactic latitude distributions of known pulsars (top panel) (Manchester, 2005) and of detected transient signals (bottom panel).

*Distribution of candidates' galactic latitudes (Fig. 9)* also has characteristic features, which can be expected of close neutron stars' distributions. The lower panel shows the distribution of "candidates" in our Survey, the upper panel – distribution of nearby pulsars with DM under 30 pc/cc and period more than 0.1 seconds. Both distributions have a maximum close to zero galactic latitude.

Remarkably, both distributions have intrinsic maxima around minus and plus 50 degrees. The data cleaning using the developed routines and processing of the next part of data caused the noticeable changes of this distribution compared with (Zakharenko, 2015, Fig. 3a). The maximum at  $-50^\circ$  latitude decreased by 40% and became smaller than the broad maximum between 0 and 60 degrees. This feature of the distribution of the closest neutron stars has to be explored in future.

#### 4. Conclusions and Prospects

Thus, it becomes clear that pulsars/transients decameter survey of the Northern sky has some unique features and during its conducting we succeeded to detect a sufficiently large number of individual pulses.

Such a result is influenced by the peculiarities of the low-frequency range, which have both negative and positive aspects:

– wide beam of the telescope does not allow to define the coordinates with high accuracy, however the large field of view can captures a large number of simultaneous events;

– large dispersion delay complicates data processing, but allows to distinguish accurately the interference and space signals with different dispersion measures;

– scattering in the propagation medium (along with the radiation cone broadening, which is characteristic of different types of NS) also increase probability of individual pulse detection.

All these features allowed detecting a relatively large number of sources, than it would be possible at high frequencies.

Currently, we are improving methods for identifying weaker and weaker interference and continue processing the remaining 30% of the data.

#### References

- Keane E. et al.: 2015, *AASKA*, **14**, 40.  
Manchester R. N. et al.: 2005, *AJ*, **129**, 1993.  
Thorsett S.E.: 1991, *ApJ*, **377**, 263.  
Ulyanov O.M. et al.: 2006, *RP&RA*, **11**, 113.  
Ulyanov O.M. et al.: 2007, *RP&RA*, **12**, 520.  
Ulyanov O.M. et al.: 2012, *Astron. Rep.*, **56**, 417.  
Vasylieva I.Y. et al.: 2014, *RP&RA*, **19**, 197.  
Vasylieva I.Y. et al.: 2013, *Odessa Astron. Publ.*, **26**, 159.  
Zakharenko V.V. et al.: 2015, *Odessa Astron. Publ.*, **28**, 252.  
Zakharenko V.V. et al.: 2013, *MNRAS*, **431**, 3624.

DOI: <http://dx.doi.org/10.18524/1810-4215.2016.29.85212>

## CONNECTION BETWEEN THE SHOCK WAVE SPEED AND II TYPE RADIO BURSTS DRIFT VELOCITY

E.A.Isaeva, R.O.Kravetz

Institute of Radio astronomy of NAS of Ukraine, URAN-4 observatory  
isaeva-ln@mail.ru

**ABSTRACT.** The substantial arguments of strong connection between shock wave speed and drift velocity of II type radio bursts in 25-180 MHz range are presented. The studied sample has included 112 proton events that were accompanied with coronal shock waves. To evaluate drift velocity and shock wave speed there was used original records of dynamic spectra from radio spectrograph in 25-180 MHz range. The velocities of shock waves were evaluated with the power mode model of solar corona density falloff.

**Keywords:** drift velocity, shock wave, II type radio bursts

### 1. Introduction

Urgency of the study of the shock waves is straight connected with the decision of the problem of the acceleration of solar cosmic rays (Tsap et al., 2012; Tsap et al., 2013). The most reliable indicator of the shock waves are II type radio bursts. It is known that for their generation is responsible the plasma mechanism of radio radiation (Cairns, et al., 2003). It is considered that meter range bursts of II type are connected with shock waves, appearing in flares (Wagner et al., 1983; Vrtnak et al., 1995), but bursts in decimeter-hectometer range are connected with propagation of the interplanetary shock waves, generated by CME (Classen et al., 2002; Gopalswamy et al., 1998).

Earlier in work (Galanin et al., 2015) it was shown that there is a fairly strong relationship between the drift velocity and shock wave speed calculated using Newkirk model (Newkirk, 1961). The Newkirk model is often used for finding of electron density in active area of the solar corona. However, Newkirk model has some restrictions. First, value of electron density when the height of the source  $R$  are equal to Sun radius Sun  $R = R_{\odot}$  cannot be more than  $1.7 \times 10^9 \text{ sm}^{-3}$ . Secondly, this model gives an averaged distribution of density for active area when distribution of density can greatly differ for miscellaneous events. The model with exponential density falloff, just allows finding distribution of density for each concrete event that allows obtaining the best coincidence to theoretical model with observations. In this connection we researched the relationship between the drift velocity and shock wave speed compute by means of exponential model of density falloff in solar corona.

### 2. Raw data, methods of the processing and results of the study

For study the relationship between the shock wave speed and drift velocity bursts of II type were used the original record dynamic spectrum, got on radio spectrograph SRS (Solar Radio Spectrograph) within the range of 25-180 MHz (<http://www.ngdc.noaa.gov/stp/space-weather/solar-data/solar-features/solar-radio/rstn-spectral/>) figure 1. An example of dynamic spectrum of the radio burst of II type of the event 31.05.2003 is showed on figure 1. As it is seen, it is possible to select two bands, corresponding to main and the second harmonica. They are enough well approximated by functions of the type (1) (the light lines on figure 1).

$$\log_{10} f_{ij} = -\gamma_j \cdot \log_{10} t_i + f_{0j} \quad \text{or} \quad f_{ij} = f_{0j} \cdot t_i^{-\gamma_j} \quad (1),$$

where  $t_i$  – time, corresponding to maximum intensity of the hits II type on frequency  $f_{ij}$ ,  $\gamma_j$  and  $f_{0j}$  – a coefficients to linear regression,  $i=1, 2 \dots n$  – a number counting out,  $j=1, 2$  – a number of the harmonica. The zero-point counting out time for all events corresponded to the beginning of the first harmonica on frequency 180 MHz.

The main frequency plasma radiation  $f_{i1}$  is proportional to electron density  $\sqrt{N_{i1}}$  (2).

$$f_{i1} = \sqrt{\frac{e^2 N_{i1}}{\pi m_e}} = 8.98 \cdot 10^{-3} \sqrt{N_{i1}} \text{ MГц} \quad (2)$$

So, using empirical dependence of the frequency from time  $f_i$  (1) and approaching model of coronal electron density  $N_i$  (3), it is possible to calculate the distance  $R_i$  (4) of the front of the shock wave.

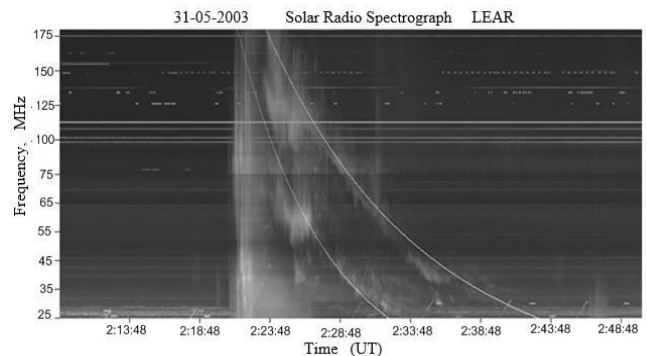


Figure 1: Dynamic spectrum of radio burst of II type of the proton event 31-05-2003

$$N_i = N_0 \cdot R_i^{-\delta}, \quad (3)$$

$$R_i = \frac{N_0}{N_i}^{\frac{1}{\delta}}, \quad (4)$$

where  $N_0$  and  $N_i$  – initial and the current values of electron density,  $R_i$  – a distance of the shock wave front in Sun corona at moment of time  $t_i$ ,  $\delta$  – a exponent of density falloff. From expression (4) it is seen that to define the distance  $R_i$  it is necessary to find  $\delta$ . Since for given moment of time  $t_i$  corresponds the definite value of the distance  $R_i$  and electron density  $N_i$ , then dependencies of density falloff  $N_0/N_i$  from distance and from time must be alike. From observations, is possible to find the dependence of the concentration falloff from time. So, knowing dependence of the frequency from time (1) from expression (2), it is possible to define the concentration  $N_i$  (5), and, consequently, the dependence of the concentrations falloff from time  $t_i$  (6).

$$N_i = \left( \frac{f_i}{0.898 \cdot 10^4} \right)^2, \quad (5)$$

$$\log_{10} N_i = -\beta \cdot \log_{10} t_i + N_0 \quad \text{or} \quad \frac{N_0}{N_i} = t_i^\beta, \quad (6)$$

where  $N_0$  and  $\beta$  – a coefficients to linear regression (6).

Using expression (4), as well as approximation of the distance  $R_i$  for event of the propagation the strong shock wave in ambience with exponential density falloff (Grechnev et. al., 2008) in the manner of

$$R_i = R_0 \cdot t_i^{\frac{2}{5-\delta}} = \frac{N_0}{N_i}^{\frac{1}{\delta}} \cdot h_0 \cdot t_i^{\frac{2}{5-\delta}},$$

it is possible to find  $\delta$ , where  $h_0$  – a scale of the distances in Sun corona. The Parameters  $\delta$ ,  $N_0$  and  $h_0$  are selected so as compute values of the concentration from time to the best advantage corresponded to observed values of the concentration, i.e.  $\frac{N_0}{N_i} = t_i^\beta$ . On figure 2 is shown dependence of the exponent of density falloff  $\delta$  from value of the exponent  $\beta$ .

Thereby to define the distance  $R_i$  and  $\delta$ , it is enough to know the dependence of the concentration falloff  $N_0/N_i$  from time  $t_i$ . Knowing  $\delta$  it is possible to find the distance

$R_i = R_0 \cdot t_i^{\frac{2}{5-\delta}}$  and to evaluate the velocity of the shock wave  $U_i$  at any time moment  $t_i$  (7). But knowing the dependence of the frequency  $f_i$  from time  $f_{ij} = f_{0j} \cdot t_i^{-\gamma_j}$  it is possible to define the drift velocity  $V_i$  (8).

$$U_i = \frac{R_{i+1} - R_i}{t_{i+1} - t_i}, \quad (7)$$

$$V_i = \frac{f_i - f_{i+1}}{t_{i+1} - t_i}. \quad (8)$$

To more exactly evaluate the relationship between of the shock wave speed  $U_i$  with the drift velocity  $V_i$ , were received dependencies  $U_i$  and  $V_i$  from time  $t_i$  in the manner of (9) and (10), accordingly.

$$\log_{10} U_i = v \cdot \log_{10} t_i + U_0 \quad \text{or} \quad U_i = U_0 \cdot t_i^v \quad (9)$$

$$\log_{10} V_i = \nu \cdot \log_{10} t_i + V_0 \quad \text{or} \quad V_i = V_0 \cdot t_i^\nu, \quad (10)$$

where  $U_0$ ,  $V_0$ ,  $v$  and  $\nu$  – a coefficients of linear regression,  $U_0$  and  $V_0$  – initial values of the shock wave speed and of the drift velocity,  $v$  and  $\nu$  – a exponents. Then, with exponents  $v$  and  $\nu$ , it is possible to judge about change of the

drift velocity and of the shock wave speed in the course of time in frequency range 25-180 MHz for all 112 proton events. Result of our study is presented on figures 3 and 4.

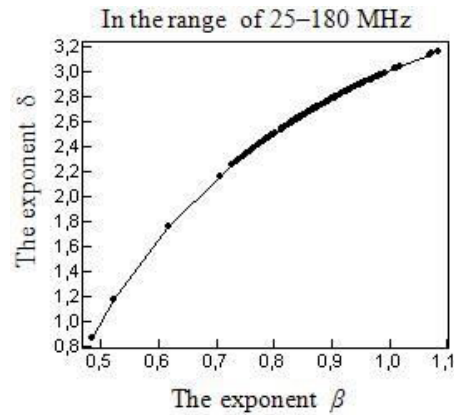


Figure 2: Relationship between  $\delta$  and  $\beta$  in exponential model of the density falloff

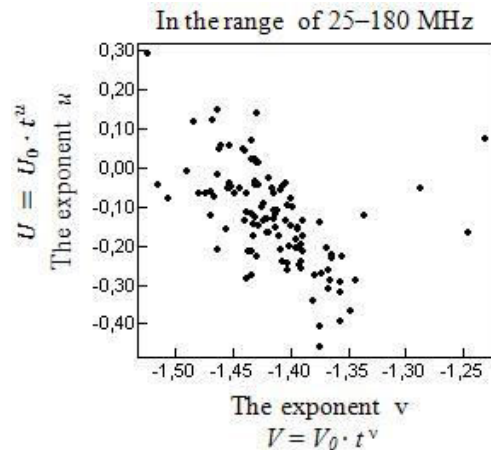


Figure 3: The relationship between the speed of the shock wave and the drift velocity in Newkirk model

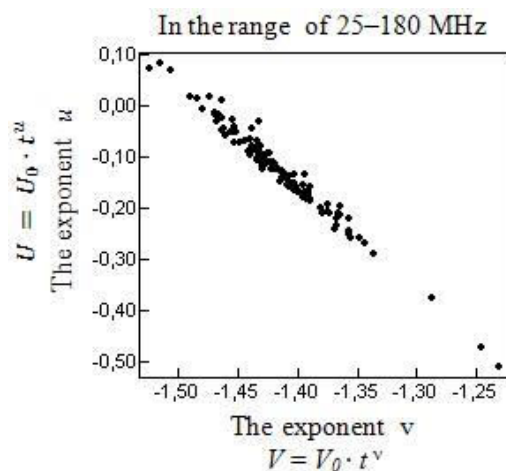


Figure 4: The relationship between the speed of the shock wave and the drift velocity in exponential model. On X axis is the exponent of falloff of the drift velocity  $\nu$ , on Y axis is the exponent of falloff of the shock wave speed  $v$

On figure 3 and figure 4 is shown the relationship between of the drift velocity and of the shock wave speed for Newkirk model and exponent model of the density falloff, accordingly. On X axis there is the exponent of the falloff of drift velocity, but on Y axis there is the exponent of the falloff of the shock wave speed. Figure 4 shows that there is a sufficiently strong relation between the shock speed  $U_i$  and the drift velocity  $V_i$  in exponential model of the density falloff. However relationship of velocity of the shock wave  $U_i$  at the drift velocity  $V_i$  in Newkirk model vastly worse figure 3. This is connected with that that Newkirk model gives averaged distribution of density in active area. While distribution of density can vastly differ from one event to another.

### Conclutions

Comparative analysis showed that there is a fairly strong relationship between the drift velocity and the speed of the shock wave in the range of 25-180 MHz.

### References

- Cairns I.H. et al.: 2003, *Space Sci. Rev.*, **107**, 27.  
Classen H.T et al.: 2002, *A&A*, **384**, 1098.  
Galanin V.V. et al.: 2015, *OAP*, **28**, 256.  
Gopalswamy N. et al.: 1998, *J. Geophys. Res.*, **103**, 307.  
Grechnev V.V. et. al.: 2008, *Solar Phys.*, **253**, 263.  
Newkirk G.: 1961, *Astrophys. J.*, **133**, 983.  
Tsap Yu.T. et al.: 2012, *G&A*, **52/7**, 921.  
Tsap Yu.T. et al.: 2013, *Cosmic Reseach*, **51/2**, 108.  
Vrsnak B. et al.: 1995, *Solar Phys.*, **158**, 331.  
Wagner W.J. et al.: 1983, *A&A*, **120**, 136.

DOI: <http://dx.doi.org/10.18524/1810-4215.2016.29.85213>

## TOOLS AND METHODS OF LOW-FREQUENCY RADIO RECOMBINATION LINES INVESTIGATIONS

A.A.Konovalenko, S.V.Stepkin, D.V.Mukha, E.V.Vasilkovskiy

Institute of Radio Astronomy of the National Academy of Sciences of Ukraine, 4, Mystetstv St., 61002, Kharkiv, Ukraine, [vasylkivskiy@mail.ua](mailto:vasylkivskiy@mail.ua)

**ABSTRACT.** In the report the tools and methods of observations of radio recombination lines which are carried out at Institute of Radio Astronomy of the National Academy of Sciences of Ukraine using the world's largest decameter radio telescope UTR-2 (arrays "South – North" and "East – West") are described. The low-frequency radio recombination lines can be used as effective means of the low-density partially ionized interstellar medium diagnostic. However, low intensities of the lines and high level of interferences makes such investigations very difficult and impose high requirements to equipment. Observations are carried out with the 4096-channel digital correlometer and new generation digital spectral processors with 8192 spectral channels. Currently, the systematic observations of radio recombination lines have been carried out in the directions of remnants of supernova stars, Galactic plane, nebulas and dust clouds. Experiments aimed to finding the redshifted line of neutral hydrogen HI which arises in the cosmological epochs of reionization in the range 8 – 32 MHz are carried out. The carbon radio recombination lines have been detected in the direction of Cassiopeia A in the broad range of frequencies from 20 to 32 MHz. The carbon radio recombination line, corresponding to the transitions to atomic level with number of 1009 (these corresponds to the Bohr size of atom near 0,1 mm) have been registered.

**Keywords:** Radio recombination lines: UTR-2 radio telescope: spectral equipment: data processing

### 1. Introduction

Radio recombination lines (RRLs) are produced by transitions of recombining electrons between two atom levels in ionized gas. Their frequencies can be calculated using Rydberg's formula:

$$\nu_n = cZ^2R \left( 1 - \frac{m_e}{M_a} \right) \left( \frac{1}{n^2} - \frac{1}{(n + \Delta n)^2} \right), \quad (1)$$

where  $c$  is speed of light,  $Z$  is the nuclear charge of the ion,  $R$  is the Rydberg constant for the taken species,  $m_e$  and  $M_a$  are electron and nuclear mass,  $n$  and  $\Delta n$  are principal quantum number and its change respectively.

The possibility of the RRLs observations was predicted by Kardashev in 1959. They were detected in 1963-1964 by Sorochenko and Borodzich at 8.9 GHz ( $n = 90$ ) and by

Dravskikh and Dravskikh at 5.7 GHz ( $n = 104$ ). A lot of high frequency RRLs has been observed towards classical hot HII regions. Also, for example, they have been detected in planetary nebulae, external galaxies, and in some circumstellar envelopes (Gordon & Sorochenko, 2002).

### 2. Detection of RRLs at Extremely Low Frequencies

The first detection of carbon RRLs was made at high frequencies. After that they were observed in the directions of a number of HII regions simultaneously with corresponding  $H\alpha$  lines. As follow from the atomic physics the mechanism of the carbon line formation is similar to that of hydrogen lines.

RRLs of high-excited interstellar carbon atoms opened in decameter range by means of radio telescope UTR-2 about 40 years ago gave a new method of cold partially-ionized plasma diagnostic. High-precision determination of fundamental parameters of the medium – temperature, density, pressure, ionization rate, movements, mechanisms of ionization and recombination and other became possible (Konovalenko & Sodin, 1980; Konovalenko & Sodin, 1981). Detection of largest bound Rydberg atoms states up to levels of the main quantum numbers 1009 in the range 10-30 MHz is important not only for an astrophysics, but also for physical science as a whole (Stepkin et al., 2007).

### 3. Equipment for Low-Frequency Radio Spectroscopic Observations

The radio telescope UTR-2, the world's biggest decameter wavelengths radio telescope (situated near Kharkiv, Ukraine), remains to the most efficient for radio spectroscopy investigations owing to a set of its merit (Braude et al., 1978). UTR-2 is a T-shaped antenna which consists of 2040 "fat" dipoles. It has an effective area of about  $140000 m^2$ , the angular resolution is high for a telescope of the decameter range ( $\sim 30'$  at 25 MHz). The telescope has an electronic beam steering which can track up to  $\pm 70^\circ$  from zenith.

#### 3.1. Digital autocorrelometer

Spectral lines at decameter range have very low relative power  $s = \Delta\nu \times \Delta T_L / T_C \sim 0.1 s^{-1}$ . It creates certain difficulties for their search and research. The strictest requirements



Figure 1: Appearance of 4096-channel autocorrelometer which used at observations in UTR-2

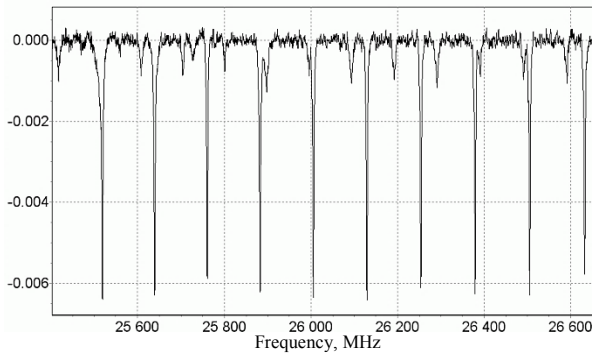


Figure 2: Spectrum obtained in the direction of Cas A with UTR-2 using autocorrelometer

are imposed to sensitivity of the radio spectrometer (not worse than 0.01%) in case of very big time of averaging. In this connection it is most suitable spectrum analyzer based on the digital sign correlometer, wherein the correlation function is determined first and then the power spectral density is determined by it. Similar multi-channel analyzers possess high stability of the operation peculiar to single-channel devices, in case of almost unlimited time of observations. Differing in simplicity of the construction connected to extremely small number of levels of quantization, such analyzers are very safe and easy-to-work. Bulky operations of Fourier transform can be executed once at the end of observations. Now on observatory of UTR-2 it is used 4096-channel correlometer (see Figure 1).

Figure 2 shows the resulting spectrum measured in the direction of Cassiopeia A (Cas A) in the frequency band around 26 MHz with UTR-2 and 4096-channel autocorrelometer, integration time is 504 hours.

### 3.2. Digital spectral processors

In recent years with the progress of digital and computer technologies made possible the creation and application of multi-bit wide-band digital receivers (Konovalenko et al., 2016). Figure 3 shows control center of UTR-2 observatory, DSPZ-receivers (Digital Spectro-Polarimeter Z-type) are assembled within standard desktop PC cases.

The digital receiver can operate in three qualitatively different regimes: waveform, full power and correlation mode. The modes are mutually exclusive. For radio spectroscopic observations correlation mode is typically used. In this mode two input signals are converted into a single output, the value of coherence between the two input signals (Ryabov et al., 2010).



Figure 3: The UTR-2 control center with new-generation back-end facilities

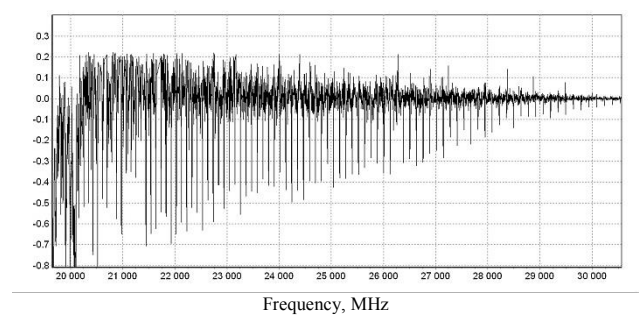


Figure 4: Carbon RRLs towards Cas A measured with the North-south arm of the UTR-2 array (using DSPZ)

Figure 4 shows the spectrum measures at UTR-2 using DSPZ in the direction of Cas A in the range 20-30 MHz. Clearly visible absorption lines in a series of about 100.

## 4. Methodology of Data Processing and Interpretation

After the observations were carried out observational data must be properly processed for their subsequent interpretation.

### 4.1. Doppler shift determination

The only ultimate criterion of the natural origin of the spectral lines in the decameter range is determination of Doppler shift of the spectral line frequency due to the orbital rotation of the Earth:

$$f = f_0 \left( 1 - \frac{v_x}{c} \right), \quad (2)$$

where  $f$  is observed frequency,  $f_0$  is the central frequency of generation,  $c$  is speed of light, and  $v_x$  is the speed of the line of sight.

If the source of monochromatic radiation is a subject that is far enough away from the Sun, the frequency of the line will change due to periodic changes in the Earth's velocity component directed to the object, due to the annual motion of the Earth around the Sun. This criterion is often used in radio astronomy for observations of pulsars and spectral lines. The maximum value of the Doppler shift plays the pipe in the directions lying in the plane of the ecliptic. At a frequency of 25 MHz, the assumption of a circular orbit

Earth at a linear speed of about  $\sim 30$  km/s causing maximum velocity differences (frequency) at times separated by an interval of 6 months, is 5.8 kHz.

#### 4.2. Interference reduction

Usually spectroscopic observations at UTR-2 are carried out using four minute frames, which are stored in computer.

In order to remove hindering signal from processed spectrum we subtract from measured autocorrelation function a model of interference. It described by

$$R[i] = \frac{2A}{r_1} \exp\left[-\sqrt{\frac{i\pi\Delta f}{(2\ln 2)^2 f_d}}\right] \cos\left(2\pi(f_0 - f)\frac{i-1}{f_d}\right), \quad (3)$$

where  $R[i]$  is the autocorrelation function of hindering signal,  $A$  is the amplitude of hindering signal,  $r_1$  is the autocorrelation function point number,  $\Delta f$  is the bandwidth of hindering signal,  $f_d$  and  $f_0$  are the sampling frequency and the frequency of the local oscillator respectively.

#### 5. Experiment to Detect 21-cm Cosmological Line Using UTR-2

The great interest in the scientific world is caused by radio astronomical investigations of physical processes taken place in the distant cosmological epochs. At least three distant epochs have been identified which have corresponding spectral windows for the redshifted HI signal (Peters et al., 2011):

1. The Dark Ages:  $100 < z < 30$  ( $15$  MHz  $< \nu < 50$  MHz);
2. First star formation:  $30 < z < 15$  ( $50$  MHz  $< \nu < 90$  MHz);
3. Epoch of Reionization:  $15 < z < 7$  ( $90$  MHz  $< \nu < 200$  MHz).

For the use of the radio telescope UTR-2 and new generation radio telescope GURT (Konovalenko et al., 2016) these epochs are of particular interest.

Observations began to be conducted from January 2015. Search the spectral lines in the observational data obtained during the daytime, it is possible only on relatively narrow frequency band. The different interfering signals will not only pose a significant challenge to detect this effect, but also RRLs arising in the interstellar medium in our epoch.

#### 6. Conclusions

Observations of low-frequency RRLs are promising means of the tenuous ISM diagnostics. Improvement of the existing low-frequency radio telescopes, spectral analyzers and methods of observation as well as the creation of new tools will open new opportunities in space plasma spectroscopy. Long-term successful observations with Ukrainian radio telescope UTR-2 gave new information about fundamental properties of the interstellar medium. Presently investigations of low-frequency RRLs with UTR-2 are continuing for many galactic objects and data processing is progressing. It is clear that RRLs studies will be important part of the scientific programs of new generation and future giant low-frequency instruments such as GURT, LOFAR, SKA, LRA.

#### References

- Gordon M.A., Sorochenko R.A.: 2002, Kluwer.  
 Konovalenko A.A., Sodin L.G.: 1980, *Nature*, **283**, 360.  
 Konovalenko A.A., Sodin L.G.: 1981, *Nature*, **294**, 135.  
 Stepkin S.V. et al.: 2007, *MNRAS*, **374**, 852.  
 Braude S.Ya. et al.: 1978, *Ap&SS*, **54**, 3.  
 Ryabov V.B. et al.: 2010, *A&A*, **510**, 16.  
 Konovalenko A.A. et al.: 2016, *ExA*, **42**, 11.  
 Peters W.M. et al.: 2011, *A&A*, **525**, 7.

DOI: <http://dx.doi.org/10.18524/1810-4215.2016.29.85214>

# THE CURRENT STATE OF DATA TRANSMISSION CHANNELS FROM PUSHCHINO TO MOSCOW AND PERSPECTIVES

D.V. Dumsky<sup>1,2</sup>, E.A. Isaev<sup>1,2</sup>, V.A. Samodurov<sup>1,2</sup>, M.V. Shatskaya<sup>3</sup>

<sup>1</sup> National research university Higher school of economics,  
Moscow, 101000, Russia

<sup>2</sup> Pushchino Radio Astronomy Observatory ASC LPI,  
Pushchino, Moscow Region, 142290, Russia

<sup>3</sup> P.N. Lebedev Physical Institute, RAS,  
53 Leninskiy Prospekt, Moscow, 119991, Russia

**ABSTRACT.** Since the work of a unique space radio telescope in the international VLBI project "Radioastron" extended to 2017 the transmission and storage of large volumes of scientific and telemetry data obtained during the experiments is still remains actual. This project is carried out by the Astro Space Center of Lebedev Physical Institute in Moscow, Russia. It requires us to maintain in operating state the high-speed link to merge into a single LAN buffer data center in Pushchino and scientific information center in Moscow. Still relevant the channel equipment monitoring system, and storage systems, as well as the timely replacement of hardware and software upgrades, backups, and documentation of the network infrastructure.

**Keywords:** Radioastron: monitoring: telecommunications.

## 1. Introduction

The spacecraft radiotelescope ground support is carried out by tracking stations. One of which is located in the Pushchino Radioastronomical Observatory. The dataflow of scientific data and telemetry information received by servers of tracking station can reach 128 Mbit/s speed. The direct communication channel witch capacity of 1 Gbit/s established for efficient data exchange. The buffer data-center created for network communication and file storage accomodation. The reliability of the channel (Fig. 1) is highly dependent on continuous monitoring of network and server equipment and communication lines. An important prerequisite for the smooth operation of the channel and the equipment to minimize downtime is monitoring 24x7x365. Monitoring involves the collection of system messages, access control, telemetry of network devices, availability of power and power consumption, temperature control in the equipment rack, as well as information about changes in the network traffic.

## 2. Monitoring system

As the monitoring system we still use well-proven over several years Zabbix system which provides availability and SLA reporting, collection of any data and great graphs and network maps. Zabbix is updated now to version 3.2, which has improved functionality and increased performance when working with a database for storing the changes history in various parameters of the "Radioastron" transmission channel equipment and servers.

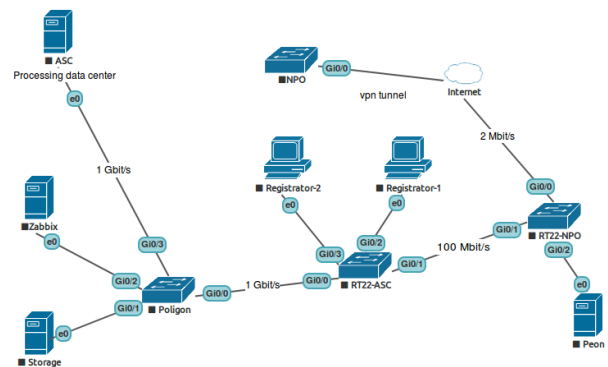


Figure 1: Radioastron data channells.

This monitoring system collects data on the performance and availability of servers, LAN and polls active network equipment by snmp. The monitoring system is installed on two servers, one of which is the virtual - is itself Zabbix server, database Postgress and Lighttpd web server. Zabbix proxy server with database Sqlite is installed on a dedicated physical server It aggregates monitoring data collected from the network equipment via SNMP and ICMP protocols. Zabbix uses postgress 9.5 database to store the history of events and

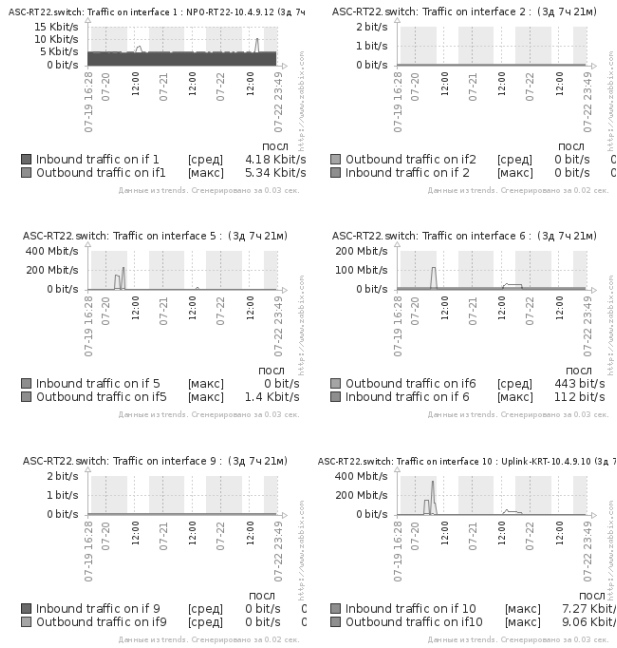


Figure 2: Graphs of channel loading.

data for graphs construction of the changing parameters. Every monitoring systems settings are made via web-interface. Monitoring system collects information about the status of the main switch interfaces, loading them (Fig. 2) and the resulting errors.

Zabbix agent is installed on the buffer storage server and sends data about status and utilization of its resources such as filling of hard disks space, as well as the status of the disks themselves, memory and cpu usage, cpu temperature (Fig. 3). Part of the equipment is monitored using the icmp ping and simple checks to identify delays and packet loss in data transmission channel. And the main features of monitoring system is alerts engineers when a fault occurs and storage of events history in DB.

### 3. Conclusion

The work of unique Russian space radio observatory in international space VLBI project "RadioAstron" extended until the end of 2017. Therefore, management and monitoring of communication channels between the tracking station in Pushchino and treatment centers in Moscow for the transmission of scientific and telemetry data is still relevant and necessary. The reliability of communication channels is highly dependent from continuous monitoring and scheduled maintenance of network, server equipment and optical communication lines.

Failsafe operation of the communication channel is especially relevant for the space telescope. For example, uninterrupted reception of telemetry data allows specialists to take further decisions on the correction

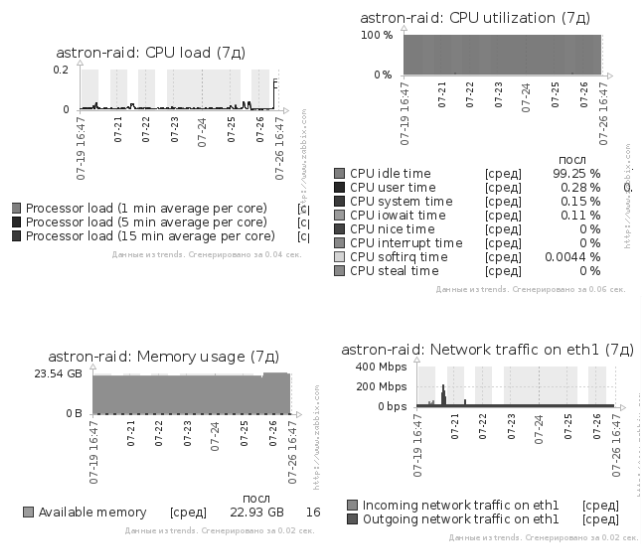


Figure 3: Graphs of storage server cpu, memory and network interface usage.

of its orbit and receive important information about the performance of the onboard equipment. The success of the scientific experiments directly related to the reliability of the transmission of scientific data. This requires solutions that can automatically detect and respond to threats and channel performance issues in real time, as well as predict possible issues in the future. Monitoring system gives us the opportunity to have the right information about data transmission at the right time.

The average data rate of the channel is typically 300-400 Gbit/s. Every day about 50 to 300 GB of unique information about the structure and evolution of various astrophysical objects (quasars, pulsars and black holes) is transmitted through the channel. The same amount of data backed up in the PRAO ASC LPI buffer data storage. The project plans to connect the new link speed 10 Tbit/s to reduce the transmission time. And we are currently performing the new channel testing and selection of appropriate equipment. The 1 Gbit/s old channel, we plan to use as a backup in the future.

The monitoring system over the past two years, allows us quickly resolved emergency situations caused by the power failure and failures of the network equipment, and cooling system of the buffer data center, as well as identify the causes of failures of channel associated with the failure of the individual switching devices and optical modules. We were promptly detected and eliminated two cases of the optical lines damage, allowing to minimize the idle time of the channel work. Monitoring of disks in buffer storage allows us for timely replacement of failed drives, that would prevent the destruction of RAID-array and prevent permanent loss of scientific data.

## SUN AND SOLAR SYSTEM

DOI: <http://dx.doi.org/10.18524/1810-4215.2016.29.85220>

## CYCLES AND ANTI-CYCLES OF SOLAR ACTIVITY

M.I. Ryabov

Odessa observatory «URAN-4» Institute of Radioastronomy NASU, [ryabov-uran@ukr.net](mailto:ryabov-uran@ukr.net)

**ABSTRACT.** Currently representation of solar cycles on average monthly data and smoothed values on various indexes from the full solar disk is generally accepted. Such representation creates an illusion of monotone change and perceptions of simultaneity of manifestations of solar activity for all solar disc. At the same time, daily monitoring data reveal the presence of discrete properties of manifestations of solar cycle. They are associated with absence of spots on the Sun in the northern and southern hemispheres at different intervals. This phenomenon is defined as anti-cycle of solar activity. Properties of discreteness of anti-cycles are presented in this paper on "spotless days' periods". On their basis the appropriate monthly and annual data was received. The basic characteristics of the manifestations of the discreteness of activity anti-cycles had been determined. It noted the «switch effect» of the existence of the solar dynamo. It manifests itself in the rapid transition from a regime of «spotless days» to the regime of continuous generation.

### 1. Introduction

The representation of the solar cycles is limited by the data of monthly values of various indexes and their annual smoothed values. On their basis, all the main indicators of the solar cycle (data minimuma, phase rise to maximum, data maximuma, phase decline to minimum and data minimuma next cycle) (Hathaway, 2010). These data make an impression of continuity of the action of the solar dynamo for generating the magnetic fields which define the appearance of sunspots. This is clearly seen in the current views of the solar cycle (<http://www.swpc.noaa.gov/products/solar-cycle-progression>).

More significant is the physical examination of the data of daily observations  $W$  index and the average monthly of sunspot groups of indexes –  $S_p$  showing the discrete nature of the manifestation of the solar cycle (Fig.1) and the difference between the northern and southern hemispheres (Fig. 2).

Using Fourier filtering and wavelet analysis allows obtaining reliable data about the existence of maximums of solar cycles and all periods of their manifestations. Cycle maximums, their amplitudes and the period sets which form the activity cycle are different for the northern and southern hemispheres (Ryabov, 2013).

Thus the problem of asymmetry N-S manifestation of the solar cycle can be solved on the basis of separate consideration of the activity of the northern and southern hemispheres of the Sun, taking into account the

discreteness manifestations activity. Consider the observational basis for such an approach (Ryabov, 2015).

### 2. Observational data of anti- cycles activity

Discrete properties are determined by the presence of the intermittent nature of the appearance and disappearance of groups of spots, which appear in all phases of the solar cycle. Periods of spots presence on the disk form the solar activity cycle.

Periods of absence of sunspots groups can be defined as the existence of "anti-cycle" activity. The basic properties of the "anti-cycle" are defined according to the «spotless days» obtained in this work for the entire set of observations of sunspots areas of the Northern and Southern hemispheres for the period of 12-24 activity cycles.

The data in the form of «spotless days» for each year is given for the entire solar disk (<http://www.spaceweather.com>). This view is not quite correct because it does not take into account the difference in the formation of the activity of the northern and southern hemispheres of the Sun.

We have determined the annual and monthly indexes which characterize the properties of the "anti-cycles" of activity of the Northern and Southern hemispheres. It is defined as the ratio of the number of «spotless days» to the total duration of a year or a month in percentage.

Thus the value '100' (upper graph scale) indicates the complete absence of spots in the time interval of a month or a year. A value of zero means the permanent presence of spot groups in the northern or southern hemispheres. Intermediate values show the interval of time "off" of solar dynamo for generating sunspots.

In this representation, the discreteness index doesn't contain any errors because the intervals of spot absence are determined in an obvious way. Dynamics of 12-24 "anti-cycle" of the solar activity for the annual and monthly values is shown in Fig. 3-4.

At minimuma 19 cycle (1964 year) of the Northern hemisphere anti-cycle showed a quick transition from the complete absence of spots (100%) to their continued existence (0%). At the same time the southern hemisphere anti-cycle demonstrates the quasi-periodic changes in the duration of time intervals of absence of sunspots range of 20-60% (Fig. 5).

In the decay phase of cycle 19 (1962 year), the anti-cycle of the Northern hemisphere demonstrates continued rise of activity from 80% to 0% (June).

Condition of low activity to 80% Northern hemisphere again comes in two months.

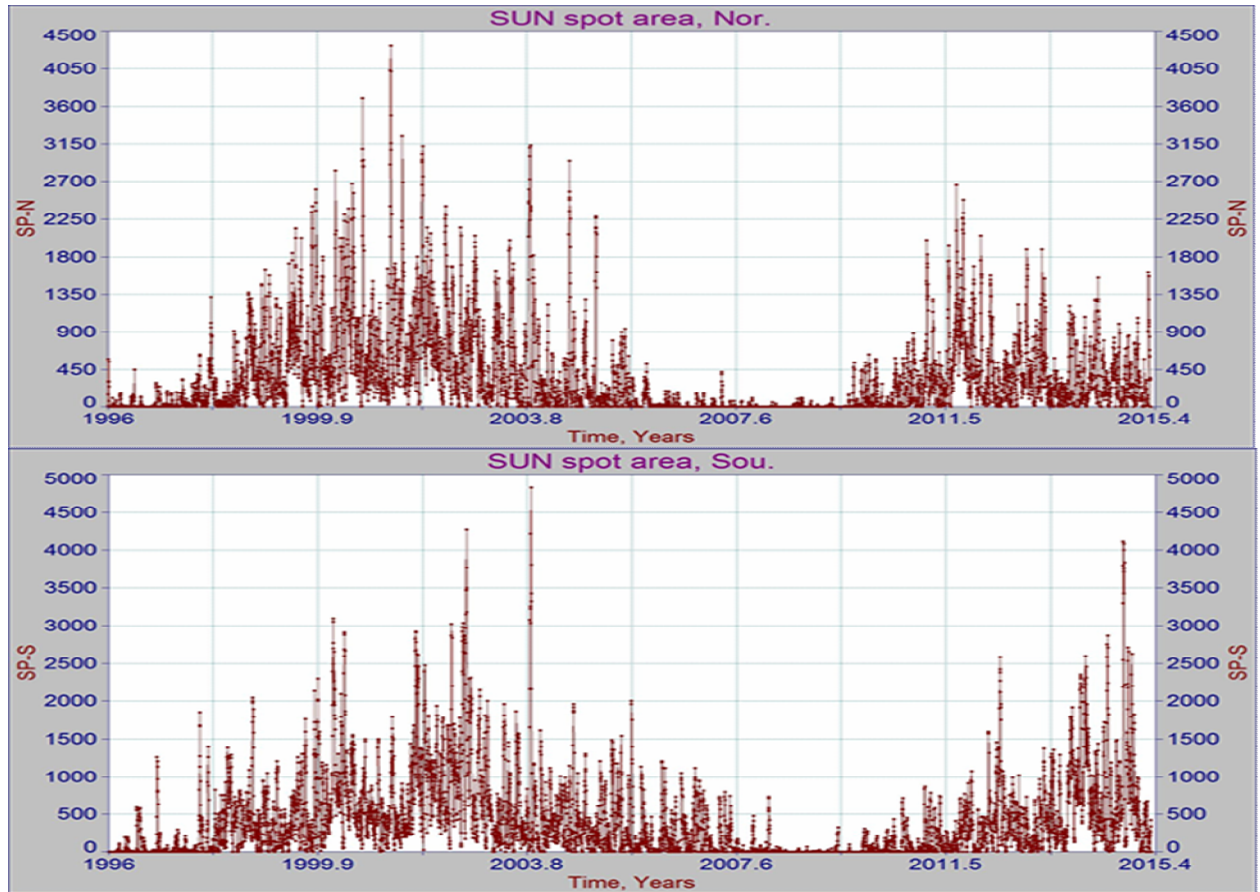


Figure 1: Daily values of the total area of sunspot groups- Sp of 23-24 cycles for the northern and southern hemispheres of the Sun.

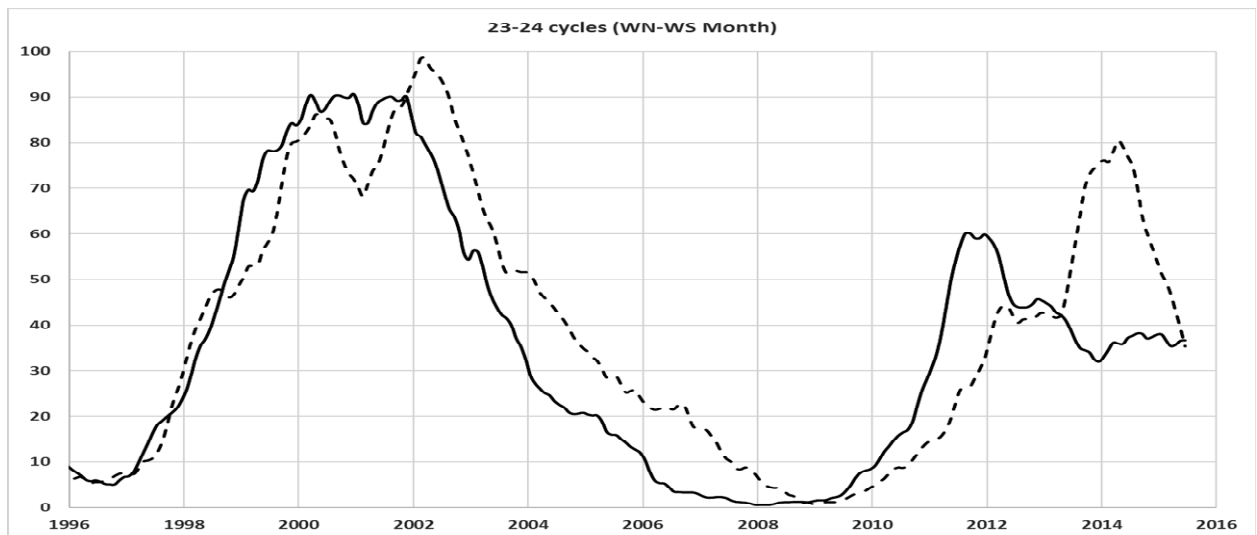


Figure 2: The average monthly Wolf number for 23-24 North and South solar cycles.

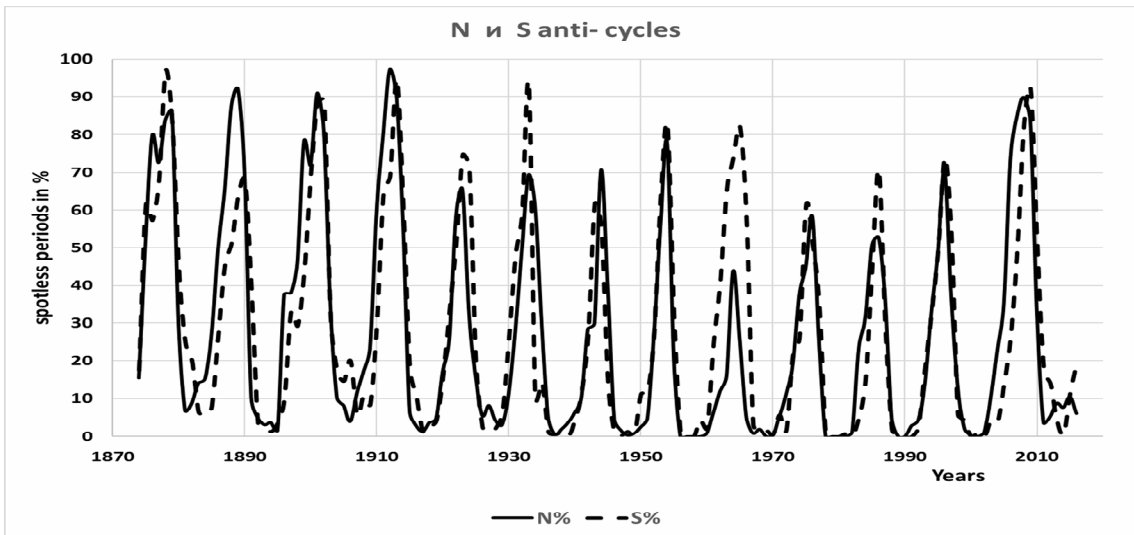


Figure 3: The annual index changes of discreteness of "anti-cycles" of the Northern and Southern hemispheres of the Sun.

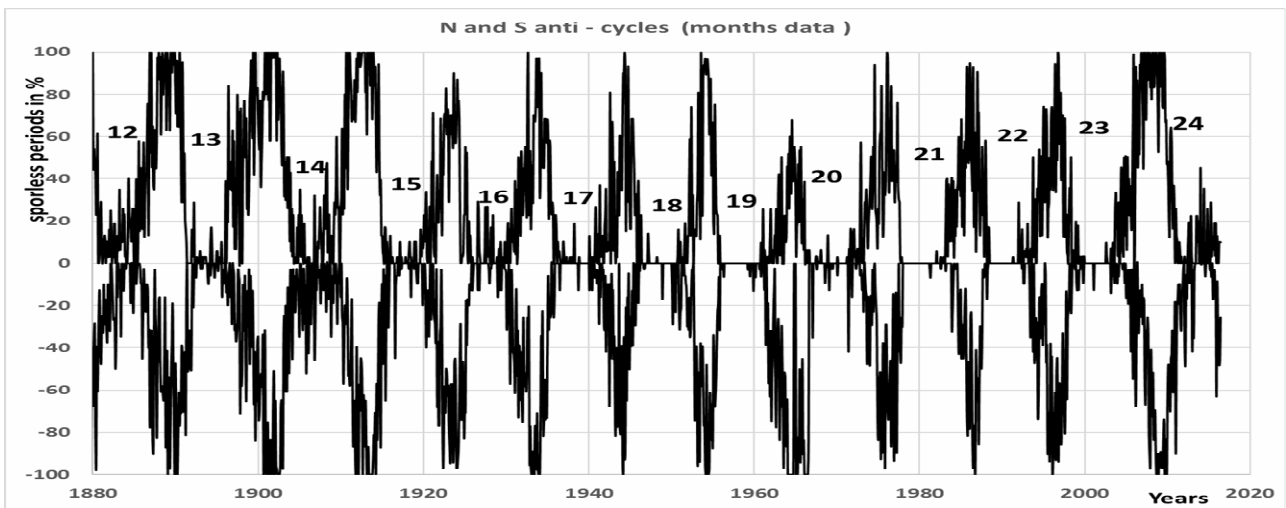


Figure 4: Monthly changes in the discreteness index of "anti-cycles" of the Northern and Southern hemispheres of the Sun (For the data separation the discrete index of the southern hemisphere is indicated with conditional negative values).

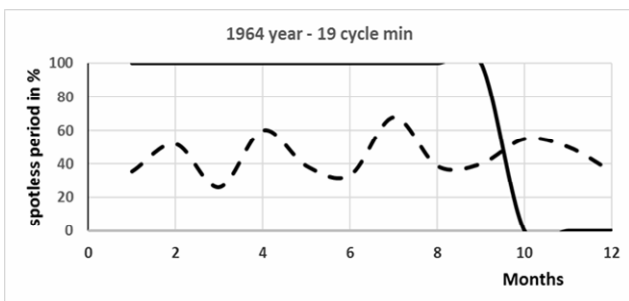


Figure 5: Anti-cycles Northern and Southern solar activity in 1964 years (19 cycle).

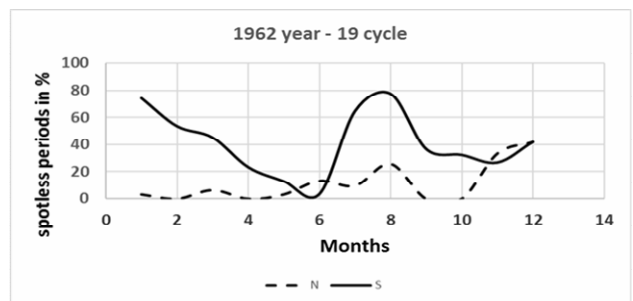


Figure 6: Anti-cycles Northern and Southern solar activity in 1962 years (19 cycle – decline to minimum).

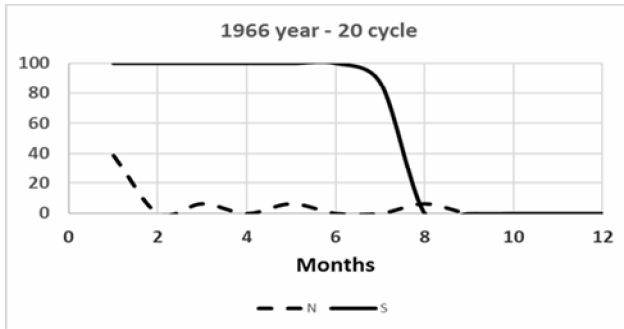


Figure 7: Anti-cycles Northern and Southern solar activity in 1966 years (20 cycle – rise to maximum)

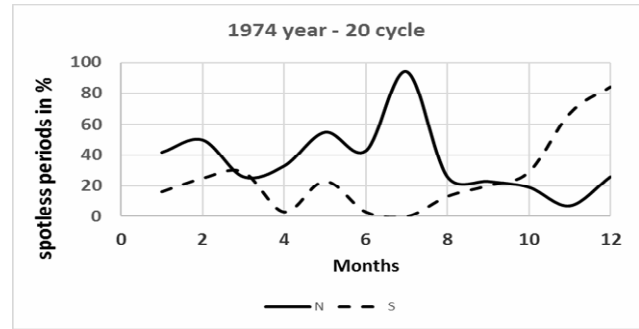


Figure 8: Anti-cycles Northern and Southern solar activity in 1974 years (20 cycle – decline to minimum)

At the same time the anti-cycle of the Southern Hemisphere showing minor deviations from the mode of existence of permanent exist sunspots (0% level) (Fig. 6).

Changes to the anti-cycles of the northern and southern hemispheres of the Sun in some years and in different phases of the solar cycle. Demonstrates manifestation «switch effect» in the solar dynamo. It manifests itself in the rapid transition from a regime of prolonged absence of sunspots to the regime of continuous generation (Fig. 5, Fig. 7).

In the rise phase of the cycle 20 (1966 year) anti-cycles of the Northern and Southern hemispheres show the same ratio as their activity in 1962 year (minimum 19 cycle) (Fig. 7).

Condition activity Northern and Southern hemispheres of the Sun during the decline to minimum 20 cycle activity (1974 years) varied widely from month to month.

However, the Southern hemisphere there has also been more active and showed no correlation with the activity of the Northern hemisphere (Fig. 8).

### 3. Conclusion

On the basis of the obtained results on presentation of the discreteness index of "anti-cycles" of the northern and southern hemispheres of the Sun a number of definite conclusions can be done.

According to the annual index values there are significant differences in the dynamics of the "anti-cycles"

in different hemispheres, including the value of the amplitude and time of the beginning and the end. And for the weaker cycles the activity duration in maximum is short.

Particular interest is the 19<sup>th</sup> cycle in which the maximum activity is provided by the abnormally high activity of the northern hemisphere. While the southern hemisphere sharply reduced its activity forming an intense and long-lasting "anti-cycle".

According to the monthly values of discrete indexes we can see that the change of sunspot regime happens within one month. During this time a complete disappearance may happen, and then the sudden appearance of groups of alternate spots in the northern and southern hemispheres.

Thus the discrete index of anti-cycles of the northern and southern hemispheres shows interesting features that are important in understanding the operation of the solar dynamo. In the continuation of this work by means of wavelet analysis the main periods of forming an "anti-cycle" of the solar activity will be identified.

### References

- Hathaway David H.: 2010, *Living Rev. Solar Phys.*, **7**, 1.  
 Ryabov M.I. et al.: 2013, *Odessa Astron. Publ.*, **26**, 276.  
 Ryabov M.I.: 2015, *Geomagnetism and Aeronomy*, **55**, 1089.

DOI: <http://dx.doi.org/10.18524/1810-4215.2016.29.85223>

## THE DECADE-LONG INSTABILITIES IN EARTH'S ROTATION AS EVIDENCE OF LITHOSPHERIC DRIFT OVER THE ASTENOSPHERE

N. S. Sidorenkov

Hydrometcenter of the Russia, Moscow, [sidorenkov@mecom.ru](mailto:sidorenkov@mecom.ru)

**ABSTRACT.** The decade instabilities in Earth's rotation (DIER) are usually explained by the interactions of the Earth's core and mantle. This hypothesis explains well a close correlation between DIER and the variations in the rate of the westward drift of the geomagnetic eccentric dipole; it corresponds quite reasonably to the possible redistribution of the angular momentum between the fluid core and the mantle of the Earth. However, the hypothesis can not explain the close correlations of DIER with the observable variations in the masses of the Antarctic and Greenland ice sheets, with the decade oscillations of the types of synoptic processes (the epochs of the atmospheric circulation), with the anomalies of the global temperature, regional anomalies of the cloudiness, precipitation, and other climatic characteristics.

It is supposed that the DIER are the fluctuations of the velocity of the lithosphere driftage along the asthenosphere. The sliding of the lithosphere over the asthenosphere is possible due to of the vibratory displacement mechanism by tidal forces. The consequences following from this hypothesis are discussed.

**Keywords:** Decade fluctuation in Earth's rotation, drift of lithosphere, plate tectonics.

### 1. Hypothesis

It is well known that seasonal variations in the Earth's rotation are determined by the redistribution of the angular momentum between the atmosphere and the Earth. When the moment of the atmosphere is increasing then the moment of the Earth is decreasing and vice versa. This regularity is well seen on Figure 7.10 (Sidorenkov, 2009) where the time series of the angular momentum of the atmosphere is compared with the time series of the angular momentum of the Earth taken with the opposite sign. Thus, the no tidal irregularities of the Earth rotation are mainly due to the exchange between the angular momentum of the solid lithosphere and its fluid environment – the atmosphere and the hydrosphere. This exchange occurs due to the moments of the frictional forces and pressure forces pushing on mountain ranges.

Special Bureau for the Atmosphere carries out the monitoring of the exchange of the angular momentum by both the momentum approach (that is, by the evaluation of the effective functions of the atmospheric and oceanic

angular momentum), and the torque approach (that is, the evaluations of the torque resulting from the wind and current stresses and pressures).

Calculations of the friction and pressure momentum forces are performed for the entire Earth surface as a whole. However, the lithosphere is cracked on a set of the lithosphere plates. The atmosphere and ocean are acting on the lithosphere plates, and only then is this action transmitted to the Earth. What is the result of the atmospheric action on the lithosphere plates? Let us recall that under the lithosphere, there is a layer of the lower viscosity – the asthenosphere in which the lithosphere plates are capable to float. Continents are frozen into the oceanic plates, and they may passively move with them (Trubitsyn and Rykov, 1998; Trubitsyn, 2000). The lithosphere plates float in the asthenospheric substratum. On the decade time scale, the lithosphere plates can move in the horizontal direction under the effect the friction and pressure (acting on mountain ranges) forces. The plates are in motion under the action of the friction stresses and pressure, which the atmosphere and ocean produce on the exterior surface of the plate. The viscous cohesive force with the asthenosphere on the soles and faces of the plates decelerates their movement, but the exterior forces overcome this resistance. Therefore, when calculating the torque, it is necessary to carry out the integration not only for the entire Earth surface but also separately for every lithosphere plate. The moment of forces affecting on an individual plate determines the vector of the movement of the plate (Sidorenkov, 2009).

### 2. Evidence

A good example of this is the situation in the Drake Passage. Strong westerly winds dominate in the 40\_S – 50\_S. They generate the powerful Antarctic Circumpolar Current (ACC) in the Southern Ocean. The South America, the Antarctic Peninsula, and the underwater lithosphere present a barrier for ACC. Westerly atmospheric winds and oceanic currents have replaced this barrier downstream and have shifted this lithosphere bridge to the east by 1500 km. This process resulted in the formation of the Scotia Sea (the South-Antilles hollow). It is bordered along the perimeter by the remains of the lithosphere bridge in the form of the South-Antilles ridge and numerous islands, the arc of the South Sandwich Islands being the principal of them. This ridge, at the drifting in the

eastward stream, has crumpled the oceanic lithosphere and has formed the deep South-Sandwich trench.

Let us present one more piece of evidence for the benefit of our hypothesis. The atmospheric circulation has a remarkable feature: at the latitudes of 35\_N and 35\_S, the wind direction alters to the opposite one. Easterly winds predominate in the tropical belt between these latitudes, and westerly winds in the moderate and high latitudes. According to this, the stresses of friction on the surface of the lithosphere are directed to the opposite sides. Therefore, the maximum stress in the lithosphere should concentrate near the latitudes of 35\_N and 35\_S. These bands should exhibit an increased seismic and tectonic activity. Really, in the Northern Hemisphere, in this band, continuous mountain ranges are extending through the Mediterranean Sea, Middle East, Iran, Pamir, Tibet, Japan and USA. Here, Earthquakes and eruptions of volcanoes occur most frequently. In the Southern Hemisphere, the band of the sign change in wind direction is located over the World Ocean. Therefore, the seismic and tectonic processes do not manifest themselves.

### 3. Estimations

Now let us estimate the order of magnitudes of the atmospheric and oceanic forces effecting on a separate plate and of the stresses of the interaction between plates.

At the common wind velocity ( $u=10$  m/s) the friction stress  $\tau$  on the surface of the plate is  $\tau = \rho u^2 = 0.004 \times 1.27 \text{ kg/m}^3 (10 \text{ m/s})^2 = 0.5 \text{ N/m}^2$ , the area of the plate is  $\approx 2 \times 10^{13} \text{ m}^2$ ; therefore, the total atmospheric force effecting on a separate plate, is  $\approx 10^{13} \text{ N}$ . Under the effect of this force the plate interacts with the circumjacent plates through the frontal contacts. The interaction takes place only at the sites of adhesion of plates, and the area of contacts may be small. The total atmospheric force concentrates on this small area. Therefore, the stresses may reach such high values ( $10^6$ – $10^7 \text{ N/m}^2$ ), at which the discontinuity and displacement of plates from each other occur. The discontinuity triggers the seismic waves. Thus, the mechanical action of the atmosphere and ocean on the lithosphere plates controls the relative movements of the lithosphere plates and can cause the earthquakes and volcanic activity.

There is a substantial body of publications in which strong correlations between the seismicity and the variations in the atmospheric indices, as well as between the seismicity and the fluctuations in the Earth's rotation (Zharov, Konov, and Smirnov, 1991; Gorkavii et al., 1994a; Gorkavii, Trapeznikov, and Fridman, 1994b; Barsukov, 2002) are found. Our hypothesis explains these correlations. The atmospheric and oceanic circulation is the initial cause of both the whole class of earthquakes and the variations in the Earth rotation. Note that the variations in the Earth rotation are very small ( $\delta\omega/\omega \approx 10^{-8}$ ) and do not affect the geophysical processes (Sidorenkov, 1961, 2002).

### 4. Variations in the ice sheet masses

Redistribution of water between the world's oceans and the ice sheets was accompanied by changes in the moment of inertia of the Earth and must have led to its irregular rotation and secular polar motion. On this basis, combined algebraic equations can be set up to relate the value of the Earth's rotational speed and the polar coordinates to the masses of ice in Antarctica and Greenland and water in the world's oceans (Sidorenkov, 2009). These equations allow one to calculate the rotational characteristics of the Earth: the polar coordinates and the rotational speed of the Earth. If the masses of ice are unknown but data on the instability of the Earth's rotation are available, it is possible to solve the inverse problem: to compute the annual values of ice masses in Antarctica and Greenland and of water in the world's oceans from the polar coordinates and the rotational speed.

It was found by Sidorenkov (2002, 2009) that the variations observed in the Antarctic ice sheet mass agreed with the mass's variations required for the explanation of the decade (5–100 year) fluctuations of the Earth's rotation rate and the secular polar motion (Fig. 1). However, this agreement proved to be only the qualitative one. As to the quantitative agreement, the variations observed in the ice masses proved to be 28 times less than the required variations.

These contradictory results indicate that the observed decades-long fluctuations in the Earth's rotation rate are not due to the rotation and polar motion of the whole Earth but rather to changes in the speed of drift of the

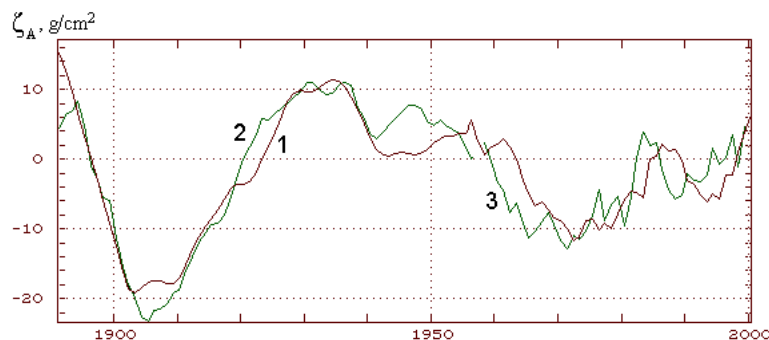


Figure 1: Temporal variations in the specific ice masses for Antarctica: 2 and 3 – data of the glaciological observations; 1 – volume required for the explanation of the decade fluctuations of the Earth's rotation velocity and the secular polar motion.

lithosphere over the asthenosphere. Indeed, the moments of the like-sign forces arising in the process of fluctuation in the global water exchange operate for decades. It is possible that, with such long-term impacts, the matter of the asthenosphere underlying the lithosphere does not behave like a solid body but rather flows like a viscous fluid. Then, the decades-long global water exchange can result in the lithosphere's sliding over the asthenosphere without having a noticeable effect on the Earth's deeper layers. In astronomical observations, changes in the lithosphere's drift rate are recorded as the irregularities in the Earth's rotation and polar motion. However, such apparent irregularities and motions require the redistribution of water masses that are 28 times lower than in the case of rotation of the whole Earth.

### 5. The lithosphere drifts over the asthenosphere

The Earth's layers that are deeper than the asthenosphere don't take part in the formation of the observed decade fluctuations. The lithosphere's moments of inertia are 28 times less than the moment of inertia of the whole Earth and therefore the variations in the Antarctic ice mass exactly correspond to the mass's variations required for the explanation of the decade fluctuations in the lithosphere's angular rotation rate.

The sliding of the lithosphere over the asthenosphere is possible in the case when the action duration  $T$  is many times longer than the characteristic relaxation time  $t$  within the asthenosphere. It is known that the relaxation

time  $t$  is determined from the relationship  $t = \mu/\eta$ , where  $\mu$  is the viscous coefficient and  $\eta$  is the rigidity. For the asthenosphere,  $\mu \approx 10^{18} - 10^{23}$  Poise and  $\eta \approx 10^{12}$  dyn cm<sup>-2</sup>. As a result,  $t = \mu/\eta = 10^6 - 10^{11}$  s or 0.03–3000 years. Clearly, the above-mentioned hypothesis could be accepted if we take a lower limit to the permissible values of  $\mu$ . At the upper limit of viscosity, the drift of the lithosphere is hardly probable.

However, this classical estimate does not take into account the effects of vibrational lithospheric displacements. Indeed, the lithospheric plates constantly vibrate in the vertical direction under the action of lunisolar tides. On the other hand, the lithospheric plates are constantly affected in the horizontal direction by shear stresses caused by friction of wind, and ocean currents. As a result, the lithospheric plates must exhibit vibrational displacements over the asthenosphere in the direction of acting tangential forces. There is abundant evidence supporting this plate drift.

Now Global Positioning System (GPS) is used to study moving of the Earth's tectonic plates (Fig. 2). Plates move as slow as a few centimeters in a year.

The differential rotation of the lithosphere and mantle is considered in many papers devoted to the tectonics of plates (Scoppola B., Boccaletti D., Bevis M. et al., 2006; Chuikova & Maksimova, 2005) have found the uncompensated masses and stresses at the crust and uppermantle. They supposed the crust's movements caused by the crust pressing on the mantle for both the isostatic and gravity nonequilibrium.

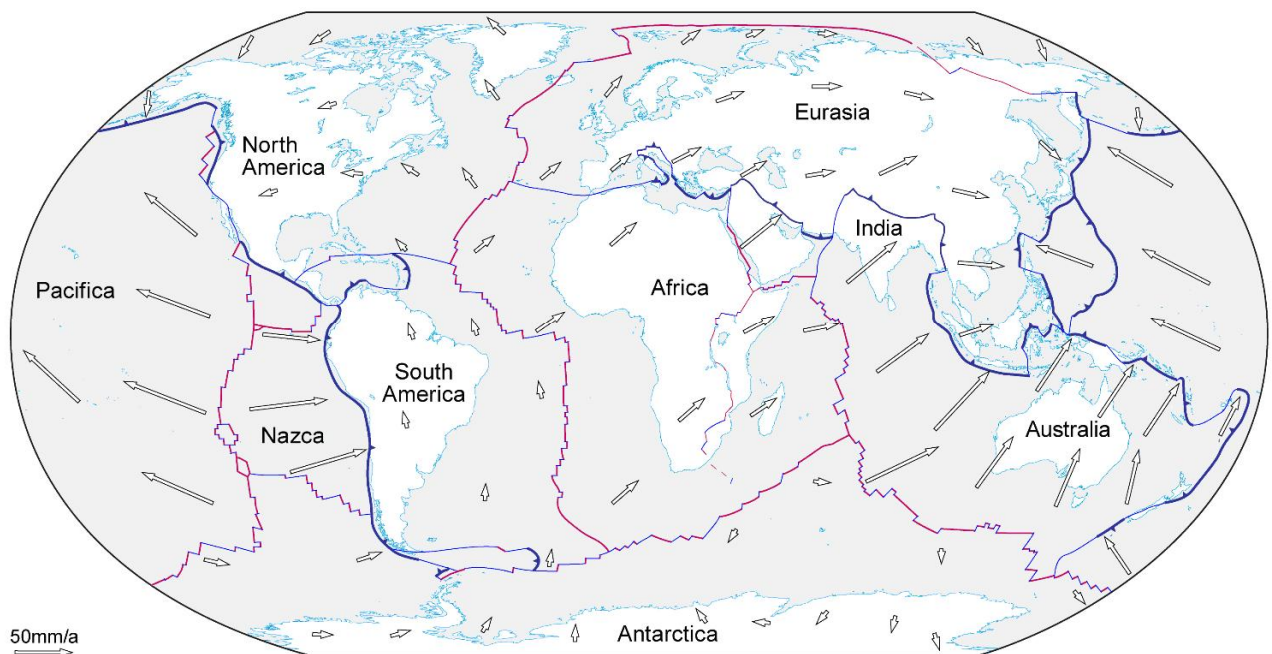


Figure 2: Current absolute plate motion from GPS information (world Robinson projection).

Length of arrows indicates rate of movement of that part of the plate

<http://www.files.ethz.ch/structuralgeology/jpb/files/english/1Introducto.pdf>

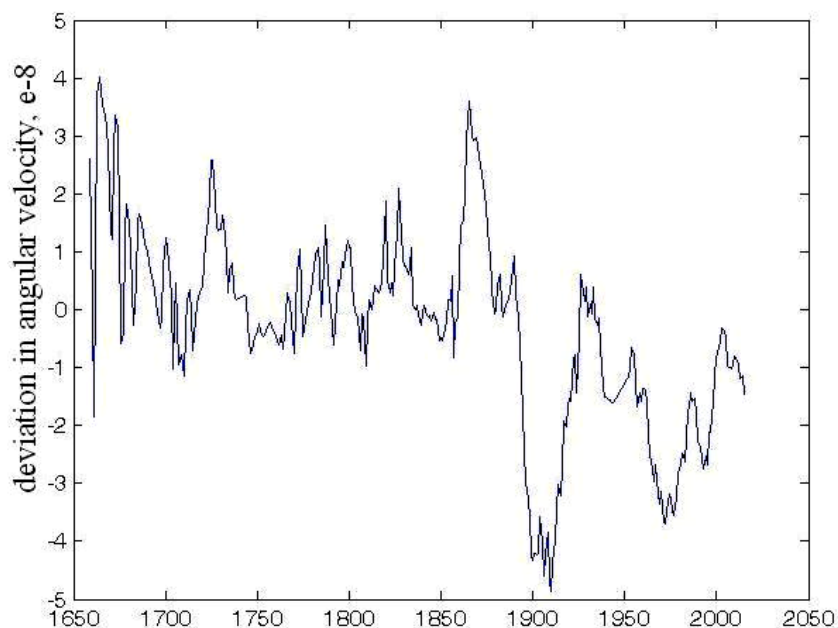


Figure 3: Fluctuations of the angular velocity of lithospheric drift over the asthenosphere in 1660-2015

Thus, the research results and observations confirm the hypothesis about the movement of the lithosphere plates under the impact of the atmospheric and oceanic circulation on the decade time scale. The total effect of the movement of all lithosphere plates is interpreted by geophysics as the decadal fluctuations of the Earth's rotation.

It can be stated that the lunisolar tidal oscillations cause the vibration displacement of continental plate. Observed by astronomers, decade variations in the Earth's angular velocity are actually variations in the angular velocity of lithospheric drift over the asthenosphere. Figure 3 demonstrates these variations over the last 350 years.

The hypothesis on the drift of the lithosphere over the asthenosphere is based not only on the analysis of the effect of redistribution of water between the ocean and the ice sheets in Antarctica and Greenland but also on a review of the mechanism of the angular momentum interchange between the atmosphere and the Earth (Section 1). The frictional forces and the pressures of the atmosphere and oceans on the lithosphere plates cause their drift over the asthenosphere. This hypothesis also agrees with the fact that there is a significant correlation between the seismic activity and the irregularities of the Earth's rotation.

The lunisolar tides affect the atmospheric and oceanic processes. On the one hand, they generate the vibrational displacement of plates and, on the other hand, influence the atmospheric and oceanic processes. That is why there are numerous relationships between the dynamics of seismicity and the peculiarities of variations of atmospheric circulation.

The state of the ice sheets in the Antarctic and Greenland depends on the climatic variations. Therefore, the decadal fluctuations in the Earth's rotation may also correlate with the fluctuations in the climatic characteristics and indices. This relationship has been found in (Lambeck, 1980; Sidorenkov, 2002; 2009). There is a close correlation between the Earth's rotation fluctuations and the frequencies of the

atmospheric circulation forms, the anomalies of the hemisphere-averaged air temperature, and many another climate characteristics (Sidorenkov, 2009). These relationships are explained given the assumption that the lithosphere drifts along the asthenosphere.

*Acknowledgements.* This study was supported by the Russian Foundation for Basic Research, project 15-05-07590.

## References

- Blekhman I.I.: *Vibrational Mechanics (Nonlinear Dynamic Effects, General Approach, Applications)*. Singapore, 2000.
- Chuikova N.A., Maksimova T.G.: 2005, *Vestnik of the Moscow State University, Ser. 3. Physics and Astronomy*, No. 4, 64–72 [in Russian].
- Lambeck K.: 1980, *The Earth's Variable Rotation: Geophysical Causes and Consequences*, Cambridge University Press, Cambridge, p. 450.
- Scoppola B., Boccaletti D., Bevis M. et al.: 2006, *GSA Bulletin*; January/February 2006; **118**; no. 1/2; p. 199–209; doi: 10.1130/B25734.1
- Sidorenkov N.S.: 1961, *Problemy Arktiki i Antarktiki.*, **9**, 45–49 [in Russian].
- Sidorenkov N.S.: 2002, *Fizika Nestabilnostey Vrasheniya Zemli (Physics of the Earth's Rotation Instabilities)* (Nauka, Fizmatlit, Moscow, 2002), p. 384 (in Russian with English summary and contents).
- Sidorenkov N.S.: 2009, *The interaction between Earth's rotation and geophysical processes*. Weinheim. WILEY-VCH Verlag GmbH & Co. KGaA, 2009, 317p.
- Trubitsyn V.P.: 2000, *Izvestiya Phys. Solid Earth*, **36 (9)**, 708–741.
- Trubitsyn V.P., Rykov V.V.: 2000, *Problemy global'noj geodinamiki*, 7–28 (in Russian).

DOI: <http://dx.doi.org/10.18524/1810-4215.2016.29.85224>

## «CHURYUMOV UNIFIED NETWORK»: NEW, IMPORTANT TASKS FOR ASTRONOMICAL OBSERVATORIES TO PROTECT SOCIETY IN THE ERA OF MODERN HYBRID WARS

**K.I.Churyumov**<sup>1</sup>, A.P.Vidmachenko<sup>2</sup>, A.F.Steklov<sup>2,3</sup>, N.G.Dashkiev<sup>3</sup>, Ya.O.Romanyuk<sup>2</sup>, I.V. Stepakhno<sup>3</sup>

<sup>1</sup> Astronomical Observatory of Taras Shevchenko National University of Kyiv,

<sup>2</sup> Main Astronomical Observatory of the National Academy of Sciences of Ukraine, [vida@mao.kiev.ua](mailto:vida@mao.kiev.ua)

<sup>3</sup> Interregional Academy of Personnel Management

**ABSTRACT.** Authors created and provided the operation of the first version of the "Bolide Network of Churyumov" for continuous recording of twilight and daytime traces of aerial and aerospace intrusions over Kiev and Kiev district during 2013-2016. A total of more than 36000 copyright photos was obtained, their classification was carried out and the first database was created. The authors recorded typical space invading meteoroids, comets nucleus fragments and traces of aerial intrusions, signs of which, as a rule, are observed at lower altitudes comparing with typical space invasions.

**Keywords:** Twilight Bolide: Comets nucleus: Space invasions: Meteoroids

We live in a very difficult time when in different parts of the globe, in different countries due to different reasons and different goals the so-called hybrid wars are provoked from the outside, break out and last for years.

The phenomenon of "hybrid war" has many definitions, but its main characteristics and key elements are the following:

1. War is clearly there, but legally it is absent.
2. The real external aggression is masked as some conflict within civil society.
3. Financial resources and often manpower, military technical systems are provided by external sources.
4. Long before the hot phase of the hybrid wars permanent active invasion of different services, systems, forces and facilities are initiated by states, geopolitical and global economic associations which are interested in conflict.
4. The hybrid wars, as a rule, cover only cover specific regions having concentrated social, economic, industrial and/or military strategic interests of the parties.

In any case, at the same time, the role of the light aviation (Churyumov et al., 2014b, d) for special purposes (e.g. drones, quadcopters) is dramatically increased. It should be emphasized that a number of the leading states have recently successfully created and tested ultra-light drones which use self-destruction function after performing a secret aggressive mission of secret invasion. This allows the aggressor state to mask his aerial aggression as "natural" invasion of fragments of disintegrated nuclei of

comets, meteoroids and even as aerospace invasion of space debris items (Brown et al., 2002, Churyumov et al., 2014e, f, 2015a, Spurny et al., 2002, Vid'Machenko, 1995, Vidmachenko et al., 2013a, b).

Realizing the danger of the above stated, the team of authors of this brief communication created and provided the operation of the first version of the "Churyumov Unified Network" for continuous recording of twilight and daytime traces of aerial and aerospace intrusions over Kiev and Kiev district during 2013 - 2016 years (Churyumov et al., 2013, 2015c, d, 2016a, b, c, d, e, f). A total of more than 36000 copyright photos were obtained, their classification was carried out and the first database was created. The authors recorded typical space invading meteoroids, comets nucleus fragments and traces of aerial intrusions, signs of which, as a rule, are observed at lower altitudes comparing with typical space invasions (Churyumov et al., 2016g).

We also managed to fix the origin and development of local, but powerful, atmospheric vortexes, which were previously not typical for Ukraine, and therefore it confirms the dangerous trends in climate evolution. Very large, long plumes of dust, aerosol emissions of Kiev enterprises are registered that may be the subject of harsh penalties. It was also obtained a large series of photos of summer fires, explosions of tank farms and even traces of special air operations during periods of hybrid escalation of the war. In created database there is also a considerable number of "footprints in the sky" over Kiev, which we have not yet managed to classify and identify (Churyumov et al., 2014a, c 2015b).

A successful and fruitful experience of authors in the grim years of Maydan, ATO and hybrid war of 2013-2016 years, clearly requires a sharp intensification of efforts of all astronomical observatories of Ukraine regarding the development and improvement of the "Churyumov United Network" for continuous recording of twilight and daytime traces of aerospace, aerial and suborbital intrusions (Churyumov et al., 2016c, e).

The operation of such a network is of prime importance for The State Emergency Service of Ukraine, Security Service of Ukraine, Ministry of Defense of Ukraine and many other departments and ministries, which should finance the creation of hybrid photo recorders for the network,



Figure 1: On the left – photo by Steklov A.F., right – photo by Dashkiev G.N.

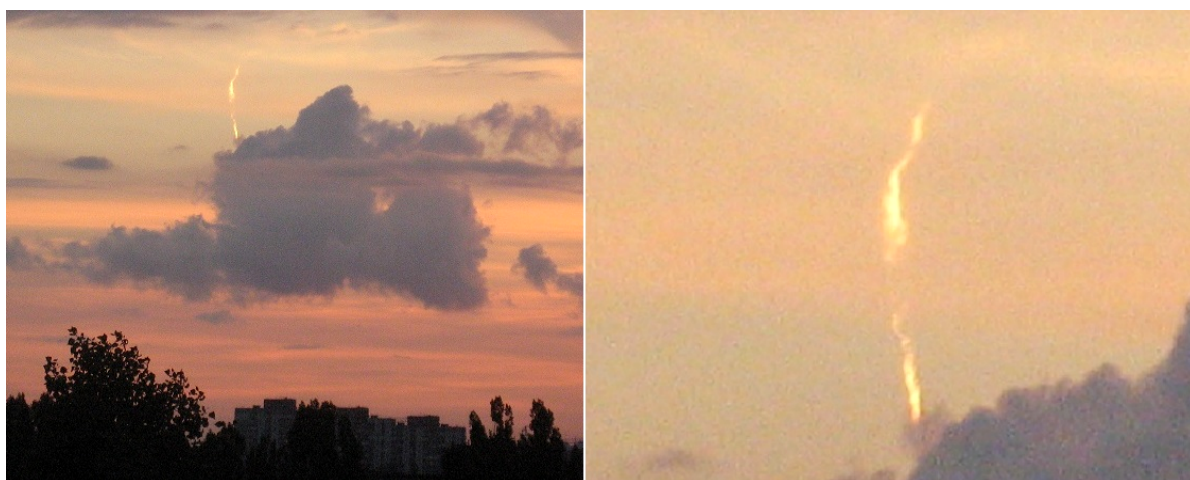


Figure 2: Bolide trace over Kiev June 31, 2013. Photo by Churyumov K.I.

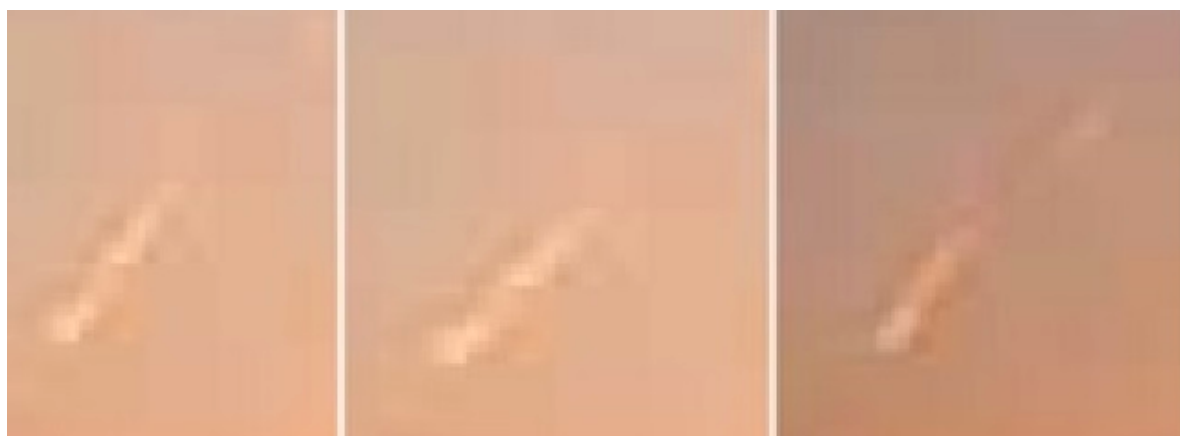


Figure 3: Variations of bolide trace over Kiev Region. July 08 2016. From left to right: UT 19.26.24, 19.26.26, 19.27.30. Photos by Steklov A.F.



Figure 4: Variations of bolide trace over Kiev Region. July 08 2016. From left to right: UT 19.27.46, 19.27.57, 19.28.28. Photos by Dashkiev G.N.

which combine the properties of modern wide-angle comet seeker and features cutting-edge video recorders. The "Churyumov Unified Network" should be supported by all astronomical, meteorological and geodetic observatories, National Academy of Sciences of Ukraine, National Academy of Pedagogical Sciences, the Academy of Sciences of Higher School, "The Planetary Society" of Ukraine; academician, universities, educational and other (national, private, amateur) observatories. Full-scale deployment of the "Churyumov United Network" requires the creation of trusted panoramic cameras, video surveillance systems with a maximum recording resolution, maintaining compression format, allowing for adequate reality color shooting in low-light conditions, in the presence of a large (long) and small (short) tracks (objects). Systems should have their own computing facility, web server, the ability to stream video over a wireless network to support transmission of multiple video streams in the required compression formats.

Our network cameras need to have not only the possibility of wired and wireless connectivity to a single and multi-channel network video servers, but also rely on the work of four-wheel drive IP-based cameras with sufficient (18x?) zoom having features of progressive scan sensor and, at the same time, multi-channel decoders should allow to connect to a large number of cameras with progressive scan technology to improve image quality. Very desirable is implementation of modes of daytime, twilight and night scenes. And so on.

The challenges that our turbulent times poses on astronomical observatories are very complex, but interesting and, finally, astronomers of Ukraine, creating systems and networks for continuous photographic twilight and daytime traces aerial, aerospace and suborbital intrusion, can take on a new critical role in the protection of society and the state in the era of hybrid wars.

In Fig. 3 (left) shows an image of "a trace in the sky", results in about a half a minute after the start of combustion body, which has flown into the atmosphere (Kruchynenko, 1995, 1997, 2004, Kruchynenko et al., 2011). Trace was observed just near the horizon. At falling this body is becoming stronger flared. Combustion occurs with elements of splashing of a yellow-orange flame. This flight-combustion continued no more than ten seconds. The object burned down and left by the Sun illuminated trail. In Fig. 3 and 4 shows the dynamics of changes in the trace form. This trace about 40 minutes was illuminated by the Sun. And then a few tens of minutes could be seen as a diffuse dark cloud against the evening sky, which is illuminated by the Moon. During this time, were obtained a few tens of trace photos, before full it's scattering in the atmosphere. The distance between the two points of observation was 25.8 km

And advanced "Churyumov Unified Network" will be only one of our responses to the challenge of time. Our other answers already in the works.

## References

- Brown P. et al.: 2002, *Nature*, **420**, 314.  
 Churyumov K.I. et al.: 2013, *Me13.ConfE*, **8**, 77.  
 Churyumov K.I. et al.: 2014a, *Asys.Conf*, **16**, 75.  
 Churyumov K.I. et al.: 2014b, *Asys.Conf*, **16**, 77.  
 Churyumov K.I. et al.: 2014c, *AstSR*, **10**(1), 37.  
 Churyumov K.I. et al.: 2014d, *MISConf.AstSP*, 86.  
 Churyumov K.I. et al.: 2014e, *MICConf.CAMMAC*, 8.  
 Churyumov K.I. et al.: 2014f, *Nasu.book.MICConf*, 98.  
 Churyumov K.I. et al.: 2015a, *Asys.Conf*, **17**, 84.  
 Churyumov K.I. et al.: 2015b, *Nea.Conf*, **9**, 22.  
 Churyumov K.I. et al.: 2015c, *Nea.Conf*, **9**, 30.  
 Churyumov K.I. et al.: 2015d, *AstSR*, **11**(2), 99.  
 Churyumov K.I. et al.: 2016a, *Asys.Conf*, **18**, 93.  
 Churyumov K.I. et al.: 2016b, *ISPCConf.A&P*, **5**, 2.  
 Churyumov K.I. et al.: 2016c, *ISPCConf.A&P*, **5**, 3.  
 Churyumov K.I. et al.: 2016d, *ISPCConf.A&P*, **5**, 33.  
 Churyumov K.I. et al.: 2016e, *ISPCConf.A&P*, **5**, 37.  
 Churyumov K.I. et al.: 2016f, *Mete.ConfP*, 63.  
 Churyumov K.I. et al.: 2016g, *ICConf.AstSPKU*, 90.  
 Kruchynenko V.G. et al.: 2011, *KPCB*, **27**(3), 109.  
 Kruchynenko V.G.: 1995, *ESOC.Workshop*, 287.  
 Kruchynenko V.G.: 1997, *A&AT*, **13**, 191.  
 Kruchynenko V.G.: 2004, *KFNT*, **20**(3), 269.  
 Spurny P. et al.: 2002, *ESASP.500*, 269.  
 Vid'Machenko A.P.: 1995, *KPCB*, **11**(4), 14.  
 Vidmachenko A.P. et al.: 2013a, *Asys.Conf*, **15**, 9.  
 Vidmachenko A.P. et al.: 2013b, *AstSR*, **9**(2), 146.

DOI: <http://dx.doi.org/10.18524/1810-4215.2016.29.85228>

# INTERNATIONAL NETWORK OF PASSIVE CORRELATION RANGING FOR ORBIT DETERMINATION OF A GEOSTATIONARY SATELLITE

Mykola Kaliuzhnyi<sup>1</sup>, Felix Bushuev<sup>1</sup>, Oleksandr Shulga<sup>1</sup>, Yevgeniya Sybiryakova<sup>1</sup>, Leonid Shakun<sup>2</sup>, Vladislavs Bezrukovs<sup>3</sup>, Sergiy Moskalenko<sup>4</sup>, Vladislav Kulishenko<sup>5</sup>, Yevgen Malynovskyi<sup>6</sup>

<sup>1</sup> Research Institute “Mykolaiv Astronomical Observatory” (RI “MAO”), Mykolaiv, Ukraine

<sup>2</sup> Astronomical Observatory of the Mechnikov Odessa National University, Odessa, Ukraine

<sup>3</sup> “Ventspils University College”, Ventspils, Latvia

<sup>4</sup> Western Center of Radio Engineering Surveillance, Mukacheve, Ukraine

<sup>5</sup> Institute of Radio Astronomy of the National Academy of Sciences of Ukraine, Kharkiv, Ukraine

<sup>6</sup> Rivne Minor Academy of Sciences of School Age Youth, Rivne, Ukraine

**ABSTRACT.** An international network of passive correlation ranging of a geostationary telecommunication satellite is considered in the article. The network is developed by the RI “MAO”. The network consists of five spatially separated stations of synchronized reception of DVB-S signals of digital satellite TV. The stations are located in Ukraine and Latvia. The time difference of arrival (TDOA) on the network stations of the DVB-S signals, radiated by the satellite, is a measured parameter.

The results of TDOA estimation obtained by the network in May-August 2016 are presented in the article. Orbital parameters of the tracked satellite are determined using measured values of the TDOA and two models of satellite motion: the analytical model SGP4/SDP4 and the model of numerical integration of the equations of satellite motion. Both models are realized using the free low-level space dynamics library OREKIT (ORbit Extrapolation KIT).

Key words: orbit of geostationary satellite, DVB-S, TDOA

## 1. Introduction

Passive correlation ranging (PaCoRa) of geostationary satellites is considered by the European Space Agency (ESA) as an alternate to classical two-way radar ranging [1]. The ESA project with the same name had been performed by the SES company during Jun. 2010 – Jan. 2013. PaCoRa system receives a satellite’s downlink signal by multiple ground stations located within the satellite’s footprint. The signal’s time difference of arrival (TDOA) is determined by the PaCoRa for each pair of the stations. Further the TDOA and known geographical coordinates of the stations are used to obtain the satellite’s position and predict its orbit. According to the ESA the PaCoRa has some advantages compare to the classical

method of ranging. In our opinion, three of them are the most important. 1) Rx-only: small antennas and standard RF front-end hardware required. 2) No uplink for ranging, therefore no impact on the satellite. 3) Orbit determination of own satellites and 3rd party satellites.

In the Research Institute “Mykolaiv astronomical observatory” (RI “MAO”) the passive correlation ranging has been employed since the first experiment in Aug. 2011 [2, 3]. The method is considered as an independent method for tracking the future Ukrainian geostationary satellite “Lybid”. Results of the passive correlation ranging of Eutelsat-13B are presented in the article. The results were obtained during 2015-2016 by an international network which consists of 5 stations located in Ukraine and Latvia.

## 2. International network of passive correlation ranging

Now the stations of the network are located in Kharkiv, Mukacheve, Rivne, Mykolaiv (Ukraine) and Ventspils (Latvia). The Rivne station had been located in Kyiv up to Feb. 2016. The Ventspils station has operated since Nov. 2015. The network has operated as a part of the four Ukrainian stations since Jan. 2015. The network also includes a data processing center, located in Mykolaiv.

The stations of the network have identical hardware and software. Each station consists of:

- The standard antenna-feeder system for the reception of DVB-S signals, with antennas of 0.9 m in diameter;
- DVB-S receiver (SkyStar1 or Skystar2) performed as a PCI-card and upgraded in terms of outputting of in-phase and quadrature signals from the receiver’s quadrature detector;
- Single-frequency ThunderBolt-E GPS receiver;

- Digital USB-oscilloscope DSO5200A with 200 MHz passband and 9-bit ADC (Analog Digital Converter);
- Personal computer (PC) with USB and RS-232 ports, operable in Windows XP environment (1 GHz CPU clock rate; 1 Gb RAM, and 100 Gb HD capacity);
- Internet connection at data rate of at least 80 Kbytes per second.

The station software consists of:

- Standard software of the DTV-S receiver and digital USB oscilloscope;
- Open source software FileZilla (FTP-client);
- Special software for synchronized measurements by the GPS and for reading and archiving samples of the DVB-S signals on the PC hard drive.

Detailed description of the station hardware and software is given in [3, 4]. The hardware and software allow each station of the network to record every second fragments of DVB-S complex signal, incoming from the quadrature detector, synchronously with PPS (Pulse-Per-Second) signals, incoming from the GPS receivers. It is shown in [3] that the complex signal should be transformed in a real signal taking into account the structure of DVB-S signal to obtain convolution and subsequently calculate TDOA. This transformation is performed on the stations now. The obtained real signal samples are archived and sent through the Internet in the data processing center. Here the correlation function of the real samples is computed and the value of TDOA is estimated by the following formula [5]:

$$\Delta\tau_i = \left( \frac{n_{xi}}{k \cdot f_n} + \tau_{PPSi} \right) - \left( \frac{n_0}{k \cdot f_n} + \tau_{PPS0} \right) - \Delta\tau_{hi}, \quad (1)$$

where  $\Delta\tau_i$  – time difference of arrival the signals received by the  $i$ -th and 0 stations,  $n_{xi}$  – offset of the maximum of the correlation function from the beginning of the sample obtained by the  $i$ -th station,  $n_0$  – given offset of the middle part of the sample obtained by the zero station,  $f_n$  – nominal sample rate of the ADC of the digital USB oscilloscope,  $k$  – measured factor between valid and nominal sample rates of the ADC,  $\Delta\tau_{hi}$  – measured value of the difference of hardware delays of the stations,  $\tau_{PPSi}$ ,  $\tau_{PPS0}$  – given initial delays of PPS signals of GPS receivers of the stations. The values of  $n_{xi}$  and  $n_0$  are measured in counts of the sampling frequency. The size of the middle part of the zero station sample is equal to the sample size of a correlator and is always less than the sample size of the ADC. The ADC sample size is equal 10240 for the employed type of USB oscilloscope. The corresponding sample length is equal 200  $\mu$ s for the sample rate  $f_n = 51.2$  МГц. The mentioned sample rate is close to Nyquist rate for the received signal. The coefficient  $k = 0.97655$  is a constant for the given type of oscilloscope. Values of  $\tau_{PPS}$  depend from geostationary position of tracked satellite and for Eutelsat-13B they are equal 1270  $\mu$ s, –215  $\mu$ s, 642  $\mu$ s, 0  $\mu$ s, 2660

$\mu$ s and 888  $\mu$ s respectively for the station in Kharkiv, Mukacheve, Rivne, Mykolaiv, Ventspils and Kyiv. The data processing center software has been written on Python to compute TDOA.

The special software has also been developed on Python to determine the orbit of tracked satellite using observed values of TDOA. Herewith orbit parameters are determined using the least square method (LS), namely, by minimizing the sum of squared differences of the observed and model values of TDOA. The LS equations are solved using the Levenberg-Marquardt method software-implemented in the Python function *leastsq* [6, 7]. The LS equations are also solved with respect to satellite coordinates in inertial coordinate system on an observing epoch. The satellite position is modeled using the free space dynamics library OREKIT (ORbit Extrapolation KIT) written in Java [8]. The developed software allows determination the satellite orbit using the SGP4/SDP4 (Simplified General Perturbation/Simplified Deep Space Perturbation) analytical model of satellite motion [9, 10], and using a numerical model of integrating the equations of satellite motion [11]. The SGP4/SDP4 model is used to determine the pseudo-keplerian elements of satellite orbit in the so called the two-line elements (TLE) format proposed by NORAD. The initial values of the satellite coordinates and velocity for this model are set in the TEME (True Equator Mean Equinox) coordinate system – the Earth-centered inertial frame used for determine the NORAD two-line elements. The following perturbations are taken into account under using the numerical model to determine satellite orbit:

- Three-body gravitational attractions of the Sun and Moon, JPL DE 405/DE 406 [12];
- Gravitational attraction of the non-spherical Earth (Earth gravity model EIGEN-6S, truncated to the 9th degree and order) [13].

The initial values of the satellite coordinates and velocity for the numerical model are set in the EME2000 (Earth's Mean Equator and Equinox) coordinate system which is also called J2000 frame.

The coordinates of the stations are necessary to determine the orbit. They are set in the Earth-fixed WGS84 system and are taken directly from the measurement data of GPS receivers used for synchronization of the stations. Initial values of the coordinates of tracked satellite are also originally set in the WGS84 assuming that the satellite is at the geographic coordinates of equal  $\varphi_{GSS}$ ,  $\lambda_{GSS} = 0$  and  $h_{GSS} = 36000$  km, where  $\varphi_{GSS}$ ,  $\lambda_{GSS}$  and  $h_{GSS}$  denote the longitude, latitude and height of the geostationary satellite. The satellite Eutelsat-13B is located in the geostationary cell at the longitude 13° East, therefore,  $\varphi_{GSS} = 13^\circ$ .

### 3. Passive correlation ranging of Eutelsat-13B

As an illustration, in Fig. 1 the graphs of slant range differences  $\Delta r$  changed in time from May 18, 2016 to Aug. 16, 2016 are given for four pairs of stations Kharkiv-Mykolaiv, Mukacheve-Mykolaiv, Ventspils-Mykolaiv and Rivne-Mykolaiv.

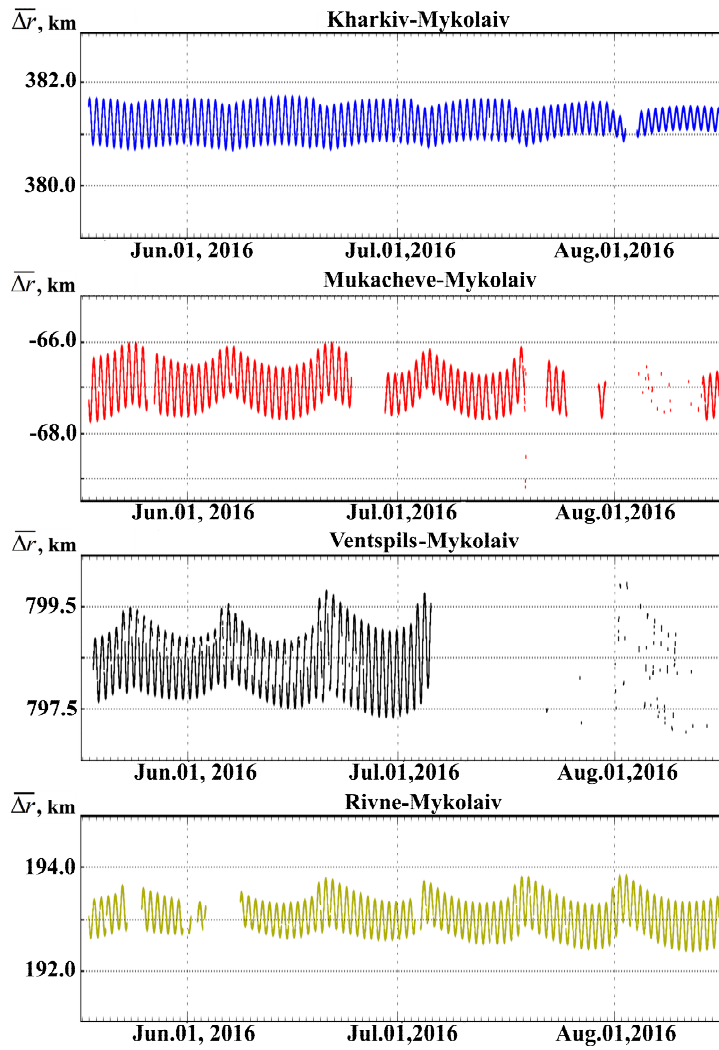


Figure 1: Slant range differences for four pairs of stations (from top to bottom): Kharkiv-Mykolaiv, Mukacheve-Mykolaiv, Ventspils-Mykolaiv and Rivne-Mykolaiv. Observation time is from May 18, 2016 to Aug. 16, 2016.

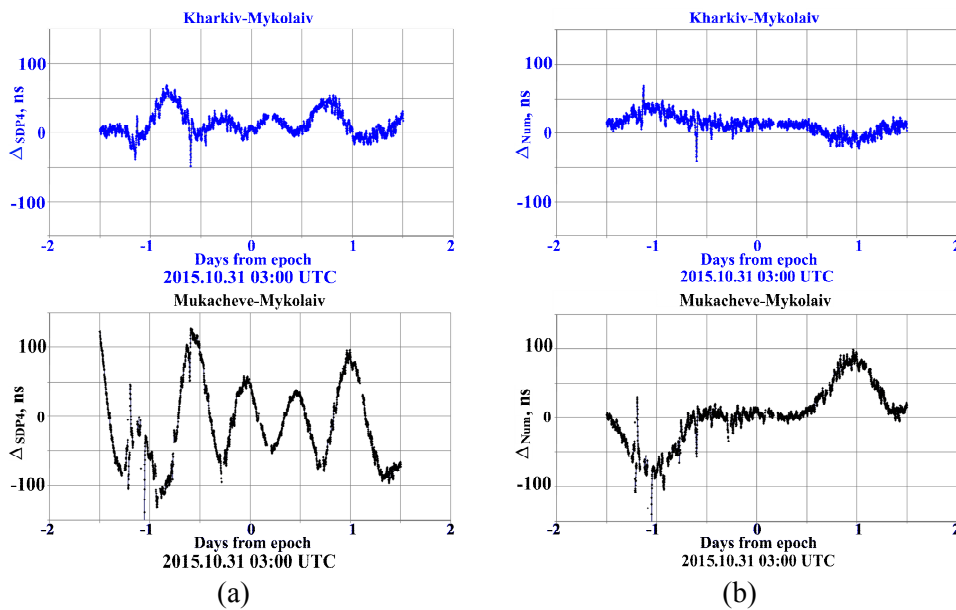


Figure 2: Residuals between model and observed TDOA for two pairs of stations (from top to bottom) Kharkiv-Mykolaiv and Mukacheve-Mykolaiv, and for two models: (a) – for SGP4/SDP4 model, and (b) – for numerical model. Fitting interval equals 24h.

Table 1. Mean and standard deviations of the residuals.

Model	Kharkiv-Mykolaiv		Mukacheve-Mykolaiv	
	$\bar{\Delta}$ , ns	$\sigma$ , ns	$\bar{\Delta}$ , ns	$\sigma$ , ns
SGP4/SDP4	11	$\pm 9$	3	$\pm 39$
Numerical	13	$\pm 5$	4	$\pm 6$

The slant range differences  $\bar{\Delta r}$  is obtained by averaging every second values  $\Delta r = \Delta \tau \cdot c$  on the interval of 60 s, where  $\Delta \tau$  – the TDOA for given pair of stations and  $c$  – the speed of light in vacuum. Statistical analysis shows that for all four pairs of stations the median of standard deviation (SD) of  $\Delta r$  is  $\pm 2.6$  m or  $\pm 8.7$  ns for the TDOA SD.

The graphs of the TDOA residuals ( $\Delta$ ) between model and observed values are shown in Fig. 2 for the interval of  $\pm 1.5$  days from the observing epoch 31.10.2015 03:00 UTC and for two pairs of stations Kharkiv-Mykolaiv and Mukacheve-Mykolaiv. Herewith the residuals obtained using the SGP4/SDP4 model are shown in Fig. 2 (a), and using the numerical model – in Fig. 2 (b). The interval for fitting the model and observed values was equal 24 hours.

From the data given in Fig. 2 (a) it follows that the SGP4/SDP4 residuals have significant periodic deviations on the fitting interval due to the inaccuracy of the model. The residuals graphs for the numerical model (Fig. 2 (b)) do not have significant periodic deviations on the fitting interval. Mean ( $\bar{\Delta}$ ) and standard deviations ( $\sigma$ ) of the residuals obtained on the fitting interval are given in Table 1. For both model there are significant deviations of the residuals outside of the fitting interval.

#### 4. Summary

1. The monitoring of Eutelsat-13B was performed by the international network of passive correlation ranging during about a year from Nov. 2015 to Aug. 2016. The network consists of five stations received DVB-S signals and spaced at 1000 km along longitude as well as latitude. Single-measurement error (1 sigma) of the TDOA is equal about  $\pm 8.7$  ns for the all pairs of the stations.

2. Special software was developed for determination orbital parameters by TDOA using the SGP4/SDP4 model and simple numerical model of satellite motion. Standard deviations and average values of the residuals between the model and observed TDOA are estimated for the pairs Kharkiv-Mykolaiv and Mukacheve-Mykolaiv. The numerical model is more accurate than the SGP4/SDP4 model. The standard deviations of the TDOA residuals on the fitting interval do not exceed  $\pm 6$  ns for the numerical model. The fitting interval should be set more than 24 hours to increase prediction accuracy of the models.

3. The considering network could be a prototype of a system of ongoing monitoring of orbits of active geostationary satellites. This system may be cheap to implement and will be fully independent, do not tied to uplink stations.

#### References

1. Passive correlation ranging (PaCoRa) [online]. Available from <https://artes.esa.int/projects/passive-correlation-ranging-pacora>.
2. Bushuev F.I., Kalyuzhny N.A., Shulga A.V., Slivinsky A.P.: 2011, The Abstract Book of the International Conference “Astronomical Research: From Near-Earth Space to the Galaxy”. Mykolaiv, Ukraine, p. 13-14.
3. Bushuev F.I., Kaliuzhnyi N.A., Slivinsky A.P., Shulga A.V.: 2012, *Radiofizika i Radioastronomia*, **17(3)**, 281–290 (in Russian).
4. Bushuev F.I., Kaliuzhnyi M.P., Sybiryakova Ye.S., Shulga O.V., Moskalenko S.S., Balagura O.A., Kulishenko V.F.: 2016, *Kosmichna nauka i tehnologia*, **22(3)**, 50–59 (in Russian).
5. Bushuev F.I., Kaliuzhnyi M.P., Sybiryakova Ye.S., Shulga O.V., Gorbanev Yu.M.: 2015, *Radiofizika i Radioastronomia*, **20(3)**, 238–246 (in Russian).
6. Least-squares fitting in Python [online]. Available from [https://python4mpia.github.io/fitting\\_data/least-squares-fitting.html](https://python4mpia.github.io/fitting_data/least-squares-fitting.html)
7. Donald W. Marquardt: 1963, *Journal of the Society for Industrial and Applied Mathematics*, **Vol. 11, No. 2**, pp. 431-441 (doi: 10.1137/0111030).
8. ORbit Extrapolation KIT 8.0 API [online]. Available from <https://www.orekit.org/static/apidocs/overview-summary.html>
9. Class TLEPropagator [online]. Available from <https://www.orekit.org/static/apidocs/org/orekit/propagation/analytical/tle/TLEPropagator.html>
10. Hoots, Felix R.; Ronald L. Roehrich (31 December 1988). "Models for Propagation of NORAD Element Sets". *United States Department of Defense Spacetrack Report* (3). Retrieved 16 June 2010.
11. Class NumericalPropagator [online]. Available from <https://www.orekit.org/static/apidocs/org/orekit/propagation/numerical/NumericalPropagator.html>
12. Standish (1998). "JPL Planetary and Lunar Ephemerides, DE405/LE405" (PDF). *JPL Interoffice Memorandum 312.F-98-048*.
13. Holmes S.A., Featherstone W.E.: 2002, *Journal of Geodesy*, **76**: 279–299 DOI 10.1007/s00190-002-0216-2.

DOI: <http://dx.doi.org/10.18524/1810-4215.2016.29.85229>

# THE CHANGE INDICES OF SOLAR AND GEOMAGNETIC ACTIVITY AND THEIR INFLUENCE ON THE DYNAMICS OF DRAG OF ARTIFICIAL SATELLITE

Komendant V.H.<sup>1</sup>, Koshkin N.I.<sup>2</sup>, Ryabov M.I.<sup>3</sup>, Sukharev A.L.<sup>3</sup><sup>1</sup>Astronomy Department of Odessa I.I.Mechnikov national university<sup>2</sup>Astronomical Observatory of Odessa I.I.Mechnikov national university<sup>3</sup>Odessa observatory «URAN-4» of Institute Radio astronomy NASU

**ABSTRACT.** The time-frequency and multiple regression analysis of the orbital parameter characterizing the drag of satellites on circular and elliptical orbits with different perigees and orbital inclinations in the atmosphere of the Earth was being conducted in 23-24 cycles of solar activity. Among the factors influencing braking dynamics of satellites were taken: W – Wolf numbers; Sp – the total area of sunspot groups of the northern and southern hemispheres of the Sun, F10.7 – the solar radio flux at 10,7 cm; E – electron flux with energies more than 0,6 MeV и 2 MeV; planetary, high latitude and middle latitude geomagnetic index Ap. In the atmospheric drag dynamics of satellites, the following periods were detected: 6–year, 2.1–year, annual, semi-annual, 27–days, 13– and 11–days. Similar periods are identified in indexes of solar and geomagnetic activity. Dependence of the periods of satellites motion on extremes of solar activities and space weather conditions was conducted.

## 1. Introduction

The state of the upper atmosphere of the Earth depends on solar and geomagnetic activity. Solar and geomagnetic activity affects the atmosphere primarily by increasing its temperature and density. Variations in the density of Earth's atmosphere cause changes in altitude satellites. In this work, satellites are used as indicators of the impact of space weather on the upper atmosphere of the Earth [1, 2]. This work is a refinement, expansion and continuation of the work [5].

## 2. Observational data

For analysis were taken twenty five satellites with different inclinations. Among them: polar, middle–latitude and equatorial satellites. There are fifteen circle orbit and ten elliptic orbit satellites. Table 1 lists: numbers of satellites, periods of observations, inclination of orbits –  $i$ , eccentricity –  $e$  and the minimum and maximum distance from the surface of the Earth at perigee –  $r$  min and  $r$  max. Study satellites moved in unmanaged mode and the satellites: 27700, 00063, 00165 – burned in the atmosphere towards the end of the observation period. Observations of these satellites cover the declining phase of solar cycle 23 and the first half of solar cycle 24. It

includes the rise phase and beginning of the maximum phase of solar cycle 24.

For the analysis the following indices were taken: W – Wolf numbers; Sp – the total area of sunspot groups of the northern and southern hemispheres of the Sun, F10.7 – the solar radio flux at 10,7 cm; E – electron flux with energies more than 0,6 MeV и 2 MeV; planetary, high latitude and middle latitude geomagnetic index Ap. Data of these indices cover time period from 2005 y. to 2014 y.

Variations of the B–star Drag Term [4] and five indices of solar and geomagnetic activity were studied in this article. Figure 1 shows an example graph of the change of the drag coefficient of the satellites: 27700, 00932 – in the investigated time interval.

Table 1.

Number of satellite	$i$	$e$	$r$ min	$r$ max
satellites with circular orbit				
06212 (2005-2012)	98.57°	0.00015	501 km	505 km
25860 (2005-2013)	98.57°	0.0002	647 km	650 km
27700 (2005-2012)	97.7°	0.0005	441 km	517 km
01814 (2005-2014)	75.9°	0.00065	675 km	684 km
04139 (2005-2014)	74.03°	0.0006	685 km	692 km
03048 (2005-2014)	74°	0.00073	693 km	702 km
04579 (2005-2014)	73.99°	0.0009	689 km	703 km
04922 (2005-2014)	65.8°	0.0027	490 km	517 km
12054 (2005-2013)	65°	0.007	522 km	546 km
00397 (2005-2014)	58.3°	0.0016	613 km	621 km
00063 (2005-2014)	48.5°	0.0027	465 km	481 km
00165 (2005-2014)	47.9°	0.0013	540 km	549 km
06153 (2005-2014)	35°	0.00077	697 km	708 km
25064 (2005-2013)	34.9°	0.0007	498 km	502 km
23757 (2005-2013)	22.9°	0.0009	487 km	498km
satellites with elliptical orbit				
00932 (2005-2014)	81.3°	0.114	522 km	2307 km
00721 (2005-2014)	78.6°	0.11	592 km	2308 km
00829 (2005-2014)	60.8°	0.3	393 km	6273 km
00746 (2005-2014)	60.8°	0.31	399 km	6409 km
00082 (2005-2014)	38.9°	0.12	631 km	2503 km
00016 (2005-2014)	34.3°	0.2	649 km	4233 km
00005 (2005-2014)	34.2°	0.19	647 km	3841 km
00020 (2005-2014)	33.4°	0.17	505 km	3310 km
00011 (2005-2014)	32.9°	0.15	551 km	2968 km
00963 (2005-2014)	19.75°	0.21	265 km	5680 km

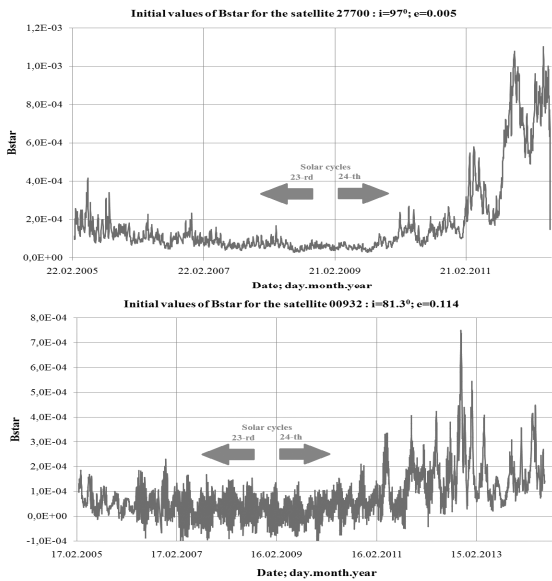


Figure 1: Initial values for polar satellites 27700 (circular orbit) and 00932 (elliptical orbit).

### 3. Methods of data processing

Packages of the statistical analysis were used for our estimations, which are: Origin Pro 8.1, STATISTICA 8 и PSELab.

For primary processing of data was used software package – Origin Pro 8.1. With it performed data interpolation by B–spline method and subtracted the trend (polynomial 3–rd order and using of frequency filtering). The primary processing of indices of solar and geomagnetic activity data wasn't used. These indexes are daily. After this package used statistical analysis software package STATISTICA 8. With this package were constructed periodograms for all satellites and indices of solar and geomagnetic activity. At the last stage was used the PSELab package for construction of the spectrograms. PSELab allows to carry out the spectral and spectral–time analysis of data.

For quantitatively characteristics of the mutual influence of the selected indices on the B–star Drag Term was used multiple correlation analysis in software package STATISTICA 8.

### 4. Results

Fig. 2 shows initial values for one of the indices of solar activity – the solar radio flux at wavelength 10,7 cm. Periodograms was built based on these initial values. This index is an indicator of ultraviolet radiation from the sun. It affects the change in the temperature and density of the upper atmosphere of the Earth.

The results of primary processing of B–star Drag Term are given in [5].

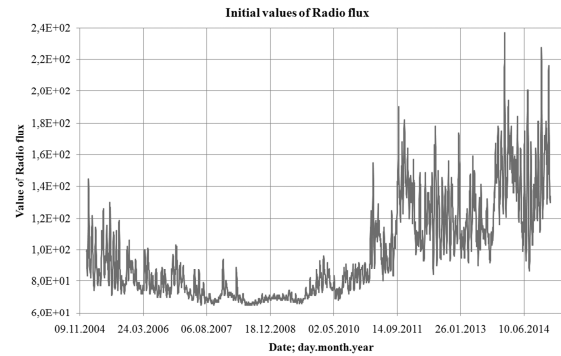


Figure 2: Initial values for index of solar activity the solar radio flux at wavelength 10,7 cm.

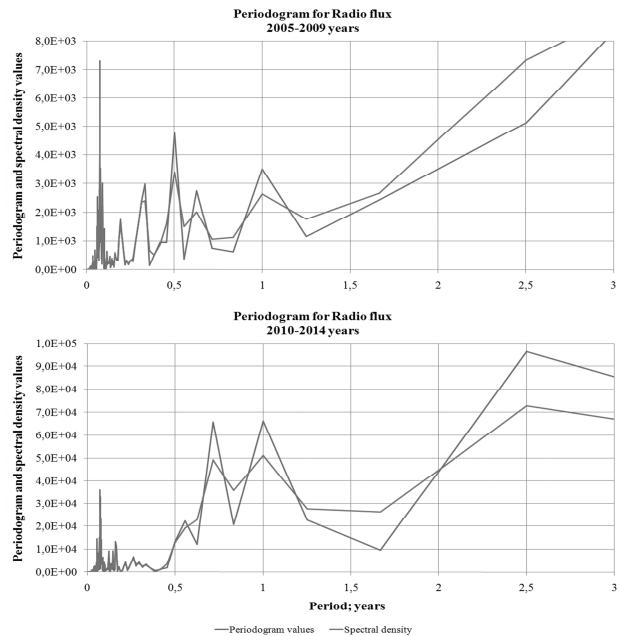


Figure 3: Periodogramm of initial values for radio flux at wavelength 10,7 cm.

#### 4.1. Dividing the data into two intervals of observations

The study period of satellites and solar and geomagnetic indexes includes phase of declining of 23–rd solar cycle, phase of rise of 24–th solar cycle. State of solar and geomagnetic activity during these periods differ significantly.

That's why observations data were divided into two periods: 2005–2009 y. and 2010–2014 y. In STATISTICA 8, using Fourier analysis, we constructed periodograms for these intervals for B–star Drag Term and five indices of solar and geomagnetic activity. An example of periodograms is shown in Figure 3.

In the resulting periodograms, for indexes of solar and geomagnetic activity, for period 2005 – 2009 y. we obtained the periods:

1. For Wolf numbers: in years (for 2005 – 2009 y. does't exist); in months (6; 3,3; 1,7; 1,2); days (28,5; 25; 21,2; 17,1; 13,4; 11,1; 8,9).

2. For the total area of sunspot groups: in years (for 2005 – 2009 y. does't exist); in months (6; 3,8; 2,4; 1,6; 1,1); days (27,7; 23; 17,2; 13,5).
3. For the solar radio flux at 10,7 cm: in years (1); in months (7,5; 6; 4; 2,3; 1,1); days (27,7; 22,8).
4. For the electron flux with energies >0.6 MeV: in years (for 2005 – 2009 y. does't exist); in months (10; 7,5; 6; 3,8; 3,2; 2,5; 1); days (26,5; 13,4; 9; 6,7; 5,4).
5. For the electron flux with energies >2 MeV: in years (2,5); in months (7,5; 6; 5; 3,8; 3,2; 1,9; 1,5; 1,3; 1); days (26,5; 20,5; 16,2; 13,9; 9; 6,8; 4,5).
6. For the planetary geomagnetic index Ap: in years (1,3); in months (7,5; 3,8; 1,9; 1,4); days (26,9; 13,5; 9; 6,7; 5,4).

In the resulting periodograms, for indexes of solar and geomagnetic activity, for period 2010 – 2014 y. we obtained the periods:

1. For Wolf numbers: in years (2,5); in months (6,7; 1,9; 1,5); days (26,1; 23,7; 21; 17,2; 16; 15,2; 13,6; 9,6).
2. For the total area of sunspot groups: in years (2,7); in months (9,1; 6,4; 3; 1,9; 1,5; 1,1); days (28,1; 27; 25,9; 24,1; 20,4; 18,6; 15,3; 13,9; 6,9).
3. For the solar radio flux at 10,7 cm: in years (2,5; 1); in months (8,6; 3,2; 1,9; 1,8; 1,5); days (26,1; 20,3).
4. For the electron flux with energies >0.6 MeV: in years (1,7); in months (7,5; 5,5; 3,7; 2,2; 1,1); days (28,1; 14,5; 12,8; 9,2; 6,7).
5. For the electron flux with energies >2 MeV: in years (1); in months (7,5; 5,5; 3,8; 2,5; 1,5; 1,2); days (28,1; 24,3; 26,1; 20,5; 17,4; 14,5; 12,8; 8,9; 7,1; 6,7).
6. For the planetary geomagnetic index Ap: in years (1); in months (5,5; 3,8; 1,9; 1,5; 1); days (28,5; 16,8; 13,3; 9; 6,6; 5,4; 4,5).

#### 4.2. Subtract of the trend component

To identify short-components, trend components were removed. In order to eliminate the influence of the trend components was subtracted the 3-rd order polynomial. In the next step was conducted frequency filtering of periodicities more than three and one years.

#### 4.3. Calculation of the spectrograms for data with subtracted trend

To identify the time of existence of periodic components used program PSELab [3]. As a result of this calculations trend periods were found (periods that do not retain their values).

For elliptic orbit satellites: from 10,2 to (=>) 9,7 days; 12=>13 days; 2,6=>1,3 month;

and for the circle orbit satellites: from 4,6=>3,7 days; 6,4=>7,2 days; 13=>11,4 days; 23=>13 days; 28 days =>1,1 month; 29,2 days =>1,2 month.

Spectrograms for the indices of solar and geomagnetic activity showed that the identified periods are present on all the studied time interval. Spectrograms for the total area of sunspot groups show periods from 5,4 to 20 days. These periods more clearly visible in the decline phase of 23-rd solar cycle.

#### 4.4. Building of multiple correlation models

One of the final stages of data processing is to build models of multiple correlation between the B–star Drag Term and indices of solar and geomagnetic activity. Building of this models consists in finding the regression and beta coefficients of model and to find multiple correlation coefficients. Models should not contain parameters that correlates with each other. Also these models must include the total number of factors influencing the studied parameter [6].

The highest correlation coefficients (between B-star and indices of solar and geomagnetic) greater than 0.7, as expected from the literature, between the B-star and radio flux at 10.7 cm, Wolf numbers and the total area of sunspot groups.

Fig. 4 and 5 show correlation between B-star and the solar radio flux at wavelength 10,7 cm for «circle» orbit and «elliptic» orbit satellites respectively.

Correlation coefficients between indices: W, Sp and F10.7 is more than 0.87. Therefore, we can't use these indexes together in the model. Thus we have built three models which we called (depending on the main influencing index): model F 10.7, model W and model Sp. The examples of models (for example model F 10.7) are shown in Table 2 and Table 3 for circle orbit and elliptic orbit satellites respectively.

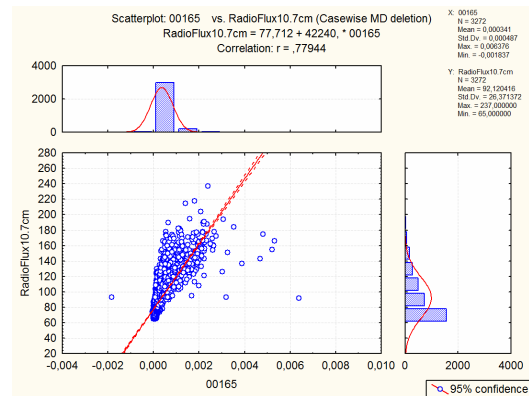


Figure 4: Graph of correlation between B-star and radio flow at a wavelength of 10.7 cm.

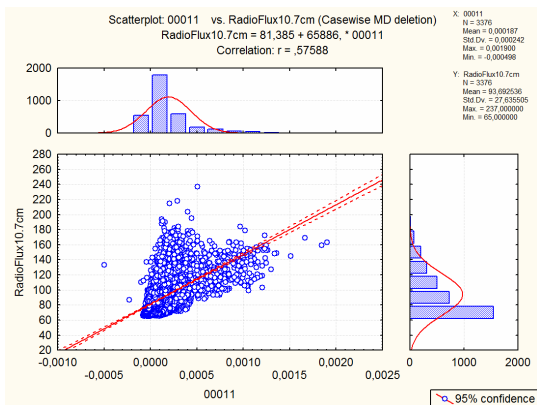


Figure 5: Graph of correlation between B-star and radio flow at a wavelength of 10.7 cm.

Table 2.

Number of satellite	Model F10.7						
	R	RadioFlux10.7cm	E>0.6 MeV	E>2 MeV	Ap Middle Latitude	Ap High Latitude	Ap Planetary
		Beta					
06212 i=98.57°	0.87	0.863265	-0.059673	0.083503			-0.021088
25860 i=97.7°	0.83	0.823517	-0.032059	0.029299			-0.070153
27700 i=97°	0.86	0.840233	-0.093921	0.109538			-0.018819
01814 i=75.9°	0.83	0.832595	-0.006108	0.018648			-0.044460
04139 i=74.03°	0.81	0.813082	-0.009609	0.022791			-0.047087
03048 i=74°	0.83	0.834077	-0.010642	0.035625			-0.034309
04579 i=73.99°	0.83	0.835709	-0.002717	0.010322			-0.042718
04922 i=65.8°	0.86	0.868181	-0.003077	0.032240		-0.042336	
12054 i=65°	0.8	0.803983	-0.001342	0.035297		-0.032477	
00397 i=58.3°	0.85	0.853947	-0.008261	0.038848		-0.047085	
00063 i=48.5°	0.85	0.842893	-0.025441	0.040645		-0.013985	
00165 i=47.9°	0.78	0.783882	-0.009629	0.015843		-0.039318	
06153 i=35°	0.74	0.754956	-0.013817	-0.008446		-0.053864	
25064 i=34.9°	0.88	0.879330	-0.005374	0.056744		-0.019261	
23757 i=22.9°	0.85	0.854784	-0.008745	0.052372			-0.052543

Table 3.

Number of satellite	Model F10.7						
	R	RadioFlux10.7cm	E>0.6 MeV	E>2 MeV	Ap Middle Latitude	Ap High Latitude	Ap Planetary
		Beta					
00932 i=81.3°	0.6	0.603455	-0.013660	0.067882			-0.025280
00721 i=78.6°	0.65	0.654942	0.026145	-0.012962			-0.028445
00746 i=60.8°	0.23	0.213755	-0.030896	0.030685	0.016173		
00829 i=60.8°	0.44	0.435915	0.011477	0.018019	0.034176		
00082 i=38.9°	0.52	0.297911	-0.460390	0.306179		-0.069210	
00016 i=34.3°	0.25	0.158849	-0.190783	0.130887		-0.001614	
00005 i=34.2°	0.25	0.179848	-0.168847	0.110631		-0.047277	
00020 i=33.4°	0.72	0.735799	0.016697	-0.018490		-0.092955	
00011 i=32.9°	0.59	0.531823	-0.139970	0.163480		0.074136	
00963 i=19.75°	0.03	0.025194	-0.015062	0.015949			0.002930

## 5. Conclusions

As a result of the calculation using the programs: OriginPro 8.1, STATISTICA 8 and PSELab have been found:

- 1) Using Fourier analysis identifies periodic components and their presence in the studied time interval.
- 2) For circle orbit satellites: in the models which include F 10.7 multiple correlation coefficient greater than 0.8, mostly for all satellite. The models which include W have the same picture as in the models of F 10.7, only the multiple correlation coefficient for the Wolf numbers slightly more than 0.7. But multiple correlation coefficient of models which includes Sp little more than 0.6, but in the last two models, the value of the beta coefficient for electrons fluxes increased significantly compared to previous models

- 3) For elliptic orbit satellites: in the models which include F 10.7 multiple correlation coefficient is slightly more than 0.6, for satellites with NORAD numbers: 00011, 00020, 00721, 00932. For other satellites multiple correlation coefficient is just above 0.2. The main contribution is making two parameters: the radio flux at a wavelength of 10.7 cm, and the electron fluxes with energies >0.6 MeV. In models which include W and Sp is the same picture as in the models which include F 10.7 only except that increases of contribution from electron fluxes with energies >0.6 MeV and the planetary geomagnetic index Ap.

Detected periods with trend probably related to the long dynamics of influence of solar and geomagnetic activity and tidal phenomena on the upper atmosphere of the Earth.

## References

1. Beletsky V.V.: The motion of an artificial satellite about the center of mass, M., 1965, 416 p.
2. Roy A.: Orbital motion, M.: Mir, 1981, 544 p.
3. PSELab [web resource] / POWER SPECTRUM ESTIMATION LABORATORY. – Access mode: <http://pselab.ru/>.
4. Kelso Ted Frequently Asked Questions: Two-Line Element Set Format, 1998.
5. Komendant V.H., Koshkin N.I., Ryabov M.I., Sukharev A.L.: 2015, *Odessa Astron. Publ.*, **28/2**, 277.
6. Mordecai Ezekiel, Karl August Fox Methods of Correlation and Regression Analysis, Linear and Curvilinear, 1966. – 560 c.

DOI: <http://dx.doi.org/10.18524/1810-4215.2016.29.85231>

# PROBLEM OF MISTAKES IN DATABASES, PROCESSING AND INTERPRETATION OF OBSERVATIONS OF THE SUN.

## II. SOLAR FLARES

N. I. Lozitska

Astronomical Observatory of Taras Shevchenko National University of Kyiv,  
Observatorna 3, Kyiv, 04053, Ukraine, [nloz@observ.univ.kiev.ua](mailto:nloz@observ.univ.kiev.ua)

**ABSTRACT.** The contribution of space-based observations of solar flares in the database for the past 50 years has increased significantly, almost completely replacing the ground observations. The statistical parameters of the temporal distribution of solar flares, obtained using ground-based and space-based observations, differ significantly. We investigated the reasons for these differences to be taken into account in the study of flare activity of the Sun in the solar activity cycles 21-24.

**Keywords:** Sun: – Solar Activity, Observations, Solar Flares, Solar Proton Events, correction the datasets.

### 1. Introduction

Database users often don't question themselves about representativity of material there, about the sunflares in particular, even though one can almost always find an answer from technical documentation or primary arrays of observations. Fairly often the gaps in observation days influence the research conclusions essentially. Statistical processing of non-uniform series sometimes has been causing incorrect results about influence of direction towards the galaxy center or position of Earth, Jupiter and Saturn on flare production in active areas.

### 2. Data of Solar flares

Series of ground-based patrol optical observations of solar flares is longer than space one. Data about flares in H $\alpha$  line from 1965 to 2008 there was composed (grouped together) earlier from reports of ten observatories in Database NGDC NOAA and recently in this database there were published results of observations of 24th cycle of solar activity for appending to this series. Based on it, we have built continuous row of annual number 176357 flares in H $\alpha$  line (1965–2016) which contains 117910 flares in period 1976–2016. Continuous uniform series of X-ray flares was possible to build only from 1976 [1]. It contains 54682 solar flares of C, M, X classes, from which 4845 flares are of classes M and X. Fraction of all optical flares are associated with X-ray flares of weaker energy class B, however amount of these flares we haven't been considering because until 1983 they were not being recorded.

### 3. The time variations of flares number

The comparison of amount of observed optical and X-ray solar flare events (SFE) is shown on Fig. 1, from which we can see, that until 2000 year number of terrestrial observations of flares (by patrolling in spectral line H $\alpha$ ) was twice as much as total number of observations of X, M and C flares by spacecraft, and even more than that in first half on 21st cycle of solar activity. During the last years number of terrestrial observatories which conduct the patrolling of flares has been decreased to four and amount of space data has become equal to that of terrestrial. Partially because of this, and not only due to century changes in solar activity, we see the larger decrease of amount of observed optical flares (by 4 times) than X-ray ones (by 2 times) during 21–24 cycles of solar activity.

To evaluate influence of astroclimate season changes on number of terrestrial registered solar flares a comparative analysis of variations of monthly average number of flares during numerous years for terrestrial and space observations (figure 2) was conducted.

From figure 2 we can see season change of frequency of optical flares by terrestrial observations (in july–august there are 20% more observed flares, than in February, the accuracy of difference existence is over 95%) compared to equal by error margin frequency of X-ray flares by satellite observations. Most observatories are situated in north hemisphere, hence in summer optical observatories register more flares.

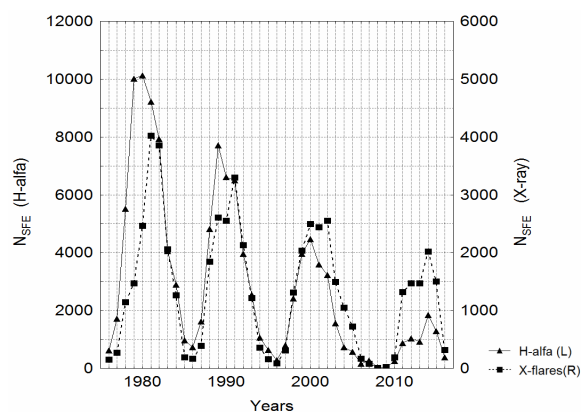


Figure 1: Annual amount of registered solar flare events

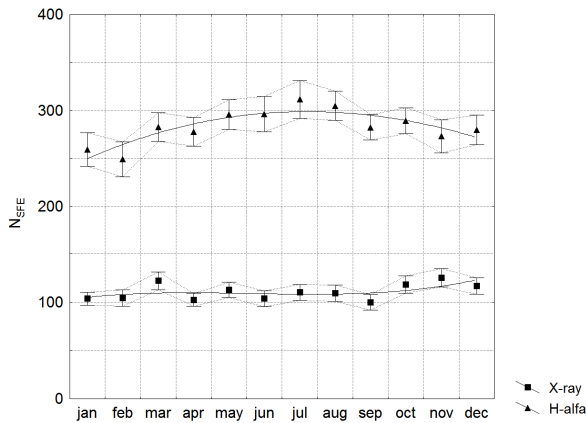


Figure 2: Distribution of number of observed optical solar flares from 1965 to 2015 and X-ray flares – from 1976 to 2016.

Analogically inter-year fluctuations of astroclimate may compromise the uniformity of optical observations series.

#### 4. Data of SPE number

Processing of series of solar proton events data and solar flares showed, that almost every 10th visible solar flare on the solar disk of class M or X (which has electromagnetic energy flux exceeding  $10^{-5}$  W/m<sup>2</sup> in maximum), is source of solar proton events. Solar proton events (solar particle events–SPE) are proton fluxes, more than 1 pfu (1 proton per cm<sup>2</sup> sr) with energies > 10 MeV at distance of 1 a.u., which are registered by orbital spacecraft after emission of high-energy neutrons and protons by powerful solar flares or particle acceleration on front of shockwave after coronal mass ejections (CME). Significant part of SPE from powerful flares are not registered by orbital spacecraft because it travels in interplanetary space at large distances from Earth.

We have built series of annual amount of SPE, based on catalogues of electronic library WDC from 1970 to 2009 and using Database SPDF NASA for 2010–2016. The list of reliably confirmed SPE in electronic library WDC contains 419 events from 1976 to 2006 yy, it is almost twice as large as list of events in NGDC NOAA base (225 SPE for the same time frame). There is no data for 24th cycle of solar activity in WDC catalogues yet, so we used the results of satellite measurements from NASA SPDF database, which contains 357 events from 1970 to 2016, and 44 events from 2010 to 2016.

Statistical analysis showed that correlation relation index of annual SPE amount with optical flares in H $\alpha$  line ( $r = 0.75$ ) is less, then with total amount of X-ray flares of C, M and X classes ( $r = 0.84$ ). Relation of number of SPE with sum of X-ray flares of classes M and X is the strongest ( $r = 0.88$ ).

#### 5. Reconstruction of true number of flares

Though this is strong statistical connection, it should be noted that series of number of X-ray solar flares received from various spacecraft of GOES series, so it is necessary

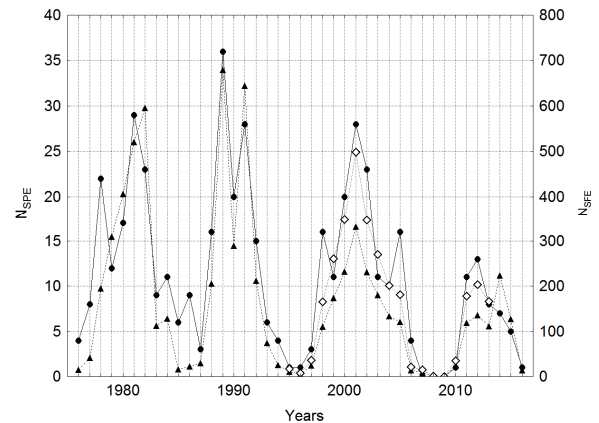


Figure 3: 11-year cycles of solar activity from 21st to 24th in number of SPE and solar flares of classes M and X. On left Y axis—annual amount of SPE (circles), on right—annual amount of M and X-flares (triangles) and the corrected curve of flare number during 1996–2013 is shown (rhombs).

to confirm its uniformity. To do this we compare it with annual amount of SPE caused by powerful flares.

From figure 3 we see, that during last two cycles of solar activity the plot of amount of SPE goes 1.5 times higher than plot of amount of solar flares. Since SPE are caused by these same flares, there cannot be such significant difference between 23–24 cycles of solar activity and 21–22. Most likely, the lowered since 1995 evaluation of amount of powerful solar flares appears due to inaccuracies in calibration of receiver of X-ray radiation, which should be considered in further work. The conducted recalculation of annual amount of M and X flares after correction of boundary energy for their classification according to correction indices, set for satellites GOES 8–GOES 15 (Database NGDC NOAA). Results of recalculation are shown on figure 3 by rhombs.

Further work on analysis and correction of data concerning flare activity of the Sun is necessary in catalogues and electronic sources, also reevaluation of research published earlier on number of flares at various time intervals. In particular, the conclusions of series of publications concerning low solar activity in 23rd cycle were incorrect.

*Acknowledgements.* We express our gratitude to all the observers, authors of catalogues and data bases

#### References

- Database SPDF NASA (Space Physics Data Facility, Goddard Space Flight Center, OMNIWeb), <http://omniweb.gsfc.nasa.gov/ow.html/>
- Database NGDC NOAA (National Geophysical Data Center), <ftp://ftp.ngdc.noaa.gov/STP/space-weather/solar-data/>
- Electronic library WDC (World Data Centers) [http://www.wdcb.ru/stp/online\\_data.ru.html#ref113\\_r/](http://www.wdcb.ru/stp/online_data.ru.html#ref113_r/)  
(Catalog of Solar Proton Events 1970–1979, 1982, 184 c.; Solar Proton Events. Catalogue 1980–1986, 1989, 159c.; Catalogue of Solar Proton Events 1987–1996, 1998, 246c.; Catalogue of Solar Proton Events in the 23rd Cycle of Solar Activity (1996 – 2008), 2016, 740 c.)

DOI: <http://dx.doi.org/10.18524/1810-4215.2016.29.85232>

# MODERN CCD OBSERVATIONS OF SELECTED MINOR PLANETS FOR THE CONNECTION OF DYNAMIC AND KINEMATIC COORDINATE SYSTEMS

A. Pomazan, N. Maigurova

Research Institute “Mykolaiv Astronomical Observatory”,  
Observatorna 1, 54030, Mykolaiv, Ukraine, [antpomaz@gmail.com](mailto:antpomaz@gmail.com)

**ABSTRACT.** One of the methods of determining the orientation parameters of the dynamic and kinematic coordinate systems is to use of long-term series of ground-based observations of selected asteroids. For achievement of the best accuracy of the link parameters the high precision and uniformly covering the asteroids orbit observations are necessary. The analysis of the available observations of selected asteroids was made with usage MPC database. The value of the true anomaly at the moment of observation was selected as parameter of orbit covering. It is shown that there are orbital segments without precise observations. This was taken into account when forming the observational list for the telescope KT-50 (Mobitel complex). 1596 positions of 50 asteroid have been obtained during 2014-2016. The comparison of the calculated positions with ephemeris obtained by on-line service HORIZONS was made. The RMS errors of the differences (O-C) were about 0.1 arcsec for both coordinates. The comparison of the obtained results with observations of the some ground based observatories and Hipparcos satellite shows high accuracy and uniformity of Nikolaev asteroid observations.

**Keywords:** astrometry, CCD observations, asteroids

## 1. Introduction

The International Celestial Reference System (ICRS) was adopted by International Astronomical Union (IAU) as new reference system in 1997. The space catalogs Hipparcos and Tycho were chosen as practical sky realization of this system in optical and near-infrared bands (HCRF). 48 asteroids have included in final list of objects to be observed by ESA satellite Hipparcos. They were regularly observed during 37 month of missions. 2282 astrometric positions of 48 asteroids reduced in parallel with the stars in the Hipparcos reference system. The one of scientific objective for these observations was obtaining of the link between dynamic and kinematic reference frames (Hestroffer, 1995). However, the results of determination of the link parameter using only these observations were not successful for some reason (Bougeard, 1995, 1997). The orientation of the dynamical ephemerides with an error less than several tenths

of mas was determined by the complete set of VLBI observations of spacecrafts (Pitjeva, 2011). It should be noted, that small period of these observations allow to get only orientation angles. It is need to have long series of observations for obtaining the rates of change of these parameters. In addition, CCD observations, which have widespread use in optical astronomy since 1990, could not be processed directly with Hipparcos catalog due to small fields of view. There were more than 30 catalogs are used as reference for astrometric reductions of asteroids. But each of these HCRF realizations has its own errors in stars positions and proper motions and the orientation of the catalog reference frames itself can also have errors. The dynamical system that are determined by the theories of motion of major planets and asteroids either didn't take in account the effect of all known asteroids due to the lack of certainty data on their masses.

Therefore, determining the mutual-orientation parameters of these frames and the rates of their changes still remains an important modern problem.

## 2. Program of observations

Currently the Minor Planet Center (MPC, <http://www.minorplanetcenter.org/iau/mpc.html>) contains the most full asteroid position database that can be used for study of mutual orientation of dynamic and kinematic systems. The problem of connection of the dynamic and kinematic coordinate system needs the right choice of the asteroid list. The observational programs of these asteroids have been discussed since last century (Numerov, 1936; Batrakov, 1990, 1999). The main selection criterion is the availability of high-precision long series of observations with a uniform filling of a few turns of the orbit.

The KT-50 observational program is combined on the base of the next overlapping lists:

- a) list of 48 asteroids that have been included in Hipparcos program. There are 2282 positions in MPC with code 248 (Hipparcos);
- b) list of 343 asteroids, whose masses are included in parameters of JPL dynamical model of motion;

c) list of 15 selected minor planet, that was adopted by IAU for observations to determine the orientation of the stellar reference frame relative to the dynamical one. Photographic observations of “h”-level accuracy of 12 asteroids from this list have been made at Nikolaev Zonal astrograph during more than 30 years.

There were selected 308 asteroids taking into account the visibility conditions and the characteristics of the KT-50 telescope. For all of these asteroids the samples with positions were chosen from MPC database. The majority of these asteroids have a long history (of over 100 years) of observations. It should be noted, that positional accuracy is very different depending on epoch of observations, place of observation, completeness of astrometric reduction etc. The evaluation of the accuracy of individual observations in one period was obtained with usage of the file residuals.txt available at MPC web-site (<http://www.minorplanetcenter.net/iau/special/residuals.txt>). The analysis of the uniformity of the distribution of observations along the arc of the orbit was performed for all asteroid positions in samples and only for positions for which the value of root mean square error (RMS) of the (O–C) differences in residuals.txt file does not exceed 0.3".

As a parameter which indicates the uniformity of filling orbit by observations was selected the value of true anomaly. True anomaly at epoch defines the position of the orbiting body along the ellipse at a specific time (the "epoch"). The values of true anomaly were calculated with on-line service HORIZONS of Jet Propulsion Laboratory (<http://ssd.jpl.nasa.gov/horizons.cgi>).

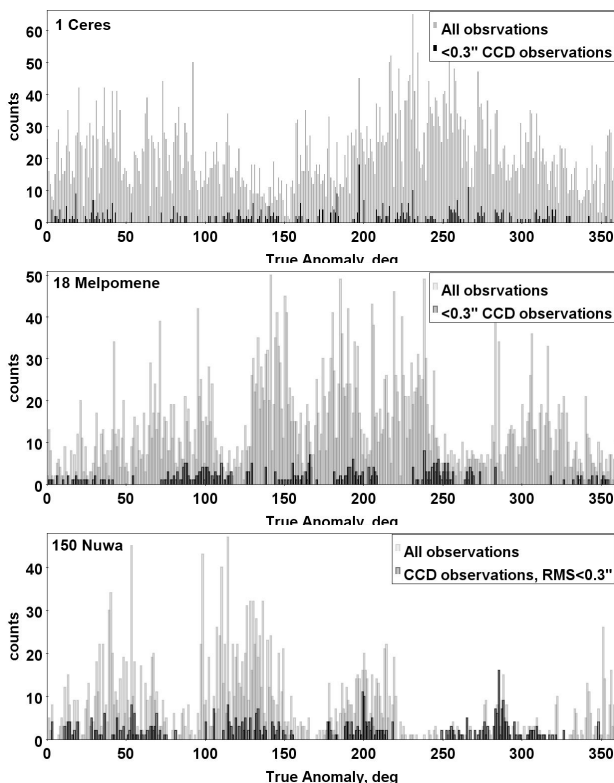


Figure 1: The distribution of the true anomaly value for a) (1) Ceres, b) (18) Melpomene, c) (150) Nuwa. Grey color correspond all MPC positions, black – only selected positions for which mean annual RMS of (O–C) differences less than 0.3".

The histograms of true anomaly distributions for (1) Ceres, (18) Melpomene and (150) Nuwa asteroids are presented in Figure 1 as an example. It is easy to notice, there are segments of the orbit not filled with observations, especially in the histogram corresponding high-precision observations. These so-called “windows” are take in account for creation of observational program. It should be note, the majority of high-precision positions relate to CCD-observation obtained after 1990 year, so Figure 1 shows necessity to continue accurate optical observations of the asteroids from foregoing lists.

### 3. Observations and Reductions

The observations of selected asteroids were carried out at telescope KT-50 (Mobitel complex) of Nikolaev Astronomical Observatory (observatory code 089). The telescope KT-50 (D=0.5 m, F=3.0 m) has begun regular observations of selected asteroids and NEO objects since 2011 (Ivantsov, 2012). The CCD camera Alta U9000 (3056x3056 pix, 12x12 mkm<sup>2</sup>) of Apogee Imaging Systems allows us to get frames with 42.0'x42.0' field of view with 0.83"/pix of scale. The observations were carried out in time delay and integration mode with time of exposure 60-85 seconds using R filter close to R photometric band of Johnson-Cousins-Bessel system. The astrometric reductions of observations were made using Astrometrica (<http://www.astrometrica.at>) software. Model of linkage of 4th order polynomial between measured and tangential CCD coordinates was chosen. The UCAC4 catalog was used as reference catalog for processing of all data.

1596 positions for 50 selected asteroids were measured from the observations during 2014-2016 at the telescope KT-50. The equatorial coordinates of the asteroids at the epoch of observation were obtained as result of standard astrometric reductions. We have used the catalogue UCAC4 as the reference astrometric catalog for reduction.

We have made the comparison of observed positions (O) with the calculated ephemeris (C) provided by on-line service HORIZONS and have calculated the residuals (O–C) in both coordinates. Since the observational time for a series of frames for one object usually did not exceed 20-40 min, the object position in the series of frames obtained during one night were calculated with a constant set of reference stars and practically in one point of the orbit. These circumstances exclude the systematic component of error connected with the reference catalog and the orbital motion and allow us to use the mean RMS of the (O–C) differences for one series of observations as an evaluation of the internal accuracy of our measurements. The mean internal accuracy of a single position is 0.061" in right ascension and 0.055" in declination for the selected asteroids in range of 10.5-15.5<sup>m</sup>. It's a little better than normal mean accuracy because the selected objects are bright enough, which made it possible to obtain the asteroid images with high signal to noise ratio. The obtained results of (O–C) differences in right ascension and declination and their RMS for some asteroids with long series of observations are given in Table 1.

To estimate external accuracy of our observations and to compare our results with other observatories open database AstDys-2 (<http://hamilton.dm.unipi.it/astdys/>) was

Table 1. Differences (O–C) and their RMS for the asteroids with long observation series.

Asteroid name	Number of images/series	Time period		RA		Dec		mag
		begin	end	O–C, "	$\sigma_{\alpha}$ , "	O–C, "	$\sigma_{\delta}$ , "	
113 Amalthea	114/8	05-07-2015	26-09-2015	0.039	0.059	-0.001	0.054	11.59-12.58
*129 Antigone	29/2	18-03-2014	21-03-2014	0.078	0.027	0.024	0.03	11.81-11.83
334 Chicago	149/11	02-07-2014	30-10-2015	0.031	0.059	0.033	0.052	13.2-14.1
*349 Dembowska	18/2	18-03-2014	21-03-2014	0.009	0.044	0.002	0.023	10.6-10.74
*451 Patientia	15/1	21-03-2014		-0.065	0.046	0.015	0.041	11.84
*704 Interamnia	30/2	18-03-2014	21-03-2014	0.081	0.042	-0.033	0.032	11.77-11.87
714 Ulula	247/4	03-08-2014	31-09-2014	0.020	0.048	0.079	0.036	13.74-14.08
778 Theobalda	80/6	02-08-2014	30-10-2014	0.019	0.058	0.004	0.047	14.45-15.18
1171 Rusthawelia	60/4	12-08-2014	30-10-2014	-0.006	0.044	0.061	0.041	13.61-14.33
909 Ulla	59/4	01-04-2014	26-07-2015	0.034	0.063	0.088	0.048	13.63-14.71
<b>Average</b>					<b>0.049</b>		<b>0.040</b>	

\* The asteroids are from list of observational program of Hipparcos space mission.

Table 2. Differences (O–C) and their RMS for the samples selected by observatory code.

Observatory code	Number of asteroids	Number of observations	Time period		RA		Dec	
			begin	end	O–C, "	$\epsilon_{\alpha}$ , "	O–C, "	$\epsilon_{\delta}$ , "
*089 Nikolaev	50	1596	03-2014	4-2016	0.023	0.090	0.048	0.101
248 Hipparcos	48	5096	11-1989	03-1993	-0.071	0.114	-0.000	0.073
673 Table Mountain Observatory	48	3812	05-1997	07-2016	-0.004	0.074	0.003	0.059
689 U.S. Naval Observatory, Flagstaff	48	18304	10-1994	05-2014	-0.006	0.082	-0.002	0.089
999 Bordeaux-Floirac	17	202	04-1997	08-2005	-0.034	0.068	-0.005	0.098

\* Data were calculated over all observed asteroids for 2014-2015 at KT-50 telescope of Mobitel complex RI NAO.

used. AstDys-2 contains dynamical information for asteroids from MPC database including differences (O–C) for each position. The samples of records corresponding to observations of the Hipparcos program asteroids were chosen from AstDys-2 for the some good in astrometric sense observatories. Only CCD observations are taking in account for calculations. The observations of the all program asteroids obtained during 2014-2016 years were used for Nikolaev observatory table data. The statistical comparison results are given in Table 2. The mean values of the (O–C) differences and their RMS were calculated with usage 3-sigma criteria. The number of outliers is not exceeds 3% of the total samples.

It can be seen that external accuracy of the modern ground-based CCD observations not worse than Hipparcos accuracy was. The mean values of the external accuracy for Nikolaev observations are 0.09" and 0.10" in right

ascension and declination, respectively. This value is comparable with the precision of the best ground-based positions definitions.

### Conclusions

The program of asteroid observations to determine the orientation parameters of the dynamic and kinematic coordinate systems was formed. It takes into account the uniformity of the distribution of already available observations along the orbit arc.

The database of 1596 accurate topocentric positions for 50 asteroids was obtained. Mean precision about 0.1" in both coordinates were achieved.

The comparison of the obtained observations with observations of space mission Hipparcos and some ground-based astronomical observatories was made. The results have

been shown the high level of accuracy of the KT-50 Nikolaev observations that is comparable to Hipparcos level of accuracy and the other ground-based observatories.

*Acknowledgements.* This research has made use of the on-line service HORIZONS and databases MPC and AstDys-2.

#### References

- AstDys-2, <http://hamilton.dm.unipi.it/astdys/>.  
Astrometrica, <http://www.astrometrica.at>.  
Batrakov Yu.V. et al: 1990, *IAU Symp.*, **141**, 69.  
Batrakov Yu. V. et al: 1999, *A&A*, **352**, 70.  
Bougeard M.L. et al.: 1995, *A&A.*, **304**, 176.  
Bougeard M.L. et al.: 1997, *ESA Symp.*, **402**, 165.  
Hestroffer D. et al.: 1995, *A&A*, **304**, 168.  
Ivantsov A. et al: 2012, *OAP*, **25**, 66.  
JPL's On-Line Solar System Data Service,  
<http://ssd.jpl.nasa.gov/horizons.cgi>.  
Minor Planet Center,  
<http://www.minorplanetcenter.org/iau/mpc.html>.  
Numerov B.: 1935, *AJ*, **45**, 105.  
Pitjeva E.V. et al: 2011, *JSR2010 Proc.*, 49.

DOI: <http://dx.doi.org/10.18524/1810-4215.2016.29.85234>

## THE OBSERVATIONS OF ARTIFICIAL SATELLITES AND SPACE DEBRIS USING KT-50 TELESCOPE IN THE ODESSA UNIVERSITY

Shakun L., Koshkin N., Korobeynikova E., Melikyants S., Strakhova S., Terpan S., Burlak N., Golubovskaya T., Dragomiretsky V., Ryabov A.

Astronomical Observatory of Odessa Mechnikov University, Odessa, 65014 Ukraine.

*nikkoshkin(a)yahoo.com*

**ABSTRACT.** In paper the equipment, images analysis techniques in the frame and the method of the satellite brightness estimation in the standard photometric system are describes. Within two years, on the KT-50 telescope were obtained measurements of about two hundred objects in more than 2,000 passages. The results of statistical analysis of actual data observations array in 2015 and 2016 are given.

### 1. Introduction

The observation of celestial bodies in near-Earth space solves two main tasks:

1. The space control, ie tracking and monitoring of active and inactive satellites and space debris in order to ensure security and the possibility of space flight (as a component of "space situational awareness").

2. The development of a entirely scientific ideas about the motion of bodies in near-Earth space, that is the nature of the forces that determine the movement of these bodies. Accumulation of the high quality observations allows you to build better models of the motion of bodies and analyze the nature of motion of bodies and the factors influencing this movement.

To control the movement of bodies in near-Earth space are apply various methods for their observation. Co-processing of these observations may allow to improve significantly the results of the study of these objects despite the significantly different methods of monitoring the same space objects. However, for the successful integration of various observations it is very important to know the particularity and accuracy of this.

On Earth orbits there is a significant number of defunct satellites that can not be observed by laser ranging. In addition, most of the space objects are an different fragments of previously launched artificial bodies, which also can not be monitored by laser ranging means. Therefore, they can be observed by active radars and passive optical telescopes. The advantages of expensive radars is the mass character of observations, all-weather, the continuity and the ability to measure the distance to object. The advantages of the optical means are an lower energy consumption and lower cost of the observation complex, better angular resolution, and passivity

(stealthy). This allows you to quickly deploy a large number of optical observation means (Shulga et al., 2015).

### 2. Objective

In the case of optical observations of space objects typically use two main strategies. The first is the satellite observation during short intervals, and accordingly the short arc (staring mode) (McGraw et al., 2015). The second strategy is the continuous tracking of the satellite along its apparent path (tracking mode) (Gasdia et al., 2016; Shakun & Koshkin, 2014). The first strategy provides significant savings in observation time for MEO and GEO objects which have a low apparent speed, at an equivalent the object orbit accuracy determination. For low-orbit objects whose apparent movement speed is high, the first strategy does not provide any significant advantages. Moreover the second strategy provides an opportunity to obtain long and continuous photometric observations and allows to obtain continuous series of pointing data, which in turn provides information on the standard deviation and local trends systematic differences between the model and satellite motion.

This paper discusses the observations of space objects received in the tracking mode. The observations were made during 2015-2016 in the Institute "Astronomical observatory" of the Odessa National Mechnikov University. This paper presents an overview of the astrometric and photometric observations, the method of obtaining and processing of observations, as well as statistics characteristics of the measurements.

### 3. Equipment

The KT-50 telescope (Fig. 1) is equipped with a digital angle encoders on axes and GPS-receiver for time measurements. In main focus of the telescope mounted CCD camera Watec-902H2 Sup, working in the TV standard mode of 25 frames/s interlaced (50 fields per second) to record a video file with the satellite image. For focal distance of 2.0 m field of view is about 12x9 arcmin. The scale of frame 768x576 is equal about 1 arcsec per pixel.



Figure 1: (Right) – Alt-azimuthal KT-50 telescope (photo); (Left) – Optical scheme of telescope.

The in-frame background stars are blurred when tracking the satellite. Therefore, the exposure accumulation can not be used to extract images of faint stars above the level of the sky background. To detect the faint stars over the noise level the low-pass filtering of the image is used.

This filter is constructed as a result of the convolution of two filters: low-pass Gaussian filter (with the width equal  $h$  and a standard deviation equal  $h/3$ ) and the  $\Pi$ -shaped filter along the direction of the satellite motion (with the length equal to the anticipated shift of the satellite during frame exposure). After filtration, the standard deviation of the noise decreases by 2 times, which makes it possible to identify additional faint stars and a blur of the image stay moderate. Limiting magnitude of detected moving objects is equal to 11m in the V-band (at an average angular speed of the telescope motion).

To determine the time of the mid exposure we using an original technique. It consists in coding of second pulses of GPS-receiver and mixing them into a video stream (Dragomiretsky et al., 2013; Shakun & Koshkin, 2014).

In this case, the random error in the determination of registration time is less than 0.0001 seconds. To estimate the systematic shift between the time of the middle of frame exposure and the time of his transfer to the video stream, we use a comparison of the measured coordinates of the satellites and its ephemerides by ILRS – international laser ranging network (Kara, 2009/2010). An estimate of the systematic shift was about 0.01 seconds. This result agrees well with the analysis of the timing diagrams of video camera Watec-902H2 Sup (Dragomiretsky et al., 2015).

#### 4. Processing of video sequences

All of the observations in this study were obtained in the video mode, the exposure duration 0.02 seconds. Method of determining the coordinates of objects in frame is described in early paper Shakun & Koshkin (2014). Estimation of the standard deviation of the object placement in the frame is in the range of 0.3 pixel for objects with high signal to noise ratio up to 0.9 pixel for objects with a signal to noise ratio of less than 3.

The determination of topocentric equatorial coordinates of the star in the reference catalogue system (J2000.0) is performed as follows.

1) In the frames containing three or more star-like objects is performed the identification with the objects configuration in catalogue (in the vicinity of the sight direction). If among the star-like objects in the frame SO can be isolated, its image is erased before the configuration identification.

2) For all frames, in which it possible to identify two or more objects with a reference stellar catalog are computed corrections to the sight direction of the telescope.

3) The slope of the frame coordinate system was specified always if identification by 3 to 5 stars. Are specified the coefficients of the transform of the frame to the celestial coordinate system in the plane if a more than 6 objects was identified.

4) The corrections to the telescope sight direction are smoothed by approximating high rigidity cubic spline.

5) Are specified the sight directions for all frames.

6) Re-processed all frames. The SO' position in the current frame is predicted based on the information about the its places in several previous frames.

7) For frames in which is possible to identify at least one star-shaped object with a reference catalogue the estimate topocentric coordinates of the satellite was done based on the average of the coordinate system in the frame. (SO previously deleted on all frames).

All obtained topocentric coordinates of satellite was approximated with use Kepler or SGP4 orbit. Erroneous estimates of the satellite coordinates are rejected.

#### 5. Method of photometric measurements processing

Method of initial processing of satellite photometric observations using analog CCD-camera thoroughly described in the (Shakun & Koshkin, 2014). The brightness of all star-like objects in images is estimated in terms of luminance volume. Transformation to the magnitudes is performed as follows.

The estimates of photometric characteristics of satellite based on comparison with measurements of catalog stars. The process can be divided into three stages. First – a linearization of the measured brightness scale. Second – a determination of the extra-atmospheric magnitude of all observed (measured) objects. Third – the transformation of the objects magnitude in the 'hardware' photometric system to the standard photometric system.

The measured brightness of all the stars in dependence on the catalog magnitudes is not linear, and to the scale correction are use the following formula:

$$m = a * \left( 2.5 \lg \frac{Vol}{const} \right)^2 + b * 2.5 \lg \frac{Vol}{const} - c ,$$

where *Vol* – "volume" of point source image on the CCD frame, *m* is its instrumental magnitude obtained using constant:  $a = -0.188001$ ,  $b = 0.563329$ ,  $c = 0.587$ ,  $const = 280000$ , which values obtained in advance.

The obtained instrumental magnitudes are distorted by absorption in the atmosphere and must be corrected by reduction to extra-atmospheric magnitudes. For this are determined a spectral extinction coefficient. For broadband photometric system, as our case, there is a dependence of the atmospheric extinction from the energy distribution in the spectrum of the star and its color-indeces.

Given these factors, the formula for atmospheric extinction is a complex function, which dependent also on the air mass  $M(z)$  and color-index  $(B-V)$  of the object and can be represented by the formula:

$$m = m^o + (K_0 + \gamma(B-V))M(z) + (K_1 + \tau(B-V))M^2(z),$$

where  $K_0$  is the coefficient of extinction. To determine coefficients  $K_0$ ,  $\gamma$ ,  $K_1$ ,  $\tau$  we used the method of successive approximations. By usage these coefficients was calculated of the extra-atmospheric magnitudes of 275 stars that measured in our photometric system.

However, change the sensitivity of a detector, temperature and other factors are lead to change of photometric system. Even more it refers to measurements taken at different times in different observatories using different equipment. This requires

to carry out the transformation of the our photometric system to some standard system. The relations between the photometric systems is generally regarded as a function of magnitude and color-indeces  $C^i$ :

$$m_1 = f(m_2, C_2^1, C_2^2, \dots, C_2^n).$$

In our case, photometric system is the wide not-standard band, so we will use conversion rates to standard V system. The measurements and calculations showed that relationship between the magnitudes of the standard photometric system ( $m_v$ ) and magnitudes of our system ( $m^o$ ) is close to the linear. Therefore we made the transformation using the following relationship:

$$m_v = Q_0 + Q_1 m^o + Q_b (B - V) + Q_r (V - R).$$

The solution of system equations for all the stars having the extra-atmospheric magnitudes give us the transformation coefficients  $Q_0$ ,  $Q_1$ ,  $Q_b$ ,  $Q_r$ . We find maximum spread of  $m_v$  is  $\pm 0.1$  mag, and standard deviation – 0.05 magnitude. These values are satisfactory for CCD photometer with sensor that works in TV-mode.

Thus, this relationship allows to determine of extra-atmospheric magnitude of artificial satellite in the standard photometric system V. For this as a color-indeces of satellite the solar color-indeces was used. The compelled assumption is accepted the satellite color are "gray" on average, which of course there is wrong, but distort the light curve of satellite insignificantly.

The final step to obtain the standard light curve of satellite, regardless of the distance to it, is "ranging" to a standard distance of 1000 km

$$m_v^{1000} = m_v - 5 * \lg R + 15 .$$

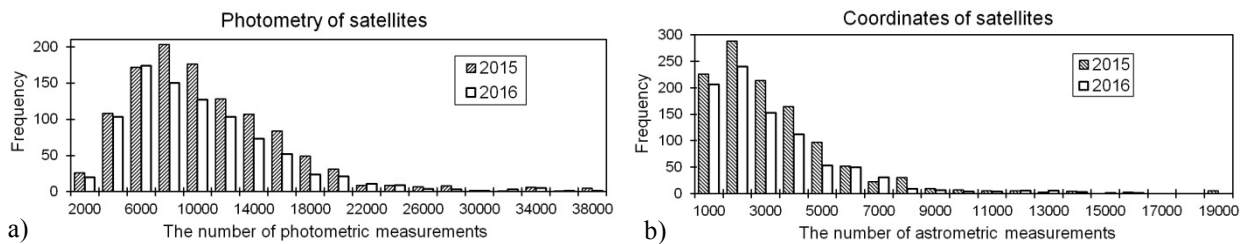


Figure 2: (a) – The frequency distribution of the photometric measurements number during single pass. (b) – The frequency distribution of the number of pointing measurements of satellite during single pass (in 2015-2016).

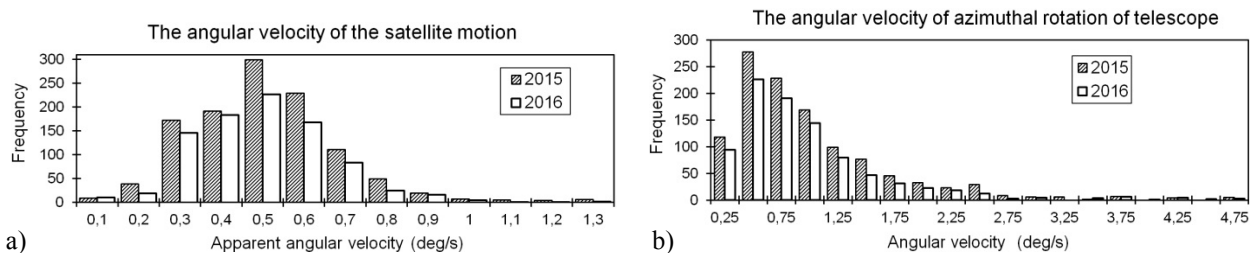


Figure 3: (a) – The frequency distribution of the maximum angular velocity of targets in the culmination. (b) – The frequency distribution of the maximum angular velocity of telescope in the azimuth movement.

## 6. Overview observations in 2015-2016

Below, are provide a brief general information about SO observations received in the past two years. In 2015, on the KT-50 telescope the observations of 182 targets in 1133 passages were obtained. Among them, 136 targets is a different payloads observed in 929 passages, and 46 is the last stages of vehicles (r/b), observed in 204 passages. In 2016, the observations of 157 objects were obtained in 974 passages during 65 nights.

To characterize the observation process, we consider some statistical parameters of the total array of the measurements in the 2015 and 2016. Fig. 2,a shows the frequency distribution versus the length of the brightness' arrays obtained in one pass. That is, the length of the photometric arrays ranged from zero to 2000 measuring in approximately 25 passages. But more often (in 195 passages) the number of measurements of the brightness during one passage was from 6000 to 8000 in 2015, and from 4000 to 6000 measurements in the 174 passages in 2016. Fig. 2,b shows the frequency distribution versus the number of astrometric measurements in the one pass. Since the background stars can not be measured in every frame of the video sequence, the number of SO coordinate measurement is substantially smaller than the photometric measurement, and the maximum of distribution is in the range from 1000 to 2000 measurements for both periods.

The KT-50 telescope is the specialized high-speed device, accordingly are observed among us to many objects moving at low altitudes above the Earth's surface. The distribution of the maximum of apparent speeds for passage to characterize the satellite speed in Fig. 3,a shown. As can see, most of the apparent angular velocity in the culmination is between 0.4 to 0.5 degrees per second, and in extreme cases exceed 1.2°/sec. However, for a biaxial mounting important characteristic is the maximum speed of telescope movement on one of the coordinates. Fig. 3,b shows the observed frequency distribution of maximum angular velocity of azimuthal telescope movement. In most cases (nearly 250 passages per year) in our observations this rate ranged from 0.25 to 0.5 degrees per second. But in many passages of the rotational speed of the telescope reaches 2.5 degrees per second, and in rare cases – 4.75 degrees per second. This index shows the limiting capabilities of the telescope for tracking of lowest LEO.

## 7. Conclusion

Tracking mode does not involve mass monitoring of many LEO space objects. The purpose of these observations to obtain very precise measurements of the position of the satellite (space debris) and its brightness throughout the visible arc over the observation point. These measurements can be used later to refine the orbit of the satellite and to development of movement theory considering their own rotation. The precise measurement of time is an important component of the high-quality measurements of the position and brightness of satellite. In this paper, images analysis techniques in the frame and the method of the satellite brightness estimation in the standard photometric system were describe. Within one year on the KT-50 telescope are always obtained a measurements of about two hundred objects in more than 1,000 passages. The results of statistical analysis of actual data observations array in 2015 and 2016 are given. This project was supported by the Ministry of Education of Ukraine, and, in part, with the support of the Main astronomical observatory of NAS of Ukraine.

## References

- Dragomiretsky V., Koshkin N. et al.: 2013, in *Bulletin of Ukrainian Earth Orientation Parameters Laboratory*, **8**, 75.
- Dragomiretsky V., Ryabov A., Koshkin N.: 2015, *Odessa Astron. Publ.*, **28/1**, 10.
- Gasdia F., Barjatya A., Bilardi S.: 2016, in *Adv. Maui Optical and Space Surveillance Technologies Conf. (AMOS)*, Hawaii, USA, Sept. 20-23 2016. (<http://www.amostech.com/TechnicalPapers/2016/Gasdia.pdf>)
- Kara I.V.: 2009/2010, *Odessa Astron. Publ.*, **22**, 20.
- McGraw J., Zimmer P., Ackermann M.: 2015, in *Adv. Maui Optical and Space Surveillance Technologies Conf. (AMOS-2015)*, Hawaii (USA), Sept.15-18 2015. ([http://www.amostech.com/TechnicalPapers/2015/Optical\\_Systems/McGraw.pdf](http://www.amostech.com/TechnicalPapers/2015/Optical_Systems/McGraw.pdf))
- Shakun L.S., Koshkin N.I.: 2014, *Advances in Space Research*, Vol. **53**, Is. **12**, 15 June 2014, 1834-1847. (<http://dx.doi.org/10.1016/j.asr.2013.12.009>)
- Shulga A.V., Kravchuk S.G. et al.: 2015, *Space science and technology*, **21 (3)**, 74.

DOI: <http://dx.doi.org/10.18524/1810-4215.2016.29.85235>

# RESONANCES IN ASTEROID SYSTEMS

V. V. Troianskyi

Astronomical Observatory, Odessa National University  
 Shevchenko Park, Odessa 65014, Ukraine,  
*v.troianskyi@onu.edu.ua*

**ABSTRACT.** Today the following types of resonances in the rotation of celestial bodies in the solar system are known, namely orbital, spin-orbit and spin-spin resonances. This paper presents our computations of these types of resonances for the known binary and multiple asteroid systems.

**Key words:** asteroid, asteroid system, resonance.

## 1. Problem statement

Resonances in the solar system have been known for a long time. They are found when investigating the orbital elements of Jupiter and Saturn, Neptune and Pluto, and they exert considerable perturbations in the motion of these planets. The moon resonances have been discovered in such systems as the Jupiter, Saturn, Uranus, Neptune and Pluto systems. The asteroid belt also has resonance structure; the Kirkwood gaps are associated with asteroid resonances with Jupiter. Trans-Neptunian objects also can be in resonance with Jupiter and Neptune. The objective of the author is to show the presence of different types of resonances in the currently known asteroid systems.

Different authors have already shown the causes of occurrence and stability of resonances in the solar system (Murray and Dermot, 2010), and in particular, in near-Earth asteroids (Fang and Margot, 2012). The spin-spin resonances in the solar system have also been studied (Batygin and Morbidelli, 2015). In this paper we examine resonances in asteroid systems based on earlier results obtained by different authors.

## 2. Orbital resonance

If the orbital periods of two moons of an asteroid are related by a ratio of small integers, such moons are in orbital resonance.

Let us consider orbital resonances in 11 known triple asteroid systems. The asteroid moons' orbital resonance ratios computed by formula (1) within the measurement accuracy are given in Table 1. The moons of Haumea (minor-planet designation 136108 Haumea) are not in orbital resonance.

$$N_1 \cdot P_1 - N_2 \cdot P_2 \approx 0 \tag{1}$$

where  $N_1$  and  $N_2$  are the orbital resonance ratios of the first and second moons, respectively;  $P_1$  and  $P_2$  are the

orbital periods of the moons. The orbital and spin periods of the asteroid moons, as well as spin periods of central asteroids were taken from Johnston's Archive: <http://www.johnstonsarchive.net/astro/asteroidmoons.html>.

Table 1. Orbital resonances of triple asteroid moons

Asteroid systems	$\frac{N_{PeriodSatelliteBeta}}{N_{PeriodSatelliteGamma}}$
(45) Eugenia	3:8
(87) Sylvia	3:8
(93) Minerva	6:13
(130) Elektra	1:5
(216) Kleopatra	1:2
(2577) Litva	143:1
(3749) Balam	1:44
(47171)1999 TC36	53:2
(136617) 1994 CC	7:1
(153591) 2001 SN263	1:9

Let us examine each of these asteroid systems, as well as the evolution of the asteroid moons, in more detail. For this purpose a numerical model of the moons' motion in the asteroid-centric Cartesian coordinate system was developed. The motion equations (2) were integrated by the 15<sup>th</sup> order Everhart numerical method (Bazyey and Kara, 2009); the coordinates of planets were taken from the numerical ephemerides DE431 (Folkner et al., 2014). We also accounted of the non-sphericity (i.e. the polar oblateness which is too approximate for the bodies with irregular shape – asteroids) of the central asteroid's gravity field (Troianskyi, 2015) and solar radiation pressure on the moons in these asteroid systems (Troianskyi and Bazyey, 2015):

$$\frac{d^2 \vec{r}}{dt^2} = \vec{a}_U + \vec{a}_P + \vec{a}_L \tag{2}$$

where  $\vec{r}$  is the radius vector;  $t$  is the time;  $\vec{a}_U$  is the acceleration due to the non-sphericity of the central asteroid's gravity field;  $\vec{a}_P$  is the acceleration due to the gravitational interaction with the solar system planets;  $\vec{a}_L$  is the solar radiation pressure induced acceleration. To account of the acceleration due to the gravity field of the oblate central asteroid, the second zonal harmonic coefficient ( $J_2$ ) should be computed using the algorithm suggested earlier (Troianskyi, 2015). The obtained coefficients  $J_2$  for the central asteroids are given in Table 2.

Table 2. The second zonal harmonic coefficients  $J_2$  for the selected asteroid systems

<i>Asteroid systems</i>	$J_2$	<i>Error</i>
(45) Eugenia	-0.01362	+0.00038 -0.00043
(87) Sylvia	-0.05319	+0.00003 -0.00024
(93) Minerva	0	0
(130) Elektra	-0.00946	+0.00108
(216) Kleopatra		-0.00138
(136617) 1994 CC	-0.01339	+0.00019 -0.00001
(153591) 2001 SN263	0	0

The changes in Keplerian elements of the asteroid moons were obtained by the integration of the motion equations. According to Kepler's modified third law (3) the square of the orbital period is directly proportional to the cube of the semi-major axis and only depends on this orbital element. The evolution of asteroid systems exhibits periodic changes in semi-major axes of asteroid moons; as a result, the ratios of their periods remain unaltered not affecting their resonances.

$$P = \frac{2\pi a^{3/2}}{k(m_A + m_{St})^{1/2}} \quad (3),$$

where  $P$  is the moon's orbital period;  $a$  is the semi-major axis of the moon;  $k$  is the gravitational constant;  $m_A$  and  $m_{St}$  are the masses of the central asteroid and its moon, respectively.

### 3. Spin-orbit and spin-spin resonances

If the spin period of the main asteroid or its moon and the moon's orbital period are related by a ratio of small integers, then such an asteroid system is in spin-orbit resonance. A special case of the spin-orbit resonance with the ratio of 1:1 is called tidal locking or captured rotation. Table 3 presents the results of computations of the spin-orbit resonances of the moons of binary and multiple asteroids using formula (1) where  $P_1$  is the spin period of the main asteroid or its moon;  $P_2$  is the moon's orbital period;  $N_1$  and  $N_2$  are the orbital resonance ratios. It is incorrect to speak about spin-orbit resonance in the (88611) Teharonhiawako and 2003 QY90 systems as their period ratios are large and exceed 1000:1.

The type of resonance when the spin period of the main component and the spin period of its moon are related by a ratio of small integers is called spin-spin resonance. Some examples of such systems are presented here below (Table 3).

Table 3. Spin-orbit and spin-spin resonances in the selected asteroid systems

<i>Asteroid systems</i>	$\frac{N_{SpinSatellite}}{N_{PeriodSatellite}}$	$\frac{N_{SpinAsteroid}}{N_{PeriodSatellite}}$	$\frac{N_{SpinAsteroid}}{N_{SpinSatellite}}$
(90) Antiope	1:1	1:1	1:1
(809) Lundia	1:1	1:1	1:1
(939) Isberga	1:1	9:1	9:1
(1139) Atami	1:1	1:1	1:1
(2006) Polonskaya	3:1	6:1	2:1
(2478) Tokai	1:1	1:1	1:1
(2577) Litva	6:1	13:1	2:1
(3309) Brorfelde	1:1	7:1	7:1
(4868) Knushevia	1:1	4:1	4:1
(4951) Iwamoto	1:1	1:1	1:1
(5381) Sekhmet	1:1	5:1	4:1
(5426) Sharp	1:1	5:1	5:1
(7369) Gavrilin	1:1	1:1	1:1
(8474) Rettig	1:1	1:1	1:1
(15430) 1998 UR31	1:1	9:1	9:1
(16525) Shumarinaiko	1:1	6:1	6:1
(16635) 1993 QO	16:1	4:1	1:4
(18890) 2000 EV26	1:1	4:1	4:1
(27568) 2000 PT6	1:1	5:1	5:1
(66391) 1999 KW4	1:1	6:1	6:1
(69230) Hermes	1:1	1:1	1:1
(88611) Teharonhiawako	-	-	1:1
(175706) 1996 FG3	1:1	6:1	6:1
(285263) 1998 QE2	24:1	7:1	1:4
(311066) 2004 DC	3:1	9:1	3:1
(399307) 1991 RJ2	1:1	5:1	5:1
(399774) 2005 NB7	1:1	4:1	4:1
2003 QY90	-	-	2:1

If the main asteroid and its moon are in a 1:1 spin-spin resonance, it is said that the system has reached the state of completed tidal de-spinning of its components (Murray and Dermot, 2010). At the close of tidal de-spinning the main asteroid and its moon are always facing each other with the same side.

#### 4. Results

The computations show that the moons in 10 out of 11 known triple asteroid systems are in orbital resonance. The numerical integration has shown that neither the effects of the non-sphericity of the main asteroid's gravity field nor the solar radiation pressure on the asteroid's moons can result in changes in the orbital resonances of the moons in these systems. If the asteroid systems do not approach to large planets in the solar system, such influence is of periodic nature. A case of close approach and destruction of systems was discussed in our earlier study (Troianskyi et al., 2015).

Most of the investigated binary and multiple asteroids are tidally locked. It means that the same side of a moon always faces the main asteroid. The most famous example of tidal locking in a planet-moon system is the Earth-Moon system.

Nine out of 36 studied asteroid systems are in the state of tidal de-spinning completed. An example of such a system is the Pluto-Charon system.

In the asteroid systems (66391) 1999 KW4, (88611) Teharonhiawako and (153591) 2001 SN263 the moons rotate about the central asteroid in retrograde orbit, i.e. in the opposite direction relative to the central asteroid's spinning, which results in decreasing semi-major axis of the moon as shown by Murray and Dermot in their study (Murray and Dermot, 2010). An example of such system is the Neptune-Triton system.

#### References

- Batygin K. & Morbidelli A.: 2015, *Astrophys. J.*, **810/2**, 110.
- Bazyey A.A., Kara I.V.: 2009, *Astronomical School's Report*, **6/2**, 155.
- Fang J., Margot J.-L.: 2012, *Ap J*, **143/1**, 25.
- Folkner W.M., Williams J.G. et al.: 2014, *The Planetary and Lunar Ephemerides DE430 and DE431*.
- Murray C.D., Dermot S.F.: 2010, *Solar System dynamics*. Cambridge, University press.
- Troianskyi V.V.: 2015, *Odessa Astron. Publ.*, **28/2**, 299.
- Troianskyi V.V., Bazyey O.A.: 2015, *Odessa Astron. Publ.*, **28/1**, 76.
- Troianskyi V.V., Radchenko K.O., Bazyey O.A.: 2015, *Astronomical School's Report*, **11/2**, 145.

DOI: <http://dx.doi.org/10.18524/1810-4215.2016.29.85236>

## IS THERE 9-TH PLANET IN OUR SOLAR SYSTEM?

A.P.Vidmachenko

Main Astronomical Observatory of the National Academy of Sciences of Ukraine,  
vida@mao.kiev.ua

**ABSTRACT.** Brown and Batygin informed on indirect evidence of existence of the ninth planet in Solar System (SS). Some evidence pointing on its possible mass in 10 Earth's mass; its distance from Sun at perihelion can be  $\sim 200$  AU, at aphelion 600-1200 AU, and orbital period about 15000 years. Authors suggest that in early SS about 4.5 billion years ago, planet has been pushed out of the field of planets formation near the Sun. But all these conclusions are based on computer calculations of orbits of several known trans-Neptunian objects (TNOs), including Sedna, 2004VN112, 2012VP113, 2010GB174, 2007TG422, 2013RF98. We draw attention to the fact that these 6 TNOs found at perihelion, when their brilliance for terrestrial observers be maximal, and orbital speed was greatest.

But just only after 50-100 years, they depart from this convenient location in space to open them. And then for thousands years, these objects will move in remote parts of their orbits. Our estimates show that the actual number of TNO with the same orbits as 6 taken into account in calculations objects should be several orders of magnitude

greater. But for the moment they are invisible for terrestrial observer, because they are very far from perihelion point. Therefore, on the basis of purely probabilistic assumptions, it should be very large number of TNOs with very eccentric orbits. Then real results of calculation for the entire ensemble of existing remote objects is strikingly different from the primary. And therefore problem of ninth planet is still on the agenda. Most likely, it is necessary to raise the question of finding the many thousands of TNOs on highly elongated orbits, and very far from terrestrial observer.

**Keywords:** Trans-Neptunian objects: Kuiper belt: 9-th planet

The distinctive orbital alignment observed within the scattered disk population of the Kuiper belt, remains largely unexplained (Vidmachenko, 2005, 2015, 2016c, d, e, g). In January 2016 M. Brown and K. Batygin informed (Batygin et al, 2016) on the indirect evidence of existence of the ninth planet in the Solar System. They are talking about circumstantial evidence pointing to its possible mass

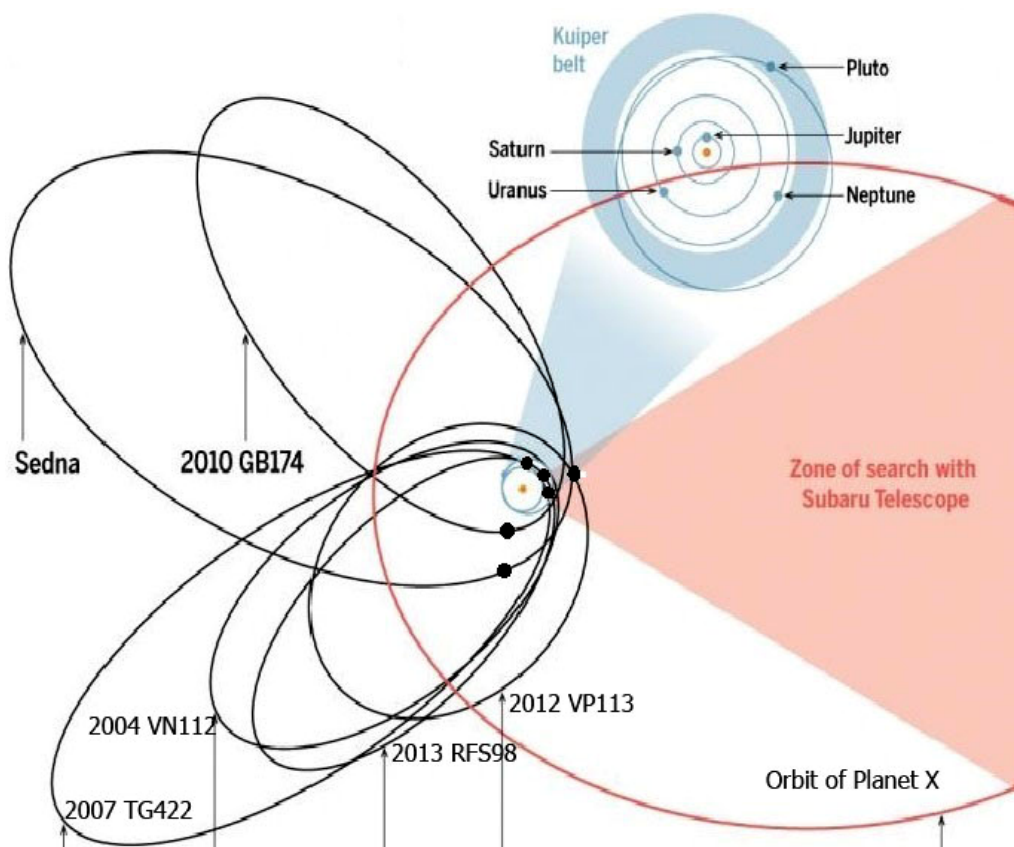


Figure 1: Orbits of TNOs and of possible planet.

in 10 times the mass of the Earth; its distance from the Sun at perihelion can be ~200 AU at aphelion – 600-1200 AU and orbital period – about 15 thousand years.

The authors suggest that in the early solar system about 4.5 billion years ago, the planet has been pushed out of the field of formation of planets near the Sun (Vidmachenko, 2009, 2016a, b, f, Vidmachenko et al., 2013b, 2014); and then it slowed down by the gas and "settled" on a remote elliptical orbit. But all these conclusions about the planet are based on computer calculations of the orbits of several known trans-Neptunian objects (TNOs), including Sedna, 2004VN112, 2007 TG422, 2010GB174, 2012VP113, 2013 RF98 (Table 1). M. Brown and K. Batygin assumed that the orientations of orbits of these objects are arranged so that they have to be influenced by of existence of a large unknown body. This may be a new planet, acting on these objects by a powerful gravitational field.

Table 1: Tans-Neptunian objects with large aphelion.

Objects	Perihelion, AU	Aphelion, AU	The size, km	Distance from the Sun at time of discovery, AU
Sedna	76,315	1006,54	995 ± 80	89,6 2003
2010 GB174	48,7	654	130 – 300	70,8 2016
2012 VP113	80,6	446	300–1000	83 2014
2007 TG422	35,6	967	343	37 2007
2004 VN112	47,3	607		47,3 2009
2013 RF98	36,28	600	50-110	36,5 2016

We draw attention to Fig. 1, which shows the orbit of TNO and possible unknown planet X. And, above all, we point out their place in orbit in moments close to their discovery.

When they were discovered, all of them were located quite close to the perihelion. In this case, whereas their brightness is maximized for the terrestrial observer - and the orbital speed was the largest (Vidmachenko et al., 2012, 2013b, 2014). But after only some 50-100 years, they depart from this convenient location in space for their possible discoveries. And then for many thousands of years, these objects will move in remote areas of their orbits.

In this regard, our estimates show that the actual number of TNOs and comet's nucleus on the same, or similar orbits, as well as for the 6 objects, which have been taken into account in the calculations in (Batygin et al., 2016), must be several orders of magnitude larger (Churyumov et al., 2013, 2014, 2015, 2016a, b, c, Vidmachenko 2005, 2016a, d, Vidmachenko et al., 2013a). But at the moment they are invisible to the terrestrial observer, because they are at a very great distance from the perihelion. Due to the enormous eccentricity of the orbit on the rate at places away from perihelion - significantly less than the current speed near perihelion for the several newly discovered TNOs (Table 1.)

Thus, on the basis of purely probabilistic assumptions, the number of TNOs on very elongated orbits, should not amount to tens and units, and they should be a lot of tens of thousands (Vidmachenko et al., 2012, 2013a, 2014). Thus, the real picture of the results of the calculation for the entire ensemble of existing remote objects is very different from the number of TNOs, which were included in the calculation in Batygin et al. (2016). The calculations of Batygin and Braun indicate the possible location of a planet to within a quadrant. Therefore, the review of such a large area of the sky may last a very long time. For the initial evaluation, we used observational data from the Space Telescope «WISE», which was launched in 2009 to study the sky at infrared wavelengths. From the results of observations at distances of up to 30000 AU, an analog of the giant planet Saturn was not registered. Our estimates indicate that up to 1000 AU would have been seen super-Earth with a radius of 11000 km (that is, it is about 10 Earth masses). Thus, either the 9-th unknown planet right now there is an even greater distance, or it is possible that these results cannot be directly scaled to the super-Earth with disproportionately smaller number of internal heat.

And so the question of the presence of the ninth planet in the solar system is still on the agenda. Most likely, it is necessary to raise the question of finding the many thousands of trans-Neptunian objects, which must be on highly elongated orbits and very far from the terrestrial observer..

### References

Batygin K., et al.: 2016, *Astron. J.* 151(2), id. 22, 12.  
 Churyumov K.I. et al.: 2013, *Me13.ConfE*, 8, 77.  
 Churyumov K.I. et al.: 2014, *AstSR*, 10(1), 37.  
 Churyumov K.I. et al.: 2015, *AstSR*, 11(2), 99.  
 Churyumov K.I. et al.: 2016a, *Apmi.book ISConf.*, 5, 33.  
 Churyumov K.I. et al.: 2016b, *Asys.Conf*, 18, 93.  
 Churyumov K.I. et al.: 2016c, *Mete.ConfP*, 63.  
 Vidmachenko A.P., et al.: 2012, *Sssr.book*, 255.  
 Vidmachenko A.P., et al.: 2013a, *AstSR*, 9(2), 146.  
 Vidmachenko A.P., et al.: 2013b, *USpT*, 110(9), 22.  
 Vidmachenko A.P., et al.: 2014, *Pese.book*, 388.  
 Vidmachenko A.P.: 2005, *AsAl.book 2006*, 52, 201.  
 Vidmachenko A.P.: 2009, *AsAl.book 2010*, 56, 225.  
 Vidmachenko A.P.: 2015, *AsAl.book 2016*. 62, 228.  
 Vidmachenko A.P.: 2016a, *Asys.Conf*, 18, 108.  
 Vidmachenko A.P.: 2016b, *Asys.Conf*, 18, 14.  
 Vidmachenko A.P.: 2016c, *Asys.Conf*, 18, 16.  
 Vidmachenko A.P.: 2016d, *Asys.Conf*, 18, 23.  
 Vidmachenko A.P.: 2016e, *GamIConf*, 16, 46.  
 Vidmachenko A.P.: 2016f, *LPICo1912*, 2002.  
 Vidmachenko A.P.: 2016g, *MISConf.AstSP*, 67.

DOI: <http://dx.doi.org/10.18524/1810-4215.2016.29.85237>

## SPECIFICATION OF LIMITS OF POSSIBLE EXISTENCE OF SATELLITES IN THE GRAVITATIONAL FIELD OF PLANETS

S.O.Yasenev<sup>1</sup>, K.O.Radchenko<sup>2</sup>

<sup>1</sup>Department "Aerospace Surveying", National Aviation University,  
*yasenev91@gmail.com*

<sup>2</sup>Department of Computer Engineering, National Technical University of Ukraine "Kyiv Polytechnic Institute", *radche000@mail.ru*

**ABSTRACT.** It is known that the satellites of the planets may exist in the area, which is bounded on one side by Roche limit, on the other – Hill sphere. The article deals with the determination of the Roche limits and Hill sphere of satellites of some planets in the solar system. This analysis revealed some features and identified the main factors influencing the setting of these parameters. Roche limits and Hill sphere parameters of the largest satellites of the planets of the solar system have been specified.

**Key words:** satellites of planets; gravitational field; Roche limit; Hill sphere; mass.

### 1. Introduction

Since the beginning of the study of the solar system by cosmic means up-to-date, the principal task stimulating the development of this area, in fact, remains unchanged. The new information, which comes as a result of numerous space missions, makes an important contribution in solving the fundamental problems of modern science, considering the origin and evolution of planets, their satellites and the solar system as a whole.

The application of this knowledge to understanding the natural processes that determine the development of our Solar system is equally important. A time is rapidly approaching when among the most urgent challenges will be the exploration of the satellites of the planets of the Solar system.

Today the vital question is specification of Roche limits of the satellites of the planets in connection with obtaining new information from astronomical observations. This is the work of scholars such as K.V.Holshevnikov, A.A.Orlov, V.L.Panteleev, R.U.Ibatullin, G.I.Shyrmin, A. Philip, N.P.Pytyev, L.V.Konstantinovskiy, E.L.Ruskol, L.L.Sokolov, B.P.Kondratyev, R.Barnes, R.Heller, B.Jones, P.Sleep, J.Noyola, S.Satyal and others.

Roche limit is determined by the difference between the acceleration, that is experienced from the planet nearest and farthest points of the satellite, and the gravity of the satellite; Roche cavity – the space that surrounds each

gravitation body moving along circular orbits around a common center of mass and the weight of the central body dominates the gravity of other bodies; Hill sphere – the space around a planet, in which the planet draws his satellite more than the object around which it revolves, that is the sun; sphere of attraction – the area in the form of a flattened ellipsoid of revolution around the celestial body within which the action of gravity on an object that rotates along an orbit around this body, emanating from this body, that is planets have a dominant influence on their satellites, despite the presence of much more massive, but more distant Sun (Vidmachenko & Morozhenko, 2014; Konstantinovskaya, 2002; Kholshchevnikov, 2015).

### 2. Formulation of the problem

In other words, the Roche limit represents the shortest distance of the satellite from the planet on which it will be not be broken into pieces, and the Hill sphere determines whether the object rotates around the planet or moves to the orbit of the Sun, that is, the farthest.

Satellites of the planets deviate from the state of hydrostatic equilibrium and have shapes that vary from spherical and have asymmetries relative to the axis of rotation and the equatorial plane.

Also, in contrast to asteroids, there are objects that evolve and have: the inner core, the magnetic field, the correct form (Ruskol, 2002). It is established that the biggest planets have radius of, approximately, from 0.002 to 0.270 times the radii of the planet. Except for the satellite of Pluto – Charon. For most of the planets (except Pluto and Earth), this limit is quite low, ranging from 0.002 to 0.042 times the radius of the planet (Konstantinovskaya, 2002).

We have identified 18 largest satellites of the planets in the Solar system as a self-gravitating formation (Yasenev, 2015). All major planetary satellites are synchronized with their planets that are rotate around the planet, in the same case as a planet around the Sun (except Triton). And they have different physical characteristics (Table 1).

Table 1. Physical characteristics of planetary satellites.

№	Name	Mass, kg 10 <sup>20</sup>	Density, kg·m <sup>-3</sup>	Average radius, km
1	Ganymede	1 481.90	1936	2 634.10
2	Titan	1 345.20	1880	2 576.00
3	Callisto	1 077.00	1835	2 410.30
4	Io	893.19	3528	1 821.00
5	Moon	734.80	3347	1 737.10
6	Europe	480.20	3019	1 561.00
7	Triton	214.00	2061	1 354.00
8	Titania	35.27	1711	788.50
9	Oberon	30.14	1630	761.50
10	Rhea	23.07	1234	764.50
11	Iapetus	18.06	1089	735.80
12	Charon	15.80	1650	606.00
13	Ariel	13.50	1670	578.90
14	Umbriel	11.75	1405	584.30
15	Dione	10.96	1479	562.00
16	Tethys	6.18	986	531.20
17	Enceladus	1.10	1610	252.20
18	Miranda	0.71	1214	236.50

3. The main part

Modern astronomical observations carried out by ground and space means led to the discovery of a large number of satellites of the planets and their number continues to grow. Most have a small mass, but their shape and sizes are held by forces of electromagnetic interactions in the minerals from which they formed. On the other side of the planets in the solar system there are massive satellites. There are relevant research questions of satellite spacecraft that require the most serious study of their celestial-mechanical characteristics.

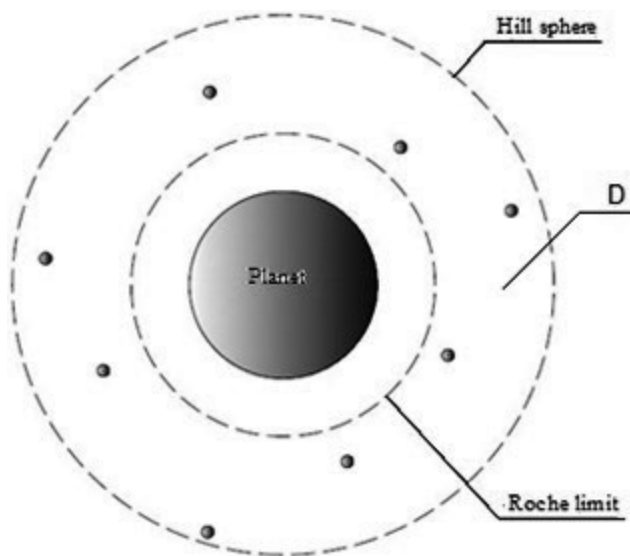


Figure 1: Field of the possible existence of satellites – the area between Roche limit and Hill sphere (D – possible existence of satellites region).

It is understood that for each of the satellites there are boundaries of their existence according to their mass and density, i.e. planets' satellites cannot be close to a planet closer than the radius of the Rocha limits and not further away than the radius of the Hill sphere (Fig. 1).

Hill sphere radius determined from the formula:

$$R_H = a(1-e) \sqrt[3]{\left(\frac{m_p}{3M_S}\right)} \tag{1}$$

where  $a$  – major axis of the orbit of the planet around the star,  $e$  – eccentricity of the orbit,  $m_p$  – mass of the planet,  $M_S$  – mass of Sun.

Radius of Roche limits determined by the formula:

$$R_R = 2.423R \left(\frac{\rho_p}{\rho_s}\right)^{\frac{1}{3}} \left(\frac{\left(1 + \frac{m_s}{3M_p}\right) + \frac{e}{3}\left(1 + \frac{m_s}{M_p}\right)}{1-e}\right)^{\frac{1}{3}} \tag{2}$$

where  $\rho_s$  – density of the satellite  $\rho_p$  – density of the planet,  $M_p$  – mass of the planet,  $m_s$  – mass of the satellite,  $e$  – polar compression of the planet. Calculate these values for some satellites of the planets (Table 2).

The orbit of the satellite can be stable at a distance of no more than 0.53 Hill sphere radius (in direct rotation) and 0.69 in the reverse. Otherwise orbit satellite will be subjected to disturbance from the Sun and other planets and satellites (Konstantinovskaya 2002, Ibatullin 2010). In other research materials, slightly different value may be given, for example (Vidmachenko & Morozhenko 2012).

All major planetary satellites in synchronization with their planets, those rotate around the planet, same as the planet around the Sun (except Triton).

It is equally clear that Roche limit is not significantly dependent on the relationship of mass of the satellite and the planet, and more dependent on the ratio of the density of the planet to the density of the satellite (Fig. 2).

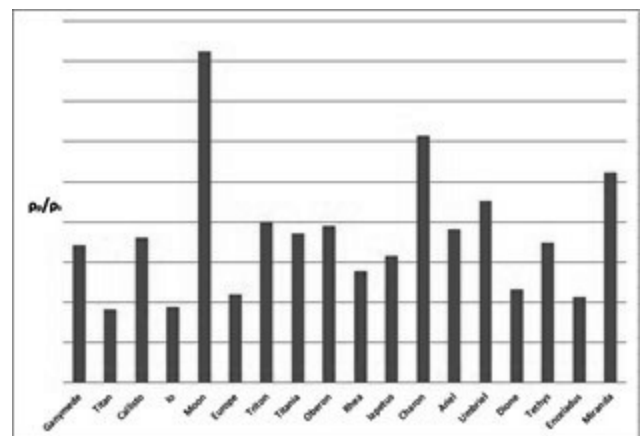


Figure 2: The ratio of density of the planet to the density of the satellite (Moon, Charon and Miranda are allocated).

Table 2. The value of Roche limits and Hill sphere for some satellites of planets in the Solar system.

№	Satellites		Planets					Roche limit, km 10 <sup>3</sup>	Hill sphere, km 10 <sup>6</sup>
	Name	Mass, kg 10 <sup>20</sup>	Name	Mass, kg	Density, kg·m <sup>-3</sup>	Average radius, km	Polar compression		
1	Ganymede	1 481.90	Jupiter	1.8986·10 <sup>27</sup>	1326	69 911	0.06487	153.787788	50.562718
2	Titan	1 345.20	Saturn	5.6846·10 <sup>26</sup>	687	58 232	0.09796	105.528511	61.825270
3	Callisto	1 077.00	Jupiter	1.8986·10 <sup>27</sup>	1326	69 911	0.06487	156.558699	50.562718
4	Io	893.19	Jupiter	1.8986·10 <sup>27</sup>	1326	69 911	0.06487	125.905842	50.562718
5	Moon	734.80	Earth	5.9742·10 <sup>24</sup>	5515	6 371	0.00335	18.285152	1.471698
6	Europe	480.20	Jupiter	1.8986·10 <sup>27</sup>	1326	69 911	0.06487	132.617227	50.562718
7	Triton	214.00	Neptune	1.0243·10 <sup>26</sup>	1638	24 622	0.01708	55.686258	114.878926
8	Titania	35.27	Uranus	8.6832·10 <sup>25</sup>	1271	25 362	0.02293	56.229532	67.118566
9	Oberon	30.14	Uranus	8.6832·10 <sup>25</sup>	1271	25 362	0.02293	57.145887	67.118566
10	Rhea	23.07	Saturn	5.6846·10 <sup>26</sup>	687	58 232	0.09796	121.424253	61.825270
11	Iapetus	18.06	Saturn	5.6846·10 <sup>26</sup>	687	58 232	0.09796	126.590511	61.825270
12	Charon	15.80	Pluto	1.305·10 <sup>22</sup>	2030	1 184	0.01670	3.1386325	5.759526
13	Ariel	13.50	Uranus	8.6832·10 <sup>25</sup>	1271	25 362	0.02293	56.685818	67.118566
14	Umbriel	11.75	Uranus	8.6832·10 <sup>25</sup>	1271	25 362	0.02293	60.046501	67.118566
15	Dione	10.96	Saturn	5.6846·10 <sup>26</sup>	687	58 232	0.09796	114.310904	61.825270
16	Tethys	6.18	Saturn	5.6846·10 <sup>26</sup>	687	58 232	0.09796	130.853307	61.825270
17	Enceladus	1.10	Saturn	5.6846·10 <sup>26</sup>	687	58 232	0.09796	111.122414	61.825270
18	Miranda	0.71	Uranus	8.6832·10 <sup>25</sup>	1271	25 362	0.02293	63.043400	67.118566

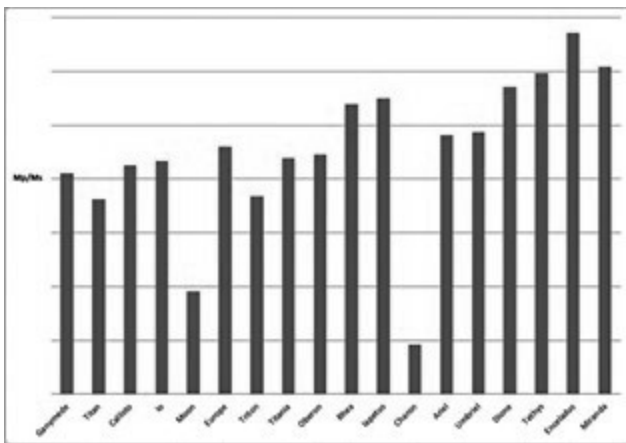


Figure 3: The ratio of the mass of the planet to the mass of the satellite (Moon and Charon are allocated) in logarithmic scale.

The calculation results show some differences in the cases of Moon and Charon, which are caused by the fact that they have large mass compared to the masses of their planets (Fig.3).

### Conclusions

1. Roche limit for planetary satellites has been determined; it is less significant depending on the relationship of mass of the satellite and the planet, and more dependent on the ratio of densities.
2. The radius of Hill sphere has been specified for the planets in the Solar system, we show that its radius is the same for all satellites of the planet.

3. The calculation results show some features in the case of Moon and Charon, which are caused by the fact that they have relatively large mass compared to the masses of the planets.

### References

- Ibatullin R.U.: 2010 *The astronomical formulas* [[http://robert-ibatullin.narod.ru/utilities/astro\\_formulas.pdf](http://robert-ibatullin.narod.ru/utilities/astro_formulas.pdf)]
- Kholshchevnikov K.V.: 2015, The Moon – a satellite or a planet? [[http://window.edu.ru/resource/045/21045/files/9808\\_077.pdf](http://window.edu.ru/resource/045/21045/files/9808_077.pdf)]
- Konstantinovskaya L.V.: 2002, *Math. Meth. Geol. Cycl.*, **9**.
- Ruskol E.L.: 2002, *Earth and Universe*, **2**.
- Vidmachenko A.P., Morozhenko O.V., 2012, *The study of the satellites surfaces and the rings of the giant planets* Kyiv, DIA, 255 pp. (in Ukrainian).
- Vidmachenko A. P., Morozhenko O. V.: 2014, K. *The physical characteristics of surface Earth-like planets, dwarf planets and small, and their companions, according to distance studies*. Kyiv, Profi, 388 pp. (in Ukrainian).
- Yasenev S.O., 2015: *Od. Astron. Publ.*, **28**(1), 88.

DOI: <http://dx.doi.org/10.18524/1810-4215.2016.29.85238>

# HIP 13962 – THE POSSIBLE FORMER MEMBER OF BINARY SYSTEM WITH SUPERNOVA

Yushchenko V.<sup>1</sup>, Yushchenko A.<sup>2</sup>, Gopka V.<sup>1</sup>, Shavrina A.<sup>3</sup>, Kovtyukh V.<sup>3</sup>, Hong K.S.<sup>4</sup>, Mkrtychian D.<sup>5</sup>, A-Thano N.<sup>5</sup>

<sup>1</sup>Astronomical observatory, Odessa National University, Odessa, 65014, Ukraine  
*vladimiryushchenko@gmail.com*

<sup>2</sup>Department of Astronomy & Space Sciences, Sejong University, Seoul, 05-006, Korea,

<sup>3</sup>Main Astronomical observatory, National Academy of Sciences of Ukraine, Kiev, 03680, Ukraine

<sup>4</sup>Korea Astronomy and Space Science Institute, Daejeon, 305-348, Korea

<sup>5</sup>National Astronomical Research Institute of Thailand, Chiangmai, 50200, Thailand

**ABSTRACT.** The runaway supergiant star HIP 13962 (spectral type G0Ia) was recently pointed as a possible former binary companion of young pulsar PSR J0826+2637. The spectra of HIP 13962 were obtained in Haute-Provence observatory (France), in Bohuynsan observatory (Korea), and also in NARIT (Thailand) with 1.9, 1.8, and 2.4 meter telescopes respectively. The spectra were obtained in 1995, 2003, 2005, 2014, and 2015. Significant variations of the spectrum are detected. The cores of strong lines show complicated structure, the brightness of the star is variable. The cycles of photometric variations have been changed. We analyzed the spectral observations and present the preliminary chemical composition for elements from iron to lead. The abundance pattern can not be fitted by solar system  $r$ - &  $s$ -process abundance distribution.

**Key words:** stars: individual: HIP 13962 – stars: abundances.

## 1. Introduction

In recent paper, published by Tetzlaff et al. (2014) it was shown that HIP 13962, G0 type runaway supergiant star of seventh magnitude, can be a former secondary member of binary system, with main component exploded as a Supernova near 3 millions years ago. The possible former main component of this system - young pulsar PSR J0826+2637 was also escaped from a small cluster Stock 7.

That is why it seems interesting to investigate the signs of contamination of the atmosphere of supergiant star HIP 13962 by nuclear processed matter. It can be a result of Supernova outburst in binary system. Note that this type contamination was predicted in many papers, for example by Proffitt & Michaud (1989), but

was never directly confirmed.

Hopefully HIP 13962 can demonstrate the results the nearby Supernova explosion in its abundance pattern because of relatively short time passed after this event.

We used the archived and new spectral and photometrical observation of the star and found the different photometric behavior at different epochs, the anomalous variable profiles of strong spectral lines, the variability of the spectrum, and the anomalous chemical composition. Here after we present the short overview of preliminary results (Yushchenko et al., 2016).

## 2. Spectral observations

The archive of observations of 1.9 telescope of Haute-Provence observatory equipped by ELODIE spectrograph with spectral resolving power  $R=42000$  was used. HIP 13962 was observed three times in 1995, 2003, and 2005 years.

Three additional spectra were observed at Bohuynsan Optical Astronomical Observatory (BOAO) 1.8 m telescope with spectral resolution near  $R=45000$ , in 2014 and 2015.

In 2014 four spectra were observed with 2.4 m telescope of National Astronomical Research Institute of Thailand (NARIT) with spectral resolution  $R=20000$ .

Signal to noise ratio of all used spectral observations exceeds 100 in the centers of echelle orders. The observed spectral regions are 4000–6800 Å, 3780–8877 Å, and 3722–8804 Å for Haute-Provence, BOAO, and NARIT observations respectively.

The initial reduction of BOAO and NARIT spectra was made using standard IRAF package, the final spectra processing, including continuum placement,

coadding of the spectra, identification of spectral lines, and equivalent widths measurements was made using URAN program (Yushchenko, 1998).

The synthetic spectrum of HIP 13962 was calculated for the whole observed wavelength region. It was taken into account in continuum placement and identification of spectral lines.

### 3. Photometry

Turner et al. (2009) performed the photometrical observations of HIP 13962 and found that the brightness of the star is variable with amplitude less than 0.1 magnitude and periods 177 and 123 days.

We investigated HIPPARSOS photometry (Perryman, 1997) of the star. Fig. 1 shows, that variability with amplitude near 0.05 magnitude was observed at the time scale of few years.

Note that Turner et al. (2009) and HIPPARSOS observations were made at different epochs (time difference is near 15 years) and it is not surprising that the values of photometrical cycles are different. Both types of brightness variations are usual for supergiant stars, but it can be also the additional argument to confirm the reality of spectrum variations, discussed here after.

### 4. Atmospheric parameters

Parameters were derived by Kovtyukh (2007) and Kovtyukh et al. (2012) as follows: the effective temperature  $T_{\text{eff}}=5871\pm130$  K, the surface gravity  $\log g=1.2$ , the microturbulent velocity 11.5 km/sec. The projected rotational velocity was found to be equal  $v \sin i = 29$  km/sec - significantly higher than the typical rotational velocities of this type stars.

To estimate parameters of HIP 13962 in this investigation we used the first of BOAO spectra, observed in 2014. Castelli and Kurucz (2003) grid of atmosphere models and the clean iron lines in the observed spectrum allowed us to accept the values 5930 K, 1.0, and 6 km/sec for effective temperature, surface gravity and microturbulent velocity respectively.

The pointed values are close to previously determined by Kovtyukh (2007) and Kovtyukh et al. (2012). Here after we present the abundances calculated with these parameters.

### 5. Chemical composition

The identification of spectral lines in observed spectrum of HIP 13962 was based on the comparison with synthetic spectrum calculated for the whole wavelength region of observed spectra. The parameters for calcu-

lations of synthetic spectrum were taken from previous section, the abundances of heavy neutron captured elements were increased by 0.5 dex.

Equivalent widths of spectral lines were measured in the the first of BOAO spectra, observed in 2014. The abundances for individual lines were calculated using Kurucz's program WIDTH9. Table 1 contains the mean values of abundances of iron and neutron captured chemical elements with respect to solar or solar system values (Grevesse et al., 2010), the errors, and the number of used lines.

More detailed description of used methodic can be found in Yushchenko et al. (2015) and in our earlier publications.

### 6. Discussion

Fig. 2 shows the chemical composition of HIP 13962 in comparison with solar system  $r$ - and  $s$ -processes abundance patterns. The abundances of elements with atomic numbers  $Z\leq 63$  and lead can be easily explained by these patterns, the discrepancies are of the order of 0.2 dex.

The most interesting feature of derived chemical composition is the relatively low abundances of lanthanides with  $Z\geq 64$ . The deviations of these elements from solar  $s$ -process abundance distribution are clearly visible.

It is worth to mention that faint lines of many heavy elements, which are not listed in Table 1, can be identified in the spectrum of HIP 13962. The high level blending of these lines requires spectrum systnesis to obtain reliable abundances for these elements.

Table 1: Chemical composition of HIP 13962

Z	Ion	$\Delta\log N$	$\sigma$	n
26	Fe I	-0.07	0.17	80
	Fe II	-0.05	0.18	18
29	Cu I	-0.52	0.12	3
39	Y II	0.39	0.22	10
40	Zr II	0.28		1
46	Pd I	0.44		1
57	La II	0.61	0.17	16
58	Ce II	0.34	0.19	19
59	Pr II	0.28	0.23	10
60	Nd II	0.39	0.23	50
62	Sm II	0.08	0.19	15
63	Eu II	0.30		1
64	Gd II	-0.10	0.24	4
65	Tb II	-0.36	0.04	3
66	Dy II	0.15	0.09	3
68	Er II	0.01	0.21	4
82	Pb II	0.23		1

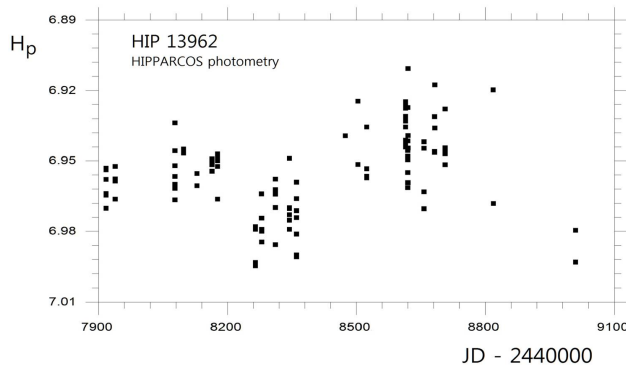


Figure 1: HIPPARCOS photometry of HIP 13962. The axes are time in Julian days and HIPPARCOS photometric system magnitude  $H_P$ .

As it was pointed here before our abundances are based on the first BOAO spectrum of HIP 13962, obtained in 2014. We found no strong differences for faint and medium strength lines between this spectrum and the other two BOAO spectra. The first Haute-Provence observatory spectrum, observed in 1995 repeats BOAO spectra for not strong lines. Tetzlaff et al. (2014) abundances were found from this spectrum.

2003 and 2005 year spectra, observed in Haute-Provence, have very different line profiles, both for strong and faint lines, as it is shown in Figures 3 and 4. The strongest lines in the spectrum are variable, it is confirmed also by NARIT spectra. The variations of hydrogen  $H\alpha$  line profiles are shown in Fig. 3.

The line profiles in 2003 and 2005 Haute-Provence spectra can be explained by strong additional light. Maybe it was an error in the reduction procedure of spectral observations. Why it happens twice? Was it a secondary light in spectrograph or in HIP 13962? It is necessary to have in mind the possibility of real variations of observed object.

Of course the probability of error in reduction procedure seems higher. It can be confirmed by Fig. 4 where cosmic ray particle produce an emission at the wavelength of promethium line in 2003 year spectrum.

If the reason of spectral anomalies is not the instrumental effect, it is possible to expect the anomalous photometrical behaviour of HIP 13962 in 2003-2005. Turner et al. (2009) collected all published photometry, unfortunately there are no data in these years.

### 7. Conclusion

HIP 13962 was investigated to find the possible signs of nuclear processed matter as a result of Supernova explosion of its former binary companion, at present time - young pulsar PSR J0826+2637. We found both

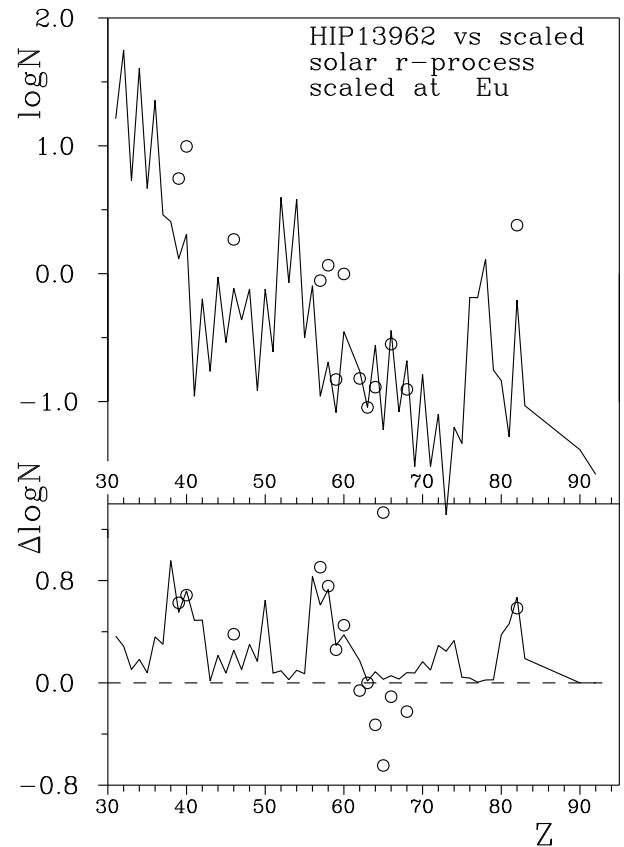


Figure 2: The top panel: comparison of surface abundances in HIP 13962 (circles) with solar system  $r$ -process abundance distribution (line) taken from Simmerer et al. (2004). and scaled to the observed abundance of europium. The bottom panel: deviations of observed abundances in HIP 13962 from scaled solar system  $r$ -process abundance distribution (circles). For comparison the solar system  $s$ -process distribution is shown by line.

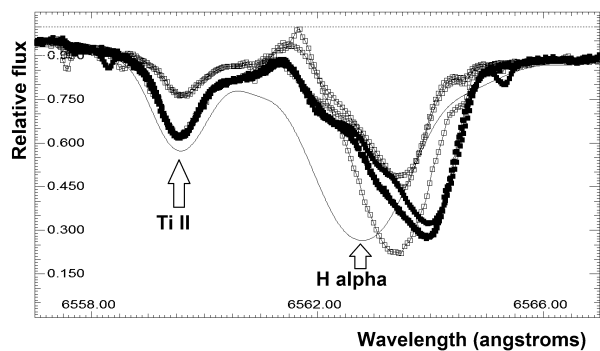


Figure 3: The spectrum of HIP 13962 in the vicinity of hydrogen  $H\alpha$  line. The axes are wavelength in angstroms and relative fluxes. Synthetic spectrum is shown by thin line. The wavelengths of  $H\alpha$  line and the strong line of ionized titanium are marked. Open squares designate Haute-Provence observatory spectra, solid squares are spectral observations obtained in Bo-huynsan observatory.

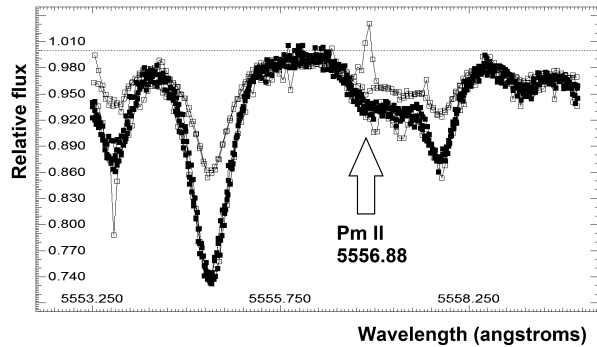


Figure 4: The spectrum of HIP 13962 in the vicinity of promethium line  $\lambda$  5556.88 Å. The axes are wavelength in angstroms and relative fluxes. The observed spectra taken from Houte-Provence and Bohuynsan observatory telescopes are pointed by open and solid squares respectively.

over and underabundances of heavy elements.

The abundances of heavy elements with atomic numbers  $Z \leq 63$  elements and lead can be approximated by solar system  $r$ - and  $s$ -processes abundance pattern. The abundances of Gd, Tb, Dy, and Er are lower than it can be expected from this solar fit.

Note that this results were made by model atmosphere method, it will be used to refine the parameters and abundances by spectrum synthesis method.

The variability of brightness and the strong variations of spectrum confirm the necessity of new spectroscopic and photometrical observations of this outstanding star.

*Acknowledgements.* This work was supported in part by the Korea Astronomy and Space Science Institute under the R&D program (Project No. 2015-1-320-18) supervised by the Ministry of Science, ICT and Future Planning. One of the authors (VY) was granted by the Swiss National Science Foundation (SCOPES project No. IZ73Z0 -128180/1) for this investigation and also for presentation of obtained result at the conference in Germany (Yushchenko et al., 2016).

## References

- Castelli F. & Kurucz R.: 2003, *IAU Symp.* 210, Poster contributions, A20, <http://wwwuser.oat.ts.astro.it/castelli/grids.html>.
- Grevesse N., Asplund M., Sauval A.J., Scott P.: 2010, *As&SpSci*, **328**, 179.
- Kovtyukh V.V.: 2007, *MNRAS*, **378**, 617.
- Kovtyukh V.V., Gorlova N.I., Belik S.I.: 2012, *MNRAS*, **423**, 3268.
- Perryman V.A.C. et al.: 1997, *The Hipparcos and Tycho Catalogues*, European Space Agency, CD-ROMs 1-8.
- Proffitt C.R., Michaud J.: 1989, *ApJ*, **345**, 998.
- Simmerer J., Sneden C., Cowan J.J., Collier J., Woolf V.M., Lawler J.E.: 2004, *ApJ*, **617**, 1091.
- Tetzlaff N., Dintel B., Neuhaeuser R., Kovtyukh V.V.: 2014, *MNRAS*, **438**, 3587.
- Turner D.G., Kovtyukh V.V., Majaess D.J., Lane D.J., Moncrieff K.E.: 2009, *Astronomische Nachrichten*, **330**, 807.
- Yushchenko A.V.: 1998, in *Proceedings of the 20th Stellar Conference of the Czech and Slovak Astronomical Institutes*, Ed. by J.Dusek (ISBN 80-85882-08-6, Brno), p. 201.
- Yushchenko A.V., Gopka V.F., Kang Y.-W., Kim C., Lee B.-C., Yushchenko V.A., Dorokhova T.N., Doikov D.N., Pikhitsa P.V., Hong K., Kim S., Lee J.-W., Rittipruk P.: 2015, *AJ*, **149**, A59.
- Yushchenko V., Yushchenko A., Gopka V., Shavrina A., Kovtyukh V., Hong K.S., Mkrtichian D., A-Thano N., presentation at the conf. *Stars on the run - a meeting on run away and hyper-velocity stars* Germany, Bamberg, August 16-19, 2016, <http://www.black-hole.eu/media/hvs2016/PDFs/Yushchenko.pdf>

*Наукове видання*

**Одеські Астрономічні Публікації**

том 29 (2016)

*Англійською мовою*

Зав. редакцією *Т. М. Забанова*  
Технічний редактор *В. В. Ковтюх*  
Комп'ютерна верстка *С. Л. Страхова*

---

Підписано до друку 24.12.16.  
Формат 60x84/8. Папір офсетний. Друк різнограф.  
Ум. друк. арк. 26,97. Обл.-вид. арк. 28,0. Тираж 300 екз. Зам. № 230.

Видавництво і друкарня «Астропринт»  
65091, м. Одеса, вул. Разумовська, 21  
Тел.: (0482) 37-07-95, 37-14-25, 33-07-17  
**[www.astroprint.odessa.ua](http://www.astroprint.odessa.ua)**  
Свідоцтво суб'єкта видавничої справи ДК №1373 від 28.05.2003 р.